Towards a Strictly Conservative Hybrid Level-Set Volume-of-Fluid Finite Volume Method for Zero Mach Number Two-Phase Flow

Dissertation

zur Erlangung des akademischen Grades eines

Doktor der Naturwissenschaften

(Dr. rer. nat.)

dem

Fachbereich für Mathematik und Informatik

der

Freien Universität Berlin

vorgelegt von

Diplom-Ingenieur

Matthias Waidmann

Berlin, 2017

Erstgutachter & Betreuer:

Prof. Dr.-Ing. Rupert Klein
Fachbereich für Mathematik & Informatik
Institut für Mathematik
Freie Universität Berlin

Zweitgutachter:

Prof. Dr.-Ing. Michael Oevermann
Fachbereich für Angewandte Mechanik
Institut für Verbrennung
Chalmers University of Technology, Göteborg, Schweden

Tag der Disputation:

02. Dezember 2016

To my wife and my daughter

ABSTRACT

Two-phase flow plays a significant role in multiple technical applications and natural phenomena. Therefore there is an increasing interest in numerical simulation of such flows for both prediction and analysis purposes. Many of these processes can be modeled as incompressible or zero Mach number flows. While there are many methods for simulation of incompressible two-phase flow at constant density, only few methods can be found, that allow for a variable density and solve the governing equations in conservative form. In principle there is no method, which consequently applies discretely conservative approximations only wherever appropriate, while remaining extendable to other flow regimes, such as the compressible or weakly-compressible low Mach number flow regime, in a conceptually consistent way. The present work is meant to serve as starting point for a Finite Volume method that satisfies these requirements while remaining extendable to equations of state beyond the assumption of a perfect gas. Within this generalized framework two key features of a numerical method for simulation of two-phase flow are focused on after deriving the zero Mach number equations for immiscible chemically reacting two-phase flow at arbitrary equation of state and presenting the underlying single-phase solver as basic building block of the numerical method in detail: On the one hand an approach for coupling of the discrete representation of the interface, sharply separating the different fluid phases, and the conserved quantities representing the fluid flow is extended, analyzed and adapted to the present framework for keeping the method stable and discretely conserving the mass of each of the fluid phases. On the other hand an approach for approximation of the influence of surface tension, which is singular at the interface, is proposed, that allows for discretely conservative treatment of these effects as well. The underlying numerical scheme for solving the resulting system of differential equations is a generalized projection method, which imposes an elliptic constraint on a hyperbolic-parabolic predictor solution in each time step. Due to the fact that projection schemes – except for the solution of linear systems for individual scalars – are iteration-free, the different building blocks presented in this work are kept iteration-free as well.

ACKNOWLEDGEMENTS

I am grateful and would like to thank the following persons for their support for making this work possible:

- **Rupert Klein** for his patient advice, interesting scientific discussions, generous funding, relaxed working atmosphere and the preliminary work on the topics covered within this thesis
- **Michael Oevermann** for extensive advice, excellent working atmosphere, implementation of the elliptic solvers, pioneering in *SAMRAI* and preliminary work
- **Stephan Gerber** for interesting scientific discussions, great working atmosphere and implementation of the basic narrow band level-set algorithms
- **Warren O'Neill** and **Tommaso Benacchio** for asking numerous questions on the implementation of the numerical methods, leading to several bug fixes and improvements
- **Maikel Nadolski** for great working atmosphere, excellent assistance in coding issues, implementation of the *Solver Test Environment* (*STE*) and improvement and documentation of the software installation process
- **Christoph Schaller** for great working atmosphere and implementation of the cut cell geometry routines
- **Paul Kermas** for great working atmosphere, debugging and documentation of the cut cell geometry routines and preparation of numerous sketches for this document
- **Jan and Jana DeWiljes** for proofreading
- **AG Klein** for the excellent working atmosphere and numerous cakes, cart races and pool matches

- **Ulrike Eickers** for great caring about several organizational issues
- **German Research Foundation (DFG)**, especially **Priority Program 1506**, lead by **Arnold Reusken** and **Dieter Bothe**, for funding and all the **contributors** for pleasant conferences and interesting discussions
- **Claus-Dieter Munz**, **Kurt Maute** and **Georg Pingen** for excellent preparation for working in the field of numerical fluid dynamics science
- **Gretar Tryggvason** and **Stéphane Zaleski** for an interesting scientific discussion
- **Wolfgang Baumann** for patient assistance concerning issues regarding the supercomputers at HLRN
- **Rob Falgout** for support concerning bug fixes in *HYPRE*
- the people at **Lawrence Livermore National Labs** for providing software packages such as *SAMRAI*, *HYPRE*, *SILO* and *VisIt*
- the people at **The HDF group** for providing *HDF5*
- the people at the **IT service** of the **math department** at **Freie Universität Berlin** for providing computer related infrastructure
- **Susanne Waidmann** for all the support of any kind, especially for taking care of the baby during the final phase of generating this document
- **Olivia Waidmann** for being the baby

CONTENTS

LIST OF TABLES

LIST OF FIGURES

LIST OF SYMBOLS

Symbol	Term	
General		
$\blacksquare$	Placeholder	
q	Scalar	
$\vec{q}$	Vector	
$\boldsymbol{Q}$	Tensor	
$\dot{q}$	Quantity per time	
$\overline{q}$	Spatial (integral) average	
$\widetilde{q}$	Temporal (integral) average	
$\widetilde{\overline{q}}$	Spatio-temporal (integral) average	
$\hat{q}$	Non-dimensional quantity	
$\breve{q}$	Dimensional reference quantity	
q	Unit of measurement	
Qq	Characteristic quantity	
A		
a	Distance	m
$\mathfrak{a}$	Scalar	
$\mathfrak{a}$	Index	
$\mathfrak{a}$	Ansatz coefficient	-
$\mathfrak{a}$	Coefficient	-
A	Area	$\mathrm{m}^{\mathfrak{d}-1}$
$\mathcal{A}$	Amplitude	-

$\mathfrak{A}$	Amplitude	-
$\mathfrak{A}$	Coefficient matrix	
$\vec{\mathfrak{A}}$	Acceleration vector	$\frac{\mathrm{m}}{\mathrm{s}^2}$
$\mathcal{A}$	Amplitude	-
α	Volume fraction	-

B

b		
$\mathfrak{b}$	Scalar	
$\mathfrak{b}$	Index	
$\mathfrak{b}$	Coefficient	
B	Inverse scaled bandwidth	$\frac{1}{\mathrm{m}}$
$\mathcal{B}$	Binomial Coefficient	-
$\mathfrak{B}$	Basis function	
$\mathfrak{B}$	Interface transition region	
$\mathfrak{B}$	Binomial Coefficient	-
$\mathcal{B}$	Binomial Coefficient	-
β	Face fraction	-

C

c	Speed of sound	$\frac{m}{s}$
c_p	Specific heat capacity at const. pressure	$\frac{m^2}{s^2 K}$
c_v	Specific heat capacity at const. volume	$\frac{m^2}{s^2 K}$
$\mathfrak{c}$	Cut cell index	-
$\mathfrak{c}$	Non-dimensional grid spacing factor	-
$\mathfrak{c}$	Index of vector component	-
$\mathfrak{c}$	Coefficient	-
C	Concentration	$\frac{\mathrm{mol}}{kg}$
$\mathcal{C}$	Constant	
$\mathfrak{C}$	Coefficient	
$\mathfrak{C}$	Corrector operator	

$\mathfrak{C}$	Cut cells	
$\mathfrak{C}$	Condition	
χ	(Adiabatic) Compressibility	$\frac{m\,s^2}{kg}$

D

d	Distance	m
$\mathfrak{d}$	Relative distance w.r.t. transition region width	-
$\mathfrak{d}$	Number of dimensions	-
$\mathfrak{d}$	Index of spatial coordinate direction	-
$\mathfrak{d}$	Real number	
D	(Binary) Diffusion coefficient	$\frac{m^2}{s}$
$\boldsymbol{D}$	(Anisotropic) Diffusion coefficient tensor	$\frac{m^2}{s}$
$\mathcal{D}$	Divergence constraint right hand side	$\frac{1}{s}$
$\mathfrak{D}$	Diagonal length	$\mathrm{m}^{\mathfrak{d}}$
Da	Damköhler number	-
$\partial\Omega$	Domain boundary	
$\partial\Omega_{\mathfrak{i}}$	Grid cell boundary	
$\partial\ddot{\Omega}$	Dual cell boundary	
$\partial\Omega^{\square}$	Boundary of computational domain	
δ	Dirac distribution	
δp	Pressure increment	$\frac{\mathrm{kg}}{\mathrm{m\,s^2}}$
$\delta\pi$	Pressure related increment	$\frac{\mathrm{kg}}{\mathrm{m\,s^2}}$
Δ	Difference	
ΔA	Grid cell face area	$\mathrm{m}^{\mathfrak{d}-1}$
Δh^0	Specific standard enthalpy of formation	$\frac{\mathrm{m}^2}{\mathrm{s}^2}$
Δt	Time step size	s
$\Delta\mathfrak{t}$	Pseudo-time step size	s
$\Delta\mathfrak{T}$	Time interval (of size Δt)	
ΔV	Grid cell volume	$\mathrm{m}^{\mathfrak{d}}$
Δx	Grid spacing	m

E

e	Total energy per unit mass	$\frac{\mathrm{m}^2}{\mathrm{s}^2}$
$\vec{\mathfrak{e}}$	Unit vector	
$\mathfrak{e}$	Index of vector component	
$\mathfrak{e}$	Small positive real number	
E	Error	
$\boldsymbol{E}$	Strain rate tensor	$\frac{1}{\mathrm{s}}$
$\mathcal{E}$	Relative error	-
$\mathfrak{E}$	Interface normal absolute strain rate component	$\frac{1}{\mathrm{s}}$
$\mathfrak{E}$	Enstrophy	$\frac{\mathrm{m}^{\mathfrak{d}}}{\mathrm{s}^2}$
$\mathfrak{E}$	Divergence error	$\frac{\mathrm{m}^{\mathfrak{d}-3}\mathrm{kgK}}{\mathrm{s}}$
$\mathcal{E}$	Relative error	-
ϵ	Bandwidth	m
ε	Scaled bandwidth	m

F

f	Flux density component	
$\vec{f}$	Flux density	
$\vec{\mathfrak{f}}$	Force density	$\frac{\mathrm{kg}}{\mathrm{m}^2\,\mathrm{s}^2}$
$\mathfrak{f}$	Real number	
$\mathfrak{f}$	Index of cell face fraction	
$\mathfrak{f}$	Cell face index	
F	Numerical flux density approximation	
$\boldsymbol{F}$	Flux density tensor	$\frac{\mathrm{kg}}{\mathrm{m}\,\mathrm{s}^2}$
$\mathcal{F}$	Numerical flux approximation	
$\mathfrak{F}$	Numerical correction flux	
$\mathfrak{F}$	Surface source	
$\widetilde{\mathcal{F}}$	Time-average space-integral flux	
Fr	Froude number	-
ϕ	Phase indicator	-
Φ	Pseudo-primitive quantity	
φ	Fluid phase index	

G

g	Gravitational acceleration	$\frac{\mathrm{m}}{\mathrm{s}^2}$
$\vec{g}$	Gravity vector	$\frac{\mathrm{m}}{\mathrm{s}^2}$
$\vec{\mathfrak{g}}$	Pressure gradient divided by density	$\frac{\mathrm{m}}{\mathrm{s}^2}$
$\mathfrak{g}$	Ghost data component	
G	Level-set function	m
$\vec{\mathcal{G}}$	Discrete level-set gradient	-
$\mathfrak{G}$	Level-set based interface representation	
γ	Heat capacity ratio	-
Γ	Interface	

H

h	Specific enthalpy	$\frac{\mathrm{m}^2}{\mathrm{s}^2}$
$\mathfrak{h}$	General relative step size w.r.t. domain size	-
$\mathfrak{h}$	Index of stencil elements	
$\mathfrak{h}$	Heat transfer coefficient	$\frac{\mathrm{kg}}{\mathrm{s}^3\,\mathrm{K}}$
H	Height	m
$\mathcal{H}$	Henry's law constant	$\frac{\mathrm{mol}\,\mathrm{s}^2}{\mathrm{kg}\,\mathrm{m}^2}$
$\mathfrak{H}$	General relative step size w.r.t. transition region	-
$\mathfrak{H}$	Real number	
$\mathcal{H}$	Heaviside step function	-
η	Scalar	

I

$\mathfrak{i}$	One-dimensional cell index	
$\mathfrak{i}$	Index	
$\mathfrak{i}$	Iteration counter	
$\boldsymbol{I}$	Identity matrix	
$\mathfrak{I}$	Interface representation	
$\mathfrak{I}$	Interface cells	

J

$\vec{j}$	(Diffusive) Flux	
$\mathfrak{j}$	Index	
$\boldsymbol{J}$	(Diffusive) Flux Tensor	
$\mathcal{J}$	Iteration index	
$\vec{\mathcal{J}}$	Space-time integral surface stress tensor component	$\frac{\mathrm{kg\,m}^{\mathfrak{D}-1}}{\mathrm{s}}$

K

k	Isotropic thermal conductivity	$\frac{\mathrm{kg\,m}}{\mathrm{s}^3\,\mathrm{K}}$
$\vec{k}$	Coefficient vector	
$\mathfrak{k}$	Index	
K	(Adiabatic) Bulk modulus	$\frac{\mathrm{kg}}{\mathrm{m\,s}^2}$
$\boldsymbol{K}$	Anisotropic thermal conductivity tensor	$\frac{\mathrm{kg\,m}}{\mathrm{s}^3\,\mathrm{K}}$
$\mathcal{K}$	Scalar coefficient	
$\mathfrak{K}$	Runge-Kutta right hand side operator	
$\mathfrak{K}$	Local sub-set of interface cells	
$\mathcal{K}$	Relative phase indicator difference	-
κ	(Mean) Curvature	$\frac{1}{m}$
$\varkappa$	Real number	

L

l	Length	m
ℓ	Level index	
$\mathfrak{l}$	Relative lower spatial bound	
$\mathfrak{l}$	Limiter weight	
L	Lower spatial bound	m
$\mathcal{L}$	Level	
$\mathfrak{L}$	Linear operator	
$\mathfrak{L}$	Limiter operator	
$\mathfrak{l}$	Limiter kernel	

$\mathfrak{L}$	Limiter function	
λ	Second viscosity coefficient	$\frac{\mathrm{kg}}{\mathrm{m\,s}}$

M

m	Mass	kg
$\mathfrak{m}$	Relative transition region size	-
$\mathfrak{m}$	Index	
$\vec{\mathfrak{m}}$	Momentum vector	$\frac{\mathrm{kg\,m}}{\mathrm{s}}$
M	Molar mass	$\frac{\mathrm{kg}}{\mathrm{mol}}$
$\boldsymbol{M}$	Transformation matrix	-
$\mathfrak{M}$	Maximum operator	
Ma	Mach number	
μ	Dynamic viscosity	$\frac{\mathrm{kg}}{\mathrm{m\,s}}$

N

n	Time level index	
$\vec{n}$	Normal vector	-
$\mathfrak{n}$	Stage index	
$\mathfrak{n}$	Index	
$\mathfrak{n}$	Relative upper temporal bound	
$\mathfrak{n}$	Local node index	
N	Upper temporal bound	s
$\mathcal{N}$	Narrow band width	
$\mathfrak{N}$	Effective narrow band width	
$\mathfrak{N}$	Narrow band	
$\mathcal{N}$	Natural number	
$\mathbb{N}$	Natural numbers	
Nu	Nusselt number	
ν	Kinematic viscosity	$\frac{\mathrm{m}^2}{\mathrm{s}}$

O

$\mathfrak{o}$	Relative lower temporal bound	
O	Lower temporal bound	
$\mathcal{O}$	Landau symbol	
$\mathfrak{O}$	Linear operator	
$\mathfrak{Op}$	Operator	
$\vec{\omega}$	Vorticity	$\frac{1}{\mathrm{s}}$
Ω	Spatial domain	
$\Omega^{\square}$	Computational domain	
$\widetilde{\Omega}$	Spatio-temporal domain	
$\Omega_{\mathfrak{i}}$	Primal grid cell	
$\ddot{\Omega}_{\mathfrak{i}}$	Dual grid cell	

P

p	Pressure	$\frac{\mathrm{kg}}{\mathrm{m\,s^2}}$
$p^{'}$	Dynamic pressure	$\frac{\mathrm{kg}}{\mathrm{m\,s^2}}$
$\vec{p}$	Specific interface tangential vector	
$\mathfrak{p}$	Norm index	
$\mathfrak{p}$	Index	
$\mathfrak{p}$	Coefficient	
$\mathfrak{p}$	Convergence order	-
P	Thermodynamic pressure	$\frac{\mathrm{kg}}{\mathrm{m\,s^2}}$
$\mathcal{P}$	Pressure related quantity	$\frac{\mathrm{kg\,K}}{\mathrm{m^3}}$
$\mathfrak{P}$	Level-set penalty function	
$\mathfrak{P}$	Predictor operator	
$\mathfrak{P}$	Primitive quantity	
$\mathfrak{P}$	Phase selector	
$\mathcal{P}$	Integer number	-
Pr	Prandtl number	
π	Predictor pressure	
Π	Product	
ϖ	Real number	

ψ	Conserved quantity per unit mass	
Ψ	Conserved quantity	

Q

q	Heat	
$\mathfrak{q}$	Source term	
$\mathfrak{q}$	Index	
$\mathfrak{q}$	Integer number	
$\vec{\mathfrak{q}}$	Coefficient vector	
$\mathcal{Q}$	Numerical source term approximation	
$\widetilde{\mathcal{Q}}$	Time-average space integral source terms	
Qr	Heat release parameter	

R

r	Radius	m
$\mathfrak{r}$	Ratio	-
$\mathfrak{r}$	Index	
$\mathfrak{r}$	Coefficient	
$\mathfrak{r}$	Step size ratio	-
R	Universal gas constant	$\frac{\mathrm{kg\,m^2}}{\mathrm{s^2\,mol\,K}}$
$\boldsymbol{R}$	Rotation matrix	
$\mathcal{R}$	Right hand side	
$\mathfrak{R}$	Recovery operator	
$\mathfrak{R}$	Ratio of radii	-
$\mathcal{R}$	Right hand side	
$\vec{\mathcal{R}}$	Right hand side vector	
$\mathbb{R}$	Real numbers	
Re	Reynolds number	
ρ	Mass density	$\frac{\mathrm{kg}}{\mathrm{m^3}}$
ϱ	Species production rate	$\frac{1}{\mathrm{s}}$

S

s	Specific entropy	$\frac{\mathrm{m}^2}{\mathrm{s}^2\,\mathrm{K}}$
$\mathfrak{s}$	Species index	
$\mathfrak{t}$	Index	
$\mathfrak{f}$	Solubility	-
$\mathfrak{f}$	Squared distance	m^2
S	Surface	$\mathrm{m}^{\mathfrak{d}}$
$\boldsymbol{S}$	Stress tensor	$\frac{\mathrm{kg}}{\mathrm{s}^2\,\mathrm{m}}$
$\boldsymbol{S}_\sigma$	Surface stress tensor	$\frac{\mathrm{kg}}{\mathrm{s}^2}$
$\mathcal{S}$	Scaled heat flow	$\frac{1}{\mathrm{s}}$
$\mathfrak{S}$	Local amplifier for level-set penalization	
$\mathfrak{S}$	Domain size	m
$\mathfrak{S}$	Separation line	
$\mathfrak{S}$	Scalar coefficient	
$\mathcal{S}$	Slope	
Sc	Schmidt number	
Sr	Strouhal number	
σ	Surface tension (coefficient)	$\frac{\mathrm{kg}}{\mathrm{s}^2}$
Σ	Sum	
ς	Real number	

T

t	Time	s
$\vec{t}$	Tangential vector	
$\mathfrak{t}$	Pseudo-time	s
t	Time slice index	
T	Temperature	K
$\boldsymbol{T}$	Translation matrix	
$\boldsymbol{\mathcal{T}}$	Viscous stress tensor	$\frac{\mathrm{kg}}{\mathrm{m}\,\mathrm{s}^2}$
$\mathfrak{T}$	Tolerance	
$\mathfrak{T}$	Final computational time	s
τ	Tangential coordinate	

θ	Potential temperature	K
Θ	Generalized potential temperature	K
ϑ	Angle	

U

u	Specific internal energy	$\frac{\mathrm{m}^2}{\mathrm{s}^2}$
$\mathfrak{u}$	Non-dimensional quantity	-
$\mathfrak{u}$	Index	
$\mathfrak{u}$	Relative upper spatial bound	
U	Upper spatial bound	
$\mathcal{U}$	Specifiy gravitational potential energy	$\frac{\mathrm{m}^2}{\mathrm{s}^2}$
$\mathfrak{U}$	Reference Velocity	$\frac{\mathrm{m}}{\mathrm{s}}$
$\mathfrak{U}$	Perimeter	m
$\vec{\mathcal{U}}$	Space-time integral update vector	

V

$\vec{v}$	Velocity vector	$\frac{\mathrm{m}}{\mathrm{s}}$
$\mathfrak{v}$	Index	
$\mathfrak{v}$	Inverse velocity component	$\frac{\mathrm{s}}{\mathrm{m}}$
$\mathfrak{v}$	Volume source	
V	Volume	$\mathrm{m}^{\mathfrak{d}}$
$\mathcal{V}$	Interface normal velocity component	$\frac{\mathrm{m}}{\mathrm{s}}$
$\mathfrak{V}$	Absolute interface normal velocity component	$\frac{\mathrm{m}}{\mathrm{s}}$
$\mathfrak{V}$	Volume-of-Fluid based interface representation	

W

$\vec{w}$	Velocity vector	$\frac{\mathrm{m}}{\mathrm{s}}$
$\mathfrak{w}$	Scalar weight	
$\mathfrak{w}$	Index	

$\mathfrak{w}$	Index of cell side w.r.t. to cell center in coord. dir.	-
W	Scalar weight	
$\mathcal{W}$	Relative scalar weight	
$\mathfrak{W}$	Minimum operator	
$\vec{\mathfrak{w}}$	Weight vector	
We	Weber number	

X

x	Spatial coordinate	m
$\mathfrak{x}$	Index	
$\mathfrak{x}$	Dual cell sub-face index	
X	Product	
$\mathcal{X}$	Integral compressibility	$\frac{m^{\mathfrak{d}+1}\,s^2}{kg}$
ξ	Real number	-
Ξ	Real number	-

Y

y	Spatial coordinate	m
$\mathfrak{y}$	Integer number	-
Y	Mass fraction	-
$\mathcal{Y}$	Scalar Poisson solution	
$\mathfrak{y}$	Real number	-
Υ	Generalized field quantity	

Z

z	Integer number	-
$\mathfrak{z}$	Integer number	-
$\mathfrak{z}$	Integer number	-
$\mathfrak{z}$	Integer number	-

$\mathfrak{z}$	Integer number	-
Z	Natural number	-
$\mathcal{Z}$	Natural number	-
$\mathfrak{Z}$	Constant	-
$\mathfrak{z}$	Coefficient	-
$\mathcal{Z}$	Integer number	-
$\mathbb{Z}$	Integer numbers	
ζ	Bulk viscosity	$\frac{\mathrm{kg}}{\mathrm{m\,s}}$

Indices

$\blacksquare_0$	Reference / background value
$\blacksquare_1$	First spatial direction
$\blacksquare_2$	Second spatial direction
$\blacksquare_3$	Third spatial direction
$\blacksquare_\mathfrak{f}$	Quantity on a certain grid cell face
$\blacksquare_\mathcal{A}$	Advection
$\blacksquare_\mathcal{C}$	Chemistry
$\blacksquare_\mathcal{D}$	Diffusion
$\blacksquare_\mathcal{E}$	Explicit
$\blacksquare_\mathcal{G}$	Acceleration
$\blacksquare_\mathcal{I}$	Implicit
$\blacksquare_\mathcal{V}$	Friction
$\blacksquare_\mathcal{X}$	Prescribed
$\blacksquare_\mathfrak{R}$	Region
$\blacksquare_m$	Midpoint
$\blacksquare_c$	Centroid
$\blacksquare_i$	Component in the first spatial dimension
$\blacksquare_j$	Component in the second spatial dimension
$\blacksquare_k$	Component in the third spatial dimension

Superscripts

$\blacksquare^{-1}$	Inverse
$\blacksquare^{T}$	Transposed
$\blacksquare^{0}$	Initial value
$\blacksquare^{(0)}$	Leading order coefficient
$\blacksquare^{(1)}$	First order coefficient
$\blacksquare^{(2)}$	Second order coefficient
$\blacksquare^{(+)}$	Fluid phase $(+)$ with $G > 0$
$\blacksquare^{(-)}$	Fluid phase $(-)$ with $G < 0$
$\blacksquare^{(L)}$	Fluid phase with **l**arger cut cell fraction
$\blacksquare^{(S)}$	Fluid phase with **s**maller cut cell fraction
$\blacksquare^{(\mathcal{L})}$	Left w.r.t. face normal direction (**l**ower)
$\blacksquare^{(\mathcal{U})}$	Right w.r.t. face normal direction (**u**pper)
$\blacksquare^{\bullet}$	Value after the first predictor stage
$\blacksquare^{*}$	Value after the entire predictor step
$\blacksquare^{**}$	Value after first projection step
$\blacksquare^{\star}$	Value before correction of volume fraction
$\blacksquare^{\star}$	Value before correction of level-set function
$\blacksquare^{\circ}$	Value at an arbitrary stage
$\blacksquare^{\oplus}$	Target value
$\blacksquare^{m}$	Pseudo-time level
$\blacksquare^{n}$	Time level

Accents

$\overline{\blacksquare}$	Spatial integral average
$\widetilde{\blacksquare}$	Temporal integral average
$\overline{\widetilde{\blacksquare}}$	Space-time average
$\hat{\blacksquare}$	Non-dimensional quantity
$\check{\blacksquare}$	Reference quantity
$\ddot{\blacksquare}$	Quantity on dual grid

Operators

$\cdot$	Inner product
$\circ$	Outer product
$\times$	Vector product
:	Frobenius inner product (double dot product)
∇	Nabla operator
$\lvert\blacksquare\rvert$	Absolute value
$[\blacksquare]$	Physical unit of $\blacksquare$
$[\![\,\blacksquare\,]\!]$	Jump of $\blacksquare$ at the Interface Γ
$\nabla\blacksquare$	Gradient of a scalar quantity
$\nabla \circ \vec{\blacksquare}$	Gradient of a vector field
$\nabla \cdot \vec{\blacksquare}$	Divergence of a vector field
$\mathrm{sgn}(\blacksquare)$	Sign of $\blacksquare$
$\Delta\blacksquare$	Difference
$\Sigma\blacksquare$	Sum
$\Pi\blacksquare$	Product
$\frac{\partial\blacksquare}{\partial\square}$	Partial derivative of $\blacksquare$ w.r.t. $\square$
$\frac{\mathrm{d}\blacksquare}{\mathrm{d}\square}$	Derivative of $\blacksquare$ w.r.t. $\square$
$\frac{\mathrm{D}\blacksquare}{\mathrm{D}t}$	Material derivative $\frac{\partial\blacksquare}{\partial t} + \vec{v} \cdot \nabla\blacksquare$

References

$\blacksquare$	Chapters & Sections
$[\blacksquare]$	Literature
$(\blacksquare)$	Equation
Fig. $\blacksquare$	Figures
Tab. $\blacksquare$	Tables

Part I

INTRODUCTION

1. NUMERICAL SIMULATION OF TWO-PHASE FLOW

Two- or multi-phase flows play a significant role in many technical applications, ranging from fuel injection in engines of vehicles, cavitation at the blades of ship's screws or icing at wings of airplanes, over either boiling of water or water cooling in reactors of larger scale power plants, flow of oil gas mixtures in pipelines, to production of food or pharmaceutics.

Numerical simulation is one of the permanent companions of design and development processes, optimization and operation of vehicles, devices or production facilities, in order to pre-estimate effects of certain actions and to reduce costs both during development and operation. Due to the availability of more and more efficient computers at moderate cost, attractiveness of numerical simulation is even gained in order to avoid elaborate and expensive experiments and to only manufacture already optimized configurations.

Two- or multi-phase flow and its numerical simulation is not only important for several engineering applications, but also for environmental events, such as formation of clouds and precipitation or flow of goundwater, free surface flows occurring during eruption of volcanoes and gush springs or during flooding and tsunami events, development and behavior of all kinds of foams, oil accidents in the sea and many more.

Classification of two-phase flows can be done due to various aspects, for example:

- the physical condition of the two-phase flow: gas-liquid, liquid-liquid, liquid-solid, gas-solid
- the way the different fluid phases combine[1]: separated (immiscible) flows, mixed flows and dispersed flows

[1] Also combinations of separated fluid phases, each being a mixture or a dispersion of different non-immiscible phases, are possible.

A larger number of these flows can be considered immiscible, consisting of different mixtures of fluids, such as, for example, air[2] and water[3], separated by a fluidic interface, at which surface forces act, arising due to surface tension. The latter can vary along the interface due to local adsorption and desorption of molecules[4] from the bulk phases.

Numerous numerical methods of all common kinds have been developed in order to simulate such two- or multi-phase flow systems and almost every combination of *flow solver*, ranging from Finite Difference (FD) [167, 176] Methods (along with Immersed Interface (e.g. [183], [108]) and Ghost Fluid (e.g. [115], [44]) Methods) over Finite Element (FE) [64, 11], Finite Volume (FV) [26, 58, 132] and Discontinuous Galerkin (DG) [122, 14] Methods to Boundary Integral Methods [78] or Particle Methods, such as Lattice Boltzmann (LB) Methods [80] on the one hand, and *interface representation* as classified below on the other hand can be found.

However, the computation of incompressible and variable density zero Mach number two-phase flow with large ratios[5] of the densities of the different fluid phases and singular momentum sources due to surface tension at the interface plus transport processes at the interface remains a challenging problem ([42]).

Due to the large variety of existing approaches, a complete overview of the field of simulation of two- or multi-phase flows is almost impossible. An certainly incomplete but nevertheless good overview of such existing methods is, for example, given in [143]. Also the introduction of [2] list several different methods. Nevertheless, there are still quite large research associations, such as, for example, recently the Priority Program (SPP) 1506 of the German research foundation (DFG) on transport processes at fluidic interfaces this work has been part of, aiming for development, enhancement and validation of such methods.

Due to more and more hybrid approaches, arising in order to overcome drawbacks of standalone methods, even the classification of the existing numerical methods is not straightforward: On the one hand, there are Lagrangian methods, which use moving grid points, that follow the fluid flow and distinguish between the different fluid phases via identification and tracking of particles with different fluid properties. On the other hand, there are Eulerian methods, which balance the change of the flow state

[2] Air consists of nitrogen, oxygen and small concentrations of various other gaseous species.
[3] In most of the natural cases many substances are dissolved in water, such as, for example, salt in the sea, air or various types of other molecules in technical applications.
[4] Molecules influencing surface tension of a fluidic interface are called **surf**ace **act**ive **a**ge**nt**s.
[5] In this context large ratios are of the order of magnitude $\mathcal{O}(1000)$ or larger.

at specified locations. In addition, hybrid Eulerian-Lagrangian methods, such as the Arbitrary-Lagrangian-Eulerian (ALE) method (e.g. [11]), combine both approaches by balancing at specific locations, the grid cells, which, however, are able to move. In [174] the following classification[6] is given:

- **Fixed-grid methods** solve the governing equations in the entire computational domain on a predefined fixed computational grid, capturing the moving interface implicitly. These **capturing methods** include
  - Marker-and-Cell (MAC) methods, in which marker particles are used to identify the different fluids [70, 69]
  - Volume-of-Fluid (VoF) methods as enhanced integral form of the MAC method, tracing regions of constant fluid identifier via a discrete function representing the scalar volume fraction of a certain domain occupied by a certain fluid [76, 29, 144, 146, 67, 57, 10]
  - Level-Set (LS) methods as implicit interface representation via a smooth scalar field [167, 156, 164, 131, 170, 39]
  - Constrained Interpolation Profile (CIP) methods, which try to construct a solution within each grid cell subject to certain constraints [138, 149]
  - Phase Field methods, which substitute the boundary condition at the interface by a partial differential equation for the evolution of a smooth auxiliary variable, identifying the various fluid phases separated by a continuous transition zone of finite thickness [68, 189]

  and hybrid combinations of the latter [152, 162, 169, 104] or with one of the following [110].

- **Tracking Methods** solve the governing equations on a fixed grid in each fluid phase, which is modified at the interface locally in order to align one of the grid cell boundary segments to the local interface segment with a separate front marking the interface

- **Moving-mesh methods** utilize separate moving and deforming interface fitted grids in each fluid phase for solving the governing equations

[6] Also combinations of the different types of methods can be applied: If, for example, the flow system consists of two different immiscible fluid phases, one of them being a mixture of various fluid phases and the other one being a dispersion of different fluid phases, then the sparse solid phases in the dispersion can be treated by an Lagrangian approach, while the continuous phase and the mixture on the other side of the interface of the two immiscible fluid phases can be treated by one of the other approaches in an Eulerian way.

- **Lagrangian methods** use moving grid points, that follow the fluid flow and distinguish between the different fluid phases via identification and tracking of moving particles with different fluid properties

An recent overview is given in [176], and up-to-date one is subject to be published via [157].

While methods with changing interface aligned grids potentially offer higher accuracy at the interface, they are difficult and expensive to apply to problems involving severe interfacial deformation and/or topological changes due to the necessity of regeneration of the computational mesh in every time step (as for example, stated in [116]) and procedures to project the present solution onto the newly generated grid. Fixed grid methods, on the other hand, either only provide a diffuse interface representation with the flow quantities smeared over several grid cells (e.g. [171]), resulting in a transition zone that is much thicker than the physical ones ([176]), or give rise to cut grid cells, if the interface is treated as sharp discontinuity of fluidic properties ([169], [185], [158], [53], [54]). The latter branch is the one this work follows.

Most of the existing methods are restricted to either the incompressible or the compressible flow regime without the option of a conceptually consistent extension to the respective other regime, including the weakly compressible transition zone. Especially most of the various approaches for incompressible flow do not solve the governing equations in conservative form, preventing straightforward extensions to other regimes and conservative solutions of the governing equations by rigorously applying discretely conservative Finite Volume methods with sharp interfaces for all features that require conservation physically. In fact, there are only few approaches dedicated to variable density zero Mach number flow in conservative form, that allow for spatial inhomogeneity of the density within each fluid phase and for a conservative discretization of the conservation laws (e.g. [150], [105]). The latter is aimed for in the present work, presenting building blocks of an unsplit numerical method for Direct Numerical Simulation of immiscible zero Mach number variable density two-phase flow based on an asymptotic low Mach number limit of the compressible Navier-Stokes equations, building the present method on projection schemes as, for example, given in [15], [17], [4], [150], [151], [92] and [180].

Projection methods[7] are very attractive for large scale computations due to the decoupling of velocity and pressure, yielding low computer storage consumption per

[7] A more detailed introduction to projection methods is given in chapter 4.1.

time step due to applicability of the fractional step[8] concept, requiring determination of solutions to linear systems for individual scalars only on the one hand, on the other hand, in constrast to, for example, application of SIMPLE- of PISO-type algorithms, there is no need for iterative procedures per time step. In this spirit all other features presented in this work are kept iteration-free as far as possible as well.

While restricting to two-phase flow examples in the incompressible regime of small length scales, focusing on the crucial issues in two-phase flow simulation of fluid phase separation, interface transport and discretization of the singular contributions due to surface tension, the present work is meant as a starting point for a discretely fully conservative Eulerian fixed Cartesian grid Finite Volume projection scheme for immiscible liquid-liquid and gas-liquid zero Mach number variable density two-phase flow, solving the governing equations in conservative form using conservative discretiztions only, additionally providing a framework that allows for conceptually straightforward transition to other flow regimes comparable to [119], [118] and [19] and equations of state[9] and consistent discretely conservative error correction in the corrector steps of the underlying predictor-corrector projection method by combining ideas from [92] and [150] and references therein.

The topicality of the present subject is emphazied by recent developments, which in principle are in line with the present approach: In [25] both incompressible and compressible two-phase flow of perfect gases is simulated using a Discontinuous Galerkin method for Direct Numerical Simulation at constant surface tension coefficient based on the Euler equations in both regimes. Another recent Discontinuous Galerkin Method for solving the low and zero Mach number equations for multi-phase flows is presented in [88]. Additional literature is cited during description of the various topics covered in the following.

Since this work is intended for serving as basis for subsequent work on open issues, extensions, enhancements and (more advanced) applications, it contains various detailed derivations and algorithms, repeating selected preliminary work by other authors in the present notation as well, if required. An overview of the content of this document is given in the next chapter.

[8] See, for example, [65] for an overview of fractional step methods, to which the projection methods, in the present context as incremental pressure correction method, belong.

[9] Especially for incompressible flows the equation of state is obsolete in the present formulation, as long as no temperature information is required and in this case potential temperature degenerates to a measure for tracking of the divergence error during the predictor step of the present predictor-corrector projection method. Therefore no discrete velocity divergence needs to be evaluated when correcting velocity divergence errors in the advective fluxes during the corrector step.

2. FRAMEWORK OF THIS THESIS

This chapter gives an overview of the scientific contributions of this work and an outline of what follows in the subsequent parts, chapters and sections.

2.1 Scientific Contributions of this Work

The following major and minor topics are covered within this work:

- presentation of the zero Mach number equations for chemically reacting two-phase flow at arbitrary equation of state
- integration of the formulation of the governing equations in [92] into the two-phase flow setting
- detailed description of the enhancement of the hybrid volume-of-fluid/level-set correction strategy from [28], advanced in [150], and its adaption to the setting of the present formulation of the governing equations and the applied numerical method as already sketched roughly in [182]
- derivation and application of a derived conservative discretization of the interface surface stress tensor as momentum boundary condition between different fluid phases via flux formulation
- proposition of a non-iterative level-set penalty strategy for keeping the absolute value of the level-set gradient close to unity
- presentation of an analytical solution for the signed distance function for elliptic contours
- presentation of the derivation of the analytical pressure solution for a test case used in [86]

- derivation of a Helmholtz-type equation for the boundary normal pressure gradient on the boundary for no-slip boundaries at variable density, corresponding to the work from [102] for constant density (see appendix section D)

The following associated research projects already have used or are about to benefit from this work and the related implementation of the newly developed flow solver[1]:

- implementation of the presented single-phase solver served as basis for other, already published, theses [18] and [133] as well as related publications [134] and [19]
- implementation of the presented solver is intended to serve as basis for different projects with in the German Research Foundation Collaborative Research Center 1114 "Scaling Cascade in Complex Systems"
- contribution to comparative studies applying the present single-phase method and its implementation to vortex-wall collision and detachment problems for analysis of drag force scaling (subject to be published in [126])

2.2 Script Organization

This script is organized as follows: After this introductory part I three more parts follow.

The first one, part II, is dedicated to the derivation of the leading order set of governing equations for chemically reacting immiscible zero Mach number two-phase flow at arbitrary equation of state (without definition of a specific reaction model) as generalization to the derivations in [90], [151], [150] and more recently [25] for ideal gas, similar to [16], and to the introduction of a resulting generalized divergence constraint as done in [5], [6] and [92].

The second one, part III, describes building blocks of a discretely conservative Finite Volume projection method for solution to the equations from part II, focussing on incompressible flow in particular. This part is divided into chapters 4 to 8.

In chapter 4 the basic concepts of the numerical method are explained.

[1] ***STAFSEA***[2] ['stæfsi: 'skwɛrd]: **ST**ructured **A**daptive **F**low **S**olver for **E**ngineering and **A**tmospheric **A**pplications, based on SAMRAI and related open source software as specified under `http://www.mi.fu-berlin.de/w/AgKlein/WelcomeSTAFSEAsquared` and in chapter 8.

Chapter 5 describes the single-phase flow solver as the basic building block of the entire numerical method. It directly applies with corresponding fluid properties to all regions of the computational domain, that are sufficiently far away from a fluidic interface, and therefore to the majority of the computational domain (which does not necessarily correspond to the majority of the grid cells, if adaptive mesh refinement with finer grid resolution in the vicinity of the interface is applied). The chapter is finalized with a section on basic numerical results for single-phase computations in order to show successful operation of the implemented method and to reproduce some standard test results for both constant and variable density flows at vanishing velocity divergence.

Chapter 6 is dedicated to building blocks extending the singe-phase method from chapter 5 to a two-phase flow solver. Therefore this chapter is split into the following sections: In section 6.1 the dual representation of the fluidic interface is described, followed by description of the strategy for numerical flux computation at cut grid cells in section 6.2, particularly focussing on determination of numerical fluxes for the explicitly treated advective part of the governing equations in the vicinity of the interface in section 6.3 and an overview of the current status regarding the overall two-phase corrector step in section 6.4. The major section 6.5 is dedicated to correction of discretization errors during the discrete two-phase transport in order to guarantee for physically reasonable states of the conserved quantities, mass conservation in each of the fluid phases and suitable necessary coupling of fluid flow and interface representation. Additionally, a non-iterative approach for stabilization of the level-set gradient is presented. The second major section 6.6 describes an approach for conservative discretization of the surface stress tensor due to surface tension. Both sections 6.5 and 6.6 comprise a final sub-section on topic-specific results each. The subsequent chapter 7 provides an overview of benefits, drawbacks and open issues of the presented approaches (as far as not already discussed in the specific sections) and in chapter 8 the software used for both production of the results presented in this work and generation of this document itself, including the various figures, is listed.

The concluding part IV contains a short summary. The appendix contains basic calculus used for the derivations within this work in chapter A, basic derivations in chapter B, a chapter on accuracy and convergence in C and derivation of the variable density equation for the boundary normal pressure gradient on no-slip boundaries in chapter D. A German version of the abstract at the beginning of the document can be found in appendix section E. The document is finalized by the list of cited literature.

Part II

MATHEMATICAL PROBLEM DESCRIPTION

3. GOVERNING EQUATIONS

The Reynolds Transport Theorem in its most general form

$$\frac{\mathrm{D}}{\mathrm{D}\,t}\left(\,\Psi\,\right) = \frac{\mathrm{d}}{\mathrm{d}t}\left(\int_{\Omega(t)} \rho\psi\,\mathrm{d}V\right) + \oint_{\partial\Omega(t)} \rho\psi\,(\vec{v}-\vec{w})\cdot\vec{n}\,\mathrm{d}A \tag{3.1}$$

according to e.g. [23], [79] or [83] links the change of any fluid property of an arbitrary fluid element (Lagrangian representation) to the change of this quantity within an arbitrarily moving and deforming control volume $\Omega \in \mathbb{R}^{\mathfrak{d}}$ in $\mathfrak{d}$ spatial dimensions (Eulerian representation). The left hand side of equation (3.1) represents the material derivative of this property $\Psi(\vec{x},t)$ with corresponding density $\rho\psi(\vec{x},t)$, value per unit mass ψ and mass density ρ, all depending[1] on both space $\vec{x}$ and time t. The total derivative

$$\frac{\mathrm{d}}{\mathrm{d}t}\left(\int_{\Omega(t)} \rho\psi\,\mathrm{d}V\right) = \int_{\Omega(t)} \left(\,\rho\psi\,\right)_t\,\mathrm{d}V + \oint_{\partial\Omega(t)} \rho\psi\,\vec{w}\cdot\vec{n}\,\mathrm{d}A \tag{3.2}$$

as first term on the right hand side of equation (3.1) consists of local changes of $\rho\psi$ with partial derivative $(\,\blacksquare\,)_t \equiv \frac{\partial\blacksquare}{\partial t}$ and fluxes across the control volume boundary $\partial\Omega$ with (outward-pointing) unit normal vector $\vec{n}$ due to changes of the time-dependent control volume. The second term on the right hand side of equation (3.1) represents net fluxes across the control volume boundary due to different velocities of fluid ($\vec{v}$) and control volume boundary ($\vec{w}$). In the most general notation the temporal change of Ψ in equation (3.1) is due to externally forced volume sources within the control volume and surface sources on the control volume boundary with production rates $\dot{\mathfrak{v}}_{(\rho\psi)}$ and

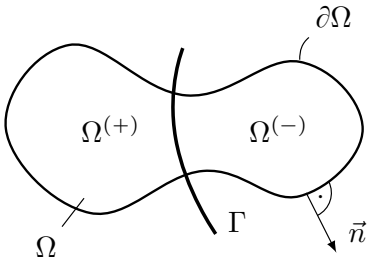

Fig. 3.1: Arbitrary domain Ω, separated by an interface Γ into sub-domains $\Omega^{(+)}$ and $\Omega^{(-)}$.

[1] Notation of the dependence on space $\vec{x}$ and time t is omitted in the above and the following notation for compactness.

$\dot{\mathfrak{F}}_{(\rho\psi)}$, resulting in the conservation law formulation

$$\int_{\Omega(t)} (\,\rho\psi\,)_t \,\mathrm{d}V + \oint_{\partial\Omega(t)} \rho\psi\,\vec{v}\cdot\vec{n}\,\mathrm{d}A = \int_{\Omega(t)} \dot{\mathfrak{v}}_{(\rho\psi)}\,\mathrm{d}V + \oint_{\partial\Omega(t)} \dot{\mathfrak{F}}_{(\rho\psi)}\,\mathrm{d}A \tag{3.3}$$

with respect to the control volume. Equation (3.3) holds in each of the sub-domains $\Omega^{(+)}$ and $\Omega^{(-)}$, resulting from separation of the control volume Ω by an interface Γ as sketched in ***Fig. 3.1***. The different sub-domains contain immiscible fluid phases with different properties. With

$$\psi \in \{1, Y_{\mathfrak{s}}, \vec{v}, e\} \tag{3.4}$$

the flow of these fluid phases is, thus, governed by the integral balances

$$\int_{\Omega^\varphi(t)} (\,\rho^\varphi\,)_t \,\mathrm{d}V = \int_{\Omega^\varphi(t)} \dot{\mathfrak{q}}^\varphi_{(\rho)}\,\mathrm{d}V - \oint_{\partial\Omega^\varphi(t)} \vec{f}^{\,\varphi}_{(\rho)}\cdot\vec{n}\,\mathrm{d}A \tag{3.5a}$$

$$\int_{\Omega^\varphi(t)} (\,\rho^\varphi Y^\varphi_{\mathfrak{s}}\,)_t \,\mathrm{d}V = \int_{\Omega^\varphi(t)} \dot{\mathfrak{q}}^\varphi_{(\rho Y_{\mathfrak{s}})}\,\mathrm{d}V - \oint_{\partial\Omega^\varphi(t)} \vec{f}^{\,\varphi}_{(\rho Y_{\mathfrak{s}})}\cdot\vec{n}\,\mathrm{d}A \tag{3.5b}$$

$$\int_{\Omega^\varphi(t)} (\,\rho^\varphi \vec{v}^{\,\varphi}\,)_t \,\mathrm{d}V = \int_{\Omega^\varphi(t)} \vec{\dot{\mathfrak{q}}}^{\,\varphi}_{(\rho\vec{v})}\,\mathrm{d}V - \oint_{\partial\Omega^\varphi(t)} \boldsymbol{F}^\varphi_{(\rho\vec{v})}\cdot\vec{n}\,\mathrm{d}A \tag{3.5c}$$

$$\int_{\Omega^\varphi(t)} (\,\rho^\varphi e^\varphi\,)_t \,\mathrm{d}V = \int_{\Omega^\varphi(t)} \dot{\mathfrak{q}}^\varphi_{(\rho e)}\,\mathrm{d}V - \oint_{\partial\Omega^\varphi(t)} \vec{f}^{\,\varphi}_{(\rho e)}\cdot\vec{n}\,\mathrm{d}A \tag{3.5d}$$

of mass (3.5a), species masses (3.5b), (linear) momentum (3.5c) and total energy (3.5d) within each fluid phase $\varphi \in \{(+),(-)\}$. In system (3.5) $Y_{\mathfrak{s}}$ is the mass fraction of species $\mathfrak{s}$ and

$$e := u + \mathcal{U} + \frac{1}{2}\,(\vec{v}\cdot\vec{v}) \tag{3.6}$$

is the total energy per unit mass without heat of formation, consisting of internal (u), potential ($\mathcal{U}$) and kinetic energy, each per unit mass. The individual volume sources – both due to internal sources, such as chemical reactions (for species mass), and external sources, such as radiation (for total energy) or gravity (for momentum) – are denoted $\dot{\mathfrak{q}}$, and the integrands of the area integrals from equation (3.3), consisting of advection and molecular transport, are summarized in the flux density vectors $\vec{f}_{(\rho\psi)}$ for scalars $\rho\psi$ and the flux density tensor $\boldsymbol{F}$ for the momentum vector.

The surface integrals in (3.5) can be split into contributions from the interface portion $\Gamma_\Omega(t) := \Omega(t) \cap \Gamma(t)$ and from sub-domain boundaries $\partial\Omega^\varphi_\Omega(t) := \partial\Omega^\varphi(t)\backslash\Gamma_\Omega(t)$

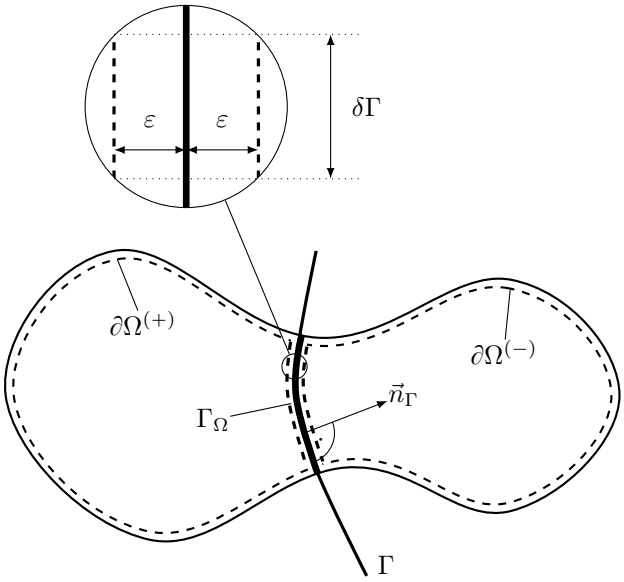

Fig. 3.2: Sub-domain boundaries $\partial\Omega^{(+)}$ and $\partial\Omega^{(-)}$, interface section Γ_Ω within Ω and interface normal vector $\vec{n}_\Gamma$.

with $\partial\Omega^\varphi(t) = \partial\Omega^\varphi_\Omega(t) \cup \Gamma_\Omega(t)$ that match the control volume boundaries:

$$\oint_{\partial\Omega^\varphi(t)} \blacksquare^\varphi \cdot \vec{n}^\varphi \,\mathrm{d}A = \int_{\partial\Omega^\varphi_\Omega(t)} \blacksquare^\varphi \cdot \vec{n}^\varphi \,\mathrm{d}A + \int_{\Gamma_\Omega(t)} \blacksquare^\varphi_\Gamma \cdot \vec{n}^\varphi_\Gamma \,\mathrm{d}S \tag{3.7}$$

The two sub-domains need to be coupled via interface conditions obtained as given in [41], [81], [176] or in [58] (and references therein) from balancing over a control volume $\delta\Omega_\Gamma := \delta\Gamma \times [-\varepsilon, \varepsilon]$ around the interface Γ as shown in ***Fig. 3.2***, with (in the limit) vanishing interface normal extent $\varepsilon \to 0$. This leads to the general interfacial balance

$$\int_{\delta\Gamma_\Omega(t)} \blacksquare^{(+)}_\Gamma \cdot \vec{n}^{(+)}_\Gamma \,\mathrm{d}S + \int_{\delta\Gamma_\Omega(t)} \blacksquare^{(-)}_\Gamma \cdot \vec{n}^{(-)}_\Gamma \,\mathrm{d}S = \int_{\delta\Gamma_\Omega(t)} \dot{\mathrm{q}}^{(\Gamma)}_\blacksquare \,\mathrm{d}S \tag{3.8}$$

in which $\dot{\mathrm{q}}^{(\Gamma)}_\blacksquare$ represents sources of quantity $\blacksquare$ at the interface, while $\vec{n}^{(+)}_\Gamma$ points from the fluid labeled $(+)$ to the one labeled $(-)$ and $\vec{n}^{(-)}_\Gamma$ points from the fluid labeled $(-)$ to the one labeled $(+)$. After definition of a unique interface normal vector

$$\vec{n}_\Gamma := \vec{n}^{(+)}_\Gamma = -\vec{n}^{(-)}_\Gamma \tag{3.9}$$

the general coupling condition for each quantity $\blacksquare$ reads

$$[\![\, \blacksquare \,]\!] \cdot \vec{n}_\Gamma = \dot{\mathrm{q}}^{(\Gamma)}_\blacksquare \tag{3.10}$$

with jump discontinuity $[\![\blacksquare]\!] := \blacksquare_\Gamma^{(+)} - \blacksquare_\Gamma^{(-)}$.

3.1 Phase Indicator

In order to distinguish between the different fluid phases, a phase indicator function (or characteristic function[2])

$$\phi^\varphi(\vec{x},t) := \begin{cases} 1 & \text{if } \vec{x} \in \Omega^\varphi(t) \\ 0 & \text{otherwise} \end{cases} \tag{3.11}$$

has to be introduced, which assigns a fixed marker value to each fluid particle, depending on its location with respect to the interface. As each fluid particle keeps its property, the material derivative

$$\frac{\mathrm{D}}{\mathrm{D}\,t}\left(\phi^\varphi\right) = \left(\phi^\varphi\right)_t + \vec{v}_\phi \cdot \nabla\phi^\varphi = 0 \tag{3.12}$$

with smooth velocity field $\vec{v}_\phi$, matching the interface velocity $\vec{w}_\Gamma$ at the interface, vanishes as shown in [45]. More precisely, as $\nabla\phi^\varphi$ is zero everywhere but at the interface, the so-called topological equation (3.12) represents the interfacial movement. Approximation of the topological equation (3.12) is one of the crucial issues in solving two-phase flow equations numerically. As shown in [173] or [176], due to

$$\nabla\phi^\varphi = -\,\vec{n}_\Gamma^\varphi\,\delta_\Gamma = -\int_\Gamma \vec{n}_\Gamma^\varphi\,\delta^{(\mathfrak{d})}\left(\vec{x}-\vec{x}_\Gamma\right)\,\mathrm{d}S \tag{3.13}$$

with surface Dirac

$$\delta_\Gamma := \int_\Gamma \delta^{(\mathfrak{d})}\left(\vec{x}-\vec{x}_\Gamma\right)\,\mathrm{d}S \tag{3.14}$$

and

$$\delta^{(\mathfrak{d})}\left(\vec{x}-\vec{x}_\Gamma\right) = \prod_{\mathfrak{d}=1}^{\mathfrak{d}} \delta\left(x_\mathfrak{d} - x_{\mathfrak{d},\Gamma}\right) \tag{3.15}$$

as the product of one-dimensional Dirac delta distributions in coordinate direction $\mathfrak{d}$,

$$\left(\phi^\varphi\right)_t = -\left(\phi^\varphi \vec{n}_\Gamma^\varphi\right)\delta_\Gamma \tag{3.16}$$

holds.

[2] As defined in [87].

3.2 One-Fluid Formulation

A reformulation of the conservation laws (3.5), that holds in the entire domain Ω in ***Fig. 3.1*** and contains both discontinuous fluid properties at the sharp interface Γ and the interface conditions as shown in [87], can be obtained by summation of the contributions in (3.5) from each fluid phase φ as described in [45], [143], [173] or [176] (originally proposed in [70]) after introduction of the generalized field quantity

$$\Upsilon\left(\vec{x},t\right) := \sum_{\varphi}\left(\phi^{\varphi}\left(\vec{x},t\right)\Upsilon^{\varphi}\left(\vec{x},t\right)\right) \tag{3.17}$$

that is valid in the entire flow domain. The benefits of such a formulation for cases, in which the detailed interface identification is necessary or desired, are emphasized, for example, in [101]. The discontinuous fluid properties are accounted for via the phase indicator ϕ introduced in section 3.1. With $\Upsilon \in \{\psi, \rho\psi, \vec{f}_{\rho\psi}, \dot{\mathrm{q}}_{\rho\psi}\}$ for each quantity ψ (including $\boldsymbol{F}$ in the case of ψ being a vector), the sum of the integral balances for $\rho\psi$ from (3.5) over the sub-domains within Ω can be written in terms of integrals over the entire domain Ω as

$$\begin{aligned}\sum_{\varphi}\Bigg(&\int_{\Omega(t)}\phi^{\varphi}\left(\left(\rho\psi\right)^{\varphi}\right)_t\,\mathrm{d}V \;-\; \int_{\Omega(t)}\phi^{\varphi}\dot{\mathrm{q}}^{\varphi}_{(\rho\psi)}\,\mathrm{d}V \\ &+\int_{\partial\Omega^{\varphi}_{\Omega}(t)}\vec{f}^{\,\varphi}_{(\rho\psi)}\cdot\vec{n}^{\varphi}\,\mathrm{d}A \;+\; \int_{\Gamma_{\Omega}(t)}\vec{f}^{\,\varphi}_{(\rho\psi),\Gamma}\cdot\vec{n}^{\varphi}_{\Gamma}\,\mathrm{d}S\Bigg) = 0\end{aligned} \tag{3.18}$$

due to

$$\int_{\Omega^{\varphi}(t)}\Upsilon^{\varphi}\,\mathrm{d}V = \int_{\Omega(t)}\phi^{\varphi}\Upsilon^{\varphi}\,\mathrm{d}V \tag{3.19}$$

after multiplication with the respective phase indicator. With

$$\phi^{\varphi}\left(\left(\rho\psi\right)^{\varphi}\right)_t = \left(\phi^{\varphi}\left(\rho\psi\right)^{\varphi}\right)_t - \left(\rho\psi\right)^{\varphi}\left(\phi^{\varphi}\right)_t = \left(\phi^{\varphi}\left(\rho\psi\right)^{\varphi}\right)_t + \left(\rho\psi\right)^{\varphi}\vec{v}_{\phi}\cdot\nabla\phi^{\varphi} \tag{3.20}$$

due to the product rule and equations (3.12) and (3.13), the generic relation

$$\int_{\Omega(t)}\left(\rho\psi\right)_t\,\mathrm{d}V - \int_{\Omega(t)}\dot{\mathrm{q}}_{(\rho\psi)}\,\mathrm{d}V + \oint_{\partial\Omega_{\Omega}(t)}\vec{f}_{(\rho\psi)}\cdot\vec{n}\,\mathrm{d}A - \int_{\Omega(t)}\dot{\mathrm{q}}^{(\Gamma)}_{(\rho\psi)}\delta_{\Gamma}\,\mathrm{d}V \;=\; 0 \tag{3.21}$$

is obtained from equation (3.18), which corresponds to the one given in [85], for example. In equation (3.21) each of the quantities $\rho\psi$, $\dot{\mathrm{q}}_{(\rho\psi)}$ and $\vec{f}_{(\rho\psi)}$ satisfies relation

(3.17). After considering

$$\vec{v}_\phi\left(\vec{x}_\Gamma, t\right) \equiv \vec{w}_\Gamma \tag{3.22}$$

at the interface and

$$\int_{\Gamma_\Omega(t)} \blacksquare \,\mathrm{d}S = \int_{\Omega(t)} \blacksquare \delta_\Gamma \,\mathrm{d}V \tag{3.23}$$

as given in [176], the interfacial surface integral from equation (3.18) can be replaced by a volume integral over the interfacial source

$$\dot{\mathfrak{q}}^{(\Gamma)}_{(\rho\psi)} = \left(\left[\!\left[\vec{f}_{(\rho\psi)} \right]\!\right] - \left[\!\left[\rho\psi \right]\!\right] \vec{w}_\Gamma \right) \cdot \vec{n}_\Gamma \tag{3.24}$$

which is restricted to the interface via the surface Dirac δ_Γ in order to obtain the representation in equation (3.21). Further, in equation (3.21) the identity

$$\begin{aligned} \oint_{\partial\Omega_\Omega(t)} \vec{f}_{(\rho\psi)} \cdot \vec{n} \,\mathrm{d}A &= \oint_{\partial\Omega_\Omega(t)} \sum_\varphi \left(\phi^\varphi \vec{f}^{\,\varphi}_{(\rho\psi)} \right) \cdot \vec{n} \,\mathrm{d}A \\ &= \sum_\varphi \left(\int_{\partial\Omega_\Omega(t)} \phi^\varphi \vec{f}^{\,\varphi}_{(\rho\psi)} \cdot \vec{n} \,\mathrm{d}A \right) = \sum_\varphi \left(\int_{\partial\Omega^\varphi_\Omega(t)} \vec{f}^{\,\varphi}_{(\rho\psi)} \cdot \vec{n}^\varphi \,\mathrm{d}A \right) \end{aligned} \tag{3.25}$$

holds, which further transforms to

$$\begin{aligned} \oint_{\partial\Omega_\Omega(t)} \vec{f}_{(\rho\psi)} \cdot \vec{n} \,\mathrm{d}A &= \sum_\varphi \left(\int_{\Omega^\varphi(t)} \nabla \cdot \vec{f}^{\,\varphi}_{(\rho\psi)} \,\mathrm{d}V - \int_{\Gamma_\Omega(t)} \vec{f}^{\,\varphi}_{(\rho\psi)} \cdot \vec{n}_\Gamma \,\mathrm{d}S \right) \\ &= \sum_\varphi \left(\int_{\Omega(t)} \phi^\varphi \nabla \cdot \vec{f}^{\,\varphi}_{(\rho\psi)} - \left(\vec{f}^{\,\varphi}_{(\rho\psi)} \cdot \vec{n}_\Gamma \delta_\Gamma \right) \,\mathrm{d}V \right) \\ &= \sum_\varphi \left(\int_{\Omega(t)} \nabla \cdot \phi^\varphi \vec{f}^{\,\varphi}_{(\rho\psi)} \underbrace{- \vec{f}^{\,\varphi}_{(\rho\psi)} \cdot \nabla \phi^\varphi - \left(\vec{f}^{\,\varphi}_{(\rho\psi)} \cdot \vec{n}_\Gamma \delta_\Gamma \right)}_{=\,0} \,\mathrm{d}V \right) \\ &= \int_{\Omega(t)} \nabla \cdot \sum_\varphi \left(\phi^\varphi \vec{f}^{\,\varphi}_{(\rho\psi)} \right) \,\mathrm{d}V = \int_{\Omega(t)} \nabla \cdot \vec{f}_{(\rho\psi)} \,\mathrm{d}V \end{aligned} \tag{3.26}$$

due to (3.13) after applying the divergence theorem in each fluid phase. Thus, equation (3.21) can be written as

$$\int_{\Omega(t)} \left(\left(\rho\psi \right)_t + \nabla \cdot \vec{f}_{(\rho\psi)} - \dot{\mathfrak{q}}_{(\rho\psi)} - \dot{\mathfrak{q}}^{(\Gamma)}_{(\rho\psi)} \delta_\Gamma \right) \,\mathrm{d}V \;=\; 0 \tag{3.27}$$

which contains volume integrals only, and, thus, also the local equation

$$(\rho\psi)_t + \nabla\cdot\vec{f}_{(\rho\psi)} - \dot{\mathfrak{q}}_{(\rho\psi)} - \dot{\mathfrak{q}}^{(\Gamma)}_{(\rho\psi)}\delta_\Gamma = 0 \tag{3.28}$$

holds. Equation (3.28) only differs from the single-phase formulation due to the singular interfacial sources (scaling with δ_Γ) and the fact that each quantity $\Upsilon \in \{\rho\psi, \vec{f}_{(\rho\psi)}, \dot{\mathfrak{q}}_{(\rho\psi)}\}$ is a generalized one according to the definition in (3.17).

In particular, the flux densities in the generic equation (3.28) are

$$\vec{f}_{(\rho)} = \rho\vec{v} \tag{3.29a}$$
$$\vec{f}_{(\rho Y_\mathfrak{s})} = \rho Y_\mathfrak{s}\vec{v} + \vec{j}_\mathfrak{s} \tag{3.29b}$$
$$\boldsymbol{F}_{(\rho\vec{v})} = \rho\vec{v}\circ\vec{v} - \boldsymbol{S} \tag{3.29c}$$
$$\vec{f}_{(\rho e)} = \rho e\vec{v} - \boldsymbol{S}\cdot\vec{v} + \vec{j}_q + \vec{j}_\mathfrak{E} \tag{3.29d}$$

with stress tensor

$$\boldsymbol{S} = \boldsymbol{\mathcal{T}} - p\boldsymbol{I} \tag{3.30}$$

and identity matrix $\boldsymbol{I}$ as well as outer product $\vec{v}\circ\vec{v} \equiv \vec{v}\vec{v}$. Molecular transport of momentum in (3.30), heat in (3.29d) and species mass in (3.29b) is modeled by the constitutive expressions for

- the viscous stress tensor

$$\boldsymbol{\mathcal{T}} = 2\mu\boldsymbol{E} + \lambda\,(\nabla\cdot\vec{v})\,\boldsymbol{I} \tag{3.31}$$

  with dynamic viscosity[3] μ and second viscosity coefficient[4] $\lambda = \zeta - \frac{2}{3}\mu$ with bulk viscosity[5] $\zeta = 0$ due to the Stokes' relation for **Newtonian fluids** as given, for example, in [24], strain rate tensor

$$\boldsymbol{E} = \frac{1}{2}\left(\nabla\circ\vec{v} + (\nabla\circ\vec{v})^T\right) \tag{3.32}$$

  and $(\blacksquare)^T$ expressing the transposed of $\blacksquare$,

- the heat flux density

$$\vec{j}_q = -\boldsymbol{K}\cdot\nabla T \tag{3.33}$$

[3] The dynamic viscosity is also called shear viscosity or second Lamé constant.
[4] The second viscosity coefficient is also called first Lamé constant.
[5] The bulk viscosity is also called volume viscosity or dilatational viscosity coefficient.

with thermal conductivity tensor $\boldsymbol{K}$ and temperature T based on **Fourier's law**, reducing to

$$\vec{j}_q = -k\boldsymbol{I} \cdot \nabla T = -k\nabla T \tag{3.34}$$

with thermal conductivity k for **isotropic materials**,

- the species diffusive flux density

$$\vec{j}_{\mathfrak{s}} = -\rho\, \boldsymbol{D}_{\mathfrak{s}} \cdot \nabla Y_{\mathfrak{s}} \tag{3.35}$$

with the species diffusivities $\boldsymbol{D}_{\mathfrak{s}}$ based on **Fick's first law**[6], reducing to

$$\vec{j}_{\mathfrak{s}} = -\rho\, D_{\mathfrak{s}} \boldsymbol{I} \cdot \nabla Y_{\mathfrak{s}} = -\rho\, D_{\mathfrak{s}} \nabla Y_{\mathfrak{s}} \tag{3.36}$$

for **isotropic materials**

while

$$\vec{j}_{\mathfrak{C}} := \sum_{\mathfrak{s}=1}^{\mathfrak{N}_{\mathfrak{s}}} h_{\mathfrak{s}}\, \vec{j}_{\mathfrak{s}} \tag{3.37}$$

in (3.29d) is defined to be the flux density responsible for the transport of the species' enthalpie $h_{\mathfrak{s}}$ via diffusion. While the interfacial sources are addressed in the next section, the volume specific production rates read

$$\dot{\mathfrak{q}}_{(\rho)} = 0 \tag{3.38a}$$

$$\dot{\mathfrak{q}}_{(\rho Y_{\mathfrak{s}})} = \rho \varrho_{\mathfrak{s}} \tag{3.38b}$$

$$\dot{\vec{\mathfrak{q}}}_{(\rho \vec{v})} = \rho \vec{g} \tag{3.38c}$$

$$\dot{\mathfrak{q}}_{(\rho e)} = \dot{q}_q - \dot{q}_\varrho \tag{3.38d}$$

[6] For multi-component systems conservative species diffusion is modeled more accurately by the Stefan-Maxwell equation, as, for example, described in [113]. In this case, the diffusive flux of species $\mathfrak{s}$, depending on its mass fraction $Y_{\mathfrak{s}}$, is

$$\vec{j}_{\mathfrak{s}} = -\rho \frac{M_{\mathfrak{s}}}{M} \left(\sum_{s=1}^{\mathfrak{N}^{(s)}} (D_{\mathfrak{s},s} \nabla Y_s) + \frac{\nabla M}{M} \sum_{s=1}^{\mathfrak{N}^{(s)}} (D_{\mathfrak{s},s} Y_s) \right)$$

as given in [113] or [27], which results in a nonlinear coupled system for all present species. Solution of such systems (with often unknown diffusivity tensor components $D_{\mathfrak{s},s}$ for complex multi-component mixtures) is beyond the scope of the present work. However, under the assumption of small amounts of solutes in a common solvent, binary diffusion of each solute in the solvent can be assumed and Fick's law with binary diffusion coefficients can be applied as a simplification as proposed e.g. in [141], where the diffusion coefficient $D_{\mathfrak{s}}$ is meant to be the binary diffusion coefficient of species $\mathfrak{s}$ in the common non-reacting abundant solvent.

with

$$\dot{q}_\varrho := \sum_{\mathfrak{s}=1}^{\mathcal{N}_\mathfrak{s}} \rho \varrho_\mathfrak{s} \left(\Delta h^0\right)_\mathfrak{s} \tag{3.39}$$

as the total amount of standard enthalpie of formation of all $\mathcal{N}_\mathfrak{s}$ species in the system per time, Δh^0 as the standard enthalpie of formation[7] of species $\mathfrak{s}$ with respect to its molar mass and

$$\varrho_\mathfrak{s} = \varrho_\mathfrak{s}\left(p, \rho, Y_\mathfrak{s}\right) \tag{3.40}$$

as the net production rate of species $\mathfrak{s}$, depending on ρ, $Y_\mathfrak{s}$ and pressure p. Further, $\vec{g}$ is the vector of gravitational acceleration and $\dot{q}_q$ represents external heat sources.

3.2.1 Closure

The thermal equation of state

$$T = T\left(p, \rho, Y_\mathfrak{s}\right) \tag{3.41}$$

and the $\mathcal{N}_\mathfrak{s}$ caloric equations of state

$$h_\mathfrak{s} = h_\mathfrak{s}\left(p, T\right) = h_\mathfrak{s}\left(p, \rho, Y_\mathfrak{s}\right) \tag{3.42}$$

for the partial specific enthalpies $h_\mathfrak{s}$ (as e.g. given in [24]) – with $\rho = \rho\left(p, s, Y_\mathfrak{s}\right)$ and specific entropy s – in combination with problem dependent initial and domain boundary conditions, as well as suitable singular interfacial source terms, yielding

$$\left(\rho\right)_t + \nabla \cdot \left(\rho \vec{v}\right) = \dot{\mathfrak{q}}_\rho^{(\Gamma)} \delta_\Gamma \tag{3.43a}$$

$$\left(\rho Y_\mathfrak{s}\right)_t + \nabla \cdot \left(\rho Y_\mathfrak{s} \vec{v}\right) + \nabla \cdot \vec{j}_\mathfrak{s} = \rho \varrho_\mathfrak{s} + \dot{\mathfrak{q}}_{\rho Y_\mathfrak{s}}^{(\Gamma)} \delta_\Gamma \tag{3.43b}$$

$$\left(\rho \vec{v}\right)_t + \nabla \cdot \left(\rho \vec{v} \circ \vec{v}\right) + \nabla p - \nabla \cdot \boldsymbol{\mathcal{T}} = \rho \vec{g} + \dot{\vec{\mathfrak{q}}}_{\rho \vec{v}}^{(\Gamma)} \delta_\Gamma \tag{3.43c}$$

$$\left(\rho e\right)_t + \nabla \cdot \left(\left(\rho e + p\right) \vec{v}\right) - \nabla \cdot \left(\left(\boldsymbol{\mathcal{T}} \cdot \vec{v}\right) - \vec{j}_q - \vec{j}_\mathfrak{e}\right) = \dot{q}_q - \dot{q}_\varrho + \dot{\mathfrak{q}}_{\rho e}^{(\Gamma)} \delta_\Gamma \tag{3.43d}$$

[7] Enthalpie of formation is positive, if it is consumed for formation of species $\mathfrak{s}$ (endothermic process), and negative, if it is released (exothermic process), resulting in the negative contribution of $\dot{q}_\varrho$ to relations (3.38d) and (3.43d).

which corresponds to the one-fluid formulation described in [87], subject to specification of the interfacial sources $\dot{\mathfrak{q}}^{(\Gamma)}$ in section 3.2.2.

3.2.2 Interface Conditions

Balance (3.8) at the interface in combination with $\vec{n}_\Gamma$ from definition (3.9) yields the interface conditions

$$\left(\left[\!\left[\vec{f}_{(\rho)} \right]\!\right] - [\![\, \rho \,]\!] \quad \vec{w}_\Gamma\right) \cdot \vec{n}_\Gamma = \dot{\mathfrak{q}}_\rho^{(\Gamma)} = \Delta\Delta\dot{m}_\Gamma \tag{3.44a}$$

$$\left(\left[\!\left[\vec{f}_{(\rho Y_\mathfrak{s})} \right]\!\right] - [\![\, \rho Y_\mathfrak{s} \,]\!]\ \vec{w}_\Gamma\right) \cdot \vec{n}_\Gamma = \dot{\mathfrak{q}}_{\rho Y_\mathfrak{s}}^{(\Gamma)} = \Delta\Delta\dot{m}_\Gamma\, Y_{\mathfrak{s},\Gamma}^{(+)} + \Delta\dot{m}_\Gamma^{(-)}\, [\![\, Y_\mathfrak{s} \,]\!] + \left[\!\left[\vec{j}_\mathfrak{s} \right]\!\right] \cdot \vec{n}_\Gamma \tag{3.44b}$$

$$\left([\![\, \boldsymbol{F}_{(\rho\vec{v})} \,]\!] - [\![\, \rho\vec{v} \,]\!] \circ \vec{w}_\Gamma\right) \cdot \vec{n}_\Gamma = \dot{\vec{\mathfrak{q}}}_{\rho\vec{v}}^{(\Gamma)} = \Delta\Delta\dot{m}_\Gamma\, \vec{v}_\Gamma^{(+)} + \Delta\dot{m}_\Gamma^{(-)}\, [\![\, \vec{v} \,]\!] - [\![\, \boldsymbol{S} \,]\!] \cdot \vec{n}_\Gamma \tag{3.44c}$$

$$\left(\left[\!\left[\vec{f}_{(\rho e)} \right]\!\right] - [\![\, \rho e \,]\!] \quad \vec{w}_\Gamma\right) \cdot \vec{n}_\Gamma = \dot{\mathfrak{q}}_{\rho e}^{(\Gamma)} = \Delta\Delta\dot{m}_\Gamma\, e_\Gamma^{(+)} + \Delta\dot{m}_\Gamma^{(-)}\, [\![\, e \,]\!] - \left[\!\left[\boldsymbol{S} \cdot \vec{v} - \vec{j}_q - \vec{j}_\mathfrak{e} \right]\!\right] \cdot \vec{n}_\Gamma \tag{3.44d}$$

with

$$\Delta\dot{m}_\Gamma^\varphi := \rho_\Gamma^\varphi \left[\left(\vec{v}_\Gamma^\varphi - \vec{w}_\Gamma\right) \cdot \vec{n}_\Gamma^\varphi\right] = \rho_\Gamma^\varphi\, \dot{\mathfrak{q}}_\phi^{(\Gamma),\varphi} \tag{3.45}$$

as the density of the mass flux of fluid phase φ across the interface due to both interface movement ($\vec{w}_\Gamma \equiv \vec{v}_{\phi,\Gamma}$) and interface normal fluid flow ($\vec{v}_\Gamma^\varphi \cdot \vec{n}_\Gamma^\varphi$), and

$$\begin{aligned} \Delta\Delta\dot{m}_\Gamma := \sum_\varphi \Delta\dot{m}_\Gamma^\varphi &= \left([\![\, \rho \,]\!] \left(\vec{v}_\Gamma^{(+)} - \vec{w}_\Gamma\right) + \rho_\Gamma^{(-)}\, [\![\, \vec{v} \,]\!]\right) \cdot \vec{n}_\Gamma \\ &= [\![\, \rho \,]\!]\, \dot{\mathfrak{q}}_\phi^{(\Gamma),(+)} + \rho_\Gamma^{(-)}\, [\![\, \vec{v} \,]\!] \cdot \vec{n}_\Gamma \end{aligned} \tag{3.46}$$

as density of the resulting effective mass flux across the interface. The other interfacial source terms $\dot{\mathfrak{q}}_\blacksquare^{(\Gamma)}$ in (3.44) represent gain or loss of species mass (in (3.44b)) at the interface, for example due to chemical reactions, the interfacial forces including surface tension (in (3.44c)) and gain or loss of interfacial total energy (in (3.44d)). Due to **conservation of mass** with the interface being a **massless surface**, $\Delta\Delta\dot{m}_\Gamma = 0$, and

$$[\![\, \vec{v} \,]\!] \cdot \vec{n}_\Gamma = \left(1 - \frac{\rho_\Gamma^{(+)}}{\rho_\Gamma^{(-)}}\right) \dot{\mathfrak{q}}_\phi^{(\Gamma),(+)} \tag{3.47}$$

as well as

$$\sum_{\mathfrak{s}} \dot{\mathfrak{q}}_{\rho Y_{\mathfrak{s}}}^{(\Gamma)} = \dot{\mathfrak{q}}_{\rho}^{(\Gamma)} = 0 \tag{3.48}$$

remain. In **absence of mass transfer across the interface**, and, thus, if there are **no phase changes**, the interface normal component of the interfacial speed $\vec{w}_\Gamma \cdot \vec{n}_\Gamma$ is equal to the interface normal fluid velocity on both sides of the interface, guaranteeing that each fluid particle remains on that side of the interface it has been on. Thus,

$$\vec{w}_\Gamma \cdot \vec{n}_\Gamma \;=\; \vec{v}_\Gamma^{(+)} \cdot \vec{n}_\Gamma \;=\; \vec{v}_\Gamma^{(-)} \cdot \vec{n}_\Gamma \;=\; \vec{v}_\phi \cdot \vec{n}_\Gamma \tag{3.49}$$

holds, yielding

$$\Delta \dot{m}_\Gamma^{(+)} = \Delta \dot{m}_\Gamma^{(-)} = 0 \tag{3.50}$$

as well as

$$\dot{\mathfrak{q}}_{\phi}^{(\Gamma),(+)} = \dot{\mathfrak{q}}_{\phi}^{(\Gamma),(-)} = \dot{\mathfrak{q}}_{\phi}^{(\Gamma)} = 0 \tag{3.51}$$

for the volume source. Therefore,

$$[\![\, \vec{v} \,]\!] \cdot \vec{n}_\Gamma = 0 \tag{3.52}$$

results, which means, that the interface normal fluid velocity is continuous. Assuming, in addition, that **no chemical reactions take place at the interface**, then for each species $\mathfrak{s}$ the relations

$$\dot{\mathfrak{q}}_{\rho Y_{\mathfrak{s}}}^{(\Gamma)} = 0 \tag{3.53}$$

as well as

$$\left[\!\!\left[\vec{j}_{\mathfrak{s}} \right]\!\!\right] \cdot \vec{n}_\Gamma = 0 \tag{3.54}$$

due to

$$\vec{j}_{\mathfrak{s}}^{(\Gamma)} = \vec{j}_{\mathfrak{s}}^{(\Gamma),(+)} = \vec{j}_{\mathfrak{s}}^{(\Gamma),(-)} \tag{3.55}$$

hold. Due to (3.54) the equation

$$\left[\!\!\left[\vec{j}_{\mathfrak{E}} \right]\!\!\right] \cdot \vec{n}_\Gamma = \sum_{\mathfrak{s}} \left[[\![\, h_{\mathfrak{s}} \,]\!] \left(\vec{j}_{\mathfrak{s}}^{(\Gamma)} \cdot \vec{n}_\Gamma \right) \right] \tag{3.56}$$

applies, which further reduces to

$$\left[\!\!\left[\vec{j}_{\mathfrak{E}} \right]\!\!\right] \cdot \vec{n}_\Gamma = 0 \tag{3.57}$$

due to

$$\vec{j}_{\mathfrak{s}}^{(\Gamma)} = \vec{j}_{\mathfrak{s}}^{(\Gamma),(+)} = \vec{j}_{\mathfrak{s}}^{(\Gamma),(-)} = 0 \tag{3.58}$$

in case of an **impermeable surface**. Equation (3.53) is considered to imply constant local surface tension over time, resulting in **continuous heat flux**

$$\left[\!\left[\vec{j}_q \right]\!\right] \cdot \vec{n}_\Gamma = \sigma_t = 0 \tag{3.59}$$

across the interface following [85]. Under these **boldly emphasized assumptions** the interfacial sources read

$$\left(\left[\!\left[\vec{f}_{(\rho)} \right]\!\right] - [\![\, \rho \,]\!] \quad \vec{w}_\Gamma \right) \cdot \vec{n}_\Gamma = \dot{\mathfrak{q}}_\rho^{(\Gamma)} = 0 \tag{3.60a}$$

$$\left(\left[\!\left[\vec{f}_{(\rho Y_{\mathfrak{s}})} \right]\!\right] - [\![\, \rho Y_{\mathfrak{s}} \,]\!] \; \vec{w}_\Gamma \right) \cdot \vec{n}_\Gamma = \dot{\mathfrak{q}}_{\rho Y_{\mathfrak{s}}}^{(\Gamma)} = 0 \tag{3.60b}$$

$$\left(\left[\!\left[\boldsymbol{F}_{(\rho\vec{v})} \right]\!\right] - [\![\, \rho\vec{v} \,]\!] \circ \vec{w}_\Gamma \right) \cdot \vec{n}_\Gamma = \dot{\vec{\mathfrak{q}}}_{\rho\vec{v}}^{(\Gamma)} = [\![\, p \,]\!]\, \vec{n}_\Gamma - [\![\, \boldsymbol{\mathcal{T}} \,]\!] \cdot \vec{n}_\Gamma \tag{3.60c}$$

$$\left(\left[\!\left[\vec{f}_{(\rho e)} \right]\!\right] - [\![\, \rho e \,]\!] \quad \vec{w}_\Gamma \right) \cdot \vec{n}_\Gamma = \dot{\mathfrak{q}}_{\rho e}^{(\Gamma)} = [\![\, p\vec{v} \,]\!] \cdot \vec{n}_\Gamma - [\![\, \boldsymbol{\mathcal{T}} \cdot \vec{v} \,]\!] \cdot \vec{n}_\Gamma \tag{3.60d}$$

with

$$\dot{\vec{\mathfrak{q}}}_{\rho\vec{v}}^{(\Gamma)} = \vec{\mathfrak{f}}_\sigma \tag{3.61a}$$

$$\dot{\mathfrak{q}}_{\rho e}^{(\Gamma)} = \vec{\mathfrak{f}}_\sigma \cdot \vec{w}_\Gamma \tag{3.61b}$$

and surface force density $\vec{\mathfrak{f}}_\sigma$ due to surface tension, dervided in the following section 3.2.4. Finally, the bottom equation (3.60d) with (3.61b) vanishes under the above conditions due to (3.49) and (3.63) below, since it leaves condition (3.60c) subject to (3.61a), multiplied by the interfacial velocity. The interface normal and interface tangential components of the momentum interface condition (3.60c) read

$$[\![\, p \,]\!] - \vec{n}_\Gamma \cdot [\![\, \boldsymbol{\mathcal{T}} \,]\!] \cdot \vec{n}_\Gamma - \vec{n}_\Gamma \cdot \vec{\mathfrak{f}}_\sigma = 0 \tag{3.62a}$$

$$(\boldsymbol{I} - \vec{n}_\Gamma \circ \vec{n}_\Gamma) \cdot \left([\![\, \boldsymbol{\mathcal{T}} \,]\!] \cdot \vec{n}_\Gamma + \vec{\mathfrak{f}}_\sigma \right) = \vec{0} \tag{3.62b}$$

with projection operator $(\boldsymbol{I} - \vec{n}_\Gamma \circ \vec{n}_\Gamma)$ onto the interface. Further, in case of **viscous flow** also the interface tangential velocity components do not jump at the interface due to friction and the resulting non-slip condition

$$[\![\, \vec{v} \,]\!] = 0 \tag{3.63}$$

at the interface yields a continuous[8] velocity field across the interface. Additionally,

$$[\![\, \phi \,]\!] = 1 \tag{3.64}$$

applies for the fluid marker as given by (3.11) in section 3.1. Further, under **isothermal** conditions

$$[\![\, T \,]\!] = 0 \tag{3.65}$$

holds, and assuming the individual species to follow Henry's law, the discontinuity of mass fractions

$$[\![\, Y_{\mathfrak{s}} \,]\!] = Y_{\mathfrak{s}}^{(+)} \left(1 - \frac{1}{\mathcal{H}_{\mathfrak{s}} \sum_{\tilde{\mathfrak{s}}} \frac{Y_{\tilde{\mathfrak{s}}}^{(+)}}{\mathcal{H}_{\tilde{\mathfrak{s}}}}} \right) \tag{3.66}$$

can be determined based on one-sided data[9] according to the definition of Henry's law $C_{\mathfrak{s}}^{(-)} = \frac{1}{\mathcal{H}_{\mathfrak{s}}} C_{\mathfrak{s}}^{(+)}$ with non-dimensional Henry's law constant $\mathcal{H}_{\mathfrak{s}}$ of species $\mathfrak{s}$ and concentration $C_{\mathfrak{s}}$.

3.2.3 Redundancy

One of the $\mathcal{N}_{\mathfrak{s}}$ scalar equations (3.5b) or (3.43b) for the partial density $\rho Y_{\mathfrak{s}}$, respectively, as well as one of the $\mathcal{N}_{\mathfrak{s}}$ caloric equations of state – say, both labeled $\mathfrak{s} = \mathfrak{s}^*$ – can be removed from the system, since the sum over all $\mathcal{N}_{\mathfrak{s}}$ species mass equations (3.43b) results in the mass equation (3.43a) due to mass conservation as given in [141], for example. Since

$$\sum_{\mathfrak{s}=1}^{\mathcal{N}_{\mathfrak{s}}} Y_{\mathfrak{s}} = 1 \tag{3.67}$$

has to hold at any point in space, the constraints

$$\sum_{\mathfrak{s}=1}^{\mathcal{N}_{\mathfrak{s}}} \vec{j}_{\mathfrak{s}} = 0, \qquad \sum_{\mathfrak{s}=1}^{\mathcal{N}_{\mathfrak{s}}} \varrho_{\mathfrak{s}} = 0, \qquad \sum_{\mathfrak{s}=1}^{\mathcal{N}_{\mathfrak{s}}} \dot{\mathfrak{q}}_{\rho Y_{\mathfrak{s}}}^{(\Gamma)} = 0 \tag{3.68}$$

arise, as shown, for example, in [141] and [95]. The caloric equation of state of species $\mathfrak{s}^*$ finally vanishes due to

$$\sum_{\mathfrak{s}=1}^{\mathcal{N}_{\mathfrak{s}}} Y_{\mathfrak{s}} h_{\mathfrak{s}} = h \tag{3.69}$$

[8] The gradient of the velocity field, however, has a discontinuity at the interface.

[9] See appendix section B.1 for the derivation of equation (3.66).

with enthalpy $h = h(p, \rho, Y_{\mathfrak{s}})$ in combination with constraint (3.67). Therefore in the following the index $\mathfrak{s}$ represents any of the $\mathcal{N}_{\mathfrak{s}} - 1$ species whose index is $\mathfrak{s} \neq \mathfrak{s}^*$.

3.2.4 Surface Tension

As shown in [176] and [187], the influence of surface tension, commonly represented as the resulting interface normal surface force $\vec{\mathfrak{f}}_\sigma$, can be written in terms of the surface divergence of a surface tension tensor

$$\boldsymbol{S}_\Gamma^{(\sigma)} := \sigma\left(\boldsymbol{I} - \vec{n}_\Gamma \circ \vec{n}_\Gamma\right) \tag{3.70}$$

with σ as the surface tension coefficient – or surface energy density – and identity matrix $\boldsymbol{I}$. This surface tension tensor was originally introduced in [82] and [100] and allows for the notation

$$\int_{\Gamma_\Omega(t)} \vec{\mathfrak{f}}_\sigma \,\mathrm{d}S = \int_{\Gamma_\Omega(t)} \nabla_\Gamma \cdot \boldsymbol{S}_\Gamma^{(\sigma)} \,\mathrm{d}S \overset{(\star)}{=} \oint_{\partial\Omega(t)\cap\Gamma(t)} \boldsymbol{S}_\Gamma^{(\sigma)} \cdot \vec{p} \,\mathrm{d}\ell = \oint_{\partial\Omega(t)\cap\Gamma(t)} \sigma\vec{p} \,\mathrm{d}\ell \tag{3.71}$$

with surface gradient operator

$$\nabla_\Gamma = \left(\boldsymbol{I} - \vec{n}_\Gamma \circ \vec{n}_\Gamma\right) \cdot \nabla \tag{3.72}$$

and $\vec{p}$ as the interface tangential vector, which is perpendicular to the boundary of a surface element in the surface, pointing outward regarding Ω as sketched in ***Fig. 3.3***. Thus, $\vec{n}_\Gamma \cdot \vec{p} \equiv 0$ at any point of the surface element boundary.

The right hand side with respect to $(\star)$ of equation (3.71) is obtained by applying the divergence theorem on the surface, yielding line integrals around the intersection of Γ and $\partial\Omega$. The vector $\vec{p}$ can be considered the projection

$$\vec{p} = \left(\boldsymbol{I} - \vec{n}_\Gamma \circ \vec{n}_\Gamma\right) \cdot \vec{n} \tag{3.73}$$

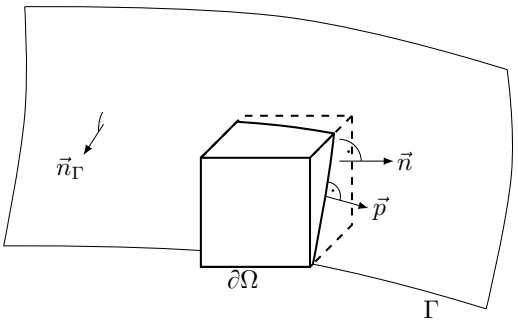

Fig. 3.3: Interface Γ intersecting a cubic control volume Ω with boundary $\partial\Omega$

of the normal vector $\vec{n}$ to the control volume boundary $\partial\Omega$ onto the surface of Γ. Due

to the identities $(\vec{n}_\Gamma \cdot \vec{n}_\Gamma) \equiv 1$ and $(\vec{n}_\Gamma \circ \vec{n}_\Gamma) \cdot \vec{n} \equiv \vec{n}_\Gamma \, (\vec{n}_\Gamma \cdot \vec{n})$ the relation

$$\begin{aligned} \boldsymbol{S}_\Gamma^{(\sigma)} \cdot \vec{p} \;&=\; \sigma \, (\boldsymbol{I} - \vec{n}_\Gamma \circ \vec{n}_\Gamma) \cdot (\boldsymbol{I} - \vec{n}_\Gamma \circ \vec{n}_\Gamma) \cdot \vec{n} \\ &=\; \sigma \, (\boldsymbol{I} - \vec{n}_\Gamma \circ \vec{n}_\Gamma) \cdot \vec{n} \;=\; \boldsymbol{S}_\Gamma^{(\sigma)} \cdot \vec{n} \end{aligned} \tag{3.74}$$

holds, since for the occuring expression $(\vec{n}_\Gamma \circ \vec{n}_\Gamma) \cdot (\vec{n}_\Gamma \circ \vec{n}_\Gamma) \cdot \vec{n}$ the identity

$$(\vec{n}_\Gamma \circ \vec{n}_\Gamma) \cdot (\vec{n}_\Gamma \circ \vec{n}_\Gamma) \cdot \vec{n} = \vec{n}_\Gamma \, (\vec{n}_\Gamma \cdot \vec{n}_\Gamma) \, (\vec{n}_\Gamma \cdot \vec{n}) = \vec{n}_\Gamma \, (\vec{n}_\Gamma \cdot \vec{n}) = (\vec{n}_\Gamma \circ \vec{n}_\Gamma) \cdot \vec{n} \tag{3.75}$$

is obtained. Therefore relation (3.73) allows for rewriting equation (3.71) as surface integral

$$\oint_{\partial\Omega(t) \cap \Gamma(t)} \boldsymbol{S}_\Gamma^{(\sigma)} \cdot \vec{p} \, \mathrm{d}\ell \;=\; \oint_{\partial\Omega(t)} \left(\boldsymbol{S}_\Gamma^{(\sigma)} \delta_\Gamma \right) \cdot \vec{p} \, \mathrm{d}A \;=\; \oint_{\partial\Omega(t)} \left(\boldsymbol{S}_\Gamma^{(\sigma)} \delta_\Gamma \right) \cdot \vec{n} \, \mathrm{d}A \tag{3.76}$$

in full space over the domain boundary $\partial\Omega$, with δ_Γ as the surface Dirac (3.14), limiting the effect of surface tension to the interface. The facts, that on the one hand

$$\boldsymbol{S}_\Gamma^{(\sigma)} \cdot \vec{p} \;=\; \sigma \vec{p} \;=\; \sigma \, (\boldsymbol{I}_\Gamma \cdot \vec{p}) \;=\; (\sigma \boldsymbol{I}_\Gamma) \cdot \vec{p} \tag{3.77}$$

with surface identity $\boldsymbol{I}_\Gamma \;=\; (\boldsymbol{I} - \vec{n}_\Gamma \circ \vec{n}_\Gamma)$ – resulting in (3.70) – and on the other hand

$$\vec{\mathrm{f}}_\sigma \;=\; \nabla_\Gamma \cdot \boldsymbol{S}_\Gamma^{(\sigma)} \;=\; \nabla_\Gamma \cdot \sigma \boldsymbol{I}_\Gamma \;=\; \sigma \, (\nabla_\Gamma \cdot \boldsymbol{I}_\Gamma) + \boldsymbol{I}_\Gamma \cdot \nabla_\Gamma \sigma \;=\; \sigma \, (\nabla_\Gamma \cdot \boldsymbol{I}_\Gamma) + \nabla_\Gamma \sigma \tag{3.78}$$

reveal the common formulation

$$\vec{\mathrm{f}}_\sigma \;=\; \sigma \kappa \vec{n}_\Gamma + \nabla_\Gamma \sigma \tag{3.79}$$

for the surface force density, split into interface normal and interface tangential contributions, with mean[10] interface curvature κ due to

$$(\nabla_\Gamma \cdot \boldsymbol{I}_\Gamma) = \kappa \vec{n}_\Gamma \tag{3.80}$$

as given in [176]. Another full space formulation involving the surface Dirac δ_Γ can

[10] κ: the mean curvature in two space dimensions and twice the mean curvature in three space dimensions.

be obtained in addition to (3.76) in terms of a volume integral due to

$$\int_{\Gamma_\Omega(t)} \dot{\vec{\mathfrak{q}}}^{(\Gamma)}_{\rho\vec{v}}\,\mathrm{d}S = \int_{\Gamma_\Omega(t)} \vec{\mathfrak{f}}_\sigma\,\mathrm{d}S \overset{(3.23)}{=} \int_{\Omega(t)} \vec{\mathfrak{f}}_\sigma\delta_\Gamma\,\mathrm{d}V = \int_{\Omega(t)} \vec{\mathfrak{f}}_\Gamma\,\mathrm{d}V \tag{3.81}$$

and, thus, with the identities (3.71) and (3.76) the relation

$$\oint_{\partial\Omega(t)} \left(\boldsymbol{S}^{(\sigma)}_\Gamma\delta_\Gamma\right)\cdot\vec{n}\,\mathrm{d}A \;=\; \int_{\Omega(t)} \vec{\mathfrak{f}}_\Gamma\,\mathrm{d}V \tag{3.82}$$

with (volume) force density $\vec{\mathfrak{f}}_\Gamma$ holds.

3.2.5 Total Energy Balance in Pressure Formulation

Enthalpy is defined as

$$h = h\left(p,\rho,Y_{\mathfrak{s}}\right) = u\left(p,\rho,Y_{\mathfrak{s}}\right) + \frac{p}{\rho} \tag{3.83}$$

while the balance for internal energy

$$u = u\left(p,\rho,Y_{\mathfrak{s}}\right) \tag{3.84}$$

results from subtracting the kinetic energy balance[11]

$$\rho\frac{\mathrm{D}}{\mathrm{D}\,t}\left(\frac{1}{2}\left(\vec{v}\cdot\vec{v}\right)\right) = \left(\rho\vec{g}+\vec{\mathfrak{f}}_\sigma\delta_\Gamma\right)\cdot\vec{v} + \nabla\cdot\left(\,\boldsymbol{S}\cdot\vec{v}\,\right) - \boldsymbol{S}:\nabla\vec{v} \tag{3.85}$$

and the potential energy balance[12]

$$\rho\frac{\mathrm{D}}{\mathrm{D}\,t}\left(\,\mathcal{U}\,\right) = -\rho\vec{g}\cdot\vec{v} \tag{3.86}$$

with time-independent specific potential energy $\mathcal{U}$ from the total energy equation (3.43d) as done in [141]. As shown in appendix section B.2.3, this yields the pressure formulation

$$\left(\,p\,\right)_t + \vec{v}\cdot\nabla p + \left(\rho c^2\right)\left(\nabla\cdot\vec{v}\right) \;=\; \Xi^{-1}\left[-\boldsymbol{\mathcal{T}}:\nabla\vec{v} + \nabla\cdot\vec{j}_q - \dot{q}_q + \dot{\mathfrak{q}}_c\right] \tag{3.87}$$

[11] See appendix section B.2.1 for derivation of the kinetic energy balance.
[12] See appendix section B.2.2 for derivation of the potential energy balance.

of the total energy balance due to $\vec{v}(\vec{x}_\Gamma) \equiv \vec{w}_\Gamma$ with

$$\dot{\mathfrak{q}}_c := \sum_{\mathfrak{s}=1}^{\mathcal{N}_\mathfrak{s}} \dot{q}_\mathfrak{s} \tag{3.88}$$

and

$$\dot{q}_\mathfrak{s} := \vec{j}_\mathfrak{s} \cdot \nabla h_\mathfrak{s} + \rho \varrho_\mathfrak{s} \left[h_\mathfrak{s} + \left(\Delta h^0 \right)_\mathfrak{s} \right] \tag{3.89}$$

as well as

$$\Xi = 1 - \rho \left(\frac{\partial h}{\partial p} \right)_{\rho, Y_\mathfrak{s}} \tag{3.90}$$

and

$$c^2 = \left(\frac{\partial p}{\partial \rho} \right)_{s, Y_\mathfrak{s}} = \frac{\rho}{\Xi} \left(\frac{\partial h}{\partial \rho} \right)_{p, Y_\mathfrak{s}} = \frac{1}{\chi \, \rho} = \frac{K}{\rho} \tag{3.91}$$

as the frozen speed of sound[13] as given in [9], [73] and [137] with specific entropy s, (frozen) adiabatic compressibility

$$\chi = -\rho \left(\frac{\partial \rho^{-1}}{\partial p} \right)_{s, Y_\mathfrak{s}} = \frac{1}{\rho} \left(\frac{\partial \rho}{\partial p} \right)_{s, Y_\mathfrak{s}} = \frac{1 - \rho \left(\frac{\partial h}{\partial p} \right)_{\rho, Y_\mathfrak{s}}}{\rho^2 \left(\frac{\partial h}{\partial \rho} \right)_{p, Y_\mathfrak{s}}} \tag{3.92}$$

and adiabatic bulk modulus K.

3.2.5.1 Perfect Gas

If the fluid phases are perfect gases, the above relations simplify due to the particular equation of state

$$T = \frac{p}{\rho} \frac{M}{R} \tag{3.93}$$

with R as the universal gas constant and M as the molar mass of the mixture of the respective fluid phase. With the heat capacity ratio

$$\gamma = \frac{c_p}{c_v} \tag{3.94}$$

and c_v and c_p as the (constant) heat capacities at constant volume and constant pressure, as well as the relations

$$c_p - c_v = \frac{R}{M} \tag{3.95}$$

[13] The speed of sound is called frozen, if all the mass fractions $Y_\mathfrak{s}$ remain constant.

and - resulting from (3.94) and (3.95) -

$$c_v = \frac{1}{\gamma - 1}\frac{R}{M}, \qquad c_p = \frac{\gamma}{\gamma - 1}\frac{R}{M} \tag{3.96}$$

the general quantities on the left hand side of ***Tab. 3.1*** for arbitrary equations of state simplify to the expressions on the right hand side of ***Tab. 3.1*** for perfect gases. Due to the caloric equation of state

$$\rho e = \frac{p}{\gamma - 1} + \frac{1}{2}\rho\left(\vec{v}\cdot\vec{v}\right) + \mathcal{U} \tag{3.97}$$

for perfect gases the results from [95] are obtained. The only difference to [95] for perfect gases is, that in [95] the standard enthalpie of formation is contained in ρe, while here it is treated separately, considering the species balance (3.43b) with (3.53), leading to the caloric equation (3.97) and to the energy balance representation (3.43d) with (3.37) and (3.38d), the latter subject to (3.39). The resulting pressure formulation of the energy equation for perfect gases reads

$$\left(p\right)_t + \vec{v}\cdot\nabla p + \left(\gamma p\right)\left(\nabla\cdot\vec{v}\right) \;=\; \left(1-\gamma\right)\left[-\boldsymbol{\mathcal{T}} : \nabla\vec{v} + \nabla\cdot\vec{j}_q - \dot{q}_q + \dot{\mathfrak{q}}_c\right] \tag{3.98}$$

in which all quantities are discontinuous at the interface according to definition (3.17) as well. The left hand side of equation (3.98) corresponds to the ones obtained in [92] and [19].

3.2.6 Dimensional System

The resulting (dimensional) system reads

$$\begin{aligned}
&\left(\rho\right)_t && + \nabla\cdot\left(\rho\vec{v}\right) && && = 0 && (3.99a)\\
&\left(\rho Y_{\mathfrak{s}}\right)_t && + \nabla\cdot\left(\rho Y_{\mathfrak{s}}\vec{v}\right) && + \nabla\cdot\vec{j}_{\mathfrak{s}} && = \rho\varrho_{\mathfrak{s}} && (3.99b)\\
&\left(\rho\vec{v}\right)_t && + \nabla\cdot\left(\rho\vec{v}\circ\vec{v}\right) && + \nabla p - \nabla\cdot\boldsymbol{\mathcal{T}} && = \rho\vec{g} + \vec{\mathfrak{f}}_\sigma\delta_\Gamma && (3.99c)\\
&\left(p\right)_t && + \vec{v}\cdot\nabla p && + \left(\rho c^2\right)\left(\nabla\cdot\vec{v}\right) && = \Xi^{-1}\Big[-\boldsymbol{\mathcal{T}} : \nabla\vec{v} + \nabla\cdot\vec{j}_q && \\
& && && && \qquad -\dot{q}_q + \dot{\mathfrak{q}}_c] && (3.99d)\\
&\left(\phi\right)_t && + \vec{v}\cdot\nabla\phi && && = 0 && (3.99e)
\end{aligned}$$

Tab. 3.1: Simplifications for two-phase flow of perfect gases

Quantity	Perfect gas representation
$T = T\left(\rho, p, Y_{\mathfrak{s}}\right)$	$T = \frac{M}{R}\left(\frac{p}{\rho}\right)$
$u = u\left(\rho, p, Y_{\mathfrak{s}}\right) = \sum_{\mathfrak{s}=1}^{\mathcal{N}_{\mathfrak{s}}} Y_{\mathfrak{s}} u_{\mathfrak{s}}$	$u = \frac{1}{\gamma-1}\left(\frac{p}{\rho}\right)$
$h = u\left(\rho, p, Y_{\mathfrak{s}}\right) + \left(\frac{p}{\rho}\right)$	$h = \left(\frac{\gamma}{\gamma-1}\right)\left(\frac{p}{\rho}\right)$
$\rho\left(\frac{\partial h}{\partial p}\right)_{\rho, Y_{\mathfrak{s}}}$	$\left(\frac{\gamma}{\gamma-1}\right)$
$\rho\left(\frac{\partial h}{\partial \rho}\right)_{p, Y_{\mathfrak{s}}}$	$-\left(\frac{\gamma}{\gamma-1}\right)\left(\frac{p}{\rho}\right)$
$c_p = \left(\frac{\partial h}{\partial T}\right)_{p, Y_{\mathfrak{s}}}$	$c_p = \left(\frac{\gamma}{\gamma-1}\right)\frac{R}{M}$
$\Xi = 1 - \rho\left(\frac{\partial h}{\partial p}\right)_{\rho, Y_{\mathfrak{s}}}$	$\Xi = -\left(\frac{1}{\gamma-1}\right)$
$\chi = \frac{1}{K} = \frac{1}{\rho}\left(\frac{\partial \rho}{\partial p}\right)_{s, Y_{\mathfrak{s}}} = \frac{\Xi}{\rho}\left(\rho\left(\frac{\partial h}{\partial \rho}\right)_{p, Y_{\mathfrak{s}}}\right)^{-1}$	$\chi = \frac{1}{K} = \frac{1}{\gamma p}$
$c = \sqrt{\left(\frac{\partial p}{\partial \rho}\right)_{s, Y_{\mathfrak{s}}}} = \sqrt{\frac{\rho}{\Xi}\left(\frac{\partial h}{\partial \rho}\right)_{p, Y_{\mathfrak{s}}}} = \frac{1}{\sqrt{\chi\rho}}$	$c = \sqrt{\gamma(p/\rho)}$

under the assumptions made so far, with the energy equation in pressure formulation due to section 3.2.5 for general fluids. The system is completed by the relations specified in ***Tab. 3.3***, suitable initial and boundary conditions and the parameters given in ***Tab. 3.4***. The units of measurement of all quantities are given in ***Tab. 3.2*** and are based on the $\mathcal{N}_d = 4$ fundamental physical dimensions mass $[\mathrm{kg}]$, length $[\mathrm{m}]$, time $[\mathrm{s}]$ and temperature $[\mathrm{K}]$.

Tab. 3.2: Units of measurement according to the International System of Units (SI)

Symbol	t	$\vec{x}$	$\vec{v}$	ρ	p, K	Y	e, u, h	ϕ	T
Unit	s	m	$\frac{\mathrm{m}}{\mathrm{s}}$	$\frac{\mathrm{kg}}{\mathrm{m}^3}$	$\frac{\mathrm{kg}}{\mathrm{s}^2\mathrm{m}}$	$\frac{\mathrm{kg}}{\mathrm{kg}}$	$\frac{\mathrm{m}^2}{\mathrm{s}^2}$	$-$	K
Symbol	D, $\boldsymbol{D}$	$\vec{g}$	k, $\boldsymbol{K}$	$\mathfrak{b}$	μ, ζ	σ	κ, $\delta(x)$	Δh^0	ϱ
Unit	$\frac{\mathrm{m}^2}{\mathrm{s}}$	$\frac{\mathrm{m}}{\mathrm{s}^2}$	$\frac{\mathrm{kg\ m}}{\mathrm{s}^3\mathrm{K}}$	$\frac{\mathrm{kg}}{\mathrm{s}^3\mathrm{K}}$	$\frac{\mathrm{kg}}{\mathrm{s\ m}}$	$\frac{\mathrm{kg}}{\mathrm{s}^2}$	$\frac{1}{\mathrm{m}}$	$\frac{\mathrm{m}^2}{\mathrm{s}^2}$	$\frac{1}{\mathrm{s}}$

Tab. 3.3: Equations for specification of quantities in order to close system (3.99)

Quantity	$\vec{j}_q$	$\dot{\mathfrak{q}}_c$		$\vec{j}_{\mathfrak{E}}$	
Equation	(3.34)	(3.88)		(3.37)	
Quantity	T	$\dot{q}_{\mathfrak{s}}$	$h_{\mathfrak{s}}$	$\vec{j}_{\mathfrak{s}}$	$\varrho_{\mathfrak{s}}$
Equation	(3.41)	(3.89)	(3.42)	(3.36)	(3.40)
Quantity	c	$\boldsymbol{\mathcal{T}}$	$\vec{\mathfrak{f}}_\sigma$		
Equation	(3.91)	(3.31)	(3.79)		
Quantity	Ξ	$\boldsymbol{E}$	κ	$\vec{n}_\Gamma$	δ_Γ
Equation	(3.90)	(3.32)	(3.80)	(3.13) (3.9)	(3.14) (3.15)

Tab. 3.4: Parameters required in system (3.99)

Symbol	Description
μ	dynamic viscosity
ζ	bulk viscosity
g	gravitational acceleration
σ_Γ	surface tension coefficient[14]
K	bulk modulus
D	diffusive coefficient
k	thermal conductivity
$\mathfrak{h}$	heat transfer coefficient
Δh^0	enthalpie of formation w.r.t. molar mass

[14] Surface tension, in general, depends on the concentration C_Γ of **surf**ace **act**ive **a**gen**t**s on the interface according to

$$\sigma\left(C_\Gamma\right) = \sigma_\Gamma\left(1 - \frac{\sigma_C\left(C_\Gamma\right)}{\sigma_\Gamma}\right)$$

as, for example, given in [121] or [175], with σ_Γ as the surface tension coefficient of the clean interface. In this case $\sigma_C\left(C_\Gamma\right)$ is a **surfactant** concentration dependent function, which can depend on other state variables in addition, and, thus, C_Γ is a function of both space and time, for which an additional transport equation on the surface has to be solved. This is, however, beyond the scope of this work. **Surfactant**s are molecules, attached to the interface, changing the interfacial properties – such as surface tension – and various so-called surface tension - concentration isotherms, as e.g. in [50], are proposed in order to model the behavior of surface tension due to influences such as **surfactant**s.

3.3 Nondimensionalization

A non-dimensional version of the system (3.99) can be obtained by choosing $\mathcal{N}_q = 14$ scalar reference quantities

$$\check{t},\ \check{l},\ \check{v},\ \check{\rho},\ \check{\chi},\ \check{g},\ \check{\mu},\ \check{\sigma},\ \check{\varrho},\ \check{D},\ \check{k},\ \check{\mathfrak{h}},\ \check{c}_p,\ (\Delta\check{h}^0) \tag{3.100}$$

with length l and $\chi = 1/K$ as well as units of measurement according to ***Tab. 3.2***. With these reference quantities $(\mathcal{N}_q - \mathcal{N}_d) = 10$ non-dimensional characteristic numbers can be defined according to [95] as listed in table ***Tab. 3.5***, with $\mathcal{N}_d$ as given in section 3.2.6. With the non-dimensional space and time coordinates $\hat{\vec{x}}$ and $\hat{t}$, satisfying

$$\vec{x} = \check{l}\,\hat{\vec{x}}, \quad t = \check{t}\,\hat{t}, \tag{3.101}$$

and the resulting operators

$$(\blacksquare)_{\hat{t}} = \check{t}\,(\blacksquare)_t\,, \quad \hat{\nabla}\blacksquare = \check{l}\nabla\blacksquare, \quad \hat{\nabla}\cdot\blacksquare = \check{l}\nabla\cdot\blacksquare \tag{3.102}$$

as well as non-dimensional state variables

$$\begin{aligned} \hat{\rho} &= \tfrac{\rho}{\check{\rho}}, & \hat{\vec{v}} &= \tfrac{\vec{v}}{\check{v}}, & \hat{p} &= p\,\check{\chi}, \\ \hat{T} &= T\,\check{c}_p\check{\rho}\check{\chi}, & \hat{h} &= h\,\check{\rho}\check{\chi}, \end{aligned} \tag{3.103}$$

parameters

$$\begin{aligned} \hat{\mu} &= \tfrac{\mu}{\check{\mu}}, & \hat{\zeta} &= \tfrac{\zeta}{\check{\mu}}, & \hat{D} &= \tfrac{D}{\check{D}}, \\ \hat{\vec{g}} &= \tfrac{\vec{g}}{\check{g}}, & \hat{\sigma} &= \tfrac{\sigma}{\check{\sigma}}, & \hat{k} &= \tfrac{k}{\check{k}}, & \hat{\kappa} &= \kappa\,\check{l}, \end{aligned} \tag{3.104}$$

and additional quantities

$$\begin{aligned} \hat{c} &= c\,\sqrt{\check{\rho}\check{\chi}}, & \hat{\dot{q}}_q &= \dot{q}_q \tfrac{\check{c}_p\check{\rho}\check{\chi}\check{l}}{\check{\mathfrak{h}}}, & \hat{\varrho} &= \tfrac{\varrho}{\check{\varrho}}, \\ (\Delta\hat{h}^0) &= \tfrac{\Delta h^0}{\Delta\check{h}^0}, & \delta(\hat{x}) &= \delta(x)\,\check{l}, \end{aligned} \tag{3.105}$$

the non-dimensional system reads

$$\mathsf{Sr}\,(\,\hat{\rho}\,)_{\hat{t}} \quad + \hat{\nabla}\cdot\hat{\rho}\hat{\vec{v}} \qquad = \; 0 \tag{3.106a}$$

$$\mathsf{Sr}\,(\,\hat{\rho}Y_{\mathfrak{s}}\,)_{\hat{t}} \; + \hat{\nabla}\cdot\hat{\rho}Y_{\mathfrak{s}}\hat{\vec{v}} \quad = \; \mathsf{Da}\;\hat{\rho}\hat{\varrho}_{\mathfrak{s}} - \frac{1}{\mathsf{Re}\,\mathsf{Sc}}\hat{\nabla}\cdot\hat{\vec{j}}_{\mathfrak{s}} \tag{3.106b}$$

$$\mathsf{Sr}\left(\hat{\rho}\hat{\vec{v}}\right)_{\hat{t}} + \hat{\nabla}\cdot\hat{\rho}\hat{\vec{v}}\circ\hat{\vec{v}} \;\; = \;\; \frac{1}{\mathsf{Re}}\hat{\nabla}\cdot\hat{\boldsymbol{\mathcal{T}}} - \frac{1}{\mathsf{Ma}^2}\hat{\nabla}\hat{p} + \frac{1}{\mathsf{Fr}^2}\,\hat{\rho}\hat{\vec{g}} + \frac{1}{\mathsf{We}}\hat{\vec{\mathsf{f}}}_{\Gamma} \tag{3.106c}$$

$$\begin{aligned}\mathsf{Sr}\,(\,\hat{p}\,)_{\hat{t}} \quad + \;\hat{\vec{v}}\cdot\hat{\nabla}\hat{p} \;+ \;\hat{\rho}\,\hat{c}^2\left(\hat{\nabla}\cdot\hat{\vec{v}}\right) \;\; = \\ \Xi^{-1}\left[\frac{1}{\mathsf{Re}\,\mathsf{Pr}}\left(\hat{\nabla}\cdot\hat{\vec{j}}_q \;- \mathsf{Nu}\,\hat{\dot{q}}_q\right) + \sum_{\mathfrak{s}=1}^{\mathcal{N}_{\mathfrak{s}}}\hat{\dot{q}}_{\mathfrak{s}} - \mathsf{Ma}^2\left(\frac{1}{\mathsf{Re}}\left(\hat{\boldsymbol{\mathcal{T}}}:\hat{\nabla}\hat{\vec{v}}\right)\right)\right]\end{aligned} \tag{3.106d}$$

using the characteristic numbers from ***Tab. 3.5***. In system (3.106) the definition

Tab. 3.5: Non-dimensional characteristic numbers

Symbol	Definition	Description
Da	$\left(\check{\varrho}\;\check{l}\right)/\check{v}$	Damköhler number [15]
Fr	$\check{v}/\sqrt{\check{l}\;\check{g}}$	Froude number [16]
Ma	$\check{v}\sqrt{\check{\rho}\,\check{\chi}}$	Mach number [17]
Nu	$\left(\check{\mathfrak{h}}\;\check{l}\right)/\check{k}$	Nusselt number [18]
Pr	$\left(\check{\mu}\;\check{c}_p\right)/\check{k}$	Prandtl number [19]
Qr	$\left(\check{\rho}\,\check{\chi}\;\Delta\check{h}^0\right)$	Heat release parameter
Re	$\left(\check{\rho}\,\check{v}\,\check{l}\right)/\check{\mu}$	Reynolds number [20]
Sc	$\check{\mu}/\left(\check{\rho}\;\check{D}\right)$	Schmidt number [21]
Sr	$\check{l}/\left(\check{t}\;\check{v}\right)$	Strouhal number [22]
We	$\left(\check{\rho}\;\check{v}^2\;\check{l}\right)/\check{\sigma}$	Weber number [23]

$$\hat{\dot{q}}_{\mathfrak{s}} := \frac{1}{\mathsf{Re}\,\mathsf{Sc}} \left(\hat{\vec{j}}_{\mathfrak{s}} \cdot \hat{\nabla} \hat{h}_{\mathfrak{s}} \right) + \mathsf{Da} \left(\hat{h}_{\mathfrak{s}} + \mathsf{Qr} (\Delta \hat{h}^0)_{\mathfrak{s}} \right) \hat{\rho} \hat{\varrho}_{\mathfrak{s}} \tag{3.107}$$

is used and it is subject to suitable initial and domain boundary conditions, constraints[24]

$$\sum_{\mathfrak{s}=1}^{\mathcal{N}_{\mathfrak{s}}} Y_{\mathfrak{s}} = 1, \quad \sum_{\mathfrak{s}=1}^{\mathcal{N}_{\mathfrak{s}}} \hat{\vec{j}}_{\mathfrak{s}} = 0, \quad \sum_{\mathfrak{s}=1}^{\mathcal{N}_{\mathfrak{s}}} \hat{\rho} \hat{\varrho}_{\mathfrak{s}} = 0, \quad \sum_{\mathfrak{s}=1}^{\mathcal{N}_{\mathfrak{s}}} Y_{\mathfrak{s}} \hat{h}_{\mathfrak{s}} = \hat{h} \tag{3.108}$$

and non-dimensional versions of the quantities specified in ***Tab. 3.3***, as well as interface jump conditions

$$\left[\!\left[\hat{\vec{v}} \right]\!\right] = 0, \qquad \left[\!\left[\hat{\vec{j}}_{\mathfrak{s}} \right]\!\right] \cdot \vec{n}_\Gamma = 0, \qquad \left[\!\left[\hat{T} \right]\!\right] = 0$$

$$\begin{aligned}
&\frac{1}{\mathsf{Ma}^2} \left[\!\left[\hat{p} \right]\!\right] - \frac{1}{\mathsf{Re}} \left(\vec{n}_\Gamma \cdot \left[\!\left[\hat{\boldsymbol{\mathcal{T}}} \right]\!\right] \cdot \vec{n}_\Gamma \right) = \frac{1}{\mathsf{We}} \hat{\sigma} \hat{\kappa}, \\
&\frac{1}{\mathsf{Re}} \left((\boldsymbol{I} - \vec{n}_\Gamma \circ \vec{n}_\Gamma) \cdot \left[\!\left[\hat{\boldsymbol{\mathcal{T}}} \right]\!\right] \cdot \vec{n}_\Gamma \right) = \frac{1}{\mathsf{We}} \left((\boldsymbol{I} - \vec{n}_\Gamma \circ \vec{n}_\Gamma) \cdot \hat{\nabla} \right) \hat{\sigma}, \\
&\frac{1}{\mathsf{Ma}^2} \left[\!\left[\frac{1}{\hat{\rho}} \hat{\nabla} \hat{p} \cdot \vec{n}_\Gamma \right]\!\right] = \frac{1}{\mathsf{Re}} \left[\!\left[\frac{1}{\hat{\rho}} \hat{\nabla} \cdot \hat{\boldsymbol{\mathcal{T}}} \right]\!\right]
\end{aligned} \tag{3.109}$$

and the species discontinuity from (3.66).

[15] Ratio of reaction rate to convective mass transport rate.
[16] Ratio of kinetic to potential energy.
[17] Ratio of flow speed to speed of sound $c = \sqrt{K/\rho} = \frac{1}{\sqrt{\rho \chi}}$
[18] Ratio of heat transfer into the fluid to heat conduction within the fluid.
[19] Ratio of viscous diffusion rate to thermal diffusion rate.
[20] Ratio of inertial forces to viscous forces.
[21] Ratio of viscous diffusion rate to mass diffusion rate.
[22] Ratio of characteristic speed of vortex shedding to flow speed.
[23] Ratio of fluid inertia to surface tension.
[24] One of the species balances does not need to be solved, if the mass equation is solved in addition, since the sum of all species masses equals the total system mass.

3.4 Zero Mach Number Limit

The non-dimensional system (3.106) reveals, that singularities arise, if one or more of the non-dimensional characteristic numbers approach zero or infinity [95]. This implicates, according to [89], [90], [95], [154] and [181], that in these regimes standard methods for numerical simulation of compressible flow become (highly) inefficient or even fail. In the limit of vanishing Mach number ($\mathsf{Ma} \rightarrow 0$), assuming the other characteristic numbers from ***Tab. 3.5*** to remain finite and non-zero, the momentum equation becomes singular, since the pressure gradient term degenerates and becomes dominant. Preventing the Froude number Fr from vanishing[25] while $\mathsf{Ma} \rightarrow 0$ (which is the case in the pseudo-incompressible limit [46]), in particular, requires length scales $\check{l} := \mathfrak{H}\check{l}_{sc}$ to be small compared to the atmospheric pressure scale height[26] $\check{l}_{sc}$ with factor $\mathfrak{H} \rightarrow 0$ and $\check{t}$ to resolve the respective advective time scale with reference velocity $\check{v}$ as shown in [91] and [92] or also more generally in [153]. In case of $\mathsf{Ma} \rightarrow 0$ elliptic properties enter the hyperbolic-parabolic system of equations as shown in [150] and [151], and both reformulation of the governing equations and application of suitable numerical methods for solving these equations is required. Following the asymptotic analysis presented in [89], [95][27] and [111], a single-length-, single-time-scale asymptotic expansion of the primitive variables

$$\hat{\rho}\left(\hat{\vec{x}},\hat{t}\right) = \hat{\rho}^{(0)}\left(\hat{\vec{x}},\hat{t}\right) + \mathsf{Ma}\,\hat{\rho}^{(1)}\left(\hat{\vec{x}},\hat{t}\right) + \mathsf{Ma}^2\,\hat{\rho}^{(2)}\left(\hat{\vec{x}},\hat{t}\right) + ... \tag{3.110a}$$

$$\hat{p}\left(\hat{\vec{x}},\hat{t}\right) = \hat{p}^{(0)}\left(\hat{\vec{x}},\hat{t}\right) + \mathsf{Ma}\,\hat{p}^{(1)}\left(\hat{\vec{x}},\hat{t}\right) + \mathsf{Ma}^2\,\hat{p}^{(2)}\left(\hat{\vec{x}},\hat{t}\right) + ... \tag{3.110b}$$

$$\hat{\vec{v}}\left(\hat{\vec{x}},\hat{t}\right) = \hat{\vec{v}}^{(0)}\left(\hat{\vec{x}},\hat{t}\right) + \mathsf{Ma}\,\hat{\vec{v}}^{(1)}\left(\hat{\vec{x}},\hat{t}\right) + \mathsf{Ma}^2\,\hat{\vec{v}}^{(2)}\left(\hat{\vec{x}},\hat{t}\right) + ... \tag{3.110c}$$

$$Y_{\mathfrak{s}}\left(\hat{\vec{x}},\hat{t}\right) = Y_{\mathfrak{s}}^{(0)}\left(\hat{\vec{x}},\hat{t}\right) + \mathsf{Ma}\,Y_{\mathfrak{s}}^{(1)}\left(\hat{\vec{x}},\hat{t}\right) + \mathsf{Ma}^2\,Y_{\mathfrak{s}}^{(2)}\left(\hat{\vec{x}},\hat{t}\right) + ... \tag{3.110d}$$

$$\phi\left(\hat{\vec{x}},\hat{t}\right) = \phi^{(0)}\left(\hat{\vec{x}},\hat{t}\right) + \mathsf{Ma}\,\phi^{(1)}\left(\hat{\vec{x}},\hat{t}\right) + \mathsf{Ma}^2\,\phi^{(2)}\left(\hat{\vec{x}},\hat{t}\right) + ... \tag{3.110e}$$

[25] $\mathsf{Fr} \gg \mathsf{Ma}$ holds for vertical length scales of $\check{l} = 10m$ since $\check{l} \geqslant \left(\check{\rho}\check{\chi}\check{\vec{g}}\right)^{-1}$ has to hold such that $\mathsf{Fr} \leqslant \mathsf{Ma}$. For water at sea level conditions on earth this corresponds to about $\check{l}_{H_2O} \geqslant 208 \cdot 10^3 m$ due to $\check{\rho}_{H_2O} \approx 1000\frac{kg}{m^3}$, $\check{\chi}_{H_2O} \approx 4.8077 \cdot 10^{-10}\frac{m\,s^2}{kg}$ and $\check{\vec{g}} \approx 9.81\frac{m}{s^2}$, for air this corresponds to $\check{l}_{air} \geqslant 10.3 \cdot 10^3 m$ due to $\check{\rho}_{air} \approx 1\frac{kg}{m^3}$ and $\check{\chi}_{air} \approx 9.901 \cdot 10^{-6}\frac{m\,s^2}{kg}$. Thus, within the regime of $\check{l} = 10m$ the ratio $\frac{1}{\mathsf{Fr}^2}$ stays finite while $\frac{1}{\mathsf{Ma}^2} \rightarrow \infty$.

[26] The height above ground level, in which the atmospheric pressure has dropped by a factor of Euler's constant compared to ground level pressure: $p = \mathfrak{e}^{-1}p_{ground}$.

[27] It is important to note, that the asymptotic analysis does not provide a simplified system of equations, but establishes a way of how to discretize the full set of equations, while overcoming numerical difficulties arising in the zero Mach number limit.

in the Mach number Ma reveals the following hierarchy of equations after application to the system (3.106) including interface conditions (3.109) and separate collection of terms of equal order of magnitude in Ma:

- Order Ma^{-2}:

$$\hat{\nabla}\hat{p}^{(0)}\left(\hat{\vec{x}},\hat{t}\right) = 0 \tag{3.111}$$

$$\left[\!\left[\hat{p}^{(0)}\right]\!\right] = 0 \tag{3.112}$$

- Order Ma^{-1}:

$$\hat{\nabla}\hat{p}^{(1)}\left(\hat{\vec{x}},\hat{t}\right) = 0 \tag{3.113}$$

$$\left[\!\left[\hat{p}^{(1)}\right]\!\right] = 0 \tag{3.114}$$

- Order Ma^{0}:

The leading order system is

$$\mathsf{Sr}\left(\hat{\rho}^{(0)}\right)_{\hat{t}} + \hat{\nabla}\cdot\hat{\rho}^{(0)}\hat{\vec{v}}^{(0)} = 0 \tag{3.115a}$$

$$\mathsf{Sr}\left(\hat{\rho}^{(0)}Y_{\mathfrak{s}}^{(0)}\right)_{\hat{t}} + \hat{\nabla}\cdot\hat{\rho}^{(0)}Y_{\mathfrak{s}}^{(0)}\hat{\vec{v}}^{(0)} = \mathsf{Da}\,\hat{\rho}^{(0)}\hat{\varrho}_{\mathfrak{s}}^{(0)} - \frac{1}{\mathsf{Re}\,\mathsf{Sc}}\hat{\nabla}\cdot\hat{\vec{j}}_{\mathfrak{s}}^{(0)} \tag{3.115b}$$

$$\mathsf{Sr}\left(\hat{\rho}^{(0)}\hat{\vec{v}}^{(0)}\right)_{\hat{t}} + \hat{\nabla}\cdot\hat{\rho}^{(0)}\hat{\vec{v}}^{(0)}\circ\hat{\vec{v}}^{(0)} = \frac{1}{\mathsf{Re}}\hat{\nabla}\cdot\hat{\boldsymbol{\mathcal{T}}}^{(0)} - \hat{\nabla}\hat{p}^{(2)} + \frac{1}{\mathsf{Fr}^2}\,\hat{\rho}^{(0)}\hat{\vec{g}} + \frac{1}{\mathsf{We}}\vec{\mathfrak{f}}_{\Gamma} \tag{3.115c}$$

$$\mathsf{Sr}\left(\hat{p}^{(0)}\right)_{\hat{t}} + \hat{\vec{v}}^{(0)}\cdot\hat{\nabla}\hat{p}^{(0)} + \hat{\rho}^{(0)}\left(\hat{c}^{(0)}\right)^2\left(\hat{\nabla}\cdot\hat{\vec{v}}^{(0)}\right) = \frac{1}{\Xi^{(0)}}\left[\frac{1}{\mathsf{Re}\,\mathsf{Pr}}\left(\hat{\nabla}\cdot\hat{\vec{j}}_q^{(0)} - \mathsf{Nu}\,\hat{\dot{q}}_q\right) + \sum_{\mathfrak{s}=1}^{\mathcal{N}_{\mathfrak{s}}}\hat{\dot{q}}_{\mathfrak{s}}^{(0)}\right] \tag{3.115d}$$

with (3.107) as well as suitable initial and domain boundary conditions, con-

straints (3.108) for the $\blacksquare^{(0)}$ quantities and interface conditions

$$\left[\!\left[\hat{\vec{v}}^{(0)} \right]\!\right] = 0, \qquad \left[\!\left[\hat{\vec{j}}_{\mathfrak{s}}^{(0)} \right]\!\right] \cdot \vec{n}_\Gamma = 0, \qquad \left[\!\left[\hat{T}^{(0)} \right]\!\right] = 0,$$

$$\begin{aligned}
&\left[\!\left[\hat{p}^{(2)} \right]\!\right] - \frac{1}{\mathsf{Re}} \left(\vec{n}_\Gamma \cdot \left[\!\left[\hat{\boldsymbol{\mathcal{T}}}^{(0)} \right]\!\right] \cdot \vec{n}_\Gamma \right) = \frac{1}{\mathsf{We}} \hat{\sigma} \hat{\kappa}, \\
&\frac{1}{\mathsf{Re}} \left((\boldsymbol{I} - \vec{n}_\Gamma \circ \vec{n}_\Gamma) \cdot \left[\!\left[\hat{\boldsymbol{\mathcal{T}}}^{(0)} \right]\!\right] \cdot \vec{n}_\Gamma \right) = \frac{1}{\mathsf{We}} \left((\boldsymbol{I} - \vec{n}_\Gamma \circ \vec{n}_\Gamma) \cdot \hat{\nabla} \right) \hat{\sigma}, \\
&\left[\!\left[\frac{1}{\hat{\rho}^{(0)}} \hat{\nabla} \hat{p}^{(2)} \cdot \vec{n}_\Gamma \right]\!\right] = \frac{1}{\mathsf{Re}} \left[\!\left[\frac{1}{\hat{\rho}^{(0)}} \hat{\nabla} \cdot \hat{\boldsymbol{\mathcal{T}}}^{(0)} \right]\!\right]
\end{aligned} \tag{3.116}$$

including the leading order verions of (3.66).

As done in [90] and [95], various conclusions can be drawn from this result of the asymptotic analysis for fully conservative numerical solution to the full set of governing equations in the zero Mach number limit:

- The leading order pressure $\hat{p}^{(0)}$ turns out to be homogeneous in space and continuous across the interface Γ due to (3.111) and (3.112) and, thus, remains a function of time only:

  $$\hat{p}^{(0)} = \hat{p}^{(0)} \left(\hat{t} \right) \tag{3.117}$$

  Therefore only the partial derivative of the leading order pressure with respect to time remains in (3.115d) while the contribution involving the pressure gradient vanishes. Further, $\hat{p}^{(0)}$ does not appear in the momentum equation of the leading order system but only occurs in the energy equation and the equation(s) of state. Thus, $\hat{p}^{(0)}$ turns out to be the thermodynamic pressure. If $\hat{p}^{(0)} \left(\hat{t} \right)$, as function of time (only), is not known a priori, e.g. as the atmospheric pressure as in [133] for the pseudo-incompressible equations, $\left(\hat{p}^{(0)} \right)_{\hat{t}}$ can be determined via integration of (3.115d) over the entire computational

domain $\Omega^{\square}$ with boundary $\partial\Omega^{\square}$, yielding

$$\left(\hat{p}^{(0)}\right)_{\hat{t}} = -\frac{1}{\hat{\mathcal{X}}^{(0)}\,\mathsf{Sr}}\left[\int_{\partial\Omega^{\square}} \hat{\vec{v}}^{(0)}\cdot\vec{n}^{\square}\,\mathrm{d}\hat{A} + \frac{\mathsf{Nu}}{\mathsf{Re}\,\mathsf{Pr}}\int_{\Omega^{\square}}\frac{\hat{\chi}^{(0)}}{\Xi^{(0)}}\hat{\dot{q}}_q\,\mathrm{d}\hat{V}\right.$$
$$\left. - \frac{1}{\mathsf{Re}\,\mathsf{Pr}}\int_{\Omega^{\square}}\frac{\hat{\chi}^{(0)}}{\Xi^{(0)}}\left(\hat{\nabla}\cdot\hat{\vec{j}}_q^{(0)}\right)\,\mathrm{d}\hat{V} - \sum_{\mathfrak{s}=1}^{\mathcal{N}_{\mathfrak{s}}}\left(\int_{\Omega^{\square}}\frac{\hat{\chi}^{(0)}}{\Xi^{(0)}}\hat{\dot{q}}_{\mathfrak{s}}^{(0)}\,\mathrm{d}\hat{V}\right)\right] \tag{3.118}$$

with suitable domain boundary conditions, $\partial\Omega^{\square}$, A, V and $\vec{n}^{\square}$ as the outer domain boundary, its area, the volume of the computational domain and the outward-pointing unit normal vector with respect to $\partial\Omega^{\square}$, as well as

$$\hat{\mathcal{X}}^{(0)} := \int_{\Omega^{\square}}\hat{\chi}^{(0)}\,\mathrm{d}\hat{V} = \int_{\Omega^{\square}}\frac{1}{\hat{\rho}^{(0)}\left(\hat{c}^{(0)}\right)^2}\,\mathrm{d}\hat{V} \tag{3.119}$$

- The first order pressure $p^{(1)}$ is both homogeneous in space and continuous across the interface Γ due to (3.113) and (3.114) and, thus, remains a function of time only as well:

$$\hat{p}^{(1)} = \hat{p}^{(1)}\left(\hat{t}\right) \tag{3.120}$$

  A multi-length-, single-time-scale asymptotic analysis, performed in [89], identifies $\hat{p}^{(1)}$ as the acoustic pressure in the low Mach number regime. In the leading order system (3.115) for the zero Mach number limit, $\hat{p}^{(1)}$ does not appear at all and sound-wave propagation, which becomes unnoticeable for $\mathsf{Ma}\to 0$ as stated in [95], is excluded from the leading order system. Therefore sound propagation does not need to be treated by a numerical scheme for solving the leading order system. This allows for significantly larger time step sizes for explicit numerical methods and, thus, for less consumption of computational time, since stability of an explicit numerical method is not limited by the speed of sound-wave propagation anymore, but by the (significantly smaller) fluid velocity[28].

- The dynamic pressure $\hat{p}^{(2)}$ occurs in the leading order momentum equation, but not in the energy equation. Thus, momentum and energy equation decouple on cost of an extra unknown quantity $\hat{p}^{(2)}$. However, no Riemann problems need

[28] The speed of sound in water at 20^oC and sea level pressure is about $c_{H_2O} = 1482\frac{m}{s}$ (e.g. [40]). If an air bubble rises in a water column at a typical rise velocity of $\vec{v} = 0.2\frac{m}{s}$ (e.g. [36]), an explicit numerical method can treat this problem using a 7410 times larger time step size and, thus, the numerical method is 7410 times faster.

to be solved in the zero Mach number limit for determination of numerical fluxes, which allows for faster numerical methods due to less time consuming determination of advective fluxes, which is the most time consuming part of explicit methods.

The interface conditions for interface normal stresses and the interface normal pressure gradient in (3.116) also contain $\hat{p}^{(2)}$ only.

- As a result of the previous conclusions, pressure decomposition according to

$$\hat{p}\left(\hat{\vec{x}},\hat{t}\right) = \hat{P}_0\left(\hat{t}\right) + \mathsf{Ma}^2\,\hat{p}'\left(\hat{\vec{x}},\hat{t}\right) \tag{3.121}$$

with spatially homogeneous thermodynamic pressure $\hat{P}_0$ in the energy balance and the equation(s) of state and perturbation pressure $\hat{p}'$ in the momentum equation, the latter guaranteeing the velocity divergence constraint to be satisfied, is appropriate for solving the leading order system (3.115).

- A velocity divergence constraint

$$\hat{\nabla}\cdot\hat{\vec{v}} = -\mathsf{Sr}\frac{\left(\hat{P}_0\right)_{\hat{t}}}{\hat{\rho}\,\hat{c}^2} + \frac{\Xi^{-1}}{\hat{\rho}\,\hat{c}^2}\left[\frac{1}{\mathsf{Re}\,\mathsf{Pr}}\left(\hat{\nabla}\cdot\hat{\vec{j}}_q - \mathsf{Nu}\,\hat{q}_q\right) + \sum_{\mathfrak{s}=1}^{\mathcal{N}_\mathfrak{s}}\hat{\dot{q}}_\mathfrak{s}\right] \tag{3.122}$$

(omitting the leading order labels) arises as a consequence of energy conservation (not due to conservation of mass) and it is driven by energy conversion and transport processes, leading to compression or expansion and in consequence to density variations.

- At non-zero flow velocity, vanishing Mach number

$$\mathsf{Ma} := \frac{|\hat{\vec{v}}|}{\hat{c}} = |\hat{\vec{v}}|\sqrt{\hat{\rho}\hat{\chi}} \tag{3.123}$$

is governed by vanishing compressibility

$$\hat{\chi} = -\hat{\rho}\left(\frac{\partial\hat{\rho}^{-1}}{\partial\hat{p}}\right)_{\hat{s}} = \frac{1}{\hat{\rho}}\left(\frac{\partial\hat{\rho}}{\partial\hat{p}}\right)_{\hat{s}} \;\rightarrow\; 0 \tag{3.124}$$

and a resulting speed of sound

$$\hat{c} = \sqrt{(\hat{\rho}\hat{\chi})^{-1}} \;\rightarrow\; \infty \tag{3.125}$$

which is arbitrarily large, leading to the common incompressibility[29] constraint

$$\hat{\nabla} \cdot \hat{\vec{v}} = 0 \tag{3.126}$$

as result of the energy balance (3.115d). With that, system (3.115) corresponds to the zero Mach number variable density equations presented in [92], however, with the dynamic pressure $\hat{p}^{(2)} \equiv \hat{p}'$ instead of the Exner pressure (which is commonly used in meteorology frameworks as originally proposed in [46]) in the momentum equation, as for example done in [19] for the pseudo-incompressible equations[30]. The same result is obtained[31] for isothermal flow[32] in absence of chemical reactions and external heat sources (adiabatic system). Due to the constraint (3.126), conservation of mass reduces to

$$(\hat{\rho})_{\hat{t}} + \hat{\vec{v}} \cdot \hat{\nabla}\hat{\rho} = 0 \tag{3.127}$$

and if $\hat{\nabla}\hat{\rho} = \vec{0}$ initially, $(\hat{\rho})_{\hat{t}} = 0$ and $\hat{\nabla}\hat{\rho} = \vec{0}$ holds for all times and with that $\hat{\rho} = \text{const.}$ within each fluid phase. Note that in the present formulation (3.115) explicit knowledge of the equation of state (3.41) is only required for cases in which $\hat{\nabla} \cdot \hat{\vec{v}} \neq 0$ holds and contributions of heat conduction to the velocity divergence right hand side are considered, and/or chemical reactions, requiring knowledge of (3.40), are present, which is beyond the scope of the subsequent work. The benefit of the present variable density formulation is, that also zero Mach number flows, satisfying (3.126), can be computed, for which initially $\hat{\nabla}\hat{\rho} \neq \vec{0}$ holds (e.g. stratified flows), leading to non-zero density changes over time. In the rest of this chapter the more general divergence

[29] Incompressibility can only be assumed for liquid phases in fluidic multi-phase systems. However, in [19], for example, an approach for extension of numerical methods for incompressible flow to weakly compressible flow is presented, in which the arising Poisson problems for the elliptic contributions transform to Helmholtz problems. For slow gaseous flow – as, for example, for rising gas bubbles in a liquid – weak compressibility can be assumed, which is, however, beyond the scope of the discussion of the numerical method presented in part III. Further, as shown in [129], the interfacial dynamics are governed by the behavior of the heavier fluid the more, the larger the density ratio of the fluids is.

[30] The zero Mach number variable density equations are the small scale limit of the pseudo-incompressible equations and the limiting case of low Mach number asymptotics

[31] In general, the same result is obtained, if the right hand side terms of equation (3.115d) balance or each of them vanishes separately (as in the isothermal case without chemical reactions and external heat sources) – or a combination of both.

[32] In case of isothermal flow both $(T)_t = \left(\frac{\partial T}{\partial P_0}\right)(P_0)_t = 0$ and $\nabla T = \left(\frac{\partial T}{\partial P_0}\right)\nabla P_0 = 0$ hold; while the latter is always satisfied in the zero Mach number regime due to vanishing gradient of the background pressure, a constant temperature in time requires $(P_0)_t = 0$ for finite non-zero $\left(\frac{\partial T}{\partial P_0}\right)$; for ideal gas $\left(\frac{\partial T}{\partial P_0}\right) = \frac{M}{\rho R}$.

constraint (3.122) is kept, in order to also apply to flows with very small but non-zero Mach number, for which the above limit considerations including pressure decomposition apply as well.

3.5 Space-Integral Dimensional Leading Order System

The resulting integral dimensional leading order system (omitting the leading order labels for compactness)

$$\int_{\Omega(t)} (\,\rho\,)_t \,\mathrm{d}V \;+\; \oint_{\partial\Omega(t)} \rho\vec{v}\cdot\vec{n}\,\mathrm{d}A \;=\; 0 \tag{3.128a}$$

$$\int_{\Omega(t)} (\,\rho Y_{\mathfrak{s}}\,)_t \,\mathrm{d}V \;+\; \oint_{\partial\Omega(t)} \rho Y_{\mathfrak{s}}\vec{v}\cdot\vec{n}\,\mathrm{d}A \;=\; \int_{\Omega(t)} \rho\varrho_{\mathfrak{s}}\,\mathrm{d}V - \oint_{\partial\Omega(t)} \vec{j}_{\mathfrak{s}}\cdot\vec{n}\,\mathrm{d}A \tag{3.128b}$$

$$\int_{\Omega(t)} (\,\rho\vec{v}\,)_t \,\mathrm{d}V \;+\; \oint_{\partial\Omega(t)} \rho\vec{v}\circ\vec{v}\cdot\vec{n}\,\mathrm{d}A \;=\; \oint_{\partial\Omega(t)} \left(\boldsymbol{\mathcal{T}} - \boldsymbol{I}p^{'} + \boldsymbol{S}_{\Gamma}^{(\sigma)}\delta_{\Gamma}\right)\cdot\vec{n}\,\mathrm{d}A + \int_{\Omega(t)} \rho\vec{g}\,\mathrm{d}V \tag{3.128c}$$

$$\oint_{\partial\Omega(t)} \vec{v}\cdot\vec{n}\,\mathrm{d}A \;=\; \int_{\Omega(t)} \mathcal{D}\,\mathrm{d}V \tag{3.128d}$$

with

$$\mathcal{D} := -\frac{1}{\rho\, c^2}\left(\Xi^{-1}\dot{q} + (\,P_0\,)_t\right) \tag{3.129}$$

and

$$\dot{q} := \dot{q}_q - \nabla\cdot\vec{j}_q - \dot{q}_c \tag{3.130}$$

is obtained from system (3.115) after reverting the steps performed in order to obtain the non-dimensional system (3.106) from the original integral equations and considering (3.82) concerning the influence of surface tension. The pressure

$$p = P_0 + p^{'} \tag{3.131}$$

consists of the background pressure P_0 and small perturbations $p^{'}$ and is extended by the (reformulated) marker transport equation

from (3.12) and the jump conditions

$$\begin{aligned} &[\![\, \vec{v} \,]\!] = 0, \qquad \left[\!\!\left[\vec{j}_{\mathfrak{s}} \right]\!\!\right] \cdot \vec{n}_\Gamma = 0, \qquad [\![\, T \,]\!] = 0, \qquad [\![\, P_0 \,]\!] = 0, \\ &\left[\!\!\left[p^{'} \right]\!\!\right] - (\vec{n}_\Gamma \cdot [\![\, \boldsymbol{\mathcal{T}} \,]\!] \cdot \vec{n}_\Gamma) = \sigma\kappa, \\ &((\boldsymbol{I} - \vec{n}_\Gamma \circ \vec{n}_\Gamma) \cdot [\![\, \boldsymbol{\mathcal{T}} \,]\!] \cdot \vec{n}_\Gamma) = ((\boldsymbol{I} - \vec{n}_\Gamma \circ \vec{n}_\Gamma) \cdot \nabla)\, \sigma, \\ &\left[\!\!\left[\frac{1}{\rho} \nabla p^{'} \cdot \vec{n}_\Gamma \right]\!\!\right] = \left[\!\!\left[\frac{1}{\rho} \nabla \cdot \boldsymbol{\mathcal{T}} \right]\!\!\right] \end{aligned} \tag{3.132}$$

according to section 3.2.2 as dimensional form of the ones given in (3.116). The constraint (3.126) corresponds to $\mathcal{D} = 0$ in (3.128d), defined through (3.129).

3.6 Generalized Divergence Constraint

In [5], [6] and [7] a generalized velocity divergence constraint of type

$$\nabla \cdot (\mathcal{P}\vec{v}) \;=\; \mathcal{P}\left(\mathcal{S} - \frac{(\,P_0\,)_t}{\rho\, c^2}\right) \;=\; \mathcal{P}\left(\mathcal{S} - \frac{(\,\ln P_0\,)_t}{\widetilde{\gamma}(P_0)}\right) \tag{3.133}$$

with

$$\widetilde{\gamma}(p) := \frac{\rho \left(\frac{\partial h}{\partial \rho}\right)_{p, Y_{\mathfrak{s}}}}{\frac{p}{\rho}\, \Xi} \tag{3.134}$$

is derived for simulation of supernovae with arbitrary equation of state, based on the relation

$$\nabla \cdot \vec{v} + \frac{1}{\rho\, c^2}\, (\vec{v} \cdot \nabla P_0) \;=\; \frac{1}{\mathcal{P}} \nabla \cdot (\mathcal{P}\, \vec{v}) \;=\; \nabla \cdot \vec{v} + \frac{1}{\mathcal{P}}\, (\vec{v} \cdot \nabla \mathcal{P}) \tag{3.135}$$

from [5]. In equation (3.133)

$$\mathcal{S} \;=\; \frac{\Xi^{-1}}{\rho\, c^2} \dot{q} \;=\; \frac{\chi}{\Xi} \dot{q} \tag{3.136}$$

summarizes the sources related to heat production and conduction and $\mathcal{P}$ is a both space and time dependent quantity (called β_0 in [5], [6] and [7]). Note that by appli-

cation of the chain rule $(\,P_0\,)_t \equiv \left(\frac{\partial P_0}{\partial t}\right) = \left(\frac{\partial P_0}{\partial \mathcal{P}}\right)\left(\frac{\partial \mathcal{P}}{\partial t}\right) = \left(\frac{\partial P_0}{\partial \mathcal{P}}\right)(\,\mathcal{P}\,)_t$ the relation

$$(\,\mathcal{P}\,)_t = \left(\frac{\partial \mathcal{P}}{\partial P_0}\right)(\,P_0\,)_t \tag{3.137}$$

is obtained, which allows to recast equation (3.133) into the form

$$(\,\mathcal{P}\,)_t + \nabla\cdot(\mathcal{P}\vec{v}) \;=\; \mathcal{P}\mathcal{S} \tag{3.138}$$

with

$$\left(\frac{\partial \mathcal{P}}{\partial P_0}\right) = \frac{\mathcal{P}}{\rho\, c^2} \tag{3.139}$$

linking $\mathcal{P}$ to the background pressure P_0. For the small scale limit, with $\nabla P_0 = 0$ due to equation (3.111) with $P_0 \equiv p^{(0)}$, space-dependency of $\mathcal{P}$ vanishes due to $\nabla\mathcal{P} \equiv 0$ from relation (3.135) for arbitrary $\vec{v}$. The generalized integral pseudo-incompressible[33] type divergence constraint[34] then reads

$$\oint_{\partial\Omega} (\mathcal{P}\vec{v}\cdot\vec{n})\,\mathrm{d}A = \underbrace{-\,(\,P_0\,)_t \int_\Omega \frac{\Theta}{c^2}\,\mathrm{d}V \underbrace{-\int_\Omega \frac{\dot{q}\,\Theta}{\Xi\, c^2}\,\mathrm{d}V}_{=:\,\int_\Omega \mathcal{P}\mathcal{S}\,\mathrm{d}V}}_{=:\,\int_\Omega \mathcal{P}\mathcal{D}\,\mathrm{d}V} \tag{3.140}$$

with

$$\Theta(\theta) := \frac{\mathcal{P}}{\rho} \tag{3.141}$$

based on (3.128d) as function of potential temperature θ. Equation (3.140) is of the same type as the divergence constraint given in [134], with both a pressure dependent temporal derivative and a source term on the right hand side. The differential equation (3.139) can be solved for $\mathcal{P}$ via integration of

$$\int_{\check{\mathcal{P}}}^{\mathcal{P}} \frac{1}{\tilde{\mathcal{P}}}\,\mathrm{d}\tilde{\mathcal{P}} = \int_{\check{P}_0}^{P} \frac{1}{\rho\, c^2}\,\mathrm{d}\tilde{P}_0 \tag{3.142}$$

after separation of variables to yield

$$\mathcal{P} = \check{\mathcal{P}}\exp\left[\int_{\check{P}_0}^{P} \frac{1}{\rho\, c^2}\,\mathrm{d}\tilde{P}_0\right] \tag{3.143}$$

[33] In the pseudo-incompressible regime $\mathcal{P}$ depends on the (vertical) space coordinate(s), but not on time, while in the small scale limit $\mathcal{P}$ is independent of spatial variations (but might depend on time in analogy to the leading order pressure P_0).

[34] $\nabla\cdot\vec{v} = \mathcal{D} \;\Rightarrow\; \mathcal{P}\,\nabla\cdot\vec{v} = \mathcal{P}\mathcal{D} \;\Rightarrow\; \nabla\cdot\mathcal{P}\vec{v} = \mathcal{P}\mathcal{D}$

with corresponding reference quantities $\check{\mathcal{P}}$ and $\check{P}_0$. The right hand side integral of equation (3.143) can be evaluated, if the equation of state is specified, yielding that $\mathcal{P}$ is constant and homogeneous if P_0 is, as shown for perfect gas in the following. For incompressible flow $\mathcal{P}$ degenerates to a homogeneous constant auxilliary quantity $\check{\mathcal{P}}$ due to $\mathcal{D} = 0$ as consequence of $c \to \infty$.

3.6.1 Perfect Gas

For perfect gases, Θ from relation (3.141) can be shown to be the potential temperature

$$\Theta(\theta) \;=\; \theta \;=\; T\left(\frac{\check{P}_0}{P_0}\right)^{\frac{R}{Mc_p}} \;=\; \frac{P_0 M}{\rho R}\left(\frac{\check{P}_0}{P_0}\right)^{\frac{\gamma-1}{\gamma}} \tag{3.144}$$

as done in [92] for a non-dimensional setting in a meteorological framework or in [19], [133] and [134] for the dimensional case, yielding

$$\mathcal{P} \;=\; \rho\Theta \;=\; \frac{\check{P}_0 M}{R}\left(\frac{P_0}{\check{P}_0}\right)^{\frac{1}{\gamma}} = \check{\mathcal{P}}\left(\frac{P_0}{\check{P}_0}\right)^{\frac{1}{\gamma}} \tag{3.145}$$

with reference background pressure $\check{P}_0$. This result is also obtained from equation (3.143) with $\rho c^2 \equiv \gamma P_0$.

3.6.1.1 Time Derivative

The partial derivative of (3.145) with respect to time reads

$$\begin{aligned}
(\,\mathcal{P}\,)_t \;&=\; \left(\frac{\check{P}_0 M}{R}\left(\frac{P_0}{\check{P}_0}\right)^{\frac{1}{\gamma}}\right)_t \;=\; \frac{\check{P}_0{}^{\frac{\gamma-1}{\gamma}} M}{R}\left(P_0^{\frac{1}{\gamma}}\right)_t \\
&=\; \left(\frac{\check{P}_0}{P_0}\right)^{\frac{\gamma-1}{\gamma}} \frac{M}{\gamma R}\,(\,P_0\,)_t \overset{(3.144)}{=} \frac{\rho\theta}{\gamma P_0}\,(\,P_0\,)_t \overset{(3.141)}{=} \frac{\mathcal{P}}{\gamma P_0}\,(\,P_0\,)_t
\end{aligned} \tag{3.146}$$

if $(\check{P}_0{}^{\frac{\gamma-1}{\gamma}} M)$ is assumed to be time-independent and with that

$$(\,\ln P_0\,)_t = \gamma\,(\,\ln \mathcal{P}\,)_t \tag{3.147}$$

is obtained. With $\widetilde{\gamma}$ reducing to the pressure independent heat capacity ratio γ for ideal gases, finally

$$\frac{\mathcal{P}}{\gamma}\,(\,\ln P_0\,)_t = \mathcal{P}\,(\,\ln \mathcal{P}\,)_t = (\,\mathcal{P}\,)_t \tag{3.148}$$

results for the corresponding relation in equation (3.133). Thus, for ideal gas the expression containing the derivative of the leading order pressure with respect to time in (3.133) matches the respective expression given in [134].

3.6.1.2 Gradient

The gradient of $\mathcal{P}$ vanishes by construction if $\nabla P_0 = 0$ as shown above, which naturally includes ideal gases due to

$$\nabla \mathcal{P} = \nabla \left(\frac{\check{P}_0 M}{R} \left(\frac{P_0}{\check{P}_0} \right)^{\frac{1}{\gamma}} \right) \overset{(3.146)}{=} \frac{\mathcal{P}}{\gamma P_0} \nabla P_0 \tag{3.149}$$

which matches (3.135), requiring $(\check{P}_0{}^{\frac{\gamma-1}{\gamma}} M)$ to be homogeneous.

3.6.1.3 Interfacial Discontinuity

For the interfacial discontinuity

$$[\![\mathcal{P}]\!] = 0 \tag{3.150}$$

is obtained for the choice

$$\check{P}_0^{(-)} = P_0 \left(\left(\frac{M^{(+)}}{M^{(-)}} \right)^{\frac{\gamma^{(-)}}{(\gamma^{(-)}-1)}} \left(\frac{\check{P}_0^{(+)}}{P_0} \right)^{\frac{(\gamma^{(+)}-1)\gamma^{(-)}}{(\gamma^{(-)}-1)\gamma^{(+)}}} \right) \tag{3.151}$$

connecting the background pressures in the different fluid phases, which simplifies to

$$\check{P}_0^{(-)} = \left(\frac{M^{(+)}}{M^{(-)}} \right)^{\frac{\gamma}{(\gamma-1)}} \check{P}_0^{(+)} \tag{3.152}$$

in case of identical heat capacity ratios $\gamma = \gamma^{(+)} = \gamma^{(-)}$ in both phases. This result is obtained by subtracting the corresponding expression of $\mathcal{P}$ on both sides of the

interface according to

$$\begin{aligned}\llbracket \mathcal{P} \rrbracket = \mathcal{P}^{(+)} - \mathcal{P}^{(-)} &= \frac{1}{R}\left(\left(\check{P}_0^{\frac{\gamma-1}{\gamma}} M\, P_0^{\frac{1}{\gamma}}\right)^{(+)} - \left(\check{P}_0^{\frac{\gamma-1}{\gamma}} M\, P_0^{\frac{1}{\gamma}}\right)^{(-)}\right) \\ &= \frac{P_0}{R}\left(\left(\frac{\check{P}_0^{(+)}}{P_0}\right)^{\frac{\gamma^{(+)}-1}{\gamma^{(+)}}} M^{(+)} - \left(\frac{\check{P}_0^{(-)}}{P_0}\right)^{\frac{\gamma^{(-)}-1}{\gamma^{(-)}}} M^{(-)}\right)\end{aligned} \tag{3.153}$$

accounting for $\llbracket P_0 \rrbracket = 0$ due to relation (3.112).

Part III

BUILDING BLOCKS FOR A FULLY CONSERVATIVE NUMERICAL METHOD

4. CONCEPTS OF THE NUMERICAL METHOD

In this chapter the basic concepts of the numerical method are outlined, starting with an overview of projection methods, followed by the equations for Finite Volume methods. The latter are derived for arbitrary control volumes with piecewise smooth boundary segments, subsequently restricted to fix Cartesian grids and the equations for Cartesian grid cells, that are intersected by an interface with different states on either side of the interface, are derived.

4.1 Projection Method

In principle, there are two classes of methods for solving the governing equations for zero Mach number or incompressible flow as a special case of low Mach number flow ([3]), both containing elliptic properties. The first class introduces an artificial compressibility as introduced in [33], the second class consists of the various widely used pressure correction approaches. Among the latter, on the one hand there are iterative implicit methods, such as the PISO and SIMPLE algorithms (including variants SIMPLER and SIMPLEC) introduced in [139], on the other hand there are fractional step methods, that split the solution procedure into different sub-steps.

An overview of projection methods is, for example, given in [65] and a history about earlier versions can be found in [56]. Projection methods can be viewed as special case of fractional step methods, [184], in which the determination of the solution at the subsequent time level is split into different sub-steps, of which the final one projects a predicted solution onto the space of solutions that satisfy an elliptic constraint. As outlined in the introduction, projection methods are especially efficient at comparable accuracy to other approaches if applied to large scale computations, which are required for the Direct Numerical Simulation of practical problems, since each projection step in the corrector of the predictor-corrector scheme only requires solving of a linear problem for a scalar quantity per time step instead of solving large linear systems. Following [65], projection methods for incompressible flow (at con-

stant density) can be split into three different classes: pressure-correction methods, velocity-correction methods and consistent splitting schemes. Both pressure- and velocity-correction methods can be sub-dividied into non-incremental, incremental and rotational incremental versions, of which the non-incremental ones directly compute updated solutions of the unknown scalar quantity, the incremental ones compute corrections to the previous known solution with the latter considered for obtaining predicted data and the rotational incremental ones additionally apply a modified pressure update including viscous effects implicitely incorporating a consistent pressure boundary condition. Similar work is done in [30].

Starting with a sketch of the original projection method, more recenty versions, especially focussing on the variable density case, are given in the following.

4.1.1 Classical Projection Method

Classical projection methods solve the momentum equation

$$\vec{v}_t + \vec{v} \cdot \nabla \vec{v} + \frac{1}{\rho} \nabla p - \frac{\mu}{\rho} \nabla \cdot \nabla \vec{v} = 0 \tag{4.1}$$

for incompressible flow in non-conservative form with constant density ρ and constant dynamic viscosity μ in combination with the velocity divergence constraint

$$\nabla \cdot \vec{v} = 0 \tag{4.2}$$

due to conservation of mass by Helmholtz-Hodge decomposition of an arbitrary velocity field

$$\vec{v}^* = \vec{v}_{\text{sol}} + \vec{v}_{\text{irrot}} = \vec{v}_{\text{sol}} + \nabla \delta\pi \tag{4.3}$$

into a solenoidal velocity field $\vec{v}_{\text{sol}}$ and an irrotational velocity field $\vec{v}_{\text{irrot}}$, where the latter can be replaced by the gradient of a scalar $\delta\pi$ due to $\nabla \times \vec{v}_{\text{irrot}} = 0 \equiv \nabla \times \nabla \delta\pi$. The divergence of (4.3) leaves

$$\nabla \cdot \vec{v}^* = \nabla \cdot \vec{v}_{\text{irrot}} = \nabla \cdot \nabla \delta\pi \tag{4.4}$$

due to $\nabla \cdot \vec{v}_{\text{sol}} = 0$, which can be solved for $\delta\pi$ for given boundary conditions of $\delta\pi$ and a given velocity field $\vec{v}^*$. In the original non-incremental method [33, 34] the

latter is obtained from a predictor step solving

$$\vec{v}^* = \vec{v}^n - \Delta t \left(\vec{v} \cdot \nabla \vec{v} - \frac{\mu}{\rho} \nabla \cdot \nabla \vec{v} \right) \tag{4.5}$$

without contribution of the pressure forces. The final velocity is obtained by adding the pressure forces

$$\vec{v}^{n+1} = \vec{v}^* - \underbrace{\frac{\Delta t}{\rho} \nabla p^{n+1}}_{=: \nabla \delta\pi} \tag{4.6}$$

after determination of $\nabla \delta\pi$ according to (4.4) due to $\nabla \cdot \vec{v}^{n+1} = 0$.

As boundary condition for solid wall boundaries, for example, $\nabla p \cdot \vec{n}_\square = 0$ is obtained[1] due to $\vec{v} \cdot \vec{n}_\square = 0$ with $\vec{n}_\square$ as the normal vector to the domain boundary. However, as this boundary condition is not the true pressure boundary condition of the Navier-Stokes equations, accuracy is reduced at the boundary. Improvement can be achieved by two different actions:

- incremental methods involving suitable pressure updates according to [30] or [65] as sketched in the following section 4.1.2 can be applied: Improved accuracy of projection methods as discovered in [60] is shown in [30] or [65], if only pressure increments are computed by the projection step and old time level pressure information is already considered in the predictor step. As shown in [30], the resulting accuracy depends on the combination of chosen predictor pressure representation π, the boundary condition for the predicted velocity $\vec{v}^*$ and computation of the new pressure $p = \pi + \mathfrak{O}(\delta\pi)$ with $\delta\pi$ as solution to the Poisson problem and $\mathfrak{O}$ as a (linear) operator yielding the pressure increment from the incremental Poisson solution. This corresponds to the rotational incremental methods as introduced above.

- boundary tangential information due to viscous stresses can be incorporated in the pressure boundary condition: In [102] an approach for solving a Helmholtz-type problem on the domain boundary for determination of the boundary normal pressure boundary condition of the Poisson problem within the domain is presented, and well-posedness of the respective problem is shown. The resulting boundary normal pressure boundary condition for application to the Poisson problem of the projection contains boundary tangential information.

[1] If the right hand side of equation (5.128) is non-zero, but consists of the gravity vector, the right hand side of the vertical pressure boundary condition is $\vec{g} \cdot \vec{n}_\square$.

A corresponding equation for solid no-slip boundaries for the variable density case is derived in appendix section D.

4.1.2 Projection Method Variants

The second order accurate projection method for incompressible flows from [15] is extended to variable density flows with divergence constraint of type

$$\nabla \cdot \frac{1}{\rho^*} \nabla \partial\pi = \mathcal{D}^* \tag{4.7}$$

with known quantities indicated by $*$ in [17]. As the original method from [33], these two methods, however, suffer from pressure discretization related issues. In contrast to these discretely exact projection methods, in [8] an approximate projection is proposed, which is extended to variable density flows in [4]. A detailed summary is given in [150], which is also compactly reviewed in [180]. In the latter, a stable discretely exact non-incremenental pressure correction projection method on staggered grids is presented.

4.1.3 Generalized Projection Method

The generalized approximate projection method for enforcing the generalized divergence constraint (3.140) is presented in [92] for inviscid flow in the context of a generalized meteorological framework and in [5] and [6] for the low Mach number model of supernovae. Application of the respective two step corrector within the present method on a staggered grid is given in detail in sections 5.2.1 and 5.2.2. While for incompressible viscous flows with constant density approaches concerning an accurate explicit pressure update and an accurate pressure boundary condition are available as sketched in section 4.1.1, the situation yet is less clear for viscous zero Mach number flows with variable density and a suitable explicit pressure update remains to be found for a corresponding rotational form of the incremental pressure-correction method. Additionally, application of an approach for determination of an accurate pressure boundary condition including boundary tangential information due to viscous stresses for variable density flows as given in appendix section D for solid no-slip wall boundaries remains to be done, which is, however, beyond the scope of this work.

4.2 Finite Volume Method

Finite Volume methods are a natural choice of approximating conservation laws of the type (3.21), as they determine volume averages of the conserved quantities, based on numerical approximation of the fluxes across the control volume boundaries and the volume averages of the source terms. A general Finite Volume discretization of equation (3.21) in a time-dependent control volume $\Omega_\mathfrak{i}$ with index $\mathfrak{i}$ and $\mathcal{N}^{(\mathfrak{f})}$ smooth boundary segments in semi-discrete space integral representation[2] reads

$$\frac{\mathrm{d}}{\mathrm{d}t}\left(\int_{\Omega_\mathfrak{i}(t)} \rho\psi \,\mathrm{d}V\right) =$$

$$\frac{\mathrm{d}}{\mathrm{d}t}\left(\,\Delta V_\mathfrak{i}(t)\,\overline{\rho\psi}_\mathfrak{i}(t)\,\right) = \Delta V_\mathfrak{i}(t)\,\overline{\mathcal{Q}}_{(\rho\psi),\mathfrak{i}}(t) - \left(\sum_{\mathfrak{f}=1}^{\mathcal{N}^{(\mathfrak{f})}} \left(\Delta A_\mathfrak{f}(t)\,\overline{\mathcal{F}}_{(\rho\psi),\mathfrak{f}}(t)\right)\right)_\mathfrak{i} \tag{4.8}$$

after taking relation (3.2) into account, and

$$\begin{aligned}\overline{\rho\psi}_\mathfrak{i}^{(n+1)} = \overline{\rho\psi}_\mathfrak{i}^{(n)} &- \left(1 - \frac{\Delta V_\mathfrak{i}^{(n)}}{\Delta V_\mathfrak{i}^{(n+1)}}\right)\overline{\rho\psi}_\mathfrak{i}^{(n)} \\ &+ \frac{\Delta t}{\Delta V_\mathfrak{i}^{(n+1)}}\left(\widetilde{\mathcal{Q}}_{(\rho\psi),\mathfrak{i}} - \left(\sum_{\mathfrak{f}=1}^{\mathcal{N}^{(\mathfrak{f})}} \widetilde{\mathcal{F}}_{(\rho\psi),\mathfrak{f}}\right)_\mathfrak{i}\right)\end{aligned} \tag{4.9}$$

is obtained after integration over a time interval $\left(t^n, t^{n+1}\right)$ with size $\Delta t := t^{n+1} - t^n$ and time level index n in a fully discrete space-time integral representation. In equation (4.8) and (4.9)

$$\overline{\rho\psi}_\mathfrak{i}(t) := \frac{1}{\Delta V_\mathfrak{i}(t)}\int_{\Omega_\mathfrak{i}(t)} \rho\psi(\vec{x},t)\,\mathrm{d}V \tag{4.10}$$

is the integral average of $\rho\psi$ within the control volume $\Omega_\mathfrak{i}$, such that

$$\int_{t^n}^{t^{n+1}} \frac{\mathrm{d}}{\mathrm{d}t}\left(\,\Delta V_\mathfrak{i}(t)\,\overline{\rho\psi}_\mathfrak{i}(t)\,\right)\,\mathrm{d}t \;= \Delta V_\mathfrak{i}^{(n+1)}\overline{\rho\psi}_\mathfrak{i}^{(n+1)} - \Delta V_\mathfrak{i}^{(n)}\overline{\rho\psi}_\mathfrak{i}^{(n)} \tag{4.11}$$

[2] A discretization technique of the interfacial surface tension contribution to the momentum equation is discussed separately in section 6.6.

is obtained and $\widetilde{\mathcal{Q}}_{\mathfrak{i}}$ and $\widetilde{\mathcal{F}}_{\mathfrak{f}}$ are suitable spatio-temporal approximations

$$\widetilde{\mathcal{Q}}_{(\rho\psi),\mathfrak{i}} :\approx \frac{1}{\Delta t}\int_{t^n}^{t^{n+1}} \Delta V_{\mathfrak{i}}(t)\,\overline{\mathcal{Q}}_{(\rho\psi),\mathfrak{i}}(t)\,\mathrm{d}t \tag{4.12a}$$

$$\widetilde{\mathcal{F}}_{(\rho\psi),\mathfrak{f}} :\approx \frac{1}{\Delta t}\int_{t^n}^{t^{n+1}} \Delta A_{\mathfrak{f}}(t)\,\overline{\mathcal{F}}_{(\rho\psi),\mathfrak{f}}(t)\,\mathrm{d}t \tag{4.12b}$$

to the volume sources with approximation

$$\overline{\mathcal{Q}}_{(\rho\psi),\mathfrak{i}}(t) \;:\approx\; \overline{\dot{\mathfrak{q}}}_{(\rho\psi),\mathfrak{i}}(t) \;:=\; \frac{1}{\Delta V_{\mathfrak{i}}(t)}\int_{\Omega_{\mathfrak{i}}(t)} \dot{\mathfrak{q}}_{(\rho\psi)}(\vec{x},t)\,\mathrm{d}V \tag{4.13}$$

to the volume integral average and approximation

$$\overline{\mathcal{F}}_{(\rho\psi),\mathfrak{f}}(t) \;:\approx\; \overline{f}_{(\rho\psi),\mathfrak{f}}(t) \;:=\; \frac{1}{\Delta A_{\mathfrak{f}}(t)}\int_{\partial\Omega_{\mathfrak{f}}(t)} \left(\vec{f}_{(\rho\psi)} - \rho\psi\vec{w}\right)_{\mathfrak{f}}(\vec{x},t)\cdot\vec{n}_{\mathfrak{f}}(\vec{x},t)\,\mathrm{d}A \tag{4.14}$$

to the face integral average of the control volume boundary normal flux. If $\rho\psi$ represents the momentum density vector instead of a scalar quantity, $\vec{f}$ has to be replaced by the tensor $\boldsymbol{F}$ and $\overline{\dot{\mathfrak{q}}}$ by the vector $\overline{\vec{\dot{\mathfrak{q}}}}$, yielding average vectors in equations (4.12), (4.13) and (4.14).

4.2.1 Fix Cartesian Grid

The computational domain $\Omega^{\square}$ is sub-divided into $\mathcal{N}^{(\mathfrak{i})}$ finite control volumes $\Omega_{\mathfrak{i}}$, the computational grid, such that

$$\Omega^{\square} = \{\Omega_{\mathfrak{i}};\, \mathfrak{i} = 1..\mathcal{N}^{(\mathfrak{i})} \in \mathbb{N}\} \tag{4.15}$$

is satisfied. A Cartesian grid with grid cell size

$$\Delta V_{\mathfrak{i}}^{(\ell)}(t) := \int_{\Omega_{\mathfrak{i}}^{(\ell)}(t)} \mathrm{d}V = \mathfrak{h}^{(\ell)} \prod_{\mathfrak{d}=1}^{\mathfrak{D}} \mathfrak{c}_{\mathfrak{d}}(t) \tag{4.16}$$

and $\mathfrak{h}^{(\ell)}$ as the one-dimensional reference grid spacing of grid refinement level ℓ as well as $\mathfrak{c}_{\mathfrak{d}}$ as scaling factor in coordinate direction $\mathfrak{d}$ is used. The grid cells are assumed to be fixed within the considered time intervals, and therefore – allowing for only one grid refinement level and therefore omitting the index (ℓ) in the following – the time

dependence in (4.16) drops, reducing to

$$\Delta V_{\mathfrak{i}} = \mathfrak{h} \prod_{\mathfrak{d}=1}^{\mathfrak{D}} \mathfrak{c}_{\mathfrak{d}} = \prod_{\mathfrak{d}=1}^{\mathfrak{D}} \Delta x_{\mathfrak{d}} \tag{4.17}$$

with fixed ratio of grid cell extensions in the different coordinate directions. Time-invariant grid cells further imply, that the boundary of the grid cells does not move. Thus,

$$\vec{w} \equiv 0 \tag{4.18}$$

as well as

$$\frac{\mathrm{d}}{\mathrm{d}t} \left(\int_{\Omega_{\mathfrak{i}}} \rho\psi \, \mathrm{d}V \right) = \int_{\Omega_{\mathfrak{i}}} \frac{\partial \rho\psi}{\partial t} \, \mathrm{d}V \tag{4.19}$$

with now time-independent grid cells $\Omega_{\mathfrak{i}}$. The Finite Volume approximation (4.8) simplifies to

$$\frac{\mathrm{d}}{\mathrm{d}t} \left(\overline{\rho\psi}_{\mathfrak{i}}(t) \right) = \overline{\mathcal{Q}}_{(\rho\psi),\mathfrak{i}}(t) - \frac{1}{\mathfrak{h}} \left(\sum_{\mathfrak{d}=1}^{\mathfrak{D}} \frac{1}{\mathfrak{c}_{\mathfrak{d}}} \sum_{\mathfrak{w}=1}^{2} \overline{\mathcal{F}}_{(\rho\psi),\mathfrak{d},\mathfrak{w}}(t) \right)_{\mathfrak{i}} \tag{4.20}$$

and (4.9) to

$$\overline{\rho\psi}_{\mathfrak{i}}^{(n+1)} = \overline{\rho\psi}_{\mathfrak{i}}^{(n)} + \Delta t \left(\widetilde{\overline{\mathcal{Q}}}_{(\rho\psi),\mathfrak{i}} - \frac{1}{\mathfrak{h}} \left(\sum_{\mathfrak{d}=1}^{\mathfrak{D}} \frac{1}{\mathfrak{c}_{\mathfrak{d}}} \sum_{\mathfrak{w}=1}^{2} \widetilde{\overline{\mathcal{F}}}_{(\rho\psi),\mathfrak{d},\mathfrak{w}} \right)_{\mathfrak{i}} \right) \tag{4.21}$$

with spatio-temporal grid cell and grid cell face average approximations

$$\begin{aligned} \widetilde{\overline{\mathcal{Q}}}_{(\rho\psi),\mathfrak{i}} &:\approx \frac{1}{\Delta t} \int_{t^n}^{t^{n+1}} \overline{\mathcal{Q}}_{(\rho\psi),\mathfrak{i}}(t) \, \mathrm{d}t \\ &\approx \frac{1}{\Delta t} \int_{t^n}^{t^{n+1}} \overline{\dot{\mathfrak{q}}}_{(\rho\psi),\mathfrak{i}}(t) \, \mathrm{d}t \\ &= \frac{1}{\Delta t \, \Delta V_{\mathfrak{i}}} \int_{t^n}^{t^{n+1}} \int_{\Omega_{\mathfrak{i}}} \dot{\mathfrak{q}}_{(\rho\psi),\mathfrak{i}} \, \mathrm{d}V \, \mathrm{d}t \end{aligned} \tag{4.22a}$$

$$\begin{aligned}
\widetilde{\overline{\mathcal{F}}}_{(\rho\psi),\mathfrak{d},\mathfrak{w}} \;&:\approx\; \frac{1}{\Delta t}\int_{t^n}^{t^{n+1}} \overline{\mathcal{F}}_{(\rho\psi),\mathfrak{d},\mathfrak{w}}(t)\,\mathrm{d}t \\
&\approx\; \frac{1}{\Delta t}\int_{t^n}^{t^{n+1}} \overline{f}_{(\rho\psi),\mathfrak{d},\mathfrak{w}}(t)\,\mathrm{d}t \\
&=\; \frac{1}{\Delta t\,\Delta A_{\mathfrak{d}}}\int_{t^n}^{t^{n+1}}\int_{\partial\Omega_{\mathfrak{d},\mathfrak{w}}} \vec{f}_{(\rho\psi),\mathfrak{d},\mathfrak{w}}\cdot\vec{n}_{\mathfrak{d},\mathfrak{w}}\,\mathrm{d}A\,\mathrm{d}t
\end{aligned} \tag{4.22b}$$

for the source terms and the grid cell boundary fluxes, with

$$\overline{f}_{(\rho\psi),\mathfrak{d},\mathfrak{w}}(t) := \frac{1}{\Delta A_{\mathfrak{d}}}\int_{\partial\Omega_{\mathfrak{d},\mathfrak{w}}} \vec{f}_{(\rho\psi),\mathfrak{d},\mathfrak{w}}(\vec{x},t)\;\cdot\vec{n}_{\mathfrak{d},\mathfrak{w}}\,\mathrm{d}A \tag{4.23}$$

as the approximation to the simplified spatial grid cell face flux average due to (4.18), fixed outward-pointing face normal $\vec{n}_{\mathfrak{f}}$ and face area ΔA. In equation (4.21) the sum over all grid cell faces has been split into a sum over the coordinate directions with index $\mathfrak{d}$, and the location of the considered grid cell face $\partial\Omega_{\mathfrak{f}}$ with respect to the grid cell center in the respective coordinate direction, indexed $\mathfrak{w}$. Expressing the outward-pointing normal vector $\vec{n}_{\mathfrak{d},\mathfrak{w}}$, pointing in negative coordinate direction $\mathfrak{d}$ for $\mathfrak{w}=1$ and in positive coordinate direction $\mathfrak{d}$ for $\mathfrak{w}=2$, by the unit vector $\vec{\mathfrak{e}}_{\mathfrak{d}}$, pointing in positive coordinate direction d, relations (4.20) and (4.21) read

$$\frac{\mathrm{d}}{\mathrm{d}t}\left(\overline{\rho\psi}_{\mathfrak{i}}(t)\right) = \overline{\mathcal{Q}}_{(\rho\psi),\mathfrak{i}}(t) - \frac{1}{\mathfrak{h}}\left(\sum_{\mathfrak{d}=1}^{\mathfrak{d}}\frac{1}{\mathfrak{c}_{\mathfrak{d}}}\sum_{\mathfrak{w}=1}^{2}(-1)^{\mathfrak{w}}\,\overline{\mathcal{F}}_{(\rho\psi),\mathfrak{d},\mathfrak{w}}(t)\right)_{\mathfrak{i}} =: \mathfrak{L}_{\mathfrak{i}}^{\{1\}}(\rho\psi(t)) \tag{4.24}$$

and

$$\overline{\rho\psi}_{\mathfrak{i}}^{(n+1)} \;=\; \overline{\rho\psi}_{\mathfrak{i}}^{(n)} \;+\; \Delta t\left(\widetilde{\overline{\mathcal{Q}}}_{(\rho\psi),\mathfrak{i}} - \frac{1}{\mathfrak{h}}\left(\sum_{\mathfrak{d}=1}^{\mathfrak{d}}\frac{1}{\mathfrak{c}_{\mathfrak{d}}}\sum_{\mathfrak{w}=1}^{2}(-1)^{\mathfrak{w}}\,\widetilde{\overline{\mathcal{F}}}_{(\rho\psi),\mathfrak{d},\mathfrak{w}}\right)_{\mathfrak{i}}\right) \tag{4.25}$$

with spatial and spatio-temporal average flux approximations

$$\overline{\mathcal{F}}_{(\rho\psi),\mathfrak{d},\mathfrak{w}}(t) \;:\approx\; \frac{1}{\Delta A_{\mathfrak{d}}}\int_{\partial\Omega_{\mathfrak{d},\mathfrak{w}}} \vec{f}_{(\rho\psi),\mathfrak{d},\mathfrak{w}}(\vec{x},t)\;\cdot\vec{\mathfrak{e}}_{\mathfrak{d}}\,\mathrm{d}A \tag{4.26a}$$

$$\widetilde{\overline{\mathcal{F}}}_{(\rho\psi),\mathfrak{d},\mathfrak{w}} \;:\approx \frac{1}{\Delta t\,\Delta A_{\mathfrak{d}}}\int_{t^n}^{t^{n+1}}\int_{\partial\Omega_{\mathfrak{d},\mathfrak{w}}} \vec{f}_{(\rho\psi),\mathfrak{d},\mathfrak{w}}(\vec{x},t)\cdot\vec{\mathfrak{e}}_{\mathfrak{d}}\,\mathrm{d}A\,\mathrm{d}t \tag{4.26b}$$

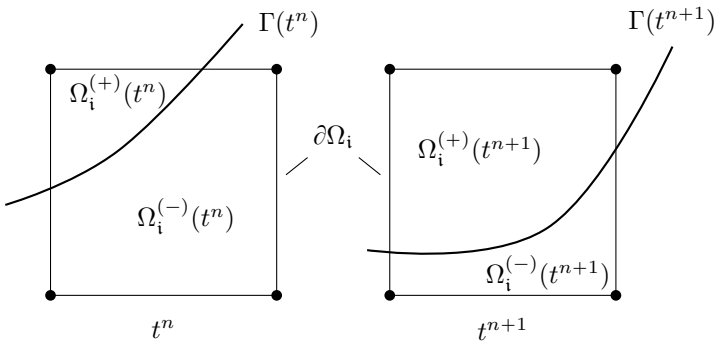

Fig. 4.1: Grid cell at two different points in time, t^n and t^{n+1}, intersected by a moving and/or deforming interface Γ

4.2.2 Cut Cells

While each Cartesian grid cell remains fixed within the considered time interval with invariant grid cell boundary, grid cell subsets $\Omega_\mathrm{i}^\varphi$ – if occupied by different fluid phases φ in case of an intersection of interface Γ and grid cell Ω_i as sketched in ***Fig. 4.1*** – remain time dependent as the interface can move and deform over time with $\vec{w}_\Gamma \neq 0$. Thus, if written in terms of these grid cell subsets, equation (4.20) yields

$$\frac{\mathrm{d}}{\mathrm{d}t}\left(\overline{\rho\psi}_\mathrm{i}(t)\right) = \sum_\varphi \overline{\mathcal{Q}}^\varphi_{(\rho\psi),\mathrm{i}}(t) - \frac{1}{\mathfrak{h}}\left(\sum_{\mathfrak{d}=1}^{\mathfrak{d}} \frac{1}{\mathfrak{c}_\mathfrak{d}} \sum_{\mathfrak{w}=1}^{2} (-1)^\mathfrak{w} \sum_\varphi \overline{\mathcal{F}}^\varphi_{(\rho\psi),\mathfrak{d},\mathfrak{w}}(t)\right)_\mathrm{i} =: \mathfrak{L}_\mathrm{i}^{\{2\}}\left(\rho\psi(t)\right) \tag{4.27}$$

for the semi-discrete space integral version, and equation (4.21) results in the fully discrete space-time integral version

$$\overline{\rho\psi}_\mathrm{i}^{(n+1)} = \overline{\rho\psi}_\mathrm{i}^{(n)} + \Delta t\left(\sum_\varphi \widetilde{\overline{\mathcal{Q}}}^\varphi_{(\rho\psi),\mathrm{i}} - \frac{1}{\mathfrak{h}}\left(\sum_{\mathfrak{d}=1}^{\mathfrak{d}} \frac{1}{\mathfrak{c}_\mathfrak{d}} \sum_{\mathfrak{w}=1}^{2} (-1)^\mathfrak{w} \sum_\varphi \widetilde{\overline{\mathcal{F}}}^\varphi_{(\rho\psi),\mathfrak{d},\mathfrak{w}}\right)_\mathrm{i}\right) \tag{4.28}$$

for the update of the integral average of $\rho\psi$ in the entire grid cell after considering relation (3.25). While $\widetilde{\overline{\mathcal{Q}}}^\varphi_{(\rho\psi),\mathrm{i}}$ and $\widetilde{\overline{\mathcal{F}}}^\varphi_{(\rho\psi),\mathfrak{d},\mathfrak{w}}$ approximate the expressions

$$\begin{aligned}\widetilde{\overline{\mathcal{Q}}}^\varphi_{(\rho\psi),\mathrm{i}} &:\approx \frac{1}{\Delta t\,\Delta V_\mathrm{i}} \int_{t^n}^{t^{n+1}} \int_{\Omega_\mathrm{i}^\varphi} \dot{\mathfrak{q}}^\varphi_{(\rho\psi),\mathrm{i}}\,\mathrm{d}V\,\mathrm{d}t \\ &= \frac{1}{\Delta t} \int_{t^n}^{t^{n+1}} \alpha_\mathrm{i}^\varphi(t)\,\bar{\dot{\mathfrak{q}}}^\varphi_{(\rho\psi),\mathrm{i}}(t)\,\mathrm{d}V\,\mathrm{d}t \end{aligned} \tag{4.29a}$$

$$\begin{aligned}\widetilde{\overline{\mathcal{F}}}^{\varphi}_{(\rho\psi),\mathfrak{d},\mathfrak{w}} &:\approx \frac{1}{\Delta t\,\Delta A_{\mathfrak{d}}}\int_{t^n}^{t^{n+1}}\int_{\partial\Omega^{(\varphi)}_{\mathfrak{d},\mathfrak{w}}} \vec{f}^{\varphi}_{(\rho\psi),\mathfrak{d},\mathfrak{w}}\cdot\vec{\mathfrak{e}}_{\mathfrak{d}}\,\mathrm{d}A\,\mathrm{d}t \\ &= \frac{1}{\Delta t}\int_{t^n}^{t^{n+1}} \beta^{\varphi}_{\mathfrak{d},\mathfrak{w}}(t)\;\overline{f}^{\varphi}_{(\rho\psi),\mathfrak{d},\mathfrak{w}}(t)\,\mathrm{d}t \qquad (4.29b)\end{aligned}$$

in (4.28), the integral averages, used in relations (4.29), read

$$\overline{\dot{\mathfrak{q}}}^{\varphi}_{(\rho\psi),\mathfrak{i}}(t) := \frac{1}{\Delta V^{\varphi}_{\mathfrak{i}}(t)}\int_{\Omega^{\varphi}_{\mathfrak{i}}}\dot{\mathfrak{q}}^{\varphi}_{(\rho\psi),\mathfrak{i}}\,\mathrm{d}V \qquad (4.30a)$$

$$\overline{f}^{\varphi}_{(\rho\psi),\mathfrak{d},\mathfrak{w}}(t) := \frac{1}{\Delta A^{\varphi}_{\mathfrak{d},\mathfrak{w}}(t)}\int_{\partial\Omega^{\varphi}_{\mathfrak{d},\mathfrak{w}}}\vec{f}^{\varphi}_{(\rho\psi),\mathfrak{d},\mathfrak{w}}\cdot\vec{\mathfrak{e}}_{\mathfrak{d}}\,\mathrm{d}A \qquad (4.30b)$$

for each grid cell subset. Further,

$$\alpha^{\varphi}_{\mathfrak{i}}(t) := \frac{\Delta V^{\varphi}_{\mathfrak{i}}(t)}{\Delta V_{\mathfrak{i}}} = \frac{\int_{\Omega^{\varphi}_{\mathfrak{i}}(t)}\mathrm{d}V}{\int_{\Omega_{\mathfrak{i}}}\mathrm{d}V} = \frac{\int_{\Omega_{\mathfrak{i}}}\phi^{\varphi}(t)\,\mathrm{d}V}{\int_{\Omega_{\mathfrak{i}}}\mathrm{d}V} \qquad (4.31a)$$

$$\beta^{\varphi}_{\mathfrak{d},\mathfrak{w}}(t) := \frac{\Delta A^{\varphi}_{\mathfrak{d},\mathfrak{w}}(t)}{\Delta A_{\mathfrak{d},\mathfrak{w}}} = \frac{\int_{\partial\Omega^{\varphi}_{\mathfrak{d},\mathfrak{w}}(t)}\mathrm{d}A}{\int_{\partial\Omega_{\mathfrak{d},\mathfrak{w}}}\mathrm{d}A} = \frac{\int_{\partial\Omega_{\mathfrak{d},\mathfrak{w}}}\phi^{\varphi}(t)\,\mathrm{d}A}{\int_{\partial\Omega_{\mathfrak{d},\mathfrak{w}}}\mathrm{d}A} \qquad (4.31b)$$

are the time-dependent grid cell (volume) fraction α in phase φ in cell $\mathfrak{i}$ and the time-dependent grid cell face (area) fraction β in phase φ on the cell face of grid cell $\mathfrak{i}$ with face normal in direction $\mathfrak{d}$ on cell side $\mathfrak{w}$ are defined. Using these definitions, corresponding time average fractions

$$\widetilde{\alpha}^{\varphi}_{\mathfrak{i}} := \frac{1}{\Delta t}\int_{t^n}^{t^{n+1}}\alpha^{\varphi}_{\mathfrak{i}}(t)\,\mathrm{d}t \qquad (4.32a)$$

$$\widetilde{\beta}^{\varphi}_{\mathfrak{d},\mathfrak{w}} := \frac{1}{\Delta t}\int_{t^n}^{t^{n+1}}\beta^{\varphi}_{\mathfrak{d},\mathfrak{w}}(t)\,\mathrm{d}t \qquad (4.32b)$$

can be specified, such that

$$\widetilde{\overline{\mathcal{Q}}}^{\varphi}_{(\rho\psi),\mathfrak{i}} \approx \widetilde{\alpha}^{\varphi}_{\mathfrak{i}}\;\overline{\overline{\mathcal{Q}}}^{\varphi}_{(\rho\psi),\mathfrak{i}} \qquad (4.33a)$$

$$\widetilde{\overline{\mathcal{F}}}^{\varphi}_{(\rho\psi),\mathfrak{d},\mathfrak{w}} \approx \widetilde{\beta}^{\varphi}_{\mathfrak{d},\mathfrak{w}}\;\overline{\overline{\mathcal{F}}}^{\varphi}_{(\rho\psi),\mathfrak{d},\mathfrak{w}} \qquad (4.33b)$$

with approximations

$$\overline{\overline{\mathcal{Q}}}^{\varphi}_{(\rho\psi),\mathfrak{i}} :\approx \frac{\int_{t^n}^{t^{n+1}}\alpha^{\varphi}_{\mathfrak{i}}(t)\;\overline{\mathcal{Q}}^{\varphi}_{(\rho\psi),\mathfrak{i}}(t)\,\mathrm{d}t}{\int_{t^n}^{t^{n+1}}\alpha^{\varphi}_{\mathfrak{i}}(t)\,\mathrm{d}t} \approx \frac{\int_{t^n}^{t^{n+1}}\alpha^{\varphi}_{\mathfrak{i}}(t)\;\overline{\dot{\mathfrak{q}}}^{\varphi}_{(\rho\psi),\mathfrak{i}}(t)\,\mathrm{d}t}{\int_{t^n}^{t^{n+1}}\alpha^{\varphi}_{\mathfrak{i}}(t)\,\mathrm{d}t} \qquad (4.34a)$$

$$\overline{\overline{\mathcal{F}}}^{\varphi}_{(\rho\psi),\mathfrak{d},\mathfrak{w}} \;:\approx\; \frac{\int_{t^n}^{t^{n+1}} \beta^{\varphi}_{\mathfrak{d},\mathfrak{w}}(t)\, \overline{\mathcal{F}}^{\varphi}_{(\rho\psi),\mathfrak{d},\mathfrak{w}}(t)\,\mathrm{d}t}{\int_{t^n}^{t^{n+1}} \beta^{\varphi}_{\mathfrak{d},\mathfrak{w}}(t)\,\mathrm{d}t} \approx \frac{\int_{t^n}^{t^{n+1}} \beta^{\varphi}_{\mathfrak{d},\mathfrak{w}}(t)\, \overline{f}^{\varphi}_{(\rho\psi),\mathfrak{d},\mathfrak{w}}(t)\,\mathrm{d}t}{\int_{t^n}^{t^{n+1}} \beta^{\varphi}_{\mathfrak{d},\mathfrak{w}}(t)\,\mathrm{d}t} \tag{4.34b}$$

For two-phase flow, in addition, the relations

$$\alpha_{\mathfrak{i}}^{(-)} = 1 - \alpha_{\mathfrak{i}}^{(+)} = 1 - \alpha_{\mathfrak{i}} \tag{4.35a}$$

$$\beta_{\mathfrak{d},\mathfrak{w}}^{(-)} = 1 - \beta_{\mathfrak{d},\mathfrak{w}}^{(+)} = 1 - \beta_{\mathfrak{d},\mathfrak{w}} \tag{4.35b}$$

and

$$\widetilde{\alpha}_{\mathfrak{i}}^{(-)} = 1 - \widetilde{\alpha}_{\mathfrak{i}}^{(+)} = 1 - \widetilde{\alpha}_{\mathfrak{i}} \tag{4.36a}$$

$$\widetilde{\beta}_{\mathfrak{d},\mathfrak{w}}^{(-)} = 1 - \widetilde{\beta}_{\mathfrak{d},\mathfrak{w}}^{(+)} = 1 - \widetilde{\beta}_{\mathfrak{d},\mathfrak{w}} \tag{4.36b}$$

apply, if the fluid phase, which is labeled $(+)$, is taken to be the reference phase with

$$\alpha_{\mathfrak{i}} \equiv \alpha_{\mathfrak{i}}^{(+)} \tag{4.37a}$$

$$\beta_{\mathfrak{d},\mathfrak{w}} \equiv \beta_{\mathfrak{d},\mathfrak{w}}^{(+)} \tag{4.37b}$$

as reference fractions[3].

[3] The choice of the reference phase is arbitrary and also the fluid phase labeled $(-)$ could have been chosen. Throughout this work, however, the reference phase is the one labeled $(+)$.

5. SINGLE-PHASE FINITE VOLUME PROJECTION METHOD

The underlying numerical method for single-phase flow, described in this chapter, applies without modification in each Finite Volume grid cell, that is sufficiently far away from the fluidic interface, assuming fluid properties of the respective fluid phase in this grid cell. The grid cell is sufficiently far away from the interface, if the entire stencil, required for numerical computation of all fluxes and source terms involved in determination of the update of the integral averages in the current grid cell, only consists of grid cells, that are entirely occupied by one of the fluid phases throughout the entire time interval considered. This applies for most of the computational domain (however, not necessarily to most of the computational grid cells if adaptive mesh refinement (AMR) is used). The single-phase set of equations corresponds to system (3.128) without the interfacial force in the momentum equation, without the transport of the phase indicator from section 3.1 and without the need of accounting for interfacial discontinuities in parameters as well as conserved and primitive quantities. Further, the divergence constraint (3.128d) is replaced by the generalized constraint (3.140). Since the resulting system (3.128) consists of both hyperbolic-parabolic and elliptic contributions, a fractional step method[1] – or, to be more specific, an approximate incremental-pressure projection method (according to the nomenclature in [30]) or incremental pressure-correction method (according to the classification in [65]) as utilized in [15], [180] and [92] – is applied, splitting the solution process into two main parts:

1. a spatially unsplit hyperbolic-parabolic predictor step $\mathfrak{P}$, ignoring both enforcement of the divergence constraint (3.140) and time dependence of the dynamic pressure $p^{'}$ and

2. an elliptic corrector step $\mathfrak{C}$, consisting of two approximate projection steps, similar to methods related to [15] as one type of projection methods as categorized in [30]:

[1] See, for example, [12] and [30] for an overview of such methods, including projection methods and pressure correction (or pressure Poisson) methods

(a) a corrector step $\mathfrak{C}_{(1)}$, enforcing the approximations of the advective flux averages to satisfy the divergence constraint

(b) a corrector step $\mathfrak{C}_{(2)}$, both enforcing the velocity divergence constraint and accounting for time-dependence of the dynamic pressure

Thus, the updated integral averages after a full numerical time step can be expressed as

$$\overline{\rho\psi}^{(n+1)} = \mathfrak{C}_{(2)} \left(\mathfrak{C}_{(1)} \left(\mathfrak{P} \left(\overline{\rho\psi}^{(n)} \right) \right) \right) \tag{5.1}$$

with superscript $n+1$ indicating values at the new time level and superscript n representing the time level at which known data is given. The steps

$$\overline{\rho\psi}^{(n+1),*} = \mathfrak{P} \left(\overline{\rho\psi}^{(n)} \right) \tag{5.2a}$$

$$\overline{\rho\psi}^{(n+1)} = \mathfrak{C} \left(\overline{\rho\psi}^{(n+1),*} \right) \tag{5.2b}$$

are described in the following sections 5.1 and 5.2, the sub-steps

$$\overline{\rho\psi}^{(n+1),**} = \mathfrak{C}_{(1)} \left(\overline{\rho\psi}^{(n+1),*} \right) \tag{5.3a}$$

$$\overline{\rho\psi}^{(n+1)} = \mathfrak{C}_{(2)} \left(\overline{\rho\psi}^{(n+1),**} \right) \tag{5.3b}$$

of the latter in sections 5.2.1 and 5.2.2.

5.1 Predictor

In this section the underlying predictor step is described, starting with reformulating a hyperbolic-parabolic auxiliary system of equations in sub-section 5.1.1. The subsequent description of the time integrator in sub-section 5.1.2 is followed by explanation of the computation of the applied numerical fluxes in sub-section 5.1.3, including the required state recovery at grid cell faces. Computation of source terms is sketched in sub-section 5.1.4, before the entire predictor procedure is summarized in sub-section 5.1.5. The predictor step advances the conserved quantities in time, ignoring on the one hand time dependence of the dynamic pressure in the momentum equation, on the other hand elliptic influences from the original system of equations, given via the divergence constraint.

5.1.1 Auxiliary System of Equations

In the predictor step elliptic contributions due to the velocity divergence constraint and time dependence of the dynamic pressure $p^{'}$ are neglected and the space integral single-phase hyperbolic-parabolic system

$$\frac{\mathrm{d}}{\mathrm{d}t}\left(\int_{\Omega}\mathcal{P}\vec{\Phi}\,\mathrm{d}V\right) = -\oint_{\partial\Omega}(\mathcal{P}\vec{v}\cdot\vec{n})\,\vec{\Phi}\,\mathrm{d}A + \oint_{\partial\Omega}\boldsymbol{J}_{\vec{\Phi}}\cdot\vec{n}\,\mathrm{d}A + \vec{\dot{\mathfrak{q}}}_{\vec{\Phi}} \tag{5.4}$$

with

$$\vec{\Phi} = \left(\frac{1}{\Theta}, \frac{Y_{\mathfrak{s}}}{\Theta}, \frac{\vec{v}}{\Theta}, 1\right) \tag{5.5a}$$

$$\boldsymbol{J}_{\vec{\Phi}} = \left[\vec{0}, -\vec{j}_{\mathfrak{s}}, \boldsymbol{\mathcal{T}}, \vec{0}\right] \tag{5.5b}$$

$$\vec{\dot{\mathfrak{q}}}_{\vec{\Phi}} = (0, \mathfrak{q}_{Y_{\mathfrak{s}}}, \vec{\mathfrak{q}}_{\vec{v}}, \mathfrak{q}_{\mathcal{P}}) \tag{5.5c}$$

and source terms

$$\mathfrak{q}_{Y_{\mathfrak{s}}} := \int_{\Omega}\rho\varrho_{\mathfrak{s}}\,\mathrm{d}V \tag{5.6a}$$

$$\vec{\mathfrak{q}}_{\vec{v}} := -\left(\oint_{\partial\Omega}\pi^{'}\vec{n}\,\mathrm{d}A + \int_{\Omega}\rho\nabla\mathcal{U}\,\mathrm{d}V\right) \tag{5.6b}$$

$$\mathfrak{q}_{\mathcal{P}} := -\left(\int_{\Omega}\frac{\mathcal{P}\,\chi\,\dot{q}}{\Xi}\,\mathrm{d}V\right) \tag{5.6c}$$

is solved instead, restricted to $\chi = 0$ for incompressible fluids, for which $\mathcal{P}$ reduces to a constant in both space and time and $\mathfrak{q}_{\mathcal{P}} = 0$ holds. The advective fluxes of all conserved quantities are referred to the common carrier flux $(\mathcal{P}\vec{v}\cdot\vec{n})$ from the left hand side of (3.140), with $\mathcal{P}\vec{\Phi}$ representing the conserved quantities and $\vec{\Phi}$ as the vector of pseudo-primitive variables according to ***Tab. 5.1***. Further, $\pi^{'}$ is the time-independent predictor pressure such that

$$p^{'}(\vec{x},t) = \pi^{'}(\vec{x}) + \partial p^{'}(\vec{x},t) \tag{5.7}$$

and $\mathcal{U}$ is the gravitational potential, while all the other quantities are defined as in section 3.

Tab. 5.1: Variable representations

	conserved	primitive	pseudo-primitive
mass	ρ	1	$\frac{1}{\theta}$
species mass	$\rho Y_{\mathfrak{s}}$	$Y_{\mathfrak{s}}$	$\frac{Y_{\mathfrak{s}}}{\theta}$
momentum	$\rho\vec{v}$	$\vec{v}$	$\frac{\vec{v}}{\theta}$
energy	$\mathcal{P}$	θ	1

Introduction of an additional partial derivative of $\mathcal{P}$ with respect to time on the left hand side of equation (3.140) during the predictor step offers the possibility of collecting deviations from the not yet enforced divergence constraint (3.140) in the expression $\mathfrak{E}$ in

$$\underbrace{\int_\Omega \left(\mathcal{P}\right)_t \,\mathrm{d}V}_{=:\,\mathfrak{E}} + \oint_{\partial\Omega} \left(\mathcal{P}\vec{v}\cdot\vec{n}\right)\,\mathrm{d}A = -\left[\left(P_0\right)_t \int_\Omega \mathcal{P}\chi\,\mathrm{d}V + \int_\Omega \frac{\mathcal{P}\,\chi\,\dot{q}}{\Xi}\,\mathrm{d}V\right] \tag{5.8}$$

since $\mathfrak{E} \overset{!}{=} 0$ is required after each full predictor-corrector time step. Collected deviations from zero in $\mathfrak{E}$ can be utilized in the subsequent corrector step to consistently correct divergence errors in the advective fluxes as $\mathfrak{E}$ contains the accumulated deviations of the carrier flux $(\mathcal{P}\vec{v}\cdot\vec{n})$, which effectively transports all conserved quantities, from the flux satisfying the divergence constraint.

5.1.2 Time Integration

Second order accurate time integration, summarized by

$$\overline{\mathcal{P}\vec{\Phi}}^{(n+1),*} = \mathfrak{P}\left(\overline{\mathcal{P}\vec{\Phi}}^{(n)}\right) + \mathcal{O}\left(\Delta t^3\right) \tag{5.9}$$

according to (5.2a), is performed via Strang operator splitting, proposed in [159], separating expressions treated implicitly from the ones treated explicitly. Depending on which of the following explicit ($\mathcal{E}$) and implicit ($\mathcal{I}$) approximations $\mathfrak{P}$ to solution

operators of sub-problems of (5.4) are the cheaper ones, either

$$\mathfrak{P}\left(\overline{\vec{\mathcal{P}\Phi}}^{(n)}\right) := \mathfrak{O}_{\mathcal{J}}\left(\Delta t/2\right)\left(\mathfrak{O}_{\mathcal{E}}\left(\Delta t/2\right)\left(\mathfrak{O}_{\mathcal{E}}^{\mathcal{C}}\left(\Delta t\right)\left(\mathfrak{O}_{\mathcal{E}}^{-1}\left(\Delta t/2\right)\left(\mathfrak{O}_{\mathcal{J}}^{-1}\left(\Delta t/2\right)\left(\overline{\vec{\mathcal{P}\Phi}}^{(n)}\right)\right)\right)\right)\right) \tag{5.10}$$

or

$$\mathfrak{P}\left(\overline{\vec{\mathcal{P}\Phi}}^{(n)}\right) := \mathfrak{O}_{\mathcal{E}}\left(\Delta t/2\right)\left(\mathfrak{O}_{\mathcal{J}}\left(\Delta t/2\right)\left(\mathfrak{O}_{\mathcal{E}}^{\mathcal{C}}\left(\Delta t\right)\left(\mathfrak{O}_{\mathcal{J}}^{-1}\left(\Delta t/2\right)\left(\mathfrak{O}_{\mathcal{E}}^{-1}\left(\Delta t/2\right)\left(\overline{\vec{\mathcal{P}\Phi}}^{(n)}\right)\right)\right)\right)\right) \tag{5.11}$$

is used for updating the integral averages of the conserved quantities, as, for example, given in [31] for splittings with more than two sub-operators involved. Superscript (n) represents the old time level of known data, $(n+1)$ the time level after time integration over the temporal increment $\Delta t = t^{n+1} - t^n$, superscript $*$ represents the state after the predictor step and $\mathfrak{O}^{-1}$ indicates reverse order of the right hand side sub-operators $\mathfrak{O}_{\blacksquare}^{\blacksquare}$ in ***Tab. 5.2***, in which an overview of reasonable treatment of the single sub-operators is given, depending on the (lowest local) Schmidt number $\mathsf{Sc}_{\mathfrak{s}}$ of the respective species $\mathfrak{s}$ and the (lowest local) Reynolds number $\mathsf{Re}_{\mathfrak{h}}$ with respect to the grid spacing $\mathfrak{h}$.

Tab. 5.2: Explicit ($\mathcal{E}$) and implicit ($\mathcal{J}$) treatment of sub-operators depending on the (lowest local) Schmidt number $\mathsf{Sc}_{\mathfrak{s}}$ and the (lowest local) Reynolds number $\mathsf{Re}_{\mathfrak{h}}$ with respect to the grid spacing $\mathfrak{h}$

	$\mathsf{Re}_{\mathfrak{h}} \geqslant \frac{\mathcal{C}_{\mathcal{A}}}{\mathcal{C}_{\mathcal{V}}}$	$\mathsf{Re}_{\mathfrak{h}} < \frac{\mathcal{C}_{\mathcal{A}}}{\mathcal{C}_{\mathcal{V}}}$
$\mathsf{Sc}_{\mathfrak{s}} \geqslant \frac{\mathcal{C}_{\mathcal{A}}}{\mathcal{C}_{\mathcal{D}}}\frac{1}{\mathsf{Re}_{\mathfrak{h}}}$	$\mathfrak{O}_{\mathcal{E}} = \mathfrak{O}_{\mathcal{E}}^{\mathcal{A}}\,\mathfrak{O}_{\mathcal{E}}^{\mathcal{V}}\,\mathfrak{O}_{\mathcal{E}}^{\mathcal{D}}$ $-$	$\mathfrak{O}_{\mathcal{E}} = \mathfrak{O}_{\mathcal{E}}^{\mathcal{A}}\,\mathfrak{O}_{\mathcal{E}}^{\mathcal{D}}$ $\mathfrak{O}_{\mathcal{J}} := \mathfrak{O}_{\mathcal{J}}^{\mathcal{D}}$
$\mathsf{Sc}_{\mathfrak{s}} < \frac{\mathcal{C}_{\mathcal{A}}}{\mathcal{C}_{\mathcal{D}}}\frac{1}{\mathsf{Re}_{\mathfrak{h}}}$	$\mathfrak{O}_{\mathcal{E}} = \mathfrak{O}_{\mathcal{E}}^{\mathcal{A}}\,\mathfrak{O}_{\mathcal{E}}^{\mathcal{V}}$ $\mathfrak{O}_{\mathcal{J}} := \mathfrak{O}_{\mathcal{J}}^{\mathcal{D}}$	$\mathfrak{O}_{\mathcal{E}} = \mathfrak{O}_{\mathcal{E}}^{\mathcal{A}}$ $\mathfrak{O}_{\mathcal{J}} := \mathfrak{O}_{\mathcal{J}}^{\mathcal{V}}\,\mathfrak{O}_{\mathcal{J}}^{\mathcal{D}}$

The subdivisions in ***Tab. 5.2*** with superscripts $\mathcal{A}$, $\mathcal{V}$ and $\mathcal{D}$ for hyperbolic, viscous and (other) diffusive effects are derived based on the maximum allowable stable ex-

plicit time steps of the single contributions, with $\mathcal{C}_\mathcal{A}$, $\mathcal{C}_\mathcal{V}$ and $\mathcal{C}_\mathcal{D}$ as defined in section 5.1.2.1. While hyperbolic contributions, such as advection, are always treated explicitly, treatment of parabolic contributions, such as species diffusion or friction (corresponding to momentum diffusion), depends on the respective time step restrictions due to explicit stability limits as given in section 5.1.2.1. If the maximum allowable explicit time step of a parabolic contribution is larger than the maximum allowable time step due to advection, the parabolic contribution can be treated explicitly as well. However, if it is smaller than the maximum allowable advective time step, implicit treatment of the respective contribution is cheaper and preferred. If the type of treatment of the different contributions can not be switched during the computation, the decision on the respective type has to be done in advance. As the local Reynolds and Schmidt numbers change during the computation, explicit treatment of the parabolic contributions is only reasonable in case the respective conditions in ***Tab. 5.2*** are fulfilled throughout the entire computation – for example if $\mathsf{Re}_\mathfrak{h} \gg \mathcal{C}_\mathcal{A}/\mathcal{C}_\mathcal{V}$ and/or $\min_\mathfrak{s} \mathsf{Sc}_\mathfrak{s} \gg \mathcal{C}_\mathcal{A}/\left(\mathcal{C}_\mathcal{V}\,\mathsf{Re}_\mathfrak{h}\right)$ – since otherwise the maximum allowable time step size can become very small.

The operator approximation $\Phi_\mathcal{E}^\mathcal{C}$ in (5.10) and (5.11) represents explicitly treated chemical reactions, entering the system (3.128) via the volume source $\rho\varrho_\mathfrak{s}$ in equation (3.128b). As the latter, if present, can become very expensive for larger numbers of species and advanced reaction models, $\Phi_\mathcal{E}^\mathcal{C}$ is always kept the "center" operator, since due to

$$\Phi_\mathcal{E}^\mathcal{C}\left(\Delta t\right) \equiv \Phi_\mathcal{E}^\mathcal{C}\left(\Delta t/2\right)\Phi_\mathcal{E}^{\mathcal{C}\,-1}\left(\Delta t/2\right) \equiv \Phi_\mathcal{E}^\mathcal{C}\left(\Delta t/2\right)\Phi_\mathcal{E}^\mathcal{C}\left(\Delta t/2\right) \tag{5.12}$$

it only needs to be evaluated once per time step, if done that way. Including chemical reactions into the numerical method is subject of current work and therefore not discussed further in the following. Preliminary studies have been done in [61]. In **absence of chemical reactions** the respective species sources vanish ($\varrho_\mathfrak{s} = 0$), the operator $\Phi_\mathcal{E}^\mathcal{C}$ drops and parameters such as D or μ are assumed to be space and time independent constants. In section 5.1.2.1 the explicit time step size limits of the different contributions are given, defining $\mathcal{C}_\mathcal{A}$, $\mathcal{C}_\mathcal{V}$ and $\mathcal{C}_\mathcal{D}$ in ***Tab. 5.2***, before the explicit time integration scheme is described in section 5.1.2.2 and the implicit one in section 5.1.2.3.

5.1.2.1 Time Step Restriction

In explicit methods, stability conditions, which restrict the size of the maximum allowable time step, need to be satisfied. For the latter

$$\Delta t \leqslant \Delta t_{\text{max}}^{\{1\}} \tag{5.13}$$

has to hold, with

$$\Delta t_{\text{max}}^{\{1\}} := \min\left(\Delta t_{\mathcal{A}},\ \Delta t_{\mathcal{V}},\ \min_{\mathfrak{s}}\left(\Delta t_{\mathcal{D},\mathfrak{s}}\right),\ \Delta t_{\mathcal{G}},\ \Delta t_{\mathcal{X}}\right) \tag{5.14}$$

as its total upper bound for single-phase flow, upper bounds $\Delta t_{\mathcal{A}}$, $\Delta t_{\mathcal{V}}$, $\Delta t_{\mathcal{D},\mathfrak{s}}$ and $\Delta t_{\mathcal{G}}$ for explicit treatment of the different physical effects as given in ***Tab. 5.3*** with $\mathfrak{d}$ as the number of spatial dimensions and $\Delta t_{\mathcal{X}}$ as an arbitrarily prescribed value.

Tab. 5.3: Explicit time step restrictions due to different physical effects

advection[2]	$\Delta t_{\mathcal{A}} \leqslant \mathcal{C}_{\mathcal{A}} \min_{\Omega}\left(\frac{\mathfrak{c}_{\mathfrak{d}}}{\lvert\vec{v}\rvert}\right) \mathfrak{h}$	$\mathcal{C}_{\mathcal{A}} := \frac{1}{\mathfrak{d}}$
friction[3]	$\Delta t_{\mathcal{V}} \leqslant \mathcal{C}_{\mathcal{V}} \min_{\Omega}\left(\frac{\rho \mathfrak{c}_{\mathfrak{d}}^2}{\mu}\right) \mathfrak{h}^2$	$\mathcal{C}_{\mathcal{V}} := \frac{1}{2\mathfrak{d}}$
diffusion[4]	$\Delta t_{\mathcal{D},\mathfrak{s}} \leqslant \mathcal{C}_{\mathcal{D}} \min_{\Omega}\left(\frac{\mathfrak{c}_{\mathfrak{d}}^2}{D_{\mathfrak{s}}}\right) \mathfrak{h}^2$	$\mathcal{C}_{\mathcal{D}} := \frac{1}{2\mathfrak{d}}$
gravity[5]	$\Delta t_{\mathcal{G}} \leqslant \mathcal{C}_{\mathcal{G}} \min_{\Omega}\left(\sqrt{\frac{\mathfrak{c}_{\mathfrak{d}}}{\lvert\vec{g}\rvert}}\right) \mathfrak{h}^{\frac{1}{2}}$	$\mathcal{C}_{\mathcal{G}} \equiv \sqrt{\mathcal{C}_{\mathcal{A}}}$

Due to the relations from ***Tab. 5.3*** dependencies on the time step size Δt are also denoted in terms of $\mathfrak{h}$ in the following.

[2] $\mathcal{C}_{\mathcal{A}}$ is the CFL number according to [37]; the maximum allowable $\mathcal{C}_{\mathcal{A}}$ depends, among others, on the time integration scheme and on the way of spatial state reconstruction, e.g. if fully multi-dimensional spatial reconstruction or dimension-by-dimension reconstruction is used as, for example, described in [150]. Details on stability limits for Runge-Kutta methods can be found in e.g. [75].

[3] In [167] the scaling $\mathcal{C}_{\mathcal{V}}$ is chosen to be $\frac{3}{14}$, in [190] it is $\frac{1}{2}$.

[4] Explicit diffusive time step restriction is e.g. given in [75].

[5] The constraint due to gravity can be derived by replacing the maximum velocity in the definition of the CFL number by the gravitational acceleration times the maximum allowable time step size $\Delta t_{\mathcal{G}}$ and solving for $\Delta t_{\mathcal{G}}$: $\Delta t_{\mathcal{G}} \leqslant \mathcal{C}_{\mathcal{A}} \min_{\Omega}\left(\frac{\mathfrak{c}_{\mathfrak{d}}}{\lvert\vec{g}\rvert \Delta t_{\mathcal{G}}}\right) \mathfrak{h} \quad \Rightarrow \quad \Delta t_{\mathcal{G}} \leqslant \mathcal{C}_{\mathcal{G}} \left(\frac{\mathfrak{h}}{\lvert\vec{g}\rvert} \min_{\Omega}\left(\mathfrak{c}_{\mathfrak{d}}\right)\right)^{1/2}$.

5.1.2.2 Explicit Time Integration Scheme

In contrast to [92] and [150], where spatial Strang operator splitting is used for explicit time integration of the hyperbolic part (5.4) of system (3.128), the present method follows the unsplit method-of-lines approach – as done in [151] and originally proposed in [148] – for approximation of (5.4) via $\mathfrak{O}_{\mathcal{E}}$. Applying the method-of-lines, the approximation (4.24) of the semi-discrete governing equations – discretized in space while kept continuous in time – is integrated on the Cartesian grid in the continuous variable, time t, via an integrator for ordinary differential equations. Second order accurate time integration can be performed using an explicit two stage strong stability preserving Runge-Kutta (SPP-RK2) type approach as given in [62] or – adapted to Finite Volume methods – in [106], requiring two evaluations of the numerical fluxes per time step for obtaining second order accuracy. In general, Runge-Kutta methods for time integration of equation (4.24) read

$$\rho\psi_{\mathfrak{i}}^{(m+1)} = \underbrace{\rho\psi_{\mathfrak{i}}^{(m)} + \Delta\mathfrak{t} \sum_{\mathfrak{n}=1}^{\mathcal{N}^{\bullet}} \left(\mathfrak{b}_{\mathfrak{n}} \, \mathfrak{K}_{\mathfrak{i},\mathfrak{n}}^{\{1\}} \right)}_{= \mathfrak{O}_{\mathcal{E},\mathfrak{i}}^{(\mathfrak{p})}\left(\rho\psi^{(m)}\right)} + \mathcal{O}\left(\Delta t^{\,\mathfrak{p}+1}\right) \tag{5.15}$$

with exponent $\mathfrak{p}$ indicating the convergence order,

$$\mathfrak{K}_{\mathfrak{i},\mathfrak{n}}^{\{1\}} := \mathfrak{L}_{\mathfrak{i}}^{\{1\}} \left(\rho\psi_{\mathfrak{n}}^{\bullet}\right) \tag{5.16}$$

with operator $\mathfrak{L}_{\mathfrak{i}}^{\{1\}}$ representing the discrete explicitly treated single-phase contributions to the right hand side of equation (5.4) according to (4.24) (with $\mathcal{P}\Phi \equiv \rho\psi$ and Φ as any component of $\vec{\Phi}$) and

$$\rho\psi_{\mathfrak{i},\mathfrak{n}}^{\bullet} := \begin{cases} \rho\psi_{\mathfrak{i}}^{(m)} & \mathfrak{n} = 1 \\ \rho\psi_{\mathfrak{i}}^{(m)} + \Delta\mathfrak{t} \, \sum_{\tilde{\mathfrak{n}}=1}^{\mathcal{N}^{\bullet}} \mathfrak{a}_{\mathfrak{n},\tilde{\mathfrak{n}}} \, \mathfrak{K}_{\mathfrak{i},\tilde{\mathfrak{n}}}^{\{1\}} & \mathfrak{n} > 1 \end{cases} \tag{5.17}$$

where $\Delta\mathfrak{t}$ represents the size of the pseudo time step[6], m indicates the pseudo time level at which data is given and $m+1$ indicates the pseudo time level at which data has to be determined. For the subset of explicit methods

$$\mathfrak{a}_{\mathfrak{n},\tilde{\mathfrak{n}}} = 0 \quad \forall \quad \mathfrak{n} \leqslant \tilde{\mathfrak{n}} \tag{5.18}$$

[6] If, for example, the operator $\mathfrak{O}_{\mathcal{E}}$ is applied for a half time step $\Delta t/2$ in (5.10) or (5.11), the pseudo time step size is $\Delta\mathfrak{t} = \Delta t/2$.

is required. As given in [160], for any explicit second order accurate two stage method (and, thus, $\mathcal{N}^\bullet = 2$)

$$\mathfrak{b}_1 = 1 - \frac{1}{2\mathfrak{d}}, \qquad \mathfrak{b}_2 = \frac{1}{2\mathfrak{d}} \tag{5.19}$$

holds, with

$$\begin{array}{c|cc} \mathfrak{c}_1 & \mathfrak{a}_{1,1} & \mathfrak{a}_{1,2} \\ \mathfrak{c}_2 & \mathfrak{a}_{2,1} & \mathfrak{a}_{2,2} \\ \hline & \mathfrak{b}_1 & \mathfrak{b}_2 \end{array} \quad = \quad \begin{array}{c|cc} 0 & 0 & 0 \\ \mathfrak{d} & \mathfrak{d} & 0 \\ \hline & 1 - \frac{1}{2\mathfrak{d}} & \frac{1}{2\mathfrak{d}} \end{array}$$

as corresponding Butcher tableau[7]. For any $\mathfrak{d} \neq 0$ the conditions $\mathfrak{b}_1 + \mathfrak{b}_2 = 1$ (required for first order accuracy) and $\mathfrak{b}_2\,\mathfrak{c}_2 = \frac{1}{2}$ (required for second order accuracy) are satisfied and $\mathfrak{c}_2 = \mathfrak{a}_{2,1}$ holds due to both $\mathfrak{c}_\mathfrak{n} = \sum_{\tilde{\mathfrak{n}}=1}^{2} \left(\mathfrak{a}_{\mathfrak{n},\tilde{\mathfrak{n}}}\right)$ and relation (5.18) for explicit methods. The SPP-RK2 version finally is obtained for

$$\mathfrak{d} := 1 \tag{5.20}$$

according to [62], reducing to the method of Heun

$$\rho\psi_\mathfrak{i}^{(m+1)} = \underbrace{\rho\psi_\mathfrak{i}^{(m)} + \Delta\mathfrak{t}\left(\mathfrak{b}_1\,\mathfrak{L}_\mathfrak{i}^{\{1\}}(\rho\psi^{(m)}) + \mathfrak{b}_2\,\mathfrak{L}_\mathfrak{i}^{\{1\}}(\rho\psi_2^\bullet)\right)}_{= \mathfrak{Phi}_{\mathcal{E},\mathfrak{i}}^{(2)}(\rho\psi^{(m)})} + \mathcal{O}\left(\Delta t^3\right) \tag{5.21}$$

with $\mathfrak{p} = 2$,

$$\rho\psi_2^\bullet = \rho\psi_\mathfrak{i}^{(m)} + \Delta\mathfrak{t}\,\mathfrak{L}_\mathfrak{i}^{\{1\}}(\rho\psi^{(m)}) \tag{5.22}$$

and

$$\mathfrak{b}_1 = \mathfrak{b}_2 = \frac{1}{2} \tag{5.23}$$

corresponding to a trapezoidal rule in time. The most efficient low-storage implementation of SPP-RK2 in the Finite Volume context requires two storage units per scalar conserved quantity $\rho\psi$ and one storage unit for the corresponding fluxes over all grid cell faces. This becomes evident after reformulation of equation (5.21) to yield

$$\rho\psi_\mathfrak{i}^{(m+1)} = \underbrace{(1 - \mathfrak{b}_1)}_{= \mathfrak{b}_2}\,\rho\psi_\mathfrak{i}^{(m)} + \mathfrak{b}_1\,\rho\psi_{\mathfrak{i},2}^\bullet + \mathfrak{b}_2\,\Delta\mathfrak{t}\,\mathfrak{L}_\mathfrak{i}^{\{1\}}(\rho\psi_{\mathfrak{i},2}^\bullet) \tag{5.24}$$

[7] See, e.g. [140].

considering relation (5.22), solved for $\mathfrak{L}_{\mathrm{i}}^{\{1\}}(\rho\psi^{(m)})$. The following algorithm summarizes the explicit time integration process:

1. keep $\rho\psi_{\mathrm{i}}^{(m)}$ in the first storage unit throughout the entire time integration process
2. compute grid cell face normal flux approximations $\overline{\mathcal{F}}_{(\rho\psi)}$, based on the required $\rho\psi^{(m)}$, for each grid cell face as described in section 5.1.3.1.
3. evaluate volume source terms as given in section 5.1.4.2
4. determine $\Delta\mathrm{t}\ \mathfrak{L}_{\mathrm{i}}^{\{1\}}(\rho\psi^{(m)})$ based on the computed numerical fluxes from 2. and store $\rho\psi_2^{\bullet}$, computed according to (5.22), in the second storage unit
5. repeat 2. with $\rho\psi_2^{\bullet}$ instead of $\rho\psi^{(m)}$. Previously computed fluxes can be overwritten.
6. repeat 4. for $\Delta\mathrm{t}\ \mathfrak{L}^{\{1\}}(\rho\psi_2^{\bullet})$ and overwrite $\rho\psi^{(m)}$ with the weighted sum (5.24).

5.1.2.3 Implicit Time Integration Scheme

The parabolic contributions[8] treated implicitly via the operator $\mathfrak{Phi}_{\mathfrak{I}}$ in (5.10) or (5.11), integrating sub-problems of the type

$$\frac{\mathrm{d}}{\mathrm{d}t}\left(\overline{\rho\psi}_{\mathrm{i}}\right) \;=\; \oint_{\partial\Omega_{\mathrm{i}}} \rho\,\mathfrak{C}\,\nabla\psi\cdot\vec{n}\,\mathrm{d}A \;\approx\; \mathfrak{L}_{\mathrm{i}}^{\mathcal{P}}\left(\rho\psi\right) \tag{5.25}$$

implicitly in time, are approximated via a (globally) second order accurate Crank-Nicolson scheme[9]

$$\overline{\rho\psi}_{\mathrm{i}}^{(m+1)} = \underbrace{\overline{\rho\psi}_{\mathrm{i}}^{(m)} + \frac{\Delta\mathrm{t}}{2}\left[\mathfrak{L}_{\mathrm{i}}^{\mathcal{P}}\left(\rho\psi^{(m+1)}\right) + \mathfrak{L}_{\mathrm{i}}^{\mathcal{P}}\left(\rho\psi^{(m)}\right)\right]}_{=\,\mathfrak{Phi}_{\mathfrak{I},\mathrm{i}}(\rho\psi)} + \mathcal{O}(\Delta\mathrm{t}^3) \tag{5.26}$$

as, for example, done in [150]. As in section 5.1.2.2, $\Delta\mathrm{t}$ is the pseudo time step with m and $m+1$ indicating the pseudo time levels with known (m) and unknown $(m+1)$ data. If the operator $\mathfrak{Phi}_{\mathfrak{I}}$ is applied for a half time step $\Delta t/2$ in the operator splitting

[8] Species diffusion, friction or heat conduction (while the latter does not apply here) are parabolic contributions.

[9] Proposed in [38] as the average of the explicit forward and the implicit backward Euler schemes.

(5.10) or (5.11), the pseudo time step $\Delta\mathfrak{t}$ in equation (5.26) has to be replaced by $\Delta t/2$, yielding an overall scaling of $\Delta t/4$. Evaluation of the approximations

$$\mathfrak{L}_{\mathfrak{i}}^{\mathcal{P}}\left(\rho\psi\right) = \frac{1}{\mathfrak{h}}\left(\sum_{\mathfrak{d}=1}^{\mathfrak{d}}\frac{1}{\mathfrak{c}_{\mathfrak{d}}}\sum_{\mathfrak{w}=1}^{2}(-1)^{\mathfrak{w}}\,\overline{\mathcal{F}}^{\mathcal{P}}_{(\rho\psi),\mathfrak{d},\mathfrak{w}}\right)_{\mathfrak{i}} = \frac{1}{\mathfrak{h}}\left(\sum_{\mathfrak{d}=1}^{\mathfrak{d}}\frac{1}{\mathfrak{c}_{\mathfrak{d}}}\sum_{\mathfrak{w}=1}^{2}(-1)^{\mathfrak{w}}\,\left(\rho\mathfrak{C}\nabla\psi\right)_{\mathfrak{d},\mathfrak{w}}\right)_{\mathfrak{i}} \tag{5.27}$$

at both pseudo time levels in (5.26) requires knowledge of $\psi^{(m+1)}$, $\rho^{(m+1)}$ and the coefficient $\mathfrak{C}^{(m+1)}$. While the operator $\mathfrak{O}_{\mathfrak{j}}$ does not change the fluid density over pseudo-time and, thus, $\rho^{(m+1)} = \rho^{(m)}$, the quantity $\psi^{(m+1)}$ – subject to be determined – remains unknown. If the temporal behavior of the coefficient is unknown[10], it has to be assumed to be constant as well and $\mathfrak{C}^{(m+1)} = \mathfrak{C}^{(m)}$. Rewriting equation (5.26), considering (5.27), yields

$$\begin{aligned}\left(\sum_{\mathfrak{d}=1}^{\mathfrak{d}}\frac{1}{\mathfrak{c}_{\mathfrak{d}}}\sum_{\mathfrak{w}=1}^{2}\left((-1)^{\mathfrak{w}}\,\widetilde{\mathfrak{C}}^{(m+1)}_{\mathfrak{d},\mathfrak{w}}\right)\,\left(\nabla\psi^{(m+1)}_{\mathfrak{d},\mathfrak{w}}\cdot\vec{\mathfrak{e}}_{\mathfrak{d}}\right)\right)_{\mathfrak{i}} &- \rho_{\mathfrak{i}}^{(m+1)}\,\psi_{\mathfrak{i}}^{(m+1)} \\ &= \mathcal{R}_{\mathfrak{i}}\left(\rho\psi^{(m)}\right) + \mathcal{O}(\mathfrak{h}^2)\end{aligned} \tag{5.28}$$

with coefficients

$$\widetilde{\mathfrak{C}}^{(m+1)}_{\mathfrak{d},\mathfrak{w}} := \frac{\Delta\mathfrak{t}}{2\,\mathfrak{h}}\,\rho^{(m+1)}_{\mathfrak{d},\mathfrak{w}}\mathfrak{C}^{(m+1)}_{\mathfrak{d},\mathfrak{w}} \tag{5.29}$$

and

$$\mathcal{R}_{\mathfrak{i}}\left(\rho\psi^{(m)}\right) := -\left[\overline{\rho\psi}_{\mathfrak{i}}^{(m)} + \frac{\Delta\mathfrak{t}}{2\,\mathfrak{h}}\left(\sum_{\mathfrak{d}=1}^{\mathfrak{d}}\frac{1}{\mathfrak{c}_{\mathfrak{d}}}\sum_{\mathfrak{w}=1}^{2}(-1)^{\mathfrak{w}}\,\left(\rho^{(m)}_{\mathfrak{d},\mathfrak{w}}\mathfrak{C}^{(m)}_{\mathfrak{d},\mathfrak{w}}\nabla\psi^{(m)}_{\mathfrak{d},\mathfrak{w}}\cdot\vec{\mathfrak{e}}_{\mathfrak{d}}\right)\right)_{\mathfrak{i}}\right] \tag{5.30}$$

as known right hand side at the old (pseudo) time level after separation of different time levels. The expression $\mathcal{O}(\mathfrak{h}^2)$ in the Helmholtz-type problem (5.28) arises due to the approximation of the integral average $\overline{\rho\psi}_{\mathfrak{i}} = \rho_{\mathfrak{i}}\psi_{\mathfrak{i}} + \mathcal{O}(\mathfrak{h}^2)$ in the "Helmholtz" part on the left hand side via the cell center values $\rho_{\mathfrak{i}}^{(m+1)}\;\psi_{\mathfrak{i}}^{(m+1)}$. Rewriting (5.28) in terms of directional indices i, j and k, referring to the different coordinate directions of the Cartesian grid, and assuming linear approximation of the slopes $\nabla\psi_{\mathfrak{d},\mathfrak{w}}\cdot\vec{\mathfrak{e}}_{\mathfrak{d}}$ at

[10] Time evolution of the coefficient $\mathfrak{C}$ is known, for example, if chemical reactions are present and treated with a suitable numerical tool such as Cantera, `http://www.cantera.org` [last visited on Aug. 1^{st}, 2016].

grid cell faces according to

$$\nabla\psi_{1,1}\cdot\vec{\mathfrak{e}}_1 \;=\; \nabla\psi_{i-\frac{1}{2},j,k}\cdot\vec{\mathfrak{e}}_1 \;=\; \frac{\psi_{i,j,k}-\psi_{i-1,j,k}}{\mathfrak{c}_1\mathfrak{h}} \;+\; \mathcal{O}(\mathfrak{h}^2) \tag{5.31a}$$

$$\nabla\psi_{1,2}\cdot\vec{\mathfrak{e}}_1 \;=\; \nabla\psi_{i+\frac{1}{2},j,k}\cdot\vec{\mathfrak{e}}_1 \;=\; \frac{\psi_{i+1,j,k}-\psi_{i,j,k}}{\mathfrak{c}_1\mathfrak{h}} \;+\; \mathcal{O}(\mathfrak{h}^2) \tag{5.31b}$$

$$\nabla\psi_{2,1}\cdot\vec{\mathfrak{e}}_2 \;=\; \nabla\psi_{i,j-\frac{1}{2},k}\cdot\vec{\mathfrak{e}}_2 \;=\; \frac{\psi_{i,j,k}-\psi_{i,j-1,k}}{\mathfrak{c}_2\mathfrak{h}} \;+\; \mathcal{O}(\mathfrak{h}^2) \tag{5.31c}$$

$$\nabla\psi_{2,2}\cdot\vec{\mathfrak{e}}_2 \;=\; \nabla\psi_{i,j+\frac{1}{2},k}\cdot\vec{\mathfrak{e}}_2 \;=\; \frac{\psi_{i,j+1,k}-\psi_{i,j,k}}{\mathfrak{c}_2\mathfrak{h}} \;+\; \mathcal{O}(\mathfrak{h}^2) \tag{5.31d}$$

$$\nabla\psi_{3,1}\cdot\vec{\mathfrak{e}}_3 \;=\; \nabla\psi_{i,j,k-\frac{1}{2}}\cdot\vec{\mathfrak{e}}_3 \;=\; \frac{\psi_{i,j,k}-\psi_{i,j,k-1}}{\mathfrak{c}_3\mathfrak{h}} \;+\; \mathcal{O}(\mathfrak{h}^2) \tag{5.31e}$$

$$\nabla\psi_{3,2}\cdot\vec{\mathfrak{e}}_3 \;=\; \nabla\psi_{i,j,k+\frac{1}{2}}\cdot\vec{\mathfrak{e}}_3 \;=\; \frac{\psi_{i,j,k+1}-\psi_{i,j,k}}{\mathfrak{c}_3\mathfrak{h}} \;+\; \mathcal{O}(\mathfrak{h}^2) \tag{5.31f}$$

equation (5.28) transforms to

$$\begin{aligned}
&\breve{\mathfrak{C}}^{(m+1)}_{(i+1,j,k)}\,\psi^{(m+1)}_{(i+1,j,k)} + \breve{\mathfrak{C}}^{(m+1)}_{(i-1,j,k)}\,\psi^{(m+1)}_{(i-1,j,k)}\\
+\;&\breve{\mathfrak{C}}^{(m+1)}_{(i,j+1,k)}\,\psi^{(m+1)}_{(i,j+1,k)} + \breve{\mathfrak{C}}^{(m+1)}_{(i,j-1,k)}\,\psi^{(m+1)}_{(i,j-1,k)}\\
+\;&\breve{\mathfrak{C}}^{(m+1)}_{(i,j,k+1)}\,\psi^{(m+1)}_{(i,j,k+1)} + \breve{\mathfrak{C}}^{(m+1)}_{(i,j,k-1)}\,\psi^{(m+1)}_{(i,j,k-1)}\\
&\qquad - \breve{\mathfrak{C}}^{(m+1)}_{(i,j,k)}\,\psi^{(m+1)}_{(i,j,k)} \;=\; \mathfrak{h}\,\mathcal{R}_{\mathfrak{i}}\left(\rho\psi^{(m)}\right) \;+\; \mathcal{O}(\mathfrak{h}^3)
\end{aligned} \tag{5.32}$$

after multiplication with $\mathfrak{h}$, with

$$\breve{\mathfrak{C}}^{(m+1)}_{(i+1,j,k)} \;:=\; \frac{\widetilde{\mathfrak{C}}_{(i+1,j,k)}+\widetilde{\mathfrak{C}}_{(i,j,k)}}{2\,\mathfrak{c}_1^2}, \qquad \breve{\mathfrak{C}}^{(m+1)}_{(i-1,j,k)} \;:=\; \frac{\widetilde{\mathfrak{C}}_{(i-1,j,k)}+\widetilde{\mathfrak{C}}_{(i,j,k)}}{2\,\mathfrak{c}_1^2} \tag{5.33a}$$

$$\breve{\mathfrak{C}}^{(m+1)}_{(i,j+1,k)} \;:=\; \frac{\widetilde{\mathfrak{C}}_{(i,j+1,k)}+\widetilde{\mathfrak{C}}_{(i,j,k)}}{2\,\mathfrak{c}_2^2}, \qquad \breve{\mathfrak{C}}^{(m+1)}_{(i,j-1,k)} \;:=\; \frac{\widetilde{\mathfrak{C}}_{(i,j-1,k)}+\widetilde{\mathfrak{C}}_{(i,j,k)}}{2\,\mathfrak{c}_2^2} \tag{5.33b}$$

$$\breve{\mathfrak{C}}^{(m+1)}_{(i,j,k+1)} \;:=\; \frac{\widetilde{\mathfrak{C}}_{(i,j,k+1)}+\widetilde{\mathfrak{C}}_{(i,j,k)}}{2\,\mathfrak{c}_3^2}, \qquad \breve{\mathfrak{C}}^{(m+1)}_{(i,j,k-1)} \;:=\; \frac{\widetilde{\mathfrak{C}}_{(i,j,k-1)}+\widetilde{\mathfrak{C}}_{(i,j,k)}}{2\,\mathfrak{c}_3^2} \tag{5.33c}$$

$$\begin{aligned}
\breve{\mathfrak{C}}^{(m+1)}_{(i,j,k)} \;:=\;& \breve{\mathfrak{C}}^{(m+1)}_{(i+1,j,k)} + \breve{\mathfrak{C}}^{(m+1)}_{(i-1,j,k)} + \breve{\mathfrak{C}}^{(m+1)}_{(i,j+1,k)} + \breve{\mathfrak{C}}^{(m+1)}_{(i,j-1,k)}\\
&+ \breve{\mathfrak{C}}^{(m+1)}_{(i,j,k+1)} + \breve{\mathfrak{C}}^{(m+1)}_{(i,j,k-1)} + \mathfrak{h}\,\rho^{(m+1)}_{(i,j,k)}
\end{aligned} \tag{5.33d}$$

for any grid cell $\mathfrak{i} \mathrel{\widehat{=}} (i,j,k)$ that is not in touch with the domain boundary, leading to a linear system of the form

$$\mathfrak{A}_{\breve{\mathfrak{C}}}\cdot\vec{\psi}^{(m+1)} \;=\; \vec{\mathcal{R}} \tag{5.34}$$

for $\psi^{(m+1)}$ with, in general, block-diagonal square matrix $\mathfrak{A}_{\breve{\mathfrak{C}}}$, depending on the coefficients $\breve{\mathfrak{C}}$ and boundary conditions. The latter, required for grid cells that touch the domain boundary, are given in section 5.4.2. If the problem is only two-dimensional, then $k \equiv 1$, $\mathfrak{c}_3 \equiv 1$, $\psi_{(i,j,k\pm1)} \equiv 0$ and $\breve{\mathfrak{C}}^{(m+1)}_{(i,j,k\pm\frac{1}{2})} \equiv 0$. The stencil for determination of cell centered values in each internal grid cell is sketched in ***Fig. 5.9*** on page 95. Once the second order accurate solution for the $\psi^{(m+1)}$ is obtained as described in section 5.5, $\mathfrak{L}^{\mathcal{P}}_{\mathfrak{i}}\left(\rho\psi^{(m+1)}\right)$ – and with that the entire right hand side of equation (5.27) – can be evaluated. The following algorithm summarizes the implicit time integration process:

1. compute coefficients (5.29) on each grid cell face
2. compute flux approximations $\overline{\mathcal{F}}^{\mathcal{P},(m)}_{(\rho\psi),\mathfrak{d},\mathfrak{w}} = \rho^{(m)}_{\mathfrak{d},\mathfrak{w}}\mathfrak{C}^{(m)}_{\mathfrak{d},\mathfrak{w}}\left(\nabla\psi^{(m)}_{\mathfrak{d},\mathfrak{w}}\cdot\vec{\mathfrak{e}}_{\mathfrak{d}}\right)$, based on known values at pseudo time level m, on each grid cell face, considering (5.31), as described in section 5.1.3.2
3. compute right hand side (5.30) of (5.28), based on the fluxes computed in 2. and the known integral average in each grid cell
4. assemble global matrix $\mathfrak{A}_{\breve{\mathfrak{C}}}$ in (5.34) by determination and accumulation[11] of coefficients $\breve{\mathfrak{C}}$ from (5.33) in each grid cell, based on the facial coefficients $\widetilde{\mathfrak{C}}$ determined in 1.
5. modify matrix and right hand side entries, depending on boundary conditions as described in section 5.4.2
6. solve the linear system (5.34) for $\psi^{(m+1)}$
7. compute fluxes $\overline{\mathcal{F}}^{\mathcal{P},(m+1)}_{(\rho\psi),\mathfrak{d},\mathfrak{w}} = \rho^{(m+1)}_{\mathfrak{d},\mathfrak{w}}\mathfrak{C}^{(m+1)}_{\mathfrak{d},\mathfrak{w}}\left(\nabla\psi^{(m+1)}_{\mathfrak{d},\mathfrak{w}}\cdot\vec{\mathfrak{e}}_{\mathfrak{d}}\right)$ at pseudo time level $m+1$, considering (5.31), as described in section 5.1.3.2
8. evaluate $\mathfrak{L}^{\mathcal{P}}_{\mathfrak{i}}\left(\rho\psi^{(m+1)}\right)$ according to (5.27)
9. compute (5.26) according to $\overline{\rho\psi}^{(m+1)}_{\mathfrak{i}} = \frac{\Delta\mathfrak{t}}{2}\mathfrak{L}^{\mathcal{P}}_{\mathfrak{i}}\left(\rho\psi^{(m+1)}\right) - \mathcal{R}_{\mathfrak{i}}\left(\rho\psi^{(m)}\right)$ with the latter computed in 3. and $\mathfrak{L}^{\mathcal{P}}_{\mathfrak{i}}\left(\rho\psi^{(m+1)}\right)$ in 8.

Note that although cell center values $\psi^{(m+1)}_{\mathfrak{i}}$ are already determined in step 6. and $\overline{\rho\psi}^{(m+1)}_{\mathfrak{i}} = \rho^{(m+1)}_{\mathfrak{i}}\,\psi^{(m+1)}_{\mathfrak{i}} + \mathcal{O}(\mathfrak{h}^2)$, steps 7. to 9. are still necessary in order to obtain a fully conservative discretization.

[11] For each grid cell a line like the one given in (5.32) arises, containing coefficients contributing to the coefficient of a neighboring cell; therefore the resulting entry in the global matrix for each grid cell has to be composed the own coefficient and contributions of neighboring grid cells.

5.1.2.3 - 1 Diffusion

If diffusion is treated implicitly via $\Phi_{\mathfrak{I}}^{\mathcal{D}}$ by the above scheme, then

$$\psi := Y_{\mathfrak{s}} \tag{5.35}$$

and the general coefficient $\mathfrak{C}$ in (5.26) is the (binary) diffusion coefficient

$$\mathfrak{C} := D_{\mathfrak{s}} \tag{5.36}$$

of species $\mathfrak{s}$ in its solvent. The above algorithm has to be performed for each species and can be done sequentially.

5.1.2.3 - 2 Friction

Friction can be treated implicitly by the above integration scheme via the operator $\Phi_{\mathfrak{I}}^{\mathcal{V}}$, if the dynamic viscosity μ does not depend on space (but can depend on time). In this case the viscous contribution

$$\begin{aligned}\nabla \cdot \boldsymbol{\mathcal{T}} &= \nabla \cdot \left(\mu \left(\nabla \circ \vec{v} + (\nabla \circ \vec{v})^T\right)\right) + \nabla \left(\lambda \left(\nabla \cdot \vec{v}\right)\right) \\ &= \nabla \cdot \left(\mu \left(\nabla \circ \vec{v}\right)\right) + \left(\mu + \lambda\right) \nabla \left(\nabla \cdot \vec{v}\right) + \left(\nabla \cdot \vec{v}\right) \nabla \lambda + \left(\nabla \circ \vec{v}\right)^T \cdot \nabla \mu\end{aligned} \tag{5.37}$$

reduces to

$$\nabla \cdot \boldsymbol{\mathcal{T}} = \nabla \cdot \left(\mu \left(\nabla \circ \vec{v}\right)\right) + \left(\mu + \lambda\right) \nabla \mathcal{D} + \mathcal{D} \nabla \lambda \tag{5.38}$$

if $\nabla \cdot \vec{v} = \mathcal{D}$ and $\mathcal{D}$ independent of $\vec{v}$. With the kinematic viscosity $\nu = \frac{\mu}{\rho}$ this can be written as

$$\left(\nabla \cdot \boldsymbol{\mathcal{T}}\right)_{\mathfrak{d}} = \nabla \cdot \left(\rho \nu \nabla v_{\mathfrak{d}}\right) + \underbrace{\left(\mu + \lambda\right) \frac{\partial \mathcal{D}}{\partial x_{\mathfrak{d}}} + \mathcal{D} \frac{\partial \lambda}{\partial x_{\mathfrak{d}}}}_{=: \mathfrak{q}_{\mathfrak{d}}} \tag{5.39}$$

for each velocity component[12]. The first term on the right hand side now represents a "diffusive" flux for velocity component $v_{\mathfrak{d}}$ with

$$\psi := v_{\mathfrak{d}} \tag{5.40}$$

[12] If the dynamic viscosity is homogeneous, kinematic viscosity ν and density ρ can still depend on space, but only in such a way that $\nabla \left(\rho \nu\right) = \nabla \mu = 0$.

and

$$\mathfrak{C} := \nu \tag{5.41}$$

as "diffusive" coefficient. For $\nabla \cdot \vec{v} = 0$ and, thus, $\mathcal{D} = 0$, the additional right hand side terms $\mathfrak{q}_{\mathfrak{d}}$ vanish. In case of $\nabla\mu = 0$, leading to (5.39), the implicit scheme described above can be applied for each momentum component separately due to decoupling of the single components. For $\mathcal{D} \neq 0$ and $\mathcal{D}$ independent of $\vec{v}$, the expression

$$-\frac{1}{2}\left(\mathfrak{q}_{\mathfrak{d},\mathfrak{i}}^{(m+1)} + \mathfrak{q}_{\mathfrak{d},\mathfrak{i}}^{(m)}\right) \tag{5.42}$$

has to be added to (5.30) and either the temporal behavior of $\mathfrak{q}_{\mathfrak{d}}$ has to be known or it has to be assumed constant in time, reducing (5.42) to $-\mathfrak{q}_{\mathfrak{d},\mathfrak{i}}^{(m)}$.

5.1.3 Flux Computation

Flux computation, required for evaluation of the explicit and/or implicit operators from (5.10) or (5.11) as determined in sections 5.1.2.2 and 5.1.2.3, is described in this section, starting with the advective fluxes, followed by diffusive and viscous fluxes.

5.1.3.1 Advective Fluxes

The advective fluxes, contributing to the explicit approximation $\mathfrak{L}_{\mathfrak{i}}^{\{1\}}$ in (5.21) as given in (4.24) as part of $\mathfrak{D}_{\mathcal{E}}$ in (5.10) or (5.11), can be computed without solving Riemann problems due to the independence of the momentum equation and the energy equation substitute (5.8). The latter decouple, since both the dynamic pressure[13] $p^{'}$ in the momentum equation and the background pressure[14] P_0 on the right hand side of equation (5.8) can be treated as "passive" source terms during the predictor step, leading to a diagonal Jacobian $(\boldsymbol{I}\, v_{\mathfrak{d}})$ of the resulting Euler-type system of equations per coordinate direction $\mathfrak{d}$, with contributions of the respective velocity component $v_{\mathfrak{d}}$ only. The advective fluxes of each scalar component of the hyperbolic auxiliary system (5.4) can thus be computed independently and sequentially. Once the grid cell face normal carrier flux $(\mathcal{P}\,\vec{v}\cdot\vec{n})$ in (5.4) is suitably approximated, exemplified by means of grid cell face $(i+\frac{1}{2}, j, k)$ as upper grid cell face of grid cell $\mathfrak{i} \mathrel{\widehat{=}} (i,j,k)$

[13] The dynamic pressure is assumed to be time-independent during the predictor step.

[14] Temporal behavior of the homogeneous background pressure has to be determined by other means as, for example, given in section 3.4.

with normal vector in x_1 direction as

$$\begin{aligned}\left(\overline{\mathcal{F}}^{\mathcal{A}}_{(\mathcal{P}),1,2}\right)_{\mathrm{i}} \equiv \overline{\mathcal{F}}^{\mathcal{A}}_{(\mathcal{P}),(i+\frac{1}{2},j,k)} &= \mathcal{P}^{\mathrm{upw}}_{(i+\frac{1}{2},j,k)} v_{1,(i+\frac{1}{2},j,k)} \\ &= \underbrace{\mathcal{P}^{(\mathcal{L})}_{(i+\frac{1}{2},j,k)} v^{(\mathcal{L})}_{1,(i+\frac{1}{2},j,k)}}_{=:\,\overline{\mathcal{F}}^{(\mathcal{L})}_{(\mathcal{P}),(i+\frac{1}{2},j,k)}} + \underbrace{\mathcal{P}^{(\mathcal{U})}_{(i+\frac{1}{2},j,k)} v^{(\mathcal{U})}_{1,(i+\frac{1}{2},j,k)}}_{=:\,\overline{\mathcal{F}}^{(\mathcal{U})}_{(\mathcal{P}),(i+\frac{1}{2},j,k)}}\end{aligned} \tag{5.43}$$

with

$$\left(\mathcal{P}^{(\mathcal{L})}_{(i+\frac{1}{2},j,k)},\ \mathcal{P}^{(\mathcal{U})}_{(i+\frac{1}{2},j,k)}\right) = \mathfrak{R}\left(\mathcal{P}_{(i+2,j,k)}, \mathcal{P}_{(i+1,j,k)}, \mathcal{P}_{(i,j,k)}, \mathcal{P}_{(i-1,j,k)}\right) \tag{5.44}$$

and second order accurate state recovery operator $\mathfrak{R}$ as described in section 5.1.3.1 - 1, the resulting advective fluxes of mass, species masses and momentum can be obtained by transporting upwind values of the respective pseudo-primitive variables from (5.5a). In approximation (5.43), $v^{(\mathcal{L})}$ is the grid cell face normal velocity component pointing in positive coordinate direction and $v^{(\mathcal{U})}$ is the grid cell face normal velocity component pointing in negative coordinate direction:

$$v^{(\mathcal{L})}_{1,(i+\frac{1}{2},j,k)} := \max\left(0, v_{1,(i+\frac{1}{2},j,k)}\right) \geqslant 0 \tag{5.45a}$$

$$v^{(\mathcal{U})}_{1,(i+\frac{1}{2},j,k)} := \min\left(0, v_{1,(i+\frac{1}{2},j,k)}\right) \leqslant 0 \tag{5.45b}$$

The normal velocity across the grid cell face is the second order accurate average

$$v_{1,(i+\frac{1}{2},j,k)} := \frac{v_{1,(i+1,j,k)} + v_{1,(i,j,k)}}{2} \tag{5.46}$$

and due to (5.45) one of the fluxes $\overline{\mathcal{F}}^{(\mathcal{L})}_{(\mathcal{P}),(i+\frac{1}{2},j,k)}$ and $\overline{\mathcal{F}}^{(\mathcal{U})}_{(\mathcal{P}),(i+\frac{1}{2},j,k)}$ in equation (5.43) is always zero, depending on the flow orientation in grid cell face normal direction, while the non-zero one is the upwind flux. The upwind fluxes of the other quantities read

$$\begin{aligned}\overline{\mathcal{F}}^{\mathcal{A}}_{(\rho\psi),(i+\frac{1}{2},j,k)} &\equiv \overline{\mathcal{F}}^{\mathcal{A}}_{(\mathcal{P}\Phi),(i+\frac{1}{2},j,k)} \\ &= \overline{\mathcal{F}}^{(\mathcal{L})}_{(\mathcal{P}),(i+\frac{1}{2},j,k)} \Phi^{(\mathcal{L})}_{(i+\frac{1}{2},j,k)} + \overline{\mathcal{F}}^{(\mathcal{U})}_{(\mathcal{P}),(i+\frac{1}{2},j,k)} \Phi^{(\mathcal{U})}_{(i+\frac{1}{2},j,k)}\end{aligned} \tag{5.47}$$

with

$$\left(\Phi^{(\mathcal{L})}_{(i+\frac{1}{2},j,k)},\ \Phi^{(\mathcal{U})}_{(i+\frac{1}{2},j,k)}\right) = \mathfrak{R}\left(\Phi_{(i+2,j,k)}, \Phi_{(i+1,j,k)}, \Phi_{(i,j,k)}, \Phi_{(i-1,j,k)}\right) \tag{5.48}$$

and Φ represents any component from (5.5a). The non-zero carrier flux contribution $\overline{\mathcal{F}}^{(\mathcal{L})}_{(\mathcal{P}),(i+\frac{1}{2},j,k)}$ or $\overline{\mathcal{F}}^{(\mathcal{U})}_{(\mathcal{P}),(i+\frac{1}{2},j,k)}$ automatically selects the upwind quantity from (5.48) if done according to (5.47). Equations (5.43) to (5.48) apply equivalently for the other coordinate directions and grid cell faces. The stencil involved in flux computation for each grid cell face is sketched in ***Fig. 5.1***, the resulting stencil for each grid cell is sketched in ***Fig. 5.2***.

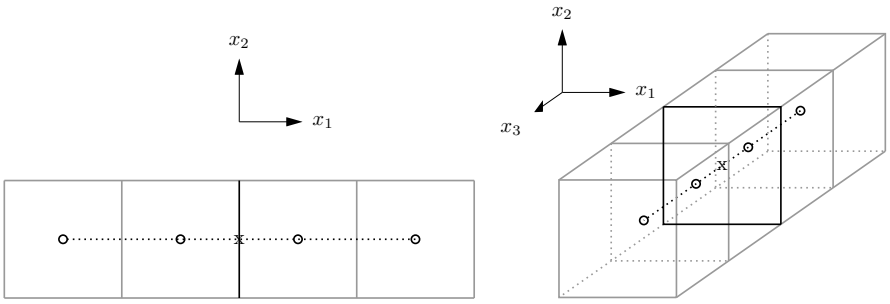

Fig. 5.1: Stencil for grid cell face normal flux computation involving one fluid phase only, left $\mathfrak{d} = 2$, right $\mathfrak{d} = 3$

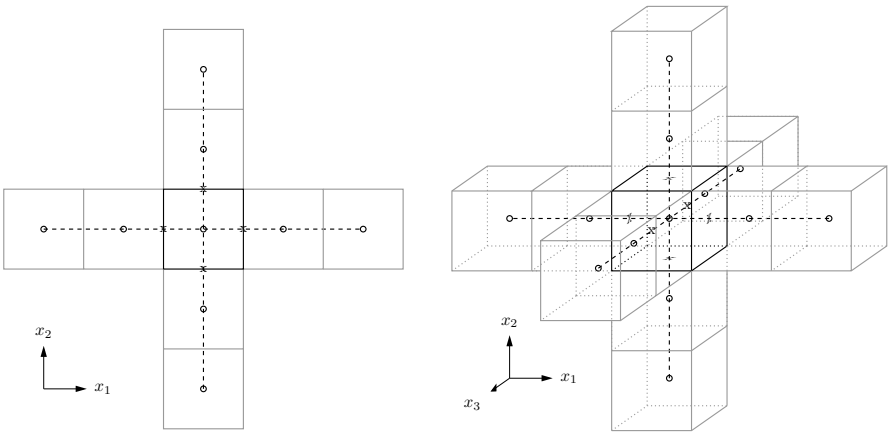

Fig. 5.2: Stencil for the update in a grid cell due to advective fluxes involving one fluid phase only, left $\mathfrak{d} = 2$, right $\mathfrak{d} = 3$

5.1.3.1 - 1 State Recovery at Grid Cell Faces

State recovery at grid cell faces, as represented in section 5.1.3.1 by $\mathfrak{R}$, is done second order accurate in a dimension-by-dimension fashion by

1. determination of slopes $\mathcal{S}^{(\Phi)}_{\mathfrak{d}}$ in grid cell face normal direction at the grid cell face considered and at the neighboring grid cell faces in grid cell face normal

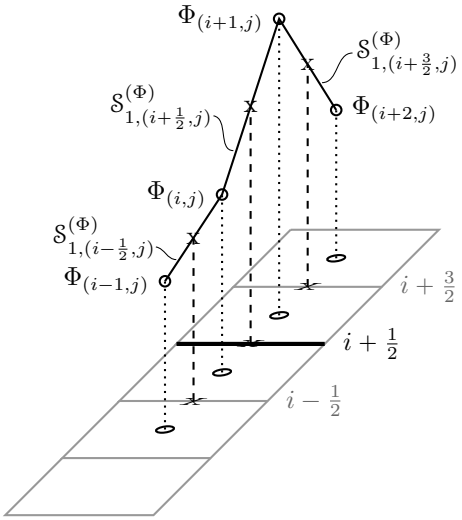

Fig. 5.3: Determination of slopes at grid cell faces ($\mathfrak{d} = 2$, analogously $\mathfrak{d} = 3$)

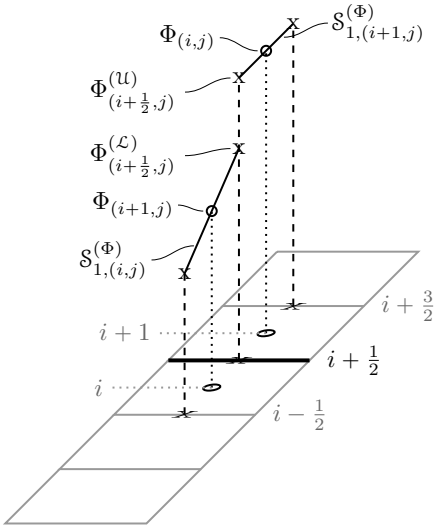

Fig. 5.4: Determination of slopes in grid cells ($\mathfrak{d} = 2$, analogously $\mathfrak{d} = 3$)

direction as sketched in ***Fig. 5.3***:

$$\mathbb{S}^{(\Phi)}_{1,(i+\frac{3}{2},j,k)} := \frac{\Phi_{(i+2,j,k)} - \Phi_{(i+1,j,k)}}{\mathfrak{c}_1\,\mathfrak{h}} \tag{5.49a}$$

$$\mathbb{S}^{(\Phi)}_{1,(i+\frac{1}{2},j,k)} := \frac{\Phi_{(i+1,j,k)} - \Phi_{(i,j,k)}}{\mathfrak{c}_1\,\mathfrak{h}} \tag{5.49b}$$

$$\mathbb{S}^{(\Phi)}_{1,(i-\frac{1}{2},j,k)} := \frac{\Phi_{(i,j,k)} - \Phi_{(i-1,j,k)}}{\mathfrak{c}_1\,\mathfrak{h}} \tag{5.49c}$$

2. determination of slopes

$$\mathbb{S}^{(\Phi)}_{1,(i+1,j,k)} := \mathfrak{L}\left(\mathbb{S}^{(\Phi)}_{1,(i+\frac{3}{2},j,k)},\ \mathbb{S}^{(\Phi)}_{1,(i+\frac{1}{2},j,k)}\right) \tag{5.50a}$$

$$\mathbb{S}^{(\Phi)}_{1,(i,j,k)} := \mathfrak{L}\left(\mathbb{S}^{(\Phi)}_{1,(i+\frac{1}{2},j,k)},\ \mathbb{S}^{(\Phi)}_{1,(i-\frac{1}{2},j,k)}\right) \tag{5.50b}$$

in grid cells (i, j, k) and $(i + 1, j, k)$, sharing the grid cell face $(i + \frac{1}{2}, j, k)$ as sketched in ***Fig. 5.4***, involving the (non-linear) extended van Leer limiter

function

$$\mathfrak{L}\left(\breve{\mathfrak{a}},\breve{\mathfrak{b}}\right) := \frac{\operatorname{sgn}(\breve{\mathfrak{a}})+\operatorname{sgn}(\breve{\mathfrak{b}})}{2}\,\mathfrak{l}\left(|\breve{\mathfrak{a}}|,|\breve{\mathfrak{b}}|\right) \tag{5.51a}$$

$$\mathfrak{l}\left(\mathfrak{a},\mathfrak{b}\right) := \begin{cases} \frac{2\,\mathfrak{a}\,\mathfrak{b}}{\mathfrak{a}+\mathfrak{b}}\;\mathfrak{k}\left(\min\left(\frac{\mathfrak{a}}{\mathfrak{b}},\frac{\mathfrak{b}}{\mathfrak{a}}\right)\right) & \operatorname{sgn}(\mathfrak{a}\mathfrak{b})>0 \\ 0 & \text{otherwise} \end{cases} \tag{5.51b}$$

$$\mathfrak{k}\left(\xi\right) := 1+\xi\left(1-\xi\right)\left(1-\xi^{\mathfrak{z}}\right) \tag{5.51c}$$

with limiter operator $\mathfrak{L}$, limiter function $\mathfrak{l}$ and limiter weight $\mathfrak{k}$ as given and discussed in [92]. This version (5.51) is within the valid range for a second order TVD limiter for $\{\mathfrak{z}\in\mathbb{Z}\mid 0\leqslant\mathfrak{z}<7\}$ and $0\leqslant\xi\leqslant 1$ (which is the only range of interest due to $0\leqslant\min\left(\frac{\mathfrak{a}}{\mathfrak{b}},\frac{\mathfrak{b}}{\mathfrak{a}}\right)\leqslant 1$) and yields a monotonous result in ξ in addition for $\{\mathfrak{z}\in\mathbb{Z}\mid 0\leqslant\mathfrak{z}\leqslant 4\}$ and $0\leqslant\xi\leqslant 1$. For $\mathfrak{z}=0$ it reduces to the original van Leer limiter[15] with $\mathfrak{k}\left(\xi\right)\equiv 1$, which is applied throughout the results sections 5.6, 6.5.6 and 6.6.4. Note that since both arguments of the limiter function (5.51b) are non-negative real numbers, the lower option of (5.51b) only applies if at least one of the two arguments $\mathfrak{a}$ and $\mathfrak{b}$ is zero.

3. determination of lower ($\mathcal{L}$) and upper ($\mathcal{U}$) recovered values at grid cell face $(i+\frac{1}{2},j,k)$, based on the cell center values – or integral averages, respectively – of cells (i,j,k) and $(i+1,j,k)$ and the slopes determined in 2. in direction $\mathfrak{d}=1$:

$$\Phi^{(\mathcal{L})}_{(i+\frac{1}{2},j,k)} = \Phi_{(i,j,k)} + \mathcal{S}^{(\Phi)}_{1,(i,j,k)}\,\frac{\mathfrak{c}_1\,\mathfrak{h}}{2} + \mathcal{O}(\mathfrak{h}^2) \tag{5.52a}$$

$$\Phi^{(\mathcal{U})}_{(i+\frac{1}{2},j,k)} = \Phi_{(i+1,j,k)} - \mathcal{S}^{(\Phi)}_{1,(i+1,j,k)}\,\frac{\mathfrak{c}_1\,\mathfrak{h}}{2} + \mathcal{O}(\mathfrak{h}^2) \tag{5.52b}$$

The values (5.52) are returned by the operator $\mathfrak{R}$ if applied to the respective cell center values in the stencil required as done in (5.44) and (5.48).

As in section 5.1.3.1, the above relations transform accordingly to the other grid cell faces and coordinate directions.

5.1.3.2 Diffusive Fluxes

Both in case of explicit treatment of species diffusion according to section 5.1.2.2 and in case of an implicit time integration operator for species diffusion according

[15] The original van Leer limiter is proposed in [179].

to section 5.1.2.3 with 5.1.2.3 - 1, the approximation of the grid cell face normal component of the diffusive flux $\vec{j}_{\mathfrak{s}} = \rho D_{\mathfrak{s}} \nabla Y_{\mathfrak{s}}$ of species $\mathfrak{s}$ for application to (5.27) is

$$\left(\overline{\mathcal{F}}^{\mathcal{D}}_{(\rho Y_{\mathfrak{s}}),1,2}\right)_{\mathfrak{i}} \equiv \overline{\mathcal{F}}^{\mathcal{D}}_{(\rho Y_{\mathfrak{s}}),(i+\frac{1}{2},j,k)} = (\rho\, D_{\mathfrak{s}})_{(i+\frac{1}{2},j,k)}\, \nabla Y_{\mathfrak{s},(i+\frac{1}{2},j,k)} \cdot \vec{\mathfrak{e}}_1 + \mathcal{O}\left(\mathfrak{h}^2\right) \tag{5.53}$$

with

$$(\rho\, D_{\mathfrak{s}})_{(i+\frac{1}{2},j,k)} := \frac{\left((\rho\, D_{\mathfrak{s}})_{(i+1,j,k)} + (\rho\, D_{\mathfrak{s}})_{(i,j,k)}\right)}{2} \tag{5.54a}$$

$$\nabla Y_{\mathfrak{s},(i+\frac{1}{2},j,k)} := \frac{\left(Y_{\mathfrak{s},(i+1,j,k)} - Y_{\mathfrak{s},(i,j,k)}\right)}{\mathfrak{c}_1\, \mathfrak{h}} \tag{5.54b}$$

for grid cell face $(i + \frac{1}{2}, j, k)$. The latter is the upper grid cell face of grid cell $\mathfrak{i} \mathrel{\widehat{=}} (i, j, k)$ with normal vector in x_1 direction and approximation (5.53) holds accordingly for all other grid cell faces and coordinate directions with corresponding indices.

5.1.3.3 Viscous Fluxes

In this section the discretization of the viscous momentum fluxes is described. The discretization used in case of implicit time integration is similar to the one used for the diffusive species fluxes, while for explicit treatment of friction the full viscous stress tensor is discretized.

5.1.3.3 - 1 Implicit

In case of implicit time integration as described in section 5.1.2.3 with 5.1.2.3 - 2, the viscous flux for momentum component $\mathfrak{c}$ across grid cell face $(i + \frac{1}{2}, j, k)$ of cell $\mathfrak{i} \mathrel{\widehat{=}} (i, j, k)$ with $\mathfrak{d} = 1$ and $\mathfrak{w} = 2$ for application to (5.27) is approximated as

$$\left(\overline{\mathcal{F}}^{\mathcal{V},\mathcal{I}}_{(\rho v_{\mathfrak{c}}),1,2}\right)_{\mathfrak{i}} \equiv \overline{\mathcal{F}}^{\mathcal{V},\mathcal{I}}_{(\rho v_{\mathfrak{c}}),(i+\frac{1}{2},j,k)} = \mu_{(i+\frac{1}{2},j,k)}\, (\nabla v_{\mathfrak{c}})_{(i+\frac{1}{2},j,k)} \cdot \vec{\mathfrak{e}}_1 + \mathcal{O}\left(\mathfrak{h}^2\right) \tag{5.55}$$

with

$$\mu_{(i+\frac{1}{2},j,k)} := \frac{\left(\mu_{(i+1,j,k)} + \mu_{(i,j,k)}\right)}{2} \tag{5.56a}$$

$$\left(\nabla v_{\mathfrak{c}}\right)_{(i+\frac{1}{2},j,k)} := \frac{\left(v_{\mathfrak{c},(i+1,j,k)} - v_{\mathfrak{c},(i,j,k)}\right)}{\mathfrak{c}_1\,\mathfrak{h}} \tag{5.56b}$$

and accordingly for all the other grid cell faces of grid cell $\mathfrak{i}$ with corresponding indices.

5.1.3.3 - 2 Explicit

In case of explicit time integration as described in section 5.1.2.2, the full viscous stress tensor (3.31), including both the symmetric part $2\mu\boldsymbol{E}$ and the asymmetric part $\boldsymbol{I}\lambda\left(\nabla\cdot\vec{v}\right)$, is discretized, since during the predictor step the velocity divergence constraint is not satisfied. The approximation of any component $\mathfrak{c}$ of the viscous momentum flux vector $\boldsymbol{\mathcal{T}}\cdot\vec{\mathfrak{e}}_{\mathfrak{d}}$ in direction $\mathfrak{d}$ can be expressed as

$$\left(\overline{\mathcal{F}}^{\mathcal{V},\mathcal{E}}_{(\rho v_{\mathfrak{c}}),\mathfrak{d},\mathfrak{w}}\right)_{\mathfrak{i}} = \left(\mu_{\mathfrak{d},\mathfrak{w}}\left(\left(\frac{\partial v_{\mathfrak{c}}}{\partial x_{\mathfrak{d}}}\right)_{\mathfrak{d},\mathfrak{w}} + \left(\frac{\partial v_{\mathfrak{d}}}{\partial x_{\mathfrak{c}}}\right)_{\mathfrak{d},\mathfrak{w}}\right) + \delta_{\mathfrak{d},\mathfrak{c}}\,\lambda_{\mathfrak{d},\mathfrak{w}}\sum_{\mathfrak{e}=1}^{\mathfrak{d}}\left(\frac{\partial v_{\mathfrak{e}}}{\partial x_{\mathfrak{e}}}\right)_{\mathfrak{d},\mathfrak{w}}\right)_{\mathfrak{i}} \tag{5.57}$$

with

$$\delta_{\mathfrak{d},\mathfrak{c}} := \begin{cases} 1, & \mathfrak{d} = \mathfrak{c} \\ 0, & \mathfrak{d} \neq \mathfrak{c} \end{cases} \tag{5.58}$$

as the Kronecker delta and $\mathfrak{w}$ as introduced on page 60. In general, the partial derivative of velocity component *i* with respect to the spatial direction *j* can be approximated second order accurate by

$$\left(\frac{\partial v_{\mathfrak{i}}}{\partial x_{\mathfrak{j}}}\right)_{\mathfrak{k}} = \frac{\left(v_{\mathfrak{i},(\mathfrak{k}+\frac{1}{2})} - v_{\mathfrak{i},(\mathfrak{k}-\frac{1}{2})}\right)}{\mathfrak{c}_{\mathfrak{j}}\,\mathfrak{h}} + \mathcal{O}(\mathfrak{h}^2) \tag{5.59}$$

at any location with $\mathfrak{k}$ as the $\mathfrak{j}^{th}$ one-dimensional location index. For approximation of $\left(\frac{\partial v_{\mathfrak{i}}}{\partial x_{\mathfrak{j}}}\right)_{\mathfrak{k}}$ in the center of a grid cell face with normal vector pointing into direction $\mathfrak{d}$, the values $v_{\mathfrak{i},(\mathfrak{k}+\frac{1}{2})}$ and $v_{\mathfrak{i},(\mathfrak{k}-\frac{1}{2})}$ are cell center values, if $\mathfrak{j}\equiv\mathfrak{d}$, and nodal values for $\mathfrak{d}=2$ or edge center values for $\mathfrak{d}=3$ for all $\mathfrak{j}\neq\mathfrak{d}$. While cell center velocity components

$$v_{\mathfrak{i}}^{(C)} = \frac{\overline{\rho v_{\mathfrak{i}}}}{\overline{\rho}} + \mathcal{O}(\mathfrak{h}^2) \tag{5.60}$$

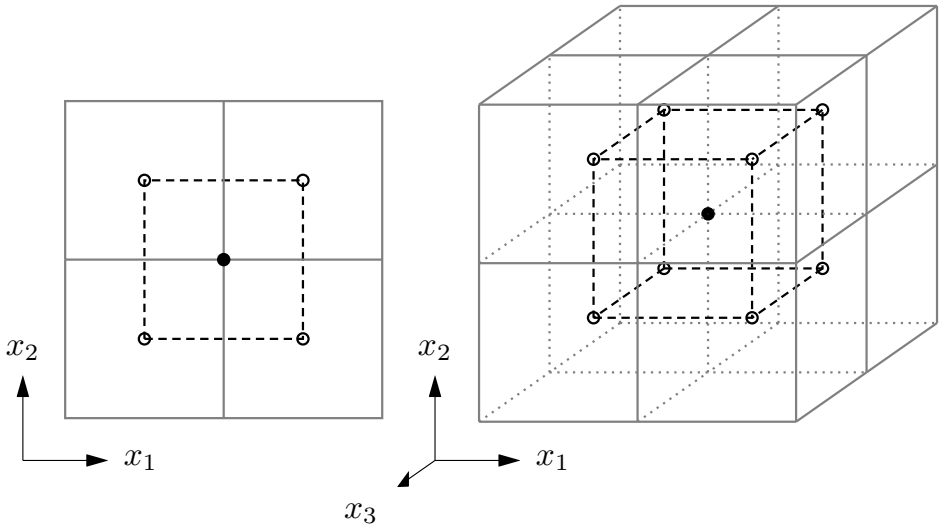

Fig. 5.5: Stencil for computation of nodal values (dot) via interpolation based on cell center values (circle), left $\mathfrak{d} = 2$, right $\mathfrak{d} = 3$

can be determined second order accurate directly based on the integral averages of the respective momentum component and the density, nodal values

$$v_{\mathfrak{i}}^{(N)} = \frac{1}{2^{\mathfrak{d}}} \sum_{\text{sur}=1}^{2^{\mathfrak{d}}} \left(v_{\mathfrak{i}}^{(C)} \right)_{\text{sur}} + \mathcal{O}(\mathfrak{h}^2) \tag{5.61}$$

need to be obtained via second order accurate interpolation from all $2^{\mathfrak{d}}$ surrounding cell center values as sketched in ***Fig. 5.5***. Edge center values

$$v_{\mathfrak{i}}^{(E)} = \frac{1}{2^{\mathfrak{d}-1}} \sum_{\text{pla}=1}^{2^{\mathfrak{d}-1}} \left(v_{\mathfrak{i}}^{(C)} \right)_{\text{pla}} + \mathcal{O}(\mathfrak{h}^2) \tag{5.62}$$

for the case of three spatial dimensions need to be determined via second order accurate interpolation from all $2^{\mathfrak{d}-1}$ neighboring cell centers, which are in the same plane as the edge center, as sketched in ***Fig. 5.6***. The resulting stencils for both $\mathfrak{d} = 2$ and $\mathfrak{d} = 3$ for determination of the grid cell face normal viscous flux across one grid cell face are sketched in ***Fig. 5.7*** as, for example, given in [20]. The viscosity coefficients μ and λ in equation (5.57) are approximated at

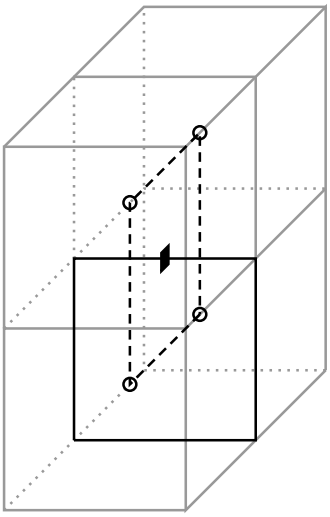

Fig. 5.6: Stencil for computation of edge center values (cross) via interpolation based on cell center values (circle)

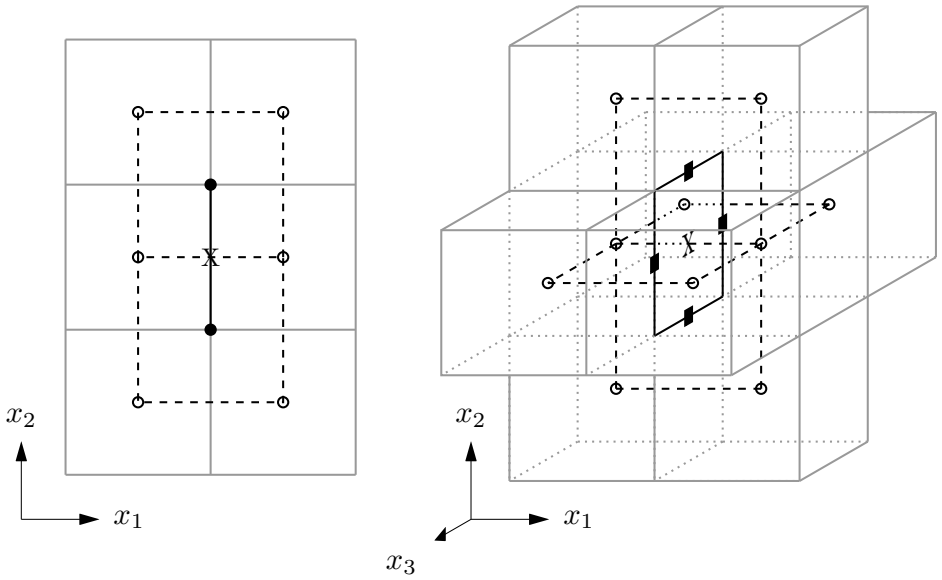

Fig. 5.7: Stencil values (circles) for computation of viscous fluxes at grid cell face centers (cross), left $\mathfrak{d} = 2$, right $\mathfrak{d} = 3$

the grid cell face second order accurate by central differences based on the cell center values of grid cells sharing the respective cell face according to (5.56a).

5.1.4 Source Terms

In this section discretization of the contributions, which are treated as (passive) source terms during the predictor step, is described, starting with the dynamic pressure, which is discretized on cell faces, in section 5.1.4.1 before discretization of the volume sources (in grid cell centers) is described in section 5.1.4.2.

5.1.4.1 Dynamic Pressure

As stated in section 5.1.3.1, the dynamic pressure contribution to the momentum equation can be treated as "passive" momentum source in the predictor step due to decoupling of momentum and energy equation and assumed time-independence of the dynamic pressure contribution to the momentum equation during the predictor step due to splitting (5.7) with predicted dynamic pressure $\pi^{'}$. The contribution

$$\int_{\Omega_\mathrm{i}} \nabla\pi^{'}\,\mathrm{d}V = \int_{\Omega_\mathrm{i}} \nabla\cdot\left(\boldsymbol{I}\pi^{'}\right)\,\mathrm{d}V = \oint_{\partial\Omega_\mathrm{i}} \boldsymbol{I}\pi^{'}\cdot\vec{n}\,\mathrm{d}A = \oint_{\partial\Omega_\mathrm{i}} \pi^{'}\vec{n}\,\mathrm{d}A \qquad (5.63)$$

to the momentum sources (5.6b) during the predictor step is added to the explicit grid cell face normal advective flux approximation, discussed in section 5.1.3.1, for conservative approximation in the course of explicit treatment of momentum contributions according to (4.24) and (5.21). Exemplary, on grid cell face $(i+\frac{1}{2},j,k)$ the predictor pressure contribution is approximated as grid cell face normal flux component

$$\left(\overline{\mathcal{F}}^{(\pi)}_{(\rho v_1),1,2}\right)_{\mathfrak{i}} \;=\; \overline{\mathcal{F}}^{(\pi)}_{(\rho v_1),(i+\frac{1}{2},j,k)} \;=\; \pi^{'}_{(i+\frac{1}{2},j,k)} \;+\; \mathcal{O}(\mathfrak{h}^2) \tag{5.64}$$

with

$$\pi^{'}_{(i+\frac{1}{2},j,k)} := \frac{1}{\mathcal{N}^{(N)}} \sum_{\mathfrak{n}=1}^{\mathcal{N}^{(N)}} \pi^{'(N)}_{\mathfrak{n}} \tag{5.65}$$

as the predictor pressure in the cell face center, resulting from interpolation based on the $\mathcal{N}^{(N)}$ pressure values

$$\pi^{'(N)}_{\mathfrak{n}} \in \begin{cases} \left(\pi^{'}_{(i+\frac{1}{2},j\pm\frac{1}{2})}\right) & \mathfrak{d}=2 \\ \left(\pi^{'}_{(i+\frac{1}{2},j\pm\frac{1}{2},k\pm\frac{1}{2})}\right) & \mathfrak{d}=3 \end{cases} \tag{5.66}$$

stored in the nodes of grid cell face $(i+\frac{1}{2},j,k)$. As previously, the above transforms analogously to the other grid cell faces and spatial directions.

5.1.4.2 Volume Source

Volume sources are addressed throughout this work as described in the following.

5.1.4.2 - 1 Gravity

The approximation of momentum gain due to gravitational acceleration $\vec{g} = -\nabla\mathcal{U}$, contributing to $\overline{\mathcal{Q}}_{(\rho\vec{v}),\mathfrak{i}} = \overline{\mathcal{Q}}_{(\rho\vec{v}),(i,j,k)}$ in (4.24) for application to (5.21) via the operator $\mathfrak{L}^{\{1\}}_{\mathfrak{i}}$, is

$$\overline{\mathcal{Q}}_{(\rho\vec{v}),(i,j,k)} := \vec{g}\,\overline{\rho}_{(i,j,k)} \tag{5.67}$$

5.1.4.2 - 2 Species Production

Discretization of species production $\varrho_{\mathfrak{s}}$ due to chemical reactions is subject of current work and, therefore, in (5.6a)

$$\mathfrak{q}_{Y_{\mathfrak{s}}} = 0 \tag{5.68}$$

is chosen throughout this work, resulting in

$$\overline{\mathcal{Q}}_{(\rho Y_{\mathfrak{s}}),\mathfrak{i}} = \overline{\mathcal{Q}}_{(\rho Y_{\mathfrak{s}}),(i,j,k)} = 0 \tag{5.69}$$

in (4.24) for application to (5.21) via the operator $\mathfrak{L}_{\mathfrak{i}}^{\{1\}}$.

5.1.4.2 - 3 Energy / Entropy Sources

The present work is restricted to cases in which

$$\mathfrak{q}_{\mathcal{P}} = 0 \tag{5.70}$$

in (5.6c), resulting in

$$\overline{\mathcal{Q}}_{(\rho\Theta),\mathfrak{i}} = \overline{\mathcal{Q}}_{(\mathcal{P}),(i,j,k)} = 0 \tag{5.71}$$

in (4.24) for application to (5.21) via the operator $\mathfrak{L}_{\mathfrak{i}}^{\{1\}}$. Relation (5.70) is obtained by one of the following options or a combination of both:

- incompressible fluids ($\chi = 0$)
- adiabatic systems ($\dot{\mathfrak{q}}_q = 0$) in equilibrium – isothermal flow ($\nabla T = 0$, $\nabla h_{\mathfrak{s}} = 0$) in absence of chemical reactions ($\varrho_{\mathfrak{s}} = 0$) – resulting in $\dot{q} = 0$ from (3.130) with (3.88) and (3.89), at constant background pressure[16] ($(\, P_0 \,)_t = 0$)

5.1.5 Summary: Predictor

After the predictor step

- all scalar conserved quantities are already advanced in time second order accurate
- yet all conserved quantities are determined based on fluxes that do not satisfy the divergence constraint (3.140) as the velocity field yet does not satisfy (3.140)
- momentum is only first order accurate in time (while second order accurate in space) as time evolution of the dynamic pressure $p^{'}$ is not yet accounted for

[16] Time-independence of the background pressure is a consequence of isothermal flow in the zero Mach number regime as shown in the footnotes of page 43

- the dynamic pressure $p^{'}$ has not changed yet as in the predictor step only the time-independent contribution $\pi^{'}$ to (5.7) is considered.
- since the divergence constraint (3.140) is not yet satisfied, in (5.8) $\mathfrak{E} \neq 0$ holds

The approximation of the integral average of any conserved quantity $\rho\psi$ after the predictor step $\mathfrak{P}$ is labeled $\overline{\rho\psi}^{(n+1),*} \equiv \overline{\mathcal{P}\Phi}^{(n+1),*}$ according to (5.2a).

5.2 Corrector

The corrector $\mathfrak{C}$ of the projection method is split into two projection steps as done in [151], [92] and [180]:

1. The first projection $\mathfrak{C}_{(1)}$ determines correction fluxes for all conserved quantities, such that the resulting fluxes, consisting of the sum of these correction fluxes and the advective fluxes (5.47) from the predictor step, satisfy the divergence constraint (3.140). This step, described in section 5.2.1, thus, inserts the elliptic contributions into the grid cell face fluxes, which gives rise to solving a Poisson problem for cell centered values as described in section 5.5.
2. The second projection $\mathfrak{C}_{(2)}$, described in section 5.2.2,
   (a) determines momentum correction fluxes, such that the final grid cell centered velocity field, derived from the corrected momentum, satisfies the divergence constraint (3.140).
   (b) updates the dynamic pressure according to (5.7) after determination of a nodal approximation to the space-time dependent pressure increment $\partial p^{'}(\vec{x},t)$. The latter is obtained by solving a Poisson problem on a staggered grid in centers of dual cells[17] as sketched in ***Fig. 5.8***. The Poisson solution both represents the pressure increment $\partial p^{'}(\vec{x},t)$ and serves as basis for determination of the momentum correction fluxes in (a).

5.2.1 Flux Correction

The flux integral approximations during the predictor step $\mathfrak{P}$, leading to second order accurate updates for all scalars and a first order update for the momentum, since time

[17] The grid cells of the staggered grid are called dual cells; centers of the dual grid cells are the nodes of the grid cells of the primal grid.

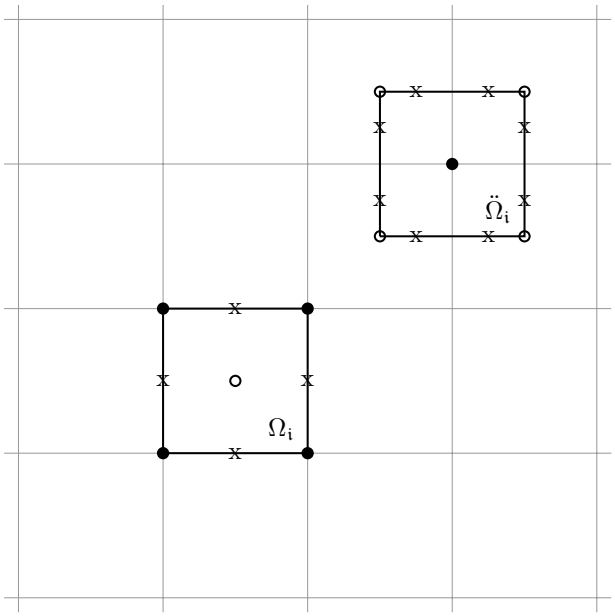

Fig. 5.8: Primal grid cell $\Omega_\mathfrak{i}$ and dual grid cell $\ddot{\Omega}_\mathfrak{i}$ for $\mathfrak{d} = 2$, *circles*: primal cell centers (dual cell nodes), *dots*: dual cell centers (primal cell nodes), *crosses*: (sub-)face centers

dependence of the dynamic pressure is omitted, yet lack the elliptic properties due to the divergence constraint (3.140). For determination of the desired grid cell face normal carrier flux $(\mathcal{P}\vec{v} \cdot \vec{n})$, that satisfies (3.140), the integral time-discrete second order accurate Poisson equation

$$\oint_{\partial\Omega_\mathfrak{i}} \left(\frac{\Delta t}{2} \Theta^{\left(n+\frac{1}{2}\right),*} \right) \nabla \partial\pi'^{\left(n+\frac{1}{2}\right)} \cdot \vec{n} \, \mathrm{d}A = -\frac{\Delta V_\mathfrak{i}}{\Delta t} \left(\overline{\mathcal{P}}_\mathfrak{i}^{(n+1),*} - \overline{\mathcal{P}}_\mathfrak{i}^{(n)} \right) + Q_\mathfrak{i}^{\left(n+\frac{1}{2}\right),*} \tag{5.72}$$

with

$$Q_\mathfrak{i}^{\left(n+\frac{1}{2}\right),*} := \int_{\partial\Omega_\mathfrak{i}} \left[\mathcal{P} \left(\mathcal{S} - \mathcal{D} \right) \right]^{\left(n+\frac{1}{2}\right),*} \mathrm{d}V \tag{5.73}$$

is obtained as sketched in the following steps, corresponding to a generalized MAC-projection – referred to as first projection tracing back to [70] – with integral Finite Volume discretization of the discrete divergence operator as done in [92] and [180]:

1. integration of (3.140) in time from t^n to t^{n+1}:

$$\int_{t^n}^{t^{n+1}} \oint_{\partial\Omega_\mathfrak{i}} \left(\mathcal{P}\vec{v} \cdot \vec{n} \right) \mathrm{d}A \, \mathrm{d}t = \int_{t^n}^{t^{n+1}} \int_{\Omega_\mathfrak{i}} \mathcal{P}\mathcal{D} \, \mathrm{d}V \, \mathrm{d}t \tag{5.74}$$

2. exchanging the order of temporal and spatial integration (which is possible due

to time-independent Ω_i):

$$\oint_{\partial\Omega_\mathrm{i}} \int_{t^n}^{t^{n+1}} (\mathcal{P}\vec{v}\cdot\vec{n})\ \mathrm{d}t\,\mathrm{d}A = \int_{\Omega_\mathrm{i}} \int_{t^n}^{t^{n+1}} \mathcal{P}\mathcal{D}\,\mathrm{d}t\,\mathrm{d}V \tag{5.75}$$

3. approximation

$$\int_{t^n}^{t^{n+1}} (\mathcal{P}\vec{v}\cdot\vec{n})\ \mathrm{d}t \ = \ \Delta t\ \widetilde{\mathcal{P}\vec{v}}\cdot\vec{n} \ = \ \Delta t\ (\mathcal{P}\vec{v})^{\left(n+\frac{1}{2}\right)}\cdot\vec{n} + \mathcal{O}\left(\Delta t^3\right) \tag{5.76}$$

in (5.75) with

$$\widetilde{\mathcal{P}\vec{v}}\cdot\vec{n} = \frac{1}{\Delta t}\int_{t^n}^{t^{n+1}} \mathcal{P}\vec{v}\cdot\vec{n}\,\mathrm{d}t \tag{5.77}$$

as temporal average, yielding

$$\Delta t \oint_{\partial\Omega_\mathrm{i}} \left((\mathcal{P}\vec{v})^{\left(n+\frac{1}{2}\right)}\cdot\vec{n}\right)\mathrm{d}A \ = \Delta t \int_{\Omega_\mathrm{i}} (\mathcal{P}\mathcal{D})^{\left(n+\frac{1}{2}\right)}\ \mathrm{d}V + \mathcal{O}(\Delta t^3) \tag{5.78}$$

4. approximation of $(\mathcal{P}\vec{v})^{\left(n+\frac{1}{2}\right)}$ in (5.78) by

$$\begin{aligned}(\mathcal{P}\vec{v})^{\left(n+\frac{1}{2}\right)} &= \Theta^{\left(n+\frac{1}{2}\right)}\,(\rho\vec{v})^{\left(n+\frac{1}{2}\right)} \\ &= \Theta^{\left(n+\frac{1}{2}\right)}\frac{\left((\rho\vec{v})^{(n+1)} + (\rho\vec{v})^{(n)}\right)}{2} + \mathcal{O}(\Delta t^2)\end{aligned} \tag{5.79}$$

5. replacement of the yet unknown $(\rho\vec{v})^{(n+1)}$ in (5.79) by

$$(\rho\vec{v})^{(n+1)} = (\rho\vec{v})^{(n+1),*} - \Delta t\,\partial\pi'^{\left(n+\frac{1}{2}\right)} + \mathcal{O}(\Delta t^2) \tag{5.80}$$

after

   (a) Integration of the non-integral form of momentum equation (3.128c) in time from t^n to t^{n+1}:

$$\begin{aligned}&(\rho\vec{v})^{(n+1)} \\ &\quad = (\rho\vec{v})^{(n)} - \Delta t\left(\nabla\rho\vec{v}\circ\vec{v} - \nabla\cdot\boldsymbol{\mathcal{T}} + \nabla p' - \rho\vec{g}\right)^{\left(n+\frac{1}{2}\right)} \\ &\qquad + \mathcal{O}(\Delta t^2)\end{aligned} \tag{5.81}$$

(b) subtraction of the prediction

$$\begin{aligned}(\rho\vec{v})^{(n+1),*} &= (\rho\vec{v})^{(n)} - \Delta t\left((\nabla\rho\vec{v}\circ\vec{v} - \nabla\cdot\boldsymbol{\mathcal{T}})^{(n+\frac{1}{2}),*} + \nabla\pi' - \rho^{(n+\frac{1}{2}),*}\vec{g}\right)\\ &\quad + \mathcal{O}(\Delta t^2)\end{aligned} \tag{5.82}$$

from (5.81), yielding (5.80) due to $\rho^{(n+\frac{1}{2})} = \rho^{(n+\frac{1}{2}),*} + \mathcal{O}(\Delta t^2)$ with

$$\begin{aligned}\nabla\partial\pi'^{\,(n+\frac{1}{2})} := \nabla\partial p'^{\,(n+\frac{1}{2})} &+ \nabla\cdot\left[(\rho\vec{v}\circ\vec{v})^{(n+\frac{1}{2})} - (\rho\vec{v}\circ\vec{v})^{(n+\frac{1}{2}),*}\right]\\ &+ \nabla\cdot\left[(\boldsymbol{\mathcal{T}})^{(n+\frac{1}{2})} - (\boldsymbol{\mathcal{T}})^{(n+\frac{1}{2}),*}\right]\end{aligned} \tag{5.83}$$

6. consideration of both

$$(\rho\vec{v})^{(n+\frac{1}{2}),*} = \frac{\left((\rho\vec{v})^{(n+1),*} + (\rho\vec{v})^{(n)}\right)}{2} + \mathcal{O}(\Delta t^2) \tag{5.84}$$

and

$$\Theta^{(n+\frac{1}{2}),*} = \Theta^{(n+\frac{1}{2})} + \mathcal{O}(\Delta t^2) \tag{5.85}$$

and, thus, in equation (5.79)

$$\Theta^{(n+\frac{1}{2})}\frac{\left((\rho\vec{v})^{(n+1),*} + (\rho\vec{v})^{(n)}\right)}{2} = (\mathcal{P}\vec{v})^{(n+\frac{1}{2}),*} + \mathcal{O}(\Delta t^2) \tag{5.86}$$

as well as

$$(\mathcal{P}\vec{v})^{(n+\frac{1}{2})} = (\mathcal{P}\vec{v})^{(n+\frac{1}{2}),*} + \mathcal{O}(\Delta t^2) \tag{5.87}$$

after inserting (5.80). This transforms (5.78) to

$$\Delta t\oint_{\partial\Omega_{\mathfrak{i}}}\left((\mathcal{P}\vec{v})^{(n+\frac{1}{2}),*}\cdot\vec{n}\right)\,\mathrm{d}A = \Delta t\int_{\Omega_{\mathfrak{i}}}(\mathcal{P}\mathcal{D})^{(n+\frac{1}{2})}\,\mathrm{d}V + \mathcal{O}(\Delta t^3) \tag{5.88}$$

7. replacement of the left hand side of (5.88) according to

$$\begin{aligned}\Delta t\oint_{\partial\Omega_{\mathfrak{i}}}\left((\mathcal{P}\vec{v})^{(n+\frac{1}{2}),*}\cdot\vec{n}\right)\,\mathrm{d}A = &-\Delta V_{\mathfrak{i}}\left(\overline{\mathcal{P}}^{(n+1),*} - \overline{\mathcal{P}}^{(n)}\right)\\ &+\Delta t\int_{\Omega_{\mathfrak{i}}}(\mathcal{P}\mathcal{S})^{(n+\frac{1}{2})}\,\mathrm{d}V\end{aligned} \tag{5.89}$$

with $\Delta V_{\mathfrak{i}} := \mathfrak{h}^{\mathfrak{d}}\left(\Pi_{\check{\mathfrak{d}}=1}^{\mathfrak{d}}\xi_{\check{\mathfrak{d}}}\right)$ from approximation of the spatio-temporal integral of $(\mathcal{P})_t + \nabla\cdot(\mathcal{P}\vec{v}) = \mathcal{P}\mathcal{D}$ during the predictor step

8. consideration of

$$\mathcal{P}^{(n+\frac{1}{2})} = \mathcal{P}^{(n+\frac{1}{2}),*} + \mathcal{O}(\Delta t^2) = \frac{\mathcal{P}^{(n+1),*} + \mathcal{P}^{(n)}}{2} + \mathcal{O}(\Delta t^2) \quad (5.90a)$$

$$\mathcal{S}^{(n+\frac{1}{2})} = \mathcal{S}^{(n+\frac{1}{2}),*} + \mathcal{O}(\Delta t^2) = \frac{\mathcal{S}^{(n+1),*} + \mathcal{S}^{(n)}}{2} + \mathcal{O}(\Delta t^2) \quad (5.90b)$$

$$\mathcal{D}^{(n+\frac{1}{2})} = \mathcal{D}^{(n+\frac{1}{2}),*} + \mathcal{O}(\Delta t^2) = \frac{\mathcal{D}^{(n+1),*} + \mathcal{D}^{(n)}}{2} + \mathcal{O}(\Delta t^2) \quad (5.90c)$$

In (5.72) $\overline{\mathcal{P}}_{\mathfrak{i}}^{(n)}$ is known as result from the previous time step, integrating the governing equations from t^{n-1} to t^n, $\overline{\mathcal{P}}_{\mathfrak{i}}^{(n+1),*}$ results from the current predictor step $\mathfrak{P}$ and $Q_{\mathfrak{i}}^{(n+\frac{1}{2}),*} = 0$ for incompressible fluids, since both $\mathcal{S} = 0$ and $\mathcal{D} = 0$ due to $\chi = \frac{1}{\rho c^2} = 0$. The benefit of formulation (5.72) is, that the divergence does not have to be evaluated explicitly as the divergence error, accumulated during the predictor step, is contained in the predictor result $\overline{\mathcal{P}}_{\mathfrak{i}}^{(n+1),*}$ and can be extracted if the true value $\overline{\mathcal{P}}_{\mathfrak{i}}^{(n+1)}$ is (approximately) known. A further advantage of the Finite Volume representation of the Poisson equation (5.72) is, that the result $\partial\pi'^{(n+\frac{1}{2})}$ can be used directly for computation of the correction fluxes for $\mathcal{P}$, since $Q_{\mathfrak{i}}^{(n+\frac{1}{2}),*}$ in (5.72) represents an approximation to the true (physical) change of $\mathcal{P}$. Therefore both left and right hand side of (5.72) represent the error $\Delta V_{\mathfrak{i}}\big(\overline{\mathcal{P}}^{(n+1),**} - \overline{\mathcal{P}}^{(n+1),*}\big)$ due to omission of the divergence constraint during the predictor step with $\overline{\mathcal{P}}^{n+1,**}$ as corrected approximation to $\overline{\mathcal{P}}_{\mathfrak{i}}^{(n+1)}$.

Equation (5.72) is solved for the unknown $\partial\pi'^{(n+\frac{1}{2})}$ after spatial discretization

$$\frac{1}{\mathfrak{h}} \sum_{\mathfrak{d}=1}^{\mathfrak{d}} \frac{1}{\mathfrak{c}_{\mathfrak{d}}} \sum_{\mathfrak{w}=1}^{2} (-1)^{\mathfrak{w}} \Delta\widetilde{\overline{\mathcal{F}}}_{(\mathcal{P}),\mathfrak{d},\mathfrak{w}} = -\frac{1}{\Delta t}\left(\overline{\mathcal{P}}_{\mathfrak{i}}^{(n+1),*} - \overline{\mathcal{P}}_{\mathfrak{i}}^{(n)}\right) \quad (5.91)$$

with $Q_{\mathfrak{i}}^{(n+\frac{1}{2}),*} = 0$ and

$$\Delta\widetilde{\overline{\mathcal{F}}}_{(\mathcal{P}),\mathfrak{d},\mathfrak{w}} := \left[\left(\frac{\Delta t}{2}\Theta^{(n+\frac{1}{2}),*}\right)_{\mathfrak{d},\mathfrak{w}} \nabla\partial\pi'^{(n+\frac{1}{2})}_{\mathfrak{d},\mathfrak{w}} \cdot \vec{\mathfrak{e}}_{\mathfrak{d}}\right] \quad (5.92)$$

involving approximations as

$$\nabla\partial\pi'^{(n+\frac{1}{2})}_{1,2} \equiv \nabla\partial\pi'^{(n+\frac{1}{2})}_{(i+\frac{1}{2},j,k)} = \frac{\partial\pi'^{(n+\frac{1}{2})}_{(i+1,j,k)} - \partial\pi'^{(n+\frac{1}{2})}_{(i,j,k)}}{\mathfrak{c}_1\,\mathfrak{h}} + \mathcal{O}(\mathfrak{h}^2) \quad (5.93)$$

of the facial gradient $\nabla\partial\pi'^{(n+\frac{1}{2})}_{(i+\frac{1}{2},j,k)}$, exemplified for grid cell face $(i+\frac{1}{2}, j, k)$ with face

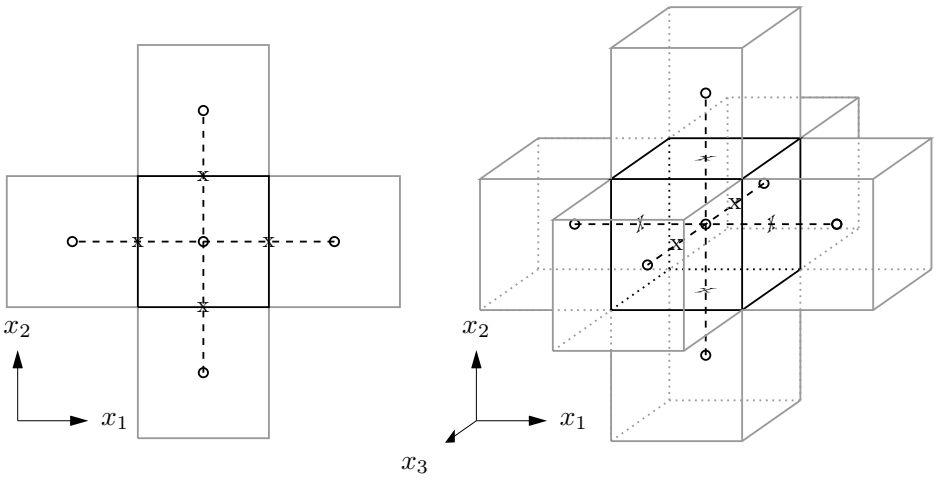

Fig. 5.9: Stencils for cell centered projection: 5-point stencil for $\mathfrak{d} = 2$ (left) and 7-point stencil for $\mathfrak{d} = 3$ (right)

normal in direction $\mathfrak{d} = 1$, with unknown cell center values ${\partial\pi'}^{\left(n+\frac{1}{2}\right)}_{(i+1,j,k)}$ and ${\partial\pi'}^{\left(n+\frac{1}{2}\right)}_{(i,j,k)}$ in the grid cells sharing cell face $(i+\frac{1}{2}, j, k)$, as well as

$$\begin{aligned}\left(\frac{\Delta t}{2}\Theta^{(n+\frac{1}{2}),*}\right)_{1,2} &= \frac{\Delta t}{2}\,\Theta^{(n+\frac{1}{2}),*}_{(i+\frac{1}{2},j,k)} \\ &= \Delta t\frac{\Theta^{(n+1),*}_{(i+1,j,k)} + \Theta^{(n+1),*}_{(i,j,k)} + \Theta^{(n)}_{(i+1,j,k)} + \Theta^{(n)}_{(i,j,k)}}{8} + \mathcal{O}(\mathfrak{h}^2)\end{aligned} \tag{5.94}$$

considering (3.141) and $\Delta t \sim \mathfrak{h}$. Approximation (5.93) leads to a linear system

$$\mathfrak{A}_\Theta \cdot \vec{\partial\pi}'^{\left(n+\frac{1}{2}\right)} = \vec{\mathcal{R}}_{\overline{\mathcal{P}}} \tag{5.95}$$

for cell center values of ${\partial\pi'}^{\left(n+\frac{1}{2}\right)}$ with 5-point stencil for each grid cell as sketched in ***Fig. 5.9***, subject to boundary conditions as given in section 5.4.2. After inserting the resulting solutions ${\partial\pi'}^{\left(n+\frac{1}{2}\right)}$ into (5.93) and the latter, together with the coefficient approximation (5.94), into (5.92), the correction flux based update

$$\Delta\overline{\mathcal{P}} := \overline{\mathcal{P}}^{(n+1),**} - \overline{\mathcal{P}}^{(n+1),*} = \Delta t\left(\frac{1}{\mathfrak{h}}\sum_{\mathfrak{d}=1}^{\mathfrak{d}}\frac{1}{\mathfrak{c}_\mathfrak{d}}\sum_{\mathfrak{w}=1}^{2}(-1)^{\mathfrak{w}}\Delta\widetilde{\overline{\mathcal{F}}}_{(\mathcal{P}),\mathfrak{d},\mathfrak{w}}\right) \tag{5.96}$$

for each grid cell can be determined from the left hand side of equation (5.91) with now known ${\partial\pi'}^{\left(n+\frac{1}{2}\right)}$, as it corrects the difference between left and right hand side in (3.140).

Since each of the other conserved quantities has been advanced based on the approximation of the same grid cell face normal carrier flux ($\mathcal{P}\vec{v}\cdot\vec{n}$) during the predictor step, correction of divergence errors in the fluxes of these conserved quantities can be done for improved stability similarly to determination of their advective flux in section 5.1.3.1, once the carrier correction flux $\Delta\widetilde{\overline{\mathcal{F}}}_{(\mathcal{P}),\mathfrak{d},\mathfrak{w}}$ is known on each grid cell face: The carrier correction flux is split into two parts according to

$$\Delta\widetilde{\overline{\mathcal{F}}}_{(\mathcal{P}),\mathfrak{d},\mathfrak{w}} = \Delta\widetilde{\overline{\mathcal{F}}}^{(\mathcal{L})}_{(\mathcal{P}),\mathfrak{d},\mathfrak{w}} + \Delta\widetilde{\overline{\mathcal{F}}}^{(\mathcal{U})}_{(\mathcal{P}),\mathfrak{d},\mathfrak{w}} \tag{5.97}$$

with one of the carrier flux contributions

$$\Delta\widetilde{\overline{\mathcal{F}}}^{(\mathcal{L})}_{(\mathcal{P}),\mathfrak{d},\mathfrak{w}} := \max\left(0, \Delta\widetilde{\overline{\mathcal{F}}}_{(\mathcal{P}),\mathfrak{d},\mathfrak{w}}\right) \geqslant 0 \tag{5.98a}$$

$$\Delta\widetilde{\overline{\mathcal{F}}}^{(\mathcal{U})}_{(\mathcal{P}),\mathfrak{d},\mathfrak{w}} := \min\left(0, \Delta\widetilde{\overline{\mathcal{F}}}_{(\mathcal{P}),\mathfrak{d},\mathfrak{w}}\right) \leqslant 0 \tag{5.98b}$$

equal to zero. The resulting correction flux of any other conserved quantity reads

$$\Delta\widetilde{\overline{\mathcal{F}}}_{(\rho\psi),\mathfrak{d},\mathfrak{w}} = \Delta\widetilde{\overline{\mathcal{F}}}^{(\mathcal{L})}_{(\mathcal{P}),\mathfrak{d},\mathfrak{w}}\,\Phi^{(\mathcal{L})}_{\mathfrak{d},\mathfrak{w}} + \Delta\widetilde{\overline{\mathcal{F}}}^{(\mathcal{U})}_{(\mathcal{P}),\mathfrak{d},\mathfrak{w}}\,\Phi^{(\mathcal{L})}_{\mathfrak{d},\mathfrak{w}} \tag{5.99}$$

with Φ as any component from (5.5a) and, for example, for grid cell face $(i+\frac{1}{2},j,k)$ with $\mathfrak{d}=1$ and $\mathfrak{w}=2$,

$$\Phi^{(\mathcal{L})}_{1,2} \equiv \Phi^{(\mathcal{L})}_{(i+\frac{1}{2},j,k)} = \Phi_{(i,j,k)} = \frac{\overline{\rho\psi}_{(i,j,k)}}{\overline{\mathcal{P}}_{(i,j,k)}} \tag{5.100a}$$

$$\Phi^{(\mathcal{U})}_{1,2} \equiv \Phi^{(\mathcal{U})}_{(i+\frac{1}{2},j,k)} = \Phi_{(i+1,j,k)} = \frac{\overline{\rho\psi}_{(i+1,j,k)}}{\overline{\mathcal{P}}_{(i+1,j,k)}} \tag{5.100b}$$

as upwind values. First order accurate upwind values are sufficient for maintaining second order accuracy as shown in [92], since the flux corrections add second order contributions to the second order accurate predicted values $\overline{\rho\psi}^{(n+1),*}$. This yields

$$\begin{aligned}\overline{\rho\psi}^{(n+1),**} &= \overline{\rho\psi}^{(n+1),*} - \Delta t\left(\frac{1}{\mathfrak{h}}\sum_{\mathfrak{d}=1}^{\mathfrak{d}}\frac{1}{\mathfrak{c}_{\mathfrak{d}}}\sum_{\mathfrak{w}=1}^{2}(-1)^{\mathfrak{w}}\Delta\widetilde{\overline{\mathcal{F}}}_{(\rho\psi),\mathfrak{d},\mathfrak{w}}\right)\\ &= \overline{\rho\psi}^{(n)} - \Delta t\left(\frac{1}{\mathfrak{h}}\sum_{\mathfrak{d}=1}^{\mathfrak{d}}\frac{1}{\mathfrak{c}_{\mathfrak{d}}}\sum_{\mathfrak{w}=1}^{2}(-1)^{\mathfrak{w}}\left(\widetilde{\overline{\mathcal{F}}}^{*}_{(\rho\psi),\mathfrak{d},\mathfrak{w}} + \Delta\widetilde{\overline{\mathcal{F}}}_{(\rho\psi),\mathfrak{d},\mathfrak{w}}\right)\right)\end{aligned} \tag{5.101}$$

with spatio-temporal flux average $\widetilde{\overline{\mathcal{F}}}^{*}_{(\rho\psi),\mathfrak{d},\mathfrak{w}}$ as effective predictor flux as determined

during evaluation of $\mathfrak{P}$ in section 5.1 and

$$\widetilde{\overline{\mathcal{F}}}_{(\rho\psi),\mathfrak{d},\mathfrak{w}} = \widetilde{\overline{\mathcal{F}}}^{*}_{(\rho\psi),\mathfrak{d},\mathfrak{w}} + \Delta\widetilde{\overline{\mathcal{F}}}_{(\rho\psi),\mathfrak{d},\mathfrak{w}} \tag{5.102}$$

as resulting flux average, satisfying the divergence constraint (3.140). The algorithm of this first projection step is as follows:

1. determine coefficients on grid cell faces according to (5.94)
2. determine right hand side of (5.91) in cell centers
3. apply boundary conditions as described in section 5.4.2
4. assemble global coefficient matrix on the left hand side of (5.95), including (cell-dependent) scaling of the coefficients from step 1. with $\frac{(-1)^{\mathfrak{w}}}{\mathfrak{c}_{\mathfrak{d}}\mathfrak{h}}$
5. assemble global right hand side vector of (5.95)
6. solve linear system (5.95) for $\partial\pi'^{\left(n+\frac{1}{2}\right)}$
7. evaluate carrier correction flux (5.92)
8. compute correction fluxes (5.99) for all other conserved quantities with (5.98) and (5.100)
9. update all conserved quantities according to (5.101)

The increment, determined by solving (5.95), is ignored in the subsequent part of the numerical scheme, since the update for the nodal pressure is determined in the second projection step described in the following.

5.2.2 Momentum Correction and Pressure Update

While scalar quantities are already second order accurate and corrected as described in section 5.2.1, such that

$$\overline{\rho\psi}^{(n+1)} \equiv \overline{\rho\psi}^{(n+1),**}, \qquad \rho\psi \neq \rho\vec{v} \tag{5.103}$$

for all scalar quantities, the momentum $\overline{\rho\vec{v}}^{(n+1),**}$ still lacks the contribution due to the time-dependent pressure increment $\partial p'$ and suffers from wrong velocity divergences in the viscous stresses considered so far. Therefore momentum is first order

accurate only at this point and needs to be corrected for a second time – referred to as second projection, tracing back to [34] and [172]. The Poisson-type equation

$$\oint_{\partial\ddot{\Omega}_\mathrm{i}} \left(\Delta t\, \Theta^{(n+1),**}\right) \nabla\partial\pi'^{\left(n+\frac{1}{2}\right)} \cdot \vec{n}\,\mathrm{d}A = \oint_{\partial\ddot{\Omega}_\mathrm{i}} (\mathcal{P}\vec{v})^{(n+1),**} \cdot \vec{n}\,\mathrm{d}A - \int_{\ddot{\Omega}_\mathrm{i}} \mathcal{P}^{(n+1),**}\mathcal{D}^{(n+1),**}\,\mathrm{d}V \tag{5.104}$$

for determination of an increment $\partial\pi'$, such that the cell centered velocity field satisfies the divergence constraint (3.140), is obtained after the following steps:

1. integration of the non-integral momentum equation (3.128c) over time:

$$(\rho\vec{v})^{(n+1)} = (\rho\vec{v})^{(n)} - \int_{t^n}^{t^{n+1}} \left(\nabla\cdot\rho\vec{v}\circ\vec{v} - \nabla\cdot\boldsymbol{\mathcal{T}} + \nabla p' - \rho\vec{g}\right)\,\mathrm{d}t \tag{5.105}$$

2. separating parts already treated before ($(\rho\vec{v})^{(n+1),**}$) from the ones not yet considered, taking into account (5.7):

$$(\rho\vec{v})^{(n+1)} = \overbrace{(\rho\vec{v})^{(n)} - \int_{t^n}^{t^{n+1}} \left(\nabla\cdot\rho\vec{v}\circ\vec{v} - \nabla\cdot\boldsymbol{\mathcal{T}}^* + \nabla\pi' - \rho\vec{g}\right)\,\mathrm{d}t}^{=(\rho\vec{v})^{(n+1),**}} - \int_{t^n}^{t^{n+1}} \nabla\partial\pi'\,\mathrm{d}t \tag{5.106}$$

with

$$\nabla\partial\pi' := \nabla\partial p' - \nabla\cdot(\boldsymbol{\mathcal{T}} - \boldsymbol{\mathcal{T}}^*) \tag{5.107}$$

or

$$\nabla\cdot\left(\boldsymbol{I}\partial\pi' - \boldsymbol{I}\partial p' + (\boldsymbol{\mathcal{T}} - \boldsymbol{\mathcal{T}}^*)\right) = \vec{0} \tag{5.108}$$

and $(\boldsymbol{\mathcal{T}} - \boldsymbol{\mathcal{T}}^*)$ as given below

3. multiplication with $\Theta^{(n+1)}$ as defined in (3.141), considering $\Theta^{(n+1),**} = \Theta^{(n+1)}$ due to both $\mathcal{P}^{(n+1),**} = \mathcal{P}^{(n+1)}$ and $\rho^{(n+1),**} = \rho^{(n+1)}$ and second order accurate approximation of the time integral:

$$(\mathcal{P}\vec{v})^{(n+1)} = (\mathcal{P}\vec{v})^{(n+1),**} - \left(\Delta t\, \Theta^{(n+1),**}\right) \nabla\partial\pi'^{\left(n+\frac{1}{2}\right)} + \mathcal{O}\left(\Delta t^3\right) \tag{5.109}$$

4. application of the (discrete) divergence operator, integration over dual control volume $\ddot{\Omega}_{\mathfrak{i}}$, application of the divergence theorem and considering (3.140)

For stability reasons, avoiding generation of checkerboard-like patterns in the numerical solution due to numerical decoupling of neighboring grid cells, the pressure increment is determined on a staggered grid, whose dual grid cells $\ddot{\Omega}_{\mathfrak{i}}$ are centered in the nodes of the original, primal, grid cells $\Omega_{\mathfrak{i}}$, as done in [92], [180], [95], [151] and [17]. The increment in the center of grid cell face $(i+\frac{1}{2},j,k)$ between primal cells (i,j,k) and $(i+1,j,k)$ is approximated similarly to (5.65) for evaluation of the approximation of the momentum flux contribution due to the predictor pressure as

$$\partial\pi_{1,2}^{'\left(n+\frac{1}{2}\right)} = \partial\pi_{(i+\frac{1}{2},j,k)}^{'\left(n+\frac{1}{2}\right)} = \frac{1}{2^{(\mathfrak{d}-1)}} \sum_{\mathfrak{n}=1}^{2^{(\mathfrak{d}-1)}} \partial\pi_{\mathfrak{n}}^{'(N)} \tag{5.110}$$

which results from interpolation based on the $2^{(\mathfrak{d}-1)}$ yet unknown increments

$$\partial\pi_{\mathfrak{n}}^{'(N)} \in \begin{cases} \left(\partial\pi'_{(i+\frac{1}{2},j\pm\frac{1}{2})}\right) & \text{for } \mathfrak{d}=2 \\ \left(\partial\pi'_{(i+\frac{1}{2},j\pm\frac{1}{2},k\pm\frac{1}{2})}\right) & \text{for } \mathfrak{d}=3 \end{cases} \tag{5.111}$$

in nodes of the primal grid cell face $(i+\frac{1}{2},j,k)$. This, as previously, holds for the other grid cell faces analogously. Both left and right hand side of (5.104) are discretized on sub-cells of the dual cell $\ddot{\Omega}_{\mathfrak{i}}$, separated by the boundary of the primal cells as sketched in ***Fig. 5.8***, by second order accurate approximation of the boundary integrals in centers of sub-cell faces and approximation of volume integrals in the center of sub-cells. Bi-linear ($\mathfrak{d}=2$) / tri-linear ($\mathfrak{d}=3$) ansatz functions

$$\partial\pi_{\mathfrak{i}}^{'}(\vec{x}) \approx \sum_{\mathfrak{k}=0}^{\mathfrak{d}-2} \sum_{\mathfrak{j}=0}^{1} \sum_{\mathfrak{i}=0}^{1} \left(\mathfrak{a}_{\mathfrak{i},\mathfrak{j},\mathfrak{k}}\left(\partial\pi^{'(N)}\right) \Pi_{\mathfrak{d}=1}^{\mathfrak{d}} \left(x_{\mathfrak{d}}^{(\mathfrak{i},\mathfrak{j},\mathfrak{k})_{\mathfrak{d}}} \right) \right) \tag{5.112}$$

for the unknown increment $\partial\pi^{'}$ on primal grid cells with coefficients $\mathfrak{a}_{\mathfrak{i},\mathfrak{j},\mathfrak{k}}(\partial\pi^{'(N)})$ as functions of the (unknown) primal cell node (or dual cell center) values $\partial\pi^{'(N)}$, lead to a 9-point stencil for $\mathfrak{d}=2$ and a 27-point stencil for $\mathfrak{d}=3$ as done in [128] and [130]. The cited literature is refered to for more details on the discretization. The stencils are sketched in ***Fig. 5.10*** and the resulting spatial discretization of (5.104)

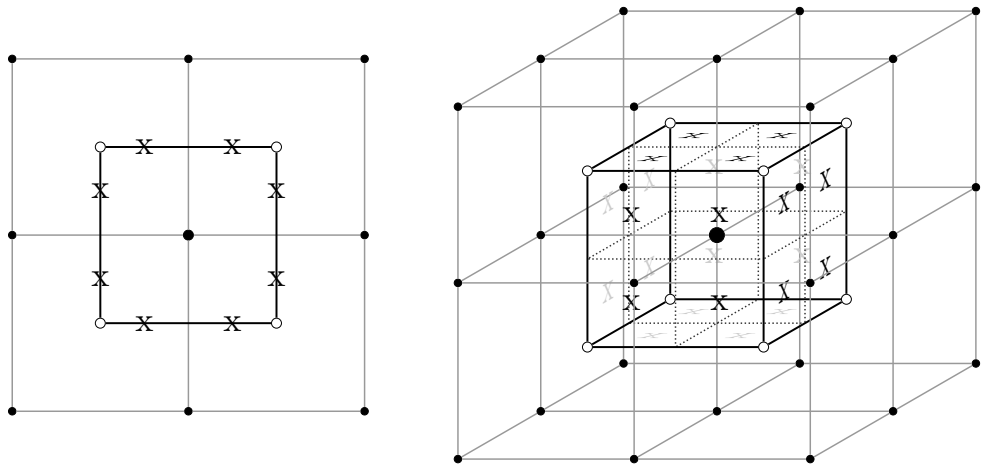

Fig. 5.10: Stencil for second projection step with *black dots* indicating dual cell centers, *circles* indicating primal cell centers and *crosses* marking locations at which flux averages are approximated: *left*: 9-point stencil ($\mathfrak{d} = 2$), *right*: 27-point stencil ($\mathfrak{d} = 3$)

reads

$$\frac{1}{\mathfrak{h}} \sum_{\mathfrak{d}=1}^{\mathfrak{d}} \frac{1}{\mathfrak{c}_{\mathfrak{d}}} \sum_{\mathfrak{w}=1}^{2} (-1)^{\mathfrak{w}} \sum_{\mathfrak{x}=1}^{2^{(\mathfrak{d}-1)}} \left[\left(\Delta t \, \Theta^{(n+1),**} \right)_{\mathfrak{d},\mathfrak{w},\mathfrak{x}} \left(\nabla \partial \pi'_{\mathfrak{i}_{\mathfrak{d},\mathfrak{w},\mathfrak{x}}} \left(\ddot{\vec{x}}_{\mathfrak{d},\mathfrak{w},\mathfrak{x}} \right) \cdot \vec{\mathfrak{e}}_{\mathfrak{d}} \right) \right]$$

$$= \frac{1}{\mathfrak{h}} \sum_{\mathfrak{d}=1}^{\mathfrak{d}} \frac{1}{\mathfrak{c}_{\mathfrak{d}}} \sum_{\mathfrak{w}=1}^{2} (-1)^{\mathfrak{w}} \sum_{\mathfrak{x}=1}^{2^{(\mathfrak{d}-1)}} \left[(\mathcal{P}\vec{v})^{(n+1),**}_{\mathfrak{d},\mathfrak{w},\mathfrak{x}} \right] - \sum_{\text{sub}=1}^{2^{\mathfrak{d}}} \overline{\mathcal{P}\,\mathcal{D}}^{(n+1),**}_{\text{sub}} \tag{5.113}$$

for each dual cell with $\mathfrak{x}$ as the index of the sub-faces on a dual cell face. In (5.113) the expression $\left(\nabla \partial \pi'_{\mathfrak{i}_{\mathfrak{d},\mathfrak{w},\mathfrak{x}}} \left(\ddot{\vec{x}}_{\mathfrak{d},\mathfrak{w},\mathfrak{x}} \right) \cdot \vec{\mathfrak{e}}_{\mathfrak{d}} \right)$ – which is discretized as done in [128] and [130] – is the $\mathfrak{d}^{th}$ component of the analytically determined gradient of the ansatz function (5.112) in that primal cell $\mathfrak{i}$, in which the sub-face with indices $\mathfrak{d}, \mathfrak{w}, \mathfrak{x}$ is located in, evaluated in dual sub-face center $\ddot{\vec{x}}_{\mathfrak{d},\mathfrak{w},\mathfrak{x}}$, and, thus, a function of the $\partial \pi'^{\,(N)}$ to be determined. This results in a linear system

$$\mathfrak{A}^{(N)}_{\Theta} \cdot \vec{\partial \pi}'^{\,(N)} \;=\; \vec{\mathcal{R}}^{(N)} \tag{5.114}$$

subject to boundary conditions as given in section 5.4.2 for determination of the unknown $\partial \pi'^{\,(N)}$. Once solved as described in section 5.5, the primal cell face centered values of $\partial \pi'$ can be obtained from (5.110), and the momenta can be updated accord-

ing to

$$\begin{aligned}\overline{\rho\vec{v}}_{\mathfrak{i}}^{(n+1)} &= \overline{\rho\vec{v}}_{\mathfrak{i}}^{(n+1),**} - \frac{1}{\Delta V_{\mathfrak{i}}}\int_{t^n}^{t^{n+1}}\oint_{\partial\Omega_{\mathfrak{i}}}\partial\pi^{'}\vec{n}\,\mathrm{d}A\,\mathrm{d}t \\ &= \overline{\rho\vec{v}}_{\mathfrak{i}}^{(n+1),**} - \Delta t\left(\frac{1}{\mathfrak{h}}\sum_{\mathfrak{d}=1}^{\mathfrak{d}}\frac{1}{\mathfrak{c}_{\mathfrak{d}}}\sum_{\mathfrak{w}=1}^{2}\left[(-1)^{\mathfrak{w}}\partial\pi_{\mathfrak{d},\mathfrak{w}}^{'\left(n+\frac{1}{2}\right)}\vec{\mathfrak{e}}_{\mathfrak{d}}\right]\right) + \mathcal{O}(\Delta t^3)\end{aligned} \tag{5.115}$$

In the special case of homogeneous density ρ, homogeneous dynamic viscosity μ and zero velocity divergence $\nabla\cdot\vec{v}=0$, the general relation (5.108) with

$$\boldsymbol{\mathcal{T}}-\boldsymbol{\mathcal{T}}^{*} = -\frac{\Delta t}{2}\left(\mu^{n+\frac{1}{2}}\left(\nabla\vec{\mathfrak{g}}+(\nabla\vec{\mathfrak{g}})^{T}\right)+\lambda^{n+\frac{1}{2}}\boldsymbol{I}\,(\nabla\cdot\vec{\mathfrak{g}})\right) \tag{5.116}$$

and

$$\vec{\mathfrak{g}} := \frac{1}{\rho^{(n+1)}}\nabla\cdot\left(\boldsymbol{I}\partial\pi^{'\left(n+\frac{1}{2}\right)}\right) \tag{5.117}$$

can be reduced to the explicit pressure increment

$$\partial p^{'\left(n+\frac{1}{2}\right)} = \partial\pi^{'\left(n+\frac{1}{2}\right)} - \frac{\Delta t}{2}\left(\frac{\mu}{\rho}\right)^{(n+1)}\nabla\cdot\nabla\partial\pi^{'\left(n+\frac{1}{2}\right)} \tag{5.118}$$

yielding the final pressure

$$p^{'\left(n+\frac{1}{2}\right)} = \pi^{'} + \underbrace{\partial\pi^{'\left(n+\frac{1}{2}\right)} - \frac{\Delta t}{2}\left(\frac{\mu}{\rho}\right)^{(n+1)}\nabla\cdot\nabla\partial\pi^{'\left(n+\frac{1}{2}\right)}}_{=\,\partial p^{'\left(n+\frac{1}{2}\right)}} \tag{5.119}$$

according to (5.7) as given in [30]. Relation (5.116) is obtained by inserting the non-integral form of (5.115) – divided by the density – into (3.31) or (3.32), respectively, during determination of $\boldsymbol{\mathcal{T}}$, eliminating velocity contributions in the difference $\boldsymbol{\mathcal{T}}-\boldsymbol{\mathcal{T}}^{*}$. The pressure update formula (5.119) is second order accurate on periodic domains and $\left(\frac{3}{2}\right)^{th}$ order accurate on more general domains as shown in [66]. As pressure is not only staggered in space but also in time,

$$\pi^{'} := p^{'\left(n-\frac{1}{2}\right)} \tag{5.120}$$

can be defined as in [15] or in [5], [6] and [7]. Determination of an explicit second order accurate pressure update on general domains without restrictions for ρ, μ and

$\nabla \cdot \vec{v}$, however, is not available yet. Thus, the first order accurate pressure update

$$p'^{\left(n+\frac{1}{2}\right)} = \pi' + \partial\pi'^{\left(n+\frac{1}{2}\right)} \tag{5.121}$$

is used throughout this work. Since (5.114) is solved with Neumann boundaries (see section 5.4.2), the solution $\partial\pi'^{\left(n+\frac{1}{2}\right)}$ is also valid, if an arbitrary constant is added. In order to keep solutions from different time-steps in similar value ranges, $\partial\pi'^{\left(n+\frac{1}{2}\right)}$ is set to be zero at a reference location and the solution in the rest of the domain is adjusted accordingly by subtracting the constant that resulted in the reference location after solving (5.114).

The algorithm for the second projection step is as follows:

1. compute coefficients $\left(\frac{\Delta t}{2}\Theta_{\mathfrak{i}}^{(n+1),**}\right) \approx \left(\frac{\Delta t}{2}\frac{\overline{\mathcal{P}}_{\mathfrak{i}}^{(n+1),**}}{\overline{\rho}_{\mathfrak{i}}^{(n+1),**}}\right)$ in primal cell centers (dual cell nodes)
2. compute approximations to $(\mathcal{P}\vec{v})_{\mathfrak{i}}^{(n+1),**} \approx \left(\overline{\mathcal{P}}_{\mathfrak{i}}\frac{\overline{\rho\vec{v}}_{\mathfrak{i}}}{\overline{\rho}_{\mathfrak{i}}}\right)^{(n+1),**}$ in primal cell centers (dual cell nodes)
3. determine contributions to right hand of (5.114) due to surface integrals over dual cell sub-faces (as given by the first expression on the right hand side (second line of (5.113)) in dual cell centers (primal cell nodes), based on the primal cell center values determined in step 2.
4. add volume integrals of source terms (second expression on the right hand side (second line of (5.113)) to the nodal right hand side determined in step 3., if applicable
5. assemble global matrix on the left hand side of (5.114), based on the left hand side of (5.113), discretized in dual cell sub-faces centers, involving
   - results from step 1.
   - weights $\Pi_{\mathfrak{d}=1}^{\mathfrak{D}}\left(x_{\mathfrak{d}}^{(\mathfrak{i},\mathfrak{j},\mathfrak{k})_{\mathfrak{d}}}\right)$ from (5.112)
   - the factor $\frac{(-1)^{\mathfrak{w}}}{\mathfrak{c}_{\mathfrak{d}}\,\mathfrak{h}}$ from (5.113)
6. apply boundary conditions as described in section 5.4.2
7. solve (5.114) for the unknown $\partial\pi'^{(N)}$

8. update momenta according to (5.115) with primal cell face center increment according to (5.110)
9. adjust Poisson solution to be zero in the reference location
10. update dynamic pressure in cell nodes according to (5.121) with $\partial\pi^{'\,(n+\frac{1}{2})} = \partial\pi^{'\,(N)}$

5.2.3 Summary: Corrector

The corrector step is split into two parts, the first one as a cell centered MAC-type projection for correction of fluxes to satisfy the divergence constraint, the second one as a node centered projection for correction of the cell centered velocity field and the node centered pressure to satisfy the divergence constraint.

After the first corrector step

- all scalar conserved quantities have attained their final values to be used as starting point for the next time step
- momentum is still only first order accurate in time (while second order accurate in space) as time evolution of the dynamic pressure $p^{'}$ is not yet accounted for
- the cell centered velocity field does not satisfy the divergence constraint
- the dynamic pressure $p^{'}$ has not been updated

The approximation of the integral average of any conserved quantity $\rho\psi$ after the first corrector step $\mathfrak{C}_{(1)}$ is labeled $\overline{\rho\psi}^{(n+1),**} \equiv \overline{\mathcal{P}\Phi}^{(n+1),**}$ according to (5.3a). For scalars $\overline{\rho\psi}^{(n+1),**} = \overline{\rho\psi}^{(n+1)}$ applies.

After the second corrector step

- all conserved quantities have attained their final values to be used as starting point for the next time step
- momentum is second order accurate as well
- the cell centered velocity field satisfies the divergence constraint
- the dynamic pressure $p^{'}$ has been updated (first order accurate)

The approximation of the integral average of any conserved quantity $\rho\psi$ after the second corrector step $\mathfrak{C}_{(2)}$ is labeled $\overline{\rho\psi}^{(n+1)} \equiv \overline{\mathcal{P}\Phi}^{(n+1)}$ according to (5.3b). Only the nodal pressure and the momentum (and from that the velocity) change during this second correction step.

5.3 Initial Conditions

Initial conditions for the integral averages need to be specified, depending on the given physical problem. Typically, initial data for the density ρ, the velocity $\vec{v}$, the background pressure P_0 and the temperature T (such that $\mathcal{P} = \rho\Theta(T)$) are available and can be specified in grid cell centers, approximating the integral average over the grid cell second order accurate. While the initial momentum is determined from the specified initial density and velocity as the integral average of each conserved quantity is approximated based on the specified primitive variables, the initial dynamic pressure $p'^{(-\frac{1}{2})}$ at time level $n = 0$, matching the specified (conserved) quantities and satisfying the divergence constraint (3.140), is determined – if not known – via the following fixed-point iteration similar to [4] and [5]:

1. in contrast to [5], an initial guess for the nodal pressure $p'^{(-\frac{1}{2})}_{[0]} \neq 0$ is computed from an initial nodal projection as described below
2. with the available guess $p'^{(-\frac{1}{2})}_{[\mathfrak{i}]}$ for the initial pressure a complete time step is performed as described in sections 5.1 and 5.2
3. the resulting pressure $p'^{(\frac{1}{2})}_{[\mathfrak{i}]}$ at time level $n = 1$ is taken as improved initial pressure
$$p'^{(-\frac{1}{2})}_{[\mathfrak{i}+1]} := p'^{(\frac{1}{2})}_{[\mathfrak{i}]} \tag{5.122}$$
while all the conserved quantities $\rho\psi$ are discarded and reset to their initial values at $n = 0$.
4. steps 2. and 3. are repeated $\mathcal{N}_{\text{iter}}$ times and the final initial pressure is
$$p'^{(-\frac{1}{2})} := p'^{(\frac{1}{2})}_{[\mathcal{N}_{\text{iter}}]} \tag{5.123}$$
where
$$\mathcal{N}_{\text{iter}} := \min\left(\mathcal{N}^{(\max)}_{\text{iter}}, \mathfrak{i}_{\text{tol}}\right) \tag{5.124}$$

with $\mathfrak{N}_{\text{iter}}^{(\max)}$ as a specified maximum number of initial iterations according to steps 2. and 3. and $\mathfrak{i}_{\text{tol}}$ as the iteration index at which

$$\left\| p_{[\mathfrak{i}_{\text{tol}}]}^{'(-\frac{1}{2})} - p_{[\mathfrak{i}_{\text{tol}}-1]}^{'(-\frac{1}{2})} \right\|_{\mathfrak{p}} < \mathfrak{T} \tag{5.125}$$

with norm $\|\blacksquare\|_{\mathfrak{p}}$, $\mathfrak{p} \in \{1, 2, \infty\}$ and $\mathfrak{T}$ as some specified tolerance.

This iterative procedure – among others – adds the influence of initially (unknown) acceleration to the pressure found during the initial guess. The initial guess is performed in order to save (at least) one of the subsequent iteration steps in comparison to starting the iteration with a zero pressure, since solving a Poisson-type problem is cheaper than performing a whole time step involving two projections and computation of predictor fluxes. The initial projection, leading to the initial guess $p_{[0]}^{'(-\frac{1}{2})}$ in step 1. of the algorithm described above, is a nodal projection, similar to the second projection step described in section 5.2.2, with the following differences:

- since the result of the initial projection is only a guess as starting point for the iterative procedure described above, and since pressure is not a conserved quantity, the initial projection is done based on the non-conservative momentum equation as described below
- no increment $\partial\pi'$ but a full pressure guess p' is determined
- no computation of right hand side volume sources is required
- the result, serving as initial guess $p_{[0]}^{'(-\frac{1}{2})}$, is not needed for updating any conserved quantity

The required discrete Poisson type equation

$$\begin{aligned}
&\frac{1}{\mathfrak{h}} \sum_{\mathfrak{d}=1}^{\mathfrak{d}} \frac{1}{\mathfrak{c}_{\mathfrak{d}}} \sum_{\mathfrak{w}=1}^{2} (-1)^{\mathfrak{w}} \sum_{\mathfrak{x}=1}^{2^{(\mathfrak{d}-1)}} \left[\left(\frac{1}{\rho^{(0)}} \right)_{\mathfrak{d},\mathfrak{w},\mathfrak{x}} \left(\nabla p_{\mathfrak{i}_{\mathfrak{d},\mathfrak{w},\mathfrak{x}}}^{'(-\frac{1}{2})} \left(\ddot{\vec{x}}_{\mathfrak{d},\mathfrak{w},\mathfrak{x}} \right) \cdot \vec{\mathfrak{e}}_{\mathfrak{d}} \right) \right] \\
&= \frac{1}{\mathfrak{h}} \sum_{\mathfrak{d}=1}^{\mathfrak{d}} \frac{1}{\mathfrak{c}_{\mathfrak{d}}} \sum_{\mathfrak{w}=1}^{2} (-1)^{\mathfrak{w}} \sum_{\mathfrak{x}=1}^{2^{(\mathfrak{d}-1)}} \left[\left(\vec{\mathfrak{A}}^{(0)} \right)_{\mathfrak{d},\mathfrak{w},\mathfrak{x}} \cdot \vec{\mathfrak{e}}_{\mathfrak{d}} \right]
\end{aligned} \tag{5.126}$$

with acceleration vector

$$\vec{\mathfrak{A}}^{(0)} := \vec{g} \; - \; \vec{v}^{(0)} \cdot \nabla \vec{v}^{(0)} \; + \; \frac{1}{\rho^{(0)}} \nabla \cdot \boldsymbol{\mathcal{T}}^{(0)} \tag{5.127}$$

and $\blacksquare^{(0)}$ indicating initial values is obtained by

1. subtracting the non-integral mass balance $(\,\rho\,)_t + \nabla \cdot (\rho\vec{v}) = 0$ from the non-integral momentum balance $(\,\rho\vec{v}\,)_t + \nabla \cdot (\rho\vec{v} \circ \vec{v}) + \nabla p^{'} - \nabla \cdot \boldsymbol{\mathcal{T}} = \rho\vec{g}$ to obtain
$$\frac{1}{\rho}\nabla p^{'} = \frac{1}{\rho}\nabla \cdot \boldsymbol{\mathcal{T}} + \vec{g} - \vec{v} \cdot \nabla\vec{v} - (\,\vec{v}\,)_t \tag{5.128}$$
after division by ρ.

2. applying the divergence operator to (5.128):
$$\nabla \cdot \frac{1}{\rho}\nabla p^{'} = \nabla \cdot \left(\frac{1}{\rho}\nabla \cdot \boldsymbol{\mathcal{T}} + g - \vec{v} \cdot \nabla\vec{v}\right) \tag{5.129}$$

3. integration over a dual cell $\ddot{\Omega}$ and application of the divergence theorem, yielding
$$\oint_{\partial\ddot{\Omega}} \left(\frac{1}{\rho}\right) \nabla p^{'} \cdot \vec{n}\,\mathrm{d}A = \oint_{\partial\ddot{\Omega}} \left(\frac{1}{\rho}\nabla \cdot \boldsymbol{\mathcal{T}} + g - \vec{v} \cdot \nabla\vec{v} - (\,\vec{v}\,)_t\right) \cdot \vec{n}\,\mathrm{d}A \tag{5.130}$$

4. ignoring the unknown contribution $(\,\vec{v}\,)_t$ which re-enters the resulting pressure after the subsequent iteration described above

As in equation (5.113), the expression $\left(\nabla p_{\mathfrak{i}_{\mathfrak{d},\mathfrak{w},\mathfrak{x}}}^{'(-\frac{1}{2})}\left(\ddot{\vec{x}}_{\mathfrak{d},\mathfrak{w},\mathfrak{x}}\right) \cdot \vec{\mathfrak{e}}_{\mathfrak{d}}\right)$ in relation (5.126) is the $\mathfrak{d}^{th}$ component of the analytically determined gradient of the ansatz[18]

$$p_{\mathfrak{i}}^{'(-\frac{1}{2})}(\vec{x}) \approx \sum_{\mathfrak{k}=0}^{\mathfrak{d}-2}\sum_{\mathfrak{j}=0}^{1}\sum_{\mathfrak{i}=0}^{1}\left(\mathfrak{a}_{\mathfrak{i},\mathfrak{j},\mathfrak{k}}\left(p_{[0]}^{'(-\frac{1}{2})}\right)\,\Pi_{\mathfrak{d}=1}^{\mathfrak{d}}\left(x_{\mathfrak{d}}^{(\mathfrak{i},\mathfrak{j},\mathfrak{k})_{\mathfrak{d}}}\right)\right) \tag{5.131}$$

in that primal cell $\mathfrak{i}$, in which the sub-face with indices $\mathfrak{d}, \mathfrak{w}, \mathfrak{x}$ is located in, evaluated in dual sub-face center $\ddot{\vec{x}}_{\mathfrak{d},\mathfrak{w},\mathfrak{x}}$, with unknown nodal values $p_{[0]}^{'(-\frac{1}{2})}$ to be determined.

The algorithm of the initial projection is as follows:

1. compute coefficients $\left(\frac{1}{\rho^{(0)}}\right)$ in primal cell centers (dual cell nodes)
2. compute primal cell center values of the right hand side contribution (5.127),

[18] The ansatz is bi-linear for $\mathfrak{d} = 2$ and tri-linear for $\mathfrak{d} = 3$.

approximating each component $\mathfrak{c}$ of the advective contribution vector $\vec{v} \cdot \nabla \vec{v}$ by

$$\begin{aligned}(\vec{v} \cdot \nabla \vec{v})_{\mathfrak{c}}^{(0)} &= \sum_{\mathfrak{d}=1}^{\mathfrak{D}} \left(v_{\mathfrak{d}}^{(0)} \left(\frac{\partial v_{\mathfrak{c}}}{\partial x_{\mathfrak{d}}} \right)^{(0)} \right) \\ &\approx \sum_{\mathfrak{d}=1}^{\mathfrak{D}} \left(v_{\mathfrak{d},(i,j,k)}^{(0)} \frac{v_{\mathfrak{c},((i,j,k)+\vec{\mathfrak{e}}_{\mathfrak{d}})}^{(0)} - v_{\mathfrak{c},((i,j,k)-\vec{\mathfrak{e}}_{\mathfrak{d}})}^{(0)}}{2\,\mathfrak{c}_{\mathfrak{d}}\,\mathfrak{h}} \right) + \mathcal{O}(\mathfrak{h}^2) \end{aligned} \tag{5.132}$$

and each component of $\nabla \cdot \boldsymbol{\mathcal{T}}$ by

$$\begin{aligned}(\nabla \cdot \boldsymbol{\mathcal{T}})_{\mathfrak{c}}^{(0)} &= \sum_{\mathfrak{d}=1}^{\mathfrak{D}} \left(\frac{\partial \boldsymbol{\mathcal{T}}_{\mathfrak{c},\mathfrak{d}}^{(0)}}{\partial x_{\mathfrak{d}}} \right) \\ &\approx \frac{1}{\mathfrak{h}} \left(\sum_{\mathfrak{w}=1}^{2} (-1)^{\mathfrak{w}} \left(\frac{\boldsymbol{\mathcal{T}}_{\mathfrak{c},\mathfrak{d},\mathfrak{w}}^{(0),\text{asym}}}{\mathfrak{c}_{\mathfrak{c}}} + \sum_{\mathfrak{d}=1}^{\mathfrak{D}} \left(\frac{\boldsymbol{\mathcal{T}}_{\mathfrak{c},\mathfrak{d},\mathfrak{w}}^{(0),\text{sym}}}{\mathfrak{c}_{\mathfrak{d}}} \right) \right) \right) + \mathcal{O}(\mathfrak{h}^2) \end{aligned} \tag{5.133}$$

with

$$\boldsymbol{\mathcal{T}}_{\mathfrak{c},\mathfrak{d},\mathfrak{w}}^{(0),\text{sym}} = \mu_{\mathfrak{d},\mathfrak{w}} \left(\left(\frac{\partial v_{\mathfrak{c}}}{\partial x_{\mathfrak{d}}} \right)_{\mathfrak{d},\mathfrak{w}} + \left(\frac{\partial v_{\mathfrak{d}}}{\partial x_{\mathfrak{c}}} \right)_{\mathfrak{d},\mathfrak{w}} \right) \tag{5.134a}$$

$$\boldsymbol{\mathcal{T}}_{\mathfrak{c},\mathfrak{d},\mathfrak{w}}^{(0),\text{asym}} = \lambda_{\mathfrak{d},\mathfrak{w}} \sum_{\mathfrak{e}=1}^{\mathfrak{D}} \left(\frac{\partial v_{\mathfrak{e}}}{\partial x_{\mathfrak{e}}} \right)_{\mathfrak{d},\mathfrak{w}} \tag{5.134b}$$

and the velocity derivatives according to the ones given in section 5.1.3.3 - 2

3. perform steps 3. to 5. on page 102 in section 5.2.2
4. apply boundary conditions as described in section 5.4.2
5. solve the resulting linear system

$$\mathfrak{A}_{\frac{1}{\rho},[0]}^{(N)} \cdot \vec{p}_{[0]}^{\,\prime\,(-\frac{1}{2})} = \vec{\mathcal{R}}_{[0]}^{(N)} \tag{5.135}$$

for the unknown $p_{[0]}^{\prime\,(-\frac{1}{2})}$

5.4 Boundary Conditions

The boundary conditions at the outer boundary $\partial\Omega^{\square}$ of the computational domain $\Omega^{\square}$ are enforced via determination of suitable values in ghost cells in a ghost region around the computational domain as sketched in ***Fig. 5.11*** in two spatial dimensions. These ghost values are determined such that the required boundary fluxes across grid cell faces at $\partial\Omega^{\square}$ are reached. While values in ghost cells in the boundary boxes along the domain boundary (dark grey in ***Fig. 5.11***) depend on the type of the boundary only, the values in the boxes at the domain corners (light grey in ***Fig. 5.11***) depend on the combination of the types of all neighboring domain boundary faces.

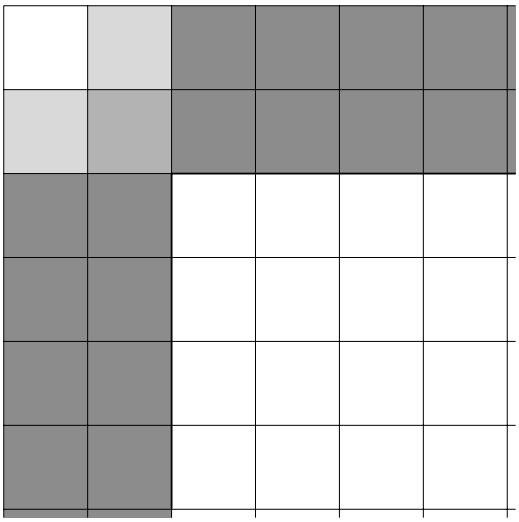

Fig. 5.11: Ghost cells around computational domain (white): *dark grey*: ghost cells in ghost boxes at the domain boundary faces; *light grey, medium light grey, medium dark grey*: ghost cells in ghost boxes at the domain corners; the different grey levels indicate which cells are required for the different stencils occurring throughout the numerical method at domain boundary faces

5.4.1 Hyperbolic-Parabolic Part

First, the specification of the boundary conditions for the hyperblic-parabolic part of the numerical method is given according to the appendix of [90], in which the corresponding formulas for the boundary conditions of primitive quantities are given.

5.4.1.1 Boundary Types

For determination of ghost values in boundary boxes along the domain boundary it is sufficient to consider the type of the respective boundary segment as listed below.

5.4.1.1 - 1 Solid Wall

At solid walls, boundary normal fluxes of mass, species mass, and momentum vanish. Thus, ghost fluid values of these quantities can be obtained by mirroring the states form the grid cells at the boundary to the ghost region as sketched in ***Fig. 5.12***. While the scalars are just copied as described, the boundary normal vector component of momentum (and velocity) needs to change its sign in addition in order to enforce a zero boundary normal velocity at $\partial\Omega^{\square}$. If friction is present at the solid wall, the boundary tangential components of momentum and velocity need to change their sign in the ghost region as well, in order to enforce a zero flow – and, thus, the no-slip condition – at the boundary. Without friction only the interface normal vector components need to change sign and slip is allowed in boundary tangential directions. The boundary normal pressure gradient, required in the correction steps, is zero at the solid wall boundary as well.

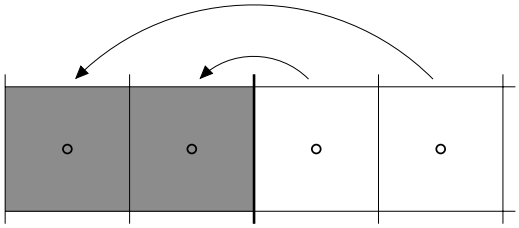

Fig. 5.12: Ghost cell values at solid walls

5.4.1.1 - 2 Inflow

The flux across inflow boundary grid cell faces is adjusted by determination of the ghost region values such that numerical flux evaluation with stencil cells both in the ghost region and within the computational domain yields the required boundary flux as sketched in ***Fig. 5.13***.

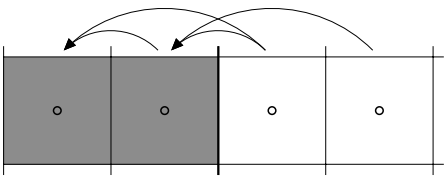

Fig. 5.13: Ghost cell values at inflow boundaries

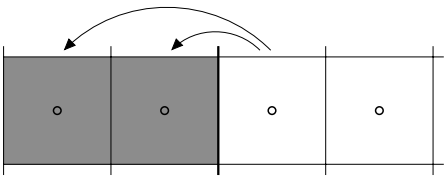

Fig. 5.14: Ghost cell values at outflow boundaries: zeroth order extrapolation

5.4.1.1 - 3 Outflow

At outflow boundaries the quantities are determined via zero order extrapolation as sketched in ***Fig. 5.14***, since linear (first order) extrapolation has the potential to cause

unphysical return flow from the boundary region into the domain and, thus, has to be avoided without further treatment.

5.4.1.1 - 4 Periodic Boundary

If the boundary is a periodic (and, thus, no outer) boundary, the values in the ghost region are set as sketched in ***Fig. 5.15*** in order to mimic the state within the computational domain in the vicinity of the partner boundary (which is periodic as well).

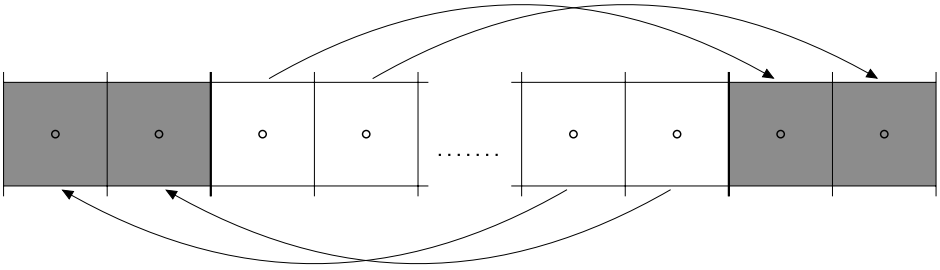

Fig. 5.15: Ghost cell values at periodic boundaries

5.4.1.2 Boundary Type Combinations

Determination of ghost values in the ghost boxes at the domain corners requires knowledge of the combination of neighboring boundary types. These ghost values are needed for computation of viscous fluxes across the boundary.

5.4.1.2 - 1 Two Space Dimensions

The ghost value determination in the domain corner ghost boxes is sketched in ***Fig. 5.16*** for different neighboring boundary types in two spatial dimensions. The numbers link cells in the ghost region to cells inside the computational domain, of which the ghost cells obtain their information. The sign vector indicates, which vector component needs to change sign in the ghost region in comparison to the linked inner domain cell.

5.4.1.2 - 2 Three Space Dimensions

For three space dimensions the boundary settings shown in ***Fig. 5.16*** for edges of the two-dimensional domain apply to domain boundary faces and the settings shown for domain corner nodes apply to domain boundary edges. Additional settings for the

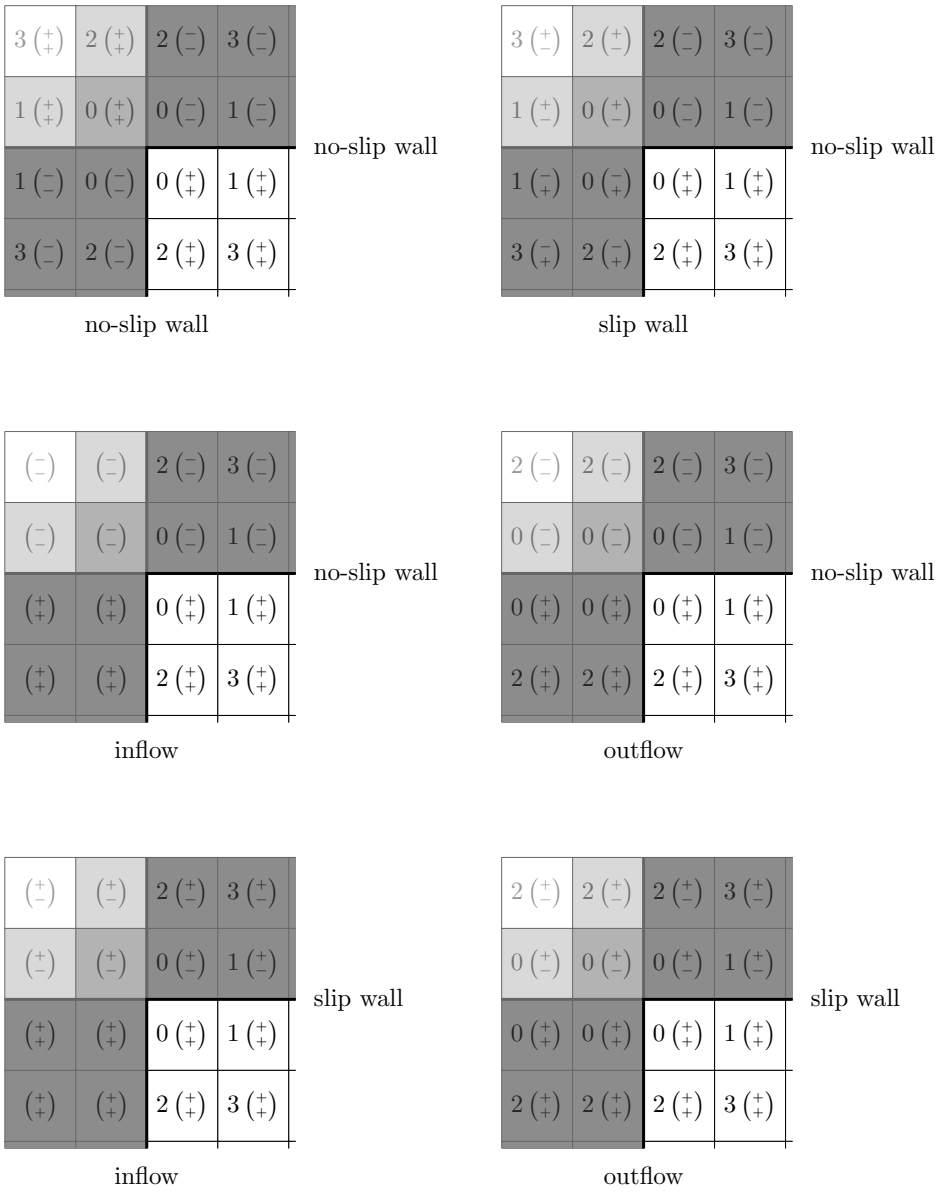

Fig. 5.16: Ghost cell values depending on combinations of adjacent boundary types: values 0,1,2 and 3 indicate the cell within the computational domain the absolute value of the ghost cell value comes from, the sign vectors indicate the sign of vector quantity components, provided all vector components within the cells labeled 0,1,2 and 3 within the computational domain have positive sign

domain corners of three dimensional domains have to be taken into account, considering the respective combinations of three adjacent domain boundary types.

5.4.2 Elliptic Problems

For solving integral elliptic problems of type

$$\oint_{\partial\Omega_i} \left(\Theta^{(\circ)}\nabla\partial\pi\right)\cdot\vec{n}\,\mathrm{d}A \;=\int_{\Omega_i}\nabla\cdot\vec{\mathcal{R}}^{\,(\circ)}\mathrm{d}V-\int_{\Omega_i}\mathcal{D}^{(\circ)}\mathrm{d}V \tag{5.136}$$

for the unknown quantity $\partial\pi$ with available[19] right hand side vector $\vec{\mathcal{R}}$ and scalar $\mathcal{D}$, a boundary condition for the control volume boundary normal flux $\Theta^{(\circ)}\nabla\partial\pi\cdot\vec{n}$ over the domain boundary has to be specified. The integrals over control volume boundary segments, which conincide with the boundary of the computational domain, can be separated from the left hand side control volume boundary integrals, yielding

$$\begin{aligned}\int_{\partial\Omega_i\setminus\partial\Omega^{\square}} \left(\Theta^{(\circ)}\nabla\partial\pi\right)\cdot\vec{n}\,\mathrm{d}A \;&=\int_{\Omega_i}\nabla\cdot\vec{\mathcal{R}}^{\,(\circ)}\mathrm{d}V-\int_{\Omega_i}\mathcal{D}^{(\circ)}\mathrm{d}V\\ &\quad-\int_{\partial\Omega^{\square}}\left(\Theta^{(\circ)}\nabla\partial\pi^{(\circ)}\right)^{\square}\cdot\vec{n}^{\square}\,\mathrm{d}A\end{aligned} \tag{5.137}$$

after shifting of the domain boundary integrals labeled $\square$ with Neumann boundary condition to the right hand side. For determination of pressure increments via (5.137) up to a constant, the velocity boundary condition has to be taken into account via the momentum balance. Following [15], the fact that the correct velocity boundary condition has already been considered during the predictor step of the incremental projection method yields the zero Neumann boundary condition

$$\left(\Theta^{(\circ)}\nabla\partial\pi^{(\circ)}\right)^{\square}\cdot\vec{n}^{\square}=0 \tag{5.138}$$

for the elliptic problems of the corrector step in order to keep the velocity boundary condition unchanged, such that the final velocity field still satisfies the physical boundary conditions. As discussed in [30], this leads to an only first order accurate pressure approximation due to the implicit assumption that the local boundary normal pressure boundary conditon does not change over time. As shown in [65] the resulting artificial boundary layer also affects accuracy of momentum and the scalars in the L_∞-norm. Improvement with respect to the accuracy of the pressure at the boundary is expected by utilization of a suitable pressure update formula, consequently allow-

[19] Available information is labeled by superscript $(\circ)$ here.

ing for a changing pressure boundary condition over time as discussed in [30], and incorporating boundary tangential information into the Neumann boundary condition of the elliptic problem by solving a Helmholtz-type problem for the boundary condition on the boundary independent of the unknown final velocity as discussed in [102] and in appendix section D. The lack of consitency of the pressure boundary condition in both incremental and full pressure projection methods is a widely discussed and still not sufficiently resolved issue, especially for variable density flows, as discussed for flows with constant density, for example, in [77], [65] or [109].

5.5 Solution of Systems of Linear Equations

The linear systems (5.34), (5.95), (5.114) and (5.135), arising throughout the solution procedure described in sections 5.1, 5.2 and 5.3, are solved by an algebraic multigrid preconditioned biconjugate gradient stabilized method (BiCGSTAB) for sparse systems, introduced in [178] as a Krylov sub-space method according to [99]. The utilized biconjugate gradient stabilized method is described in [13], implemented as presented in [35], [52] and related publications[20]. The algebraic multigrid preconditioner (BoomerAMG) is described in [74] and references therein. A more recent introduction to algebraic multigrid preconditioner can be found in [51].

5.6 Validation and Results

This section is meant to show, that the present single-phase method – as basis for the following chapters – is implemented well, second order accurate, conservative and stable. Therefore the following test cases are presented, in each of which the reference values $\check{\Phi}$ from ***Tab. 5.4*** are considered, if not stated otherwise, and the relations $\Phi = \hat{\Phi}\check{\Phi}$, $P_0(\vec{x}, 0) = \check{P}_0$ and $\mathcal{P}(\vec{x}, 0) = \check{\mathcal{P}}$ apply.

Tab. 5.4: Reference quantities $\check{\Phi}$ as used for single-phase solver tests

$\check{\Phi}$	$\check{l}$	$\check{t}$	$\check{v}$	$\check{T}$	$\check{\rho}$	$\check{P}_0$	$\check{\mathcal{P}}$
Unit	m	s	K	$\frac{\mathrm{m}}{\mathrm{s}}$	$\frac{\mathrm{kg}}{\mathrm{m}^3}$	$\frac{\mathrm{kg}}{\mathrm{m\,s}^2}$	$\frac{\mathrm{kg}}{\mathrm{m}^3}\mathrm{K}$
Size	1	1	1	300	1.1768	101325	$\frac{\check{P}_0}{\frac{\check{R}}{\check{M}}} = \check{\rho}\check{T} = \check{\rho}\check{\theta}$

[20] https://computation.llnl.gov/project/linear_solvers/publications.php, [last visited on Jul. 27^{th}, 2016]

5.6.1 Smoothed Gresho Vortex

The two-dimensional analytical solution to a vortex problem, initially described in [63] and smoothed as done in [86], is

$$\hat{\rho}(\vec{x},t) = \begin{cases} \left(1+(1-\hat{r}^2)^6\right) & \text{if} \quad \hat{r}<1 \\ 1 & \text{otherwise} \end{cases} \tag{5.139}$$

for the non-dimensional density $\hat{\rho}$ and

$$\hat{v}_1(\vec{x},t) = \hat{v}_1^{(\infty)} \begin{cases} \left(1-\eta\,\varpi_1\,(1-\hat{r})^6\,\hat{r}^6\,\sin(\vartheta)\right) & \text{if} \quad \hat{r}<1 \\ 1 & \text{otherwise} \end{cases} \tag{5.140a}$$

$$\hat{v}_2(\vec{x},t) = \hat{v}_2^{(\infty)} \begin{cases} \left(1+\eta\,\varpi_2\,(1-\hat{r})^6\,\hat{r}^6\,\cos(\vartheta)\right) & \text{if} \quad \hat{r}<1 \\ 1 & \text{otherwise} \end{cases} \tag{5.140b}$$

for the non-dimensional velocity $\hat{\vec{v}}$ of an inviscid ($\mu = 0$) fluid in absence of gravity ($\vec{g} = \vec{0}$). In equations (5.139) and (5.140)

$$\hat{r} = \frac{\hat{d}}{\hat{r}_\circ} \tag{5.141}$$

is the time-dependent relative radius with $\hat{r}_\circ = 0.4$ as the non-dimensional radius of the vortex and

$$\hat{d} := \left|\Delta\hat{\vec{x}}\right| \tag{5.142}$$

as the time-dependent non-dimensional local distance to the vortex center, resulting from

$$\Delta\hat{\vec{x}} := \hat{\vec{x}} - \hat{\vec{x}}_\circ(\hat{t}) \tag{5.143}$$

with

$$\hat{\vec{x}}_\circ\left(\hat{t}\right) = \begin{pmatrix} 0.5 \\ 0.5 \end{pmatrix} + \hat{t}\begin{pmatrix} \hat{v}_1^{(\infty)} \\ \hat{v}_2^{(\infty)} \end{pmatrix} \tag{5.144}$$

as the non-dimensional time-dependent position of the vortex center. Further,

$$\hat{\vec{v}}^{(\infty)} = \begin{pmatrix} 1 \\ 1 \end{pmatrix}, \quad \hat{w} = 1 \tag{5.145}$$

are the non-dimensional magnitudes of the advective and rotational velocity components with ratios

$$\varpi_i := \frac{\hat{w}}{\hat{v}_i^{(\infty)}} \tag{5.146}$$

and

$$\eta = \xi \,\mathrm{sgn}\left(\Delta\hat{x}_1\right), \qquad \xi = 1024, \qquad \vartheta = \tan^{-1}\left(\frac{\Delta\hat{x}_2}{\Delta\hat{x}_1}\right) \tag{5.147}$$

are the signed scaling factor η and the angle ϑ.

The pressure $\hat{p}^{'}$ can be obtained by considering a one-dimensional path between the vortex center (5.144) at $\hat{r} = 0$ and the outer boundary of the vortex at $\hat{r} = 1$. Due to the rotational velocity and the non-constant density along this path, centrifugal forces $\vec{\mathfrak{f}}_z$ try to pull mass away from the moving vortex center. Therefore, the closer one gets to $\vec{x}^{(0)}(t)$, the stronger a pressure force $\vec{\mathfrak{f}}_p$, balancing $\vec{\mathfrak{f}}_z$, has to be, in order to keep the vortex stable. This yields the equilibrium

$$\underbrace{\int_{dS} p^{'}(\vec{x},t)\mathrm{d}S}_{=\vec{\mathfrak{f}}_p} = \underbrace{\int_{dV} \frac{\rho(r)\vec{v}_r^{\,2}(r)}{r}\,\mathrm{d}V}_{=\vec{\mathfrak{f}}_z} = \int_{dV} \frac{\hat{\rho}(r)\left(v_{1,r}^2(r) + v_{2,r}^2(r)\right)}{r}\,\mathrm{d}V \tag{5.148}$$

where

$$\vec{v}_r := \vec{v} - \breve{\vec{v}}\begin{pmatrix}\hat{v}_1^{(\infty)}\\ \hat{v}_2^{(\infty)}\end{pmatrix} \tag{5.149}$$

is only the rotational part of the original velocity field $\vec{v}$. Along the one-dimensional path, the corresponding non-dimensional pressure equation is

$$\hat{p}^{'}(\hat{r},\hat{t}) = \int_1^{\hat{r}} \frac{\hat{\rho}(\tilde{r})\hat{\vec{v}}_r^{\,2}(\tilde{r})}{\tilde{r}}\,\mathrm{d}\tilde{r} = \int_1^{\hat{r}} \frac{\hat{\rho}(\tilde{r})\left(\hat{v}_{1,r}^2(\tilde{r}) + \hat{v}_{2,r}^2(\tilde{r})\right)}{\tilde{r}}\,\mathrm{d}\tilde{r} \tag{5.150}$$

after non-dimensionalizing with $\frac{1}{(\breve{\rho}\breve{v}^2)}$ due to $\mathrm{d}V = \mathrm{d}S\mathrm{d}\tilde{r}$. Choosing the integration path to start at the right outer boundary of the vortex ($\hat{r} = 1$ holds everywhere at the outer vortex boundary), approaching its center from the right (which is possible due to the rotational symmetry of the problem), the following simplifications apply:

$$\Delta\hat{x}_2 = 0, \quad \vartheta = 0, \quad \sin(\vartheta) = 0, \quad \cos(\vartheta) = 1, \quad \mathrm{sgn}\left(\Delta\hat{x}_1\right) = 1 \tag{5.151}$$

Therefore the simplified non-dimensional rotational velocity field

$$\hat{v}_{1,r}(\hat{r},t) = 0 \tag{5.152a}$$

$$\hat{v}_{2,r}(\hat{r},t) = \begin{cases} \xi\hat{w}\,(1-\hat{r})^6\,\hat{r}^6 & \text{if} \quad \hat{r}<1 \\ 0 & \text{otherwise} \end{cases} \tag{5.152b}$$

with square

$$\hat{\vec{v}}_r^{\,2}(\hat{r},\hat{t}) = \begin{cases} \xi^2\hat{w}^2\,(1-\hat{r})^{12}\,\hat{r}^{12} & \text{if} \quad \hat{r}<1 \\ 0 & \text{otherwise} \end{cases} \tag{5.153}$$

can be used for pressure determination via integration from 1 to $\hat{r}$ according to equation (5.150) to yield the non-dimensional pressure

$$\hat{p}^{'}(\hat{\vec{x}},\hat{t}) = \begin{cases} \hat{p}_r^{'}(\hat{r},\hat{t}) - \hat{p}_r^{'}(1,\hat{t}) & \text{if} \quad \hat{r}<1 \\ 0 & \text{otherwise} \end{cases} \tag{5.154}$$

with

$$\hat{p}_r^{'}(\hat{r},\hat{t}) = \int \frac{\hat{\rho}(\tilde{r})\hat{\vec{v}}_r^{\,2}(\tilde{r})}{\tilde{r}}\,\mathrm{d}\tilde{r} = \begin{cases} 2\,\xi^2\hat{w}^2\hat{\rho}\left(\sum_{k=12}^{36}\left(\mathcal{C}_k\,\tilde{r}^k\right)\right) & \text{if} \quad \tilde{r}<1 \\ 0 & \text{otherwise} \end{cases} \tag{5.155}$$

and coefficients $\mathcal{C}_k$ according to ***Tab. 5.5***.

Tab. 5.5: Coefficients of the analytical representation of pressure $p^{'}$ for the smoothed Gresho vortex

k	12	13	14	15	16	17	18	19	20	21
$\mathcal{C}_k$	$\frac{1}{12}$	$-\frac{12}{13}$	$\frac{9}{2}$	$-\frac{184}{15}$	$\frac{609}{32}$	$-\frac{222}{17}$	$-\frac{38}{9}$	$\frac{54}{19}$	$\frac{783}{20}$	$-\frac{558}{7}$
k	22	23	24	25	26	27	28	29	30	31
$\mathcal{C}_k$	$\frac{1053}{22}$	$\frac{1014}{23}$	$-\frac{1473}{16}$	$\frac{204}{5}$	$\frac{510}{13}$	$-\frac{1564}{27}$	$\frac{153}{8}$	$\frac{450}{29}$	$-\frac{269}{15}$	$\frac{174}{31}$
k	32	33	34	35	36	-	-	-	-	-
$\mathcal{C}_k$	$\frac{57}{32}$	$-\frac{74}{33}$	$\frac{15}{17}$	$-\frac{6}{35}$	$\frac{1}{72}$	-	-	-	-	-

This analytical solution for $\hat{\rho}$, $\hat{\vec{v}}$ and $\hat{p}^{'}$ is used for a convergence study of the advective part of the single-phase solver, including the influence of the pressure $\hat{p}^{'}$. As in [86], by the choice (5.145) the vortex is transported diagonally in a periodic domain at CFL-number $\mathcal{C}_{\mathcal{A}} = 0.4$ without limiter until $\hat{t} = 1.0$, where the vortex arrives at the domain center position again. In ***Fig. 5.17*** the initial conditions and exact solution

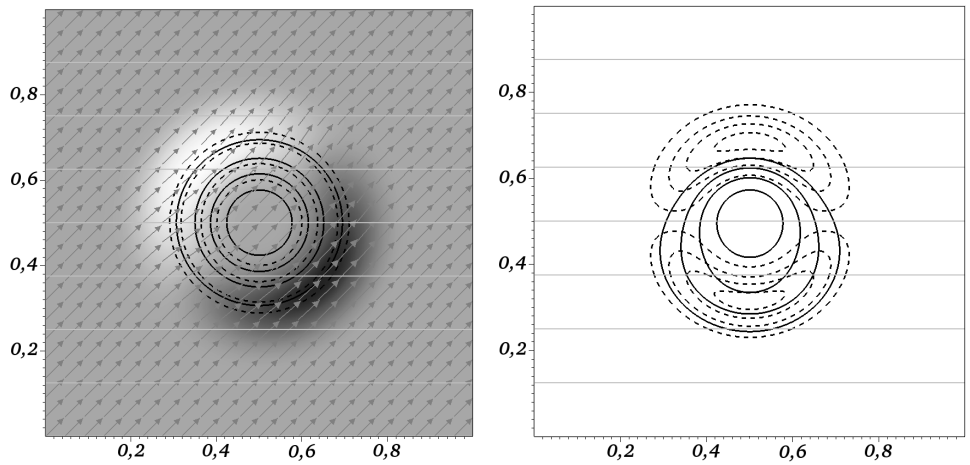

Fig. 5.17: Smoothed Gresho vortex; *left*: initial conditions and exact solution at $\hat{t} = 1$: *greyscale*: velocity magnitude between 1.164 (white) and 1.664 (anthracite) in domain diagonal flow at $\hat{v}_1^{(\infty)} = \hat{v}_2^{(\infty)} = 1$ (*grey arrows*); *solid black lines*: density iso-contours $\hat{\rho} \in (0.5, 0.6, 0.7, 0.8, 0.9)$; *dashed black lines*: pressure iso-contours $\hat{p}^{'} \in (-0.0025, -0.0075, -0.0125, -0.0175)$; *right*: iso-contours $(0.6, 0.7, 0.8, 0.9)$ of the $\hat{x}_1$-component of momentum (*solid lines*) and iso-contours $(\pm 0.175, \pm 0.125, \pm 0.075, \pm 0.025)$ of the $\hat{x}_2$-component of the pressure gradient $\hat{\nabla}\hat{p}^{'}$ (*dashed lines*) at $\hat{t} = 1$ on 1024×1024 grid cells; *light grey lines* in both picture represent the fixed patch distribution due to domain decomposition into 8 sub-domains for parallel convergence analysis

at $\hat{t} = 1.0$, as well as results for momentum and pressure gradient at $\hat{t} = 1.0$ are shown. Numerical solutions are obtained on a hierarchy of grids of resolution 64×64, 128×128, 256×256, 512×512 and 1024×1024 grid cells. The exact solution at $\hat{t} = 1.0$ – corresponding to the initial condition – is evaluated on a fine reference grid of 4096×4096 grid cells. Error norms $\| E \|_{\mathfrak{p}}$ according to relation (C.26) in appendix section C.3 and corresponding convergence orders[21] $\mathfrak{p}$ according to relation (C.30) for density, momentum and pressure are given in ***Tab. 5.6***, corresponding plots are shown in ***Fig. 5.18***. No convergence results are specified for $\mathcal{P}$, since $\mathcal{P}$ is constant at the accuracy[22] of the elliptic solver of the first corrector step, which is chosen to be 10^{-9}, already on the coarsest grid. The convergence order of the pressure $p^{'}$ breaks down towards finer grids, since the error norm approaches the accuracy of the elliptic solver of the second corrector step, which is chosen to be 10^{-6}. Momentum,

[21] Note that for determination of the errors between solutions on different grids only second order accurate integration is used for obtaining average data on the finer grid at the location, at which data is available on the coarser grid. Therefore the presented results for $\mathfrak{p}$ have an upper bound of (about) 2. This, however, is sufficient, as the present method aims for second order accuracy and the analysis, nevertheless, assures that the method is not worse than second order accurate.

[22] Magnitude of the relative residual at which the solver terminates.

Tab. 5.6: Convergence results for flow at $\mu = 0$, $D = 0$ and $\vec{g} = \vec{0}$

$\mathcal{P}$						
$\mathfrak{h}$	$\parallel E \parallel_1$	$\mathfrak{p}_1$	$\parallel E \parallel_2$	$\mathfrak{p}_2$	$\parallel E \parallel_\infty$	$\mathfrak{p}_\infty$
$2^{-\mathcal{N}}$	10^{-9}	-	10^{-9}	-	10^{-9}	-
$\mathcal{N} = 6$	12.930	-	8.312	-	22.042	-
$\mathcal{N} = 7$	7.814	-	4.865	-	15.188	-
$\mathcal{N} = 8$	11.358	-	8.000	-	38.160	-
$\mathcal{N} = 9$	9.002	-	6.590	-	43.634	-
$\mathcal{N} = 10$	11.663	-	8.709	-	143.823	-
ρ						
$\mathfrak{h}$	$\parallel E \parallel_1$	$\mathfrak{p}_1$	$\parallel E \parallel_2$	$\mathfrak{p}_2$	$\parallel E \parallel_\infty$	$\mathfrak{p}_\infty$
$2^{-\mathcal{N}}$	10^{-3}	-	10^{-3}	-	10^{-3}	-
$\mathcal{N} = 6$	50.099	-	23.338	-	34.069	-
$\mathcal{N} = 7$	13.809	1.859	6.564	1.830	11.409	1.578
$\mathcal{N} = 8$	3.549	1.960	1.698	1.951	3.085	1.887
$\mathcal{N} = 9$	0.896	1.987	0.429	1.983	0.788	1.968
$\mathcal{N} = 10$	0.225	1.993	0.108	1.992	0.199	1.981
$\rho\vec{v}$						
$\mathfrak{h}$	$\parallel E \parallel_1$	$\mathfrak{p}_1$	$\parallel E \parallel_2$	$\mathfrak{p}_2$	$\parallel E \parallel_\infty$	$\mathfrak{p}_\infty$
$2^{-\mathcal{N}}$	10^{-3}	-	10^{-3}	-	10^{-3}	-
$\mathcal{N} = 6$	14.345	-	10.643	-	18.877	-
$\mathcal{N} = 7$	3.764	1.930	2.877	1.887	5.636	1.744
$\mathcal{N} = 8$	0.951	1.984	0.736	1.967	1.427	1.981
$\mathcal{N} = 9$	0.238	1.996	0.185	1.992	0.352	2.019
$\mathcal{N} = 10$	0.059	1.999	0.046	1.998	0.087	2.007
$p^{'}$						
$\mathfrak{h}$	$\parallel E \parallel_1$	$\mathfrak{p}_1$	$\parallel E \parallel_2$	$\mathfrak{p}_2$	$\parallel E \parallel_\infty$	$\mathfrak{p}_\infty$
$2^{-\mathcal{N}}$	10^{-3}	-	10^{-3}	-	10^{-3}	-
$\mathcal{N} = 6$	2.059	-	1.413	-	2.335	-
$\mathcal{N} = 7$	0.470	2.129	0.303	2.219	0.511	2.191
$\mathcal{N} = 8$	0.093	2.331	0.057	2.417	0.128	1.996
$\mathcal{N} = 9$	0.029	1.697	0.018	1.653	0.036	1.814
$\mathcal{N} = 10$	0.014	0.956	0.011	0.655	0.019	0.907

nevertheless, converges second order accurate since only first order accurate flux densities (involving pressure) are required for second order accuracy in momentum.

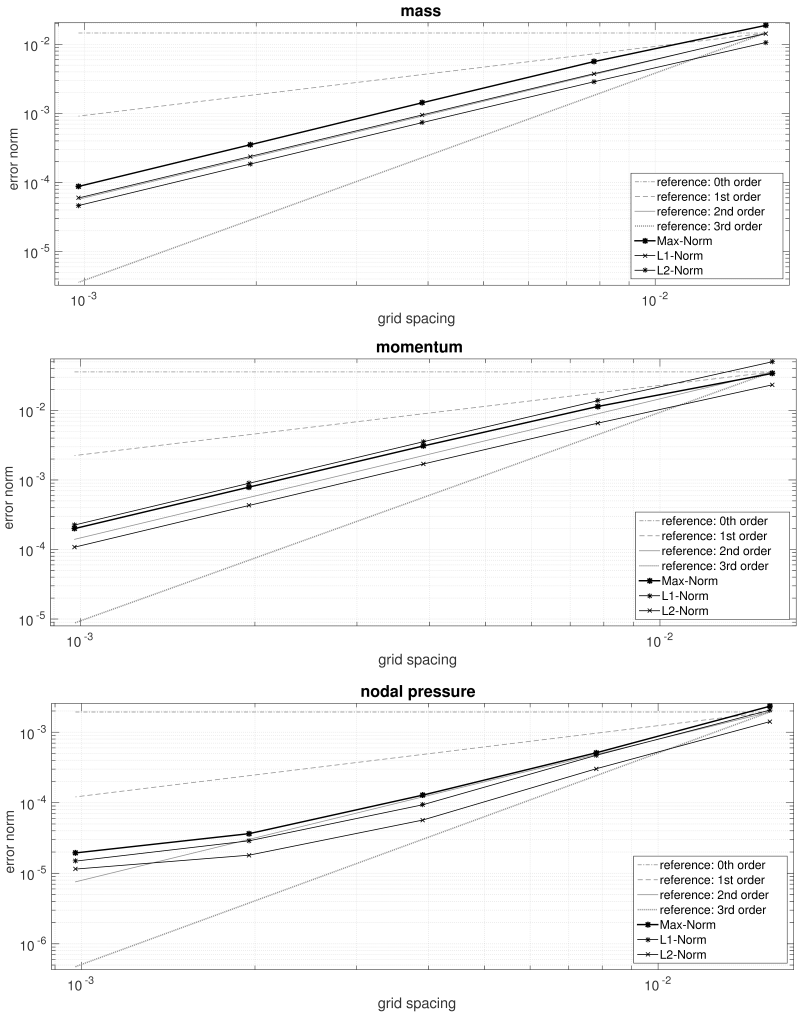

Fig. 5.18: Double logarithmic plot of error norms of mass (ρ), momentum ($\rho\vec{v}$) and nodal pressure ($p^{'}$) over grid spacing $\mathfrak{h}$ with reference slopes for different convergence rates

5.6.2 Species Diffusion

In this two-dimensional basic example the implementation of species diffusion is tested in a closed box with solid walls everywhere, using an initial contact disconti-

nuity, represented via the piecewise constant mass fraction distribution

$$Y(\hat{\vec{x}},0) := \begin{cases} 0.75 & \text{if} \quad 0.25 < \hat{x}_1, \hat{x}_2 \leqslant 0.75 \\ 0.25 & \text{otherwise} \end{cases} \tag{5.156}$$

with relative coordinates $0 < \hat{x}_1, \hat{x}_2 < 1$ in the squared domain. All other physical effects are neglected and especially

$$\hat{\vec{v}}(\hat{\vec{x}},0) = 0, \qquad \hat{p}'(\hat{\vec{x}},0) = 0 \tag{5.157}$$

at arbitrary homogeneous fluid density ($\hat{\rho}(\hat{\vec{x}},0) = 1$ is chosen here). By the choice (5.156), initially 75% of the total species mass are located within 25% of the domain. Thus, after a successful diffusive balancing process the species mass fraction should be equal to 0.375 everywhere in the domain. This process is plotted in ***Fig. 5.20*** on page 121 for the (artificially high) diffusion coefficients D of $10^{-3}\ \frac{\mathrm{m}^2}{\mathrm{s}}$, $10^{-4}\ \frac{\mathrm{m}^2}{\mathrm{s}}$ and $10^{-5}\ \frac{\mathrm{m}^2}{\mathrm{s}}$. As expected, the initially squared contact discontinuity first diffuses towards a circular distribution until the solid domain boundaries are reached and diffusion continues towards the domain corners. As also expected, the same structures, that are obtained for $D = 10^{-3}\ \frac{\mathrm{m}^2}{\mathrm{s}}$ after $\hat{t} = 5$ and $\hat{t} = 10$ (grey solid lines in the top right and second left picture) is obtained for $D = 10^{-5}\ \frac{\mathrm{m}^2}{\mathrm{s}}$ after $\hat{t} = 500$ and $\hat{t} = 1000$ (grey dashed lines in the bottom pictures). At the latter times, the iso-contours for $D = 10^{-3}\ \frac{\mathrm{m}^2}{\mathrm{s}}$ (grey solid lines) have already vanished, as the target mass fraction of 0.375 is reached everywhere more accurately than the precision of the computational data.

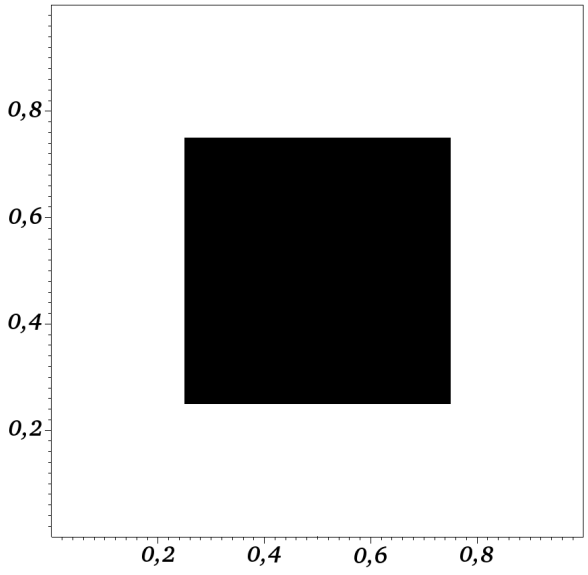

Fig. 5.19: Initial species mass fraction: *white*: $Y = 0.25$, *black*: $Y = 0.75$

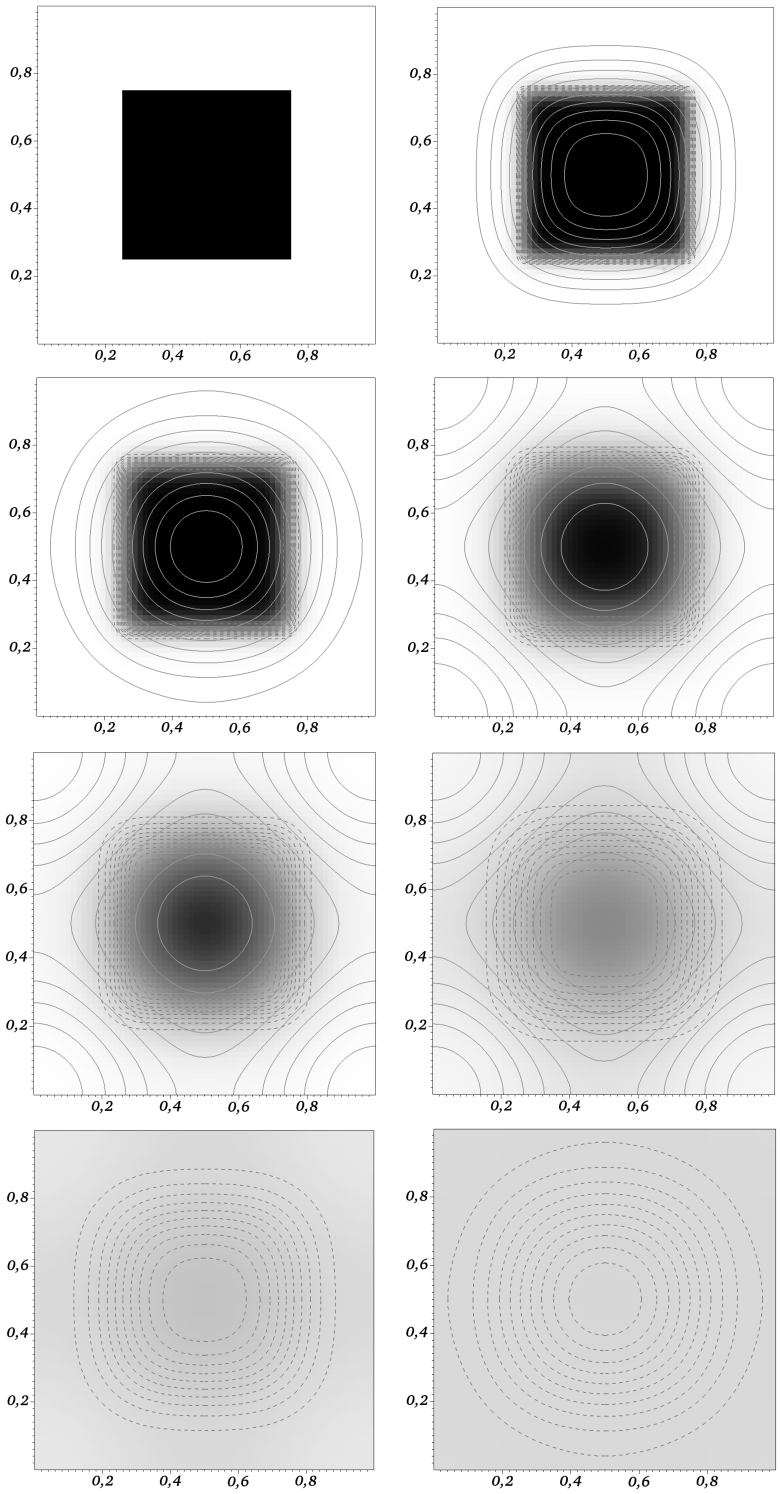

Fig. 5.20: Diffusion of a species with mass fraction 0.75 (*black*), initially covering 25% of the domain (*top left*), into areas in which this species has only a mass fraction of 0.25 (*white*) with (artificial) diffusion coefficients of $10^{-3}\,\frac{\mathrm{m}^2}{\mathrm{s}}$ (*grey solid iso-contours*), $10^{-4}\,\frac{\mathrm{m}^2}{\mathrm{s}}$ (*greyscale areas*) and $10^{-5}\,\frac{\mathrm{m}^2}{\mathrm{s}}$ (*grey dashed iso-contours* at $\hat{t} \in \{\{0,5\},\{10,50\},\{100,250\},\{500,1000\}\}$; the final mass fraction (*grey area, bottom right*) is 0.375; grid resolution is 64×64 grid cells

5.6.3 Viscous Channel Flow

In this basic two-dimensional example the implementation of viscous fluxes is tested using a viscous laminar channel flow with constant inflow on the left side, no-slip boundaries on top and bottom and outflow boundary on the right as shown in ***Fig. 5.21***. Due to viscosity, development of both a laminar boundary layer along the no-slip walls and a parabolic velocity profile towards the outflow boundary is expected. In this example the reference quantities

$$\breve{v} = 10^{-2}\,\frac{\mathrm{m}}{\mathrm{s}}, \qquad \breve{\mu} = 10^{-3}\,\frac{\mathrm{kg}}{\mathrm{m\,s}}, \qquad \breve{\rho} = 10^{3}\,\frac{\mathrm{kg}}{\mathrm{m}^3}, \qquad \breve{l} = 10^{-1}\,\mathrm{m} \tag{5.158}$$

are chosen, corresponding to a Reynolds number of $1000 = \mathsf{Re} < 2300$ at $\hat{t} = 0$ with respect to the length of the channel with non-dimensional extensions $[0, 1] \times [0, 0.1]$, for which laminar flow is expected. The grid consists of 512×256 rectangular grid cells with 5 times finer grid resolution in wall normal direction x_2 than in flow direction x_1. The non-dimensional inflow velocity on the left is chosen to be constant and homogeneous, $\hat{\vec{v}}((0, \hat{x}_2)\,, \hat{t}) = 1$, and both the dynamic viscosity and density are homogeneous and constant according to $\hat{\mu}(\hat{\vec{x}}, \hat{t}) = 1$ and $\hat{\rho}(\hat{\vec{x}}, \hat{t}) = 1$, maintained due to inflow conditions $\hat{\mu}((0, \hat{x}_2)\,, \hat{t}) = 1$ and $\hat{\rho}((0, \hat{x}_2)\,, \hat{t}) = 1$. The pressure drop along the channel is obtained via the initial iterative procedure described in section 5.3. The resulting pressure profile also accounts for initial accelerations. The theoretical

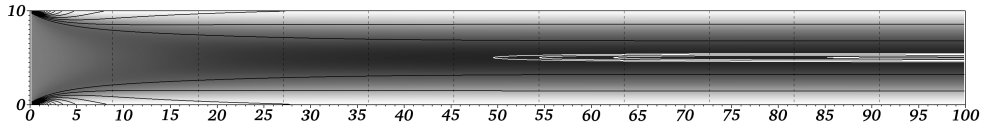

Fig. 5.21: Channel flow at constant inflow velocity over the entire inflow boundary (*left*) and resulting parabolic outflow (*right*); *greyscale*: non-dimensional velocity magnitude between 0 (white) and 1.5 (dark grey); *solid black lines*: iso-contours of the vertical (wall normal) velocity gradient component; *dashed black lines*: iso-contours of pressure $p^{'}$, *solid white lines*: iso-contours of velocity magnitude at $(0.99, 0.9925, 0.995, 0.9975)\,\hat{v}_1^{(max)}$; length scales scale with 10^{-2}

parabolic target velocity profile

$$\begin{pmatrix} \hat{v}_1 \\ \hat{v}_2 \end{pmatrix} = \begin{pmatrix} \hat{\mathcal{A}}\,\hat{x}_2\left(\hat{H} - \hat{x}_2\right) \\ 0 \end{pmatrix}, \qquad \hat{\mathcal{A}} := \frac{4\,\hat{v}_1^{(max)}}{\hat{H}^2} \tag{5.159}$$

with non-dimensional channel height $\hat{H} = 0.1$ is reached at the outflow boundary, while for the maximum velocity in flow direction $\hat{v}_1^{(max)} = \frac{3}{2}\,\hat{\vec{v}}((0, \hat{x}_2)\,, \hat{t}) = 1.5$,

resulting from global mass conservation

$$\hat{\mathcal{A}} \int_0^{\hat{H}} \hat{\rho}((\hat{l}, \hat{x}_2), \hat{t}) \left(\hat{x}_2 \left(\hat{H} - \hat{x}_2 \right) \right) \mathrm{d}\hat{x}_2 = \int_0^{\hat{H}} \hat{\rho}((0, \hat{x}_2), \hat{t}) \, \hat{\vec{v}}((0, \hat{x}_2), \hat{t}) \, \mathrm{d}\hat{x}_2 \tag{5.160}$$

for incompressible channel flows with non-dimensional channel length $\hat{l} = 1$, is obtained accurately as shown in the time series plot in ***Fig. 5.22***.

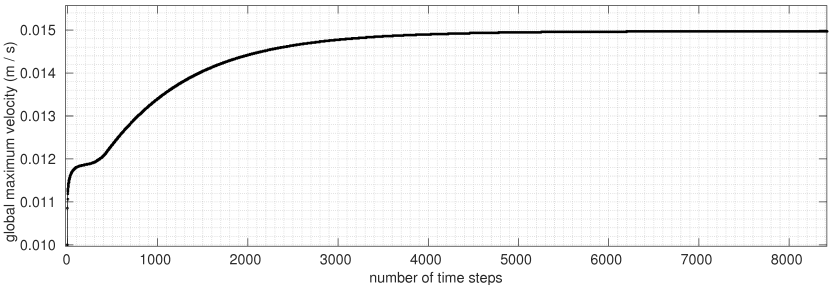

Fig. 5.22: Global maximum velocity over number of time steps of an explicit-implicit computation for channel flow; friction is treated implicitly; initial time step size at CFL-number $\mathcal{C}_{\mathcal{A}} = 0.48$: $\Delta t_0 = 1.875 \cdot 10^{-3}$, final time step size: $\Delta t = 1.25275 \cdot 10^{-3}$

Fig. 5.21 shows the velocity magnitude (greyscale) and iso-contours of the gradient of the wall normal velocity component (black solid), pressure $p^{'}$ (black dashed) and velocity magnitude at $\hat{v}_1 \in (0.99,\ 0.9925,\ 0.995,\ 0.9975)\, \hat{v}_1^{(max)}$ (white) at $\hat{t} = 10$, and ***Fig. 5.23*** shows the corresponding velocity profiles at $\hat{x}_1 \in (0.1,\ 0.2,\ 0.3,\ 0.4, 0.5, 1.0)$. A maximum velocity of $0.99\, \hat{v}_1^{(max)}$ is obtained at $\hat{x}_1 = 0.495$. In ***Fig. 5.24*** on page 124 velocity profiles and wall normal gradients at the outflow boundary at different points in time are shown, which develop as expected.

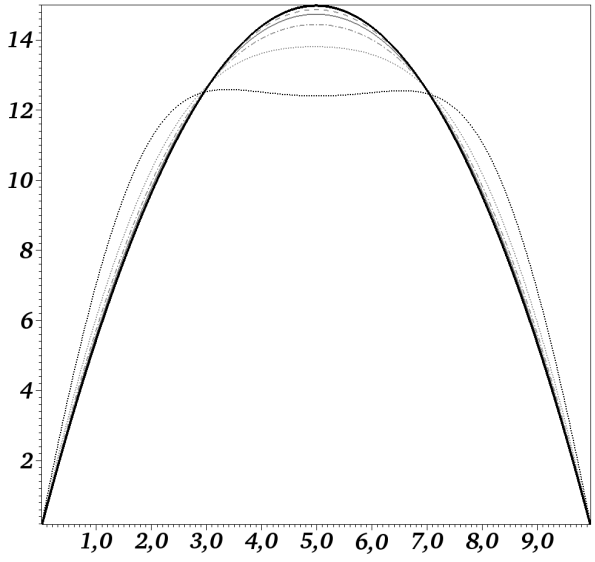

Fig. 5.23: Profiles of velocity component v_1 (*vertical axis*), depending on coordinate direction x_2 (*horizontal axis*), at $\hat{x}_1 \in (0.1, 0.2, 0.3, 0.4, 0.5, 1.0)$ and $\hat{t} = 10$; horizontal axis scales with 10^{-2}, vertical axis scales with 10^{-3}

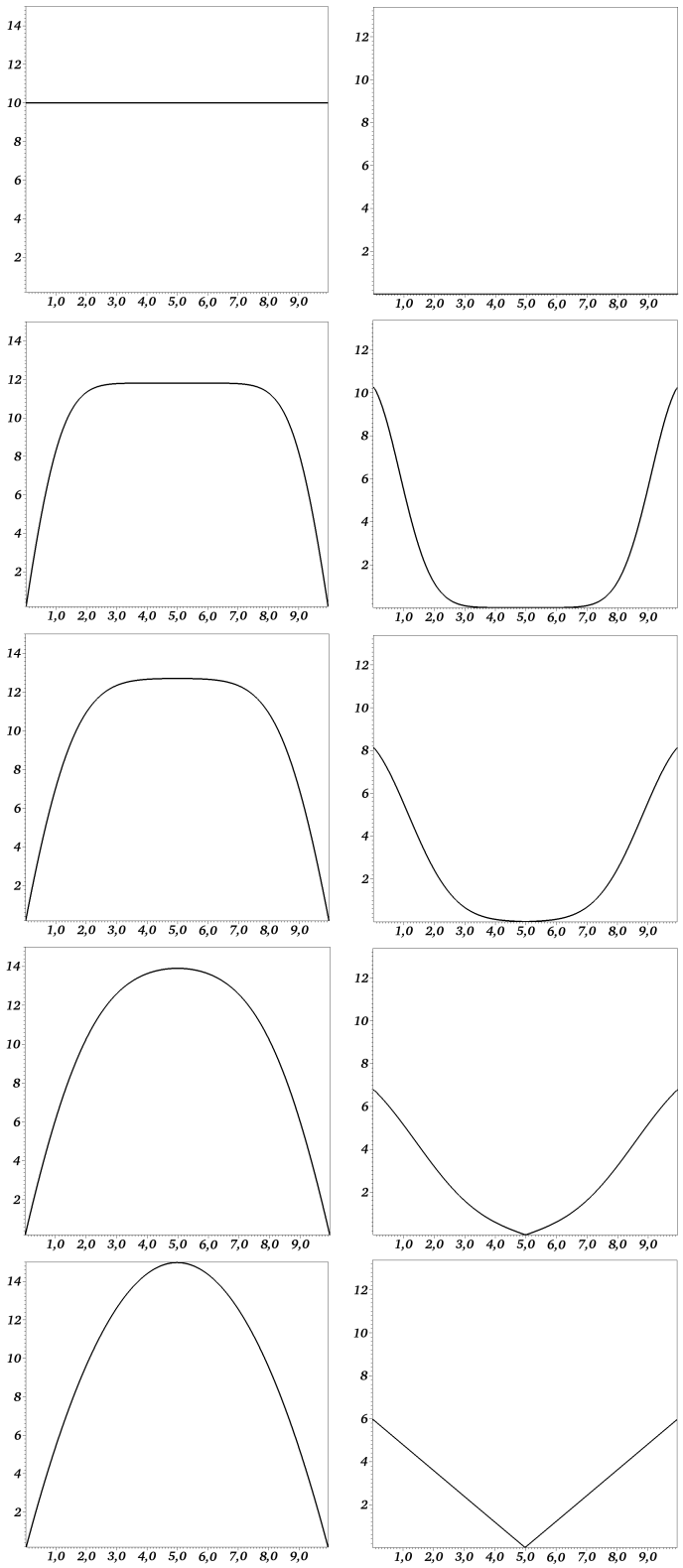

Fig. 5.24: Velocity profiles (*left)* and absolute value of vertical (wall normal) velocity gradient components (*right*) in at the channel outflow boundary ($\hat{\vec{x}}_1 = \hat{l} = 1$) at $\hat{t} \in (0.0, 0.5, 1.0, 2.0, 10.0)$ over $\hat{x}_2$; the final outflow profile (*bottom*) is parabolic in $\hat{x}_2$, with 1.5 times the inflow value as maximum value and linear wall normal gradient component. The horizontal coordinates in all pictures scale with 10^{-2}, the non-dimensional velocity magnitudes on the left scale with 10^{-3} and the vertical axes in the right pictures scale with 10^{-1}

5.6.4 Falling Drop

As in [150], the single-phase version of an inviscid ($\hat{\mu} = 0$) falling drop example is computed at $\mathsf{Fr} = 1$ ($\check{\vec{v}} = 1\frac{\mathrm{m}}{\mathrm{s}}$, $\check{l} = 1\mathrm{m}$, $\check{g} = 1\frac{\mathrm{m}}{\mathrm{s}^2}$) in both two and three spatial dimensions in a closed box at

$$\check{\rho} = 1000\frac{\mathrm{kg}}{\mathrm{m}^3}, \qquad \check{P}_0 = 101325\frac{\mathrm{kg}}{\mathrm{m}\,\mathrm{s}^2} \tag{5.161}$$

in order to show, that on the one hand the entire method – yet without numerical representation of a fluidic interface[23] – is able to handle large density ratios within few grid cells, on the other hand, three dimensional computations are possible as well, while restricting to two space dimensions in the rest of this work. The upper half of the box is filled with a light fluid of density $\hat{\rho} = 0.001$ at rest, initially containing a static circular ($\mathfrak{d} = 2$) / spherical ($\mathfrak{d} = 3$) drop of a heavy fluid of density $\hat{\rho} = 1$. The lower half of the box is filled with the heavy fluid, at rest as well, leading to the following initial setting:

$$\hat{\rho}(\hat{\vec{x}}, 0) = \begin{cases} 1 & \text{if} \quad 0 \leqslant \hat{x}_{\mathfrak{d}} \leqslant 1 \quad \vee \quad \hat{r} \leqslant 0.2 \\ 0.001 & \text{if} \quad 1 < \hat{x}_{\mathfrak{d}} \leqslant 2 \quad \wedge \quad \hat{r} > 0.2 \end{cases} \tag{5.162a}$$

$$\hat{\vec{v}}(\hat{\vec{x}}, 0) = \vec{0} \tag{5.162b}$$

$$\hat{r} = \left| \hat{\vec{x}} - \hat{\vec{x}}^{(\mathfrak{d})} \right| \tag{5.162c}$$

$$\hat{\vec{x}}^{(2)} = \begin{pmatrix} 0.5 \\ 0.75 \end{pmatrix} \qquad \hat{\vec{x}}^{(3)} = \begin{pmatrix} 0.5 \\ 0.5 \\ 0.75 \end{pmatrix} \tag{5.162d}$$

$$\hat{\vec{x}} = \frac{\vec{x}}{\check{l}} \tag{5.162e}$$

The dynamic pressure $\hat{p}^{'}$ results from the procedure described in section 5.3. After acceleration due to gravity the drop hits the surface of the heavy fluid as shown in ***Fig. 5.25*** on page 126 and in ***Fig. 5.26*** on page 127, corresponding to the snapshots given in [150], which are well reproduced. However, in the present method numerical diffusion seems to be larger than in [150]. In this example the elliptic solver for determination of the nodal pressure $p^{'}$ terminates, if the relative residual is smaller than 10^{-3}.

[23] See chapter 6 for two-phase flow.

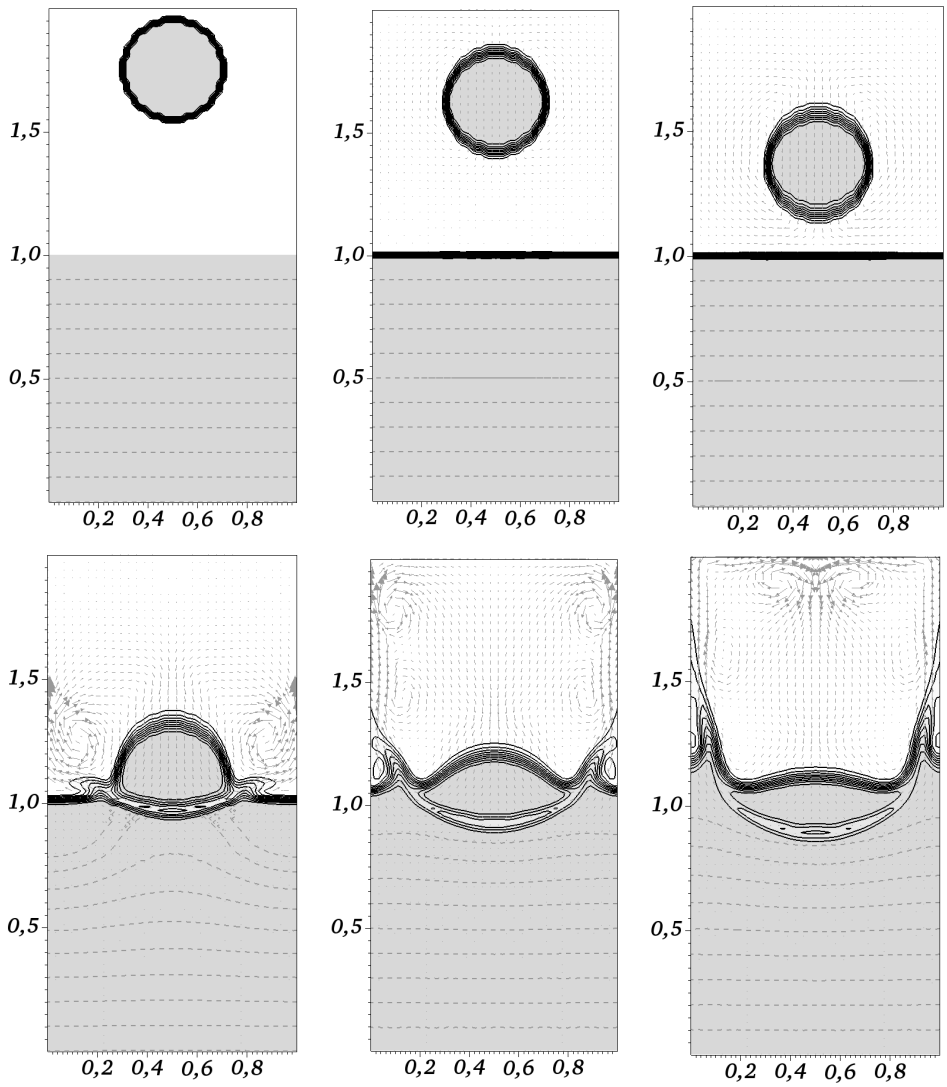

Fig. 5.25: Single-phase computation of a two-dimensional circular fluid drop of density $\hat{\rho} = 1$, falling within a fluid of density $\hat{\rho} = 0.001$ (*white*, top half domain) in a closed box into a fluid of density $\hat{\rho} = 1$ (*light grey*, bottom half domain); the pressure iso-contours $\hat{p}^{'} \in (-0.1, -0.2, -0.3, -0.4, -0.5, -0.6, -0.7, -0.8, -0.9)$, the density iso-contours at $\hat{\rho} \in (0.1, 0.2, 0.3, 0.4, 0.5, 0.6, 0.7, 0.8, 0.9)$ (*black solid lines*) and velocity vectors (*grey arrows*) are plotted at $\hat{t} \in ((0, 0.5, 0.875), (1.125, 1.25, 1.375))$

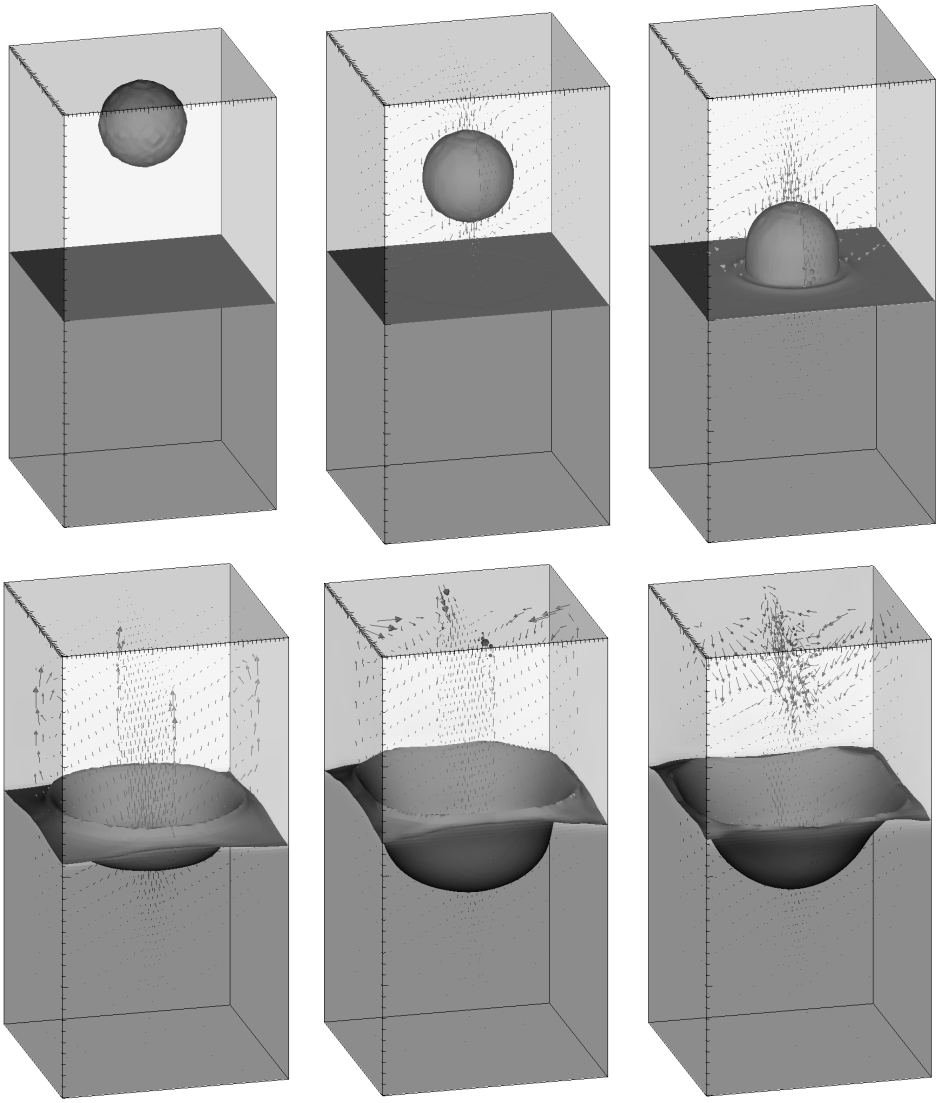

Fig. 5.26: Single-phase computation of a three-dimensional spherical fluid drop of density $\hat{\rho} = 1$, falling within a fluid of density $\hat{\rho} = 0.001$ (*light grey*, top half domain) in a closed box into a fluid of density $\hat{\rho} = 1$ (*medium grey*, bottom half domain); the density iso-contour at $\hat{\rho} = 0.5$ (*dark grey*) and velocity vectors in the $\hat{x}_1$-$\hat{x}_3$- and the $\hat{x}_2$-$\hat{x}_3$-plane are plotted at $\hat{t} \in ((0, 0.75, 1.125), (1.5, 1.875, 2.25))$

5.6.5 Density Disturbances in Stratified Setting

The initial condition for the non-dimensional density in this two-dimensional setting is

$$\hat{\rho}(\hat{\vec{x}},0) = \left[\frac{1}{2} - \mathcal{C}_0\left(\hat{x}_2 - \frac{1}{2}\right)^3 + \Delta\hat{\rho}\right] \tag{5.163}$$

with Gaussian disturbance

$$\Delta\hat{\rho} := \sum_{\mathcal{N}=-10}^{10}\left(\mathcal{C}_1\,\mathrm{e}^{-\left(\hat{r}^{(1)}(\mathcal{N})\right)^2} - \mathcal{C}_2\,\mathrm{e}^{-\left(\hat{r}^{(2)}(\mathcal{N})\right)^2}\right) \tag{5.164}$$

subject to

$$\left(\hat{r}^{(i)}(\mathcal{N})\right)^2 = \left(\frac{\hat{x}_1 - \hat{x}_1^{(i)} - \mathcal{N}}{\mathcal{C}_3}\right)^2 + \left(\frac{\hat{x}_2 - \hat{x}_2^{(i)}}{\mathcal{C}_3}\right)^2 \tag{5.165}$$

and

$$\hat{\vec{x}}^{(1)} = \begin{pmatrix}0.5\\0.75\end{pmatrix}, \qquad \hat{\vec{x}}^{(2)} = \begin{pmatrix}0.5\\0.25\end{pmatrix} \tag{5.166a}$$

$$\mathcal{C}_0 = 0.5, \qquad \mathcal{C}_1 = \mathcal{C}_2 = 0.05, \qquad \mathcal{C}_3 = 0.1 \tag{5.166b}$$

on a $([0,1]\times[0,1])$ domain as specified in [86], periodic in the horizontal direction and bounded by solid no-slip walls on top and bottom. The system is initially at rest and, thus,

$$\hat{\vec{v}}(\hat{\vec{x}},0) = 0 \tag{5.167}$$

applies for the initial velocity. Physically, this setting corresponds to a cold air parcel on top of a hot one in a stratified surrounding with

$$g = 9.81\,\frac{\mathrm{m}}{\mathrm{s}^2}, \qquad \mu = 1.846\cdot 10^{-5}\,\frac{\mathrm{m}^2}{\mathrm{s}}, \qquad \hat{p}'(\vec{0},t) = 0 \tag{5.168a}$$

and a resulting stratification in $\hat{p}'$ as shown in the first picture of ***Fig. 5.27*** on page 129. The other snapshots in ***Fig. 5.27*** show, that also in non-trivial flow situations with locally large velocity gradients symmetry is maintained by the present method, wherever only physically symmetric influences act on the flow. While horizontal symmetry is well maintained, the upper part is not symmetric to the lower one with respect to the horizontal center axis due to an initial pressure profile, which is only horizontally symmetric with respect to the vertical center axis.

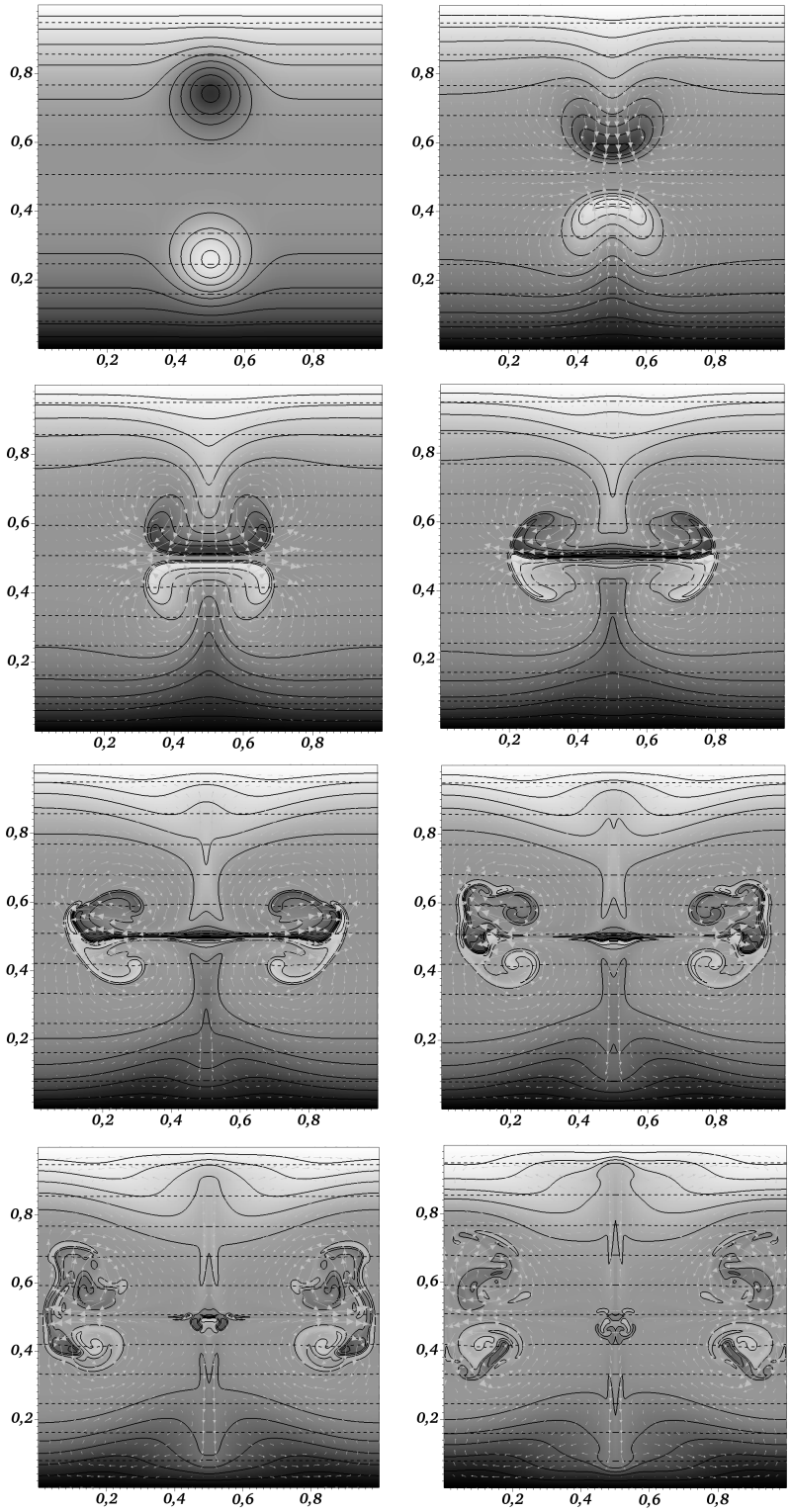

Fig. 5.27: Density disturbances under the influence of gravity in stratified environment on a two-dimensional grid of 256×256 grid cells: Snapshots at $\hat{t} \in \{\{0, 1.0\}, \{1.5, 2.0\}, \{2.5, 3.0\}, \{3.5, 4.0\}\}$; *greyscale:* density $\hat{\rho}$ (initial values between 0.4382 (white) and 0.5618 (black)); *solid black lines*: equidistant density iso-contours; *dashed black lines*: iso-contours of pressure $\hat{p}'$ at $(-0.5, -1.0, -1.5, -2.0, -2.5, -3.0, -3.5, -4.0, -4.5, -5.0, -5.5, -6.0)$; *grey arrows*: velocity field

This can be seen more clearly, if the density disturbances $\Delta\hat{\rho}$ are amplified by a factor of 10 as shown in ***Fig. 5.28*** on page 130. Therefore horizontal acceleration of the lower center flow feature in ***Fig. 5.27*** is slightly larger than the one of the top center flow feature. Advection including pressure is treated explicitly at a CFL-number $\mathcal{C}_{\mathcal{A}} = 0.48$ as described in section 5.1.3.1 and friction is treated implicitly as described in section 5.1.3.3 - 1.

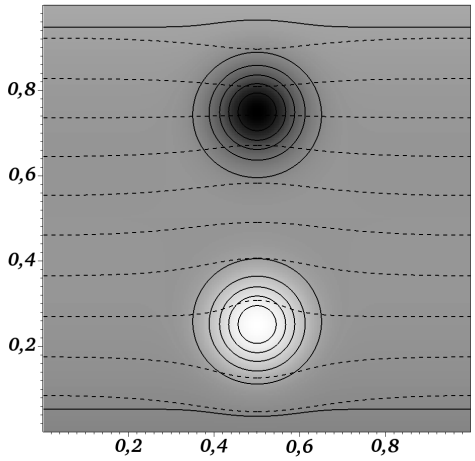

Fig. 5.28: Density disturbances – $\Delta\hat{\rho}$ amplified by a factor of 10 – under the influence of gravity between $\hat{\rho} = 0.00801$ (white) and $\hat{\rho} = 0.99235$ (black); iso-contours of density (*solid*) and pressure (*dashed*)

5.6.6 Gravity Driven Instability

The two-dimensional initial conditions are basically the ones specified in the previous test case 5.6.5. However, in addition to the influence of gravity, a shear flow

$$\hat{\vec{v}}(\hat{\vec{x}}, 0) := \frac{1}{2} \begin{pmatrix} \tanh\left(\frac{\hat{x}_2 - \frac{1}{2}}{\varepsilon}\right) \\ 0 \end{pmatrix} \tag{5.169}$$

with

$$\varepsilon = 0.02 \tag{5.170}$$

according to [86] is acting on the density distribution (5.163) to (5.166a) with

$$\mathcal{C}_0 = 0.0156, \qquad \mathcal{C}_1 = \mathcal{C}_2 = 0.00156, \qquad \mathcal{C}_3 = 0.25 \tag{5.171}$$

instead of the coefficients given in section 5.6.5 in equation (5.166b). Further, viscosity is neglected ($\mu = 0$) and, thus, the top and bottom domain boundaries are slip-walls. ***Fig. 5.29*** on page 131 shows the initial distribution of density $\hat{\rho}$ (black solid lines), pressure $\hat{p}'$ (dashed lines) and two-dimensional vorticity $\frac{\partial \hat{v}_2}{\partial \hat{x}_1} - \frac{\partial \hat{v}_1}{\partial \hat{x}_2}$ (greyscale areas) in the left plot, and the state of these variable at $\hat{t} = 2.5$ in the right

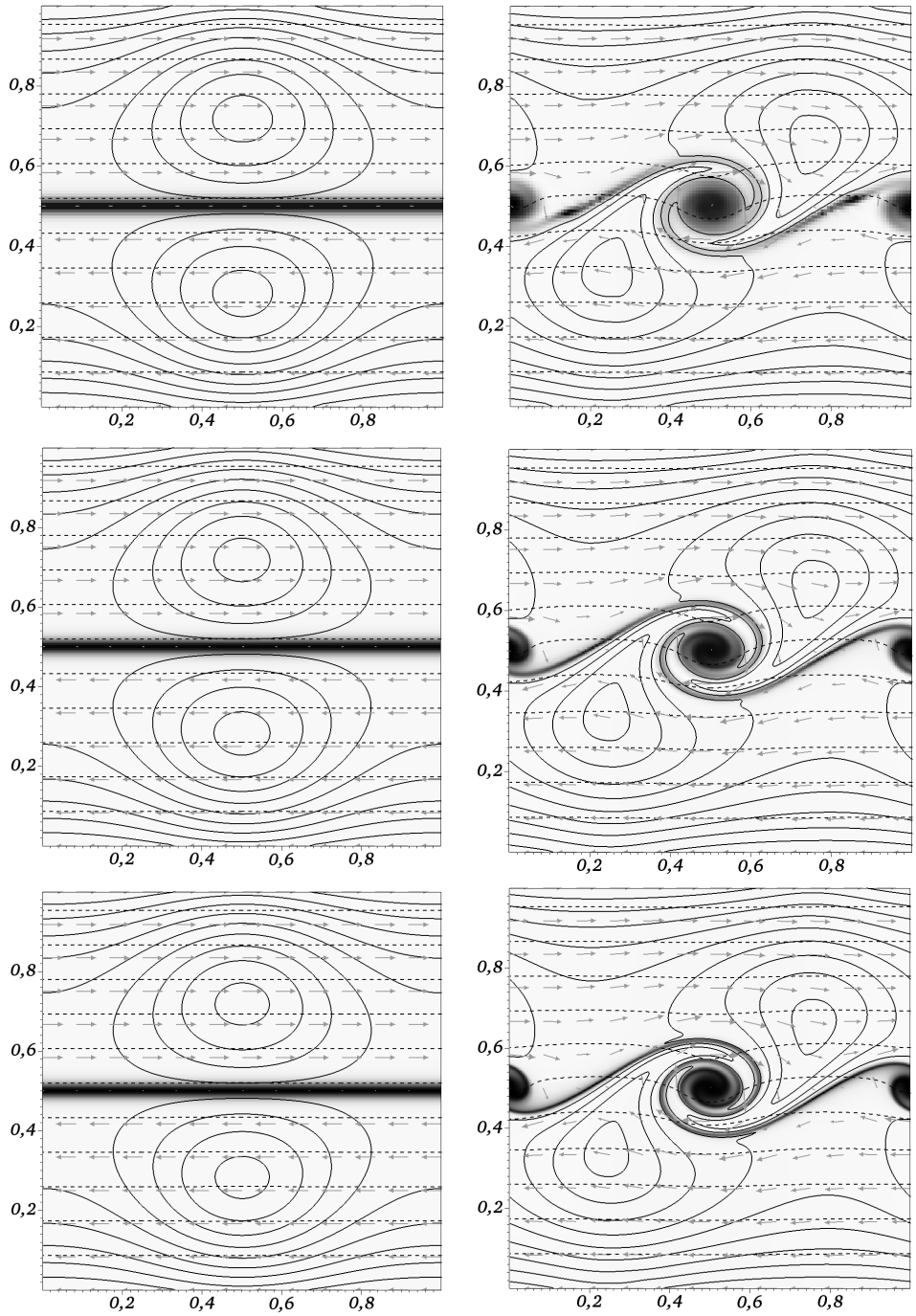

Fig. 5.29: Gravity driven instability on two-dimensional grids of 128×128 (*top*), 256×256 (*center*) and 512×512 (*bottom*) grid cells at $\hat{t} = 0$ (*left*) and $\hat{t} = 2.5$ (*right*): *greyscale:* two-dimensional vorticity between -25.0 (black) and 1.5 (white); *solid black lines*: equidistant density iso-contours; *dashed black lines*: pressure iso-contours at $(-0.5, -1.0, -1.5, -2.0, -2.5, -3.0, -3.5, -4.0, -4.5, -5.0, -5.5, -6.0)$; *grey arrows*: velocity field

plot for different grid resolutions. The results from [86] are well reproduced.

5.6.7 Vortex-Wall Collision

The present single-phase method has been applied both fully explicit and semi-implicit for comparative studies in two space dimensions to contribute to [124], [125] and [126], in which the Reynolds number dependent scaling of the drag force at high Reynolds numbers is studied on a vortex-wall collision and detachment test problem in weakly viscous incompressible fluids at different viscosities as described in [123] and references therein. Within the present context, this example provides another test for the viscous flux discretization. The setting shown in ***Fig. 5.30*** represents the lower left quarter of a domain, periodic in x_2 direction, containing a quadrupole consisting of two pairs of oppositely rotating vortices in a (weakly) viscous fluid. Due to that constellation and direction of rotation, the vortices start traveling along the horizontal center axes of the domain until they hit a wall as done in [123] and [98], slide along the wall for a certain period and detach from the wall due to small scale flow structures, which develop near the solid wall due to friction. Since the symmetry lines of the problem can be modeled by slip wall boundaries of the quarter domain, it is sufficient to only compute solutions within that quarter of the domain – containing only one of the four vortices as shown in ***Fig. 5.30*** – in order to capture the phenomena of the traveling vortices, hitting the solid no-slip boundary. Therefore, in the current setting the top, bottom and right boundaries are slip walls and the left boundary is the no-slip wall. The (arbitrary) density is constant everywhere and

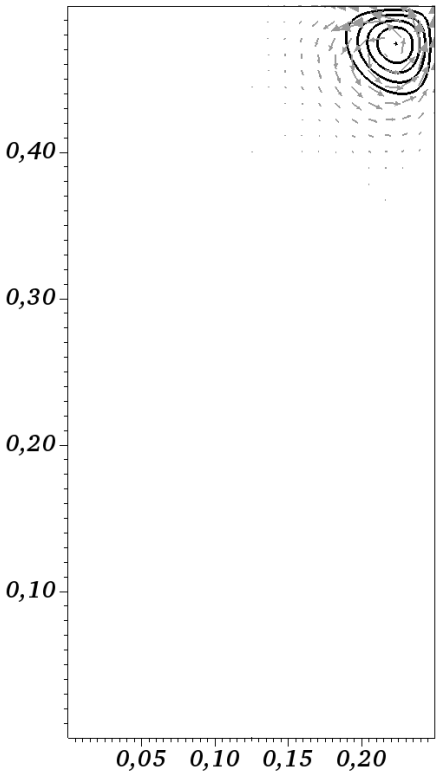

Fig. 5.30: Lower left quarter of a $[0.0, 0.5] \times [0.0, 1.0]$ domain with one vortex of a quadrupole, centered at (0.5, 0.5); *black solid lines*: iso-contours of vorticity at $0.2, 0.4, 0.6, 0.8, 1.0$; *grey arrows*: velocity vectors

chosen to be $\hat{\rho}(\hat{\vec{x}}, 0) = 1$. Gravity is neglected ($\hat{\vec{g}} = \vec{0}$) and the initial velocity field

$$\hat{\vec{v}}(\hat{\vec{x}}, 0) = \mathcal{A}\,\eta\,\mathrm{e}^{-\frac{1}{2}(\hat{\vec{x}}\cdot\hat{\vec{x}})} \begin{pmatrix} \hat{x}_1\left(1-\hat{x}_2^2\right) \\ \hat{x}_2\left(\hat{x}_1^2-1\right) \end{pmatrix} \tag{5.172}$$

with

$$\mathcal{A} = 0.625847306637464, \qquad \eta = 0.031830988618379 \tag{5.173}$$

and relative non-dimensional coordinates

$$\hat{x}_i = \frac{\hat{x}_i - \hat{x}_{\circ,i}}{\eta} \tag{5.174}$$

as well as origin

$$\hat{\vec{x}}_\circ = \begin{pmatrix} 0.25 \\ 0.5 \end{pmatrix} \tag{5.175}$$

corresponds to the initial two-dimensional local vorticity magnitude

$$|\hat{\vec{\omega}}| = \left|\frac{\partial \hat{v}_2}{\partial \hat{x}_1} - \frac{\partial \hat{v}_1}{\partial \hat{x}_2}\right| = \mathcal{A}\,\hat{x}_1\,\hat{x}_2\left(6 - \hat{\vec{x}}\cdot\hat{\vec{x}}\right)\,\mathrm{e}^{-\frac{1}{2}(\hat{\vec{x}}\cdot\hat{\vec{x}})} \tag{5.176}$$

with initial enstrophy

$$\hat{\mathfrak{E}}^0 = \frac{1}{2}\int_{\hat{\Omega}} |\hat{\vec{\omega}}|^2 \mathrm{d}V = \frac{1}{2}\int_{\hat{\Omega}} \left|\hat{\nabla}\hat{\vec{v}}\right|^2 \mathrm{d}V \approx 1.195 \cdot 10^{-3} \tag{5.177}$$

and Frobenius norm (or Hilbert-Schmidt norm) $\left|\hat{\nabla}\hat{\vec{v}}\right|$. Computations on the quarter domain $[0, 0.25] \times [0, 0.5]$ are performed at a grid resolution of 4096×1024 grid cells (corresponding to a factor of 8 between no-slip wall normal and no-slip wall tangential resolution). As shown in ***Fig. 5.32*** and ***Fig. 5.33*** for an initial Reynolds number $\mathsf{Re} \approx 36109$ due to the maximum initial rotation speed $\check{v}^{(max)} \approx 1.418 \cdot 10^{-2}\,\frac{\mathrm{m}}{\mathrm{s}}$, vortex size $2\eta\check{l} \approx 6.3662{\cdot}10^{-2}\,\mathrm{m}$ and dynamic viscosity $\check{\mu} = 0.25{\cdot}10^{-7}\,\frac{\mathrm{kg}}{\mathrm{m\,s}}$, similar flow features as in [98] develop: Due to large vorticity in the boundary layer at $\mathsf{Re} > \mathcal{O}(10^4)$, the vortex detaches from the wall and small scale vortices from the boundary layer merge to a second oppositely rotating vortex as described in [98], causing the entire structure to fall back onto the no-slip wall.

In ***Fig. 5.31*** time series of the global maximum absolute vorticity, the global enstrophy (5.177) and the global kinetic energy are shown. As in [145] for another, three-dimensional, example, different phases can be identified from the enstrophy

plot: In the first phase, enstrophy remains nearly constant while the vortex is sliding along the top slip wall boundary until $\hat{t} \lesssim 30$. From $\hat{t} \approx 30$, already before the vortex hits the no-slip wall, a boundary layer is developing at the latter due to the globally induced velocity field, which becomes more evident from the plot of global maximum vorticity. At $\hat{t} \approx 40$ the vortex starts hitting the no-slip wall and between $40 \lesssim \hat{t} \lesssim 56.5$ a secondary vortex develops in the boundary layer after the vortex has hit the no-slip wall. This phase is followed by a deformation phase of the primary boundary layer from $56.5 \lesssim \hat{t} \lesssim 59.5$, in which a secondary boundary layer of opposite vorticity develops at the no-slip wall underneath the primary one, causing the latter to deform and to finally detach in the sequel. Detachment of a secondary vortex from the primary boundary layer starts from $\hat{t} \lesssim 59.5$. The following peaks in the plots of enstrophy and maximum vorticity in ***Fig. 5.31*** indicate generation, deformation and detachment of other sub-layers and vortices as shown in the wake of the pair of primary (black) and secondary (white) vortex in ***Fig. 5.34*** on page 137.

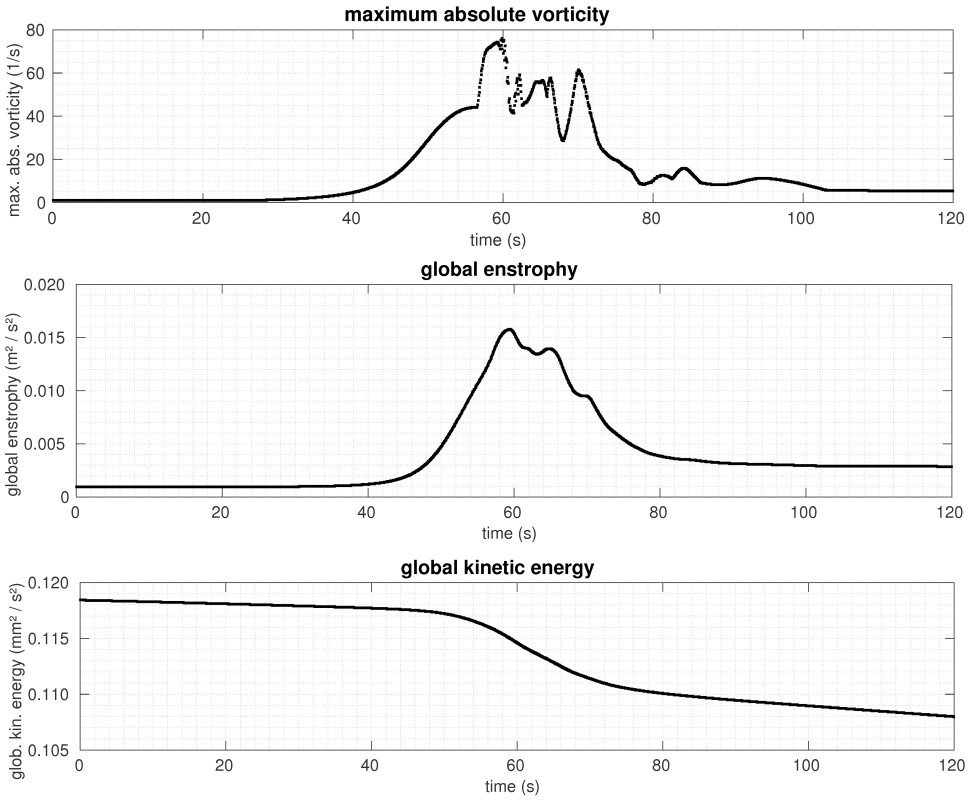

Fig. 5.31: Global time series of vortex-wall collision at $\mathsf{Re} = 36109$: *top*: global maximum absolute vorticity; *top*: global enstrophy, *bottom*: global kinetic energy

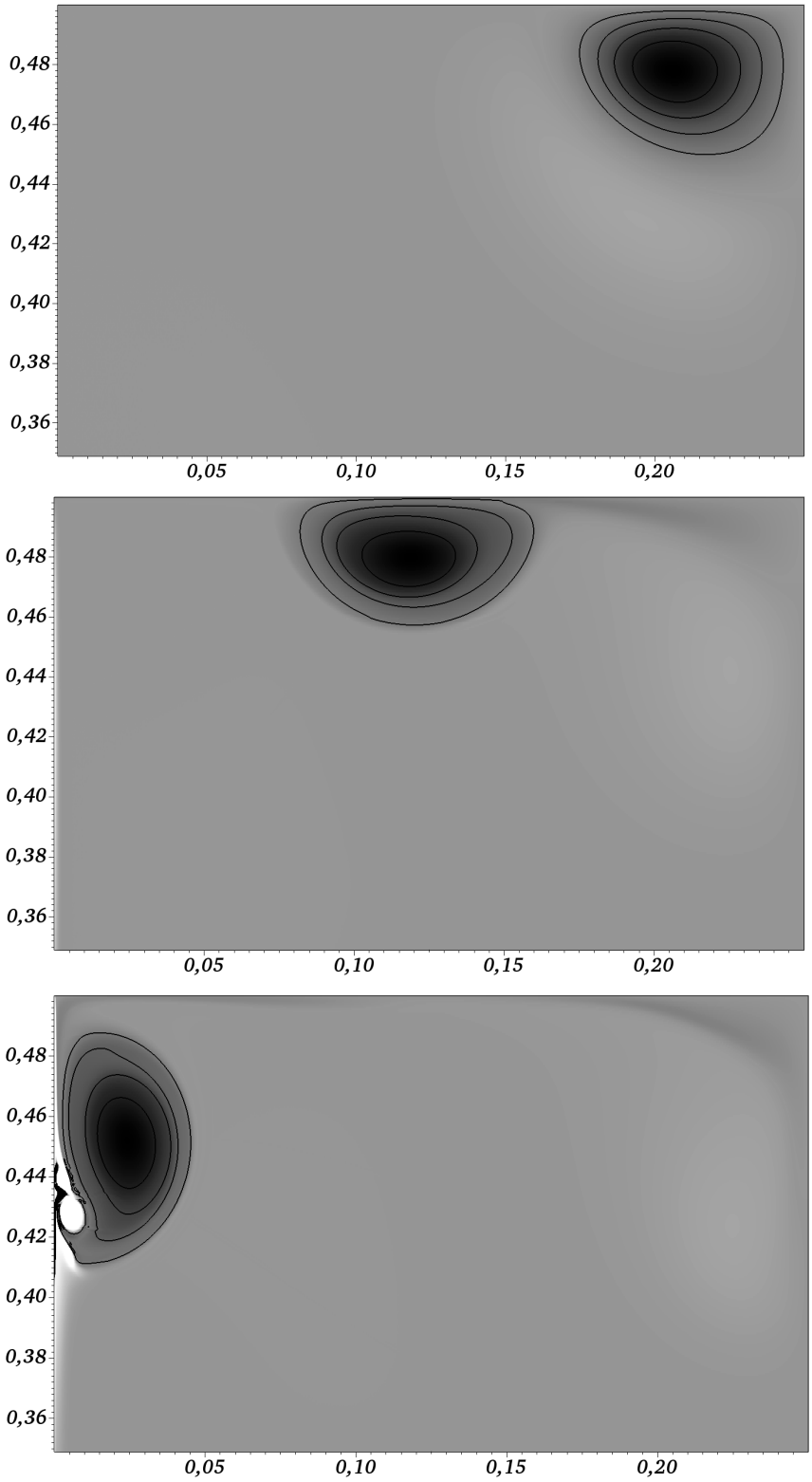

Fig. 5.32: Vorticity during vortex-wall collision in upper part of the lower left quarter domain at $\hat{t} \in (0, 30, 60)$ for $\mathsf{Re} = 36109$); *black*: positive vorticity above 1, *white*: negative vorticity below -1; *grey*: absolute vorticity values smaller than 1; *solid black lines*: iso-contours of vorticity a $(0.2, 0.4, 0.6, 0.8, 1.0)$

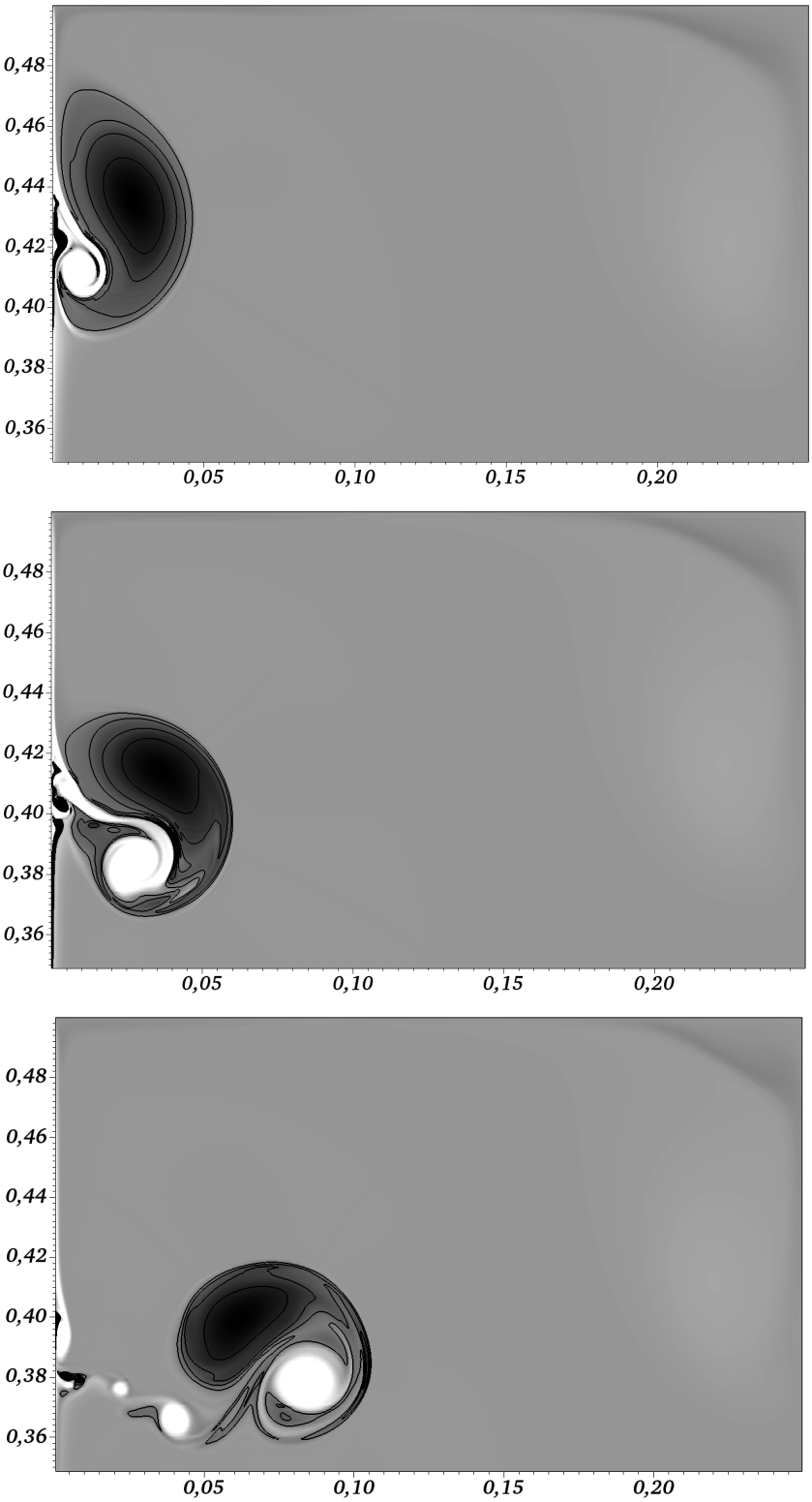

Fig. 5.33: Vorticity during vortex-wall collision in upper part of the lower left quarter domain at $\hat{t} \in (66, 75, 90)$ for $\mathsf{Re} = 36109$); *black*: positive vorticity above 1, *white*: negative vorticity below -1; *grey*: absolute vorticity values smaller than 1; *solid black lines*: iso-contours of vorticity a $(0.2, 0.4, 0.6, 0.8, 1.0)$

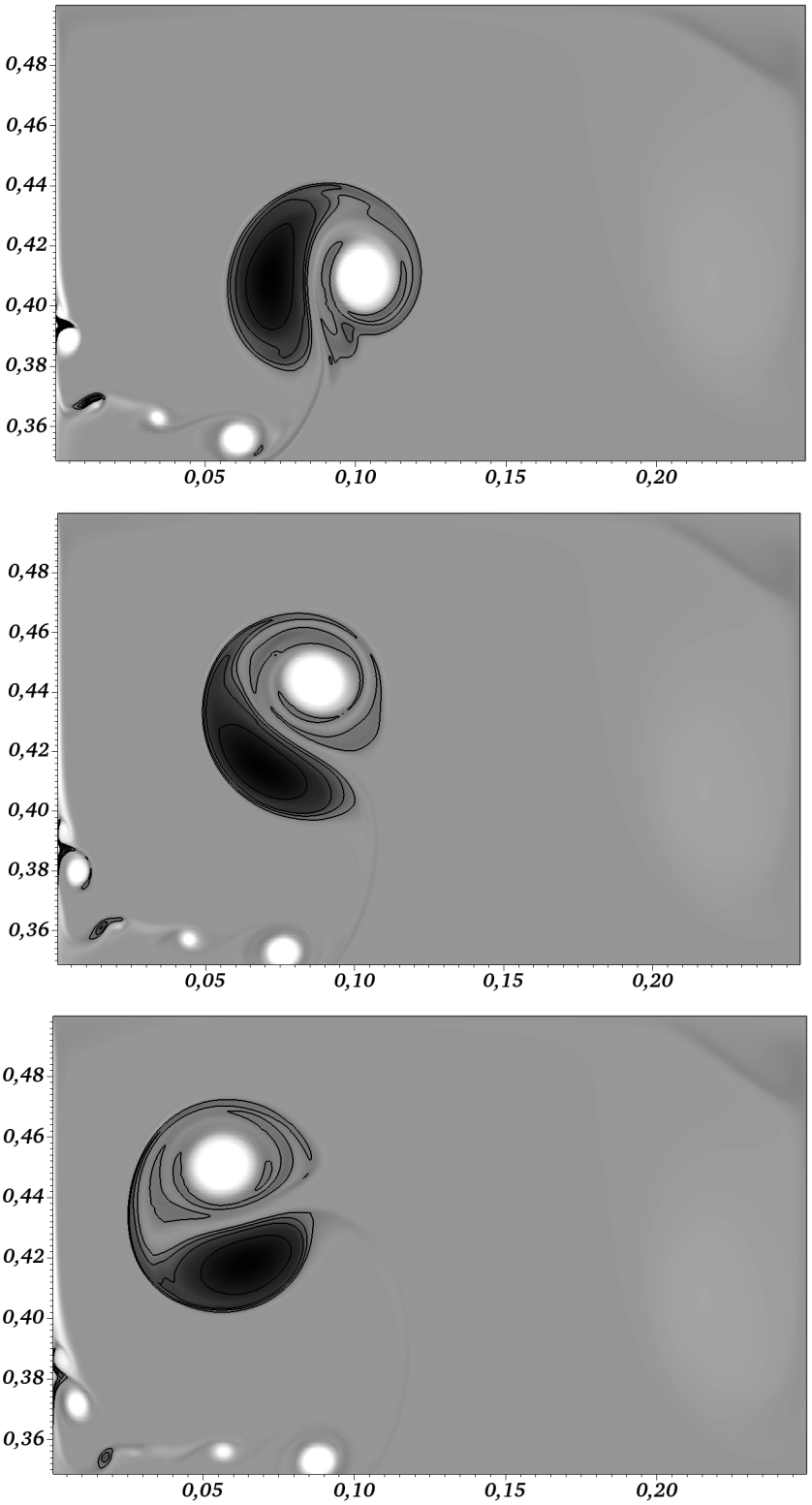

Fig. 5.34: Vorticity during vortex-wall collision in upper part of the lower left quarter domain at $\hat{t} \in (100, 110, 120)$ for $\mathsf{Re} = 36109$); *black*: positive vorticity above 1, *white*: negative vorticity below -1; *grey*: absolute vorticity values smaller than 1; *solid black lines*: iso-contours of vorticity a $(0.2, 0.4, 0.6, 0.8, 1.0)$

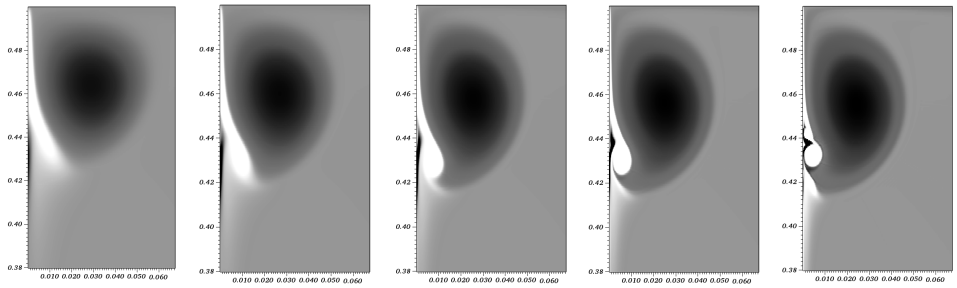

Fig. 5.35: Vorticity during vortex-wall collision in the left upper corner of the lower left quarter domain at $t = 60$ for $\mathsf{Re} \in (1923, 3845, 7690, 15381, 30761)$ from left to right; *black*: vorticity above 1, *white*: vorticity below -1; *grey* absolute vorticity values smaller than 1

Further, results for the maximum vorticity and the time of maximum vorticity for $|\vec{v}|^{(max)}(t = 0\,\mathrm{s}) \approx 1.208 \cdot 10^{-2}\,\frac{\mathrm{m}}{\mathrm{s}}$ are given in ***Tab. 5.7***, and the corresponding plots at $t = 60\,\mathrm{s}$ are given in ***Fig. 5.35***.

Tab. 5.7: Maximum enstrophy and maximum vorticity during vortex-wall collision for different Reynolds numbers at maximum initial velocity $|\vec{v}|^{(max)}(t = 0\,\mathrm{s}) \approx 1.208 \cdot 10^{-2}\,\frac{\mathrm{m}}{\mathrm{s}}$

Re	μ	$\lvert\vec{\omega}\rvert^{(max)}$	$t_{\lvert\vec{\omega}\rvert^{(max)}}$
	$\frac{\mathrm{kg}}{\mathrm{m\,s}}$	$\frac{1}{\mathrm{s}}$	s
	10^{-7}		
1923	4.00	8.742	59.11
3845	2.00	14.085	57.50
7690	1.00	21.308	56.75
15381	0.50	36.465	59.68
30761	0.25	74.184	59.24

5.6.8 Rising Thermal Bubble

In [59] a test case is proposed, in which an air parcel, that is slightly warmer than its surrounding, rises due to the influence of gravity and the resulting pressure stratification on atmospheric length scales of magnitude $\mathcal{O}(10^3)$. The potential temperature with reference value $\breve{\theta} = 300\,\mathrm{K}$ is initially disturbed according to

$$\hat{\theta}\left(\hat{\vec{x}}, \hat{t}\right) := \hat{\theta}_0 \begin{cases} 1 + \frac{\hat{\theta}'}{2}\left(1 + \cos\left(\pi \hat{r}\right)\right) & \hat{r} \leqslant 1 \\ 1 & \hat{r} > 1 \end{cases} \tag{5.178}$$

with

$$\hat{\theta}_0 := 1 \tag{5.179a}$$

$$\hat{\theta}' := \frac{1}{600} \tag{5.179b}$$

and $\hat{r}$ as defined in (5.141) to (5.143), with $\hat{r}_\circ = 0.25$ and

$$\hat{\vec{x}}_\circ(0) = \begin{pmatrix} 0.5 \\ 0.35 \end{pmatrix} \tag{5.180}$$

as the initial center of the potential temperature disturbance. Results for this test case are, for example, given in [59] and [117]. Since the present method, however, is derived for small length scales of magnitude $\mathcal{O}(1)$, several parameters need to be transformed in order to perform the test at the same governing characteristic numbers Fr, Re and Sr besides of the vanishing Mach number Ma. While for atmospheric scales the reference quantities

$$\check{l}^{(atm)} = 1000\,\mathrm{m}, \qquad \check{t}^{(atm)} = 1000\,\mathrm{s}, \qquad \check{\mu}^{(atm)} = 0.1\,\frac{\mathrm{kg}}{\mathrm{m\,s}} \tag{5.181}$$

are chosen in [117], yielding

$$\mathsf{Ma} = 0, \qquad \mathsf{Sr} = \frac{\check{l}^{(atm)}}{\check{t}^{(atm)}\check{v}^{(atm)}} = 1, \qquad \mathsf{Fr} = \frac{\check{v}^{(atm)}}{\sqrt{\check{l}^{(atm)}\check{g}}}, \qquad \mathsf{Re} = \frac{\check{l}^{(atm)}\check{v}^{(atm)}\check{\rho}}{\check{\mu}^{(atm)}} \tag{5.182}$$

for the relevant characteristic numbers with

$$\check{\rho} = 1.177\,\frac{\mathrm{kg}}{\mathrm{m}^3}, \qquad \check{g} = 9.81\,\frac{\mathrm{m}}{\mathrm{s}^2} \tag{5.183}$$

for both the atmospheric and the present small scale setting, in the latter the reference quantities

$$\check{v} = \eta\,\check{v}^{(atm)}, \qquad \check{t} = \eta\,\check{t}^{(atm)}, \qquad \check{\mu} = \eta^3\,\check{\mu}^{(atm)} \tag{5.184}$$

with

$$\eta := \frac{1}{\sqrt{1000}} \approx 3.162277660168 \cdot 10^{-2} \tag{5.185}$$

have to be chosen at length scales of

$$\check{l} = \eta^2\,\check{l}^{(atm)} = 1\,\mathrm{m} \tag{5.186}$$

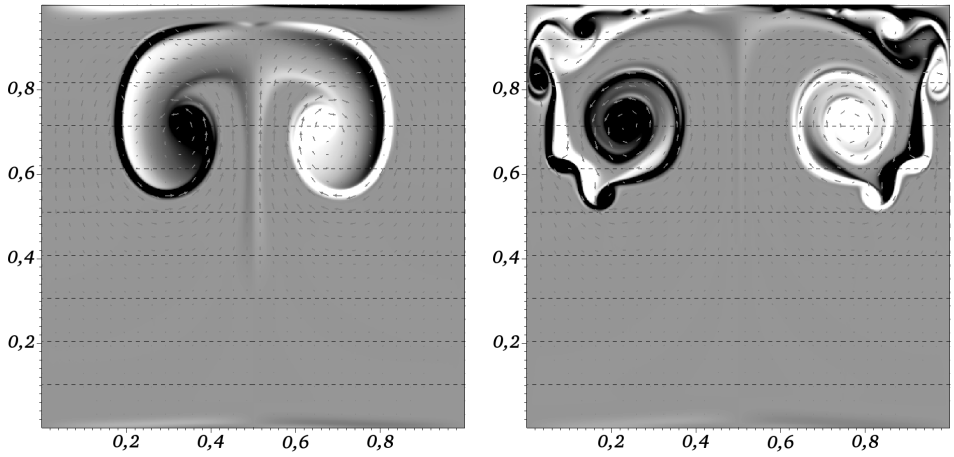

Fig. 5.36: Two-dimensional vorticity of rising thermal bubble on a grid of 512×512 Cartesian cells in a $[0,1] \times [0,1]$ domain with no-slip walls at bottom and top and both constant background density and potential temperature at $\hat{t} \in (0.7, 1.0)$; *black*: vorticity values larger than 1; *white*: vorticity values smaller than -1; *grey*: vorticity values with absolute value smaller than 1; *black dashed lines*: iso-contours of $\hat{p}^{'} \in (-1,-2,-3,-4,-5,-6,-7,-8,-9)\,\eta^{-2}$ (bottom to top); *grey arrows*: velocity vectors $\hat{\vec{v}}$;

in order to preserve all characteristic numbers from (5.182). With this rescaling and periodic boundary conditions to the left and right, good agreement with the results from [117] is achieved as shown in ***Fig. 5.39*** on page 142, in which snapshots at the points in time corresponding to the results in [117] are plotted, and the correct rise velocities are obtained. The differences to [59] and [117] at the top of the domain towards the end of the simulation are due to the fact, that – in contrast to [59] and [117] – no-slip boundaries are used at top and bottom of the domain for the present computations. Therefore, a lower and an upper boundary layer develop in the resulting velocity field as shown in ***Fig. 5.36***, in which the two-dimensional vorticity $\frac{\partial \hat{v}_2}{\partial \hat{x}_1} - \frac{\partial \hat{v}_1}{\partial \hat{x}_2}$ is plotted. Note that due to homogeneous constant $\hat{\mathcal{P}}(\hat{\vec{x}}, \hat{t}) = 1$ and $\hat{P}_0(\hat{\vec{x}}, 0) = 1$ in the small scale limit with $\check{\mathcal{P}} = 300\,\mathrm{K}\frac{\mathrm{kg}}{\mathrm{m}^3}$ and $\check{P}_0 = 101325\,\frac{\mathrm{kg}}{\mathrm{m\,s}^2}$, the density ρ shows the (scaled) inverse behavior of potential temperature θ according to relations (3.141) and (3.144). In contrast to the atmospheric setting, in which P_0 is stratified, in the present small scale limit pressure stratification due to the influence of gravity drops in via $p^{'}$. ***Fig. 5.40*** on page 143 emphazises one of the strength of the present variable density method in comparison to methods restricted to incompressible flow with constant density. It illustrates the same snapshots as ***Fig. 5.39***, but with weakly stably

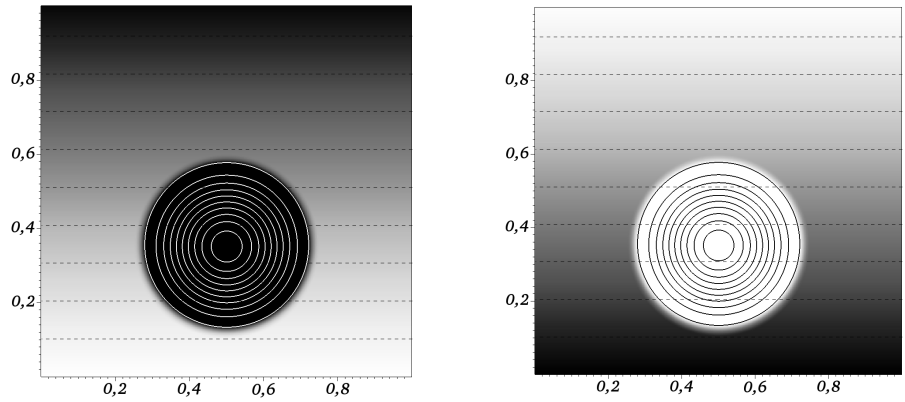

Fig. 5.37: Background stratification for rising thermal bubble at $\hat{t} = 0$: *left*: potential temperature difference $0 < (\hat{\theta} - 1) \leqslant \frac{1}{12000}$ with white representing 0, *right*: density $-8.25 \cdot 10^{-5} \leqslant (\hat{\rho} - 1) \leqslant 0$ with black representing 0; *white/black solid lines*: iso-contours of $(\hat{\theta} - 1) \in (1, 3, 5, 7, 9, 11, 13, 15, 17, 19)\, \frac{\hat{\theta}'}{20}$ (outer to inner); *black dashed lines*: iso-contours of $\hat{p}' \in (-1, -2, -3, -4, -5, -6, -7, -8, -9)\, \eta^{-2}$ (bottom to top)

stratified – and therefore spatially inhomogeneous – distribution

$$\hat{\theta}_0 := \left(1 - \left(1 - \frac{1}{\gamma}\right)\left(\frac{\check{l}\check{g}\check{\rho}}{\check{P}_0}\right)\hat{x}_{\mathfrak{d}}\right)^{-\frac{1}{\gamma-1}} \tag{5.187}$$

of background potential temperature $\hat{\theta}_0$ instead of (5.179a) for application to (5.178).

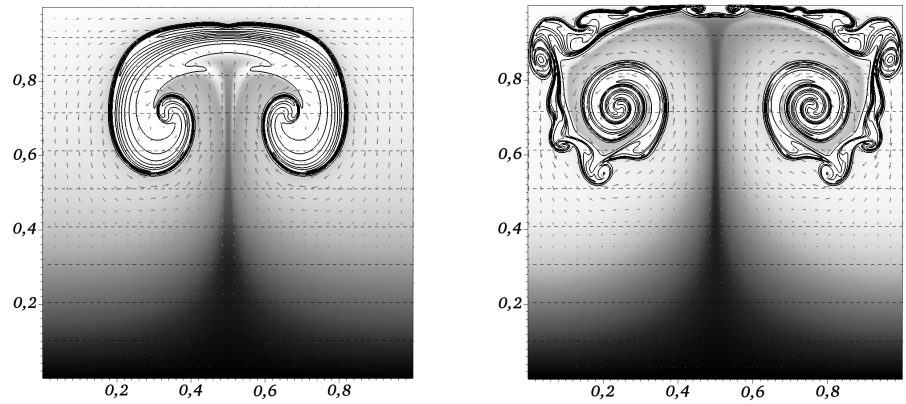

Fig. 5.38: Background density for rising thermal bubble at $\hat{t} = 0.7$ (*left*) and $\hat{t} = 1.0$ (*right*); *black solid lines*: iso-contours of $(\hat{\theta} - 1) \in (1, 3, 5, 7, 9, 11, 13, 15, 17, 19)\, \frac{\hat{\theta}'}{20}$ (outer to inner); *black dashed lines*: iso-contours of $\hat{p}' \in (-1, -2, -3, -4, -5, -6, -7, -8, -9)\, \eta^{-2}$ (bottom to top)

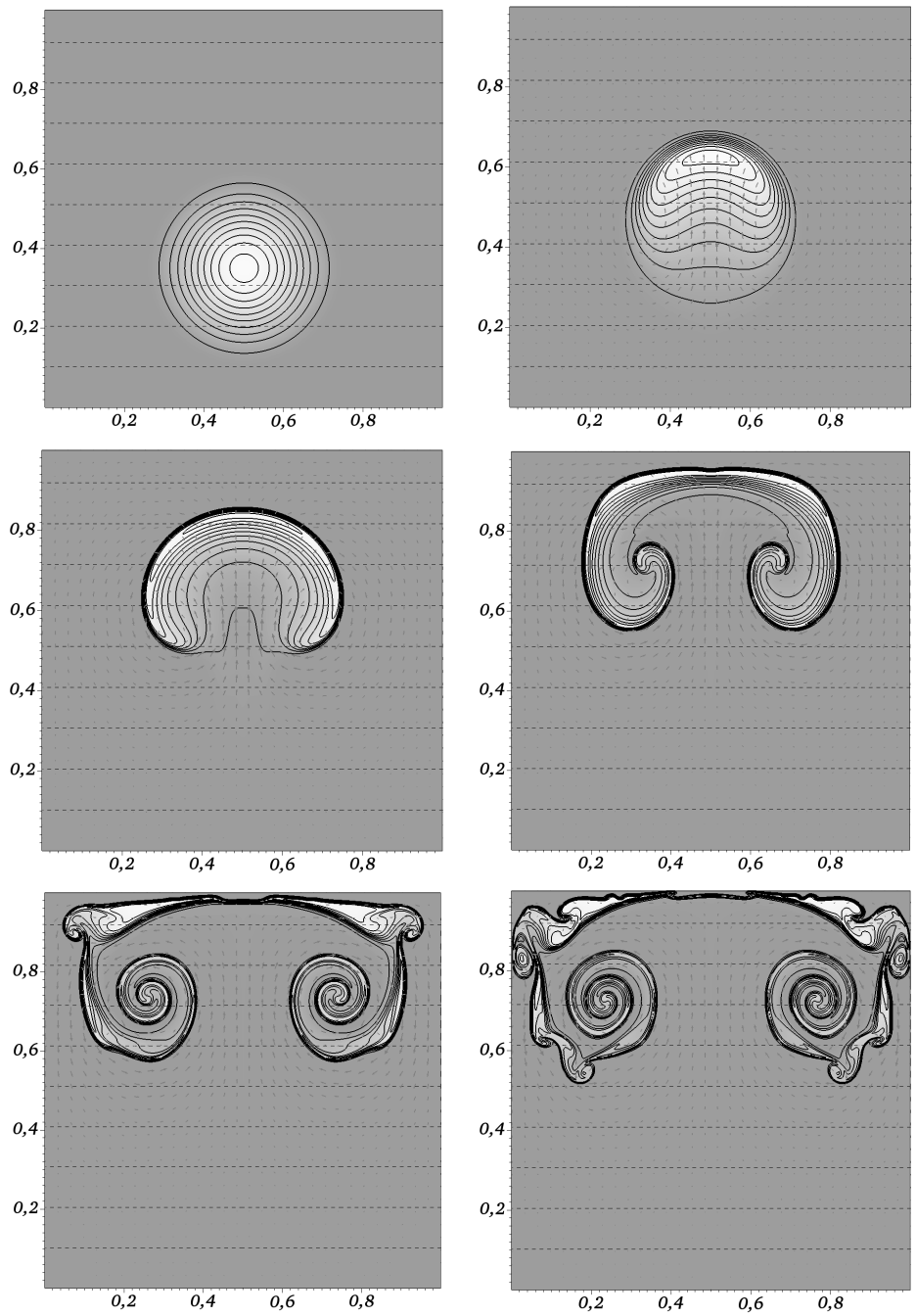

Fig. 5.39: Rising thermal bubble on a grid of 512×512 Cartesian cells in a $[0,1] \times [0,1]$ domain with no-slip walls at bottom and top and both **constant background density and potential temperature** at $\hat{t} \in ((0,0.3),(0.5,0.7),(0.9,1.0))$; *black solid lines*: iso-contours of $(\hat{\theta}-1) \in (1,3,5,7,9,11,13,15,17,19)\,\frac{\hat{\theta}'}{20}$ (outer to inner); *black dashed lines*: iso-contours of $\hat{p}' \in (-1,-2,-3,-4,-5,-6,-7,-8,-9)\,\eta^{-2}$ (bottom to top); *grey arrows*: velocity vectors $\hat{\vec{v}}$; *grey*: (initial) density $\hat{\rho} = 1$; *white*: (initial) density $\hat{\rho} \approx 0.9983$

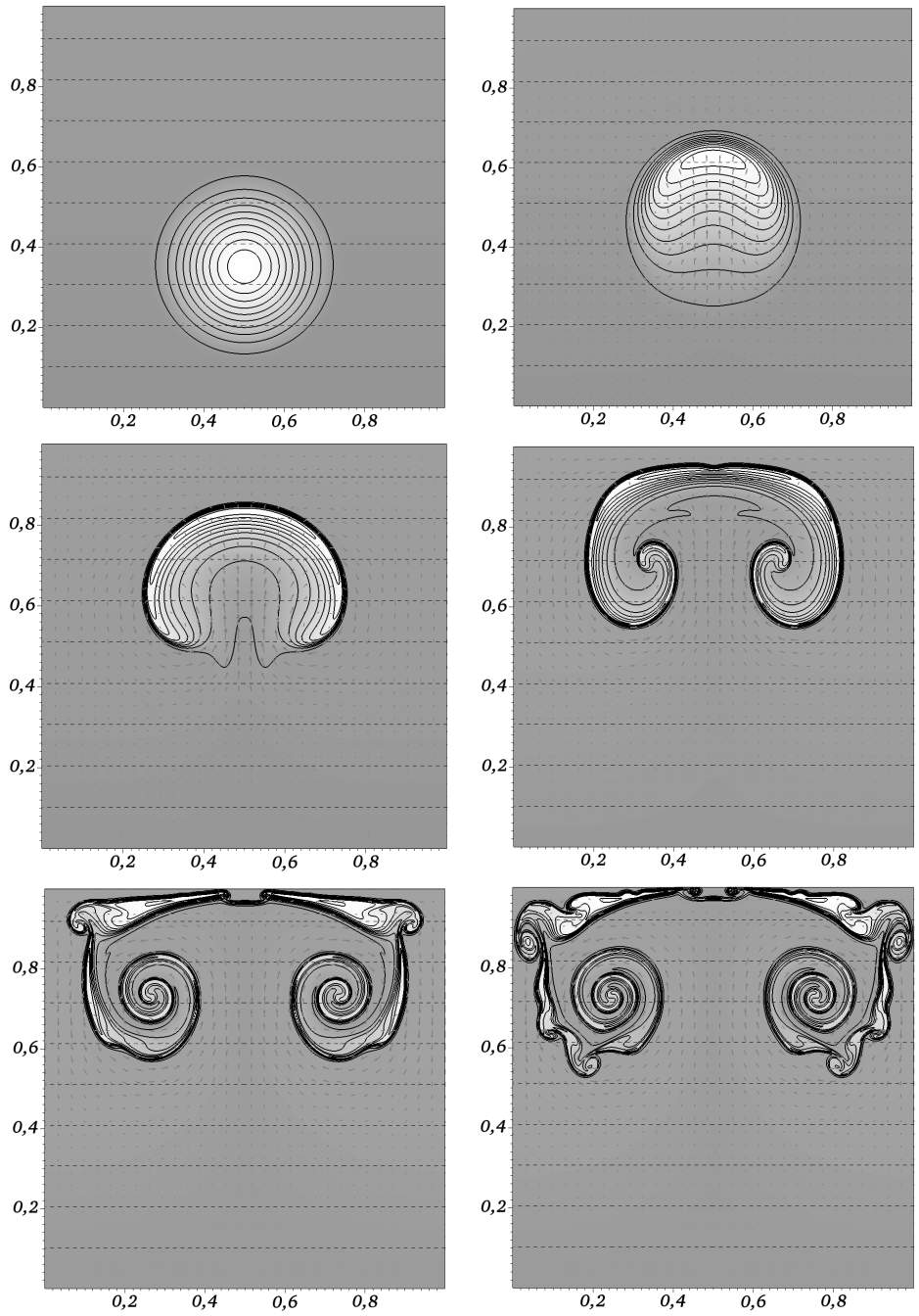

Fig. 5.40: Rising thermal bubble on a grid of 512×512 Cartesian cells in a $[0,1] \times [0,1]$ domain with no-slip walls at bottom and top and both **weakly stratified background density and potential temperature** at $\hat{t} \in ((0,0.3),(0.5,0.7),(0.9,1.0))$; *black solid lines*: iso-contours of $(\hat{\theta}-1) \in (1,3,5,7,9,11,13,15,17,19)\,\frac{\theta'}{20}$ (outer to inner); *black dashed lines*: iso-contours of $\hat{p}' \in (-1,-2,-3,-4,-5,-6,-7,-8,-9)\,\eta^{-2}$ (bottom to top); *grey arrows*: velocity vectors $\hat{\vec{v}}$; *grey*: (initial) density $\hat{\rho}=1$; *white*: (initial) density $\hat{\rho} \approx 0.9983$

This results in a scaled inverse stratification of the background density due to homogeneous $\mathcal{P}$ as shown in ***Fig. 5.37*** for the initial condition. The respective circular disturbance, subject to rise, has been faded out in ***Fig. 5.37***, in order to make the stratification visible.

The explanation for the differences between ***Fig. 5.39*** and ***Fig. 5.40*** can be found in ***Fig. 5.38***, in which the density is shown at $\hat{t} = 0.7$ and $\hat{t} = 1.0$ according to the initial setting in the right picture of ***Fig. 5.37***: Due to the induced velocity field heavier fluid is transported upward in the wake of the rising bubble.

5.7 Enhancements

An application of the particular implementation of the present single-phase method is published in [133] and [134], where the method is extended to the pseudo-incompressible regime ([46], [7], [92]) for moist flow of ideal gases on atmospheric length scales, with a height- and time-dependent leading order background pressure with $\frac{\partial P_0}{\partial x_{\mathfrak{d}}} \neq 0$ and $x_{\mathfrak{d}}$ as the vertical coordinate. As in the present method, the dynamic pressure is used in the momentum equation instead of the Exner function, which is commonly used in atmospheric flow simulations ([142], [46], [92], [93]), allowing for thermodynamic consistency according to [96] for general equations of state. Further, a well-balanced discretization of vertical leading order pressure gradient and gravity is presented. Particularly, the relations in ***Tab. 5.8*** hold for the transition of the present method to [134].

Tab. 5.8: Transition from present method (left) to [134] (right); the notation on the right hand side of each arrow is the one used in [134]

$\mathcal{P}$	$\rightarrow$	P_0
$\mathcal{P}\,\mathcal{D}$	$\rightarrow$	$\mathcal{S} - (P_0)_t$
$\mathcal{S}$	$\rightarrow$	$\left(\frac{L_v}{c_p T} - \frac{1}{\epsilon + q_v}\right) C$
$\frac{\partial \Theta}{\partial \theta}$	$\rightarrow$	$\frac{1+q_v/\epsilon}{1+q}$

Another extension of the presented single-phase method to the low Mach number and compressible regimes of slow[24] atmospheric flow is presented in [18] and [19], in which the Poisson problems in the corrector steps are extended to Helmholtz problems to account for compressibility effects via a fading factor for smooth transition between the different regimes within few time-steps.

[24] Slow compared to the speed of sound.

6. EXTENSIONS TOWARDS A CONSERVATIVE TWO-PHASE FLOW PROJECTION METHOD

In this chapter building blocks are described, extending the single-phase method from chapter 5 towards a fully conservative zero Mach number variable density two-phase flow method with a sharp fluidic interface, starting with the description of the latter in section 6.1. In section 6.2 the solution strategy in arising cut Cartesian grid cells is sketched, before the extensions of the advective kernel of the predictor step are presented in detail is section 6.3. In section 6.4 a brief overview of both existing and yet missing approaches for treatment of sharp interfaces in the corrector step is given, followed by the two major sections 6.5 and 6.6, which are dedicated to required corrections for stable conservative transport of each fluid phase and an approach for discretization of the surface stress tensor from section 3.2.4.

6.1 Interface Respresentation

The sharp moving interface Γ, separating the domain Ω into fluid phases labeled $(+)$ and $(-)$, is represented by the transport of the marker introduced in section 3.1. Discretization of the latter, as stressed in [176], is one of the crucial parts of a two-phase flow method. While interface tracking methods require the computational grid to adjust according to the changing interface, interface capturing methods are compliant with fixed grids and represent an interface implicitly via a scalar field, allowing for easier treatment of topological changes and severe interface changes. The most common capturing methods are the level-set (LS) method, discussed in section 6.1.1, and the volume-of-fluid (VOF) method, presented in section 6.1.2. However, stand-alone discretizations of both methods suffer from drawbacks concerning maintenance of physical properties at the fluidic interface as stressed below. Therefore hybrid LS-VOF methods[1], such as CLSVOF in [168] and advancements (as, for ex-

[1] A hybrid level-set/ghost fluid approach ACLS (without volume-of-fluid) is, for example, presented in [42]. Further methods focusing on improvement of conservation properties of level-set methods comprise spectrally refined level-set methods [43], particle level-set methods [49] and other

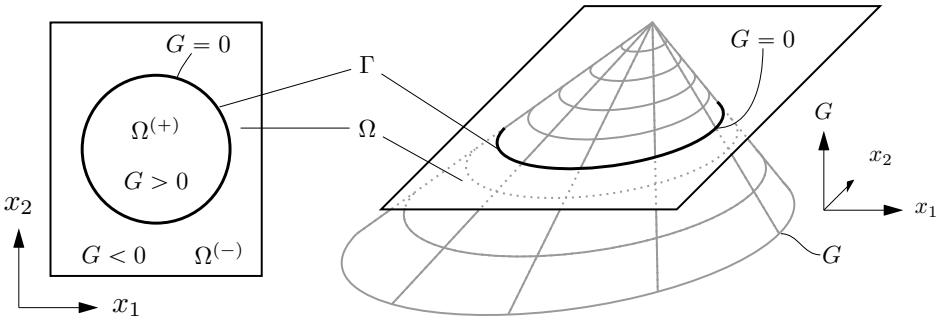

Fig. 6.1: Level-set function $G \in \mathbb{R}^{\mathfrak{d}+1}$ for representation of a contour in $\mathbb{R}^{\mathfrak{d}}$, here $\mathfrak{d} = 2$

ample, [163] and [165] or [84] (CLSVOFM)), ACLSVOF in [186], VOSET in [161], MCSL in [177] or, more recently, [104], are introduced, in order to combine the advantages and overcome the drawbacks of each standalone method. Many of these hybrid schemes, however, still suffer from conservation issues. The present hybrid method – detailed in sections 6.1.3 and 6.5 in order to spell out the brief sketch in [182] – follows a hybrid LS-VOF approach, initiated in [28] and advanced in [150], adapted to the present two-phase flow method, in order to couple and synchronize both discrete interface movement and discrete fluid flow and conserve mass of each fluid phase while avoiding elaborate interface reconstructions.

6.1.1 Level-Set Method

Level-set (LS) methods, introduced in [135], represent the moving interface implicitly as approximation to an iso-surface – usually the zero level – of the space- and time-dependent level-set function $G(\vec{x}, t)$ as sketched in ***Fig. 6.1***. Typically, G is initialized to be a signed distance function and the phase indicator ϕ from section 3.1 is essentially represented by the sign of G. Evolution of the different levels of constant interface distance is governed by

$$\frac{\mathrm{D}G}{\mathrm{D}t} \equiv G_t + \vec{v}_G \cdot \nabla G = 0, \qquad G(\vec{x}, t) \begin{cases} > 0 & \forall \ \vec{x} \in \Omega^{(+)}(t) \\ = 0 & \forall \ \vec{x} \in \Gamma(t) \\ < 0 & \forall \ \vec{x} \in \Omega^{(-)}(t) \end{cases} \tag{6.1}$$

as special form of the Hamilton-Jabobi equation

$$G_t = -\mathcal{V}_G |\nabla G| \tag{6.2}$$

conservative level-set methods such as [131] as listed in [104].

with interface normal speed

$$\mathcal{V}_G := \vec{v}_G \cdot \frac{\nabla G}{|\nabla G|} \tag{6.3}$$

and velocity $\vec{v}_G$, that has to match the interface velocity $\vec{w}_\Gamma$ at the zero level $G = 0$ and is arbitrary otherwise. Due to the assumptions in section 3.2.2, the level-set function can be considered to be transported by the fluid velocity $\vec{v}$. However, the choice

$$\vec{v}_G := \vec{v} \tag{6.4}$$

does not preserve the signed distance property of the level-set function, which needs to be considered as shown towards the end of this section, if the signed distance property is required.

The major advantage of level-set methods is the availability of an accurate but simple continuous (implicit) representation of interfaces of arbitrarily changeable shape and topology, allowing for determination of quantities such as the local interface normal vector

$$\vec{n}_\Gamma = -\frac{\nabla G}{|\nabla G|} \tag{6.5}$$

or the local interface mean curvature

$$\kappa = -\nabla \cdot \vec{n}_\Gamma \tag{6.6}$$

with sign convention as in [176] smoothly and cheaply. The main drawback, however, is, that there is no inherent mechanism to conserve mass in the sub-domains, separated by the zero level $G = 0$, on the discrete level, resulting in significant local non-physical mass transition across the discrete interface as nicely shown in [104], even if the signed distance property is maintained, as stated, for example, in [136]. Even if (6.1) is transformed to a conservation law and discretized via fluxes across grid cell faces, conservation of the respective quantity is not related to conservation of conserved quantities of the individual fluid phases, separated by the zero level of the level-set function.

Therefore in the present work the level-set equation (6.1) is discretized non-conservatively in a narrow band $\mathfrak{N}$ around the interface location using a spatially unlimited third order accurate upstream central finite difference approach UC3 according to [72] and [71] and explicit second order accurate SPP-RK2 time integration as presented in section 5.1.2.2, while the conservation issue remains to be fixed. The dis-

cretization of the operator $\mathfrak{L}$ in equation (5.21) on page 73 for time integration of the level-set function transport (6.1), thus, reads

$$\mathfrak{L}_{(G)}\left(\nabla G_{(i,j,k)}, \vec{v}_{(i,j,k)}\right) = \frac{1}{2}\left(\vec{v}_{(i,j,k)} \cdot \vec{\mathcal{G}}^{[-]}_{(i,j,k)} + \left(\sum_{\mathfrak{d}=1}^{\mathfrak{D}} \left(\left|v_{\mathfrak{d},(i,j,k)}\right| \vec{\mathfrak{e}}_{\mathfrak{d}}\right)\right) \cdot \vec{\mathcal{G}}^{[+]}_{(i,j,k)}\right) \tag{6.7}$$

with

$$\vec{\mathcal{G}}^{[\pm]}_{(i,j,k)} := \vec{\mathcal{G}}^{\{-\}}_{(i,j,k)} \pm \vec{\mathcal{G}}^{\{+\}}_{(i,j,k)} \tag{6.8}$$

such that

$$\nabla G^{\{\pm\}}\Big|_{(i,j,k)} = \vec{\mathcal{G}}^{\{\pm\}}_{(i,j,k)} + \mathcal{O}\left(\mathfrak{h}^3\right) \tag{6.9}$$

and

$$\mathcal{G}^{\{-\}}_{\mathfrak{c},(i,j,k)} := \frac{1}{6\,\mathfrak{c}_{\mathfrak{c}}\,\mathfrak{h}}\left(G_{((i,j,k)-2\vec{\mathfrak{e}}_{\mathfrak{c}})} - 6\,G_{((i,j,k)-\vec{\mathfrak{e}}_{\mathfrak{c}})} + 3\,G_{(i,j,k)} + 2\,G_{((i,j,k)+\vec{\mathfrak{e}}_{\mathfrak{c}})}\right) \tag{6.10a}$$

$$\mathcal{G}^{\{+\}}_{\mathfrak{c},(i,j,k)} := \frac{1}{6\,\mathfrak{c}_{\mathfrak{c}}\,\mathfrak{h}}\left(-G_{((i,j,k)+2\vec{\mathfrak{e}}_{\mathfrak{c}})} + 6\,G_{((i,j,k)+\vec{\mathfrak{e}}_{\mathfrak{c}})} - 3\,G_{(i,j,k)} - 2\,G_{((i,j,k)-\vec{\mathfrak{e}}_{\mathfrak{c}})}\right) \tag{6.10b}$$

for any component $\mathfrak{c}$ of $\vec{\mathcal{G}}^{\{\pm\}}$. As before, $\mathfrak{h}$ is the grid spacing, $\mathfrak{c}_{\mathfrak{c}}$ the scaling in direction $\mathfrak{c}$ and $\vec{\mathfrak{e}}_{\mathfrak{c}}$ the unit vector in coordinate direction $\mathfrak{c}$. If a cell of the UC3 stencil is not in $\mathfrak{N}$, then a first order upwind stencil is used, and cells on the boundary of $\mathfrak{N}$ are not updated, such that only data from within $\mathfrak{N}$ is used, since data beyond $\mathfrak{N}$ is arbitrary. Thus, accuracy increases within $\mathfrak{N}$ towards the interface and full accuracy at the interface Γ is only obtained if $\mathfrak{N}$ is sufficiently expanded. The narrow band is assembled as the set union of all $(2\mathcal{N})^{\mathfrak{d}}$ sized boxes around each cut grid cell. The narrow band width on each side of the interface results from

$$d_{\mathfrak{N}} \geqslant \mathcal{N}\,\mathfrak{h}\,\max_{\mathfrak{d}}\left(\mathfrak{c}_{\mathfrak{d}}\right) \tag{6.11}$$

and

$$\mathcal{N} = 5 \tag{6.12}$$

is chosen throughout this work, such that for any element of the set $\mathfrak{C}$ of cut grid cells (or $\mathfrak{I}$ of interface cells[2], respectively) each narrow band cell within the corresponding UC3 stencil for evaluation of (6.10) can be updated using a full UC3 stencil as well. In grid cells, that newly enter the narrow band around the interface due to movement

[2] See equation (6.168) for definition.

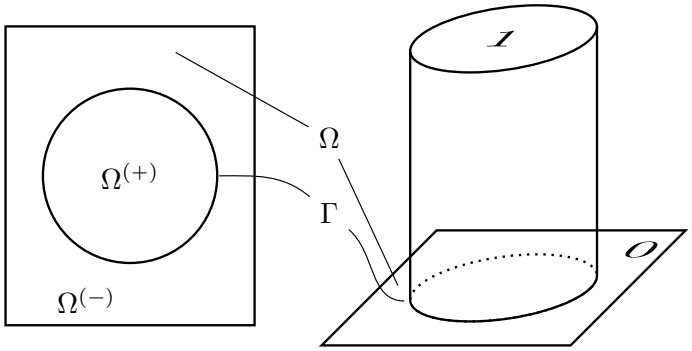

Fig. 6.2: Phase indicator ϕ of reference phase $(+)$

of the latter, level-set values are initialized via the fast marching method according to [155] or [32], respectively.

6.1.2 Volume-of-Fluid Method

Volume-of-fluid (VOF) methods, introduced in [76], approximate evolution of the phase indicator function (3.11) in an integral discrete fashion by following regions of constant fluid identifier ϕ as sketched in ***Fig. 6.2***. Therefore the transport equation (3.12) of the phase indicator (3.11) of reference phase $(+)$ is rewritten in divergence form in terms of the fluid velocity as

$$\left(\phi^{(+)}\right)_t + \nabla \cdot \left(\phi^{(+)}\vec{v}\right) = \phi^{(+)}\mathcal{D} - \delta_\Gamma \left(\vec{v} - \vec{v}_\phi\right) \cdot \vec{n}_\Gamma \tag{6.13}$$

and integrated over each grid cell to yield

$$\left(\alpha_\phi\right)_t + \oint_{\partial\Omega_\mathrm{i}} \phi^{(+)}\vec{v} \cdot \vec{n}\,\mathrm{d}A = \int_{\Omega_\mathrm{i}} \phi^{(+)}\mathcal{D}\,\mathrm{d}V - \int_\Gamma \left(\vec{v} - \vec{v}_\phi\right) \cdot \vec{n}_\Gamma\,\mathrm{d}S \tag{6.14}$$

after division by the cell volume (4.17) with grid cell volume fraction

$$\alpha_\phi\left(t\right) := \overline{\phi}^{(+)}\left(t\right) = \frac{1}{\Delta V_\mathrm{i}} \int_{\Omega_\mathrm{i}} \phi^{(+)}\left(\vec{x}, t\right)\,\mathrm{d}V \tag{6.15}$$

occupied by the reference fluid. Thus, $0 \leqslant \alpha \leqslant 1$ has to hold. If equation (6.13) is multiplied with the local fluid density, the conservation equation

$$\overline{\rho\phi}^{(+)}\left(t\right) + \oint_{\partial\Omega_\mathrm{i}} \rho\phi^{(+)}\vec{v} \cdot \vec{n}\,\mathrm{d}A = \int_{\Omega_\mathrm{i}} \rho\phi^{(+)}\mathcal{D}\,\mathrm{d}V - \int_\Gamma \rho\left(\vec{v} - \vec{v}_\phi\right) \cdot \vec{n}_\Gamma\,\mathrm{d}S \tag{6.16}$$

for the reference fluid mass is obtained after application of the product rule, subtraction of the local mass balance and integration over a control volume (grid cell), with sources due to volume expansion on the right hand side, which vanish due to the assumptions in sections 3.2.2 and 3.4. The formulations (6.13) and (6.16) contain the interface implicitly in the grid cells, in which $\mathfrak{e} < \alpha_\phi < (1 - \mathfrak{e})$ and $\mathfrak{e}$ as a small positive number, which is the major drawback of volume-of-fluid methods: Extensive interface reconstruction procedures (such as the commonly used Piecewise Linear Interface Construction (PLIC) method from [188], for example) are required, if the smooth interface needs to be known explicitly, since

- by default interface approximations in each grid cell due to the volume fraction distribution do not match continuously to the corresponding interface approximation in the neighboring grid cell containing the interface, yielding a discontinuous explicit interface representation and
- the interface position and orientation within the control volume is arbitrary subject to the volume fraction, if no surrounding information is used in addition.

A volume-of-fluid representation, that suits the numerical method described in chapter 5, is obtained after multiplication of (6.13) with $\mathcal{P}$ as introduced in section 3.6, application of the product rule considering equation (3.138) and integration over the control volume to yield

$$\overline{\mathcal{P}\phi}^{(+)}(t) + \oint_{\partial\Omega_\mathfrak{i}} (\mathcal{P}\vec{v}\cdot\vec{n})\,\phi^{(+)}\,\mathrm{d}A \;=\; \int_{\Omega_\mathfrak{i}} \mathcal{P}\phi^{(+)}\mathcal{S}\,\mathrm{d}V - \int_\Gamma \mathcal{P}\,(\vec{v}-\vec{v}_\phi)\cdot\vec{n}_\Gamma\,\mathrm{d}S \tag{6.17}$$

with vanishing right hand side in absence of volume expansions of the reference phase. Due to the properties of $\mathcal{P}$ in the small scale limit,

$$\begin{aligned}\overline{\mathcal{P}\phi}^{(+)}(t) \;&=\; \frac{1}{\Delta V_\mathfrak{i}}\int_{\Omega_\mathfrak{i}} \mathcal{P}(t)\,\phi^{(+)}(\vec{x},t)\;\mathrm{d}V \;=\; \mathcal{P}(t)\left(\frac{1}{\Delta V_\mathfrak{i}}\int_{\Omega_\mathfrak{i}} \phi^{(+)}(\vec{x},t)\;\mathrm{d}V\right)\\ &=\; \mathcal{P}(t)\,\alpha_\phi(t) \;=\; \overline{\mathcal{P}}(t)\,\alpha_\phi(t) \;+\; \mathcal{O}\left(\mathfrak{h}^2\right)\end{aligned} \tag{6.18}$$

holds. Equation (6.17), integrated in time from t^n to t^{n+1}, can be treated as any other scalar quantity in chapter 5, since the hyperbolic equation shares the same grid cell face normal carrier flux density $(\mathcal{P}\vec{v}\cdot\vec{n})$. Therefore $\mathcal{P}\phi$ is discretely conserved both locally and globally. However, discretization errors, arising from numerical treatment as described in section 6.5.1 below, cause occurrence of both $\alpha_\phi < 0$ and $\alpha_\phi > 1$, both without any physically reasonable interpretation, since $\alpha_\phi = 1$ means that the

entire grid cell is occupied by the reference fluid $(+)$ and $\alpha_\phi = 0$ means, that there is no reference fluid at all in the respective grid cell. In many methods involving a volume-of-fluid type interface representation, these over- and undershoots are simply truncated to satisfy $\mathfrak{e} < \alpha_\phi < (1 - \mathfrak{e})$. However, if they have been obtained with a discretely conservative method, truncation of its results causes discrete defects in the masses of the individual fluid phases. Additionally, intermediate values beyond the interface lead to smearing of the volume-of-fluid based interface representation.

While for incompressible flow with constant densities in each fluid phase, in fact the volume-of-fluid equation (6.17) and the variable density equation (3.128a) are redundant, this redundancy vanishes once a variable density and/or a non-zero divergence constraint occurs in at least one of the fluid phases.

6.1.3 Hybrid Level-Set Volume-of-Fluid Method

The drawbacks of both the level-set based interface representation and the one due to a volume-of-fluid based representation as described in the previous sections 6.1.1 and 6.1.2 can be overcome by combining both representations, yielding a dual interface representation according to

$$\mathfrak{J}^{(+)} \quad \Longrightarrow \quad \begin{cases} \mathfrak{G} \\ \mathfrak{V} \end{cases} \tag{6.19}$$

with $\mathfrak{J}^{\varphi}$ representing equation (3.12) with (3.11), $\mathfrak{G}$ representing equation (6.1) and $\mathfrak{V}$ representing equation (6.17) – also subject to (3.11) – with corresponding discretizations of $\mathfrak{G}$ and $\mathfrak{V}$ as given in sections 6.1.1 and 6.1.2 (or chapter 5 for the latter, respectively).

The present conservative hybrid level-set volume-of-fluid method follows the corresponding strategy in [152] and [150], avoiding elaborate volume-of-fluid related interface reconstruction and deriving all interface related quantities, which need to be known explicitly, from the level-set representation, from which they can be obtained easily and accurately due to the higher order discretization of the level-set function in space as given in section 6.1.1. The level-set function, which serves as interface reference representation, is corrected based on the conservatively transported volume-of-fluid type indicator distribution (as introduced initially in [28]), the latter serving as a measure for the deviation of the level-set interface representation from a conservatively transported interface. Therefore, in the present hybrid level-set

volume-of-fluid method, truncation of over- and undershooting discrete volume fraction values, as described in section 6.1.2, is replaced by a flux correction algorithm as given in section 6.5.2, which is applied each time discrete fluxes for the phase indicator of the reference phase have been computed, in order to keep the volume fractions bounded within $0 < \alpha < 1$ and the interface sharp at any time. Due to the different natures of discretization of $\mathfrak{G}$ and $\mathfrak{V}$, both interface representations need synchronization in order to prevent decoupling of level-set based interface representation and conserved quantities of the fluid flow. The necessary two-way coupling between level-set, phase indicator, as well as all other conserved quantities is described in section 6.5, after presentation of the relevant extensions to the numerical method from chapter 5 in the vicinity of the interface in section 6.3.

6.1.4 Explicit Interface Discretization

The explicit discrete interface representation, separating the fluidic phases within the Cartesian grid cells, is derived from the level-set representation in cell nodes and corrected based on the interface duality described in section 6.1.3 according to section 6.5. Therefore,

1. cell center values of the level-set are advected as described in section 6.1.1
2. level-set values in the nodes (N) of the grid cells are obtained by second order accurate interpolation based on the cell center values (C) surrounding the respective node according to

$$G^{(N)} = \frac{1}{2^{\mathfrak{d}}} \sum_{\mathrm{sur}=1}^{2^{\mathfrak{d}}} G_{\mathrm{sur}}^{(C)} + \mathcal{O}(\mathfrak{h}^2) \tag{6.20}$$

3. the level-set function between each pair of nodes is approximated linearly based on the nodal level-set values
4. locations, at which the piecewise linear approximation of the level-set function vanishes, approximate points on the interface
5. the interface is recovered piecewise linearly between the found approximate interface locations at cell faces ($\mathfrak{d} = 2$) or cell edges ($\mathfrak{d} = 3$)
6. the discrete interface position is corrected as described in section 6.5.3 in order to impose mass conservation properties

Steps 3. to 5. are sketched in ***Fig. 6.3*** for $\mathfrak{d} = 2$. The size of both volume fractions, α, and cell face fractions, β, as well as the interface normal vector $\vec{n}_\Gamma$ and the centroids of both the Cartesian grid cell fractions and the particular cell face fractions are determined based on this explicit piecewise linear interface discretization and are, thus, functions of the nodal level-set values (which depend on the surrounding cell center level-set values). Based on level-set values in the $2^{\mathfrak{d}}$ cell nodes at a certain time level the aforesaid spatial properties are determined. As sketched in ***Fig. 6.4***, replacement of $2^{\mathfrak{d}-1}$ neighboring nodal values – say, in nodes 4 to 7 – by values in the remaining nodes – 0 to 3 – at another time level provides the spatio-temporal properties of the discrete manifold spanned by the remaining nodes (0 to 3).

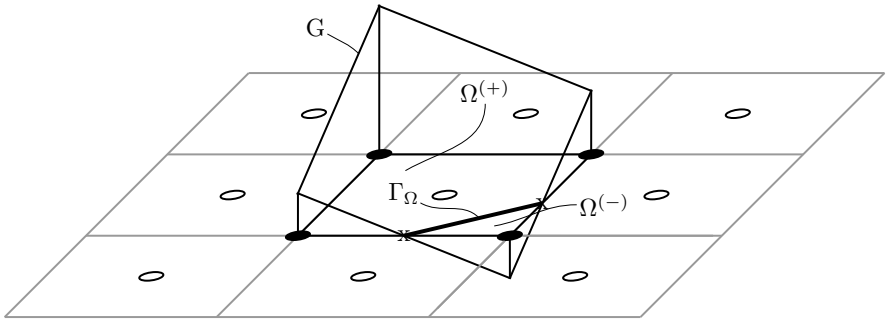

Fig. 6.3: Determination of in-cell interface approximation, based on level-set data in cell nodes

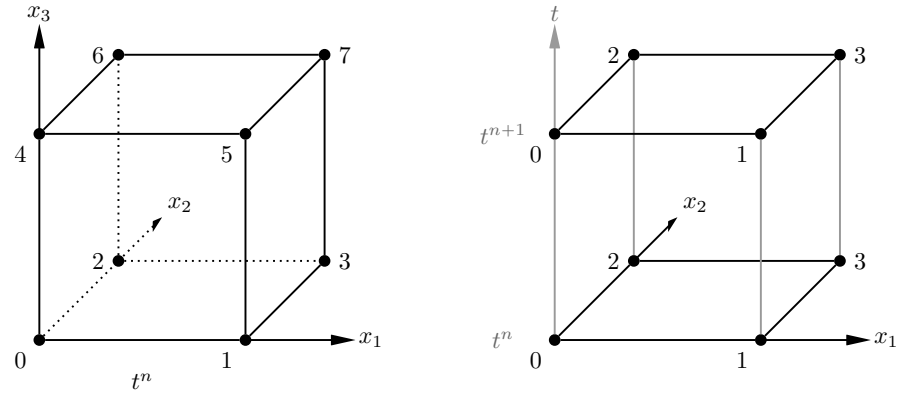

Fig. 6.4: *Left:* Spatial domain at $\mathfrak{d} = 3$ with $2^{\mathfrak{d}}$ spatial cell nodes; *right:* Spatio-temporal domain at $\mathfrak{d} = 2$ with twice a set of $2^{\mathfrak{d}}$ spatial cell nodes; the right sketch also applies for grid cell faces at $\mathfrak{d} = 3$ with twice a set of $2^{\mathfrak{d}-1}$ spatial nodes

6.2 Solution Strategy in Cut Grid Cells

For the solution to a single-phase flow problem using a standard Finite Volume method, incremental updates for the cell averages of the conserved quantities are computed per time interval as described in chapter 5. For determination of these incremental updates, based on - among others - a balance of control volume boundary fluxes, knowledge of an effective numerical flux per grid cell face is required. This numerical flux approximates the average flux over both the grid cell face and the time interval considered. The accuracy of this average flux approximation depends on the information that is used for the numerical flux computation, i.e. the cell face surrounding cell average values.

Following the strategy in [156], this standard Finite Volume machinery is also used in case of two-phase flow for determination of the incremental updates in any grid cell, no matter if it is located completely within one of the two fluid phases or cut by the approximation of the fluidic interface Γ at any time during the corresponding time interval. In the cut cells, resulting averages

$$\begin{aligned}\overline{\rho\psi}(t) &= \frac{1}{\Delta V}\int_{\Omega}\rho\psi(\vec{x},t)\,\mathrm{d}V \\ &= \frac{1}{\Delta V}\sum_{\varphi=1}^{2}\left(\int_{\Omega^{\varphi}(t)}(\rho\psi)^{\varphi}(\vec{x},t)\,\mathrm{d}V\right) = \sum_{\varphi=1}^{2}\left(\alpha^{\varphi}(t)\,\overline{\rho\psi}^{\varphi}(t)\right)\end{aligned} \tag{6.21}$$

are stored at specific points in time t and updates approximating the change over a finite time interval Δt are determined for the entire grid cell as done for single-phase flow. Avoiding the computation of separate updates and average values $\overline{\rho\psi}^{\varphi}$ in each cut grid cell fraction prevents a severe CFL stability restriction [37], which would result in arbitrarily small allowable time step sizes and therefore in a stiff method due to potentially arising arbitrarily small irregular grid cell fractions α^{φ}. However, as a consequence, in analogy to regular grid cell faces, for each conserved quantity

- computation of one single effective numerical flux is required per time interval on each cut grid cell face as approximation of the space-time flux average
- computation of an effective source term approximation is required per time interval and cut grid cell

according to section 4.2.2 and section 6.3.2 below.

For all grid cell faces, which are not cut by the interface during the corresponding time interval, numerical flux computation can be done as in the standard single-phase Finite Volume method with fluid properties according to the respective fluid phase as described chapter 5. However, grid cell faces, that are not cut by the interface during that time interval, might be or become close enough to the interface, that one ore more grid cells in the stencil used for numerical flux computation are cut by the interface as shown in ***Fig. 6.7*** in section 6.3.3.1. In that case ghost fluid extrapolation as described in the section 6.3.3.3 needs to be performed in order to provide the necessary information for interface state recovery and flux computation in the corresponding fluid phase.

6.3 Predictor

While the description of the discretization of viscous and diffusive fluxes at cut grid cell faces and volume sources in cut grid cells is deferred to a future publication, in this section the advective kernel of the two-phase flow predictor step is described. While for grid cells, which are sufficiently far away from the interface, the single-phase method as described in chapter 5 – extended by the transport equations for the two scalar fields representing the interface as described in section 6.1 – applies with fluid properties of the respective fluid phase, the advection procedure has to be modified in the vicinity of the interface with respect to advective flux computation and correction of discretization errors for conservation purposes.

6.3.1 Auxiliary System of Equations

The advective kernel

$$\frac{\mathrm{d}}{\mathrm{d}t}\left(\int_{\Omega}\mathcal{P}\vec{\Phi}\,\mathrm{d}V\right) = -\oint_{\partial\Omega}\left(\mathcal{P}\vec{v}\cdot\vec{n}\right)\vec{\Phi}\,\mathrm{d}A \tag{6.22a}$$

$$G_t = -\vec{v}\cdot\nabla G \tag{6.22b}$$

for two-phase flow is obtained from the two-phase flow predictor auxiliary system

$$\frac{\mathrm{d}}{\mathrm{d}t}\left(\int_{\Omega}\mathcal{P}\vec{\Phi}\,\mathrm{d}V\right) = -\oint_{\partial\Omega}\left(\mathcal{P}\vec{v}\cdot\vec{n}\right)\vec{\Phi}\,\mathrm{d}A + \oint_{\partial\Omega}\boldsymbol{J}_{\vec{\Phi}}\cdot\vec{n}\,\mathrm{d}A + \dot{\vec{\mathrm{q}}}_{\vec{\Phi}} \tag{6.23a}$$

$$G_t = -\vec{v}\cdot\nabla G \tag{6.23b}$$

with

$$\vec{\Phi} = \left(\frac{1}{\Theta}, \frac{Y_{\mathfrak{s}}}{\Theta}, \frac{\vec{v}}{\Theta}, 1, \phi^{(+)}\right) \tag{6.24a}$$

$$\boldsymbol{J}_{\vec{\Phi}} = \left[\vec{0}, -\vec{j}_{\mathfrak{s}}, \left(\boldsymbol{\mathcal{T}} + \boldsymbol{S}_{\Gamma}^{(\sigma)}\delta_{\Gamma}\right), \vec{0}, \vec{0}\right] \tag{6.24b}$$

$$\dot{\vec{\mathfrak{q}}}_{\vec{\Phi}} = (0, \mathfrak{q}_{Y_{\mathfrak{s}}}, \vec{\mathfrak{q}}_{\vec{v}}, \mathfrak{q}_{\mathcal{P}}, \mathfrak{q}_{\phi}) \tag{6.24c}$$

and source terms

$$\mathfrak{q}_{Y_{\mathfrak{s}}} := \int_{\Omega} \rho \varrho_{\mathfrak{s}} \,\mathrm{d}V \tag{6.25a}$$

$$\vec{\mathfrak{q}}_{\vec{v}} := -\left(\oint_{\partial\Omega} \pi^{'} \vec{n} \,\mathrm{d}A + \int_{\Omega} \rho \nabla \mathcal{U} \,\mathrm{d}V\right) \tag{6.25b}$$

$$\mathfrak{q}_{\mathcal{P}} := -\left(\int_{\Omega} \mathcal{P}\,\mathcal{S} \,\mathrm{d}V\right) \tag{6.25c}$$

$$\mathfrak{q}_{\phi} := -\left(\int_{\Omega} \mathcal{P}\,\mathcal{S}\,\phi^{(+)} \,\mathrm{d}V\right) \tag{6.25d}$$

with $\mathcal{S} = \frac{\chi}{\Xi}\dot{q}$ according to definition (3.136) and $\chi = 0$ by assuming

$$\mu = \zeta = D = \varrho = k = 0 \tag{6.26a}$$

$$\vec{g} = -\nabla \mathcal{U} = \vec{0} \tag{6.26b}$$

$$\pi^{'} = 0 \tag{6.26c}$$

$$\sigma = 0 \tag{6.26d}$$

yielding

$$\boldsymbol{J}_{\vec{\Phi}} = \left[\vec{0}, \vec{0}, \mathbf{0}, \vec{0}, \vec{0}\right] \tag{6.27a}$$

$$\dot{\vec{\mathfrak{q}}}_{\vec{\Phi}} = \left(0, 0, \vec{0}, 0, 0\right) \tag{6.27b}$$

6.3.2 Time Integration

The explicit two-phase predictor update $\Delta\rho\psi_{\mathfrak{i}}$ of an integral average in a cut grid cell $\mathfrak{i}$ in

$$\overline{\rho\psi}_{\mathfrak{i}}^{(m+1)} = \overline{\rho\psi}_{\mathfrak{i}}^{(m)} + \Delta\overline{\rho\psi}_{\mathfrak{i}} \tag{6.28}$$

reads

$$\begin{aligned}\Delta\overline{\rho\psi}_{\mathfrak{i}} = &\frac{1}{\Delta V}\int_{t^m}^{t^{m+1}} \sum_{\varphi=1}^{2} \int_{\Omega_{\mathfrak{i}}^{\varphi}(t)} \dot{\mathfrak{q}}_{(\rho\psi)}^{\varphi}\,\mathrm{d}V\,\mathrm{d}t \\ &- \frac{1}{\Delta V}\int_{t^m}^{t^{m+1}} \sum_{\mathfrak{d}=1}^{\mathfrak{d}} \sum_{\mathfrak{w}=1}^{2} (-1)^{\mathfrak{w}} \sum_{\varphi=1}^{2} \int_{\left(\partial\Omega_{\mathfrak{d},\mathfrak{w}}^{\varphi}\right)_{\mathfrak{i}}(t)} \vec{f}_{(\rho\psi)}^{\varphi}\cdot\vec{\mathfrak{e}}_{\mathfrak{d}}\,\mathrm{d}A\mathrm{d}t\end{aligned} \tag{6.29}$$

and transforms to

$$\begin{aligned}\Delta\overline{\rho\psi}_{\mathfrak{i}} = &\frac{1}{\Delta V}\sum_{\varphi=1}^{2}\int_{t^m}^{t^{m+1}} \int_{\Omega_{\mathfrak{i}}^{\varphi}(t)} \dot{\mathfrak{q}}_{(\rho\psi)}^{\varphi}\,\mathrm{d}V\,\mathrm{d}t \\ &- \frac{1}{\Delta V}\sum_{\mathfrak{d}=1}^{\mathfrak{d}} \sum_{\mathfrak{w}=1}^{2} (-1)^{\mathfrak{w}} \left[\sum_{\varphi=1}^{2}\left(\int_{t^m}^{t^{m+1}} \int_{\left(\partial\Omega_{\mathfrak{d},\mathfrak{w}}^{\varphi}\right)_{\mathfrak{i}}(t)} \vec{f}_{(\rho\psi)}^{\varphi}\cdot\vec{\mathfrak{e}}_{\mathfrak{d}}\,\mathrm{d}A\mathrm{d}t\right)\right]\end{aligned} \tag{6.30}$$

after exchanging order of summation and time integration. After summarizing the integration over the respective spatial domains and time to integrals over the spatio-temporal domains

$$\widetilde{\Omega}^{\varphi} := \left(\Omega^{\varphi}(t)\times(t^m,t^{m+1})\right) \in \mathbb{R}^{\mathfrak{d}+1} \tag{6.31}$$

$$\widetilde{\partial\Omega}^{\varphi} := \left(\partial\Omega^{\varphi}(t)\times(t^m,t^{m+1})\right) \in \mathbb{R}^{\mathfrak{d}} \tag{6.32}$$

and defining

$$f_{(\rho\psi),\mathfrak{d},\mathfrak{w}}^{\varphi} := \vec{f}_{(\rho\psi),\mathfrak{w}}^{\varphi}\cdot\vec{\mathfrak{e}}_{\mathfrak{d}} \tag{6.33}$$

as well as space-time averages

$$\widetilde{\dot{\mathfrak{q}}}^{\varphi} := \frac{1}{\widetilde{\alpha}\,\Delta\mathfrak{t}\,\Delta V}\int_{\widetilde{\Omega}^{\varphi}} \dot{\mathfrak{q}}_{(\rho\psi)}^{\varphi}\,\mathrm{d}\widetilde{V} \tag{6.34a}$$

$$\widetilde{f}_{(\rho\psi),\mathfrak{d},\mathfrak{w}}^{\varphi} := \frac{1}{\widetilde{\beta}_{\mathfrak{d},\mathfrak{w}}\,\Delta\mathfrak{t}\,\Delta A_{\mathfrak{d}}}\int_{\widetilde{\partial\Omega}_{\mathfrak{d},\mathfrak{w}}^{\varphi}} f_{(\rho\psi),\mathfrak{d},\mathfrak{w}}^{\varphi}\,\mathrm{d}\widetilde{A} \tag{6.34b}$$

per fluid phase φ, the expression

$$\begin{aligned}\Delta\overline{\rho\psi}_{\mathfrak{i}} = &\frac{1}{\Delta V}\sum_{\varphi=1}^{2}\left(\int_{\widetilde{\Omega}_{\mathfrak{i}}^{\varphi}}\dot{\mathfrak{q}}_{(\rho\psi)}^{\varphi}\,\mathrm{d}\widetilde{V}\right)\\ &-\frac{1}{\Delta V}\sum_{\mathfrak{d}=1}^{\mathfrak{d}}\sum_{\mathfrak{w}=1}^{2}(-1)^{\mathfrak{w}}\left[\sum_{\varphi=1}^{2}\left(\int_{\left(\widetilde{\partial\Omega}_{\mathfrak{d},\mathfrak{w}}^{\varphi}\right)_{\mathfrak{i}}}\vec{f}_{(\rho\psi),\mathfrak{w}}^{\varphi}\cdot\vec{\mathfrak{e}}_{\mathfrak{d}}\,\mathrm{d}\widetilde{A}\right)\right]\\ &=\Delta\mathfrak{t}\left(\sum_{\varphi=1}^{2}\left(\widetilde{\alpha}^{\varphi}\,\widetilde{\overline{\dot{\mathfrak{q}}}}^{\varphi}\right)-\frac{1}{\mathfrak{h}}\sum_{\mathfrak{d}=1}^{\mathfrak{d}}\frac{1}{\mathfrak{c}_{\mathfrak{d}}}\sum_{\mathfrak{w}=1}^{2}(-1)^{\mathfrak{w}}\left[\sum_{\varphi=1}^{2}\left(\widetilde{\beta}_{\mathfrak{d},\mathfrak{w}}^{\varphi}\,\widetilde{\overline{f}}_{(\rho\psi),\mathfrak{d},\mathfrak{w}}^{\varphi}\right)\right]\right)\end{aligned}\tag{6.35}$$

is obtained. With Taylor expansions

$$\dot{\mathfrak{q}}_{(\rho\psi)}^{\varphi} = \dot{\mathfrak{q}}_{(\rho\psi)}^{\varphi}\left(\vec{x}_0^{\widetilde{\Omega}^{\varphi}}\right) + \frac{\partial f_{(\rho\psi),\mathfrak{d}}^{\varphi}}{\partial\vec{x}^{\widetilde{\Omega}^{\varphi}}}\left(\vec{x}_0^{\widetilde{\Omega}^{\varphi}}\right)\cdot\left(\vec{x}^{\widetilde{\Omega}^{\varphi}}-\vec{x}_0^{\widetilde{\Omega}^{\varphi}}\right)+\mathcal{O}(\mathfrak{h}^2)\tag{6.36a}$$

$$f_{(\rho\psi),\mathfrak{d},\mathfrak{w}}^{\varphi} = f_{(\rho\psi),\mathfrak{d},\mathfrak{w}}^{\varphi}\left(\vec{x}_0^{\widetilde{\partial\Omega}_{\mathfrak{d},\mathfrak{w}}^{\varphi}}\right)+\frac{\partial f_{(\rho\psi),\mathfrak{d},\mathfrak{w}}^{\varphi}}{\partial\vec{x}^{\widetilde{\partial\Omega}^{\varphi}}}\left(\vec{x}_0^{\widetilde{\partial\Omega}_{\mathfrak{d},\mathfrak{w}}^{\varphi}}\right)\cdot\left(\vec{x}^{\widetilde{\partial\Omega}_{\mathfrak{d},\mathfrak{w}}^{\varphi}}-\vec{x}_0^{\widetilde{\partial\Omega}_{\mathfrak{d},\mathfrak{w}}^{\varphi}}\right)+\mathcal{O}(\mathfrak{h}^2)\tag{6.36b}$$

in each fluid phase φ with $\vec{x}^{\widetilde{\Omega}^{\varphi}}\in\mathbb{R}^{\mathfrak{d}+1}$ as spatio-temporal coordinate vector, consisting of both the $\mathfrak{d}$ spatial coordinates and time, and $\vec{x}_{\mathfrak{d},\mathfrak{w}}^{\widetilde{\partial\Omega}^{\varphi}}\in\mathbb{R}^{\mathfrak{d}}$ as spatio-temporal coordinate vector, consisting of the $\mathfrak{d}-1$ spatial coordinates perpendicular to the respective grid cell face normal direction $\mathfrak{d}$ and time, the space-time averages (6.34) can be approximated by

$$\widetilde{\overline{\dot{\mathfrak{q}}}}^{\varphi} = \underbrace{\left(\dot{\mathfrak{q}}_{(\rho\psi)}^{\varphi}\left(\vec{x}_0^{\widetilde{\Omega}^{\varphi}}\right)+\frac{\partial\dot{\mathfrak{q}}_{(\rho\psi)}^{\varphi}}{\partial\vec{x}^{\widetilde{\Omega}^{\varphi}}}\left(\vec{x}_0^{\widetilde{\Omega}^{\varphi}}\right)\cdot\left(\vec{x}_c^{\widetilde{\Omega}^{\varphi}}-\vec{x}_0^{\widetilde{\Omega}^{\varphi}}\right)\right)}_{\approx\widetilde{\overline{\mathcal{Q}}}^{\varphi}}+\mathcal{O}\left(\mathfrak{h}^2\right)\tag{6.37a}$$

$$\begin{aligned}\widetilde{\overline{f}}_{(\rho\psi),\mathfrak{d},\mathfrak{w}}^{\varphi} = &\underbrace{\left(f_{(\rho\psi),\mathfrak{d},\mathfrak{w}}^{\varphi}\left(\vec{x}_0^{\widetilde{\partial\Omega}_{\mathfrak{d},\mathfrak{w}}^{\varphi}}\right)+\frac{\partial f_{(\rho\psi),\mathfrak{d},\mathfrak{w}}^{\varphi}}{\partial\vec{x}^{\widetilde{\partial\Omega}_{\mathfrak{d},\mathfrak{w}}^{\varphi}}}\left(\vec{x}_0^{\widetilde{\partial\Omega}_{\mathfrak{d},\mathfrak{w}}^{\varphi}}\right)\cdot\left(\vec{x}_c^{\widetilde{\partial\Omega}_{\mathfrak{d},\mathfrak{w}}^{\varphi}}-\vec{x}_0^{\widetilde{\partial\Omega}_{\mathfrak{d},\mathfrak{w}}^{\varphi}}\right)\right)}_{\approx\widetilde{\overline{\mathcal{F}}}^{\varphi}}\\ &+\mathcal{O}\left(\mathfrak{h}^2\right)\end{aligned}\tag{6.37b}$$

for application to (6.35). In (6.37)

$$\vec{x}_c^{\,\widetilde{\Omega}^{\varphi}} := \frac{\int_{\left(\widetilde{\Omega}^{\varphi}\right)_{\mathfrak{i}}} \left(\phi^{(+)} \vec{x}^{\,\widetilde{\Omega}^{\varphi}}\right) \mathrm{d}\widetilde{V}}{\int_{\left(\widetilde{\Omega}^{\varphi}\right)_{\mathfrak{i}}} \phi^{(+)} \, \mathrm{d}\widetilde{V}} = \frac{\int_{\left(\widetilde{\Omega}^{\varphi}\right)_{\mathfrak{i}}} \left(\phi^{(+)} \vec{x}^{\,\widetilde{\Omega}^{\varphi}}\right) \mathrm{d}\widetilde{V}}{\Delta t \, \Delta V \, \widetilde{\alpha}^{\varphi}} \tag{6.38a}$$

$$\vec{x}_c^{\,\widetilde{\partial\Omega}^{\varphi}_{\mathfrak{d},\mathfrak{w}}} := \frac{\int_{\left(\widetilde{\partial\Omega}^{\varphi}_{\mathfrak{d},\mathfrak{w}}\right)_{\mathfrak{i}}} \left(\phi^{(+)} \vec{x}^{\,\widetilde{\partial\Omega}^{\varphi}_{\mathfrak{d},\mathfrak{w}}}\right) \mathrm{d}\widetilde{A}}{\int_{\left(\widetilde{\partial\Omega}^{\varphi}_{\mathfrak{d},\mathfrak{w}}\right)_{\mathfrak{i}}} \phi^{(+)} \, \mathrm{d}\widetilde{A}} = \frac{\int_{\left(\widetilde{\Omega}^{\varphi}_{\mathfrak{d},\mathfrak{w}}\right)_{\mathfrak{i}}} \left(\phi^{(+)} \vec{x}^{\,\widetilde{\partial\Omega}^{\varphi}_{\mathfrak{d},\mathfrak{w}}}\right) \mathrm{d}\widetilde{A}}{\Delta t \, \Delta A_{\mathfrak{d}} \, \widetilde{\beta}^{\varphi}_{\mathfrak{d},\mathfrak{w}}} \tag{6.38b}$$

are the spatio-temporal centroids of $\widetilde{\Omega}^{\varphi}$ and $\widetilde{\partial\Omega}^{\varphi}_{\mathfrak{d},\mathfrak{w}}$. Relation (6.37) provides a fully second order accurate approximation, if

1. either $\vec{x}_0^{\,\widetilde{\Omega}^{\varphi}} := \vec{x}_c^{\,\widetilde{\Omega}^{\varphi}}$ and $\vec{x}_0^{\,\widetilde{\partial\Omega}^{\varphi}_{\mathfrak{d},\mathfrak{w}}} := \vec{x}_c^{\,\widetilde{\partial\Omega}^{\varphi}_{\mathfrak{d},\mathfrak{w}}}$ are chosen, which requires approximation of $\dot{\mathfrak{q}}^{\varphi}_{(\rho\psi)} \left(\vec{x}_c^{\,\widetilde{\Omega}^{\varphi}}\right)$ and $f^{\varphi}_{(\rho\psi),\mathfrak{d}} \left(\vec{x}_c^{\,\widetilde{\partial\Omega}^{\varphi}_{\mathfrak{d},\mathfrak{w}}}\right)$ with an error not larger than $\mathcal{O}\left(\mathfrak{h}^2\right)$,
2. or if $\dot{\mathfrak{q}}^{\varphi}_{(\rho\psi)} \left(\vec{x}_0^{\,\widetilde{\Omega}^{\varphi}}\right)$ and $f^{\varphi}_{(\rho\psi),\mathfrak{d}} \left(\vec{x}_0^{\,\widetilde{\partial\Omega}^{\varphi}_{\mathfrak{d},\mathfrak{w}}}\right)$ are approximated for $\vec{x}_0^{\,\widetilde{\Omega}^{\varphi}} \neq \vec{x}_c^{\,\widetilde{\Omega}^{\varphi}}$ and $\vec{x}_0^{\,\widetilde{\partial\Omega}^{\varphi}_{\mathfrak{d},\mathfrak{w}}} \neq \vec{x}_c^{\,\widetilde{\partial\Omega}^{\varphi}_{\mathfrak{d},\mathfrak{w}}}$ with an error not larger than $\mathcal{O}\left(\mathfrak{h}^2\right)$ and, in addition, both $\frac{\partial \dot{\mathfrak{q}}^{\varphi}_{(\rho\psi)}}{\partial \vec{x}^{\,\widetilde{\Omega}^{\varphi}}} \left(\vec{x}_0^{\,\widetilde{\Omega}^{\varphi}}\right)$ and $\frac{\partial f^{\varphi}_{(\rho\psi),\mathfrak{d}}}{\partial \vec{x}^{\,\widetilde{\partial\Omega}^{\varphi}_{\mathfrak{d},\mathfrak{w}}}} \left(\vec{x}_0^{\,\widetilde{\partial\Omega}^{\varphi}_{\mathfrak{d},\mathfrak{w}}}\right)$ are approximated with an error not larger than $\mathcal{O}\left(\mathfrak{h}\right)$.

The present method-of-lines approach yields a first order accurate approximation, as it replaces the single-phase update contributions

$$\mathfrak{K}^{\{1\}}_{\mathfrak{i},\mathfrak{n}} = \left(\overline{\mathcal{Q}}_{(\rho\psi),\mathfrak{n}} - \frac{1}{\mathfrak{h}} \sum_{\mathfrak{d}=1}^{\mathfrak{D}} \left(\frac{1}{\mathfrak{c}_{\mathfrak{d}}} \sum_{\mathfrak{w}=1}^{2} \left((-1)^{\mathfrak{w}} \left(\overline{\mathcal{F}}_{(\rho\psi)\mathfrak{d},\mathfrak{w}} \right)_{\mathfrak{n}} \right) \right) \right)_{\mathfrak{i}} \tag{6.39}$$

in

$$\Delta \overline{\rho\psi}^{\{1\}}_{\mathfrak{i}} := \Delta t \sum_{\mathfrak{n}=1}^{2} \left(\mathfrak{b}_{\mathfrak{n}} \, \mathfrak{K}^{\{1\}}_{\mathfrak{i},\mathfrak{n}} \right) \tag{6.40}$$

$$\mathfrak{b}_{\mathfrak{n}} = \frac{1}{2}, \qquad 1 \leqslant \mathfrak{n} \in \mathbb{N} \leqslant 2 \tag{6.41}$$

according to relations (5.15), (5.16) and (5.23), described in section 5.1.2.2, by

$$\mathfrak{K}_{\mathfrak{i},\mathfrak{n}}^{\{2\}} = \sum_{\varphi=1}^{2} \left(\widetilde{\alpha}^{\varphi} \, \overline{\mathcal{Q}}_{(\rho\psi),\mathfrak{n}}^{\varphi} \right)_{\mathfrak{i}} - \frac{1}{\mathfrak{h}} \left(\sum_{\mathfrak{d}=1}^{\mathfrak{d}} \left(\frac{1}{\mathfrak{c}_{\mathfrak{d}}} \sum_{\mathfrak{w}=1}^{2} \left((-1)^{\mathfrak{w}} \sum_{\varphi=1}^{2} \left(\widetilde{\beta}_{\mathfrak{d},\mathfrak{w}}^{\varphi} \, \left(\overline{\mathcal{F}}_{(\rho\psi),\mathfrak{d},\mathfrak{w}}^{\varphi} \right)_{\mathfrak{n}} \right) \right) \right) \right)_{\mathfrak{i}} \tag{6.42}$$

with approximations $\overline{\mathcal{Q}}_{(\rho\psi)}^{\varphi}$ and $\overline{\mathcal{F}}_{(\rho\psi),\mathfrak{d},\mathfrak{w}}^{\varphi}$ of the spatial averages per fluid phase. Thus, $\dot{\mathfrak{q}}_{(\rho\psi)}^{\varphi}$ and $f_{(\rho\psi),\mathfrak{d},\mathfrak{w}}^{\varphi}$ in (6.37) are effectively evaluated at the half time level $\frac{t^m + t^{m+1}}{2}$ for both fluid phases instead of the individual spatio-temporal centroids $\vec{x}_c^{\,\widetilde{\Omega}^{\varphi}}$ and $\vec{x}_c^{\,\widetilde{\partial\Omega}_{\mathfrak{d},\mathfrak{w}}^{\varphi}}$ of each fluid phase φ. This yields an $\mathcal{O}(\mathfrak{h})$ error as result of the loss of topological symmetry in space-time as sketched in ***Fig. 6.5***, if an arbitrarily moving interface separating two different fluids is involved.

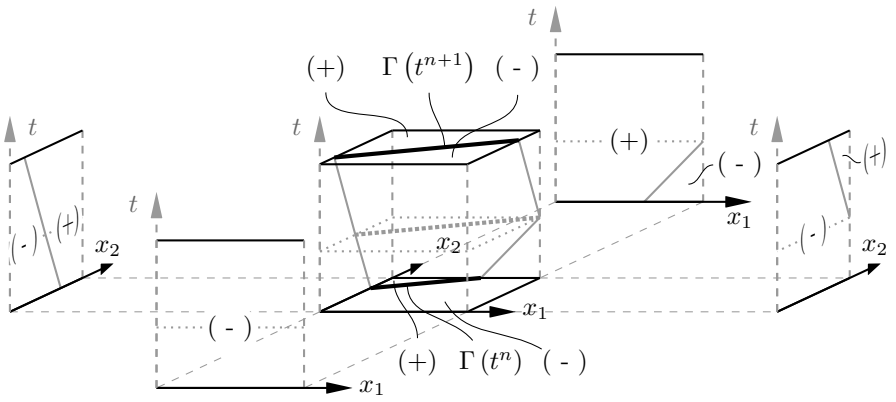

Fig. 6.5: Distribution of fluid phases over space-time domains, sketched for two-dimensional grid cells and its cell faces over time ($\mathfrak{d} = 2$). The center sketch for the two-dimensional grid cell holds for grid cell faces in three space dimensions as well ($\mathfrak{d} = 3$).

A locally second order accurate approximation in time is subject of current research and beyond the scope of this work, as it requires individual coefficients $\mathfrak{b}_{\mathfrak{n}}$ in (6.40) for each cell face fraction and each volume fraction and might require the use of (at least) a third time level, either in form of a third evaluation within a single-step method (as, for example, explicit Runge-Kutta methods with (at least) three stages) or using multi-step methods with more than one time level of known data in order to cope with the lack of topological symmetry in each fluid phase in (space-)time.

However, for grid cells, which are only cut in $\mathcal{N}_{\text{cut}}^{(t)} \ll \mathcal{N}_{\mathfrak{T}}^{(t)} = \mathcal{C}^{(t)} \frac{\mathfrak{T}}{\mathfrak{h}}$ time steps during the computation with total time $\mathfrak{T}$ as the sum of all time steps, the order of magnitude

of the time-global error $E^{(t)}$ in a grid cell $\mathfrak{i}$ is the same as if the cell had been regular throughout the entire computation due to

$$\begin{aligned} E_{\mathfrak{i}}^{(t)} &:= \mathcal{C}_2^{(t)} \mathcal{N}_{\text{cut}}^{(t)} \mathcal{O}\left(\mathfrak{h}^2\right) + \mathcal{C}_3^{(t)} \left(\mathcal{N}_{\mathfrak{T}}^{(t)} - \mathcal{N}_{\text{cut}}^{(t)}\right) \mathcal{O}\left(\mathfrak{h}^3\right) + ... \\ &= \mathcal{C}_2^{(t)} \mathcal{N}_{\text{cut}}^{(t)} \mathcal{O}\left(\mathfrak{h}^2\right) + \mathcal{C}_3^{(t)} \left(\frac{\mathcal{C}^{(t)} \mathfrak{T} - \mathcal{N}_{\text{cut}}^{(t)} \mathfrak{h}}{\mathfrak{h}}\right) \mathcal{O}\left(\mathfrak{h}^3\right) + ... \\ &= \mathcal{C}_2^{(t)} \left(\mathcal{N}_{\text{cut}}^{(t)} + \frac{\mathcal{C}_3^{(t)}}{\mathcal{C}_2^{(t)}} \mathcal{C}^{(t)} \mathfrak{T}\right) \mathcal{O}\left(\mathfrak{h}^2\right) - \mathcal{C}_3^{(t)} \mathcal{N}_{\text{cut}}^{(t)} \mathcal{O}\left(\mathfrak{h}^3\right) + ... \\ &= \mathcal{O}\left(\mathfrak{h}^2\right) + ... \end{aligned} \tag{6.43}$$

with $\mathcal{C}^{(t)}$, $\mathcal{C}_2^{(t)}$ and $\mathcal{C}_3^{(t)}$ as constants with suitable dimension. Further, since only a small number $\mathcal{N}_{\text{cut},\Delta t}^{(\vec{x})} \ll \mathcal{N}_{\Delta t}^{(\vec{x})} := \min_{\mathfrak{d}} \left(\frac{\mathfrak{S}}{\Delta x}\right)_{\mathfrak{d}} = \frac{\mathcal{C}_0^{(\vec{x})}}{\max_{\mathfrak{d}} \mathfrak{c}_{\mathfrak{d}}} \frac{\max_{\mathfrak{d}} \mathfrak{S}_{\mathfrak{d}}}{\mathfrak{h}}$ of the overall grid cells is cut during each time step with $0 < \mathcal{C}_0^{(\vec{x})} \in \mathbb{R} < 1$, $\max_{\mathfrak{d}} \mathfrak{c}_{\mathfrak{d}} \equiv 1$ and $\mathfrak{S}_{\mathfrak{d}}$ as the one-dimensional domain extension in direction $\mathfrak{d}$ with $\mathcal{C}^{(\vec{x})} := \mathcal{C}_0^{(\vec{x})} \frac{\max_{\mathfrak{d}} \mathfrak{S}_{\mathfrak{d}}}{\max_{\mathfrak{d}} \mathfrak{c}_{\mathfrak{d}}}$, the space-global error in each time step, $E_{\Delta t}^{(\vec{x})}$, is of the same order of magnitude as if all cells would have been regular:

$$\begin{aligned} E_{\Delta t}^{(\vec{x})} &:= \mathcal{C}_2^{(\vec{x})} \mathcal{N}_{\text{cut},\Delta t}^{(\vec{x})} \mathcal{O}\left(\mathfrak{h}^2\right) + \mathcal{C}_3^{(\vec{x})} \left(\mathcal{N}_{\Delta t}^{(\vec{x})} - \mathcal{N}_{\text{cut},\Delta t}^{(\vec{x})}\right) \mathcal{O}\left(\mathfrak{h}^3\right) + ... \\ &= \mathcal{C}_2^{(\vec{x})} \mathcal{N}_{\text{cut},\Delta t}^{(\vec{x})} \mathcal{O}\left(\mathfrak{h}^2\right) + \mathcal{C}_3^{(\vec{x})} \left(\frac{\mathcal{C}^{(\vec{x})} - \mathcal{N}_{\text{cut},\Delta t}^{(\vec{x})} \mathfrak{h}}{\mathfrak{h}}\right) \mathcal{O}\left(\mathfrak{h}^3\right) + ... \\ &= \mathcal{C}_2^{(\vec{x})} \left(\mathcal{N}_{\text{cut},\Delta t}^{(\vec{x})} + \frac{\mathcal{C}_3^{(\vec{x})}}{\mathcal{C}_2^{(\vec{x})}} \mathcal{C}^{(\vec{x})}\right) \mathcal{O}\left(\mathfrak{h}^2\right) - \mathcal{C}_3^{(\vec{x})} \mathcal{N}_{\text{cut},\Delta t}^{(\vec{x})} \mathcal{O}\left(\mathfrak{h}^3\right) + ... \\ &= \mathcal{O}\left(\mathfrak{h}^2\right) + ... \end{aligned} \tag{6.44}$$

with $\mathcal{C}^{(\vec{x})}$, $\mathcal{C}_2^{(\vec{x})}$ and $\mathcal{C}_3^{(\vec{x})}$ as constants with suitable dimension. Thus, while $\mathcal{N}_{\text{cut},\Delta t}^{(\vec{x})} \ll \mathcal{N}_{\Delta t}^{(\vec{x})}$ can be assumed to hold in any case, for $\mathcal{N}_{\text{cut}}^{(t)} \ll \mathcal{N}_{\mathfrak{T}}^{(t)}$ the global error is

$$E = \mathcal{O}\left(\mathfrak{h}^2\right) \tag{6.45}$$

while the local error in cut grid cells is

$$E_{\text{cut}} = \mathcal{O}\left(\mathfrak{h}^2\right) \tag{6.46}$$

and

$$E_{\text{reg}} = \mathcal{O}\left(\mathfrak{h}^3\right) \tag{6.47}$$

in regular grid cells. However, in cases in which $\mathcal{N}_{\text{cut}}^{(t)} = \mathcal{C}_{\text{cut}}^{(t)} \frac{\mathfrak{T}}{\mathfrak{h}} \approx \mathcal{C}^{(t)} \frac{\mathfrak{T}}{\mathfrak{h}} = \mathcal{N}_{\mathfrak{T}}^{(t)}$ (when a grid cell is cut throughout (almost) the entire computation, e.g. either due to very small local velocities or due to an oscillating interface), the time-global error

$$\begin{aligned} E_{\mathfrak{i}}^{(t)} &:= \mathcal{C}_2^{(t)} \mathcal{N}_{\text{cut}}^{(t)} \mathcal{O}\left(\mathfrak{h}^2\right) + \mathcal{C}_3^{(t)} \left(\mathcal{N}_{\mathfrak{T}}^{(t)} - \mathcal{N}_{\text{cut}}^{(t)}\right) \mathcal{O}\left(\mathfrak{h}^3\right) + ... \\ &= \mathcal{C}_2^{(t)} \left(\mathcal{C}_{\text{cut}}^{(t)} \mathfrak{T}\right) \mathcal{O}\left(\mathfrak{h}\right) + \mathcal{C}_3^{(t)} \left(\frac{\mathfrak{T}\left(\mathcal{C}^{(t)} - \mathcal{C}_{\text{cut}}^{(t)}\right)}{\mathfrak{h}}\right) \mathcal{O}\left(\mathfrak{h}^3\right) + ... \\ &= \left(\mathcal{C}_2^{(t)} \mathcal{C}_{\text{cut}}^{(t)} \mathfrak{T}\right) \mathcal{O}\left(\mathfrak{h}\right) + \mathcal{C}_3^{(t)} \mathfrak{T} \left(\mathcal{C}^{(t)} - \mathcal{C}_{\text{cut}}^{(t)}\right) \mathcal{O}\left(\mathfrak{h}^2\right) + ... \\ &= \mathcal{O}\left(\mathfrak{h}\right) + ... \end{aligned} \tag{6.48}$$

in the respective grid cells is reduced as well.

As the interface approximation at the new time level has to be known a priori, the Runge-Kutta time integration scheme, used for the single-phase flow solver as described in section 5.1.2.2, needs to be extended beyond replacement of $\mathfrak{K}_{\mathfrak{i},\mathfrak{n}}^{\{1\}}$ in (5.15) by $\mathfrak{K}_{\mathfrak{i},\mathfrak{n}}^{\{2\}}$ from (6.42) by coupling to the level-set transport scheme for the two-phase flow predictor step. The level-set time integration is also done using a two stage Runge-Kutta scheme as described in section 6.1.1 and the necessary nested procedure is as follows, resulting in a three-stage method with an incomplete pre-stage and two full stages for consistent propagation[3]:

1. a first order propagation step is done with the level-set based on the known fluid velocity at the old time level m. This is the **first stage** of the **level-set** propagating Runge-Kutta scheme.

2. a first order propagation step is done for the **conserved quantities**, based on the old time level information and knowledge of the interface position at the new time level $m + 1$ as predicted by the first level-set propagation stage in step 1. above. This **pre-predictor step** corresponds to the first stage of the Runge-Kutta time integration scheme of the conservation laws. It is necessary to obtain the intermediate velocity – as basis for the second level-set propagation stage – at the time level of the level-set intermediate information and in order to obtain the intermediate phase indicator for the subsequent correction step.

[3] In a pure two-stage method, in which each level-set time integration stage is performed together with the corresponding stage for time integration of the conserved quantities, different volume and face fractions would be used in the different stages, which can lead to $\mathcal{O}(1)$ errors due to the discrete restriction to only one intersection per grid cell face as described in section 7.2.

3. a phase indicator based correction of the conserved quantities needs to be done as described in section 6.5 in order to **get rid of discretization errors** in the conserved quantities **that affect discrete mass conservation**. The chosen interface discretization causes flux weights at cut grid cell faces, which are accurate enough in terms of the truncation error of the numerical method, but not in terms of discrete mass conservation. This fact becomes evident in the phase indicator values, which serve as basis for the correction that needs to be done after each step in which flux weights at cut grid cell faces are involved in flux computation.

4. the velocity field resulting from the previous propagation and correction procedure is needed for the **second stage** of the Runge-Kutta scheme for **level-set** propagation. After this second stage the level-set, representing the interface, is known second order accurate in both space and time[4], and the **approximate interface position** at the end of the time step is known.

5. since now the interface position at the new time level $m+1$ is known, the **first stage** of the Runge-Kutta scheme for propagation of the **conserved quantities** is repeated, based on the (reset) information at the old time level m and with knowledge of both interface positions at time levels m and $m+1$.

6. the resulting values need to be **corrected according to step 3.**

7. the resulting information serves as basis for the **second stage** of the Runge-Kutta time integration scheme for the **conserved quantities** based on predicted values at time level $m+1$ and known (unchanged) interface positions at both time levels m and $m+1$.

8. the **final values** of the performed propagation of the **conserved quantities** again need to be **corrected according to step 3.** After that, the predictor step is completed.

6.3.2.1 Time Step Restriction

The maximum allowable time step $\Delta t_{\max}^{\{2\}\#}$ for the setting in section 6.3.1 corresponds to $\Delta t_{\max}^{\{1\}}$ from equation (5.14), with contributions $\Delta t_{\mathcal{V}}$ and $\Delta t_{\mathcal{D},\mathfrak{s}}$ according to ***Tab. 5.3*** subject to $\max_{\varphi}\left(\frac{\mu}{\rho}\right)^{\varphi}$ and $\max_{\varphi}\left(\mathcal{D}_{\mathfrak{s}}\right)^{\varphi}$ with $\varphi \in \{(+),(-)\}$.

[4] While the level-set gradient is discretized third order accurate in space as described in section 6.1.1, the velocity field is only second order accurate in space, yielding a second order accurate scheme in total.

6.3.3 Advective Flux Computation

In this section extensions to the single-phase method for advective flux computation in the vicinity of the interface are described in detail, starting with definition of different cell types in section 6.3.3.1. Sections 6.3.3.2 to 6.3.3.4 are dedicated to determination of the state information per fluid phase around the interface, required for the subsequent flux computation in section 6.3.3.5 based on the single-phase procedure from section 5.1.3.

6.3.3.1 Cartesian Grid Cell Types and Space-Time Scenarios

In principal, only two types of grid cells exist in a Cartesian grid two-phase Finite Volume scheme:

- **type 0**: cells which are not cut by the interface and, thus, are located completely in one of the existing fluid phases
- **type 1**: cells which are cut by the interface

However, since the Finite Volume balances are drawn over a certain time interval and the fluidic interface is not necessarily static but can move through the Cartesian grid during that time interval considered, separation into cells cut by the interface and cells which are not cut is not sufficient anymore for flux determination, but more different types of grid cells need to be distinguished with respect to

- the geometric configuration,
- the stencil for computation of the respective numerical flux,
- spatio-temporal scenarios during the time interval.

Thus, the following types of cells and spatio-temporal scenarios can occur as sketched in ***Fig. 6.6*** and ***Fig. 6.7*** for the stencil of advective fluxes:

- **type 0/0**:
  grid cells which are *not cut by the interface throughout the entire time interval*.
  These cells can be further split into

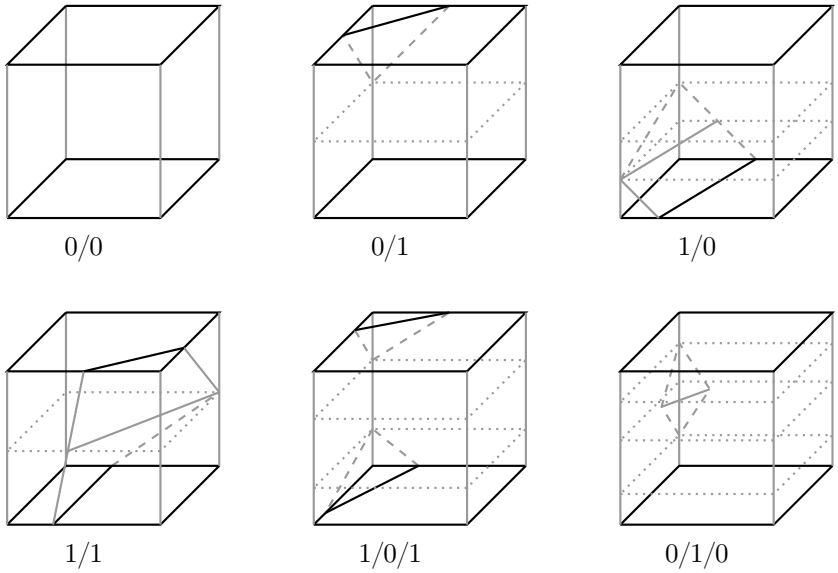

Fig. 6.6: Space-time cell types for $\mathfrak{d} = 2$; vertical grey edges represent the temporal axis

– **type 0/0 - 0**:
grid cells, which are located far enough from the interface, such that no surrounding grid cell involved in flux computation for the Finite Volume update of the respective grid cell is cut by the interface during the entire time interval. In these grid cells the standard single-phase Finite Volume method can be applied, using the fluid properties of the fluid phase which occupies the entire grid cell during the entire time interval.

– **type 0/0 - 1**:
grid cells, which are located in the vicinity of the interface, such that at least one of the surrounding grid cell face neighbors is cut by the interface during the time interval, and is, thus, not of any type 0/0. For type 0/0 - 1 grid cells, computation of fluxes across grid cell faces can be done as in the standard single-phase Finite Volume method. However, determination of states at the grid cell faces for flux computation, as well as state recovery in the cut surrounding grid cell(s), involved in cell face state recovery for flux computation, need a non-standard treatment. A grid cell of this type is also called "layer 1 cell" within this document.

– **type 0/0 - 2**:
grid cells, which are located in the vicinity of the interface, such that

  * no grid cell face neighbor cell is cut by the interface throughout the entire time interval, all grid cell face neighbor cells are of any type

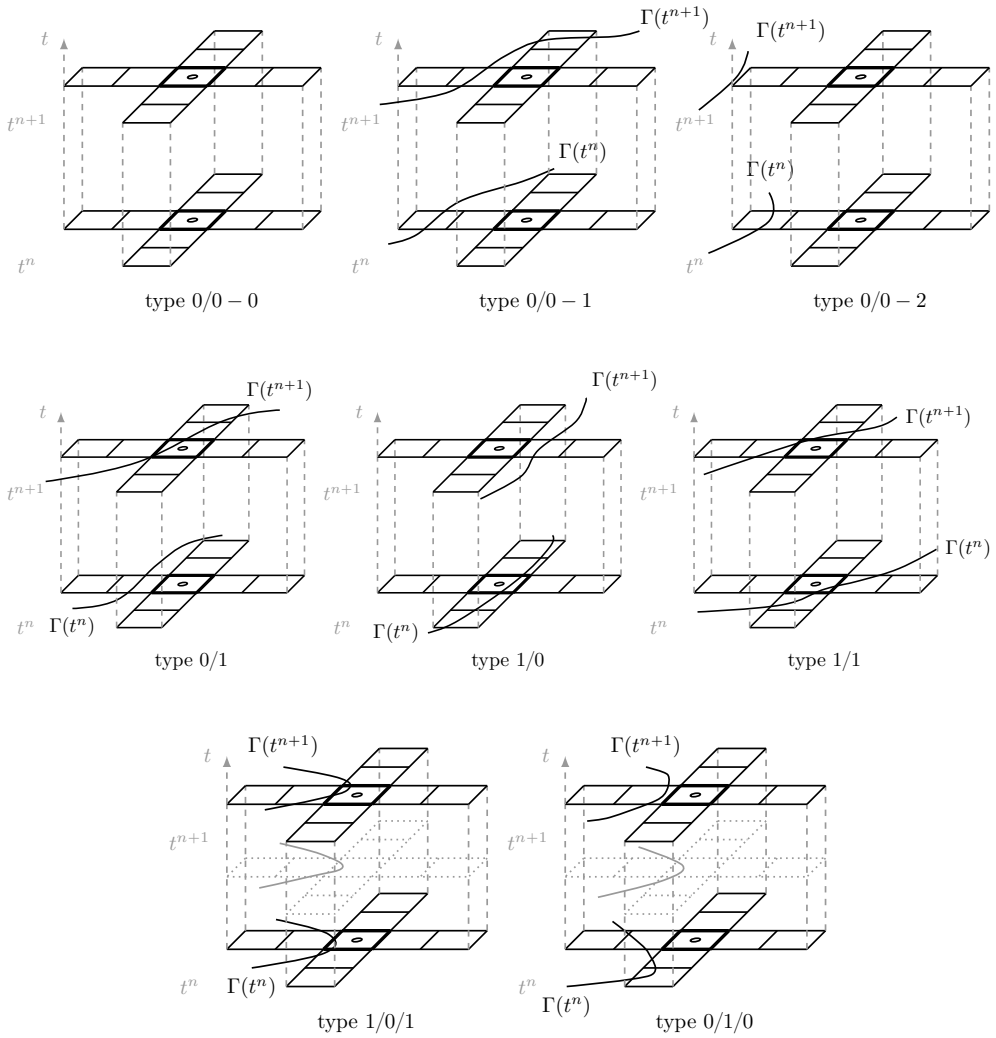

Fig. 6.7: Space-time cell types for $\mathfrak{d} = 2$ and stencil for advective flux computation

0/0.

- at least one of the surrounding grid cells involved in flux computation for the Finite Volume update of the respective grid cell is cut by the interface during the time interval and is, thus, not of any type 0/0.

For these grid cells flux computation and the necessary determination of states at the grid cell faces for flux computation can be done as in the standard single-phase Finite Volume method. However, state recovery in the cut surrounding grid cell(s) involved in cell face state recovery for flux computation needs a non-standard treatment. This type of cell is a "layer 2 cell". Information from layer 2 cells is necessary for determination of fluxes across grid cell faces of cut grid cells in a second order accurate

method.

Each type 0/0 cell is available in both fluid phases $(+)$ and $(-)$ with the physical fluid properties of the corresponding fluid phase.

- **type 0/1**:
  grid cells which are *cut by the interface at the end of the time interval but not at its beginning*.

- **type 1/0**:
  grid cells which are *cut by the interface at the beginning of the time interval but not at its end*.

- **type 1/1**:
  grid cells which are *cut by the interface throughout the entire time interval*.

- **type 1/0/1**:
  grid cells which are *cut both at the beginning and at the end of the time interval but not for some period within the time interval*. This type of cell can occur since a grid cell face is not allowed to be cut by the interface more than once.

- **type 0/1/0**:
  grid cells which are *neither cut at the beginning nor at the end of the time interval but for some period during the time interval*. This is the "inverse" of the type 1/0/1 cell and exists for the same reason as the type 1/0/1 cell.

These cut cell types and spatio-temporal scenarios allow for derivation of corresponding scenarios for each grid cell face of the respective grid cell considered, leading to grid cell face individual scenario-dependent flux computation procedures. On grid cell faces, which are cut by the interface at any time during the time interval considered, fluxes of both fluid phases need to be determined in order to compute the resulting flux for that grid cell face, while it is sufficient to compute only the flux of the respective fluid phase if the grid cell face remains within one fluid phase throughout the entire time interval. On grid cell faces, on which a flux for both fluid phases needs to be determined, also the time-average face fractions $\widetilde{\beta}$ according to sections 4.2.2 and 6.3.3.6 are required for application to the split sum for flux computation given in section 6.3.3.5.

6.3.3.2 State Recovery in Cut Cells

At the end of each time step only updated integral average values for entire grid cells, including intersected ones, are available. For computation of an effective flux across an intersected grid cell face, fluxes across fractions of this cell face need to be determined for each fluid phase as described in section 6.2 and specified in section 6.3.3.5. In order to determine these fluxes, suitable data needs to be available in each fluid phase which needs to be recovered in advance.

As shown in appendix section B.3, the integral average

$$\overline{\rho\psi} = \alpha\, \overline{\rho\psi}^{(+)} + (1-\alpha)\, \overline{\rho\psi}^{(-)} \tag{6.49}$$

of a conserved quantity $\rho\psi$ is the volume fraction weighted sum of the integral averages in the different fluid phases within the grid cell. With definition of the operators

$$\mathfrak{M}(\xi) := \max(\xi, 1-\xi) \tag{6.50a}$$

$$\mathfrak{W}(\xi) := \min(\xi, 1-\xi) \equiv 1 - \mathfrak{M}(\xi) \tag{6.50b}$$

equation (6.49) can be rewritten as

$$\overline{\rho\psi} = \mathfrak{M}(\alpha)\, \overline{\rho\psi}^{(L)} + (1 - \mathfrak{M}(\alpha))\, \overline{\rho\psi}^{(S)} \tag{6.51}$$

in which $\overline{\rho\psi}^{(L)} \in \left(\overline{\rho\psi}^{(+)}, \overline{\rho\psi}^{(-)}\right)$ is the integral average in the cut cell fraction with the larger (L) volume fraction and $\overline{\rho\psi}^{(S)} \in \left(\overline{\rho\psi}^{(+)}, \overline{\rho\psi}^{(-)}\right)$ with $\overline{\rho\psi}^{(S)} \neq \overline{\rho\psi}^{(L)}$ is the integral average in the cut cell fraction with the smaller (S) volume fraction, yielding

$$\overline{\rho\psi}^{(L)} = \frac{\overline{\rho\psi} - (1 - \mathfrak{M}(\alpha))\, \overline{\rho\psi}^{(S)}}{\mathfrak{M}(\alpha)} \tag{6.52}$$

after reorganization. Since the denominator is the larger volume fraction, equation (6.52) is always well defined due to $0.5 \leqslant \mathfrak{M}(\alpha) \leqslant 1$. The integral averages

$$\overline{\rho\psi}^{(L)/(S)} = \rho\psi\left(\vec{x}_c^{(L)/(S)}\right) + \mathcal{O}\left(\mathfrak{h}^2\right) \tag{6.53}$$

in the individual fluid phases are approximated second order accurate by the states in the centroids $\vec{x}_c^{(L)/(S)}$ of the respective grid cell fractions. As shown in ***Fig. 6.8*** for the case, in which fluid phase $(+)$ occupies the smaller volume fraction, but has the

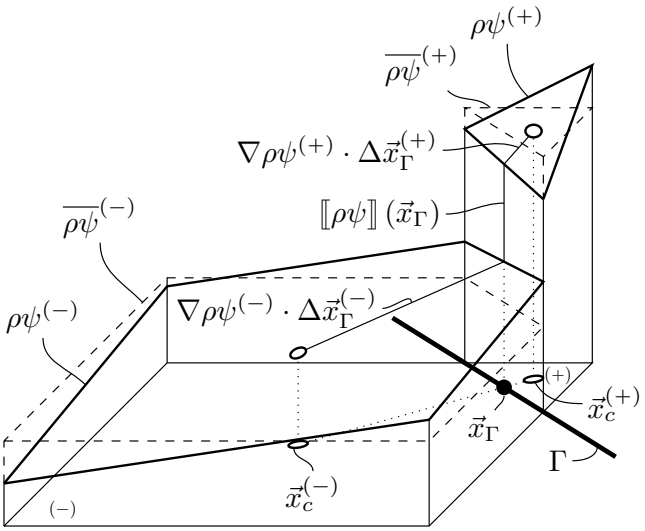

Fig. 6.8: Integral averages and states in cut cell fractions, separated by an sharp interface Γ, at which the respective quantity is discontinuous

larger average, one of the states $\rho\psi\left(\vec{x}_c^{(L)/(S)}\right)$ can be expressed in terms of the other one according to

$$\rho\psi\left(\vec{x}_c^{(S)}\right) = \rho\psi\left(\vec{x}_c^{(L)}\right) + \Delta\rho\psi^{(L)/(S)} \tag{6.54}$$

with

$$\Delta\rho\psi^{(L)/(S)} := \nabla\rho\psi^{(L)} \cdot \Delta\vec{x}_\Gamma^{(L)} - \nabla\rho\psi^{(S)} \cdot \Delta\vec{x}_\Gamma^{(S)} \pm [\![\,\rho\psi\,]\!](\vec{x}_\Gamma) \tag{6.55}$$

in which

$$\Delta\vec{x}_\Gamma^{(\eta)} := \vec{x}_\Gamma - \vec{x}_c^{(\eta)} \tag{6.56}$$

with $\vec{x}_\Gamma$ as the intersection of interface Γ and the line connecting the centroids $\vec{x}_c^{(L)}$ and $\vec{x}_c^{(S)}$.

The sign in front of the discontinuity $[\![\,\rho\psi\,]\!](\vec{x}_\Gamma) := \rho\psi^{(+)}(\vec{x}_\Gamma) - \rho\psi^{(-)}(\vec{x}_\Gamma)$ in equation (6.55) depends on which of the fluid phases occupies the larger volume fraction. For $(S) \equiv (+)$ the $+$ sign has to be chosen, for $(S) \equiv (-)$ the $-$ sign applies. Substitution of equation (6.53) into equation (6.52) and replacement of $\rho\psi\left(\vec{x}_c^{(S)}\right)$ by equation (6.54) with definition (6.55) yields

$$\rho\psi\left(\vec{x}_c^{(L)}\right) = \overline{\rho\psi} - (1 - \mathfrak{M}(\alpha))\,\Delta\rho\psi^{(L)/(S)} + \mathcal{O}\left(\mathfrak{h}^2\right) = \overline{\rho\psi}^{(L)} + \mathcal{O}\left(\mathfrak{h}^2\right) \tag{6.57}$$

and

$$\rho\psi\left(\vec{x}_c^{(S)}\right) = \overline{\rho\psi} + \quad \mathfrak{M}(\alpha) \quad \Delta\rho\psi^{(L)/(S)} + \mathcal{O}\left(\mathfrak{h}^2\right) = \overline{\rho\psi}^{(S)} + \mathcal{O}\left(\mathfrak{h}^2\right) \quad (6.58)$$

after substitution of the result (6.57) into (6.54). Transformation from $(L)/(S)$ back to $(+)/(-)$ finally yields

$$\overline{\rho\psi}^{(+)} = \overline{\rho\psi} - (1-\alpha)\,\Delta\rho\psi^{(+)/(-)} \quad (6.59a)$$

$$\overline{\rho\psi}^{(-)} = \overline{\rho\psi} + \quad \alpha \quad \Delta\rho\psi^{(+)/(-)} \quad (6.59b)$$

with

$$\Delta\rho\psi^{(+)/(-)} := \nabla\rho\psi^{(+)} \cdot \Delta\vec{x}_\Gamma^{(+)} - \nabla\rho\psi^{(-)} \cdot \Delta\vec{x}_\Gamma^{(-)} - [\![\,\rho\psi\,]\!](\vec{x}_\Gamma) \quad (6.60)$$

which necessitates knowledge of the size of the local discontinuity $[\![\,\rho\psi\,]\!]$, the gradients of $\rho\psi$ in each cut cell fraction and the location of the centroids of each cut cell fraction. The state at any point within the cut grid cell then can be approximated based on the recovered centroid value in the respective fluid phase. At the grid cell center $\vec{x}_m$, which is located in the phase occupying the larger volume fraction, the recovered state can be obtained by

$$\rho\psi^{(\pm)}(\vec{x}_m) := \overline{\rho\psi}^{(\pm)} + \nabla\rho\psi^{(\pm)} \cdot \left(\vec{x}_m - \vec{x}_c^{(\pm)}\right) \quad (6.61)$$

For fitting the present scheme, the resulting values (6.59) need to be transformed by division by $\overline{\mathcal{P}}$ in order to contribute to determination of upwind values with respect to the reference flux $(\mathcal{P}\vec{v}\cdot\vec{n})$ for the respective fluxes $(\mathcal{P}\vec{v}\cdot\vec{n})\left(\frac{\overline{\rho\psi}}{\overline{\mathcal{P}}}\right)^{(+)/(-)}_{\text{upwind}}$ at the grid cell faces as described in section 5.1.3.1.

For constant data within each fluid phase the jump $[\![\,\rho\psi\,]\!]$ is independent of the position on the interface and independent of time, yielding

$$\overline{\rho\psi}^{(+)} = \overline{\rho\psi} - (1-\alpha)\,[\![\,\rho\psi\,]\!] \quad (6.62a)$$

$$\overline{\rho\psi}^{(-)} = \overline{\rho\psi} + \quad \alpha \quad [\![\,\rho\psi\,]\!] \quad (6.62b)$$

due to vanishing gradients as given in the appendix of [90]. In the present work the described state recovery in cut grid cells is approximated by an one-sided averaged extrapolation, utilized for creation of ghost data around the interface as described in the following section 6.3.3.3 and sketched for cut grid cells in ***Fig. 6.10***.

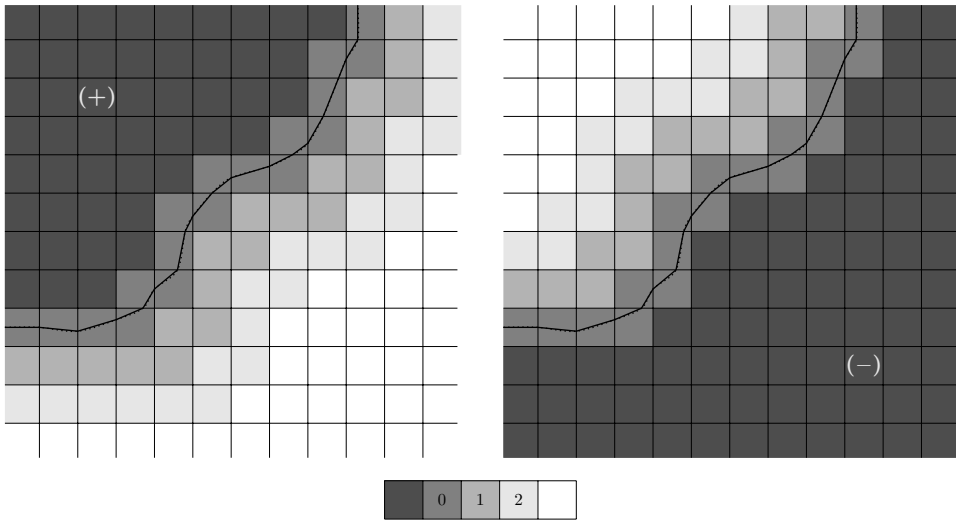

Fig. 6.9: Ghost fluid; *left:* fluid phase $(+)$, *right:* fluid phase $(-)$; the numbers indicate layers of ghost fluid, starting with layer 0 in cut grid cells

6.3.3.3 Ghost Fluid around the Interface

For determination of numerical fluxes in the vicinity of the interface, suitable data for $\mathcal{P}$ as introduced in section 3.6, the flow velocity $\vec{v}$, and the pseudo-primitive quantities $\vec{\Phi}$ as defined in equation (5.5a) has to be available for both fluid phases around the interface in order to apply standard single-phase stencils as given in section 5.1.3. As the involved stencils, however, extend into the other fluid phase beyond the interface, ghost data needs to be recovered for both fluid phases in the vicinity of the interface in the sub-domain of the respective other fluid phase as sketched in ***Fig. 6.9*** for all cells different from type 0/0 - 0 according to section 6.3.3.1.

While the velocity $\vec{v}$ is treated as a continuous field, subject to the assumptions in section 3.2.2 and the resulting equation (3.63), ghost data for any component of $\mathcal{P}$ and $\vec{\Phi}$, assumed to be represented by $\mathfrak{g}$, is recovered by the following multi-step extrapolation procedure for each fluid phase in a halo around the interface, based on available data in the respective fluid phase:

1. initialize a recovery marker in all narrow band cells $\Omega_\mathrm{i} \in \mathfrak{N}$ with value -1
2. ghost fluid states are recovered in cut grid cells, which have a sufficient amount of un-cut neighbor grid cells in the current fluid phase. The recovered ghost

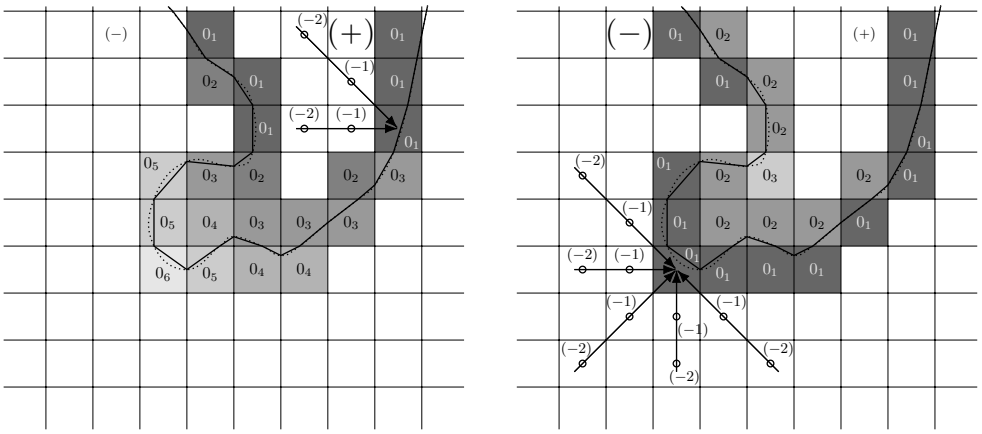

Fig. 6.10: Multi-step ghost fluid recovery in cut grid cells, *left:* fluid phase $(+)$, *right:* fluid phase $(-)$

fluid states

$$\mathfrak{g}_{\mathfrak{i}}^{\varphi} = \frac{1}{\mathcal{N}_{(\text{sten})}^{\varphi}} \sum_{\mathfrak{h}=1}^{\mathcal{N}_{(\text{sten})}^{\varphi}} \left(2\,\mathfrak{g}_{\mathfrak{i}^{(-1)}}^{\varphi} - \mathfrak{g}_{\mathfrak{i}^{(-2)}}^{\varphi} \right)_{\mathfrak{h}} \tag{6.63}$$

in each of these cut grid cells are obtained by averaging over the $\mathcal{N}_{(\text{sten})}^{\varphi}$ values obtained by linear extrapolation of available neighboring data in $\mathcal{N}_{(\text{sten})}^{\varphi} > 1$ available pseudo-one-dimensional stencils in the current fluid phase as sketched in ***Fig. 6.10***. Index superscript (-1) indicates a face or node neighbor cell of the cut grid cell in the current fluid phase, in which data for the respective quantity is already available, and index superscript (-2) indicates the neighbor of the cell labeled (-1) in the same direction, in which data is already available for the respective quantity as well as sketched in ***Fig. 6.10***.

3. cut grid cells, in which data is recovered, are labeled 0. In ***Fig. 6.10*** these are all cells labeled 0_1, where the subscript 1 indicates, that states in these cut grid cells have been recovered within the first ghost fluid recovery cycle due to sufficient available surrounding information in the respective fluid phase.

4. until all cut grid cells are labeled 0, repeat the following cycle:

   (a) perform step 2. for all cut grid cells still marked by -1, that have $\mathcal{N}_{(\text{sten})}^{\varphi} > 1$ valid stencils available in the current fluid phase, now considering not only regular grid cells in this fluid phase as valid neighbor cells, but also the cut grid cells, in which states have already been determined previously (cut grid cells which are already labeled 0)

   (b) mark these cut grid cells with 0; in ***Fig. 6.10*** the indices of the zero labels

indicate, in which cycle states in the respective cut grid cell can be recovered due to availability of sufficient surrounding data in the illustrated setting for both fluid phases

If cut cells remain with only one or even no suitable stencil available, the geometric configuration has to be considered under-resolved.

5. after states have been recovered in all cut grid cells and all of the latter are labeled 0, repeat the following steps for as many layers of grid cells around the cut grid cells, as required in the respective other fluid phase for application of the standard single-phase stencils for flux computation in the vicinity of the interface as sketched in ***Fig. 6.11***. For flux computation across each grid cell face of cut grid cells, a layer depth of at least 2 is required for application of the standard single-phase second order stencils:

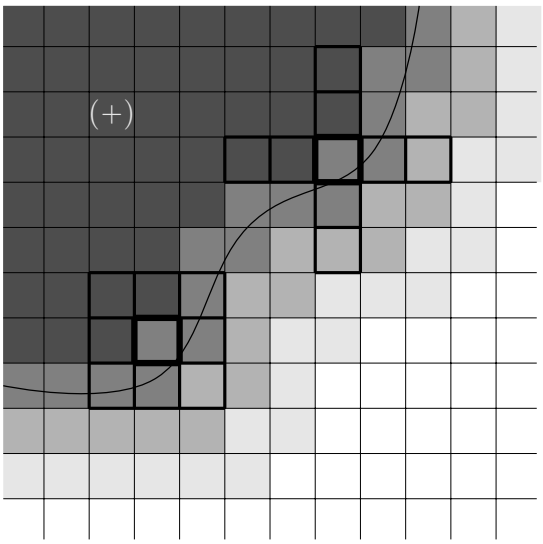

Fig. 6.11: Single-phase stencils in ghost fluid region

   (a) find regular cells of the current layer in which data of the other fluid phase is not yet available (recovery marker is -1)

   (b) for each of these cells...

      i. ... find neighbor cells which already carry data of the respective fluid phase, labeled (-1).

      ii. ... find neighbors of the neighbors from 5(b)i. in the same direction, labeled (-2), which already carry data of the respective fluid phase. The latter should be satisfied by default.

      iii. ... recover data according to equation (6.63), involving all available stencils resulting from 5(b)i. and 5(b)ii.

      iv. ... mark cells, in which data is recovered, by the index of the current layer (1 for all neighbors of cut grid cells, labeled 0, 2 for neighbors of these neighbors off the interface and so on as shown in ***Fig. 6.9***).

6.3.3.4 Interpolation of Ghost Data

Once data in the ghost region around the interface is available (obtained as described in section 6.3.3.4), there are several choices for determination of the individual numerical fluxes in the respective fluid phase, representing averages over corresponding fractions of the grid cell faces.

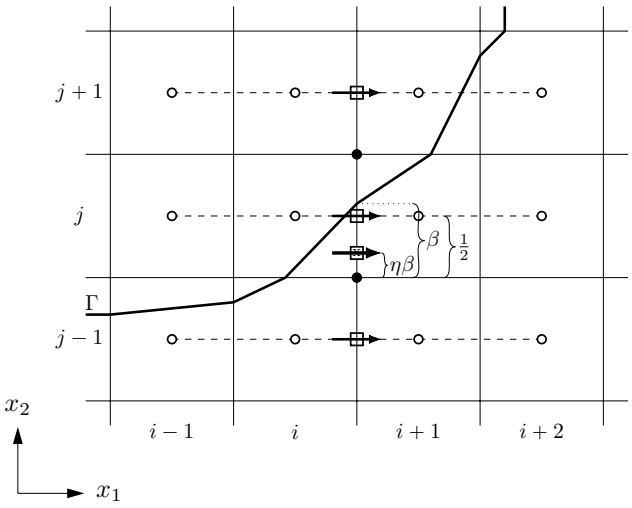

Fig. 6.12: Flux recovery at cut cell face fractions: Standard cell face centered flux averages are approximated before they are interpolated in order to obtain a flux approximation at the desired location

One possibility is to compute ghost fluxes based on the recovered ghost data in grid cell face centers for each fluid phase using standard procedures from section 5.1.3, and then interpolate the fluxes to the location of interest as sketched in ***Fig. 6.12***. A second option is to interpolate the ghost data onto a grid cell face normal line through the location, in which the flux should be approximated as sketched in ***Fig. 6.13*** for advective flux computation, and then apply the standard procedures from section 5.1.3 for flux computation to these interpolated data. While the first option, depending on the interpolation strategy,

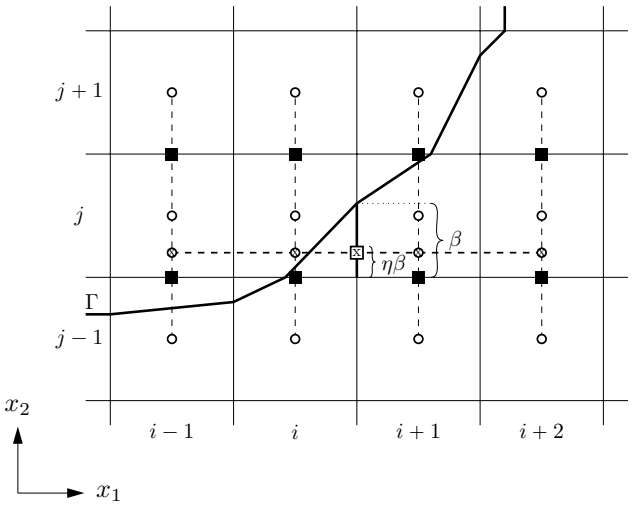

Fig. 6.13: State recovery at cut cell face fractions: States are recovered in the locations marked by a *circle filled with a cross* based on cell center data (*circles*) for application to standard Finite Volume flux approximation procedures in the desired location

yields flux approximations F for fluid phase φ according to

$$F^{\varphi}_{j,\eta^{\varphi}\beta^{\varphi}} = \frac{\eta^{\varphi}\beta^{\varphi}}{2}F^{\varphi}_{j+1} + \frac{1}{2}F^{\varphi}_{j} + \frac{1-\eta^{\varphi}\beta^{\varphi}}{2}F^{\varphi}_{j-1} \tag{6.64}$$

or

$$F^{\varphi}_{j,\eta^{\varphi}\beta^{\varphi}} = \left(\eta^{\varphi}\left(\beta^{\varphi} - \frac{1}{2}\right)\right)F^{\varphi}_{j+1} + \left(\frac{1}{2} + \left(1-\beta^{\varphi}\right)\eta^{\varphi}\right)F^{\varphi}_{j} + \frac{1-\eta^{\varphi}}{2}F^{\varphi}_{j-1} \tag{6.65}$$

with limit

$$\lim_{\beta^{\varphi}\to 1,\eta^{\varphi}\to\frac{1}{2}}\left(F^{\varphi}_{j,\eta^{\varphi}\beta^{\varphi}}\right) = \frac{1}{4}\left(F^{\varphi}_{j+1} + 2F^{\varphi}_{j} + F^{\varphi}_{j-1}\right) \tag{6.66}$$

for the example in ***Fig. 6.12*** each, the second option yields corresponding stencil data Φ for fluid phase φ for flux computation according to

$$\Phi^{\varphi}_{j,\eta^{\varphi}\beta^{\varphi}} = \frac{\eta^{\varphi}\beta^{\varphi}}{2}\Phi^{\varphi}_{j+1} + \frac{1}{2}\Phi^{\varphi}_{j} + \frac{1-\eta^{\varphi}\beta^{\varphi}}{2}\Phi^{\varphi}_{j-1} \tag{6.67}$$

or

$$\Phi^{\varphi}_{j,\eta^{\varphi}\beta^{\varphi}} = \left(\eta^{\varphi}\left(\beta^{\varphi} - \frac{1}{2}\right)\right)\Phi^{\varphi}_{j+1} + \left(\frac{1}{2} + \left(1-\beta^{\varphi}\right)\eta^{\varphi}\right)\Phi^{\varphi}_{j} + \frac{1-\eta^{\varphi}}{2}\Phi^{\varphi}_{j-1} \tag{6.68}$$

on the dashed horizontal line in ***Fig. 6.13*** with limit[5]

$$\lim_{\beta^{\varphi}\to 1,\eta^{\varphi}\to\frac{1}{2}}\left(\Phi^{\varphi}_{j,\eta^{\varphi}\beta^{\varphi}}\right) = \frac{1}{4}\left(\Phi^{\varphi}_{j+1} + 2\Phi^{\varphi}_{j} + \Phi^{\varphi}_{j-1}\right) \tag{6.69}$$

each. Both limits (6.66) and (6.69) do not correspond to the standard results

$$\lim_{\beta^{\varphi}\to 1,\eta^{\varphi}\to\frac{1}{2}}\left(F^{\varphi}_{j,\eta^{\varphi}\beta^{\varphi}}\right) = F^{\varphi}_{j} \tag{6.70a}$$

$$\lim_{\beta^{\varphi}\to 1,\eta^{\varphi}\to\frac{1}{2}}\left(\Phi^{\varphi}_{j,\eta^{\varphi}\beta^{\varphi}}\right) = \Phi_{j} \tag{6.70b}$$

for single-phase flow. Application of limited state recovery and slope computation according to section 5.1.3.1 - 1 also in grid cell face tangential directions within the respective stencil – allowing for computation of the states on the dashed horizontal

[5] While for second order accuracy in space $\eta^{\varphi} = \frac{1}{2}$ has to be chosen, second order accuracy in space-time might require $\eta^{\varphi} \neq \frac{1}{2}$ with $0 < \eta^{\varphi} < 1$, depending on the spatial coordinate of the spatio-temporal centroid of the cell face fractions in the respective fluid phase. However, this is beyond the scope of this work.

line in ***Fig. 6.13*** according to

$$\Phi^{\varphi}_{j,\eta^{\varphi}\beta^{\varphi}} = \Phi^{\varphi}_{j} \pm \mathcal{S}^{(\Phi)}_{2,(i,j,k)} \left(\frac{1}{2} - \eta^{\varphi}\beta^{\varphi} \right) \mathfrak{c}_2 \mathfrak{h} \tag{6.71}$$

in which the index 2 indicates the grid cell face tangential direction in ***Fig. 6.13*** and the sign $\pm$ depends on whether the dashed horizontal line is located above $(+)$ or below $(-)$ the respective grid cell center – satisfies the limit (6.70b)[6] and the corresponding fluxes can be computed using standard stencils and procedures from section 5.1.3 with the results of (6.71) as stencil data for each fluid phase. If the slopes for both fluid phases and all coordinate directions are pre-computed in the region, in which ghost data is available, no additional computational cost arises. However, the pre-computed slopes need to be stored for each quantity and fluid phase in this region around the interface for subsequent flux computation. Note that in case of constant data per fluid phase all described methods conincide. Since this approach, however, results in different limits on adjacent grid cell faces if the interface coincides with their common node, in the present method the approach

$$\Phi^{\varphi}_{j,\eta^{\varphi}\beta^{\varphi}} = \Phi^{\varphi}_{j} - \varsigma^{\varphi} \left(\Phi^{\varphi}_{j} - \Phi^{\varphi}_{j\mp\varsigma^{\varphi}} \right) \left(\frac{1}{2} - \eta^{\varphi}\beta^{\varphi} \right) \tag{6.72}$$

with

$$\varsigma^{\varphi} := \begin{cases} 1 & \text{if} \quad \left(\frac{1}{2} - \eta^{\varphi}\beta^{\varphi}\right) \geqslant 0 \\ -1 & \text{if} \quad \left(\frac{1}{2} - \eta^{\varphi}\beta^{\varphi}\right) < 0 \end{cases} \tag{6.73}$$

is used for determination of interpolated states, yielding

$$\Phi^{\varphi}_{j,\frac{1}{2}} = \Phi_j, \qquad \Phi^{\varphi}_{j,0} = \frac{\Phi_j + \Phi_{j-1}}{2}, \qquad \Phi^{\varphi}_{j,1} = \frac{\Phi_j + \Phi_{j+1}}{2} \tag{6.74a}$$

$$\Phi^{\varphi}_{j,\frac{1}{4}} = \frac{3\Phi_j + \Phi_{j-1}}{4}, \qquad \Phi^{\varphi}_{j,\frac{3}{4}} = \frac{3\Phi_j + \Phi_{j+1}}{4} \tag{6.74b}$$

for the setting from ***Fig. 6.13*** as expected. The sign $\mp$ in the index of equation (6.72) depends on whether the node at $j - \frac{1}{2}$ $(-)$ as in ***Fig. 6.13*** or the one at $j + \frac{1}{2}$ $(+)$ serves as reference location for determination of η^{φ} of the respective fluid phase φ. Instead of determination of stencil data according to (6.72) for application to standard single-phase flux computation procedures as described in section 5.1.3, the

[6] More advanced versions can be composed as weighted sums of the approaches (6.71), (6.67) and (6.68), that – in addition to (6.70b) – satisfy the limits $\lim_{\beta^{\varphi}\to 0, \eta^{\varphi}\to 0} \left(\Phi^{\varphi}_{j,\eta^{\varphi}\beta^{\varphi}} \right) = \frac{\Phi^{\varphi}_{j} + \Phi^{\varphi}_{j-1}}{2}$ and $\lim_{\beta^{\varphi}\to 1, \eta^{\varphi}\to 1} \left(\Phi^{\varphi}_{j,\eta^{\varphi}\beta^{\varphi}} \right) = \frac{\Phi^{\varphi}_{j+1} + \Phi^{\varphi}_{j}}{2}$.

above considerations with the corresponding result

$$F^{\varphi}_{j,\eta^{\varphi}\beta^{\varphi}} = F^{\varphi}_{j} - \varsigma^{\varphi}\left(F^{\varphi}_{j} - F^{\varphi}_{j\mp\varsigma^{\varphi}}\right)\left(\frac{1}{2} - \eta^{\varphi}\beta^{\varphi}\right) \tag{6.75}$$

can be made directly based on the fluxes as sketched in ***Fig. 6.12***, using pre-computed standard fluxes in grid cell face centers for both fluid phases as in the case of single-phase flow from section 5.1.3. Note, however, that these two options yield different results since in the flux based one the limiter function from section 5.1.3.1 - 1 is applied for each basis flux before the interpolated flux is determined, while in the state based option the limiter function is only involved once per computation of flux $F^{\varphi}_{j,\eta^{\varphi}\beta^{\varphi}}$ based on the interpolated stencil data from (6.72).

6.3.3.5 Flux Splitting

The effective numerical flux F, representing the spatio-temporal flux average and required for determination of a single update for the entire grid cell, is split at cut grid cell faces according to

$$F_{j} := \sum_{\varphi}\widetilde{\beta}^{\varphi}_{j}F^{\varphi}_{j} = \widetilde{\beta}_{j}F^{(+)}_{j} + \left(1 - \widetilde{\beta}_{j}\right)F^{(-)}_{j} \tag{6.76}$$

as proposed in [156] and performed in [150]. The individual flux contributions F^{φ}_{j} per fluid phase φ are determined as given in section 6.3.3.4 by equation (6.75) or (6.72), respectively, the latter applied as stencil data to standard single-phase standard flux determination procedures as given in section 5.1.3.1, based on recovered ghost data around the interface.

6.3.3.6 Time-Average Cell Face Fractions

Time-average cell face fractions $\widetilde{\beta}^{\varphi}$ for fluid phase φ are determined based on the nodal level-set values at both the old time level n and the new time level $n+1$ as indicated for $\mathfrak{d} = 3$ in the left plot of ***Fig. 6.4*** on page 155. For determination of the time-average cell face fractions $\widetilde{\beta}^{\varphi}$ in case of $\mathfrak{d} = 2$ basic geometric considerations are sufficient, for $\mathfrak{d} = 3$ the corresponding values for the space-space-time volume

$$\widetilde{\partial\Omega}^{\varphi} := \left(\partial\Omega^{\varphi}(t) \times (t^{n}, t^{n+1})\right) \in \mathbb{R}^{\mathfrak{d}} \tag{6.77}$$

can be obtained by integration of

$$\int_{\widetilde{\partial\Omega}^{\varphi}} \mathrm{d}\widetilde{V} = \frac{1}{3}\int_{\widetilde{\partial\Omega}^{\varphi}} \widetilde{\nabla}\cdot\widetilde{\vec{x}}\,\mathrm{d}\widetilde{V} = \sum_{\mathfrak{f}}\int_{\widetilde{\partial\partial\Omega}_{\mathfrak{f}}^{\varphi}} \widetilde{\vec{x}}\,\mathrm{d}\widetilde{A} \tag{6.78}$$

over the boundary

$$\widetilde{\partial\partial\Omega}^{\varphi} := \left(\partial\partial\Omega^{\varphi}(t)\times(t^n,t^{n+1})\right) \in \mathbb{R}^{\mathfrak{d}-1} \tag{6.79}$$

of the space-space-time volume after application of the divergence theorem with $\widetilde{\vec{x}}$ as vector consisting of $\mathfrak{d}-1$ spatial and 1 temporal coordinate and corresponding divergence operator $\widetilde{\nabla}\cdot$.

6.4 Corrector

Elliptic solvers for solving Poisson- and Helmholtz-type problems, arising within the present numerical method, are readily available through [128, 130, 129] and also able to handle grid cells, which are intersected by a sharp interface. Instead of only one bi- ($\mathfrak{d}$=2) / tri- ($\mathfrak{d}$=3) linear ansatz function per grid cell as in the single-phase setting, in cut grid cells two ansatz functions are used for approximation of the unknown quantity with two different states. These solvers are based on asymptotic analysis both in order to overcome the problem of arbitrarily small grid cell fractions ([128, 130]) and to obtain solutions in each fluid phase separately for fluids with large density ratio ([129]) by determination of a leading order solution in the heavier fluid only, before computing a higher order correction in the entire domain. However, while these methods work second order accurate for stationary interfaces, for nonsteady problems, time dependence due to the moving interface has to be included in the system since the Cartesian grid is not aligned with the interface and locations, in which solutions, coefficients and right hand side contributions are determined, might have changed the phase during the time step considered, which has to be accounted for. Since this is subject of current research for sharp interfaces, throughout this work the solvers described in sections 5.2 and 5.5 for single-phase flow are used with space-time average coefficients, providing a smoothed space time average solution for the quantity to be determined.

6.5 Sharp Conservative Fluid Phase Separation

A strictly conservative two-phase flow method not only needs to discretely maintain

- **global conservation** via the balance between the integral change of a conserved quantity within the computational **domain** and the flux across the outer domain boundary

and

- **local conservation** in each computational **grid cell** via the balance between the change of a conserved quantity in the grid cell and the fluxes across the grid cell boundary segments

but also

- **conservation of each fluid phase**, which is, for example, neither given by default by a purely level-set based approximation of the fluidic interface nor uniquely maintained by a purely volume-of-fluid based approximation as described in section 6.1,

is required. While – like, for example, in [156] – the first two issues are covered by the present method as described so far, conservative phase separation is not yet addressed and is covered in this section. Due to the different natures of the implicit interface approximations via the level-set transport from section 6.1.1 on the one hand and the volume-of-fluid evolution from section 6.1.2 on the other hand, these two discrete interface representations will never match exactly and non of them represents the exact interface. However, a two-way coupling of both representations as introduced in [28] and advanced in [152] and [150] keeps both interface representations close to each other, avoiding elaborate interface reconstruction procedures. While in [152] and [150] primarily volume-of-fluid information, obtained from the field of constant densities within each fluid phase, guides the correction procedure, in the adaption to the present method the level-set representation serves as governing basis for the discrete interface, as it is always resolved on the finest available grid level in case multiple degrees of grid resolution are involved, and the level-set gradients are discretized third order accurate as given in section 6.1.1. The conservation property is adopted from the additional volume-of-fluid field, which is transported discretely conservative as

described in section 6.1.2, while all conserved quantities pass through the correction procedure required for the volume-of-fluid field in turn due to discretization errors in the discrete volume-of-fluid field that can not remain uncorrected as described in sections 6.5.1 and 6.5.2. Since these errors, however, are extractable and produced by a discretely conservative scheme, a discretely conservative correction procedure as specified in section 6.5.2 is able to reset the volume-of-fluid field in grid cells beyond the interface to the exact volume-of-fluid values and all conserved quantities can be corrected accordingly as they suffer from the same deficiencies due to a common transport algorithm as described in sections 6.3 and 6.4 based on chapter 5. This discretely conservative correction allows for determination of a level-set correction velocity as specified in section 6.5.3 for application to the level-set correction step introduced in section 6.5.3.1, that pulls the level-set based interface representation towards the conservative one due to the volume-of-fluid and, with that, towards all other conserved quantities. That way the interface due to the level-set representation remains coupled to the flow and the later sharply separated by the interface, while interface reconstruction procedures are avoided and the separated fluid phases are conserved. In the subsequent time step, this corrected level-set based interface representation in turn serves as basis for the flux splitting at cut grid cell faces as described in section 6.2 for further advancing the conserved quantities of the flow in time. This procedure is already briefly outlined in [182], which can be considered as continuative introduction to this section. The latter contains the detailed description in the following, starting with specification of both origin and effects of the discretization errors in section 6.5.1, which are subject to the correction procedure specified afterwards in sections 6.5.2 and 6.5.3. Section 6.5.2 deals with the correction procedure for the conserved quantities, distinguishing between different types of grid cells in sections 6.5.2.4 - 1 to 6.5.2.4 - 3, based on information from the discretization error of the volume-of-fluid field. Section 6.5.3 is dedicated to determination of a suitable level-set correction, followed by presentation of various correction strategies in sections 6.5.4 and 6.5.5 before results are presented in section 6.5.6.

6.5.1 Origin and Effects of Phase Separation Related Errors

Regarding stable conservative fluid phase separation two different errors, resulting from truncation errors of components of the respective numerical methods, need to be overcome: Propagation of the level-set function as described in section 6.1.1 suffers from numerical truncation errors of both the level-set propagation algorithm and the

approximation of the velocity field used for this propagation as stated in [155]. These deviations from exact propagation appear as volume changes of fluidic structures bounded by the level-set zero level, causing a mass shift between the fluid phases which is not motivated by physics and can accumulate over time if left untreated as already stated in section 6.1.1. In consequence, conservation of conserved quantities in each fluid phase is violated, if pure level-set information is used during flux computation for representation of the interface, separating the different fluid phases, and related quantities such as grid cell face fractions in the respective fluid phases. Due to the piecewise linear approximation

$$\widetilde{\beta} = \frac{1}{\Delta t} \sum_{m=0}^{\mathcal{N}_{\text{slice}}} \left(\int_{t_m}^{t_{m+1}} \beta_m(t) \, \mathrm{d}t \right) \tag{6.80}$$

of the time-average cell face fractions in time over time slices between $t_0 \equiv t^n$ and $t_{\mathcal{N}_{\text{slice}}} \equiv t^{n+1}$, indexed m, with

$$\beta_m(t) \approx \beta(t_m) + (\beta(t_{m+1}) - \beta(t_m)) \, \frac{(t - t_m)}{(t_{m+1} - t_m)} \tag{6.81}$$

as sketched in the right plot of ***Fig. 6.14*** for a single time slice between t^n and t^{n+1}, the conserved quantities even not remain bounded within their physically reasonable range, which becomes evident in the volume-of-fluid value $\mathcal{P}\alpha$ from equation (6.18). As examined in [150] for the volume fraction α (called f there), the leading order contribution of this error is in the order of magnitude of the truncation error of the numerical scheme for determination of $\widetilde{\beta}$. If not treated suitable, these errors cause smearing of the states around the interface and artificial mass changes in the differrent fluid phases, if over- and undershoots are simply trunctated to the physically reasonable range of the respective quantity. Additional approximation errors, that affect the face fractions β of cut grid cell faces and therefore also the flux weights $\widetilde{\beta}$, are introduced during determination of the intersections of approximated interface and grid cell faces by assuming a piecewise linear interface on grid cell faces as sketched in ***Fig. 6.3***.

6.5.2 Discretely Conservative Volume-of-Fluid Based Correction of Conserved Quantities

The approach presented in this section aims for correction of all conserved quantities, based on restoring the violated boundedness of the disturbed volume-of-fluid average

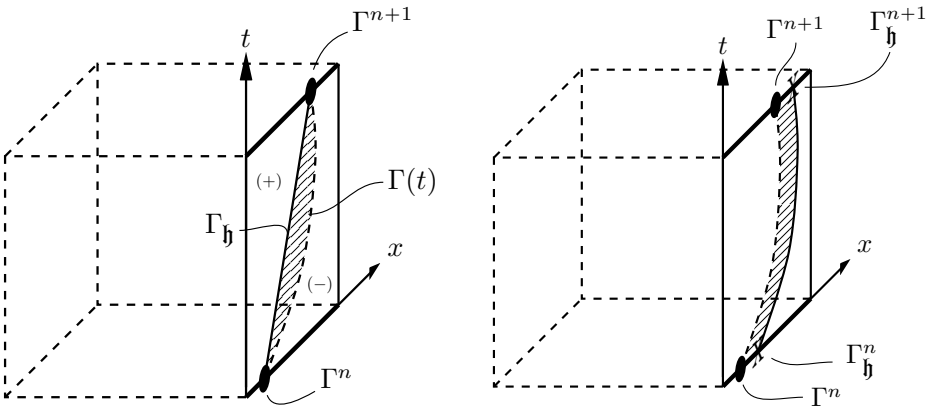

Fig. 6.14: Sources of phase related mass defects: *left*: linear approximation of temporal evolution of intersection points, *right*: approximate determination of intersection points due to piecewise linear approximation of the level-set function accoding to ***Fig. 6.3***

$\overline{\mathcal{P}\phi}^{\star}$, resulting from discretization of (6.17) in each grid cell according to sections 6.2 to 6.4 on basis of chapter 5. Therefore first a general consistent correction scheme is derived in section 6.5.2.1, which is then specified due to the available data in sections 6.5.2.2 and 6.5.2.3 and applied to different types of grid cells in section 6.5.2.4.

6.5.2.1 General Consistent Correction Scheme

For two-phase flow a consistent correction scheme for the integral averages of an arbitrary number of conserved quantities can be derived, if the errors of two of these conserved quantities are known, since scaled errors of the same kind have been generated consistently for all conserved quantities by the present numerical scheme. An increment $\Delta\overline{\rho\psi}^{(\text{err.})}$, which represents the error of an arbitrary conserved quantity $\rho\psi$ with integral average $\overline{\rho\psi}$ (omitting the grid cell index $\mathfrak{i}$), is determined by

$$\Delta\overline{\rho\psi}^{(\text{err.})} = -\frac{\Delta t}{\Delta V}\sum_{\mathfrak{f}=1}^{2\mathfrak{d}}\left[\Delta A\,\Delta\widetilde{\overline{\mathcal{F}}}^{(\text{err.})}_{\rho\psi}\right]_{\mathfrak{f}} \tag{6.82}$$

with $2\mathfrak{d}$ as the number of grid cell faces of a Cartesian grid cell. Integration of flux densities over inaccurate space-time domains $\widetilde{\partial\Omega}^{(+),\star}_{\mathfrak{f}}$ and $\widetilde{\partial\Omega}^{(-),\star}_{\mathfrak{f}}$ is the source of this error, which can be eliminated by addition of

$$\Delta\overline{\rho\psi} = -\Delta\overline{\rho\psi}^{(\text{err.})} \tag{6.83}$$

as corresponding correction. Therefore, due to equation (6.82), also

$$\sum_{\mathfrak{f}} \left[\Delta A \, \Delta \widetilde{\overline{\mathcal{F}}}_{\rho\psi} \right]_{\mathfrak{f}} = - \sum_{\mathfrak{f}} \left[\Delta A \, \Delta \widetilde{\overline{\mathcal{F}}}^{(\mathrm{err.})}_{\rho\psi} \right]_{\mathfrak{f}} \tag{6.84}$$

with

$$\Delta \widetilde{\overline{\mathcal{F}}}_{\rho\psi} = \Delta \left(\sum_{\varphi} \left(\widetilde{\beta}^{\varphi} \, \widetilde{\overline{\mathcal{F}}}^{\varphi}_{\rho\psi} \right) \right) \tag{6.85}$$

and

$$\widetilde{\beta}^{(+)} \equiv \widetilde{\beta} \tag{6.86a}$$

$$\widetilde{\beta}^{(-)} \equiv 1 - \widetilde{\beta} \tag{6.86b}$$

as well as $\varphi \in \{(+), (-)\}$ has to hold, while in general

$$\Delta \widetilde{\overline{\mathcal{F}}}_{\rho\psi,\mathfrak{f}} \neq - \Delta \widetilde{\overline{\mathcal{F}}}^{(\mathrm{err.})}_{\rho\psi,\mathfrak{f}} \tag{6.87}$$

for each individual average correction flux density $\Delta \widetilde{\overline{\mathcal{F}}}_{\rho\psi,\mathfrak{f}}$ across cell face $\mathfrak{f}$. Thus, due to relation (6.85) each of the corrective flux densities $\Delta \left(\widetilde{\beta}^{\varphi} \, \widetilde{\overline{\mathcal{F}}}^{\varphi}_{\rho\psi} \right)$ needs to be determined for the different fluid phases φ. Assuming, that the required resulting correction flux $\Delta \mathfrak{F}_{\rho\psi,\mathfrak{f}}$ across grid cell face $\mathfrak{f}$ contributes to the overall corrective increment $\Delta \overline{\rho\psi}$ in the respective grid cell to a certain, yet unknown, extent $\mathcal{W}_{\mathfrak{f}}$, this correction flux can be written as

$$\Delta \mathfrak{F}_{\rho\psi,\mathfrak{f}} \; := \; \mathcal{W}_{\mathfrak{f}} \, \Delta \overline{\rho\psi} \; = \; \mathfrak{v}_{\mathfrak{f}} \, \Delta \widetilde{\overline{\mathcal{F}}}_{\rho\psi,\mathfrak{f}} \overset{(6.85)}{=} \mathfrak{v}_{\mathfrak{f}} \, \Delta \left[\left(\sum_{\varphi} \left(\widetilde{\beta}^{\varphi} \, \widetilde{\overline{\mathcal{F}}}^{\varphi}_{\rho\psi} \right) \right) \right]_{\mathfrak{f}} \tag{6.88}$$

in which

$$\mathfrak{v}_{\mathfrak{f}} := \frac{\Delta t}{\Delta V} \Delta A_{\mathfrak{f}} \tag{6.89}$$

and

$$\sum_{\mathfrak{f}} \mathcal{W}_{\mathfrak{f}} \equiv 1 \tag{6.90}$$

for a conservation maintaining correction. With the transformation

$$\mathfrak{v}_{\mathfrak{f}} \, \Delta \left(\widetilde{\beta}^{\varphi}_{\mathfrak{f}} \, \widetilde{\overline{\mathcal{F}}}^{\varphi}_{\rho\psi,\mathfrak{f}} \right) = (\rho\psi)^{\varphi}_{\mathfrak{f}} \, \left[\Delta \mathfrak{F}^{\varphi}_{\mathrm{basic}} \right]_{\mathfrak{f}} \tag{6.91}$$

in which

$$\left[\Delta \mathfrak{F}^{\varphi}_{\mathrm{basic}} \right]_{\mathfrak{f}} := \mathfrak{v}_{\mathfrak{f}} \, \Delta \left(\left(\vec{v}^{\,\varphi}_{(\mathrm{corr.})} \cdot \vec{n} \right)_{\mathfrak{f}} \, \widetilde{\beta}^{\varphi}_{\mathfrak{f}} \right) \tag{6.92}$$

are phase-dependent common non-dimensional basic fluxes for all conserved quantities,

$$\Delta\mathfrak{F}_{\rho\psi,\mathfrak{f}} = \sum_{\varphi} \left((\rho\psi)_{\mathfrak{f}}^{\varphi} \; \left[\Delta\mathfrak{F}_{\text{basic}}^{\varphi}\right]_{\mathfrak{f}} \right) \tag{6.93}$$

results from equation (6.88) for each correction flux $\mathfrak{F}_{\rho\psi,\mathfrak{f}}$, since the unknown correction velocities $\vec{v}_{(\text{corr.})}^{\,(+)}$ and $\vec{v}_{(\text{corr.})}^{\,(-)}$ are identical for each conserved quantity $\rho\psi$ as all $\rho\psi$ have been propagated with the same transport mechanism causing the errors subject to be corrected.

With the **known error** $\Delta\overline{\rho\psi}_{(1)}^{(\text{err.})}$ **for an arbitrary first quantity** $\rho\psi_{(1)}$ (and, thus, a first given correction $\Delta\overline{\rho\psi}_{(1)}$ due to (6.83)), equation (6.93) can be solved for $\Delta\mathfrak{F}_{\text{basic}}^{(-)}$, yielding

$$\left[\Delta\mathfrak{F}_{\text{basic}}^{(-)}\right]_{\mathfrak{f}} = \frac{1}{\left(\rho\psi_{(1)}\right)_{\mathfrak{f}}^{(-)}} \left(\mathcal{W}_{\mathfrak{f}} \, \Delta\overline{\rho\psi}_{(1)} - \left(\rho\psi_{(1)}\right)_{\mathfrak{f}}^{(+)} \; \left[\Delta\mathfrak{F}_{\text{basic}}^{(+)}\right]_{\mathfrak{f}} \right) \tag{6.94}$$

Analogously, **knowledge of the error** $\Delta\overline{\rho\psi}_{(2)}^{(\text{err.})}$ **of an arbitrary second quantity** $\rho\psi_{(2)}$ results in

$$\left[\Delta\mathfrak{F}_{\text{basic}}^{(-)}\right]_{\mathfrak{f}} = \frac{1}{\left(\rho\psi_{(2)}\right)_{\mathfrak{f}}^{(-)}} \left(\mathcal{W}_{\mathfrak{f}} \, \Delta\overline{\rho\psi_{(2)}} - \left(\rho\psi_{(2)}\right)_{\mathfrak{f}}^{(+)} \; \left[\Delta\mathfrak{F}_{\text{basic}}^{(+)}\right]_{\mathfrak{f}} \right) \tag{6.95}$$

and equating expressions (6.94) and (6.95), solving for $\left[\Delta\mathfrak{F}_{\text{basic}}^{(+)}\right]_{\mathfrak{f}}$, reveals the non-dimensional basic correction fluxes

$$\left[\Delta\mathfrak{F}_{\text{basic}}^{\varphi}\right]_{\mathfrak{f}} = \frac{\mathfrak{f}_{\mathfrak{f}}}{\left(\rho\psi_{(1)}\right)_{\mathfrak{f}}^{\varphi}} \; \left[\Delta\mathfrak{F}_{\text{ref}}^{\varphi}\right]_{\mathfrak{f}} \tag{6.96}$$

in which

$$\begin{aligned} \left[\Delta\mathfrak{F}_{\text{ref}}^{(\pm)}\right]_{\mathfrak{f}} &:= \pm \, \mathcal{W}_{\mathfrak{f}} \left(\Delta\overline{\rho\psi}_{(2)} - \left(\frac{\psi_{(2)}^{(\mp)}}{\psi_{(1)}^{(\mp)}} \right)_{\mathfrak{f}} \Delta\overline{\rho\psi}_{(1)} \right) \\ &= \pm \left(\Delta\mathfrak{F}_{\rho\psi_{(2)},\mathfrak{f}} - \left(\frac{\psi_{(2)}^{(\mp)}}{\psi_{(1)}^{(\mp)}} \right)_{\mathfrak{f}} \Delta\mathfrak{F}_{\rho\psi_{(1)},\mathfrak{f}} \right) \end{aligned} \tag{6.97}$$

is defined to be the reference correction flux for all other conserved quantities and

$$\mathfrak{f}_{\mathfrak{f}} := \frac{1}{\left(\frac{\psi_{(2)}^{(+)}}{\psi_{(1)}^{(+)}} - \frac{\psi_{(2)}^{(-)}}{\psi_{(1)}^{(-)}}\right)_{\mathfrak{f}}} \tag{6.98}$$

is a common scaling. With that, the **consistent correction flux** across cell face $\mathfrak{f}$ for any conserved quantity $\rho\psi$ with yet unknown correction $\Delta\overline{\rho\psi}$ finally yields

$$\Delta\mathfrak{F}_{\rho\psi,\mathfrak{f}} = \mathfrak{f}_{\mathfrak{f}} \sum_{\varphi} \left(\left(\frac{\psi^{\varphi}}{\psi_{(1)}^{\varphi}} \right)_{\mathfrak{f}} \left[\Delta\mathfrak{F}_{\mathrm{ref}}^{\varphi} \right]_{\mathfrak{f}} \right) \tag{6.99}$$

based on relation (6.93), if corrections $\Delta\overline{\rho\psi}_{(1)}$ and $\Delta\overline{\rho\psi}_{(2)}$ or correction fluxes $\Delta\mathfrak{F}_{\rho\psi_{(1)}}$ and $\Delta\mathfrak{F}_{\rho\psi_{(2)}}$ for two of these conserved quantities are known. Corrective updates can then be determined from the resulting fluxes according to

$$\Delta\overline{\rho\psi} = -\sum_{\mathfrak{f}=1}^{2\mathfrak{d}} \Delta\mathfrak{F}_{\rho\psi,\mathfrak{f}} = -\frac{\Delta t}{\mathfrak{h}} \sum_{\mathfrak{d}=1}^{\mathfrak{d}} \frac{1}{\mathfrak{c}_{\mathfrak{d}}} \sum_{\mathfrak{w}=1}^{2} \left[\frac{\Delta\mathfrak{F}_{\rho\psi}}{\mathfrak{v}} \right]_{\mathfrak{d},\mathfrak{w}} = -\frac{\Delta t}{\mathfrak{h}} \sum_{\mathfrak{d}=1}^{\mathfrak{d}} \frac{1}{\mathfrak{c}_{\mathfrak{d}}} \sum_{\mathfrak{w}=1}^{2} \Delta\widetilde{\overline{\mathcal{F}}}_{\rho\psi,\mathfrak{d},\mathfrak{w}} \tag{6.100}$$

as done during both the predictor time evolution step and the corrector steps from chapter 5. For Cartesian grids, the sum over all cell faces in the previous equation indexed $\mathfrak{f}$ can be split into a sum over the coordinate directions ($\mathfrak{d}$) and a sum over the cell faces per coordinate direction ($\mathfrak{w}$).

6.5.2.2 Specific Consistent Correction Scheme

With definition (3.141) the two quantities with known – or at least determinable – corrections required for determination of correction fluxes according to section 6.5.2.1 are found in $\rho\psi_{(1)} := \mathcal{P} = \rho\Theta$ and $\rho\psi_{(2)} := \mathcal{P}\phi = \rho\Theta\phi$ as described in the following:

Since potential deviations in $\overline{\mathcal{P}}$ due to divergence errors are corrected in the first projection step in the corrector for any type of grid cell, $\overline{\mathcal{P}}$ is left untouched during the present correction procedure. Therefore,

$$\Delta\overline{\mathcal{P}} \equiv 0 \tag{6.101}$$

and, thus, $\Delta\overline{\rho\psi}_{(1)} = \Delta\overline{\mathcal{P}} \equiv 0$. While in general (6.101) does not mean, that each of

the contributing fluxes has to vanish, in the present case nevertheless

$$\Delta \mathfrak{F}_{\mathcal{P},\mathfrak{f}} \equiv 0 \tag{6.102}$$

has to hold for each corresponding correction flux $\Delta \mathfrak{F}_{\rho\psi_{(1)},\mathfrak{f}} = \Delta \mathfrak{F}_{\mathcal{P},\mathfrak{f}}$ across any involved grid cell face $\mathfrak{f}$ in order to leave the respective flux unchanged. This leaves

$$\left[\Delta \mathfrak{F}^{(\pm)}_{\text{ref}}\right]_{\mathfrak{f}} = \pm \mathcal{W}_{\mathfrak{f}} \Delta\overline{\rho\psi}_{(2)} = \pm \Delta \mathfrak{F}_{\rho\psi_{(2)},\mathfrak{f}} \tag{6.103}$$

from equation (6.97) to be determined for application to equation (6.99). The deviation of the volume-of-fluid variable $\overline{\mathcal{P}\phi}$ from its target value serves as second known increment $\Delta\overline{\rho\psi}_{(2)} = \Delta\overline{\mathcal{P}\phi}$. In this case, the scaling factor

$$\mathfrak{f}_{\mathfrak{f}} = \frac{1}{[\![\,\phi\,]\!]} \equiv 1 \tag{6.104}$$

remains and with

$$\left[\Delta \mathfrak{F}^{(\pm)}_{\text{ref}}\right]_{\mathfrak{f}} = \pm \mathcal{W}_{\mathfrak{f}} \Delta\overline{\mathcal{P}\phi} = \pm \Delta \mathfrak{F}_{\mathcal{P}\phi,\mathfrak{f}} \tag{6.105}$$

equation (6.99) transforms to

$$\Delta \mathfrak{F}_{\rho\psi,\mathfrak{f}} = \frac{1}{[\![\,\phi\,]\!]} \sum_{\varphi} \left(\left(\frac{\psi^{\varphi}}{\Theta^{\varphi}} \right)_{\mathfrak{f}} \left[\Delta \mathfrak{F}^{\varphi}_{\text{ref}}\right]_{\mathfrak{f}} \right) \tag{6.106}$$

$$= \left[\left(\frac{\psi^{(+)}}{\Theta^{(+)}} \right)_{\mathfrak{f}} \Delta \mathfrak{F}_{\mathcal{P}\phi,\mathfrak{f}} \right] + \left[\left(\frac{\psi^{(-)}}{\Theta^{(-)}} \right)_{\mathfrak{f}} \left(-\Delta \mathfrak{F}_{\mathcal{P}\phi,\mathfrak{f}} \right) \right] \tag{6.107}$$

for the correction fluxes of the remaining conserved quantities besides of $\mathcal{P}$ and $\mathcal{P}\phi$. While (6.102) retains the average overall flux of $\mathcal{P}$ on grid cell face $\mathfrak{f}$ to avoid changes of $\mathcal{P}$ maintaining (6.101), the flux $\Delta \mathfrak{F}_{\mathcal{P}\phi,j}$ is responsible for how this average flux of $\mathcal{P}$ is effectively distributed among the fluid phases as basis for the correction of all other conserved quantities.

Since the required corrections equal the negative discretization errors according to equation (6.83) and discretization errors are of the order of magnitude of the numerical method for determination of the time-average face fractions used as flux weights as examined in [150], first order accurate correction flux approximations are sufficient for removal of the leading order error. Therefore $\left(\frac{\psi^{(+)}}{\Theta^{(+)}}\right)_{\mathfrak{f}}$ and $\left(\frac{\psi^{(-)}}{\Theta^{(-)}}\right)_{\mathfrak{f}}$ at grid cell face $\mathfrak{f}$ can be approximated by first order accurate upwind values with respect

to the direction of the corresponding reference fluxes (6.105), which remain to be determined based on the not yet specified volume-of-fluid based target values $\overline{\mathcal{P}\phi}^{\oplus}$.

6.5.2.3 Volume-of-Fluid Target Value

Disturbed volume-of-fluid values $\overline{\mathcal{P}\phi}^{\star}$, indicated by $\star$, can end up beyond the reasonable value range after each update involving flux splitting (6.76) at grid cell faces which have been cut during the time interval considered. Since this potential over-/undershooting effectively means integration over control volumes and cell faces fractions of wrong size as sketched in ***Fig. 6.15*** with dashed lines, in general only corresponding values $\overline{\mathcal{P}\phi}_G$, based on geometric information due to the level-set, indicated by subscript G, can be reasonably split according to

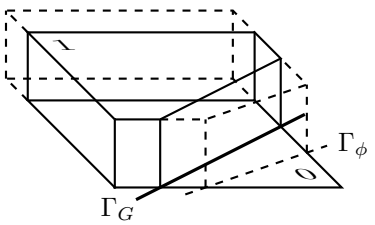

Fig. 6.15: Phase separation due to uncorrected level-set (G, *solid*) and volume-of-fluid (ϕ, *dashed*) information

$$\overline{\mathcal{P}\phi}_G = \alpha_G\, \overline{\mathcal{P}\phi}_G^{(+)} + (1-\alpha_G)\; \overline{\mathcal{P}\phi}_G^{(-)} \tag{6.108}$$

as shown for an arbitrary integral average in appendix section B.3. In equation (6.108)

$$\alpha_G = \alpha_G^{(+)} = \frac{\int_{\Omega_G^{(+)}} \mathrm{d}V}{\int_{\Omega} \mathrm{d}V} \tag{6.109}$$

is the level-set based volume fraction, which always remains bounded within $0 \leqslant \alpha_G \leqslant 1$, and $\overline{\mathcal{P}\phi}_G^{(+)}$ and $\overline{\mathcal{P}\phi}_G^{(-)}$ are the corresponding level-set based averages

$$\overline{\mathcal{P}\phi}_G^{\varphi} := \frac{\int_{\Omega_G^{\varphi}} (\mathcal{P}\phi)_G\,(\vec{x},t)\; \mathrm{d}V}{\int_{\Omega_G^{\varphi}} \mathrm{d}V} = \frac{\int_{\Omega_G^{\varphi}} (\mathcal{P}\phi)^{\varphi}\,(\vec{x},t)\; \mathrm{d}V}{\int_{\Omega_G^{\varphi}} \mathrm{d}V} \tag{6.110}$$

in the respective fluid phases. As $\phi^{(+)}$ and $\phi^{(-)}$ are constants within the corresponding fluid phases, relation (6.108) equals

$$\overline{\mathcal{P}\phi}_G = \alpha_G\, \phi^{(+)}\, \overline{\mathcal{P}}_G^{(+)} + (1-\alpha_G)\; \phi^{(-)}\, \overline{\mathcal{P}}_G^{(-)} \tag{6.111}$$

assuming a general scalar $\mathcal{P}$ with interface discontinuity at first, depending on both

space and time. Equation (6.111) can also be written as[7]

$$\overline{\mathcal{P}\phi}_G = \overline{\mathcal{P}}_G \left[\alpha_G\, \phi^{(+)} + (1-\alpha_G)\ \phi^{(-)}\right] + [\![\, \phi \,]\!]\, \alpha_G\, (1-\alpha_G) \left(\overline{\mathcal{P}}_G^{(+)} - \overline{\mathcal{P}}_G^{(-)}\right) \tag{6.112}$$

due to the identity

$$\phi^{(+)} \equiv \alpha_G\, \phi^{(+)} + (1-\alpha_G)\ \phi^{(+)} \tag{6.113}$$

and the relation

$$\overline{\mathcal{P}}_G = \alpha_G\, \overline{\mathcal{P}}_G^{(+)} + (1-\alpha_G)\ \overline{\mathcal{P}}_G^{(-)} \tag{6.114}$$

with

$$\overline{\mathcal{P}}_G^{\varphi} := \frac{\int_{\Omega_G^{\varphi}} \mathcal{P}\,(\vec{x},t)\ \mathrm{d}V}{\int_{\Omega_G^{\varphi}} \mathrm{d}V} \tag{6.115}$$

according to appendix section B.3.

The correction procedure described here in section 6.5.2 is applied each time fluxes at cut grid cell faces have been determined throughout the time stepping procedure in order to provide corrected information with sharply separated flow quantities for the subsequent sub-step. As $\overline{\mathcal{P}}_G$ does not necessarily correspond to the expected value at the corresponding time level after each of the individual sub-steps (e.g. before the first corrector step), $\overline{\mathcal{P}}_G$ can be split into its target value $\overline{\mathcal{P}}_G^{\oplus}$ at the respective time level and the current deviation $\Delta\overline{\mathcal{P}}_G := \overline{\mathcal{P}}_G - \overline{\mathcal{P}}_G^{\oplus}$. With that, equation (6.112) transforms to

$$\begin{aligned}
\overline{\mathcal{P}\phi}_G^{\bigstar,\circ} = {} & \overline{\mathcal{P}}_G^{\oplus,\circ} \left[\alpha_G^{\bigstar,\circ}\, \phi^{(+)} + \left(1-\alpha_G^{\bigstar,\circ}\right)\ \phi^{(-)}\right] \\
& + \left(\overline{\mathcal{P}}_G^{\circ} - \overline{\mathcal{P}}_G^{\oplus,\circ}\right) \left[\alpha_G^{\bigstar,\circ}\, \phi^{(+)} + \left(1-\alpha_G^{\bigstar,\circ}\right)\ \phi^{(-)}\right] \\
& + [\![\, \phi \,]\!]\, \alpha_G^{\bigstar,\circ} \left(1-\alpha_G^{\bigstar,\circ}\right) \left(\overline{\mathcal{P}}_G^{\oplus,(+)} - \overline{\mathcal{P}}_G^{\oplus,(-)}\right)^{\circ} \\
& + [\![\, \phi \,]\!]\, \alpha_G^{\bigstar,\circ} \left(1-\alpha_G^{\bigstar,\circ}\right) \left[\left(\overline{\mathcal{P}}_G^{\bigstar} - \overline{\mathcal{P}}_G^{\oplus}\right)^{(+),\circ} - \left(\overline{\mathcal{P}}_G^{\bigstar} - \overline{\mathcal{P}}_G^{\oplus}\right)^{(-),\circ}\right]
\end{aligned} \tag{6.116}$$

[7] $\overline{\mathcal{P}\phi}_G = \alpha_G\, \phi^{(+)}\, \overline{\mathcal{P}}_G^{(+)} + (1-\alpha_G)\ \phi^{(-)}\, \overline{\mathcal{P}}_G^{(-)}$
$= \alpha_G\, \phi^{(+)}\, \overline{\mathcal{P}}_G^{(+)} + \left[(1-\alpha_G)\ \phi^{(+)}\, \overline{\mathcal{P}}_G^{(-)} - (1-\alpha_G)\ \phi^{(+)}\, \overline{\mathcal{P}}_G^{(-)}\right] + (1-\alpha_G)\ \phi^{(-)}\, \overline{\mathcal{P}}_G^{(-)}$
$= \overline{\mathcal{P}}_G\, \phi^{(+)} - [\![\, \phi \,]\!]\, (1-\alpha_G)\ \overline{\mathcal{P}}_G^{(-)}$
$= \overline{\mathcal{P}}_G \left(\alpha_G\, \phi^{(+)} + (1-\alpha_G)\ \phi^{(+)}\right) - [\![\, \phi \,]\!]\, (1-\alpha_G)\ \overline{\mathcal{P}}_G^{(-)}$
$= \overline{\mathcal{P}}_G \left(\alpha_G\, \phi^{(+)} + (1-\alpha_G)\ \phi^{(-)}\right) + [\![\, \phi \,]\!]\, (1-\alpha_G)\ \left(\overline{\mathcal{P}}_G - \overline{\mathcal{P}}_G^{(-)}\right)$
$= \overline{\mathcal{P}}_G \left(\alpha_G\, \phi^{(+)} + (1-\alpha_G)\ \phi^{(-)}\right) + [\![\, \phi \,]\!]\, (1-\alpha_G)\ \left(\alpha_G\, \overline{\mathcal{P}}_G^{(+)} + (1-\alpha_G)\ \overline{\mathcal{P}}_G^{(-)} - \overline{\mathcal{P}}_G^{(-)}\right)$
$= \overline{\mathcal{P}}_G \left(\alpha_G\, \phi^{(+)} + (1-\alpha_G)\ \phi^{(-)}\right) + [\![\, \phi \,]\!]\, \alpha_G\, (1-\alpha_G)\ \left(\overline{\mathcal{P}}_G^{(+)} - \overline{\mathcal{P}}_G^{(-)}\right)$

with superscript $\star$ indicating, that the level-set function $G = G^\star$ is not yet corrected as well, and superscript $\circ$ representing any of the superscripts n, $n+1$, $\bullet$, $*$ and $**$ with $\bullet$, $*$ and $**$ indicating different incomplete intermediate states at time level $n+1$ after the first predictor stage ($\bullet$), after the full predictor ($*$) and after the first correction step ($**$). The third line of the right hand side of (6.116) is the contribution due to the final gradient[8] of $\mathcal{P}$ at the corresponding stage $\circ$, causing different target values for the integral averages of $\mathcal{P}$ in the different fluid phases, and the last line represents the contribution due to current deviations from this gradient.

Due to spatial homogeneity of $\mathcal{P}$ as given in section 3.6, with deviations in $\overline{\mathcal{P}}$ from the constant value $\overline{\mathcal{P}}^{\oplus}_{G} \equiv \mathcal{P}_0$ only due to accumulated divergence errors, the relations

$$\nabla \mathcal{P} = 0 \tag{6.117}$$

$$[\![\, \mathcal{P} \,]\!] = 0 \tag{6.118}$$

hold, yielding

$$\begin{aligned}
\overline{\mathcal{P}\phi}_G^{\star,\circ} = {} & \overline{\mathcal{P}}_G^{\oplus,\circ} \left[\alpha_G^{\star,\circ}\ \phi^{(+)} + \left(1 - \alpha_G^{\star,\circ}\right)\ \phi^{(-)} \right] \\
& + \left(\overline{\mathcal{P}}_G^{\circ} - \overline{\mathcal{P}}_G^{\oplus,\circ} \right) \left[\alpha_G^{\star,\circ}\ \phi^{(+)} + \left(1 - \alpha_G^{\star,\circ}\right)\ \phi^{(-)} \right] \\
& + [\![\, \phi \,]\!]\, \alpha_G^{\star,\circ} \left(1 - \alpha_G^{\star,\circ}\right) \left[\left(\overline{\mathcal{P}}_G^{\star} - \overline{\mathcal{P}}_G^{\oplus} \right)^{(+),\circ} - \left(\overline{\mathcal{P}}_G^{\star} - \overline{\mathcal{P}}_G^{\oplus} \right)^{(-),\circ} \right]
\end{aligned} \tag{6.119}$$

due to

$$\left(\overline{\mathcal{P}}^{\oplus,(+)} - \overline{\mathcal{P}}^{\oplus,(-)} \right)^{\circ} \equiv 0 \tag{6.120}$$

for the present flow regime. Therefore,

- in regular grid cells in general, as well as
- in cut grid cells
  - at the beginning of the time step ($\overline{\mathcal{P}}^{\,\circ} \equiv \overline{\mathcal{P}}^{\oplus,\circ} \equiv \overline{\mathcal{P}}^{\,(n)}$),

[8] The difference of target values in the different fluid phases can be written as $\overline{\mathcal{P}}_G^{\oplus,(+)} - \overline{\mathcal{P}}_G^{\oplus,(-)}$
$= \mathcal{P}_c^{(+)} - \mathcal{P}_c^{(-)} + \mathcal{O}(\mathfrak{h}^2)$
$= \mathcal{P}_\Gamma^{(+)} - \nabla\mathcal{P}^{(+)}|_\Gamma \cdot \left(\vec{x}_\Gamma - \vec{x}_c^{\,(+)} \right) - \mathcal{P}_\Gamma^{(-)} + \nabla\mathcal{P}^{(-)}|_\Gamma \cdot \left(\vec{x}_\Gamma - \vec{x}_c^{\,(-)} \right) + \mathcal{O}(\mathfrak{h}^2)$
$= [\![\, \mathcal{P} \,]\!] - [\![\, \nabla\mathcal{P} \,]\!] \cdot \left(\vec{x}_\Gamma - \vec{x}_c^{\,(+)} \right) + \nabla\mathcal{P}_\Gamma^{(-)} \cdot \left(\vec{x}_c^{\,(+)} - \vec{x}_c^{\,(-)} \right) + \mathcal{O}(\mathfrak{h}^2)$
according to ***Fig. 6.8*** on page 171.

- after the first Runge-Kutta predictor time integrator stage ($\overline{\mathcal{P}}^{\circ} \equiv \overline{\mathcal{P}}^{\oplus,\circ} \equiv \overline{\mathcal{P}}^{\bullet}$) due to the use of the old time level velocity field during the first predictor stage,
- after the first corrector step ($\overline{\mathcal{P}}^{\circ} \equiv \overline{\mathcal{P}}^{\oplus,\circ} \equiv \overline{\mathcal{P}}^{**} = \overline{\mathcal{P}}^{n+1}$) since then all scalars are effectively treated with advective fluxes satisfying the divergence constraint (3.140)

equation (6.116) reduces to

$$\overline{\mathcal{P}\phi}_G^{\star,\circ} = \overline{\mathcal{P}}^{\circ}\,\overline{\phi}_G^{\star,\circ} = \overline{\mathcal{P}}^{\oplus,\circ}\,\overline{\phi}_G^{\star,\circ} \tag{6.121}$$

with generalized[9] volume fraction

$$\overline{\phi}_G^{\star,\circ} := \alpha_G^{\star,\circ}\,\phi^{(+)} + \left(1-\alpha_G^{\star,\circ}\right)\,\phi^{(-)} \tag{6.122}$$

due to $\overline{\mathcal{P}}^{\oplus,\circ} \equiv \overline{\mathcal{P}}^{\circ}$ both in each fluid phase and in the entire grid cell. Therefore, the level-set based value $\overline{\mathcal{P}\phi}_G^{\star,\circ}$ is within the valid range

$$\overline{\mathcal{P}}^{\oplus,\circ}\min\left(\phi^{(+)},\phi^{(-)}\right) \;\leqslant\; \overline{\mathcal{P}\phi}_G^{\star,\circ} \;\leqslant\; \overline{\mathcal{P}}^{\oplus,\circ}\max\left(\phi^{(+)},\phi^{(-)}\right) \tag{6.123}$$

for all the cases listed above.

In cut grid cells (C) at stage $*$ (after the first predictor stage, but before the first projection step), however, in general $\overline{\mathcal{P}}^{\oplus,*} \neq \overline{\mathcal{P}}^{*}$ is true, making the expressions in the second and third line of equation (6.116) non-zero. Due to the second line the quantity $\overline{\mathcal{P}}$ in (6.123) has to be replaced by $\overline{\mathcal{P}}^{*}$. In addition, since

- both second and third line of the right hand side of (6.119) are zero at the beginning of the time step (and, thus, at the end of the previous one) and
- time step local deviations from a scalar integral average of a homogeneous quantity without interfacial discontinuity are of $\mathcal{O}(\mathfrak{h}^3)$ accuracy after the entire second order accurate predictor step as the quantity is treated in a singe-phase fashion,

[9] For the choice of $\phi^{(+)} := 1$ and $\phi^{(-)} := 0$ (6.122) reduces to $\overline{\phi}_G^{\star,\circ} = \alpha^{\star,\circ}$ representing the volume fraction in fluid phase $(+)$ as given based on level-set information. Nevertheless, during the present derivation the more general notation is kept.

the relation

$$\begin{aligned}\overline{\mathcal{P}\phi}_G^{\star,*} &= \overline{\mathcal{P}}^{\,*}\,\overline{\phi}_G^{\star,*} + \mathcal{O}(\mathfrak{h}^3)\\ &= \overline{\mathcal{P}}^{\,*}\,\overline{\phi}_G^{\star,n+1} + \mathcal{O}(\mathfrak{h}^3)\end{aligned} \tag{6.124}$$

with

$$\overline{\mathcal{P}}^{\,*}\min\left(\phi^{(+)},\phi^{(-)}\right) - \mathcal{O}(\mathfrak{h}^3) \;\leqslant\; \overline{\mathcal{P}\phi}_G^{\star,*} \;\leqslant\; \overline{\mathcal{P}}^{\,*}\max\left(\phi^{(+)},\phi^{(-)}\right) + \mathcal{O}(\mathfrak{h}^3) \tag{6.125}$$

is obtained in each time step, for example immediately after the predictor is completed, exceeding the limits from relation (6.123). Keeping $\overline{\mathcal{P}\phi}^{\,*}$ bounded according to (6.123) at any stage $\circ$ of the numerical time step via (6.121), thus, introduces an $\mathcal{O}(\mathfrak{h}^3)$ error if applied to cut grid cells at stage $*$. This error does not appear in all other cases as listed on page 191 and is especially limited to cut grid cells. This contribution vanishes, if (6.117) can be assumed to hold at any stage of the numerical method, yielding

$$\overline{\mathcal{P}}^{\,\circ}\min\left(\phi^{(+)},\phi^{(-)}\right) \;\leqslant\; \overline{\mathcal{P}\phi}_G^{\star,\circ} \;\leqslant\; \overline{\mathcal{P}}^{\,\circ}\max\left(\phi^{(+)},\phi^{(-)}\right) \tag{6.126}$$

as bounds for the values to be determined. The level set-based integral average $\overline{\mathcal{P}\phi}_G^{\star,\circ}$, nevertheless, involves a conservation related deviation in cut grid cells in general due to not yet corrected level-set discretization errors as stated in section 6.1.1. This deviation only vanishes, if evaluated at time level n with level-set correction being performed in the previous time step or after level-set correction in the current time step is already applied. Thus, while directly serving as target value in all grid cells, which end up regular (= not intersected by the interface) at the end of the time interval, $\overline{\mathcal{P}\phi}_G^{\star,\circ}$ according to (6.121) can not be used as target value in cut grid cells. As shown below in section 6.5.2.4, during reference correction flux determination, however, it can be used as bounded reference value for construction of a conservation maintaining target value for cut grid cells at time level $n+1$ anyway.

6.5.2.4 Reference Correction Flux Determination

As already indicated in the previous section 6.5.2.3, it is necessary for the present correction scheme to distinguish between different types of grid cells based on the interface representation due to the level-set. The following sub-sections address reference correction flux computation across faces of grid cells of these different types.

In this regard, grid cells are called

- "regular" (R) within the time interval $\Delta\mathfrak{T} = [t^n, t^{n+1}]$, if they are never intersected by the (level-set based) interface Γ during $\Delta\mathfrak{T}$ (type $0/0$ cells)[10],
- "abandoned" (A), if they have been intersected at any point in time during time interval $\Delta\mathfrak{T}$, but not anymore at its end at time level $n+1$ (type $1/0$ cells) and
- "cut" (C), if they end up intersected by the (level-set based) interface Γ at time level $n+1$ (type $0/1$, type $1/1$ and type $1/0/1$ cells)

as shown in ***Fig. 6.16***, taken from [182].

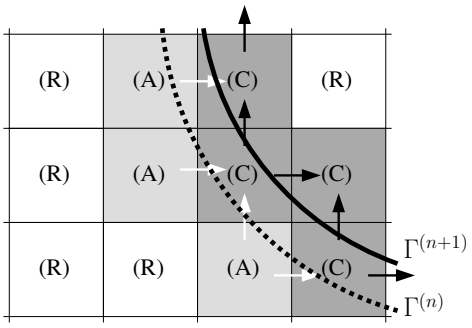

Fig. 6.16: Cartesian grid cell types: (A) abandoned, (C) cut, (R) regular, and possible correction fluxes (*white arrows*: (A), *black arrows*: (C)) at time level $n+1$ in the vicinity of a moving interface Γ; (from [182] (`https://dx.doi.org/10.1007/978-3-319-05684-5_45`) with permission of Springer)

6.5.2.4 - 1 Regular Grid Cells (R)

Regular grid cells, which never have been cut by the interface during $\Delta\mathfrak{T}$, do not need any interface discretization related correction, since these cells do not suffer from an interface related discretization error due to weighted flux splitting (6.76), as only standard single-phase Finite Volume procedures are applied for flux and update computation. Thus, corrections for all conserved quantities in all type (R) cells are zero and these cells do not have to be treated.

In particular, correction fluxes between (R) cells and neighboring cells of any type need to vanish. This way all (R) cells are left unaffected by the correction procedure and the region, in which correction is required, is decoupled from the regular surrounding. This decoupling keeps the correction problem interface local and is achieved by setting

$$\mathcal{W}_{\mathfrak{f}} \equiv 0 \tag{6.127}$$

[10] Cells of type $0/1/0$ are also considered as (R) cells since the numerical method is not able to resolve the intersection within the time interval and, thus, no split fluxes at cut grid cell faces are computed.

on each grid cell face $\mathfrak{f}$ of all type (R) cells in equation (6.105).

6.5.2.4 - 2 Abandoned Grid Cells (A)

In grid cells, which are left by the interface Γ during $\Delta\mathfrak{T}$, with only one fluid phase remaining in the so-called abandoned grid cell at the end of $\Delta\mathfrak{T}$, the volume-of-fluid target value is immediately given by

$$\overline{\mathcal{P}\phi}^{\oplus,\circ} = \overline{\mathcal{P}}^{\circ}\,\overline{\phi}_G^{\star,\circ} \tag{6.128}$$

as shown in section 6.5.2.3. This allows for a *local* correction approach due to either $\overline{\phi}_G^{\star,\circ} = \phi^{(+)}$ or $\overline{\phi}_G^{\star,\circ} = \phi^{(-)}$, depending on which fluid phase is left in the respective type (A) grid cell with either $\alpha^{\star,\circ} = 0$ or $\alpha^{\star,\circ} = 1$. Instead of directly resetting $\overline{\mathcal{P}\phi}$ to its target value via addition of the known correction

$$\Delta\overline{\mathcal{P}\phi}^{\circ} = -\left(\overline{\mathcal{P}\phi}^{\star,\circ} - \overline{\mathcal{P}\phi}^{\oplus,\circ}\right) = \overline{\mathcal{P}}^{\circ}\,\overline{\phi}_G^{\star,\circ} - \overline{\mathcal{P}\phi}^{\star,\circ} \tag{6.129}$$

to the disturbed value $\overline{\mathcal{P}\phi}^{\star,\circ}$, reference correction fluxes between type (A) and type (C) cells are determined via equation (6.105) as sketched in ***Fig. 6.17***, allowing for correction of the other conserved quantities accordingly as described in sections 6.5.2.1 and 6.5.2.2. This step is crucial in order to avoid development of a wake of intermediate and/or under- or overshooting phase indicator values over time – primarily in upwind direction with respect to the interface as shown in ***Fig. 6.29*** on page 234 in the results section 6.5.6 – and to prevent smearing of the conserved quantities around the interface and loss of sharp fluid phase separation.

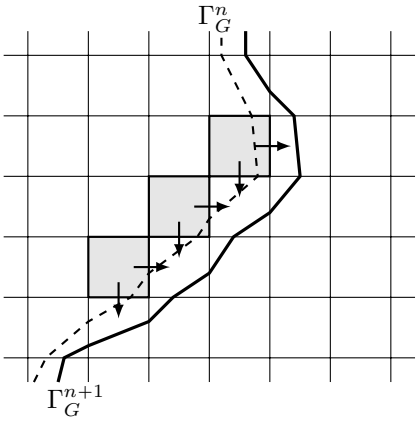

Fig. 6.17: Abandoned grid cells (A), depending on the movement of the explicit level-set based approximation of the interface Γ

The weights $\mathcal{W}_\mathfrak{f}$ in (6.105) need to satisfy (6.90) for conservative error distribution, which is given by default, if

$$\mathcal{W}_\mathfrak{f} := \frac{W_\mathfrak{f}}{\sum_i W_i} \tag{6.130}$$

with arbitrary (non-negative) weights $W_\mathfrak{f}$ is defined. However, only grid cell faces cut

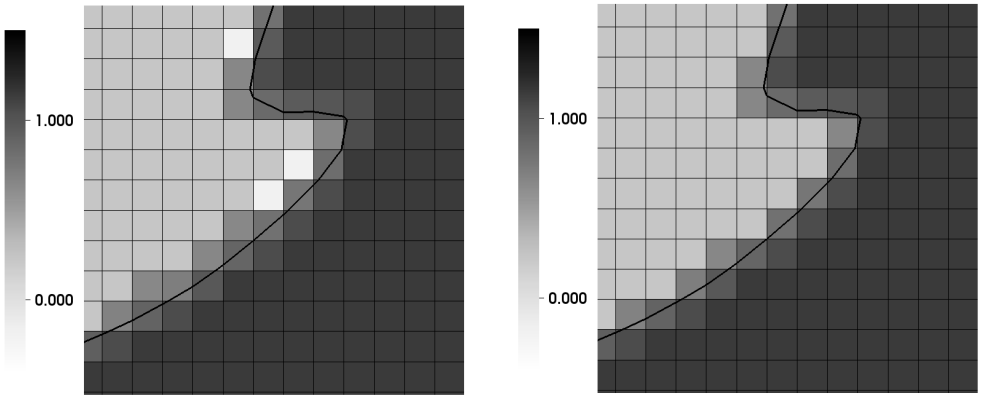

Fig. 6.18: $\overline{\mathcal{P}\phi}/\overline{\mathcal{P}}$, ***left:*** before correction with two intermediate-valued and three undershooting (*white*) type (A) cells, ***right:*** after correction in type (A) cells

or run over by the interface during $\Delta\mathfrak{T}$ are allowed to have non-zero fluxes and, thus, non-zero weights $W_{\mathfrak{f}}$. This avoids influence on other neighboring (A) or (R) cells, as only (C) cells are possible exchange partners. ***Fig. 6.18*** shows $\frac{\overline{\mathcal{P}\phi}}{\overline{\mathcal{P}}}$ of a scenario from a simulation performing the present correction scheme, in which three undershooting (white) and two intermediate-valued (A) cells (second full cell from left in fourth row from bottom and fifth full cell from left in sixth row from bottom) need to be corrected in the left plot. The setting after correction of (A) cells is shown in the right plot. Due to the CFL stability condition [37] for the explicit predictor part, an abandoned grid cell has at least one cut neighbor cell in a well resolved setting[11]. In order to be able to treat slightly under-resolved settings as well, the present correction step is embedded into a loop, which first checks, whether or not there are type (A) cells, which have no type (C) face neighbor, and if such cells are found, the present correction step is applied to these cells in a first cycle as shown in ***Fig. 6.19***, with standard[12] type (A) cells in-

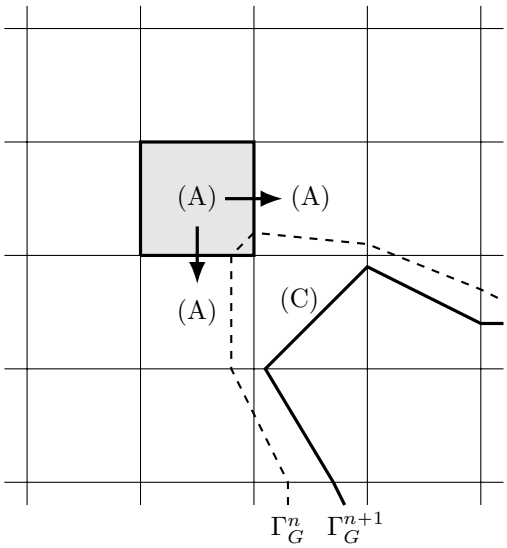

Fig. 6.19: Type (A) cell for which no type (C) face neighbor is available

[11] Treatment of under-resolved settings is discussed in section 7.2.
[12] Type (A) cells which have at least one type (C) face neighbor cell.

stead of type (C) cells as exchange partners, before the latter are corrected.

Non-physical over- or undershoots in neighboring type (C) cells, however, could only be avoided in general, if exactly that weighting was used, that is responsible for the discretization error due to weighted flux splitting (6.76).

This, however, is not possible to reproduce by the present correction scheme in an directionally unsplit method, since fluxes across grid cell faces, which do not have a cut neighbor cell at the end of $\Delta\mathfrak{T}$ anymore, might have contributed to the present errors. This happens, if a grid cell face, which is not cut at time level $n+1$ anymore, has been cut at any point in time during $\Delta\mathfrak{T}$. Yet, to keep possibly resulting temporary over- and undershoots in cut grid cells (which are corrected in the subsequent step described in section 6.5.2.4 - 3) as small and the resulting error distribution in cut grid cells as smooth as possible,

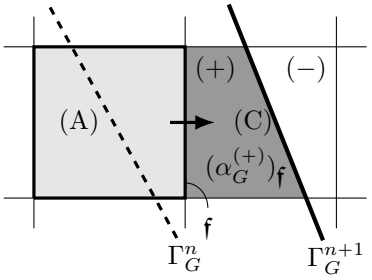

Fig. 6.20: Type (A) cell for which type (C) face neighbor is available

$$W_\mathfrak{f} := \left(\alpha_G^{(\pm)}\right)_\mathfrak{f} \tag{6.131}$$

is chosen[13], with $\left(\alpha_G^{(\pm)}\right)_\mathfrak{f}$ being the level-set based volume fraction of that part of the neighboring type (C) cell sharing grid cell face $\mathfrak{f}$, which is within the same fluid phase as the type (A) cell considered, as sketched in ***Fig. 6.20***. Due to (6.130) and (6.131) each surrounding receiver cell accepts contributions according to its fraction within the respective fluid phase, keeping the relative change due to the error shift into receiver cells equally distributed while resetting $\overline{\mathcal{P}\phi}$ in type (A) cells exactly to its target value.

With equations (6.129), (6.130) and (6.131), the reference correction fluxes (6.105) can be determined and end up zero on grid cell faces shared with type (R) or other type (A) cells, and non-zero only on grid cell faces shared with type (C) cells. Based on these reference fluxes, correction fluxes for each conserved quantity $\rho\psi$ can be computed between type (A) and type (C) via (6.106), and corrective updates can be determined according to standard Finite Volume procedures based on these fluxes.

[13] Investigation of effects of different weightings $W_\mathfrak{f}$ is subject to future research.

6.5.2.4 - 3 Cut Grid Cells (C)

After volume-of-fluid values $\overline{\mathcal{P}\phi}$ – and with those all other conserved quantities – have been completely corrected with respect to (6.123) in type (A) cells, based on correction fluxes according to (6.106), errors in the distribution of both $\overline{\mathcal{P}\phi}$ and any other conserved quantity $\rho\psi$ remain contained in cut grid cells (C) only. If correction of these errors is done conservatively, the sum of all inappropriately distributed $\overline{\mathcal{P}\phi}^{\star,\circ}$ in the $\mathcal{N}_{\mathfrak{C}}$ cut cells equals the sum of the corrected, yet unknown, distribution of $\overline{\mathcal{P}\phi}^{\oplus,\circ}$, and therefore

$$\sum_{\mathfrak{c}=1}^{\mathcal{N}_{\mathfrak{C}}} \overline{\mathcal{P}\phi}_{\mathfrak{c}}^{\star,\circ} = \sum_{\mathfrak{c}=1}^{\mathcal{N}_{\mathfrak{C}}} \overline{\mathcal{P}\phi}_{\mathfrak{c}}^{\oplus,\circ} \tag{6.132}$$

holds. However, due to unknown target values for the generalized level-set based volume fraction $\overline{\phi}_G^{\star,\circ}$ in cut grid cells[14], the target value $\overline{\mathcal{P}\phi}^{\oplus,\circ}$ is not as trivially available as for the type (A) cells in (6.129). Further, the weight $\mathcal{W}_{\mathfrak{f}}$ for error distribution based reference correction flux computation on grid cell face $\mathfrak{f}$ via (6.105) cannot be determined locally uniquely, since values in possible neighboring exchange partner cells, which are type (C) cells as well, are – in contrast to the correction of type (A) cells – also subject to be corrected as sketched in ***Fig. 6.21***.

This leads to a *non-local spatial coupling*, limited to type (C) cells only, as all other cells can not serve as receiver cells for errors from neighboring grid cells anymore. Defining

$$\Delta\mathfrak{F}_{\mathcal{P}\phi,\mathfrak{f}}^{(C)} := \frac{\Delta t}{\Delta V}\Delta A_{\mathfrak{f}}\,(\nabla\mathcal{Y}\cdot\vec{n})_{\mathfrak{f}} \tag{6.133}$$

with unknown scalar $\mathcal{Y}$ for each cut grid cell (C), a Poisson-type problem for obtaining correction fluxes $\Delta\mathfrak{F}_{\mathcal{P}\phi}^{(C)}$ between cut grid cells can be defined, applying vanishing Neumann-type boundary conditions to all grid cell faces, which are

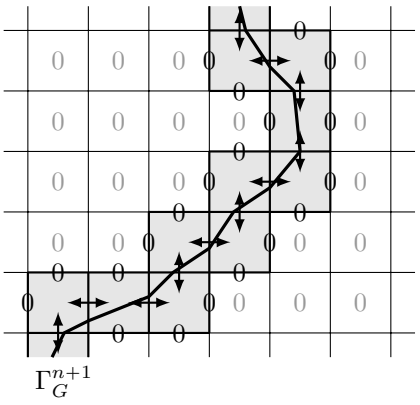

Fig. 6.21: Cut grid cells (C) after interface movement and correction in type (A) cells; possible exchange partner cells for type (C) correction are linked via arrows

[14] The volume fraction $\alpha_G^{\star,\circ}$, needed for determination of the generalized level-set based volume fraction $\overline{\phi}_G^{\star,\circ}$ according to relation (6.122), has not yet reached its final value as well, as described in section 6.5.2.3.

not shared by two type (C) cells as indicated in ***Fig. 6.21***, in order to force the fluxes across such grid cell faces to vanish. This is similar to the problem solved in [152] and [150] for both type (C) and (A) cells – called "mixed cells" there – at once, yielding

$$\left(\sum_{\mathfrak{f}} \Delta \mathfrak{F}^{(C)}_{\mathcal{P}\phi,\mathfrak{f}} \right)_{\mathfrak{c}} = \Delta \overline{\mathcal{P}\phi}_{\mathfrak{c}} = - \left(\overline{\mathcal{P}\phi}^{\star,\circ} - \overline{\mathcal{P}\phi}^{\oplus,\circ} \right)_{\mathfrak{c}} \tag{6.134}$$

for each cut grid cell, indexed $\mathfrak{c}$. While the level-set based value $\overline{\mathcal{P}}^{\circ}\, \overline{\phi}_G^{\star,\circ}$ cannot serve as target value $\overline{\mathcal{P}\phi}^{\oplus,\circ}$ in type (C) cells directly without violating conservation, definition of the **target value**

$$\overline{\mathcal{P}\phi}_{\mathfrak{c}}^{\oplus,\circ} := \overline{\mathcal{P}}_{\mathfrak{c}}^{\circ}\, \overline{\phi}_{G,\mathfrak{c}}^{\star,\circ} + \delta \overline{\mathcal{P}\phi}_{\mathfrak{c}}^{\oplus,\circ} \tag{6.135}$$

does maintain conservation, if the **local adjustment** is chosen to be

$$\delta \overline{\mathcal{P}\phi}_{\mathfrak{c}}^{\oplus,\circ} := \left(\frac{\varkappa_{\mathfrak{c}}^{\circ}}{\sum_{\tilde{\mathfrak{c}}=1}^{\mathcal{N}_{\mathfrak{C}}} \varkappa_{\tilde{\mathfrak{c}}}^{\circ}} \right) \Delta \overline{\mathcal{P}\phi}_{\mathfrak{C}} \tag{6.136}$$

wherein the **global deviation**

$$\Delta \overline{\mathcal{P}\phi}_{\mathfrak{C}} := \sum_{\mathfrak{c}=1}^{\mathcal{N}_{\mathfrak{C}}} \delta \overline{\mathcal{P}\phi}_{\mathfrak{c}}^{\star,\circ} \tag{6.137}$$

is the sum of the **local deviation**s between uncorrected volume-of-fluid and level-set based values

$$\delta \overline{\mathcal{P}\phi}_{\mathfrak{c}}^{\star,\circ} := \overline{\mathcal{P}\phi}_{\mathfrak{c}}^{\star,\circ} - \overline{\mathcal{P}}_{\mathfrak{c}}^{\circ}\, \overline{\phi}_{G,\mathfrak{c}}^{\star,\circ} \tag{6.138}$$

over all $\mathcal{N}_{\mathfrak{C}}$ type (C) cells of a closed contour and $\varkappa$ is a yet arbitrary weight. Maintenance of conservation can be checked easily, independent of $\varkappa$, by summing equation (6.135) with (6.136) to (6.138) over all $\mathcal{N}_{\mathfrak{C}}$ type (C) cells, taking into account that

$$\sum_{\mathfrak{c}=1}^{\mathcal{N}_{\mathfrak{C}}} \delta \overline{\mathcal{P}\phi}_{\mathfrak{c}}^{\star,\circ} \equiv \sum_{\mathfrak{c}=1}^{\mathcal{N}_{\mathfrak{C}}} \overline{\mathcal{P}\phi}_{\mathfrak{c}}^{\oplus,\circ} - \sum_{\mathfrak{c}=1}^{\mathcal{N}_{\mathfrak{C}}} \overline{\mathcal{P}}_{\mathfrak{c}}^{\circ}\, \overline{\phi}_{G,\mathfrak{c}}^{\star,\circ} \tag{6.139}$$

holds due to relation (6.132). Once $\varkappa$ in (6.136) is specified properly, the **resulting Poisson-type problem with vanishing Neumann boundary conditions for type**

(C) cells

$$\Delta t \left(\frac{1}{\Delta V} \sum_{\mathfrak{f}} \Delta A_{\mathfrak{f}} \left(\nabla \mathcal{Y} \cdot \vec{n} \right)_{\mathfrak{f}} \right)_{\mathfrak{c}} = \delta \overline{\mathcal{P}\phi}_{\mathfrak{c}}^{\oplus,\circ} - \delta \overline{\mathcal{P}\phi}_{\mathfrak{c}}^{\star,\circ} \tag{6.140}$$

is solved for $\mathcal{Y}$ in the entire computational domain by enforcing a trivial zero solution in all un-cut grid cells (type (R) and (A) cells) and by decoupling the type (C) cells from the surrounding via zero fluxes between cut and un-cut grid cells, representing the vanishing Neumann-type boundary condition as shown in ***Fig. 6.21***.

The discrete left hand side contributions

$$\Delta t \left(\frac{1}{\Delta V} \sum_{\mathfrak{d}=1}^{\mathfrak{D}} \frac{\Delta A_{\mathfrak{d}}}{\mathfrak{c}_{\mathfrak{d}}\mathfrak{h}} \left(\mathcal{Y}_{(i,j,k)+\vec{\mathfrak{e}}_{\mathfrak{d}}} - 2\,\mathcal{Y}_{(i,j,k)} + \mathcal{Y}_{(i,j,k)-\vec{\mathfrak{e}}_{\mathfrak{d}}} \right) \right) \tag{6.141}$$

of (6.140) to the resulting matrix from a single type (C) cell (i, j, k) on the Cartesian grid, with $k = 1$ in the two-dimensional case $\mathfrak{d} = 2$, result from discretization of the grid cell face normal gradient $\nabla \mathcal{Y} \cdot \vec{n}$ on grid cell faces via divided differences of cell center values. Care has to be taken at grid cell faces, which do not contribute a non-zero correction flux. While (6.141) assumes, that each of the grid cell faces, and therefore each neighbor cell, is involved in the corrective exchange, the latter is only allowed between neighboring type (C) cells. Therefore the resulting global matrix needs to be modified in order to separate type (C) cells from the already corrected surrounding and suppress correction fluxes to (R) and (A) cells. If each neighbor cell is involved (such as for a standard global Poisson problem), the corresponding diagonal matrix entry has the value $-2\,\mathfrak{d}$, while $2\,\mathfrak{d}$ entries of value 1 can be found in each matrix row and each matrix column the diagonal entry belongs to. To exclude (R) and (A) cells, as they are not involved in the present corrective exchange, first each matrix row, belonging to a (R) or (A) cell is overwritten with zeros besides of a matrix diagonal element of 1. Since the right hand side of (6.140) is zero for these grid cells, an initial zero solution does not change during the solution process, if the (R) and (A) cells are completely decoupled from the (C) cells. To achieve that, all off-diagonal matrix entries in columns with diagonal element of value 1 need to be zero for a complete decoupling. Now only exchange between type (C) cells is possible. The reduced Poisson type problem is solved on the entire domain. While all (R) and (A) cells just keep their initial (zero) solution, redistribution of $\overline{\mathcal{P}\phi}$ is done among type (C) cells only.

The resulting right hand side of equation (6.140) is the cut cell local difference between the representations of $\overline{\mathcal{P}\phi}$ due to level-set and volume-of-fluid information, adjusted by a certain fraction of the sum of the very same difference over all type (C) cells. The relative formulation $\varkappa_{\mathfrak{c}}^{\circ}\left(\sum_{\tilde{\mathfrak{c}}=1}^{\mathcal{N}_{\mathbb{C}}}\varkappa_{\tilde{\mathfrak{c}}}^{\circ}\right)^{-1}$ in equation (6.136) with

$$\sum_{\mathfrak{c}=1}^{\mathcal{N}_{\mathbb{C}}}\left(\frac{\varkappa_{\mathfrak{c}}^{\circ}}{\sum_{\tilde{\mathfrak{c}}=1}^{\mathcal{N}_{\mathbb{C}}}\varkappa_{\tilde{\mathfrak{c}}}^{\circ}}\right) \equiv \frac{\sum_{\mathfrak{c}=1}^{\mathcal{N}_{\mathbb{C}}}\varkappa_{\mathfrak{c}}^{\circ}}{\sum_{\tilde{\mathfrak{c}}=1}^{\mathcal{N}_{\mathbb{C}}}\varkappa_{\tilde{\mathfrak{c}}}^{\circ}} \equiv 1 \tag{6.142}$$

already guarantees maintenance of conservation and the solvability condition for (6.140) is satisfied by default, as the sum of its right hand side over all type (C) cells vanishes, leading to a vanishing sum of the right hand side over the entire computational domain due to only non-zero contributions in cut grid cells.

Once (6.140) is solved, the fluxes (6.133) can be determined from the resulting cell center values of $\mathcal{Y}$ via the divided differences used for discretization of $\nabla\mathcal{Y}\cdot\vec{n}$ on each grid cell face for obtaining (6.141).

However, the weight $\varkappa$, which still remains to be determined, needs to be specified such that the target value $\overline{\mathcal{P}\phi}^{\oplus,\circ}$ from (6.135) is within the range given in (6.123). Further, change of cell type has to be avoided in each grid cell since grid cells of type (R) and (A) are not allowed to be affected anymore. Thus, the conditions

$$\overline{\mathcal{P}}^{\circ}\max\left(\phi^{(+)},\phi^{(-)}\right)-\overline{\mathcal{P}\phi}^{\oplus,\circ} > 0 \tag{6.143a}$$

$$\overline{\mathcal{P}}^{\circ}\min\left(\phi^{(+)},\phi^{(-)}\right)-\overline{\mathcal{P}\phi}^{\oplus,\circ} < 0 \tag{6.143b}$$

have to be satisfied in order to meet (6.123). With relation (6.135) and the definition

$$\overline{\phi}^{\oplus,\circ} := \frac{\overline{\mathcal{P}\phi}^{\oplus,\circ}}{\overline{\mathcal{P}}^{\circ}} \tag{6.144}$$

as well as

$$\max\left(\phi^{(+)},\phi^{(-)}\right) > \overline{\phi}_{G}^{\star,\circ} \tag{6.145a}$$

$$\min\left(\phi^{(+)},\phi^{(-)}\right) < \overline{\phi}_{G}^{\star,\circ} \tag{6.145b}$$

due to $0 < \alpha^{\star,\circ} < 1$, the constraints

$$1 - \frac{\varkappa_{\mathfrak{c}}^{\circ}}{\left(\sum_{\tilde{\mathfrak{c}}=1}^{\mathcal{N}_{\mathfrak{L}}} \varkappa_{\tilde{\mathfrak{c}}}^{\circ}\right)} \frac{\frac{\Delta\overline{\mathcal{P}\phi}_{\mathfrak{L}}}{\overline{\mathcal{P}}^{\circ}}}{\left(\max\left(\phi^{(+)}, \phi^{(-)}\right) - \overline{\phi}_G^{\star,\circ}\right)} = \frac{\max\left(\phi^{(+)}, \phi^{(-)}\right) - \overline{\phi}^{\oplus,\circ}}{\max\left(\phi^{(+)}, \phi^{(-)}\right) - \overline{\phi}_G^{\star,\circ}} > 0 \tag{6.146a}$$

$$1 + \frac{\varkappa_{\mathfrak{c}}^{\circ}}{\left(\sum_{\tilde{\mathfrak{c}}=1}^{\mathcal{N}_{\mathfrak{L}}} \varkappa_{\tilde{\mathfrak{c}}}^{\circ}\right)} \frac{\frac{\Delta\overline{\mathcal{P}\phi}_{\mathfrak{L}}}{\overline{\mathcal{P}}^{\circ}}}{\left(\overline{\phi}_G^{\star,\circ} - \min\left(\phi^{(+)}, \phi^{(-)}\right)\right)} = \frac{\overline{\phi}^{\oplus,\circ} - \min\left(\phi^{(+)}, \phi^{(-)}\right)}{\overline{\phi}_G^{\star,\circ} - \min\left(\phi^{(+)}, \phi^{(-)}\right)} > 0 \tag{6.146b}$$

or, respectively,

$$-\left(\overline{\phi}_G^{\star,\circ} - \min\left(\phi^{(+)}, \phi^{(-)}\right)\right) < \frac{\varkappa_{\mathfrak{c}}^{\circ}}{\left(\sum_{\tilde{\mathfrak{c}}=1}^{\mathcal{N}_{\mathfrak{L}}} \varkappa_{\tilde{\mathfrak{c}}}^{\circ}\right)} \frac{\Delta\overline{\mathcal{P}\phi}_{\mathfrak{L}}}{\overline{\mathcal{P}}^{\circ}} < \left(\max\left(\phi^{(+)}, \phi^{(-)}\right) - \overline{\phi}_G^{\star,\circ}\right) \tag{6.147}$$

arise from conditions (6.143a) and (6.143b). The **weight**

$$\varkappa^{\circ} := \begin{cases} \overline{\mathcal{P}}^{\circ}\left(\max\left(\phi^{(+)}, \phi^{(-)}\right) - \overline{\phi}_G^{\star,\circ}\right) & \text{if} \quad \Delta\overline{\mathcal{P}\phi}_{\mathfrak{L}} > 0 \\ \overline{\mathcal{P}}^{\circ}\left(\overline{\phi}_G^{\star,\circ} - \min\left(\phi^{(+)}, \phi^{(-)}\right)\right) & \text{if} \quad \Delta\overline{\mathcal{P}\phi}_{\mathfrak{L}} \leqslant 0 \end{cases} \tag{6.148}$$

finally transforms these conditions for $\Delta\overline{\mathcal{P}\phi}_{\mathfrak{L}} > 0$ into

$$1 - \mathcal{K}^{(\mathrm{hi})} = \frac{\max\left(\phi^{(+)}, \phi^{(-)}\right) - \overline{\phi}^{\oplus,\circ}}{\max\left(\phi^{(+)}, \phi^{(-)}\right) - \overline{\phi}_G^{\star,\circ}} > 0 \tag{6.149a}$$

$$1 + \mathcal{K}^{(\mathrm{hi})}\, \Delta\phi_{\mathrm{rel}} = \frac{\overline{\phi}^{\oplus,\circ} - \min\left(\phi^{(+)}, \phi^{(-)}\right)}{\overline{\phi}_G^{\star,\circ} - \min\left(\phi^{(+)}, \phi^{(-)}\right)} > 0 \tag{6.149b}$$

and for $\Delta\overline{\mathcal{P}\phi}_{\mathfrak{C}} \leqslant 0$ into

$$1 - \mathcal{K}^{(\mathrm{lo})} \, \frac{1}{\Delta\phi_{\mathrm{rel}}} \quad = \quad \frac{\max\left(\phi^{(+)}, \phi^{(-)}\right) - \overline{\phi}^{\oplus,\circ}}{\max\left(\phi^{(+)}, \phi^{(-)}\right) - \overline{\phi}_G^{\star,\circ}} \quad > \quad 0 \tag{6.150a}$$

$$1 + \mathcal{K}^{(\mathrm{lo})} \quad = \quad \frac{\overline{\phi}^{\oplus,\circ} - \min\left(\phi^{(+)}, \phi^{(-)}\right)}{\overline{\phi}_G^{\star,\circ} - \min\left(\phi^{(+)}, \phi^{(-)}\right)} \quad > \quad 0 \tag{6.150b}$$

once the expressions

$$\mathcal{K}^{(\mathrm{hi})} := \frac{\Delta\overline{\mathcal{P}\phi}_{\mathfrak{C}}}{\sum_{\tilde{\mathfrak{c}}=1}^{\mathcal{N}_{\mathfrak{C}}} \overline{\mathcal{P}}^{\circ} \left(\max\left(\phi^{(+)}, \phi^{(-)}\right) - \overline{\phi}_G^{\star,\circ}\right)_{\tilde{\mathfrak{c}}}} \tag{6.151a}$$

$$\mathcal{K}^{(\mathrm{lo})} := \frac{\Delta\overline{\mathcal{P}\phi}_{\mathfrak{C}}}{\sum_{\tilde{\mathfrak{c}}=1}^{\mathcal{N}_{\mathfrak{C}}} \overline{\mathcal{P}}^{\circ} \left(\overline{\phi}_G^{\star,\circ} - \min\left(\phi^{(+)}, \phi^{(-)}\right)\right)_{\tilde{\mathfrak{c}}}} \tag{6.151b}$$

$$\Delta\phi_{\mathrm{rel}} := \frac{\left(\max\left(\phi^{(+)}, \phi^{(-)}\right) - \overline{\phi}_G^{\star,\circ}\right)}{\left(\overline{\phi}_G^{\star,\circ} - \min\left(\phi^{(+)}, \phi^{(-)}\right)\right)} \tag{6.151c}$$

are defined. While $\mathcal{K}^{(\mathrm{hi})} > 0$ holds in (6.149a) and (6.149b) for each type (C) cell due to $\Delta\overline{\mathcal{P}\phi}_{\mathfrak{C}} > 0$ and $\mathcal{K}^{(\mathrm{lo})} \leqslant 0$ holds in (6.150a) and (6.150b) for each type (C) cell due to $\Delta\overline{\mathcal{P}\phi}_{\mathfrak{C}} \leqslant 0$, the ratio $\Delta\phi_{\mathrm{rel}}$ from (6.151c) is always positive (without finite upper bound). Thus, conditions (6.149b) and (6.150a) are always satisfied, and therefore

$$\overline{\phi}^{\oplus,\circ} > \min\left(\phi^{(+)}, \phi^{(-)}\right) \qquad \text{if} \qquad \Delta\overline{\mathcal{P}\phi}_{\mathfrak{C}} > 0 \tag{6.152a}$$

$$\overline{\phi}^{\oplus,\circ} < \max\left(\phi^{(+)}, \phi^{(-)}\right) \qquad \text{if} \qquad \Delta\overline{\mathcal{P}\phi}_{\mathfrak{C}} \leqslant 0 \tag{6.152b}$$

holds. Condition (6.149a), however, is only satisfied, if

$$0 < \mathcal{K}^{(\mathrm{hi})} < 1 \tag{6.153}$$

is met, and condition (6.150b) is only satisfied, if

$$-1 < \mathcal{K}^{(\mathrm{lo})} \leqslant 0 \tag{6.154}$$

holds. Since both $\mathcal{K}^{(\mathrm{hi})}$ and $\mathcal{K}^{(\mathrm{lo})}$ have the same value in each cut grid cell, as they only consist of sums over all type (C) cells, violation of (6.153) in case of $\Delta\overline{\mathcal{P}\phi}_{\mathfrak{C}} >$

0 or of (6.154) in case of $\Delta\overline{\mathcal{P}\phi}_{\mathfrak{L}} \leqslant 0$ causes $\overline{\phi}^{\oplus,\circ}$ to exceed its lower or upper bound in all type (C) cells simultaneously, indicating, that conservation has already been violated in a preceding (sub-)step. On the other hand, if conditions (6.153) and (6.154) are satisfied,

$$\overline{\phi}^{\oplus,\circ} < \max\left(\phi^{(+)}, \phi^{(-)}\right) \quad \text{if} \quad \Delta\overline{\mathcal{P}\phi}_{\mathfrak{L}} > 0 \tag{6.155a}$$

$$\overline{\phi}^{\oplus,\circ} > \min\left(\phi^{(+)}, \phi^{(-)}\right) \quad \text{if} \quad \Delta\overline{\mathcal{P}\phi}_{\mathfrak{L}} \leqslant 0 \tag{6.155b}$$

is true for all cut cells. Finally, due to (6.152a) and (6.155a) in case of $\Delta\overline{\mathcal{P}\phi}_{\mathfrak{L}} > 0$ or due to (6.152b) and (6.155b) in case of $\Delta\overline{\mathcal{P}\phi}_{\mathfrak{L}} \leqslant 0$, respectively, the target value $\overline{\mathcal{P}\phi}^{\oplus,\circ}$ used for construction of the right hand side of the Poisson-type problem (6.140) is always bounded by (6.123) as demanded, if the weight $\varkappa^{\circ}$ is chosen according to (6.148): If $\Delta\overline{\mathcal{P}\phi}_{\mathfrak{L}} > 0$ holds and, consequently, the resulting target value $\overline{\mathcal{P}\phi}^{\oplus,\circ}$ is larger than the level-set based reference $\overline{\mathcal{P}}^{\circ}\,\overline{\phi}_G^{\star,\circ}$ in each cut grid cell, the weight (6.148) prevents the target value from exceeding $\overline{\mathcal{P}}^{\circ}\max\left(\phi^{(+)}, \phi^{(-)}\right)$, while it keeps $\overline{\mathcal{P}\phi}^{\oplus,\circ}$ from falling below $\overline{\mathcal{P}}^{\circ}\min\left(\phi^{(+)}, \phi^{(-)}\right)$ for $\delta\overline{\mathcal{P}\phi}^{\circ} < 0$ in case of $\overline{\mathcal{P}\phi}^{\oplus,\circ} < \overline{\mathcal{P}}^{\circ}\,\overline{\phi}_G^{\star,\circ}$. The special case $\Delta\overline{\mathcal{P}\phi}_{\mathfrak{L}} \equiv 0$ will not occur numerically and is therefore considered in the second line of equation (6.148) as random choice, since in this situation $\varkappa_{\mathfrak{c}}^{\circ}\left(\sum_{\tilde{\mathfrak{c}}=1}^{\mathcal{N}_{\mathfrak{L}}}\varkappa_{\tilde{\mathfrak{c}}}^{\circ}\right)^{-1}\delta\overline{\mathcal{P}\phi}^{\circ} \equiv 0$ holds anyway.

In the upper left picture of ***Fig. 6.22*** the local deviation (6.138) in cut grid cells in the flow field of the simulation from ***Fig. 6.18*** is plotted. The size of the local deviations is governed by (at least) three different mechanisms:

- the size of the fraction of the time interval, in which flux weights $\widetilde{\beta}$, different from 0 or 1, apply as indicated by the old (dashed) and new (solid) time level interface approximation in the upper left plot
- the size of the (final) volume fraction, and therefore of $\mathfrak{r} := \min\left(\Delta\phi_{\text{rel}}, \frac{1}{\Delta\phi_{\text{rel}}}\right)$
- the sign of the discretization error of $\widetilde{\beta}$

It can be seen, that the longer a type (C) cell is cut throughout the time interval considered, the larger the local deviations $\delta\overline{\mathcal{P}\phi}_{\mathfrak{c}}^{\star,\circ}$ are, since in this case the respective grid cell is exposed to discretization errors in the face fractions β due to flux splitting on cut grid cell faces for the maximum period. Additionally, these errors have the largest relative impact on small cut cell fractions in the respective fluid phase. The upper right picture shows the distribution of the weight $\varkappa$ for this special case. The

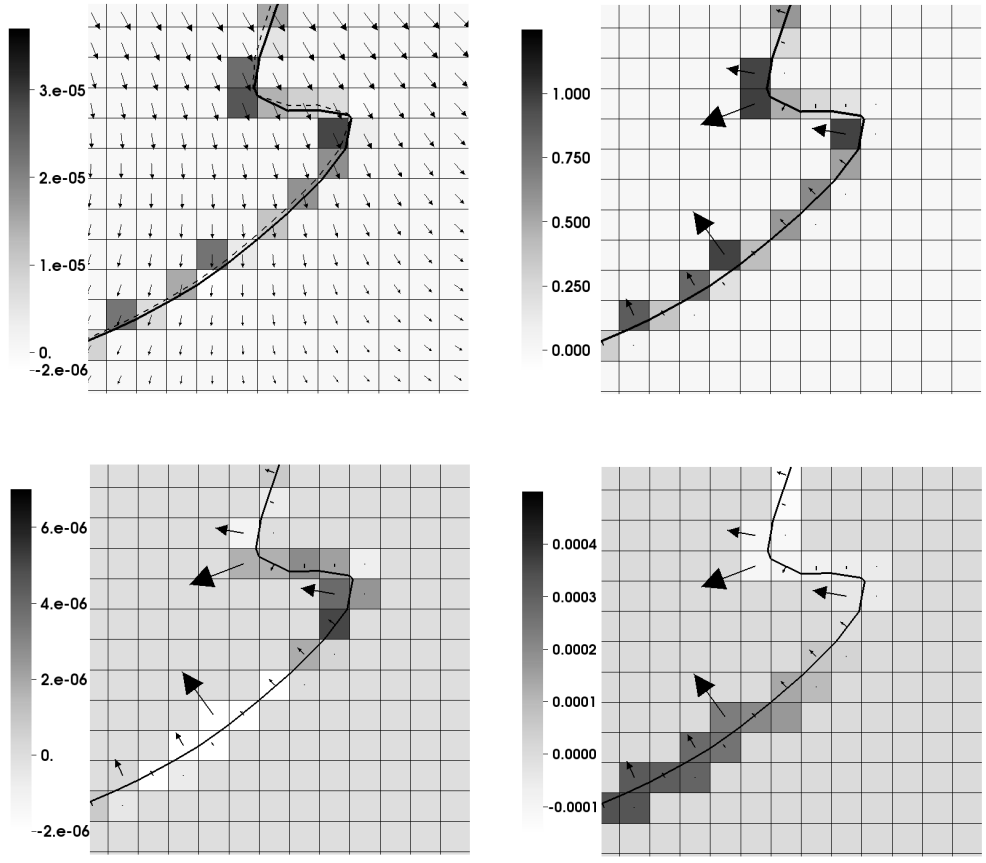

Fig. 6.22: Different quantities during volume-of-fluid redistribution: Examples for *(upper left)* scaled local deviation (6.138), including old (*dashed*) and new (*solid*) time level interface approximation, *(upper right)* weight $\varkappa$ in (6.136), *(lower left)* scaled right hand side of (6.140) and *(lower right)* scaled solution $\overline{\mathcal{P}^\circ}\mathcal{Y}$ of (6.140); scaling by $\Delta V/(\Delta t\,\overline{\mathcal{P}^\circ})$; arrows of velocity field *(upper left)* and interface correction *(others)* not equally scaled

magnitude of $\varkappa$ is distributed according to the one of the deviations. The bottom row of ***Fig. 6.22*** shows the right hand side of (6.134) or (6.140), respectively, on the left and the scaled solution $\mathcal{Y}$ of (6.134) or (6.140), respectively, on the right. From the latter it can be seen, that mass is continuously redistributed along the interface. In this special case, mass is effectively transported from the light to the dark area.

At the end, the weight $\varkappa$ governs the level-set correction velocity discussed in section 6.5.3.2 - 2. The better the weight distribution matches the distribution of local deviations, the better the correction is. In [182] the weight

$$\varkappa^\circ = \alpha_G^{\star,\circ}\left(1-\alpha_G^{\star,\circ}\right) \tag{6.156}$$

is used in contrast to the one specified in (6.148). This choice (6.156), in fact, introduces a trust region for level-set and volume-of-fluid based representations of $\overline{\mathcal{P}\phi}$, preferring level-set based values the more, the smaller one of two phase fractions in the corresponding grid cell gets, since in this case over- and undershoots beyond (6.123) in the volume-of-fluid based values are more likely and need to be prevented during target value computation. However, in contrast to (6.148), for (6.156) boundedness of the resulting values for $\overline{\mathcal{P}\phi}$ remains to be shown, while with weights according to (6.148), which maintain boundedness and correct the difference between level-set and volume-of-fluid based representation of $\overline{\mathcal{P}\phi}$ in each cut grid cell by that relative amount of the overall deviation $\Delta\overline{\mathcal{P}\phi}_{\mathfrak{C}}$, the respective cell has contributed to, interface correction can become quite local as shown in section 6.5.3.2 - 2.

Summarizing, once the reference correction fluxes (6.133) across grid cell faces between type (C) cells are determined by solving (6.134) or (6.140), respectively, for $\mathcal{Y}$ in cut cell centers, based on target value determination according to relation (6.135) including weights according to (6.148), again resulting correction fluxes (6.106) for all other conserved quantities can be computed. The correction fluxes for $\mathcal{P}$ vanish. With available correction fluxes the respective updates for all conserved quantities in each cut cell can be determined via standard Finite Volume procedures, assuming all other fluxes between cells which are not both of type (C) to vanish.

While the (A) step keeps the flow sharply separated by the interface, the present redistribution along the interface between (C) cells can be understood as conservative re-shaping of the interface representation due to the volume-of-fluid field $\overline{\mathcal{P}\phi}$ according to information provided by the (not yet corrected) level-set interface representation. The (C) step already prepares the subsequent level-set correction, which pulls the level-set representation towards the conservatively redistributed one of the volume-of-fluid field. Therefore the shape is governed by the level-set while conservation is governed by the volume-of-fluid.

6.5.2.5 Correction Algorithm Summary

This section summarizes the correction algorithm[15] for the conserved quantities

1. determine level-set based volume fraction $\alpha_G^\star$ of fluid phase $(+)$ in each type (C) cell based on nodal level-set values as sketched in section 6.3.3.6

[15] In order to pre-correct type (A) cells, which might not have a type (C) face neighbor, steps 3. to 9. have to be performed as initial cycle before step 3. with that type (A) cells as receiver cells, which have a type (C) face neighbor cell.

2. compute level-set based generalized volume fraction $\overline{\phi}_G^\star$ according to (6.122)
3. determine $\Delta\overline{\mathcal{P}\phi}$ in type (A) cells according to (6.129), using $\overline{\phi}_G^\star$ and the known $\overline{\mathcal{P}}^\star$ and $\overline{\mathcal{P}\phi}^\star$
4. determine volume fraction of all type (C) face neighbors of any type (A) cell in the fluid phase of the respective type (A) cell (either $\alpha_G^\star$ or $(1-\alpha_G^\star)$ of the neighboring type (C) cell)
5. determine weight $W_\mathfrak{f}$ for each grid cell face $\mathfrak{f}$, cut during the corresponding time interval, according to (6.130) and (6.131)
6. determine reference correction flux according to (6.105) using results from steps 3. and 5.
7. compute correction fluxes for any other conserved quantity $\rho\psi$ between type (A) and type (C) cells according to (6.106)
8. compute corrective updates for all conserved quantities in type (A) and type (C) cells
9. update all conserved quantities in type (A) and type (C) cells
10. compute difference $\delta\overline{\mathcal{P}\phi}_\mathfrak{c}^{\star,\circ}$ in each type (C) cell according to (6.138)
11. compute global sum $\Delta\overline{\mathcal{P}\phi}_\mathfrak{C}$ of the local differences from step 10. in all type (C) cells as specified in (6.137)
12. determine local weight $\varkappa$ in (6.136) according to (6.148) based on the sign of $\Delta\overline{\mathcal{P}\phi}_\mathfrak{C}$
13. determine global sum of weights $\varkappa$ in all type (C) cells as required for evaluation of (6.136)
14. compute right hand side of (6.140) in type (C) cells using results from steps 10. to 13. via (6.136) and (6.138)
15. set right hand side of (6.140) to zero in all other grid cells (A) and (R)
16. set correction fluxes between grid cells to zero if at least one of the two grid cells sharing this grid cell face is not of type (C)
17. solve Poisson-type problem (6.140) in entire computational domain

18. compute reference correction fluxes between type (C) cells according to (6.133)
19. compute correction fluxes for any other conserved quantity $\rho\psi$ between type (C) cells according to (6.106)
20. determine corrective updates for all conserved quantities in type (C) cells
21. update all conserved quantities in type (C) cells

6.5.3 Level-Set Correction

The benefits of level-set methods as described in section 6.1.1 come along with two crucial shortcomings when applied to interfaces separating different fluids due to the discrete approximation of equation (6.1). The resulting level-set representation $G^{\star,(n+1)}$, obtained through $\mathfrak{L}_{(G)}\left(\left(\nabla G\right), \vec{v}_G\right)$ with discrete approximations of the level-set gradient ∇G and the velocity field $\vec{v}_G$ as given via (6.7), applied to (5.21), on the one hand does not maintain the initially imposed signed distance property due to deviations of the level-set gradient from $|\nabla G| = 1$, on the other hand fluidic structures with boundary represented by the zero level of the level-set function do not maintain their volume (and mass) by default. While deviation from the signed distance function can cause the numerical method to fail once the local level-set gradient becomes to steep or to flat, accumulation of discetization error based volume changes of fluidic structures effectively yield artificial mass changes of the individual fluid phases. Both deficiencies are due to discretizations errors resulting from discrete treatment of equation (6.1) and need to be fixed for stable and accurate transport of fluidic structures. The following sections describe how these issues are overcome in this work by solving an additional correction equation

$$G'_{\mathfrak{t}} + \vec{v}'_G \cdot \nabla G = \dot{\mathfrak{q}}'_{(G)} \tag{6.157}$$

in pseudo-time $\mathfrak{t}$ according to solving (6.1) as described in 6.1.1 in order to include the leading order effects of the yet ignored features into the final level-set value $G^{(n+1)}$, with $\vec{v}'_G$ and $\dot{\mathfrak{q}}'_{(G)}$ as described below.

6.5.3.1 Penalization of Deviations from the Signed Distance Function

As mentioned above, movement of the level-set function does not maintain the initial signed distance property of the level-set function in general, and, thus, the absolute

value of the level-set gradient deviates from unity over time and the level-set function can become very flat and/or very steep, resulting – among others – in inaccurate interface normal vectors and/or unstable methods. Since (mostly non-trivial iterative) re-initialization procedures are very time-consuming and often affect the position of the level-set zero level – which is equivalent to a discrete artificial mass shift across the interface and/or non-physical displacement of a fluidic structure as, for example, described in [42] – the following non-iterative hybrid strategy is applied:

- in **all narrow band cells** $\Omega_{\mathfrak{i}} \in \mathfrak{N}$ a regularization is used throughout the present work in order to penalize deviations from $|\nabla G| = 1$, as, for example, done in [107]. While in the latter a diffusive penalization[16] is used during level-set propagation, the present penalization acts as a local source term $\dot{\mathfrak{q}}'_{(G)}$ in the correction equation (6.157) with corresponding discrete correcting operator

$$\mathfrak{L}'_{(G)} = \mathfrak{L}_{(G)} \left(\nabla G_{(i,j,k)}, \vec{v}'_{G,(i,j,k)} \right) + Q^{(G)}_{(i,j,k)} \tag{6.158}$$

and $\mathfrak{L}_{(G)}$ as given by equation (6.7) for application to the method-of-lines time integration (5.21). In equation (6.158) the expression

$$Q^{(G)}_{(i,j,k)} := \mathcal{C}\, \mathfrak{U} \mathfrak{P}^{(\eta)}_{(i,j,k)}\, \mathfrak{S}_{(i,j,k)} \left(1 - |(\nabla G)|_{(i,j,k)} \right) \tag{6.159}$$

approximates $\dot{\mathfrak{q}}_{(G)}$ in grid cell centers. Besides of the level-set gradient deviation, equation (6.159) consists of

$$\mathcal{C} := \frac{1}{2} \tag{6.160a}$$

$$\mathfrak{U} := \mathfrak{u}\, \breve{v} \tag{6.160b}$$

$$\mathfrak{P}^{(\eta)}_{(i,j,k)} := \mathfrak{P}^{(\Gamma),(\eta)}_{(i,j,k)}\, \mathfrak{P}^{(\mathfrak{N}),(\eta)}_{(i,j,k)} \tag{6.160c}$$

$$\mathfrak{S}_{(i,j,k)} := \max \left(\mathcal{C}_{\mathfrak{E}} \frac{\mathfrak{E}_{(i,j,k)}}{\max_{\mathfrak{N}} \mathfrak{E}}, \mathcal{C}_{\mathfrak{V}} \frac{\mathfrak{V}_{(i,j,k)}}{\max_{\mathfrak{N}} \mathfrak{V}} \right) \tag{6.160d}$$

$$\mathfrak{E}_{(i,j,k)} := |\vec{n}_\Gamma \cdot \boldsymbol{E} \cdot \vec{n}_\Gamma|_{(i,j,k)} \tag{6.160e}$$

$$\mathfrak{V}_{(i,j,k)} := |\vec{v} \cdot \vec{n}_\Gamma|_{(i,j,k)} \tag{6.160f}$$

$$\mathcal{C}_{\mathfrak{E}} := 10 \tag{6.160g}$$

$$\mathcal{C}_{\mathfrak{V}} := 0.5 \tag{6.160h}$$

with nondimensional velocity $\mathfrak{u}$, strain rate tensor $\boldsymbol{E}$ from (3.32) and local

[16] With diffusion coefficient proportional to the absolute value of the local flow velocity.

interface normal vector $\vec{n}_\Gamma$ from (6.5). The global penalty function $\mathfrak{P}$ is defined to be the product of the basic interface normal penalty profile

$$\mathfrak{P}^{(\Gamma),(\eta)}_{(i,j,k)} := \sqrt{\left|\hat{G}^{(\eta)}_{(i,j,k)}\right|}\,\frac{\arctan\left(\hat{G}^{(\eta)}_{(i,j,k)}\right)}{\arctan\left(1\right)} \tag{6.161}$$

with index

$$\eta \in \{0,1,2\} \tag{6.162}$$

and the corresponding choice

$$\mathfrak{P}^{(\mathfrak{R}),(0)}_{(i,j,k)} := \sqrt{2}\left(\mathfrak{Z}\left[\cos\left(\hat{G}^{(0)}_{(i,j,k)}\right)\right]^{\mathfrak{Z}}\right) \tag{6.163a}$$

$$\mathfrak{P}^{(\mathfrak{R}),(1)}_{(i,j,k)} := \left[1+\exp\left(-\left(\hat{G}^{(1)}_{(i,j,k)}\right)^2\right)\right]\exp\left(-\left(\frac{\hat{G}^{(1)}_{(i,j,k)}}{\mathfrak{N}^{(1)}}\right)^2\right) \tag{6.163b}$$

$$\mathfrak{P}^{(\mathfrak{R}),(2)}_{(i,j,k)} := \mathfrak{P}^{(\mathfrak{R}),(1)}_{(i,j,k)}\exp\left(-\left(\frac{\hat{G}^{(2)}_{(i,j,k)}}{\mathfrak{N}^{(2)}}\right)^2\right) \tag{6.163c}$$

with

$$\mathfrak{Z} := 2 \tag{6.164}$$

in case of $\eta = 0$. While (6.161)

- governs the behavior of $\mathfrak{P}$ in the vicinity of the interface Γ,
- guarantees, that the penalization smoothly vanishes at Γ,
- carries along the correct sign for the penalization, depending on the sign of the local level-set function,

the corresponding choice from (6.163) governs the behavior of $\mathfrak{P}$ towards the boundary of the narrow band $\mathfrak{R}$ as shown in ***Fig. 6.23***, in which $\mathfrak{P}^{(\Gamma),(\eta)}_{(i,j,k)}\,\mathfrak{P}^{(\mathfrak{R}),(\eta)}_{(i,j,k)}$ is sketched for narrow band width $\mathcal{N} = 5$ and grid spacing $\mathfrak{h} = 0.5$. The product (6.160c) with definitions (6.161) and (6.163) finally guarantees, that enough penalization is performed between interface and narrow band boundary but not at the interface, simultaneously preventing too heavy penalization at the narrow band boundary, which would lead to accumulation of destabilizing level-set deviations. In equations (6.161) and (6.163)

$$\hat{G}^{(\eta)}_{(i,j,k)} := \frac{G_{(i,j,k)}}{\mathfrak{N}^{(\eta)}\;\left(\|\vec{n}_\Gamma\|_1\right)_{(i,j,k)}\,\mathfrak{h}\,\max_{\mathfrak{b}}\left(\mathfrak{G}_{\mathfrak{b}}\right)} \tag{6.165}$$

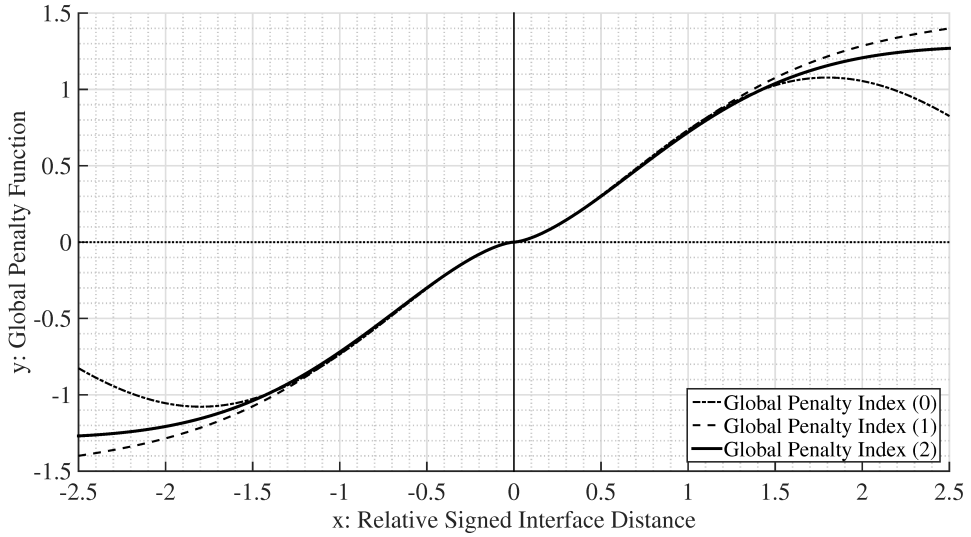

Fig. 6.23: Interface normal level-set penalty functions $\mathfrak{P}^{(\eta)}$ in narrow band $\mathfrak{N}$ around the interface Γ. The version $\mathfrak{P}^{(2)}$ is drawn solid. The interface is assumed to be located at $x = 0$, with a grid spacing of $\mathfrak{h} = 0.5$ with $\mathcal{N} = 5$ narrow band cells on each side of the interface; y represents the strength of the penalization depending on the distance from the interface and the narrow band boundary.

with

$$\mathfrak{N}^{(0)} := \mathcal{N}, \qquad \mathfrak{N}^{(1)} = \mathfrak{N}^{(2)} = (\mathcal{N} - 1) \tag{6.166}$$

is the non-dimensional relative approximation to the interface distance with respect to the narrow band size. The point-wise one-norm

$$1 \quad \leqslant \quad \|\vec{n}_\Gamma\|_1 := \sum_{\mathfrak{d}=1}^{\mathfrak{D}} \left(\frac{1}{|\nabla G|} \left| \frac{\partial G}{\partial x_\mathfrak{d}} \right| \right) \quad \leqslant \quad \sqrt{2} \tag{6.167}$$

in (6.165) stretches the penalty function the more, the smaller the angle between interface normal vector $\vec{n}_\Gamma$ and diagonal of the Cartesian grid cell is. In addition to the global penalty function, which only depends on the (disturbed) distance from the interface, the local penalization amplifier $\mathfrak{S}$ from definition (6.160d) accounts for the sources of the local deviations of the magnitude of the level-set gradient as proposed in [114]: On the one hand, relative motion of the level-set iso-contours due to shear in the velocity field, measured by the interface normal component of the strain rate tensor $\boldsymbol{E}$, causes the level-set gradient to deviate from unity the faster, the stronger this interface normal shear is. On the other hand, numerical diffusion, which is proportional to the interface normal velocity component, perturbs the level-set gradient magnitude. Therefore

multiplication of these local sources of disturbance $\mathfrak{S}$ due to local flow conditions with the global penalty function $\mathfrak{P}$ allows for keeping the magnitude of the level-set gradient bounded by penalizing the level-set the more, the larger the disturbing sources are, leaving the interface itself untouched. The choice $\eta = 2$ yield the most stable results and is therefore used throughout this work for obtaining the results in sections 6.5.6, 6.6.4.2 and 6.6.4.3. The scalings (6.160g) and (6.160h) are adopted from [114].

- in **interface cells**[17]

$$\mathfrak{I} := \begin{cases} \left\{ \Omega_{(i,j)} \ : \ \left(\Pi^{(i,j)}_{(i',j)} G \leqslant 0 \right) \ \vee \ \left(\Pi^{(i,j)}_{(i,j')} G \leqslant 0 \right) \right\} & \mathfrak{d} = 2 \\ \left\{ \Omega_{(i,j,k)} : \left(\Pi^{(i,j,k)}_{(i',j,k)} G \leqslant 0 \right) \vee \left(\Pi^{(i,j,k)}_{(i,j',k)} G \leqslant 0 \right) \vee \left(\Pi^{(i,j,k)}_{(i,j,k')} G \leqslant 0 \right) \right\} & \mathfrak{d} = 3 \end{cases} \tag{6.168}$$

with

$$\Pi^{(\mathfrak{p},\mathfrak{q},\mathfrak{r})}_{(\mathfrak{a},\mathfrak{b},\mathfrak{m})} G := G_{(\mathfrak{a},\mathfrak{b},\mathfrak{m})} G_{(\mathfrak{p},\mathfrak{q},\mathfrak{r})} \tag{6.169}$$

and $i^{'} \in \{i+1, i-1\}$, $j^{'} \in \{j+1, j-1\}$ and $k^{'} \in \{k+1, k-1\}$ the non-iterative direct CR-2 re-initialization procedure from [72] is applied, which incorporates a zero displacement of an anchor point on the piecewise linearly approximated interface Γ, represented via the level-set zero level $G = 0$. The set of interface cells $\mathfrak{I}$ is sub-divided into regions $\mathfrak{I}^{(+)}$ and $\mathfrak{I}^{(-)}$ in order to only use information from one side of the zero-level for each of the following sub-steps as proposed in [147]:

1. in

$$\mathfrak{I}^{(+)} := \begin{cases} \left\{ \Omega_{(i,j)} \ \in \mathfrak{I} : \ G^{\star}_{(i,j)} \ > 0 \right\} & \mathfrak{d} = 2 \\ \left\{ \Omega_{(i,j,k)} \in \mathfrak{I} : \ G^{\star}_{(i,j,k)} > 0 \right\} & \mathfrak{d} = 3 \end{cases} \tag{6.170}$$

with * indicating not yet re-initialized level-set function values, the signed distance function is recovered via

$$\begin{cases} d_{(i,j)} \ = \dfrac{G^{\star}_{(i,j)}}{\sqrt{\sum_{\mathfrak{d}=1}^{\mathfrak{d}} \left[\partial_{x_{\mathfrak{d}}} G^{\star}_{(i,j)} \right]^2}} & \mathfrak{d} = 2 \\ d_{(i,j,k)} = \dfrac{G^{\star}_{(i,j,k)}}{\sqrt{\sum_{\mathfrak{d}=1}^{\mathfrak{d}} \left[\partial_{x_{\mathfrak{d}}} G^{\star}_{(i,j,k)} \right]^2}} & \mathfrak{d} = 3 \end{cases} \tag{6.171}$$

[17] Interface cells are cells with cell center within a distance of $\left(\mathfrak{h} \max_{\mathfrak{d}} \left(\mathfrak{c}_{\mathfrak{d}} \right) \right)$ around the level-set zero level

in which, for example for direction $\mathfrak{d} = 1$,

$$\begin{cases} \left[\partial_{x_1} G^{\star}_{(i,j)}\right] & = \frac{G^{\star,+}_{(i,j)} - G^{\star,-}_{(i,j)}}{\max\left(\left(x^{+}_{1,(i,j)} - x^{-}_{1,(i,j)}\right), \mathfrak{e}_{\mathfrak{d}}\right)} \qquad \mathfrak{d} = 2 \\ \left[\partial_{x_1} G^{\star}_{(i,j,k)}\right] & = \frac{G^{\star,+}_{(i,j,k)} - G^{\star,-}_{(i,j,k)}}{\max\left(\left(x^{+}_{1,(i,j,k)} - x^{-}_{1,(i,j,k)}\right), \mathfrak{e}_{\mathfrak{d}}\right)} \qquad \mathfrak{d} = 3 \end{cases} \tag{6.172}$$

with

$$\mathfrak{e}_{\mathfrak{d}} := \frac{\mathfrak{c}_{\mathfrak{d}}\, \mathfrak{h}}{1000} \tag{6.173}$$

and

$$\begin{cases} \eta^{\pm}_{1,(i,j)} & := \begin{cases} \eta_{1,(i,j)} & \text{if } \Omega_{i\pm1,j} \notin \mathfrak{F} \wedge ((A_2)_1 \vee (B_2)_1) \\ \eta_{1,(i\pm1,j)} & \text{otherwise} \end{cases} \Bigg\} \mathfrak{d} = 2 \\ \eta^{\pm}_{1,(i,j,k)} & := \begin{cases} \eta_{1,(i,j,k)} & \text{if } \Omega_{i\pm1,j,k} \notin \mathfrak{F} \wedge ((A_3)_1 \vee (B_3)_1) \\ \eta_{1,(i\pm1,j,k)} & \text{otherwise} \end{cases} \Bigg\} \mathfrak{d} = 3 \end{cases} \tag{6.174}$$

for $\eta_1 \in \{G^{\star}, x_1\}$ hold. Further, in (6.174)

$$\begin{cases} (A_{\mathfrak{d}})_1 & \text{if } \left(a^{(1)}_{\mathfrak{d}}\right)_1 \wedge \left(a^{(2)}_{\mathfrak{d}}\right)_1 \\ (B_{\mathfrak{d}})_1 & \text{if } \left(b^{(1)}_{\mathfrak{d}}\right)_1 \vee \left(b^{(2)}_{\mathfrak{d}}\right)_1 \vee \left(b^{(3)}_{\mathfrak{d}}\right)_1 \end{cases} \tag{6.175}$$

with

$$\begin{cases} \left(a^{(1)}_2\right)_1 & \text{if } \Pi^{(i-1,j)}_{(i+1,j)}\, G < 0 \\ \left(a^{(1)}_3\right)_1 & \text{if } \Pi^{(i-1,j,k)}_{(i+1,j,k)} G < 0 \end{cases} \tag{6.176a}$$

$$\begin{cases} \left(a^{(2)}_2\right)_1 & \text{if } \left(\Delta^{+}_{(i,j)}\, G\right)_1 \left(\Delta^{-}_{(i,j)}\, G\right)_1 < 0 \\ \left(a^{(2)}_3\right)_1 & \text{if } \left(\Delta^{+}_{(i,j,k)} G\right)_1 \left(\Delta^{-}_{(i,j,k)} G\right)_1 < 0 \end{cases} \tag{6.176b}$$

$$\begin{cases} \left(b^{(1)}_2\right)_1 & \text{if } \Pi^{(i-1,j)}_{(i-2,j)}\, G < 0 \\ \left(b^{(1)}_3\right)_1 & \text{if } \Pi^{(i-1,j,k)}_{(i-2,j,k)} G < 0 \end{cases} \tag{6.176c}$$

$$\begin{cases} \left(b^{(2)}_2\right)_1 & \text{if } \Pi^{(i+1,j)}_{(i+2,j)}\, G < 0 \\ \left(b^{(2)}_3\right)_1 & \text{if } \Pi^{(i+1,j,k)}_{(i+2,j,k)} G < 0 \end{cases} \tag{6.176d}$$

$$\begin{cases} \left(b^{(3)}_2\right)_1 & \text{if } \left|\mathfrak{e}_{\mathfrak{d}} + \left(\Delta^{\pm}_{(i,j)} G\right)_1\right| - \left|\left(\Delta^{\mp}_{(i,j)} G\right)_1\right| < 0 \\ \left(b^{(3)}_3\right)_1 & \text{if } \left|\mathfrak{e}_{\mathfrak{d}} + \left(\Delta^{\pm}_{(i,j,k)} G\right)_1\right| - \left|\left(\Delta^{\mp}_{(i,j,k)} G\right)_1\right| < 0 \end{cases} \tag{6.176e}$$

and

$$\begin{cases} \left(\Delta^{+}_{(i,j)}\ G\right)_1 := G_{(i+1,k)} - G_{(i,j)} \\ \left(\Delta^{+}_{(i,j,k)} G\right)_1 := G_{(i+1,j,k)} - G_{(i,j,k)} \end{cases} \tag{6.177a}$$

$$\begin{cases} \left(\Delta^{-}_{(i,j)}\ G\right)_1 := G_{(i,k)} - G_{(i-1,j)} \\ \left(\Delta^{-}_{(i,j,k)} G\right)_1 := G_{(i,j,k)} - G_{(i-1,j,k)} \end{cases} \tag{6.177b}$$

represent conditions for decision on the stencil to be used for approximation of the derivatives (6.172). In contrast to [72], $\mathfrak{I}^{(+)}$ (called $\mathcal{R}$ there) is determined without considering the local level-set based curvature κ, since considering κ in cases in which κ is close to but different from zero, scenarios can occur, in which either to many interface cells are excluded from $\mathfrak{I}^{(+)}$ or tagged cells are on the wrong side of the interface, leading to wrong re-initialization in the following step

2. in

$$\mathfrak{I}^{(-)} := \mathfrak{I} \backslash \mathfrak{I}^{(+)} \tag{6.178}$$

the signed distance function is directly re-initialized via

$$\begin{cases} d_{(i,j)} = G^{\star}_{(i,j)} \dfrac{\left(\sum_{\mathfrak{l}=1}^{\mathcal{N}^{\mathfrak{K}^{(+)}}_{(i,j)}} d_{(i,j)_{\mathfrak{l}}}\right)^{(+)}}{\left(\sum_{\mathfrak{l}=1}^{\mathcal{N}^{\mathfrak{K}^{(+)}}_{(i,j)}} G^{\star}_{(i,j)_{\mathfrak{l}}}\right)^{(+)}} & \mathfrak{d} = 2 \\ d_{(i,j,k)} = G^{\star}_{(i,j,k)} \dfrac{\left(\sum_{\mathfrak{l}=1}^{\mathcal{N}^{\mathfrak{K}^{(+)}}_{(i,j,k)}} d_{(i,j,k)_{\mathfrak{l}}}\right)^{(+)}}{\left(\sum_{\mathfrak{l}=1}^{\mathcal{N}^{\mathfrak{K}^{(+)}}_{(i,j,k)}} G^{\star}_{(i,j,k)_{\mathfrak{l}}}\right)^{(+)}} & \mathfrak{d} = 3 \end{cases} \tag{6.179}$$

based on already re-initialized values d and on old values $G^{\star}$ in $\mathfrak{I}^{(+)}$ as well as the local not yet re-initialized value $G^{\star}$. In (6.179), $\mathcal{N}^{\mathfrak{K}^{(+)}}$ is the number of face neighbor cells of the current grid cell with cell centers on the other side of the zero-level (as re-initialized data is already available there) with $\mathfrak{K}^{(+)}$ as the respective sub-set of $\mathfrak{I}^{(+)}$ containing these $\mathcal{N}^{\mathfrak{K}^{(+)}}$ face neighbor cells.

3. the re-initialized distances d, computed in the two previous steps in both $\mathfrak{I}^{(+)}$ and $\mathfrak{I}^{(-)}$, are assigned to the level-set function in the entire $\mathfrak{I}$.

Consequently, by application of the above steps, the level-set function remains close to a signed distance function in the vicinity of the interface without application of iterative procedures and the approximation

$$d(\vec{x},t) \approx \frac{G}{|\nabla G|} \tag{6.180}$$

holds in that area.

6.5.3.2 Interface-Flow Coupling

As stated above and in section 6.1.1, the level-set lacks the conservation property, if not corrected. On the one hand, this affects conservation of the different fluid phases in each time step, since the ratio of fluxes in the different fluid phases at cut grid cell faces as determined in section 6.3.3 depends on the explicit level-set based interface position, determined according to section 6.1.4, and this unphysical change of shape and size of fluidic structures eventually leads to artificial gain or loss of mass of the different fluid phases. On the other hand, as there is no control on the sign of the local level-set discretization errors, the latter can accumulate over time if not corrected, leading to a decoupling of interface representation and fluid flow, which finally results in failure of the numerical method once the level-set based interface representation and the one based on the volume-of-fluid treat different grid cells as intersected ones.

While the discretization errors are of the order of magnitude of the truncation error of the numerical method in each time step, the above issues nevertheless need to be overcome for a stable method conserving each fluid phase. Therefore, the level-set based interface representation is corrected and coupled to the conserved quantities by solving equation (6.157) over a pseudo time interval of size $\Delta\mathfrak{t}$ with the interface correction velocity $\vec{v}_G^{\,\prime}$ remaining to be determined. Non-zero contributions to this correction velocity field

$$\vec{v}_G^{\,\prime} = \begin{cases} \vec{v}_G^{(\phi)} & \forall\ \Omega_{\mathfrak{i}} \in \mathfrak{C} \\ 0 & \forall\ \Omega_{\mathfrak{i}} \notin \mathfrak{C} \end{cases} \tag{6.181}$$

are only computed in grid cells, which are cut by the interface, $\mathfrak{C}$, leading to modification of level-set values G in these grid cells only. This way the level-set zero level, representing the interface Γ, is effectively moved along its normal (6.5) indirectly via level-set gradient manipulation (see ***Fig. 6.24*** for a one-dimensional sketch), as can

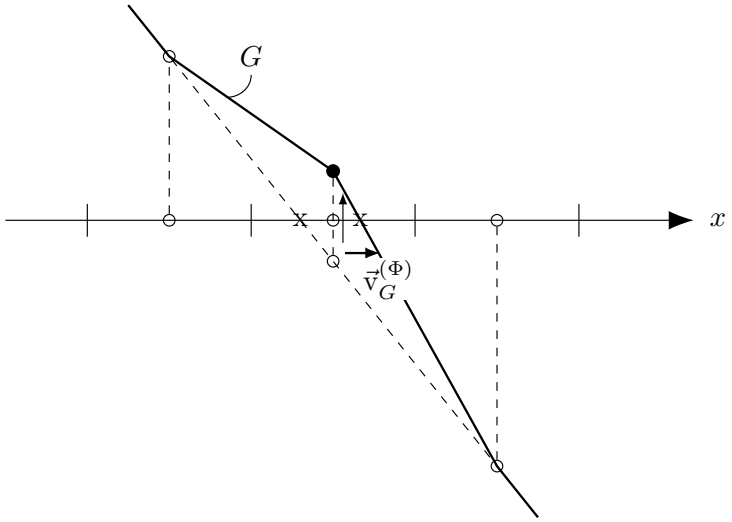

Fig. 6.24: Shift of intersection (X) of level-set (G) zero level approximation and grid cell face via (indirect) level-set gradient manipulation due to cut-cell local non-zero interface normal level-set correction velocity

be seen after transformation of equation (6.157) to

$$G_{\mathfrak{t}} + \mathcal{V}_G^{'} |\nabla G| = \dot{\mathfrak{q}}_{(G)}^{'} \tag{6.182}$$

with definition of

$$\mathcal{V}_G^{'} := \vec{v}_G^{'} \cdot \vec{n}_\Gamma \tag{6.183}$$

as interface normal correction velocity, avoiding elaborate computation of extension velocities in (narrow band) grid cells beyond the ones cut by the interface. The perturbation of the level-set gradient is corrected by the penalizing source term $\dot{\mathfrak{q}}_{(G)}^{'}$, which does not affect the interface position, as described in section 6.5.3.1. The size of the pseudo time interval is arbitrary. However, by choosing $\Delta\mathfrak{t}$ to equal the size of the time interval of the respective time step, $\Delta\mathfrak{t} = \Delta t$, the ratio of the magnitudes of interface movement during the respective time interval and necessary interface correction is directly given by the ratio of the magnitudes of correction velocities and fluid flow velocities as the numerical correction procedure according to (6.157) is subject to the CFL stability restriction as well.

Several strategies for determination of the interface normal correction velocity $\mathcal{V}_G^{'}$ are discussed in the following.

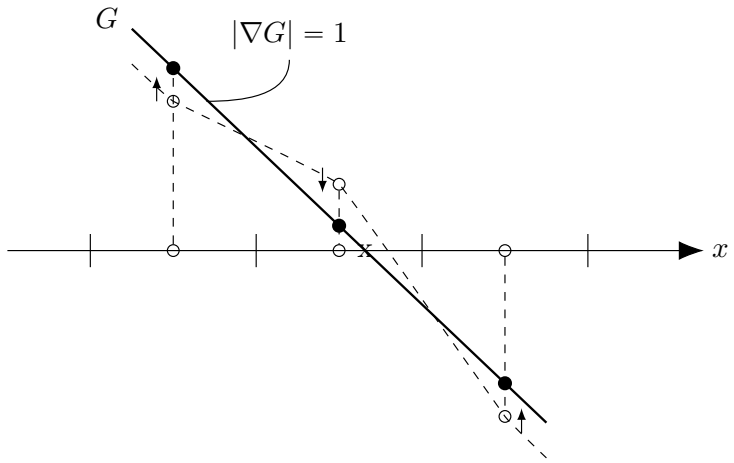

Fig. 6.25: Level-set gradient adjustment, keeping the location of the intersection (X) of level-set (G) zero level approximation and grid cell face unchanged

6.5.3.2 - 1 Globally Uniform Interface Correction Velocity

In this approach the level-set function – and with that the level-set based interface representation – is corrected using a globally uniform interface normal correction velocity $\mathcal{V}'_{G,\text{glob}}$ in each cut grid cell. Therefore a uniform (small) trial normal correction velocity $\mathcal{V}'_{G,\text{trial}}$ is applied to (6.182) and based on the resulting volume change ΔV_{trial} the final normal correction velocity

$$\begin{aligned}\mathcal{V}'_{G,\text{glob}} &= \mathcal{V}'_{G,\text{trial}} + \Delta\mathcal{V}'_{G,\text{glob}} \\ &= \mathcal{V}'_{G,\text{trial}} \left(1 + \frac{\Delta V^{(+)}_{G\to\phi} - \Delta V_{\text{trial}}}{\Delta V_{\text{trial}}} \right) = \mathcal{V}'_{G,\text{trial}} \frac{\Delta V^{(+)}_{G\to\phi}}{\Delta V_{\text{trial}}} \end{aligned} \tag{6.184}$$

for application to (6.182) is obtained by scaling of the trial velocity with the ratio of global volume error to be corrected, $\Delta V^{(+)}_{G\to\phi}$, and global volume correction ΔV_{trial}, obtained using the trial velocity $\mathcal{V}'_{G,\text{trial}}$ according to the following algorithm:

1. set the correction velocity field $\vec{v}'_G$ to zero
2. determine the necessary volume correction $\Delta V^{(+)}_{G\to\phi}$
   (a) compute level-set based volume $V^\star_G$ of the reference fluid phase $(+)$ before correction, indicated by superscript $\star$
   (b) compute difference between level-set based overall volume $V^\star_G$ in the ref-

erence fluid phase before correction and the known[18] overall target volume $V^{\oplus}$ of the same fluid phase

3. choose a (uniform) interface normal trail velocity size $\mathcal{V}'_{G,\text{glob}}$, which is small compared to the level-set propagation velocity.

4. determine trial velocity field $\vec{v}'_{G,\text{trial}}$ for application to (6.157) by splitting the interface normal trial velocity $\mathcal{V}'_{G,\text{trial}}$ into components in the coordinate directions, based on the interface normal vector (6.5). The sign of the interface normal correction velocity can be determined based on the sign of the difference determined in 2.

5. move level-set with trial velocity field $\vec{v}'_{G,\text{trial}}$ as described in 6.1.1

6. determine the resulting total volume change ΔV_{trial}

7. scale the trial velocity according to (6.184) and determine the missing interface normal level-set correction velocity for the final level-set correction $\Delta\mathcal{V}'_{G,\text{glob}} := \mathcal{V}'_{G,\text{glob}} - \mathcal{V}'_{G,\text{trial}}$.

   Alternatively, this correction velocity can be computed via determination of the missing total volume change $\Delta V^{(+)}_{G\to\phi} - \Delta V_{\text{trial}} = V^{\oplus} - (V^{\star} + \Delta V_{\text{trial}})$ as difference of target volume $V^{\oplus}$ and volume $V^{\star} + \Delta V_{\text{trial}}$ obtained after the trial step, and scaling of the trial velocity by the ratio of missing overall volume change to the already achieved volume change:

$$\Delta\mathcal{V}'_{G,\text{glob}} = \mathcal{V}'_{G,\text{trial}} \frac{\Delta V^{(+)}_{G\to\phi} - \Delta V_{\text{trial}}}{\Delta V_{\text{trial}}} \tag{6.185}$$

   Instead of resetting the result of the trial step and applying correction velocity (6.184) to the level-set algorithm for correction, the result from the trial step can be kept, applying (6.185) to the second evaluation of the level-set algorithm.

8. determine correction velocity field $\vec{v}'_{G,\text{glob}}$ or $\Delta\vec{v}'_{G,\text{glob}}$, respectively, as done in 4., based on the interface normal velocity $\mathcal{V}'_{G,\text{glob}}$ or $\Delta\mathcal{V}'_{G,\text{glob}}$, respectively, from 7.

[18] Since the global approach with uniform interface normal velocity can change the set of cut grid cells, either the correction of conserved quantities has to be done both before and after interface correction, or interface correction has to be done before the final (and only) correction of conserved quantities according to section 6.5.2. In the latter case, the target volume $V^{\oplus}$ of the reference fluid phase has to be known. Therefore, this approach in the second version is only applicable to cases, in which the volume of fluidic structures does not change.

9. move level-set with resulting correction velocity field as described in section 6.1.1

10. accept resulting interface position as accurate enough or repeat steps 6. - 10. (which is not done, since iterative procedures should be avoided) until the interface position can be regarded accurate enough

While providing accurate results without repeating steps 6. - 10. as shown in section 6.5.6.1[19], this globally uniform normal level-set correction velocity approach has the following drawbacks:

- as the described algorithm is the initial phase of an iterative Newton scheme already, all operations including level-set movement need to be done twice (2.-5. and 6.-9.) which increases computational cost
- interface correction is performed independent of local flow or geometric phenomena, which can cause interface movement due to the correction at locations at which the flow and the interface velocity vanishes
- as a uniform normal correction velocity can cause changes in the sets of cut and un-cut grid cells, interface correction needs to be done before correction of the conserved quantities as described in section 6.5.2, if an iterative scheme should be avoided. The latter should be done, since on the one hand it is one of the basic concepts of the present method and on the other hand each evaluation of the procedure from section 6.5.2 involves solving a global elliptic problem as described in section 6.5.2.4 - 3 and, with that, solution to a linear system, which is more expensive than local operations. Since in this approach conserved quantities are not yet corrected at this stage and may still contain under- and overshoots, the target volume $V^{\oplus}$ can not be computed from volume-of-fluid information, but has to be determined by other means in advance. Thus, the volume change – if there is one – has to be known a priori.

To overcome these issues, local level-set normal correction velocity determination is focused on in the following.

[19] The advected circular structure in section 6.5.6.1 is supposed to maintain its shape and constant interface curvature. Therefore the globally uniform correction fits the geometric properties of the given problem, which is not necessarily the case in general flow situation with arbitrary local changes of shape and interface position.

6.5.3.2 - 2 Local Interface Correction Velocity

In the present method, the level-set is the spatially more accurate interface representation, compared to the available volume-of-fluid information. Therefore the topology of cut and un-cut grid cells is kept fix during correction of the conserved quantities in section 6.5.2, which is based on the interface as predicted by the level-set zero level approximation as described in section 6.1.1 and 6.1.4.

After the correction from section 6.5.2 is done, in each grid cell local volume-of-fluid based information on the corrected interface position is implicitly available for level-set correction, in order to couple the level-set zero level to the fluid flow and to keep the amount of mass on each side of the interface stable, if there is no physical mechanism to change it.

As explicit reconstruction of an elaborate not necessarily continuous volume-of-fluid based interface representation should be avoided, the final interface position is not directly accessible, but contained in the corrected volume-of-fluid volume fraction distribution in cut grid cells.

However, assuming an interface normal correction of the interface position similar to [150], this information can be used for determination of local level-set correction velocities. As the correction is performed over a pseudo time interval of size $\Delta\mathfrak{t}$, for computation of a local normal correction velocity

$$\mathcal{V}'_{G,\mathrm{loc}} \;:=\; \mathfrak{P}\left(-1,1;\alpha^{\star}_{G}\right)\frac{d_{\mathrm{loc}}}{\Delta\mathfrak{t}} \;=\; \mathcal{O}\left(\frac{d_{\mathrm{loc}}}{\mathfrak{h}}\right) \tag{6.186}$$

the cut cell individual signed distance d_{loc}, by which the interface needs to be shifted in interface normal direction, remains to be determined from the known difference of level-set and volume-of-fluid based volume fractions in cut grid cells. While the sign of d_{loc} governs increase or decrease of the level-set based volume fraction towards the one due to the volume-of-fluid, $\mathfrak{P}\left(-1,1;\alpha^{\star}_{G}\right)$ with operators

$$\mathfrak{P}\left(\mathfrak{a},\mathfrak{b};\xi\right) := \begin{cases} \mathfrak{a} & \forall \quad \mathfrak{M}\left(\xi\right) \equiv \xi \\ \mathfrak{b} & \forall \quad \mathfrak{M}\left(\xi\right) \equiv 1-\xi \end{cases} \tag{6.187}$$

and

$$\mathfrak{M}\left(\xi\right) := \max\left(\xi, 1-\xi\right) \tag{6.188}$$

adjusts the effective sign, depending on if the resulting correction velocity points in positive or negative direction of the interface normal vector $\vec{n}_{\Gamma}$ as sketched in ***Fig.***

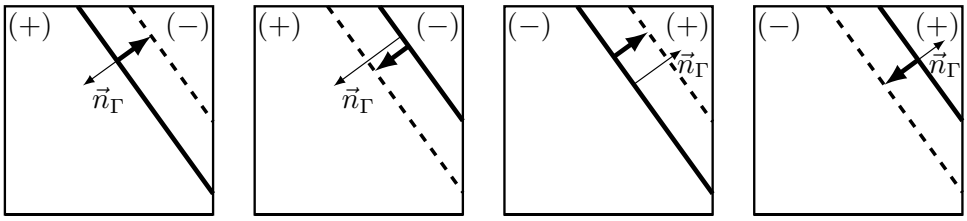

Fig. 6.26: Adjustment of level-set based interface representation: the level-set zero level is pushed towards the volume-of-fluid based interface representation, which has already been corrected based on uncorrected level-set information

6.26, with $\vec{n}_\Gamma$ pointing from $(-)$ to $(+)$.

Determination of the corresponding signed volume difference

$$\delta\Delta V_{G\to\phi} := \delta\alpha_{G\to\phi}\,\Delta V \tag{6.189}$$

between level-set and volume-of-fluid based interface representation in the cut grid cells according to

$$\delta\alpha_{G\to\phi} \;:=\; \left[\mathfrak{P}\left(\frac{\overline{\mathcal{P}\phi}}{\overline{\mathcal{P}}},\left(1-\frac{\overline{\mathcal{P}\phi}}{\overline{\mathcal{P}}}\right);\alpha_G^\star\right)-\mathfrak{M}\left(\alpha_G^\star\right)\right] \;=\; \mathcal{O}\left(\mathfrak{h}^3\right) \tag{6.190}$$

guarantees, that the volume difference is computed based on volume fractions in the same fluid phase[20]. Since the correction is performed after the first projection step with already corrected $\mathcal{P}$, the expression $\frac{\overline{\mathcal{P}\phi}}{\overline{\mathcal{P}}}$ directly represents the volume-of-fluid based volume fraction $\alpha_\phi = \overline{\phi}$ in analogy to the level-set based one, α_G, which is not corrected yet and therefore written as $\alpha_G^\star$.

In two space dimensions, two different geometric basic settings can be distinguished[21] for determination of the distance d_{loc}:

- if two (neighboring) cell nodes are located in the same fluid phase each (superscript (2)), determined based on the not yet corrected level-set representation,

[20] Since the interface representations due to level-set and volume-of-fluid information do not match exactly, the larger volume fraction due to level-set information can represent the same fluid phase as the smaller one due to volume-of fluid information and vice versa, if the volume fractions of both fluid phases are around $\frac{1}{2}$. Definition of the volume-of-fluid based volume fraction via operator (6.187) as applied in equation (6.190) guarantees, that exactly that volume fraction due to volume-of-fluid information is chosen, which represents the same fluid phase as the one considered due to level-set information.

[21] Note that in three space dimensions more different settings arise.

the local distance is

$$d_{\text{loc}}^{(2)} := \frac{\delta\Delta V_{G\to\phi}}{\Delta S_{G\to\phi}} = \frac{\delta\alpha_{G\to\phi}\Delta V}{\Delta S_{G\to\phi}} = \frac{\delta\alpha_{G\to\phi}}{\frac{\Delta S_{G\to\phi}}{\Delta S_G^\star}}\, d_{\text{loc}}^{(2),\star} = \mathcal{O}\left(\mathfrak{h}^4\right) \tag{6.191}$$

with known reference distance

$$d_{\text{loc}}^{(2),\star} := \frac{\Delta V}{\Delta S_G^\star} = \mathcal{O}(\mathfrak{h}) \tag{6.192}$$

and $\Delta S_G^\star$ as the area of the interface within the grid cell due to uncorrected level-set information. The average surface area

$$\Delta S_{G\to\phi} = \frac{1}{2}\left(\Delta S_G^\star + \Delta S_\phi\right) \tag{6.193}$$

is determined assuming the identity

$$\Delta S_\phi \equiv \Delta S_G^\star \tag{6.194}$$

to hold for ΔS_ϕ of the interface segment within the grid cell due to volume-of-fluid information as shown in ***Fig. 6.27***.

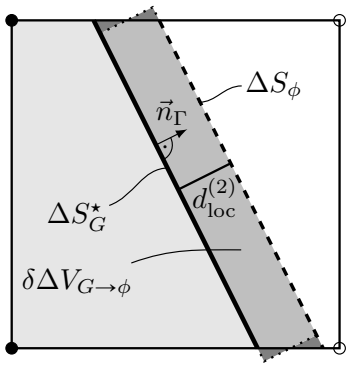

Fig. 6.27: Level-set correction in two space dimensions for a volume increment represented by a parallelogram

- if only one cell node is located in another fluid phase than the other cell nodes as shown in ***Fig. 6.28***, indicated by superscript (1) and again determined based on the not yet corrected level-set representation, the local signed distance

$$d_{\text{loc}}^{(1)} := 2\, d_{\text{loc}}^{(1),\star}\left[\sqrt{\mathfrak{W}\left(\alpha_G^\star\right)} - \sqrt{\mathfrak{W}\left(\alpha_G^\star\right) - \delta\alpha_{G\to\phi}}\right] = \mathcal{O}\left(\delta\alpha_{G\to\phi}\,\mathfrak{h}\right) \tag{6.195}$$

with known reference distance

$$d_{\text{loc}}^{(1),\star} := \frac{\Delta V}{\Delta S_G^\star}\sqrt{\mathfrak{W}\left(\alpha_G^\star\right)} = \frac{\sqrt{\Delta V}}{\sqrt{2\left(\frac{1}{\tan(\vartheta)} + \tan(\vartheta)\right)}} = \mathcal{O}(\mathfrak{h}) \tag{6.196}$$

and operator

$$\mathfrak{W}(\xi) := 1 - \mathfrak{M}(\xi) \tag{6.197}$$

as well as (smallest) angle ϑ between interface normal vector and grid coordi-

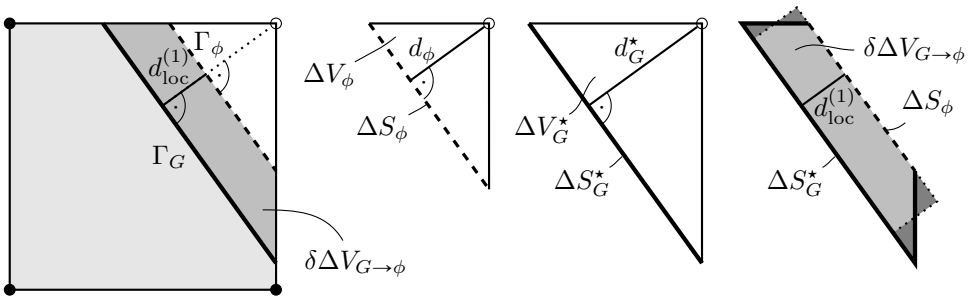

Fig. 6.28: Level-set correction in two space dimensions for a volume increment represented by a trapezoid

nate direction x_1 results from solving

$$\left(d^{(1)}_{loc}\right)^2 - 4\, d^{(1),\star}_{\mathrm{loc}} \left(d^{(1)}_{loc} \sqrt{\mathfrak{W}\left(\alpha^\star_G\right)} - \delta\alpha_{G\to\phi}\, d^{(1),\star}_{\mathrm{loc}} \right) = 0 \tag{6.198}$$

for $d^{(1)}_{\mathrm{loc}}$. The quadratic equation (6.198) in $d^{(1)}_{\mathrm{loc}}$ results from equating relation (6.189) with the area of a trapezoid yielding

$$\left(\frac{\Delta S_\phi}{\Delta V} + \frac{\sqrt{\mathfrak{W}\left(\alpha^\star_G\right)}}{d^{(1),\star}_{\mathrm{loc}}} \right) d^{(1)}_{\mathrm{loc}} - 2\,\delta\alpha_{G\to\phi} = 0 \tag{6.199}$$

after division by $\frac{\Delta V}{2}$, while representing the unknown side

$$\begin{aligned}
\Delta S_\phi = 2\frac{\Delta V_\phi}{d_\phi} &= 2\frac{1-\mathfrak{P}\left(\frac{\overline{\mathcal{P}_\phi}}{\overline{\mathcal{P}}}, \left(1-\frac{\overline{\mathcal{P}_\phi}}{\overline{\mathcal{P}}}\right); \alpha^\star_G\right)}{d^\star_G - d^{(1)}_{\mathrm{loc}}} \Delta V \\
&= 2\frac{\left(1-\mathfrak{M}\left(\alpha^\star_G\right) - \delta\alpha_{G\to\phi}\right)}{\frac{2\Delta V^\star_G}{\Delta S^\star_G} - d^{(1)}_{\mathrm{loc}}} \Delta V \\
&= 2\frac{\left(1-\mathfrak{M}\left(\alpha^\star_G\right) - \delta\alpha_{G\to\phi}\right)}{\frac{2\left(1-\mathfrak{M}\left(\alpha^\star_G\right)\right)\Delta V}{\Delta S^\star_G} - d^{(1)}_{\mathrm{loc}}} \Delta V \\
&= \frac{\left(\mathfrak{W}\left(\alpha^\star_G\right) - \delta\alpha_{G\to\phi}\right)}{d^{(1),\star}_{\mathrm{loc}} \sqrt{\mathfrak{W}\left(\alpha^\star_G\right)} - \frac{d^{(1)}_{\mathrm{loc}}}{2}} \Delta V
\end{aligned} \tag{6.200}$$

of the trapezoid by known quantities and the unknown $d^{(1)}_{\mathrm{loc}}$. The order of magnitude of expression (6.195) is determined with definition of the bounded ratio

$$\mathfrak{r} := \left(-\frac{\delta\alpha_{G\to\phi}}{\mathfrak{W}\left(\alpha_G^\star\right)} \right) = -\left(\frac{\mathfrak{p}\left(\frac{\overline{\mathcal{P}\phi}}{\overline{\mathcal{P}}}, \left(1-\frac{\overline{\mathcal{P}\phi}}{\overline{\mathcal{P}}}\right); \alpha_G^\star \right) - \mathfrak{M}(\alpha_G^\star)}{1-\mathfrak{M}(\alpha_G^\star)} \right) \tag{6.201}$$

via series expansion[22] of the root

$$\begin{aligned}
&\sqrt{\mathfrak{W}\left(\alpha_G^\star\right)} - \sqrt{\mathfrak{W}\left(\alpha_G^\star\right) - \delta\alpha_{G\to\phi}} \\
&= \sqrt{\mathfrak{W}\left(\alpha_G^\star\right)} \left(1 - \sqrt{1 - \frac{\delta\alpha_{G\to\phi}}{\mathfrak{W}\left(\alpha_G^\star\right)}} \right) \\
&= \sqrt{\mathfrak{W}\left(\alpha_G^\star\right)} \left(1 - \sqrt{1+\mathfrak{r}} \right) \\
&= \sqrt{\mathfrak{W}\left(\alpha_G^\star\right)} \left(1 - \left(1 + \frac{1}{2}\mathfrak{r} - \frac{1}{8}\mathfrak{r}^2 + \mathcal{O}\left(\mathfrak{r}^3\right) \right) \right) \\
&= -\frac{\mathfrak{r}}{2}\sqrt{\mathfrak{W}\left(\alpha_G^\star\right)} \left(1 - \frac{\mathfrak{r}}{4} + \mathcal{O}\left(\mathfrak{r}^2\right) \right) \\
&= \frac{1}{2}\left(\frac{\delta\alpha_{G\to\phi}}{\mathfrak{W}\left(\alpha_G^\star\right)} \right) \sqrt{\mathfrak{W}\left(\alpha_G^\star\right)} \left(1 + \frac{1}{4}\left(\frac{\delta\alpha_{G\to\phi}}{\mathfrak{W}\left(\alpha_G^\star\right)} \right) + ... \right) \;=\; \mathcal{O}\left(\delta\alpha_{G\to\phi}\right)
\end{aligned} \tag{6.202}$$

for $\mathfrak{W}\left(\alpha_G^\star\right) \neq 0$. For $\mathfrak{W}\left(\alpha_G^\star\right) = 0$ the expression

$$\begin{aligned}
&\sqrt{\mathfrak{W}\left(\alpha_G^\star\right)} - \sqrt{\mathfrak{W}\left(\alpha_G^\star\right) - \delta\alpha_{G\to\phi}} \\
&= -\sqrt{-\delta\alpha_{G\to\phi}} \\
&= -\sqrt{\mathfrak{M}(\alpha_G^\star) - \mathfrak{p}\left(\frac{\overline{\mathcal{P}\phi}}{\overline{\mathcal{P}}}, \left(1-\frac{\overline{\mathcal{P}\phi}}{\overline{\mathcal{P}}}\right); \alpha_G^\star \right)}
\end{aligned} \tag{6.203}$$

with

$$\mathfrak{M}(\alpha_G^\star) - \mathfrak{p}\left(\frac{\overline{\mathcal{P}\phi}}{\overline{\mathcal{P}}}, \left(1-\frac{\overline{\mathcal{P}\phi}}{\overline{\mathcal{P}}}\right); \alpha_G^\star \right) \;>\; 0 \tag{6.204}$$

due to already corrected

$$0 \;\leqslant\; \mathfrak{p}\left(\frac{\overline{\mathcal{P}\phi}}{\overline{\mathcal{P}}}, \left(1-\frac{\overline{\mathcal{P}\phi}}{\overline{\mathcal{P}}}\right); \alpha_G^\star \right) \;\leqslant\; 1 \tag{6.205}$$

is obtained. Therefore equation (6.195) in combination with (6.186) is always

[22] The issue can be also proofed without utilization of the series expansion via $\sqrt{\mathfrak{W}\left(\alpha_G^\star\right)} - \sqrt{\mathfrak{W}\left(\alpha_G^\star\right) - \delta\alpha_{G\to\phi}} = \sqrt{\mathfrak{W}\left(\alpha_G^\star\right)}\left(1 - \sqrt{1 - \frac{\delta\alpha_{G\to\phi}}{\mathfrak{W}\left(\alpha_G^\star\right)}} \right) = \sqrt{\mathfrak{W}\left(\alpha_G^\star\right)}\frac{\left(1-\sqrt{1+\mathfrak{r}}\right)\left(1+\sqrt{1+\mathfrak{r}}\right)}{\left(1+\sqrt{1+\mathfrak{r}}\right)} = \sqrt{\mathfrak{W}\left(\alpha_G^\star\right)}\frac{-\mathfrak{r}}{\left(1+\sqrt{1+\mathfrak{r}}\right)} = \mathcal{O}\left(\mathfrak{r}\right)$, since $\lim_{\mathfrak{r}\to 0}\left(\sqrt{\mathfrak{W}\left(\alpha_G^\star\right)}\frac{-1}{\left(1+\sqrt{1+\mathfrak{r}}\right)} \right) = -\frac{\sqrt{\mathfrak{W}\left(\alpha_G^\star\right)}}{2} < \infty$.

well defined, which can be also seen from the following examples:

- if the level-set based volume fraction has to increase in order to reach the volume fraction distribution due to volume-of fluid information, then $\delta\alpha_{G\to\phi} > 0$ and $d_{loc}^{(1)} > 0$ as in the first and third picture in ***Fig. 6.26***. If, however, the larger volume fraction is the one in fluid phase $(+)$ as in the first picture of ***Fig. 6.26***, then the required interface movement for increasing the larger volume fraction points against the interface normal vector, which is pointing from $(-)$ to $(+)$, and the resulting interface normal velocity has to become negative in order to increase the respective volume fraction against the normal vector, which is governed by $\mathfrak{P}\left(-1, 1; \alpha_G^\star\right)$ in equation (6.186).
- as shown above, if $\mathfrak{W}\left(\alpha_G^\star\right) = 0$ and the grid cell is labeled as cut cell, the interface is located in one of the cell nodes or covers an entire cell face. In this case equation (6.190) yields $\delta\alpha_{G\to\phi} \leqslant 0$ due to $\mathfrak{M}\left(\alpha_G^\star\right) = 1$ and

$$0 \leqslant \mathfrak{P}\left(\frac{\overline{\mathcal{P}\phi}}{\overline{\mathcal{P}}}, \left(1 - \frac{\overline{\mathcal{P}\phi}}{\overline{\mathcal{P}}}\right); \alpha_G^\star\right) \leqslant 1 \tag{6.206}$$

  which keeps $d_{\text{loc}}^{(1)} \leqslant 0$ real-valued and the correction can only decrease the larger volume fraction or increase the smaller one, respectively, leading to a positive interface normal correction velocity if the cell is entirely occupied by fluid phase $(+)$ and to a negative one, if the cell is entirely occupied by fluid phase $(-)$. In both case the correction points into the cell
- in general, the roots in (6.195) always yield real valued results due to equation (6.206) and

$$\begin{aligned} 0 \;\leqslant\; \mathfrak{W}\left(\alpha_G^\star\right) \;&=\; 1 - \mathfrak{M}\left(\alpha_G^\star\right) && \text{(6.207a)} \\ \mathfrak{W}\left(\alpha_G^\star\right) - \delta\alpha_{G\to\phi} \;&=\; \left(1 - \mathfrak{M}\left(\alpha_G^\star\right)\right) - \delta\alpha_{G\to\phi} && \text{(6.207b)} \\ &= 1 - \mathfrak{P}\left(\frac{\overline{\mathcal{P}\phi}}{\overline{\mathcal{P}}}, \left(1 - \frac{\overline{\mathcal{P}\phi}}{\overline{\mathcal{P}}}\right); \alpha_G^\star\right) \end{aligned}$$

- if there is no correction due to $\delta\alpha_{G\to\phi} = 0$, the resulting $d_{\text{loc}}^{(1)}$ vanishes for any $0 \leqslant \mathfrak{W}\left(\alpha_G^\star\right) \leqslant \frac{1}{2}$ and a zero correction velocity from (6.186) is applied.

Although theoretically excluded by the above approach, phase change of grid nodes

(and with that generation of new cut grid cells) can nevertheless occur due to the present correction in rare cases, since the explicit interface representation is not moved directly but the underlying level-set function is transported. This occurs, for example, if the intersection of grid cell face and interface is already close to the cell node before correction and the correction velocity moves the interface further in the direction of the cell node and beyond. If such a case occurs, the correction of the conserved quantities as described in section 6.5.2 needs to be repeated for a suitable interface-flow coupling. However, as observed during numerical tests, these events occur in about 1% of the time steps and repetition of the procedure from 6.5.2 can therefore be tolerated.

In order to prevent large ratios of neighboring level-set correction velocities – as their magnitude is independent of neighboring information yet – an additional filter can be introduced, which transforms the local level-set correction velocities in cut grid cells to regional ones considering neighboring information, in order to prevent unfavorable local effects on the shape of a fluidic structure in absence of leading order smoothing effects, such as surface tension. Development of suitable filters, that still conserve the masses of the fluid phases, however, is subject of future work. The filter sketched in the following, for example, requires determination of suitable weights η satisfying the mass conservation property:

A filtered level-set velocity can be defined as

$$\vec{v}^{\,\prime} := (1-\eta)\,\vec{v}^{\,\prime}_{\text{loc}} + \eta\,\vec{v}^{\,\prime}_{\text{reg}} \tag{6.208}$$

with local correction velocity given by equation (6.186) and related equations from above as well as regional correction velocity

$$\vec{v}^{\,\prime}_{\text{reg}} = \mathcal{V}^{\prime}_{G,\text{reg}}\vec{n}_{\Gamma} := \frac{\Delta V}{\Delta \mathfrak{t}}\left(\frac{\sum_{c=1}^{\mathcal{N}_{\mathfrak{R}}}\left(\delta\alpha_{G\to\phi}\right)_c}{\sum_{c=1}^{N_{\mathfrak{R}}}\left(\Delta S^{\star}_{G}\right)_c}\right)\vec{n}_{\Gamma} \tag{6.209}$$

with $\mathcal{N}_{\mathfrak{R}}$ as the number of considered neighboring cut cells, including the present one. The local weight η governs the ratio between local and regional influence and needs to be determined such that the overall mass conservation property for each fluid phase is still satisfied and local geometric and flow features are accounted for.

6.5.4 Combined Correction Strategy for Interface and Conserved Quantities

Different correction strategies can be assembled with the corrective elements described in sections 6.5.2 and 6.5.3.2. These strategies are described in this section.

6.5.4.1 Global Interface Correction

A possible correction strategy for adjusting conserved quantities and interface, the latter globally, is as follows:

1. correct the level-set function – and with that the interface position – **globally** uniformly according to section 6.5.3.2 - 1
2. correct the phase indicator – and with that the volume distribution of the different fluid phases – followed by all the other conserved quantities based on the new interface position due to the resulting level-set representation, split into the following steps:
   (a) phase indicator based correction of conserved quantities in grid cells, which are cut during the current time interval but not anymore at its end (type (A) cells) via reference correction flux computation as described in section 6.5.2.4 - 2 and correction flux determination as described in section 6.5.2.2
   (b) phase indicator based correction of conserved quantities in grid cells, which are cut at the end of the current time interval (type (C) cells) via reference correction flux determination as described section 6.5.2.4 - 3 and correction flux determination as described in section 6.5.2.2

The **advantage** of this strategy is, that the interface can leave a cut grid cell during step 1. The formerly cut grid cell is left behind regular (making it a type (A) cell), while a neighboring grid cell is cut instead. This property is especially beneficial for circular interfaces, that are supposed to maintain their circular shape as shown in section 6.5.6.1, which, however, represent a limited special subset of geometric settings occurring in physically relevant applications. Since the interface has obtained its final position already when the conserved quantities are adjusted, no iterative correction scheme besides of the two level-set evaluations in correction step 1. is needed.

The **drawbacks** of this strategy, however, are the following:

- in order to correct the interface globally, allowing the interface to move into neighboring grid cells
  - either the change of the volume, occupied by the different fluid phases between old and new time level, has to be known a priori, since knowledge of the correct volumes for each fluid phase at the new time level is necessary, which might not necessarily be given in all relevant flow cases,
  - or step 2. has to be performed both before and after step 1.; the first time in order to provide correct information on the volume distribution, the second time to adjust the flow to the resulting interface position after step 1., since new cut cells might have been generated. Since each evaluation of step 2b. requires determination of the solution to a linear problem, this version is more expensive.
- regions of the interface, which did not contribute to the error subject to be corrected, are nevertheless modified by the uniform interface correction, although the interface might already have its correct position locally. This is the case, if the interface position is left unchanged locally during the current time interval
  - either due to the local geometric properties in combination with the local velocity, that causes the interface movement, such as, for example, in the case of straight interface segments in a segment-tangential viscous flow,
  - or if the local velocity, which is moving the interface, is zero, and the interface does not move locally at all.

  In both cases the interface should not be moved locally at all, and therefore also not by the interface correction, unless for resetting interface displacements due to the uncorrected transport algorithm. However, a globally uniform correction is changing interface position everywhere, no matter if the correct position is already obtained locally before the correction or not.

6.5.4.2 Local Interface Correction

This second strategy is similar to the one presented in [152]:

1. perform step 2. from section 6.5.4.1
2. correct the level-set function - and with that the interface position - **locally** as described in section 6.5.3.2 - 2

The **advantages** of this strategy are the following:

- the volumes, occupied by the different fluid phases at the end of the time interval, do not have to be known in advance, since interface correction is done after correction of the phase indicator and the conserved quantities, and the resulting final fluid distribution is given after the conservative propagation and conservative correction of both divergence errors and flux weighting errors via phase indicator values.
- locally vanishing velocity magnitude, leading to no production of local discretization errors, requires no correction locally, which can only be achieved by application of local correction velocities. Application of the latter is also the cheapest option for the ultimate strategy of including all level-set corrections – both the ones affecting interface position (section 6.5.3.2) and gradient magnitude (section 6.5.3.1) – into the predictor step and evaluating the level-set transport algorithm only once per time step.

The **drawbacks** of this strategy are the following:

- the ratio of the magnitudes of neighboring interface normal correction velocities in cut grid cells is not bounded, as the size of each correction velocity is obtained due to local geometric information only, based on the locally required volume modification. Therefore, in absence of leading order smoothing effects, such as surface tension, and in case of recurring geometric patterns with large neighboring correction velocity ratios, the shape of the fluidic structure can be affected unfavorably, which gives rise to development of regional filters as sketched in section 6.5.3.2 - 2 in future work.
- the strength of the local level-set correction can not be utilized completely, since the volume redistribution with reference correction flux determination according to section 6.5.2.4 - 3, to which the interface position is adjusted, represents a cut cell global feature, which can yield volume corrections in cut grid cells, in which the local flow velocity vanishes. This effect is inherent to the setting of the present dimensionally unsplit method and can only be avoided by either including an additional constraint due to the local velocity magnitude (for example via the filter weights as proposed towards the end of section 6.5.3.2 - 2), or application of a dimensionally split method in the predictor step, in which locally produced errors can be corrected purely local at the respective

grid cell face, without requiring a global redistribution procedure[23]. The latter is necessary in the present approach, since in a dimensionally unsplit method the sources of local flux errors can not be traced back completely, and therefore these errors can not be corrected exactly where they have been generated.

The differences and advantages compared to [152] are the following:

- In the present numerical method, predictor fluxes, which both suffer from divergence and flux weighting related errors, are referred to fluxes of $\mathcal{P}$ for all conserved quantities according to sections 5.1.1 and 6.3.1. Just as the fluxes for correcting divergence errors in the first projection step, described in section 5.2.1 and 6.4, are also referred to correction fluxes for $\mathcal{P}$ for a consistent divergence error correction, correction fluxes for flux weighting related errors are referred to fluxes of $\mathcal{P}$ – or $\mathcal{P}\phi$, respectively – for consistency reasons as well.

- While step 1. is split into sub-steps (a) and (b), specified in section 6.5.4.1 in step 2., this step is done at once in [152] by combining both sub-steps. Splitting of step 1. into the sub-steps (a) and (b) as listed above, however, has the advantage, that both the solvability condition for the resulting elliptic problem in sub-step (b) is given by default, and the solution in sub-step (a) is not dependent on the solution accuracy of an elliptic solver for the occuring linear system, but is exact regarding volume fractions due to the knowledge of the exact target values.

- In [152] the weights for target value determination – called δ there – are determined purely based on volume-of-fluid type information based on the maximum possible local change and the question, whether the values are physically reasonable or not in order to avoid smearing. Thus, volume-of-fluid information is used as fixed reference for the level-set and the resulting interface correction. In contrast, in the present method the corresponding weights $\varkappa$ and resulting corrections contain information on the level-set based geometric setting as reference in addition, since the level-set interface representation is

[23] While beyond the scope of this work, it should be noted, that using a dimensionally split method also requires non-straight forward procedures in case of geometric settings as sketched in ***Fig. 7.2*** and ***Fig. 7.4*** in section 7.2. In such cases, despite of the dimensional splitting, corrections in all coordinate directions can be required in each of the single one-dimensional sub-steps. As in the present method, even geometric cases can be constructed, in which there is no receiver cell left for correction in the corresponding coordinate direction due to truncation of the geometric representation and the accompanying limitation to one intersection per grid cell face, which gives rise to effectively grid diagonal correction to nodal neighbor cells, which share no grid cell face.

considered to represent the geometic setting more accurately. Utilizing the resulting implicit phase indicator based geometry distribution, the level-set interface representation can be corrected such that a stable conservative continuous interface representation is obtained in the end.

6.5.4.3 Global-Local-Hybrid Interface Correction

In principle, this strategy is the same as in the previous section 6.5.4.2. However, step 2., involving local single stage determination of the level-set correction velocity based on geometric considerations as described in 6.5.3.2 - 2, is replaced by a two-stage correction velocity determination similar to the one in section 6.5.3.2 - 1, in which the second stage of final correction velocity determination by a globally uniform approach is replaced by a local volume difference depending scaling for obtaining the final local level-set correction velocity. This results in the following procedure:

1. perform step 2. from section 6.5.4.1
2. correct the level-set involving a hybrid global-local correction velocity determination by
   (a) determination of the local volume difference in each cut grid cell as described in section 6.5.3.2 - 2 by equation (6.190)
   (b) performing the global trial step, involving a small globally uniform trial velocity, described in section 6.5.3.2 - 1 in steps 3. to 6.
   (c) determination of the still remaining local volume difference $\Delta\delta\alpha_{G\to\phi}\,\Delta V$ as in step 2a., however, with the pre-corrected volume fraction $\alpha_G^{(\text{trial})}$ applied to equation (6.190) instead of the uncorrected one $\alpha_G^\star$
   (d) determination of the correction velocity (6.185) for the second application to (6.157), however, based on local relative volume differences

$$\frac{\delta\alpha_{G\to\phi} - \delta\alpha_{\text{trial}}}{\delta\alpha_{\text{trial}}} = \frac{\Delta\delta\alpha_{G\to\phi}}{\delta\alpha_{G\to\phi} - \Delta\delta\alpha_{G\to\phi}} \tag{6.210}$$

   in each cut grid cell

Benefits and drawbacks are as described in the previous section 6.5.4.2.

However, replacement of step 2. by the one described above has the additional **advantage**, that the level-set correction velocity, which has to be applied for a pseudo correction time increment, is determined with the same accuracy in all cut grid cells, independent of the individual geometric setting of the interface section in the corresponding cut grid cell during the time interval. An additional **drawback** is the increased cost of performing two pseudo level-set propagation steps for level-set interface correction, and an increased risk of generating new cut cells during the trial step, requiring step 1. to be performed at the end again, leading to further cost increase.

6.5.5 Final Level-Set Correction Strategy

In terms of efficiency, the pure local level-set correction approach 6.5.4.2 is desirable, as it allows for a shift of the level-set correction to the interface predictor of the subsequent time step by adding the local level-set correction velocity, determined towards the end of the current time step, to the level-set advection velocity of the next time step during the first level-set time integration stage of the involved Runge-Kutta time integrator as described in section 6.1.1, yielding

$$G_t \; + \; \left(\vec{v} + \vec{v}\,'^{(n-\frac{1}{2})} \right) \cdot \nabla G \; = \; \dot{\mathfrak{q}}_{(G)} \tag{6.211}$$

with level-set correction velocity $\vec{v}\,'^{(n-\frac{1}{2})}$ from the respective preceding time step. If the locally determined level-set correction velocity is used, the level-set transport algorithm has to be evaluated only once throughout each entire time step in the predictor step. If the global-local-hybrid level-set correction velocity is used, a second evaluation of the level-set algorithm for determination of the trial update as basis for the local corrections of the level-set correction velocity remains in the corrector step. Determination of the level-set correction velocity $\vec{v}\,'^{(n-\frac{1}{2})}$, computed throughout the preceding time step and only non-zero in cut grid cells in the first stage during time integration, is given in section 6.5.3.2 - 2 and the approximation to the source term, penalizing deviations from the signed distance function, is described in section 6.5.3.1.

6.5.6 Results and Open Issues

In this section, effects of the application of the procedure described in sections 6.5.2 and 6.5.3 are described, restricting the set of equations to the explicitly treated advective part from section 6.3.1 only due to the lack of a not yet available corrector for sharp moving interfaces. If not stated otherwise, level-set correction strategy 6.5.4.2 with level-set gradient correction 6.5.3.1 and both $\mathfrak{u} := 1$ and $\breve{v} = 1\,\frac{\mathrm{m}}{\mathrm{s}}$ is used.

6.5.6.1 Advection of a Circle

In ***Fig. 6.29***, taken from [182], two-dimensional horizontal advection of a circular bubble of density $\hat{\rho}^{(+)} = 1$ and radius $\hat{r} := 0.25$ within a fluid of density $\hat{\rho}^{(-)} = 1000$ is shown, initially centered within a $[0,1]\times[0,1]$ domain on a Cartesian grid, consisting of 128×128 grid cells, both with and without the correction procedures described in sections 6.5.2 and 6.5.3. With periodic boundary conditions in flow direction and slip walls on top and bottom, 1024 time steps have been computed, corresponding to 4 revolutions with velocity $\hat{\vec{v}}(\hat{\vec{x}},\hat{t}) = (1,0)$ at CFL-number $\mathcal{C}_{\mathcal{A}} = 0.5$. The illustrations of the phase indicator $\overline{\phi}$ to the left are composed of two semi-transparent plots of the two phase indicator distributions $\overline{\phi}^{(+)} = 1$ and $\overline{\phi}^{(-)} = 0$, the amplitude of each limited to a narrow value range $\overline{\phi}^{(\pm)} \pm \varepsilon$ with small ε around the target values 0 and 1. The bottom left picture shows the result applying the present correction procedure with the darker grey area representing $\overline{\phi}^{(-)} = 0$ and lighter grey area representing $\overline{\phi}^{(+)} = 1$, while the top left illustration shows the result without correction, with the initial interface (which is located at the same position) plotted for guidance. The black area indicates the region in which $\overline{\phi}^{(-)} < 0$ and the white area represents the region in which $\overline{\phi}^{(-)} > 1$. Intermediate grey, deviating from the two grey colors representing 0 and 1, indicate intermediate values $0 < \overline{\phi}^{(+)}, \overline{\phi}^{(-)} < 1$. Thus, while the interface is smeared without the present correction procedure with a wake of off-target-values developing behind the front although sharp flux splitting is performed at cut grid cell faces, the present correction procedure is able to keep the flow sharply separated by the interface with intermediate integral averages in cut grid cells only. The right plot of ***Fig. 6.29*** shows the relative error of the "volume" of the circular bubble (which is, in fact, the area within the circle) with respect to the initial value, both with and without interface correction. While without correction the bubble volume rapidly deviates from the initial value, which is expected to be maintained by an accurate method, as shown by the dotted line, application of the present correction

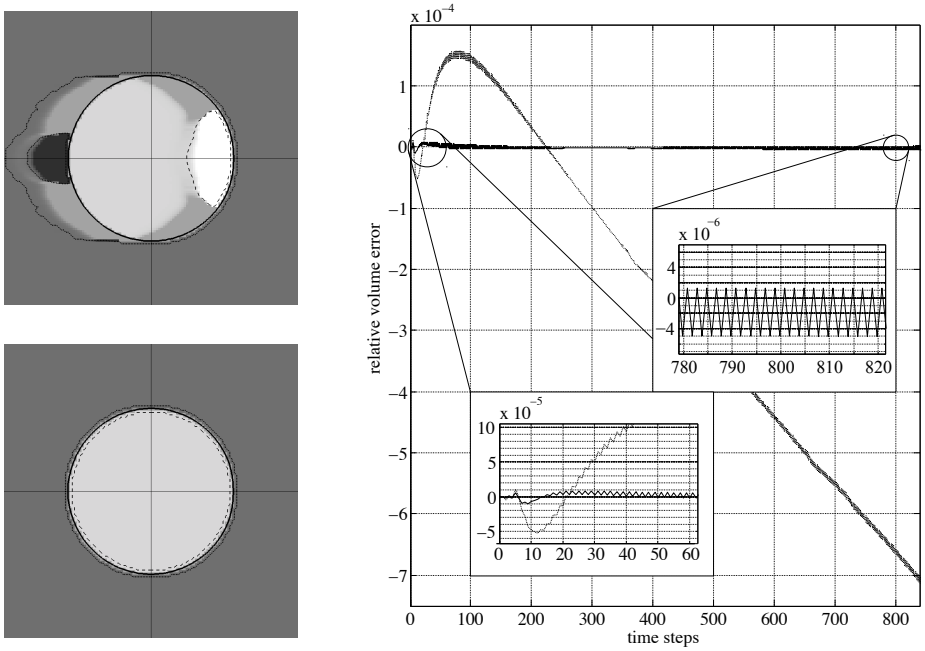

Fig. 6.29: Advection of a circle; **Left:** Volume fraction $\overline{\phi}^{(\pm)}$ after 1024 time steps on a Cartesian grid of 128x128 cells, constant homogeneous velocity $\hat{\vec{v}}(\hat{\vec{x}}, \hat{t}) = (1, 0)$ from left to right; ***top:*** without adjustment, ***bottom:*** synchronized; *black/white areas*: over-/undershoots; *dashed line*: iso-contour of $\phi^{(+)} = 1$; *dotted line*: iso-contour of $\phi^{(-)} = 0$; *thick continuous line*: level-set zero level Γ; *thin continuous lines*: patch boundaries, each patch computed on another processor. **Right:** relative error of circle area ("bubble volume") based on level-set information (α) w.r.t. initial data over time; *dotted line*: without adjustment, *solid line*: synchronized; (from [182] (`https://dx.doi.org/10.1007/978-3-319-05684-5_45`) with permission of Springer)

scheme keeps the bubble volume stable, oscillating around it's target value at high frequency and amplitudes which are smaller by orders of magnitudes. The regular oscillation in the zoomed right center extract is due to the CFL-number $\mathcal{C}_{\mathcal{A}} = 0.5$, which leads to an alternating repeating set of cut cell configurations contributing to the volume computation. For arbitrary CFL-numbers $\mathcal{C}_{\mathcal{A}} < 0.5$ arbitrary oscillation has to be expected. For obtaining the results in ***Fig. 6.29*** level-set correction velocity determination strategy 6.5.3.2 - 2 has been applied as given in [182]. ***Fig. 6.30*** shows the time series of relative errors of the interface-flow coupling (in terms of the reference phase mass based on the level-set interface representation with respect to its initial value) for the different strategies given in section 6.5.4 with choice (6.148) for redistribution of conserved quantities among cut grid cells. The comparison, however, is actually not fair, since the global approach 6.5.4.1, shown in the top plot of ***Fig. 6.30***, uses two level-set advection steps for correction, both with globally uni-

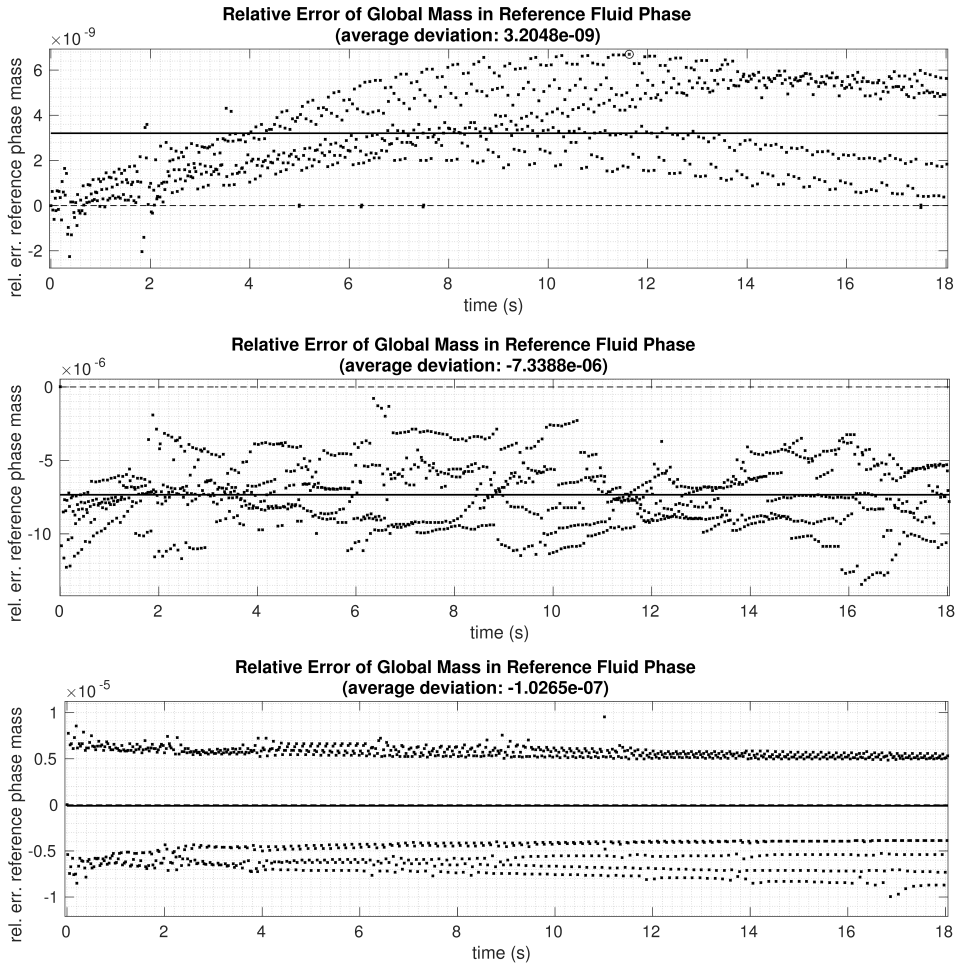

Fig. 6.30: Relative error of reference phase mass due to interface-flow coupling via different approaches: *top*: global two-stage interface correction according to section 6.5.4.1; *center*: local single-stage interface correction according to section 6.5.4.2; *bottom*: hybrid global-local two-stage interface correction according to section 6.5.4.3

form interface normal correction velocity at known target volume, corresponding to the first two steps of a fix point iteration, and afterwards the conserved quantities are adjusted to the interface which already encloses the correct volume. The hybrid global-local approach 6.5.4.3 also performs two corrective level-set advection steps, the first one with the globally uniform interface normal trial velocity and the second one with locally adjusted correction velocities, which can be seen in the bottom plot of ***Fig. 6.30***. However, in this approach the conserved quantities are already corrected before the interface is adjusted to the flow. The local approach 6.5.4.2, shown in the center plot of ***Fig. 6.30***, only performs one level-set correction step with local correction velocities, determined as described in section 6.5.3.2 - 2 with already

corrected flow quantities. While the latter is the least accurate (and least expensive) approach, it nevertheless converges second order accurate as shown in ***Tab. 6.1***, in which the convergence order

$$\mathfrak{p}_\ell := \frac{\ln\left(\frac{\left|\Delta E_\rho^{(+)}\right|_{\ell-1}}{\left|\Delta E_\rho^{(+)}\right|_{\ell}}\right)}{\ln\left(\frac{\mathcal{C}_{\ell-1}}{\mathcal{C}_\ell}\right)} \tag{6.212}$$

of the local interface-flow coupling is given. In (6.212)

$$\left|\Delta E_\rho^{(+)}\right| \quad \in \quad \left\{\left|\widetilde{\Delta E}_\rho^{(+)}\right|, \ \left|\left(\Delta E_\rho^{(+)}\right)_{\max}\right|\right\} \tag{6.213}$$

with $\left|\widetilde{\Delta E}_\rho^{(+)}\right|$ as the magnitude of the temporal average

$$\widetilde{\Delta E}_\rho^{(+)} := \frac{1}{\hat{t}_1 - \hat{t}_0}\int_{\hat{t}_0}^{\hat{t}_1} \mathcal{E}_{\hat{m}^{(+)}}\left(\hat{t}\right)\,\mathrm{d}\hat{t} \tag{6.214}$$

of the relative error

$$\mathcal{E}_{\hat{m}^{(+)}}\left(\hat{t}\right) := \frac{\left(\hat{m}^{(+)}(\hat{t}) - \hat{m}^{(+)}(\hat{t_0})\right)}{\hat{m}^{(+)}(\hat{t}_0)} \tag{6.215}$$

of the level-set based reference fluid phase mass

$$\hat{m}^{(+)}(\hat{t}) := \int_{\hat{\Omega}_{\hat{G}}^{(+)}(\hat{t})} \hat{\rho}(\hat{\vec{x}}, \hat{t})\,\mathrm{d}\hat{V} \tag{6.216}$$

with respect to its initial value at $\hat{t}_0 = 0$, and $\left|\left(\Delta E_\rho^{(+)}\right)_{\max}\right|$ as the magnitude of the maximum occurring deviation

$$\left(\Delta E_\rho^{(+)}\right)_{\max} := \max_{\hat{t}}\left(\mathcal{E}_{\hat{m}^{(+)}}\left(\hat{t}\right)\right) \tag{6.217}$$

during $[\hat{t}_0, \hat{t}_1]$ for the example of the advected circle with velocity $\hat{\vec{v}} = (0.2, 0)$ and $\hat{t}_1 = 5$. As before, the density ratio is chosen to be $\hat{\rho}^{(-)}/\hat{\rho}^{(+)} = 1000$. Second order accuracy is obtained for both error measures and the mass within the circle is kept stable over time within this range of accuracy in terms of the level-set, while the fluid phase masses are conserved up to machine accuracy in terms of the volume-of-fluid.

An additional convergence study on a sequence of grids of different resolutions for

the density, representing the scalar quantities in the system, further revealed (average) convergence orders of 2.027 in the L_1-norm, 1.506 in the L_2-norm and 0.759 in the L_∞-norm at density ratio of 1:1000, CFL-number of $\mathcal{C}_\mathcal{A} = 0.4$ and level-set correction approach 6.5.4.3. Due to the locally only first order accurate time integrator actually not more than a value around 1 has to be expected in the L_∞-norm. Numerical solutions have been obtained on two-dimensional grids of 64×64, 128×128 and 256×256 grid cells and the respective error norms have been determined by comparison with a reference solution on a grid consisting of 4096×4096 grid cells. The reference solution has been chosen to be the discrete initial condition on the latter fine grid, since it represents the discrete exact solution after full revolutions of the circular bubble in a periodic domain. One revolution on a $[0,1] \times [0,1]$ domain with velocity $\hat{\vec{v}} = (1,0)$ and final time $\hat{\mathfrak{T}} = 1$ has been analyzed.

Tab. 6.1: Convergence order $\mathfrak{p}$ for interface-flow coupling of an advected circle: $\left|\widetilde{\Delta E}_\rho^{(+)}\right|$ represents the absolute value of the temporal average of the relative error of the reference phase mass with respect to its initial value

		reference phase mass error			
ℓ	$\frac{1}{\mathcal{C}_\ell}$	$\left\|\widetilde{\Delta E}_\rho^{(+)}\right\|_\ell$	$\mathfrak{p}_\ell$	$\left\|\left(\Delta E_\rho^{(+)}\right)_{\max}\right\|_\ell$	$\mathfrak{p}_\ell$
		10^{-5}	-	10^{-5}	-
0	64	3.0851	-	8.2018	-
1	96	1.3617	2.017	3.1831	2.334
2	128	0.7357	2.140	1.6152	2.358
3	196	0.3479	1.847	0.7381	1.931
4	256	0.1779	2.331	0.4012	2.119
5	384	0.0784	2.021	0.1342	2.700

Fig. 6.31 on page 238 shows the maximum positive and the maximum negative local relative error of the magnitude of the level-set gradient with respect to its initial value of $|\nabla G| = 1$ on the two-dimensional Cartesian grid consisting of 96×96 grid cells, applying the level-set penalization presented in section 6.5.3.1 to the advection of a circle in a constant homogeneous velocity field in a periodic domain for the first 3 revolutions. Since there is no shear in the velocity field, the penalization is only due to the interface normal velocity component in order to penalize different local amplitudes of the numerical diffusion of the underlying numerical method. ***Fig. 6.33*** on page 239 shows the corresponding plot without the present level-set gradient correction procedure.

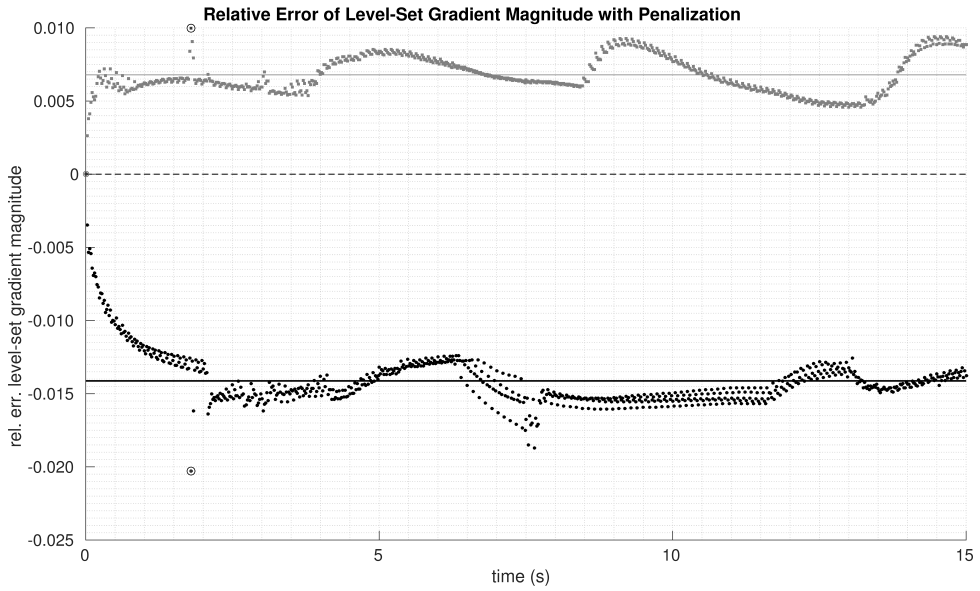

Fig. 6.31: Relative error of the magnitude of the level-set gradient with respect to its initial value of $|\nabla G| = 1$ due to level-set gradient correction for 3 revolutions of an advected circle at velocity $\hat{\vec{v}} = (0.2, 0)$ on a Cartesian grid of 96×96 grid cells in a periodic domain: *grey*: maximum positive deviation; *black*: maximum negative deviation; *solid lines*: average deviations

Note the different scalings of the vertical axes in ***Fig. 6.31*** and ***Fig. 6.33***. The magnitude of the deviation of the level-set gradient from $|\nabla G| = 1$ is significantly reduced and stabilized over time by the present approach.

Fig. 6.34 on page 240 shows the corresponding distribution of the magnitude of the level-set gradient after two revolutions of the circle at $\hat{t} = 10$ on the grid of 96×96 cells, both without (left) and with (right) the present level-set gradient correction procedure applied. Not only the magnitudes of the largest deviations are reduced, but also the distribution of the deviations is much more homogenous after application of the present approach,

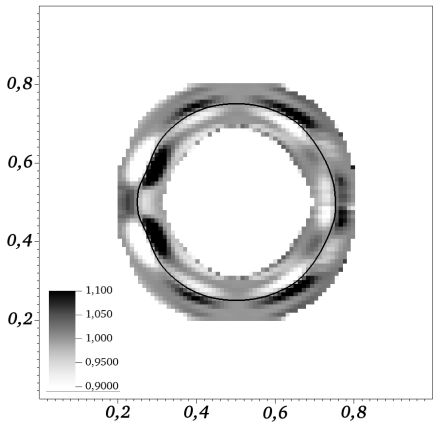

Fig. 6.32: Magnitude of the level-set gradient at $\hat{t} = 5$ after one revolution of a circle in a constant homogeneous velocity field $\vec{v} = (0.2, 0)$ on a Cartesian grid of 96×96 grid cells in a periodic $[0, 1] \times [0, 1]$ domain, applying only level-set re-initialization in interface cells without penalization in the rest of the narrow band

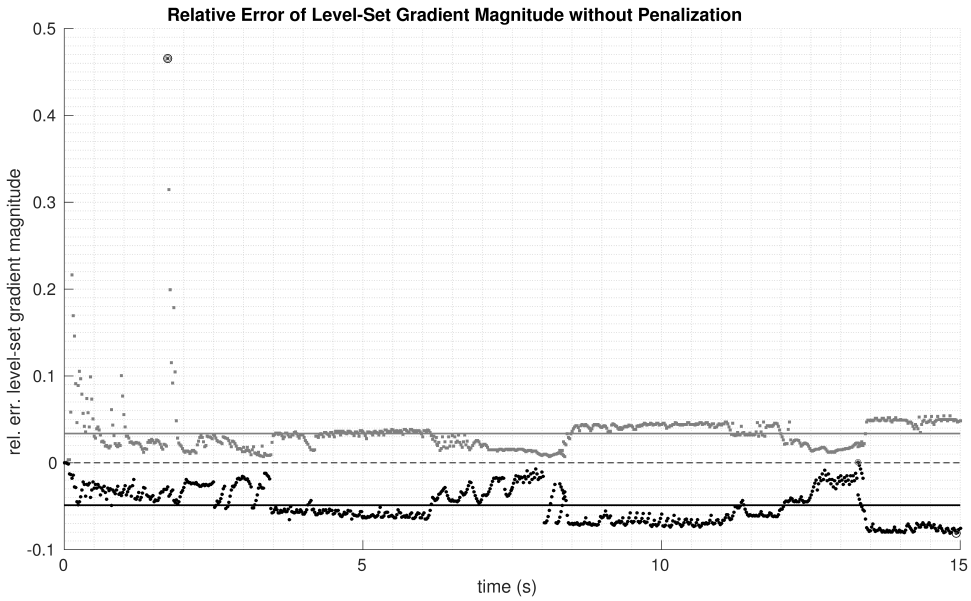

Fig. 6.33: Relative error of the magnitude of the level-set gradient with respect to its initial value of $|\nabla G| = 1$ without level-set gradient correction for 3 revolutions of an advected circle at velocity $\vec{\tilde{v}} = (0.2, 0)$ on a Cartesian grid of 96×96 grid cells in a periodic domain: *grey*: maximum positive deviation; *black*: maximum negative deviation; *solid lines*: average deviations

which is crucial for maintaining the shape of the fluidic structure applying the local interface correction for mass conservation.

In ***Fig. 6.32*** on the previous page the magnitudes of the level-set gradient after only one revolution of an advected circle in a constant homogeneous velocity field in a periodic domain are displayed, omitting the level-set penalization in the narrow band beyond the interface cells, but keeping the re-initialization in interface cells only in order to artificially produce a field of level-set gradient magnitudes within the narrow band, which is non-smooth with large local deviations. It can be seen due to the deteriorated interface in ***Fig. 6.32*** after only one revolution, that is crucial to keep the deviations in the magnitude of the level-set gradient small and their distribution within the narrow band smooth in order to maintain the shape of the fluidic structure in combination with the local mass conservation governed interface correction according to 6.5.3.2.

Level-set gradient correction according to section 6.5.3.1 on the one hand, and level-set gradient correction via application of a local level-set correction velocity in cut grid cells only according to sections 6.5.3.2 - 1 and 6.5.3.2 - 2 on the other hand, however, can act against each other, as both corrections modify the local level-set

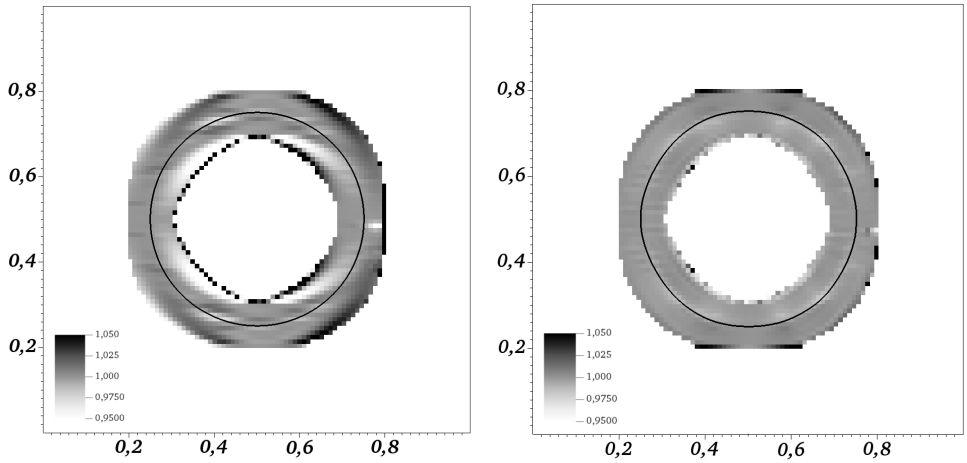

Fig. 6.34: Magnitude of the level-set gradient at $\hat{t} = 10$ after two revolutions of a circle in a constant homogeneous velocity field $\vec{v} = (0.2, 0)$ on a Cartesian grid of 96×96 grid cells in a periodic $[0, 1] \times [0, 1]$ domain: *left*: without level-set gradient correction, *right*: with level-set gradient correction

gradient. Improvement is expected by extending the level-set correction velocities into the entire narrow band (which is subject of future work), instead of using only non-zero correction velocities in cut grid cells, since in case of a smooth correction velocity field in the entire narrow band the effect of the interface correction due to the mass constraint on the level-set gradient is much smaller around the interface, and level-set gradient manipulation is primarily governed by the level-set gradient correction procedure 6.5.3.1. Further, in absence of leading order interface smoothing effects, such as surface tension, the local level-set correction velocity approach can lead to local unfavorable shape deformations in cases, in which the same local level-set correction velocity distribution is recurring permanently. This can be improved by smoothing the local level-set correction velocities with information from neighboring cut grid cells, making the correction regional instead of local or global, avoiding large local differences in local neighboring level-set correction velocities. Finding suitable smoothing filters, which maintain the mass conservation property of each fluid phase while improving shape constraints, is also subject of future work. Another topic of future investigations is the question whether it is worth to add an additional diffusive term as done in [107] to the non-iterative correction of the level-set equation solving

$$G'_{\mathfrak{t}} + \vec{v}'_G \cdot \nabla G \;=\; \nabla \cdot \left(\left[1 - \frac{1}{|\nabla G|} \right] \nabla G \right) + \dot{\mathfrak{q}}'_{(G)} \tag{6.218}$$

in order to improve smoothness of the distribution of the level-set gradient magnitude.

6.5.6.2 Rider-Kothe-Vortex

Already during advection of a circle in a constant homogeneous velocity field, as described in the previous section 6.5.6.1, various cut cell scenarios occur, while the circular interface is traveling through the grid. Nevertheless, the present advection algorithm with both level-set and level-set gradient correction is tested in this section in a less trivial flow situation, similar to the one given in [146]:

An initially circular structure of radius $\hat{r}_\circ = 0.125$, initially located at

$$\hat{\vec{x}}^{(0)} = \begin{pmatrix} 0.50 \\ 0.75 \end{pmatrix} \tag{6.219}$$

within a square domain of size[24] $[0, 1.024] \times [0, 1.024]$ with periodic boundary conditions, starts moving within a vortex with velocity field

$$\hat{\vec{v}} = 4 \sin(\pi \hat{x}_1) \sin(\pi \hat{x}_2) \begin{pmatrix} -\sin(\pi \hat{x}_1) \cos(\pi \hat{x}_2) \\ \sin(\pi \hat{x}_2) \cos(\pi \hat{x}_1) \end{pmatrix} \tag{6.220}$$

that vanishes at the domain boundaries and satisfies $\hat{\nabla} \cdot \hat{\vec{v}} = 0$. The density is set to

$$\hat{\rho} := \begin{cases} 1 & \forall\ \hat{r} > 1 \\ 10^{-4} & \forall\ \hat{r} \leqslant 1 \end{cases} \tag{6.221}$$

with relative radius $\hat{r}$ with respect to $\hat{r}_\circ$ as defined in (5.141) with (5.142) and (5.143) on page 114. The choice (6.221) corresponds to a density ratio that is about ten times larger than the one between water and air. Since gravity and friction are neglected ($\hat{g} = 0$, $\hat{\mu} = 0$) and the divergence-free velocity field is kept fix over time, the pressure $\hat{p}'$ is constant in both space and time and can be set to zero. Further, $\hat{\mathcal{P}}$ remains at its initial value and the following results on a grid of 256×256 grid cells reveal the pure interplay of the volume fractions due to the level-set and volume-of-fluid based interface representations. The relevant reference quantities are chosen to be

$$\check{l} = 1\,\mathrm{m}, \qquad \check{t} = 1\,\mathrm{s}, \qquad \check{\vec{v}} = 1\,\frac{\mathrm{m}}{\mathrm{s}}, \qquad \check{\rho} = 10^4\,\frac{\mathrm{kg}}{\mathrm{m}^3} \tag{6.222}$$

for this test case. ***Fig. 6.35*** shows the initial setting on the left hand side and the state after 300 explicit time steps of size $\Delta\hat{t} = 9.6009 \cdot 10^{-4}$ at $\hat{t} = 0.288027$ on the right. It can be seen, that despite of the large ratio of densities the flow remains separated

[24] The value of 1.024 is chosen in order to obtain simple values for the grid spacing, if the number of grid cells per coordinate direction is a power of 2.

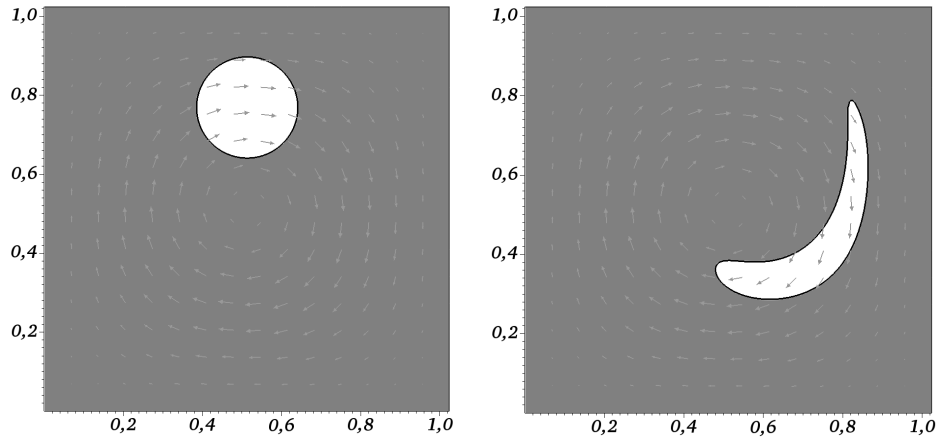

Fig. 6.35: Initial density (*left*) and density after 300 explicit time steps (*right*) for the Rider-Kothe vortex example in a fixed velocity field (*grey arrows*): *dark grey* corresponds to $\hat{\rho} = 1$, *white* corresponds to $\hat{\rho} = 10^{-4}$

sharply. This is emphasized by ***Fig. 6.36***, in which the density is plotted[25] each. On the left hand side the allowable values are limited to the range $9.99999 \cdot 10^{-5} < \hat{\rho} < 1.00001 \cdot 10^{-4}$ and on the right hand side to the range $9.99999 \cdot 10^{-1} < \hat{\rho} < 1.00001$. If these bounding values were reached or exceeded, pure black regions – in case of $1.00001 \cdot 10^{-4}$ (left) and 1.00001 (right) – or pure white ones – in case of $9.99999 \cdot 10^{-5}$ (left) and $9.99999 \cdot 10^{-1}$ (right) – would be present in the plots. However, since the individual fluid phases carry a constant grey value each, the constant initial values of $\hat{\rho} = 10^{-4}$ within the (initial) circle and $\hat{\rho} = 1$ beyond the (initial) circle are maintained everywhere within the respective fluid phase. This is confirmed by the time series plots of relative errors with respect to the respective initial value of global data from ***Fig. 6.37*** (from top to bottom) for

- global mass
- mass of the reference phase $(+)$ (interior of the circle), based on the geometry given by the level-set zero level
- global volume-of-fluid variable $\overline{\mathcal{P}\phi}$
- volume-of-fluid variable $\overline{\mathcal{P}\phi}^{(+)}$ in reference phase $(+)$
- circle area, based on volume-of-fluid information in reference phase $(+)$ according to the interface as given by the level-set zero level

[25] The left pictures in ***Fig. 6.29*** on page 234 are composed of two semi-transparent pictures corresponding to the two plots in ***Fig. 6.35*** each.

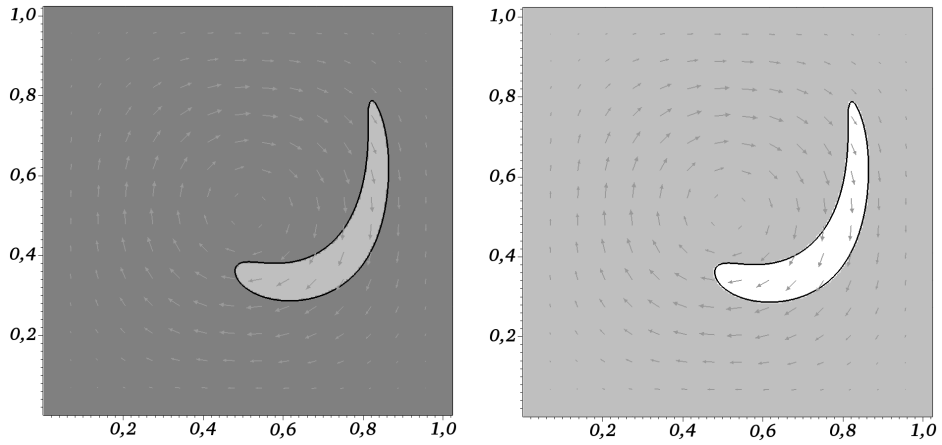

Fig. 6.36: Density after 300 explicit time steps for the Rider-Kothe vortex example: *left*: illustration limited to (*white*) $9.99999 \cdot 10^{-5} < \hat{\rho} < 1.00001 \cdot 10^{-4}$ (*black*) ; *right:* illustration limited to (*white*) $9.99999 \cdot 10^{-1} < \hat{\rho} < 1.00001$ (*black*); both fluid phases are kept sharp, since neither white nor black as boundaries of the narrow value ranges specified occur anywhere in the plots

The relative errors in all but the second plot are in the order of magnitude of machine accuracy, emphasized by the discrete levels of occuring values. This actually indicates, that only the last significant digit of the relative error is non-zero due to round-off errors. While zero is given by the dashed horizontal line in each plot, the solid horizontal line represents the average deviation from zero over time with corresponding value given in the header of each plot. The bottom plot shows the relative error of the circle area based on volume-of-fluid information, however, obtained in all regular cells within the circle and the portion within the circle in all cells which are cut by the interface due to the zero level of the level-set function. The fact, that this quantity is at machine accuracy as well, indicates, that there is no deviation between cells cut by the level-set zero level and cells carrying intermediate volume-of-fluid values. Thus, the interface representations due to level-set and volume-of-fluid can only deviate up to the magnitude of the grid spacing in each time step and the two interface representations are coupled well. A measure for this coupling is given in ***Fig. 6.37*** in the second plot from top, which represents the relative error of the reference phase mass with respect to its initial value, obtained from volume-of-fluid information but based on the volume fractions α given by the level-set based interface representation. The average deviation is due to the different natures of level-set and volume-of-fluid based interface representation and the fact, that they will not match exactly. However, successful coupling of these two interface representations and, as a result, successful coupling of the level-set based interface representation to the fluid

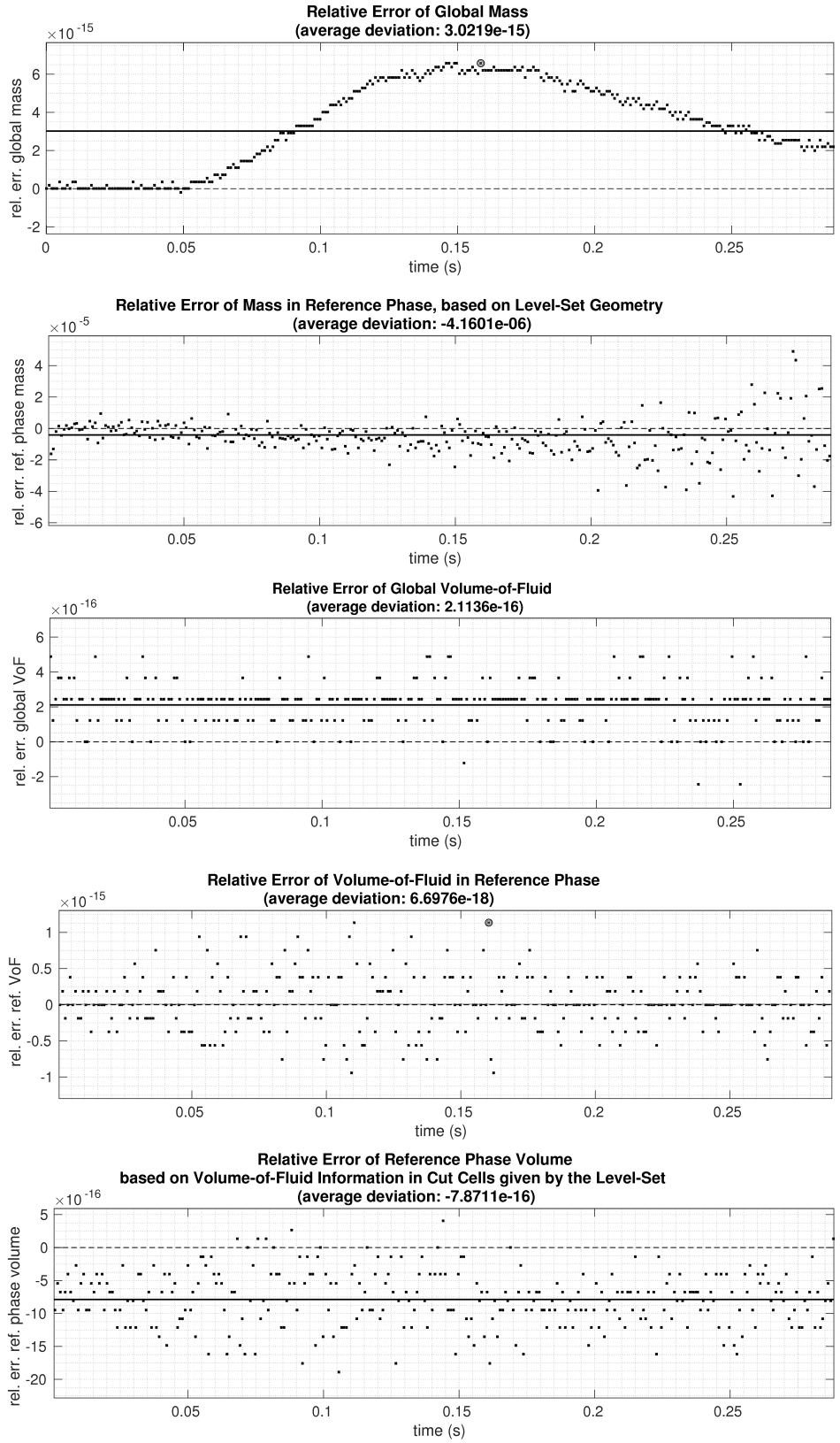

Fig. 6.37: Time series of relative errors of global data with respect to its initial data for the initial phase (first 300 explicit time steps) of the Rider-Kothe vortex example; *dots*: respective global datum at specific point in time; *solid line*: average deviation from the exact value (zero); *dashed line*: zero

flow, is shown due to the fact that the average deviation from zero over time is much smaller ($\mathcal{O}(10^{-6})$) than the individual contributions to this deviation ($\mathcal{O}(10^{-5})$).

Finally, ***Fig. 6.38*** is dedicated to the level-set penalization for keeping the local magnitude of the gradient of the level-set function $|\nabla G|$ from deviating rapidly from its target value of 1. The first and second plot on the left hand side show $|\nabla G|$ in an intermediate state after 100 explicit time steps ($\hat{t} = 0.096009$) within the narrow band around the interface without level-set penalization, in the top picture limited to the value range $0.5 < |\nabla G| < 1.5$, in the second picture without lower and upper bounds. It can be seen, that $|\nabla G|$ approaches both values close to zero and values that are much larger than one (black in the second picture on the left) very rapidly without penalization. While $|\nabla G|$ exceeds the value of 1.5 in all areas colored black in the top left picture, it has fallen below a value of 0.5 in the areas colored white. In contrast, the top right picture shows the same situation within the same value range applying the level-set penalization/re-initialization procedure: Within the core narrow band the values for $|\nabla G|$ remain close to 1 (medium grey), which can be seen more clearly in the other pictures on the right, in which the plotted allowable value range is limited more restrictively: Only few values are beyond values of 0.9 and 1.1 and significant local deviation are only present within a small range around 1. The lower left plot in ***Fig. 6.38*** shows the magnitude of the local interface normal strain rate tensor component $|\vec{n}_\Gamma \cdot \boldsymbol{E} \cdot \vec{n}_\Gamma|$ with $\boldsymbol{E}$ as given in equation (3.32) on page 21. It can be seen – comparing to the lower right plot of remaining deviations in $|\nabla G|$ – that the distribution of the required penalization matches the distribution of the magnitude of the interface normal strain rate tensor component, which has already been used for the penalization applied as given in section 6.5.3.1.

6.5.6.3 Rider-Kothe-Deformation

In principle the setting of this example, also proposed in [146], is the one from the previous section 6.5.6.2. However, instead of the velocity field specified by equation (6.220), a fix divergence-free velocity field

$$\hat{\vec{v}} = 2 \begin{pmatrix} \sin\left(4\pi\left(\hat{x}_1 + \frac{1}{2}\right)\right) \sin\left(4\pi\left(\hat{x}_2 + \frac{1}{2}\right)\right) \\ \cos\left(4\pi\left(\hat{x}_1 + \frac{1}{2}\right)\right) \cos\left(4\pi\left(\hat{x}_2 + \frac{1}{2}\right)\right) \end{pmatrix} \tag{6.223}$$

is used, which rapidly causes severe deformations as shown in ***Fig. 6.39***. This results in very steep level-set gradients, if not penalized, which cause inappropriate interface deformation and finally failure of the numerical method. The corresponding plots to

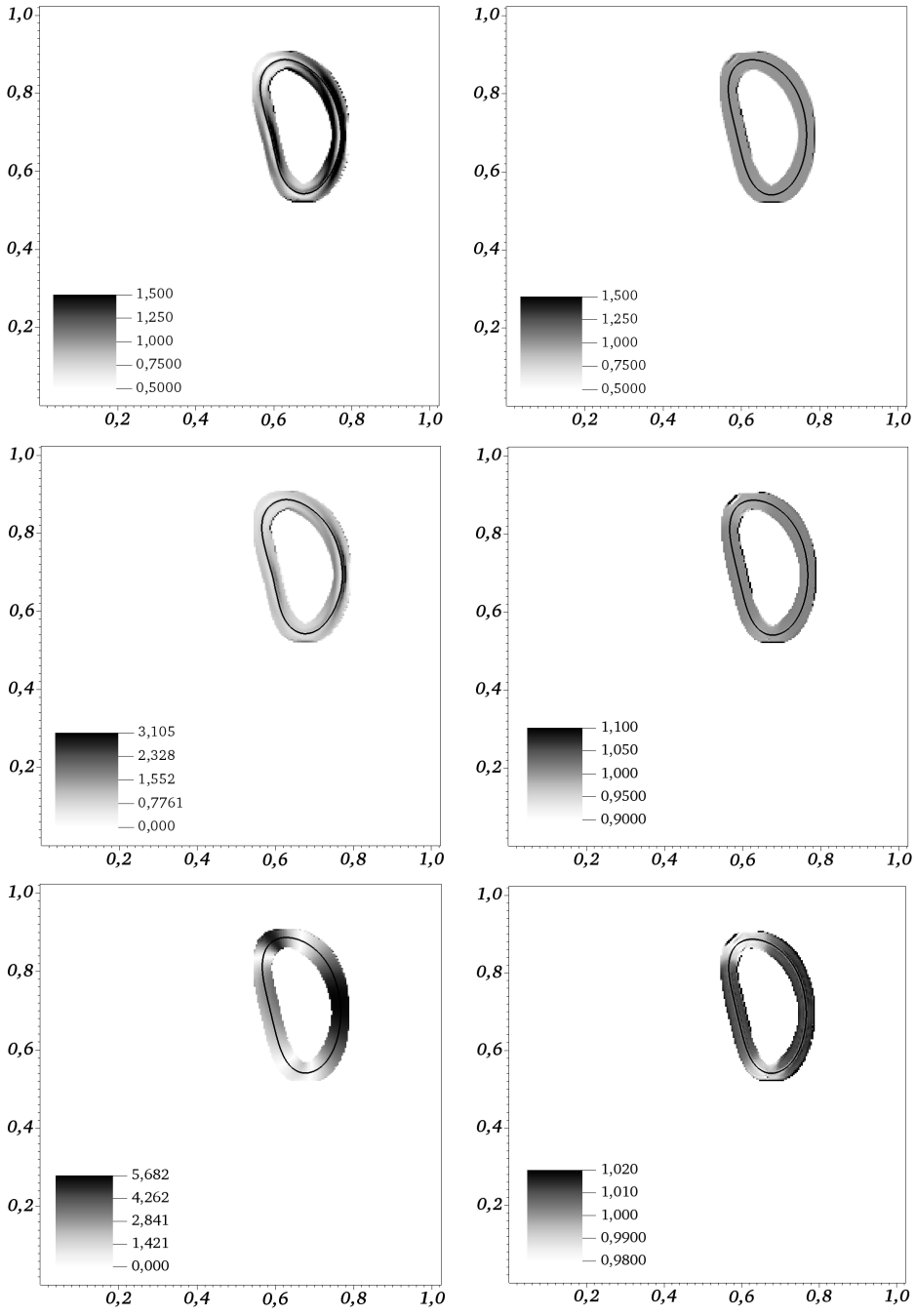

Fig. 6.38: Level-set gradient magnitude after 100 explicit time steps for the Rider-Kothe vortex example: ***left***: *top*: level-set gradient without penalization, limited to $0.5 < |\nabla G| < 1.5$; *center*: level-set gradient without penalization; *bottom*: interface normal component of the strain rate tensor $\boldsymbol{E}$ within the narrow band $\Re$; ***right***: level-set gradient with penalization of level-set gradient deviations from $|\nabla G| = 1$: *top*: illustration limited to $0.5 < |\nabla G| < 1.5$, *center*: illustration limited to $0.9 < |\nabla G| < 1.1$, *bottom*: illustration limited to $0.98 < |\nabla G| < 1.02$

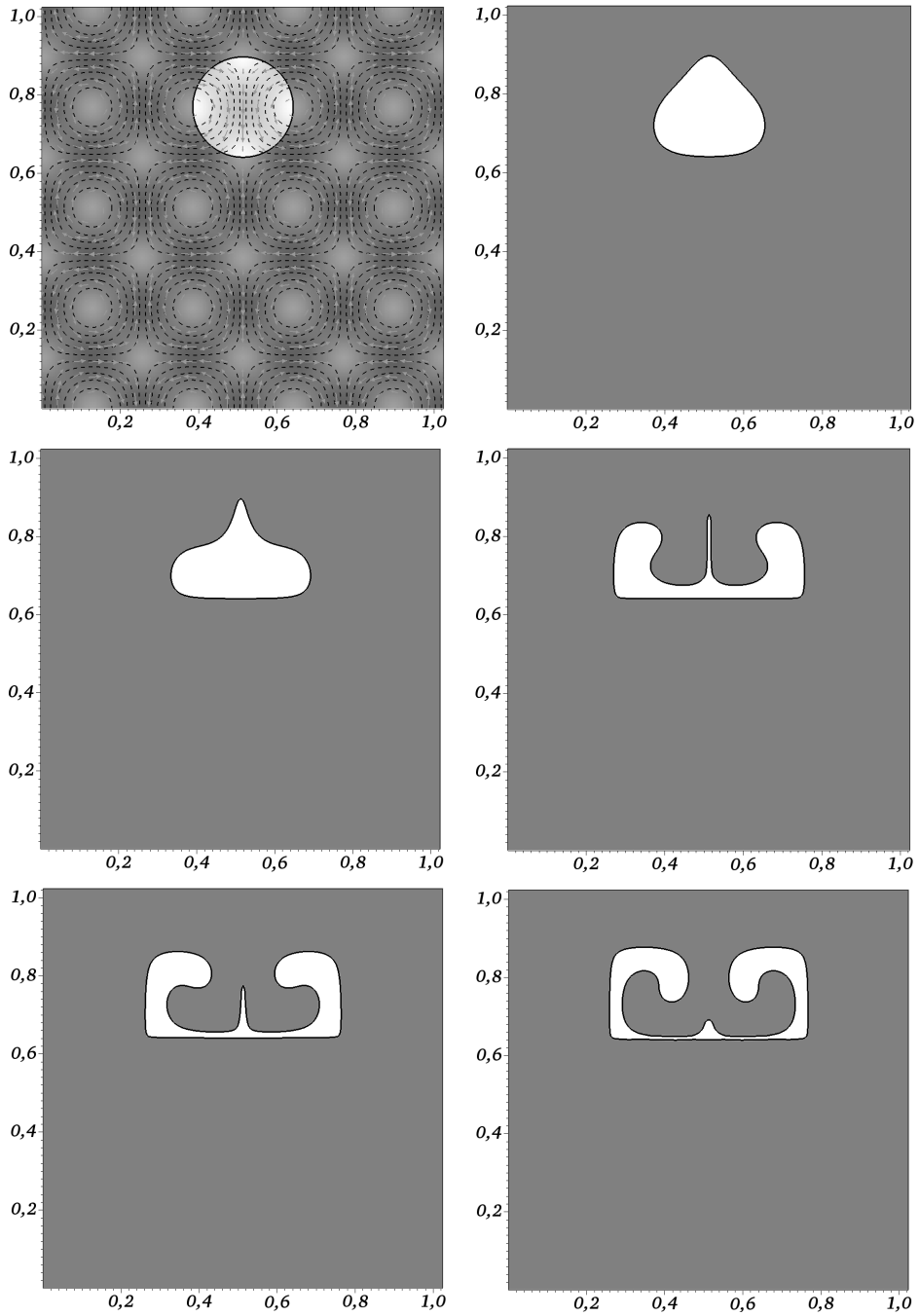

Fig. 6.39: Circle in a deforming velocity field: density of $\hat{\rho} = 10^{-4}$ (*white*), separated by the interface (*solid black line*) from the surrounding at density $\hat{\rho} = 1$ (*dark grey*) on a Cartesian grid of 256×256 grid cells at $\hat{t} \in ((0, 0.02), (0.05, 0.15), (0.20, 0.25))$; the upper left plot of the initial condition additionally shows the two-dimensional vorticity (*dashed lines*), the velocity vectors (*grey arrows*) and the velocity magnitude (*grey shades*) with darker areas representing larger velocity magnitudes

the ones in ***Fig. 6.37*** are given in ***Fig. 6.40*** with the same results as in section 6.5.6.2: Despite of the large density ratio, the rapid deformations and the locally very thin filaments in the fluidic structure, the relative errors of global mass, the volume-of-fluid quantity both globally and within the reference phase, and the reference phase volume, determined with volume-of-fluid information based on cut cells as given by the level-set geometry, only deviate by the magnitude of machine accuracy from zero and the fluid phases are kept sharply separated. In ***Fig. 6.41*** the corresponding plots for the magnitudes of the level-set gradient within bounds $0.5 < |\nabla G| < 1.5$, the interface normal level-set penalty function and both the interface normal strain rate tensor component and the interface normal velocity component are given for $\hat{t} = 0.15$, the last two governing the local penalization strength. The choice (6.160g) and (6.160h), however, does not seem to be universally optimal for all test cases. While a universal set of parameters remains to be determined, the choice

$$\mathcal{C}_{\mathfrak{E}} := 1\mathrm{m}\,\frac{\max_{\mathfrak{R}}\mathfrak{E}}{\max_{\mathfrak{R}}\mathfrak{V}}\mathcal{C}_{\mathfrak{V}} \tag{6.224}$$

with $\mathfrak{E}$ and $\mathfrak{V}$ as given in (6.160e) and (6.160f) is applicable to a wider range of test problems, however, with less optiomal results, depending on the given setting. ***Fig. 6.42*** shows the same picture as in the upper left plot of figure ***Fig. 6.41***, however, both with (6.224) instead of (6.160g) and limited to the range $0.8 < |\nabla G| < 1.2$ in order to emphasize the differences. The less black and white regions occur, the smoother the distribution of the magnitude of the level-set gradient is, and the smaller the amplitude of the deviation from $|\nabla G| = 1$ is. On the chosen grid the thin filaments in ***Fig. 6.39***, ***Fig. 6.41*** and ***Fig. 6.42*** are not well resolved. Therefore, on the one hand, recovery of ghost fluid data according to section 6.3.3.3 depends on less surrounding information, influencing both accuracy and stability of the method. On the other hand, the magnitude of the level-set gradient has decreased after the coalescence of two initially different narrow band regions. In the later case, level-set re-initialization as used in the present approach is not sufficient to keep the level-set gradient close to $|\nabla G| = 1$ and additional actions need to be taken in future work, involving adaptive mesh refinement and/or another level-set re-initialization procedure once different narrow band sections collide, in order to provide a reset starting point for the present algorithms to work properly. These numerical issues, responsible for the locally reduced discrete level-set gradient magnitude as indicated by white regions within the narrow band in ***Fig. 6.42***, explain the differences in the results in ***Fig. 6.39*** from the ones given in [146] due to a discrete underestimation of the expression $\mathcal{V}_G^{'}|\nabla G|$.

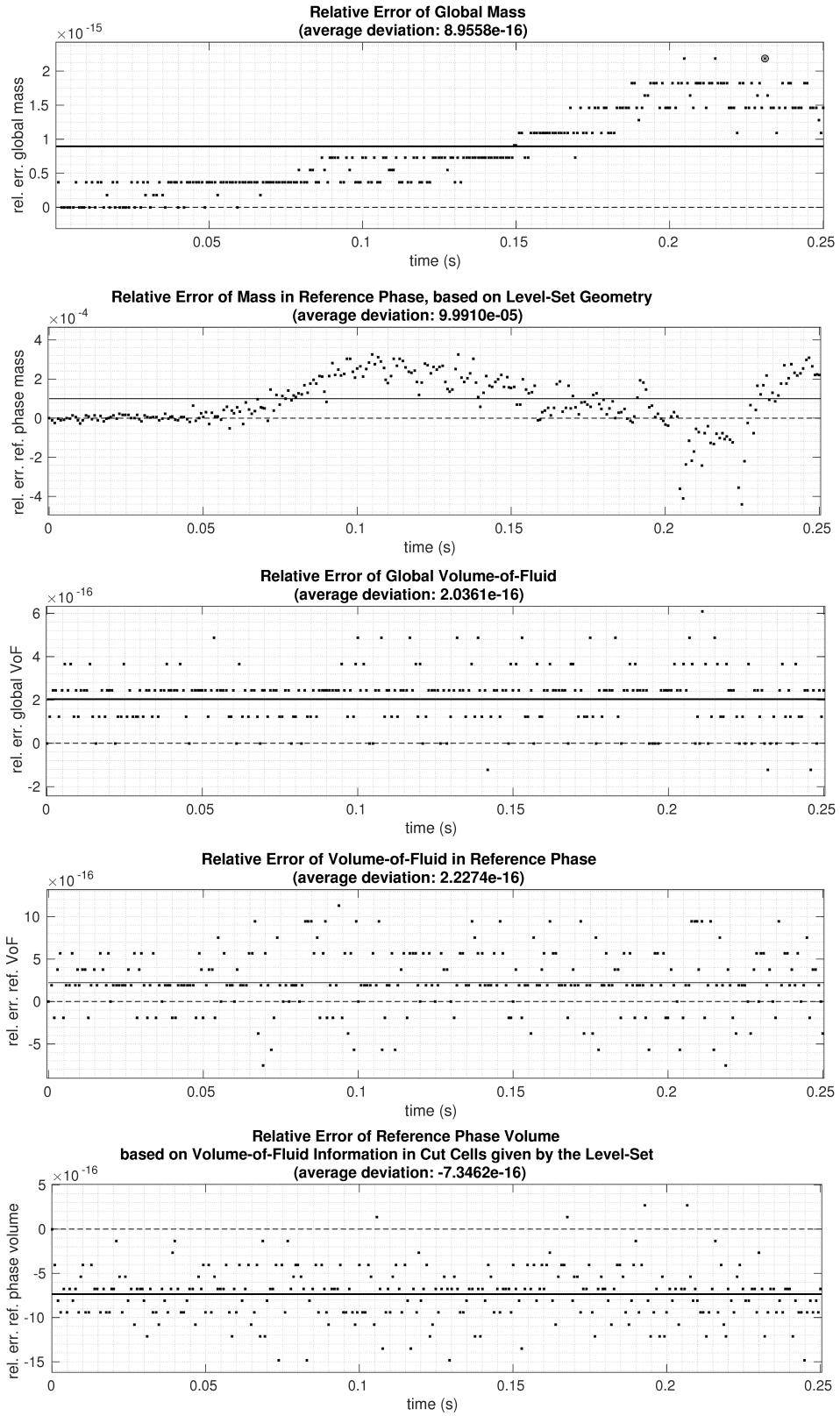

Fig. 6.40: Time series of relative errors of global data with respect to its initial data for $0 \leqslant \hat{t} \leqslant 0.25$ of the Rider-Kothe deformation example; *dots*: respective global datum at specific point in time; *solid line*: average deviation from the exact value (zero); *dashed line*: zero

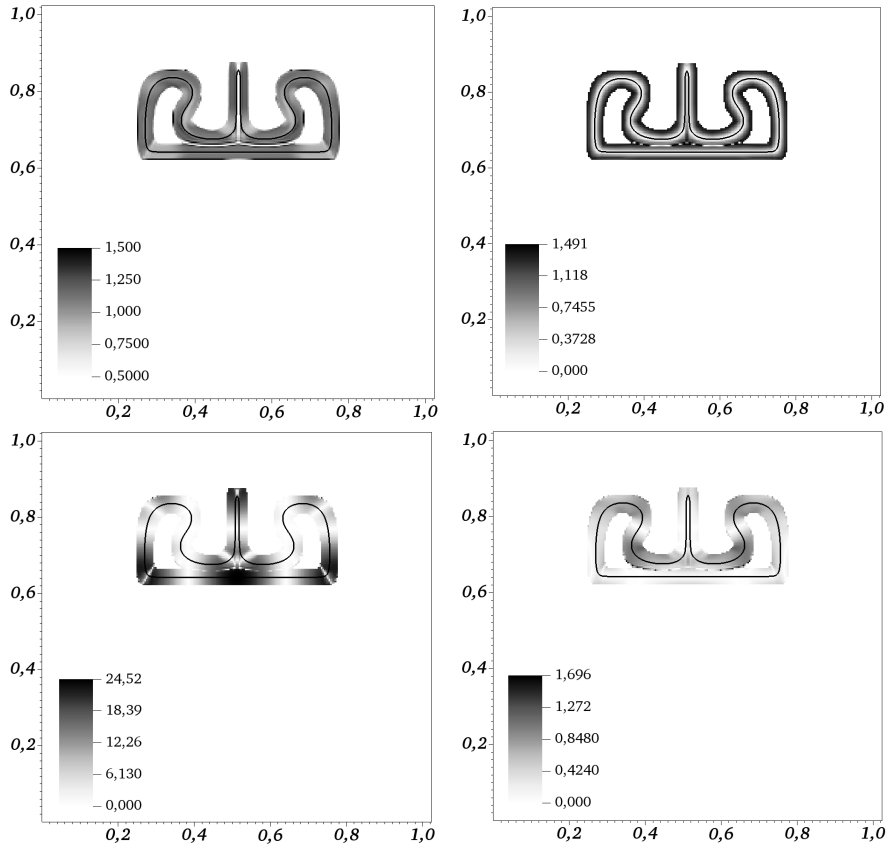

Fig. 6.41: Level-set gradient correction for the Rider-Kothe-deformation at $\hat{t} = 0.15$: *top left*: magnitude of the level-set gradient. Shown values limited to a range of $0.5 < |\nabla G| < 1.5$; *top right*: penalty function $\mathfrak{P}$; *bottom left*: magnitude of interface normal strain rate tensor component $|\vec{n}_\Gamma \cdot \boldsymbol{E} \cdot \vec{n}_\Gamma|$; *bottom right*: magnitude of interface normal velocity component $|\vec{v} \cdot \vec{n}_\Gamma|$

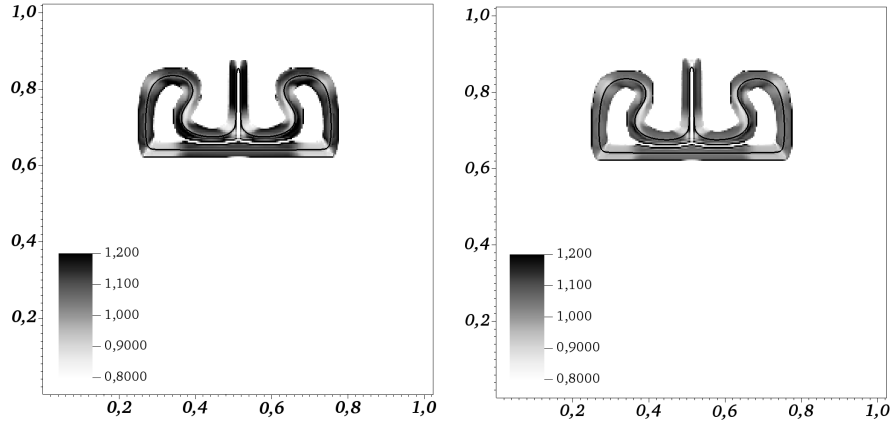

Fig. 6.42: Level-set gradient correction for the Rider-Kothe-deformation test problem at $\hat{t} = 0.15$ with different parameters: magnitude of the level-set gradient with values limited to a range of $0.8 < |\nabla G| < 1.2$, *left*: applying (6.160g) as proposed in [114]; *right*: applying (6.224)

6.6 Discretization of the Surface Stress Tensor

Surface tension as a material interface property due to molecular forces only acts along the interface. While its interface normal effective net impact balances[26] with the discontinuities of pressure and viscous stresses across the interface Γ and drives the interface towards a state of minimal energy (and, thus, minimal surface area), its interface tangential effect causes the fluid to move along the surface gradient of the surface tension coefficient due to an induced distorsion of the surrounding velocity field via friction.

Besides the discrete interface representation as discussed in section 6.1, proper discretization of surface tension and pressure forces within the conservation law of momentum are key features of a numerical method for simulation of immiscible two-phase flow. A subtle balance is mandatory in order to keep effects of spurious currents in the vicinity of the fluidic interface Γ small, and the numerical method accurate and stable. As shown in [55, 127], it is required for a suitable balance, that both pressure gradient and surface tension are treated as a single unit in each step of the numerical scheme. This implies discretization of both contributions at the same location in a compatible fashion.

In Finite Volume schemes, the pressure gradient is usually discretized as a space-time average pressure integral at grid cell faces as shown in section 5.1.4.1. Thus, the influence of surface tension needs to be discretized at grid cell faces as well, in order to allow for a suitable balance between pressure and surface tension.

While sharp conservative well-balanced representations are currently under development, in this section a continuous approximation of the surface stress tensor as given in section 3.2.4, only non-zero within a thin transition region $\mathfrak{B}$ of thickness 2ε around Γ as sketched in ***Fig. 6.43***, is presented, leading to a continuous approximation of the interfacial pressure jump within $\mathfrak{B}$.

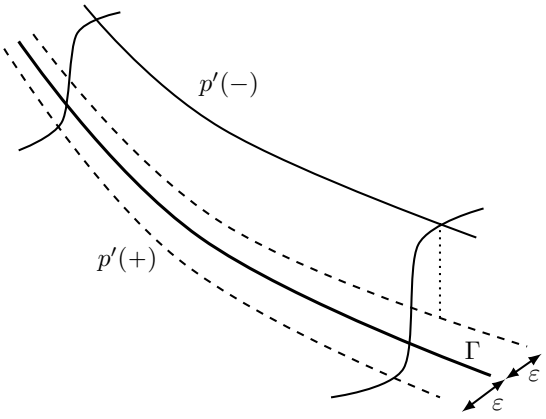

Fig. 6.43: Transition zone $\mathfrak{B}$ of thickness 2ε around the interface Γ

[26] See, for example, equation (3.132).

Most approaches for treating surface tension as a continuous force within $\mathfrak{B}$ (e.g. [167, 164, 150, 176, 47, 1]) trace back to the continuous surface force (CSF, [29]) method, which discretizes the force due to surface tension as a momentum source term in grid cell centers, involving a cosine-based approximation of the occurring Dirac delta distribution and relying on a volume-of-fluid (VOF) based interface representation. A fully conservative two-phase flow method, however, requires a conservative and locally well balanced discretization of all terms contributing to the conservation law, including forces due to surface tension, arising from arbitrarily complex surfaces and variable surface tension coefficients in both space and time.

While a suitable balance with the pressure and both stable and conservative treatment within the discrete momentum balance for density ratios $\frac{\rho^{(-)}}{\rho^{(+)}} \neq 1$ is subject of future work, such a conservative discretization of surface tension based forces at grid cell faces for interfaces, governed by a conservative level-set (LS) formulation as outlined in [182] and described in section 6.5, is presented in the following. It is based on the surface stress (CSS, [100]) or surface tension (CST, [82]) tensor formulation, discussed in e.g. [176, 187], as well as in section 3.2.4. This tensor allows for a flux density representation of forces due to surface tension via surface stresses at grid cell faces.

As shown in the following section 6.6.1, combination of

- bi-($\mathfrak{d} = 2$) or tri-($\mathfrak{d} = 3$) linear approximation of the tensor components on grid cell faces in space-time ($\mathfrak{d} = 2$) or space-space-time ($\mathfrak{d} = 3$),
- approximation of the Dirac delta distribution via interface normal linear hat functions as proposed in [48], and
- analytical space-time integration of the resulting polynomial representation

leads to the following benefits:

- no need for explicit evaluation of the interfacial curvature,
- no need for explicit evaluation of interface tangential information (and, thus, no conceptual difference between $\mathfrak{d} = 2$ and $\mathfrak{d} = 3$),
- the surface tension coefficient σ can be an arbitrary (smooth) function in space and time, e.g. depending on a surfactant[27] concentration on Γ, suitably extended into $\mathfrak{B}$ for numerical treatment,

[27] **surf**ace **act**ive **a**ge**nt**: see footnote on page 34.

- possibility of balancing space-time integral pressure and surface tension based stresses on each grid cell face separately, and
- well defined and robust behavior in the limit $\mathfrak{B} \to 0$ due to $\varepsilon \to 0$, provided the pressure is able to follow the continuous surface tension profile within $\mathfrak{B}$ due to analytic space-time integration over $\mathfrak{B}$ on sub-grid scale cell face fractions.

6.6.1 Discretization of Surface Tension Based Momentum Flux Contributions

The spatio-temporal effect of surface tension on the momentum balance can be represented via the vector integral

$$\vec{\mathcal{U}} := \frac{1}{|\Omega|} \int_{t^n}^{t^{n+1}} \oint_{\partial\Omega} \underbrace{\left(\boldsymbol{S}_\Gamma^{(\sigma)} \delta_\Gamma \right)}_{=:\, \boldsymbol{F}_S} \cdot \vec{n} \, \mathrm{d}A \, \mathrm{d}t \tag{6.225}$$

with surface integral from (3.76) on page 28. On a fixed Cartesian grid, this integral can be split into a sum of integrals over space-time sub-sections per grid cell face $\partial\Omega_{\mathfrak{d},\mathfrak{w}}$, characterized via time slices $\mathfrak{t}$ and space-time sections $\mathfrak{f}$ therein. With $\mathfrak{d}$ as grid cell face normal direction and $\mathfrak{w}$ as the side with respect to the grid cell center in the respective direction, the integral (6.225) reads

$$\begin{aligned}
\vec{\mathcal{U}} \; &= \Delta t \sum_{\mathfrak{d}=1}^{\mathfrak{d}} \frac{\Delta A_\mathfrak{d}}{\Delta V} \sum_{\mathfrak{w}=1}^{2} \left(\frac{1}{\Delta t \, \Delta A_\mathfrak{d}} \sum_{\mathfrak{t}=1}^{\mathcal{N}_{\mathfrak{t}_{\mathfrak{d},\mathfrak{w}}}} \sum_{\mathfrak{f}=1}^{\mathcal{N}^{\mathfrak{f}}_{\mathfrak{t}_{\mathfrak{d},\mathfrak{w}}}} \left[\int_{t_\mathfrak{t}^{\mathrm{lo}}}^{t_\mathfrak{t}^{\mathrm{hi}}} \int_{\partial\Omega_{\mathfrak{d},\mathfrak{w},\mathfrak{t},\mathfrak{f}}} \boldsymbol{F}_S \cdot \vec{n}_{\mathfrak{d},\mathfrak{w}} \, \mathrm{d}A \, \mathrm{d}t \right] \right) \\
&= \Delta t \sum_{\mathfrak{d}=1}^{\mathfrak{d}} \frac{1}{\mathfrak{c}_\mathfrak{d} \mathfrak{h}} \sum_{\mathfrak{w}=1}^{2} (-1)^{\mathfrak{w}} \underbrace{\left(\sum_{\mathfrak{t}=1}^{\mathcal{N}_{\mathfrak{t}_{\mathfrak{d},\mathfrak{w}}}} \sum_{\mathfrak{f}=1}^{\mathcal{N}^{\mathfrak{f}}_{\mathfrak{t}_{\mathfrak{d},\mathfrak{w}}}} \left[\frac{1}{\Delta t \, \Delta A_\mathfrak{d}} \int_{t_\mathfrak{t}^{\mathrm{lo}}}^{t_\mathfrak{t}^{\mathrm{hi}}} \int_{\partial\Omega_{\mathfrak{d},\mathfrak{w},\mathfrak{t},\mathfrak{f}}} \boldsymbol{F}_S \cdot \vec{\mathfrak{e}}_\mathfrak{d} \, \mathrm{d}A \, \mathrm{d}t \right] \right)}_{=:\, \widetilde{\overline{\mathcal{F}}}^{(\sigma)}_{\varepsilon,(\mathfrak{d},\mathfrak{w})}}
\end{aligned} \tag{6.226}$$

where $\mathcal{N}_{\mathfrak{t}_{\mathfrak{d},\mathfrak{w}}}$ represents the number of required time slices per grid cell face within Δt and $\mathcal{N}^{\mathfrak{f}}_{\mathfrak{t}_{\mathfrak{d},\mathfrak{w}}}$ is the number of sub-sections per time slice as shown in ***Fig. 6.44***.

For evaluation of the spatio-temporal flux average $\widetilde{\overline{\mathcal{F}}}^{(\sigma)}_{\varepsilon,(\mathfrak{d},\mathfrak{w})}$ per grid cell face $(\mathfrak{d},\mathfrak{w})$,

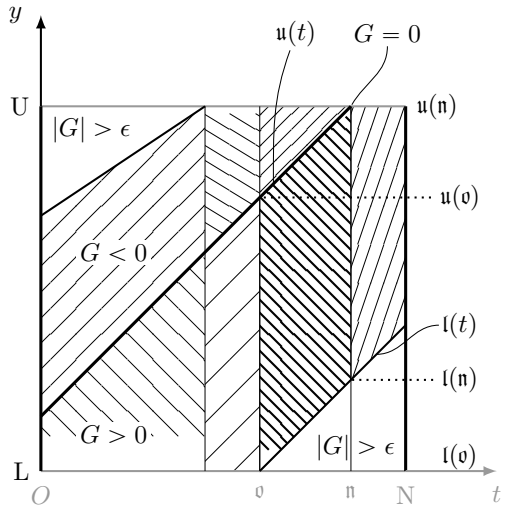

Fig. 6.44: Grid cell face (y) over time (t), cut by an interface Γ (*thick black line at* $G = 0$): Time slices (separated by vertical lines), depending on the grid cell face local spatio-temporal geometric scenario as described in detail in section 6.6.1.6, and space-time sub-sections (*differently shaded areas*), each with bounds $\mathfrak{o}$, $\mathfrak{n}$, $\mathfrak{l}(t)$ and $\mathfrak{u}(t)$ in a transition region $\mathfrak{B}$ (*entire shaded area*) around Γ

the integrals

$$\vec{\mathcal{J}}_{\mathfrak{d},\mathfrak{w},\mathfrak{t},\mathfrak{f}} := \int_{t_{\mathfrak{t}}^{\mathrm{lo}}}^{t_{\mathfrak{t}}^{\mathrm{hi}}} \int_{\partial\Omega_{\mathfrak{d},\mathfrak{w},\mathfrak{t},\mathfrak{f}}} \boldsymbol{F}_S \cdot \vec{\mathfrak{e}}_{\mathfrak{d}} \,\mathrm{d}A \,\mathrm{d}t \tag{6.227}$$

over each of the space-time sub-sections $(\mathfrak{t},\mathfrak{f})$ of face $(\mathfrak{d},\mathfrak{w})$ over time have to be evaluated. In **two space dimensions**, with y representing the coordinate perpendicular to the respective grid cell face normal vector $\vec{n}_\Gamma$ (and, thus, to coordinate direction $\vec{\mathfrak{e}}_{\mathfrak{d}}$), these integrals can be written as

$$\vec{\mathcal{J}}^{[2]}_{\mathfrak{d},\mathfrak{w},\mathfrak{t},\mathfrak{f}} = \int_{\mathfrak{o}}^{\mathfrak{n}} \int_{\mathfrak{l}}^{\mathfrak{u}} \boldsymbol{F}_S \cdot \vec{\mathfrak{e}}_{\mathfrak{d}} \,\mathrm{d}y \,\mathrm{d}t \tag{6.228}$$

with definitions

$$\mathfrak{o} := t_{\mathfrak{t}}^{\mathrm{lo}} \qquad \mathfrak{n} := t_{\mathfrak{t}}^{\mathrm{hi}} \qquad \mathfrak{l} := \mathfrak{l}(t) = y^{\mathrm{lo}}_{\mathfrak{d},\mathfrak{w},\mathfrak{t},\mathfrak{f}}(t) \qquad \mathfrak{u} := \mathfrak{u}(t) = y^{\mathrm{hi}}_{\mathfrak{d},\mathfrak{w},\mathfrak{t},\mathfrak{f}}(t) \tag{6.229}$$

and superscripts lo and hi indicating the lower and higher space and time coordinate as sketched in ***Fig. 6.44*** as well. Evaluation of each $\vec{\mathcal{J}}^{[2]}_{\mathfrak{d},\mathfrak{w},\mathfrak{t},\mathfrak{f}}$ is done via analytical integration of the integrand $\boldsymbol{F}_S \cdot \vec{\mathfrak{e}}_{\mathfrak{d}}$ using suitable ansatz functions in order to avoid discretization of the Dirac delta distribution on the underlying Cartesian grid beyond

the approximation given in section 6.6.1.1. As a result, only non-critical contributions to $\boldsymbol{F}_S$ with finite gradients of moderate sizes are discretized as described in the following.

6.6.1.1 Dirac approximation

For numerical evaluation, the singular Dirac delta distribution (3.14) requires smoothing within a narrow transition region $\mathfrak{B}$ of total width 2ε around the interface Γ (see [48]):

$$\delta_\Gamma \approx \delta^{(1)}\left(d(\vec{x},t)\right) \approx \delta_\varepsilon^{(1)}\left(d(\vec{x},t)\right) := \begin{cases} \frac{\mathfrak{A}}{\varepsilon}\mathfrak{B}\left(\frac{d(\vec{x},t)}{\varepsilon}\right) & |d(\vec{x},t)| \leqslant \varepsilon = \mathfrak{m}\,\mathfrak{h} \\ 0 & |d(\vec{x},t)| > \varepsilon = \mathfrak{m}\,\mathfrak{h} \end{cases} \tag{6.230}$$

where $d(\vec{x},t)$ is the signed distance function, m is a non-negative scaling factor with respect to the smooth transition region width and

$$\mathfrak{B}(\eta) := \left(1 - \mathrm{sgn}(\eta)^{\mathfrak{p}}\eta^{\mathfrak{p}}\right)^{\mathfrak{q}} \tag{6.231}$$

is at first chosen to be a general polynomial, acting in interface normal direction, with sgn as the sign function. As shown in [48], with smoothing (6.230) and the assumption that

$$d(\vec{x},t) \approx \frac{G(\vec{x},t)}{|\nabla G|} \tag{6.232}$$

is a valid approximation for the distance function in the vicinity of the interface Γ as shown in the box on page 256, the approximated one-dimensional Dirac delta distribution can be rewritten in terms of the (non-distance) level-set function G as

$$\begin{aligned} \delta_\varepsilon^{(1)}\left(d(\vec{x},t)\right) &= \delta_\varepsilon^{(1)}\left(\frac{G(\vec{x},t)}{|\nabla G|}\right) = \frac{\mathfrak{A}}{\varepsilon}\mathfrak{B}\left(\frac{\frac{G(\vec{x},t)}{|\nabla G|}}{\varepsilon}\right) = |\nabla G|\,\frac{\mathfrak{A}}{\epsilon}\mathfrak{B}\left(\frac{G(\vec{x},t)}{\epsilon}\right) \\ &= |\nabla G|\;\delta_\epsilon^{[1]}\left(G(\vec{x},t)\right) \end{aligned} \tag{6.233}$$

with

$$\epsilon := \varepsilon\,|\nabla G| = \mathfrak{m}\,\mathfrak{h}\,|\nabla G| =: \frac{1}{B} \tag{6.234}$$

as the modified variable bandwidth. Here,

$$\mathfrak{m} := \widetilde{\mathfrak{m}}_{glob}\,\widetilde{\mathfrak{m}}_{loc} \tag{6.235}$$

Level-Set vs. Signed Distance Function: The level-set function - although initialized as a signed distance function - does not necessarily remain a signed distance function and, depending on the processes that act on the level-set function, the level-set gradient can deteriorate from unity rapidly. However, as long as the resulting function maintains linear behavior within the region of interest in interface normal direction, the unknown distance d can be approximated as follows: If

1. the two linear functions

$$\mathcal{G}_0 = \mathcal{G}(d) - \text{sgn}(\mathcal{G}(d))|\nabla\mathcal{G}(d)|\,|d| \tag{6.236}$$
$$\mathcal{D}_0 = \mathcal{D}(d) - \text{sgn}(\mathcal{D}(d))|\nabla\mathcal{D}(d)|\,|d| \tag{6.237}$$

   with sign function sgn describe the same value $\mathcal{G}_0 = \mathcal{D}_0 = \mathcal{G}_\Gamma = \mathcal{D}_\Gamma\,(=0)$

2. both $\mathcal{G}(d)$ and $\mathcal{D}(d)$ have the same sign

$$\text{sgn}(\mathcal{G}(d)) = \text{sgn}(\mathcal{D}(d)) \tag{6.238}$$

3. the absolute value of d is replaced by d times its sign

$$|d| = \text{sgn}(d)\,d \tag{6.239}$$

4. one of the functions – say, $\mathcal{D}(d)$ – is the signed distance function $\mathcal{D}(d) = d$ with $|\nabla\mathcal{D}(d)| = |\nabla d| = 1$

then equating both expressions (6.236) and (6.237) leads to

$$\begin{aligned}
\mathcal{G}(d) &\overset{1.}{=} \mathcal{D}(d) - |d|\big[\text{sgn}(\mathcal{D}(d))|\nabla\mathcal{D}(d)| - \text{sgn}(\mathcal{G}(d))|\nabla\mathcal{G}(d)|\big] \\
&\overset{2.}{=} \mathcal{D}(d) - \text{sgn}(\mathcal{D}(d))\,|d|\,\big[|\nabla\mathcal{D}(d)| - |\nabla\mathcal{G}(d)|\big] \\
&\overset{3.}{=} \mathcal{D}(d) - \text{sgn}(\mathcal{D}(d))\,\text{sgn}(d)\,d\,\big[|\nabla\mathcal{D}(d)| - |\nabla\mathcal{G}(d)|\big] \\
&\overset{4.}{=} d\Big(1 - \underbrace{\text{sgn}(d)\,\text{sgn}(d)}_{=1}\,\big[\underbrace{|\nabla d|}_{=1} - |\nabla\mathcal{G}(d)|\big]\Big) \\
&= d\,|\nabla\mathcal{G}(d)|
\end{aligned} \tag{6.240}$$

is composed of a global and a local scaling factor, $\widetilde{\mathfrak{m}}_{glob}$ and $\widetilde{\mathfrak{m}}_{loc}$, to be specified in

section 6.6.1.5. Integration of (6.230) in interface normal direction – assuming $|\nabla G|$ to be constant (but not necessarily equal to 1) in that direction – according to

$$\begin{aligned}\int_{-\infty}^{\infty} \delta_\varepsilon^{(1)}\left(d(\vec{x},t)\right) \mathrm{d}d &= \int_{-\varepsilon}^{0} \delta_\varepsilon^{(1)}\left(d(\vec{x},t)\right)\, \mathrm{d}d + \int_{0}^{\varepsilon} \delta_\varepsilon^{(1)}\left(d(\vec{x},t)\right)\, \mathrm{d}d \\ &= \int_{-\epsilon}^{0} \delta_\epsilon^{[1]}\left(G\right)\, \mathrm{d}G + \int_{0}^{\epsilon} \delta_\epsilon^{[1]}\left(G\right)\, \mathrm{d}G \\ &= \int_{-\epsilon}^{0} \frac{\mathfrak{A}_{\mathfrak{p},\mathfrak{q}}}{\epsilon}\left(1-(-1)^{\mathfrak{p}}\left(\frac{G}{\epsilon}\right)^{\mathfrak{p}}\right)^{\mathfrak{q}} \mathrm{d}G \\ &\quad + \int_{0}^{\epsilon} \frac{\mathfrak{A}_{\mathfrak{p},\mathfrak{q}}}{\epsilon}\left(1-\left(\frac{G}{\epsilon}\right)^{\mathfrak{p}}\right)^{\mathfrak{q}} \mathrm{d}G \\ &\overset{!}{=} 1 \end{aligned} \tag{6.241}$$

results in

$$\mathfrak{A}_{\mathfrak{p},\mathfrak{q}} = \frac{1}{2}\left[\sum_{i=0}^{\mathfrak{q}} \frac{(-1)^i}{\mathfrak{p}i+1}\binom{\mathfrak{q}}{i}\right]^{-1} \tag{6.242}$$

with the binomial coefficient

$$\binom{\mathfrak{z}}{\mathfrak{s}} = \prod_{\eta=1}^{\mathfrak{s}} \frac{\mathfrak{z}+1-\eta}{\eta} = \frac{\mathfrak{z}!}{\mathfrak{s}!\,(\mathfrak{z}-\mathfrak{s})!} \tag{6.243}$$

for the amplitude $\mathfrak{A}$.

6.6.1.2 Integrand

The integrand of equation (6.228) – contributing the flux density across grid cell face $(\mathfrak{d},\mathfrak{w})$ with the latter indices omitted for brevity – reads

$$\left(\boldsymbol{F}_S\cdot\vec{\mathfrak{e}}_{\mathfrak{d}}\right)_{(\mathfrak{t},\mathfrak{f})}^{(\mathfrak{p},\mathfrak{q})} = \underbrace{\mathfrak{A}_{\mathfrak{p},\mathfrak{q}}\, B\left[1-\left(\mathrm{sgn}_{(\mathfrak{t},\mathfrak{f})}(G)\right)^{\mathfrak{p}} B^{\mathfrak{p}}\, G^{\mathfrak{p}}\right]^{\mathfrak{q}}}_{=\,\delta_\epsilon^{(1)}(G)} \underbrace{\sigma\,|\nabla G|\left(\vec{\mathfrak{e}}_{\mathfrak{d}}-\vec{n}_\Gamma\left(\vec{n}_\Gamma\cdot\vec{\mathfrak{e}}_{\mathfrak{d}}\right)\right)}_{=:\vec{f}(\nabla G)} \tag{6.244}$$

considering the identities

$$\vec{n}_\Gamma = \frac{\nabla G}{|\nabla G|}, \qquad \boldsymbol{I}\cdot\vec{\mathfrak{e}}_{\mathfrak{d}} \equiv \vec{\mathfrak{e}}_{\mathfrak{d}}, \qquad \left(\vec{n}_\Gamma\circ\vec{n}_\Gamma\right)\cdot\vec{\mathfrak{e}}_{\mathfrak{d}} \equiv \vec{n}_\Gamma\left(\vec{n}_\Gamma\cdot\vec{\mathfrak{e}}_{\mathfrak{d}}\right) \tag{6.245}$$

as well as the previous section and definition of the surface stress tensor (3.70).

The present formulation (6.244) allows the surface tension coefficient σ to be a function of e.g. a surface surfactant concentration C, which can be computed by extend-

ing the surface concentration C to the Cartesian grid in the respective vicinity of the interface Γ, if σ is not a constant and the relation $\sigma(C)$ is known.

In order to evaluate the integral (6.228) over integrand (6.244), the quantities $\vec{f}(\nabla G)$, G and B can be approximated bi-linearly in space-time:

$$\vec{f}(\nabla G) \approx \vec{F}_{\mathfrak{h}} := \vec{k}^{\vec{f}}_{00} + \vec{k}^{\vec{f}}_{10}\, t + \vec{k}^{\vec{f}}_{01}\, y + \vec{k}^{\vec{f}}_{11}\, t\, y \tag{6.246a}$$

$$G \approx G_{\mathfrak{h}} := \mathcal{K}^{G}_{00} + \mathcal{K}^{G}_{10}\, t + \mathcal{K}^{G}_{01}\, y + \mathcal{K}^{G}_{11}\, t\, y \tag{6.246b}$$

$$B \approx B_{\mathfrak{h}} := \mathcal{K}^{B}_{00} + \mathcal{K}^{B}_{10}\, t + \mathcal{K}^{B}_{01}\, y + \mathcal{K}^{B}_{11} t\, y \tag{6.246c}$$

Fig. 6.45 illustrates the different scenarios occurring in space-time domains within the spatio-temporal transition region around the interface, consisting of the grid cell boundary and the temporal axis. The quantities in equations (6.246) can be assumed to be approximated bi-linearly (grey) on the entire space-time cell based on nodal values of the latter, no matter if the cell is located completely within the spatio-temporal transition region (left sketch), at the transition region boundary with the grey shaded space-time fraction beyond the transition region (center sketch) or around the interface Γ (right sketch). The resulting approximation of the spatio-temporal integrand (6.244) obtains its sub-cell features (black) due to the interface normal Dirac approximation, sketched for $\mathfrak{p} = \mathfrak{q} = 1$.

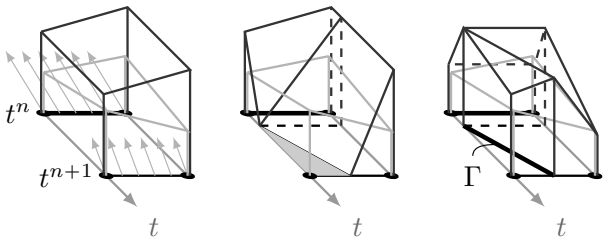

Fig. 6.45: Bi-linear ansatz function (grey) in space-time and resulting spatio-temporal approximation of the integrand $\boldsymbol{F}_S \cdot \vec{\mathfrak{e}}_{\mathfrak{d}}$ for $\mathfrak{p} = \mathfrak{q} = 1$ (black) for different positions of the space-time cell with respect to the spatio-temporal transition region $\mathfrak{B}$ around the interface Γ

After the coefficients $\vec{k}^{\vec{f}}_{ij}$, $\mathcal{K}^{G}_{ij}$ and $\mathcal{K}^{B}_{ij}$ with $i \in \{0,1\}$, $j \in \{0,1\}$ from equations (6.246) are determined according to equations (6.249a) - (6.249d) on page 259, based on the respective values

$$\{\vec{f}(\nabla G\,(L,O)), \vec{f}(\nabla G\,(U,O)), \vec{f}(\nabla G\,(L,N)), \vec{f}(\nabla G\,(U,N))\} \tag{6.247a}$$

$$\{G\,(L,O)\,, G\,(U,O)\,, G\,(L,N)\,, G\,(U,N)\} \tag{6.247b}$$

$$\{B\,(L,O)\,, B\,(U,O)\,, B\,(L,N)\,, B\,(U,N)\} \tag{6.247c}$$

Bi-Linear Ansatz in Space-Time: The general coefficients η_{ij} of a bi-linear ansatz with $i \in \{0,1\}$, $j \in \{0,1\}$ (in case of both scalars and vectors) can be determined on the two-dimensional Cartesian space-time cell, consisting of the time and one spatial coordinate y, via the 4 values $\{R_L^O, R_U^O, R_L^N, R_U^N\}$ in the corresponding space-time nodes (L,O), (U,O), (L,N) and (U,N):

$$\mathcal{R}_L^O = \eta_{00} + \eta_{10}\, O + \eta_{01}\, L + \eta_{11}\, O\, L \tag{6.248a}$$
$$\mathcal{R}_U^O = \eta_{00} + \eta_{10}\, O + \eta_{01}\, U + \eta_{11}\, O\, U \tag{6.248b}$$
$$\mathcal{R}_L^N = \eta_{00} + \eta_{10}\, N + \eta_{01}\, L + \eta_{11}\, N\, L \tag{6.248c}$$
$$\mathcal{R}_U^N = \eta_{00} + \eta_{10}\, N + \eta_{01}\, U + \eta_{11}\, N\, U \tag{6.248d}$$

Solution of the above linear system yields the coefficients

$$\eta_{00} = \varpi\left(N\,U\,\mathcal{R}_L^O - N\,L\,\mathcal{R}_U^O - O\,U\,\mathcal{R}_L^N + O\,L\,\mathcal{R}_U^N\right) \tag{6.249a}$$
$$\eta_{10} = -\varpi\left(U\,\mathcal{R}_L^O - L\,\mathcal{R}_U^O - U\,\mathcal{R}_L^N + L\,\mathcal{R}_U^N\right) \tag{6.249b}$$
$$\eta_{01} = -\varpi\left(N\,\mathcal{R}_L^O - N\mathcal{R}_U^O - O\,\mathcal{R}_L^N + O\,R_U^N\right) \tag{6.249c}$$
$$\eta_{11} = \varpi\left(\mathcal{R}_L^O - \mathcal{R}_U^O - \mathcal{R}_L^N + \mathcal{R}_U^N\right) \tag{6.249d}$$

with

$$\varpi := \frac{1}{(N-O)(U-L)} \tag{6.250}$$

in nodes (L,O), (U,O), (L,N) and (U,N) of space-time cell

$$\widetilde{\partial\Omega}_{\mathfrak{d},\mathfrak{w}} = \left(\partial\Omega_{\mathfrak{d},\mathfrak{w}} \in \mathbb{R}^{(\mathfrak{d}-1)} \times t \in \mathbb{R}\right) \tag{6.251}$$

with

$$O := t^n \qquad N := t^{n+1} = t^n + \Delta t \qquad L := y_0 \qquad U := y_1 = y_0 + \Delta y \tag{6.252}$$

as the bounds of $\widetilde{\partial\Omega}_{\mathfrak{d},\mathfrak{w}}$ as sketched in ***Fig. 6.44***, the integrand (6.244) reads

$$(\boldsymbol{F}_S \cdot \vec{\mathfrak{e}}_{\mathfrak{d}})_{(\mathfrak{t},\mathfrak{f})}^{(\mathfrak{p},\mathfrak{q})} = \mathfrak{A}_{\mathfrak{p},\mathfrak{q}} \left(\sum_{i=0}^{1}\sum_{j=0}^{1} \mathcal{K}_{ij}^B\, t^i\, y^j\right)\left(\sum_{i=0}^{2\mathfrak{p}\mathfrak{q}}\sum_{j=0}^{2\mathfrak{p}\mathfrak{q}} \mathfrak{S}_{ij\mathfrak{p}\mathfrak{q}}^{(\mathfrak{t},\mathfrak{f})}\, t^i\, y^j\right)\left(\sum_{i=0}^{1}\sum_{j=0}^{1} \vec{k}_{ij}^{\vec{f}}\, t^i\, y^j\right) \tag{6.253}$$

with $(2\mathfrak{p}\mathfrak{q}+1)^2$ coefficients $\mathfrak{S}_{ij\mathfrak{p}\mathfrak{q}}^{(\mathfrak{t},\mathfrak{f})}$ remaining to be specified in each space-time sub-

section $\mathfrak{t}$, $\mathfrak{f}$ as functions of $\mathcal{K}_{ij}^{G}$ and $\mathcal{K}_{ij}^{B}$. Equation (6.253) can be summarized to read

$$(\boldsymbol{F}_S \cdot \vec{\mathfrak{e}}_d)_{(\mathfrak{t},\mathfrak{f})}^{(\mathfrak{p},\mathfrak{q})} = \mathfrak{A}_{\mathfrak{p},\mathfrak{q}} \sum_{i=0}^{2(\mathfrak{p}\mathfrak{q}+1)} \sum_{j=0}^{2(\mathfrak{p}\mathfrak{q}+1)} \vec{\mathfrak{q}}_{ij}^{\,(\mathfrak{t},\mathfrak{f})}\, t^i\, y^j \tag{6.254}$$

with now $(2\mathfrak{p}\mathfrak{q}+3)^2$ vector coefficients $\vec{\mathfrak{q}}_{ij}^{\,(\mathfrak{t},\mathfrak{f})}$ remaining to be specified as functions of $\mathcal{K}_{ij}^{B}$, $\mathfrak{S}_{ij\mathfrak{p}\mathfrak{q}}^{(\mathfrak{t},\mathfrak{f})}$ and $\vec{k}_{ij}^{\vec{f}}$ as done in section 6.6.1.4.

6.6.1.3 Space-Time Integration

Neglecting integration constants, as they vanish after application of the integral bounds,

$$\begin{aligned}
\vec{\mathcal{J}}_{\mathfrak{d},\mathfrak{w},\mathfrak{t},\mathfrak{f}}^{[2]} &:= \int_{\mathfrak{o}}^{\mathfrak{n}} \int_{\mathfrak{l}}^{\mathfrak{u}} \boldsymbol{F}_S \cdot \vec{\mathfrak{e}}_{\mathfrak{d}}\, \mathrm{d}y\, \mathrm{d}t \\
&= \mathfrak{A}_{\mathfrak{p},\mathfrak{q}} \int_{\mathfrak{o}}^{\mathfrak{n}} \int_{\mathfrak{l}(t)}^{\mathfrak{u}(t)} \left(\sum_{i=0}^{2(\mathfrak{p}\mathfrak{q}+1)} \sum_{j=0}^{2(\mathfrak{p}\mathfrak{q}+1)} \vec{\mathfrak{q}}_{ij}^{\,(\mathfrak{t},\mathfrak{f})}\, t^i\, y^j \right) \mathrm{d}y\, \mathrm{d}t \\
&= \mathfrak{A}_{\mathfrak{p},\mathfrak{q}} \int_{\mathfrak{o}}^{\mathfrak{n}} \left[\sum_{i=0}^{2(\mathfrak{p}\mathfrak{q}+1)} \sum_{j=0}^{2(\mathfrak{p}\mathfrak{q}+1)} \frac{\vec{\mathfrak{q}}_{ij}^{\,(\mathfrak{t},\mathfrak{f})}}{j+1}\, t^i\, y^{j+1} \right]_{\mathfrak{l}(t)}^{\mathfrak{u}(t)} \mathrm{d}t
\end{aligned} \tag{6.255}$$

is obtained for the sub-section space-time integrals (6.228) after analytical integration in space on a grid cell face of a two dimensional spatial domain. With spatial bounds

$$\mathfrak{l} = \mathfrak{l}(t) \;= \mathfrak{l}(\mathfrak{o}) + \frac{\mathfrak{l}(\mathfrak{n}) - \mathfrak{l}(\mathfrak{o})}{\mathfrak{n} - \mathfrak{o}}\, (t - \mathfrak{o}) \tag{6.256}$$

$$\mathfrak{u} = \mathfrak{u}(t) \;= \mathfrak{u}(\mathfrak{o}) + \frac{\mathfrak{u}(\mathfrak{n}) - \mathfrak{u}(\mathfrak{o})}{\mathfrak{n} - \mathfrak{o}}\, (t - \mathfrak{o}) \tag{6.257}$$

which are assumed to depend linearly on time t, evaluation of the resulting polynomial in t of (at most) degree $(2\,(2(\mathfrak{p}\mathfrak{q}+1)+1))$ yields

$$\vec{\mathcal{J}}_{\mathfrak{d},\mathfrak{w},\mathfrak{t},\mathfrak{f}}^{[2]} \;=\; (\mathfrak{n} - \mathfrak{o})\, \frac{\mathfrak{A}_{\mathfrak{p},\mathfrak{q}}}{2}\, \vec{\mathcal{W}}_{(2(\mathfrak{p}\mathfrak{q}+1))}^{(\mathfrak{d},\mathfrak{w},\mathfrak{t},\mathfrak{f})} \tag{6.258}$$

with vectors

$$\vec{\mathcal{W}}_{z}^{(\mathfrak{d},\mathfrak{w},\mathfrak{t},\mathfrak{f})} := \sum_{i=0}^{z} \sum_{j=0}^{z-i} \left(\vec{\mathfrak{w}}_{ij}^{\,(\mathfrak{t},\mathfrak{f})}\, \mathfrak{n}^i\, \mathfrak{o}^j \right) \tag{6.259}$$

after analytical integration of (6.255) in time, subject to time slice bounds $\mathfrak{o}$ and $\mathfrak{n}$. In definition (6.259) the vector weights $\vec{\mathfrak{W}}_{ij}^{(\mathfrak{t},\mathfrak{f})}$ read

$$\begin{aligned}\vec{\mathfrak{W}}_{ij}^{(\mathfrak{t},\mathfrak{f})} &:= \frac{1}{\breve{\mathcal{B}}_{ij}} \sum_{\mathfrak{v}=0}^{2(\mathfrak{p}\mathfrak{q}+1)} \left(\frac{\vec{\mathfrak{q}}_{(i+j)\mathfrak{v}}^{(\mathfrak{t},\mathfrak{f})}}{\breve{\mathfrak{B}}_{ij\mathfrak{v}}} \sum_{\mathfrak{z}=0}^{\mathfrak{v}+1} \left[\breve{\mathcal{B}}_{ij\mathfrak{v}\mathfrak{z}}\, \mathcal{Y}_{\mathfrak{v}\mathfrak{z}} \right] \right) \\ &= \frac{1}{\mathcal{B}_{(i+j)}} \sum_{\mathfrak{v}=0}^{2(\mathfrak{p}\mathfrak{q}+1)} \left(\frac{\vec{\mathfrak{q}}_{(i+j)\mathfrak{v}}^{(\mathfrak{t},\mathfrak{f})}}{\mathfrak{B}_{(i+j)\mathfrak{v}}} \sum_{\mathfrak{z}=0}^{\mathfrak{v}+1} \left[\mathcal{B}_{(\mathfrak{v}+1-\mathfrak{z})i}\, \mathcal{B}_{\mathfrak{z}j}\, \mathcal{Y}_{\mathfrak{v}\mathfrak{z}} \right] \right) \\ &= \frac{1}{\mathcal{B}_{(i+j)}} \sum_{\mathfrak{v}=0}^{2(\mathfrak{p}\mathfrak{q}+1)} \left(\vec{\mathfrak{q}}_{(i+j)\mathfrak{v}}^{(\mathfrak{t},\mathfrak{f})} \mathfrak{w}_{ij\mathfrak{v}}^{(\mathfrak{t},\mathfrak{f})} \right) \end{aligned} \tag{6.260}$$

with $\vec{\mathfrak{q}}^{\,(\mathfrak{t},\mathfrak{f})}$ as specified in section 6.6.1.4 and

$$\mathfrak{w}_{ij\mathfrak{v}}^{(\mathfrak{t},\mathfrak{f})} := \frac{1}{\mathfrak{B}_{(i+j)\mathfrak{v}}} \sum_{\mathfrak{z}=0}^{\mathfrak{v}+1} \left[\mathcal{B}_{(\mathfrak{v}+1-\mathfrak{z})i}\, \mathcal{B}_{\mathfrak{z}j}\, \mathcal{Y}_{\mathfrak{v}\mathfrak{z}} \right] \tag{6.261}$$

as scalar base weights. The latter depend both on the space-time geometry via powers of the spatial limits $\mathfrak{l}$ and $\mathfrak{u}$ at the time slice boundaries $\mathfrak{o}$ and $\mathfrak{n}$ according to

$$\mathcal{Y}_{\mathfrak{v}\mathfrak{z}} := \mathfrak{u}(\mathfrak{n})^{\mathfrak{v}+1-\mathfrak{z}} \mathfrak{u}(\mathfrak{o})^{\mathfrak{z}} - \mathfrak{l}(\mathfrak{n})^{\mathfrak{v}+1-\mathfrak{z}} \mathfrak{l}(\mathfrak{o})^{\mathfrak{z}} \tag{6.262}$$

and on scalar coefficients

$$\breve{\mathcal{B}}_{ij} := \binom{2+(i+j)}{(i+j)} =: \mathcal{B}_{(i+j)} \tag{6.263a}$$

$$\breve{\mathfrak{B}}_{ij\mathfrak{v}} := \binom{2+(i+j)+\mathfrak{v}}{\mathfrak{v}} =: \mathfrak{B}_{(i+j)\mathfrak{v}} \tag{6.263b}$$

$$\breve{\mathcal{B}}_{ij\mathfrak{v}\mathfrak{z}} := \mathcal{B}_{(\mathfrak{v}+1-\mathfrak{z})i}\, \mathcal{B}_{\mathfrak{z}j}, \qquad \mathcal{B}_{\hat{i}\hat{j}} := \binom{\hat{i}+\hat{j}}{\hat{j}} \tag{6.263c}$$

which can be found as series in Pascal's triangle with binomial coefficients according to definition (6.243) as shown for $\mathfrak{p} = \mathfrak{q} = 1$ in ***Fig. 6.46*** and in (6.264).

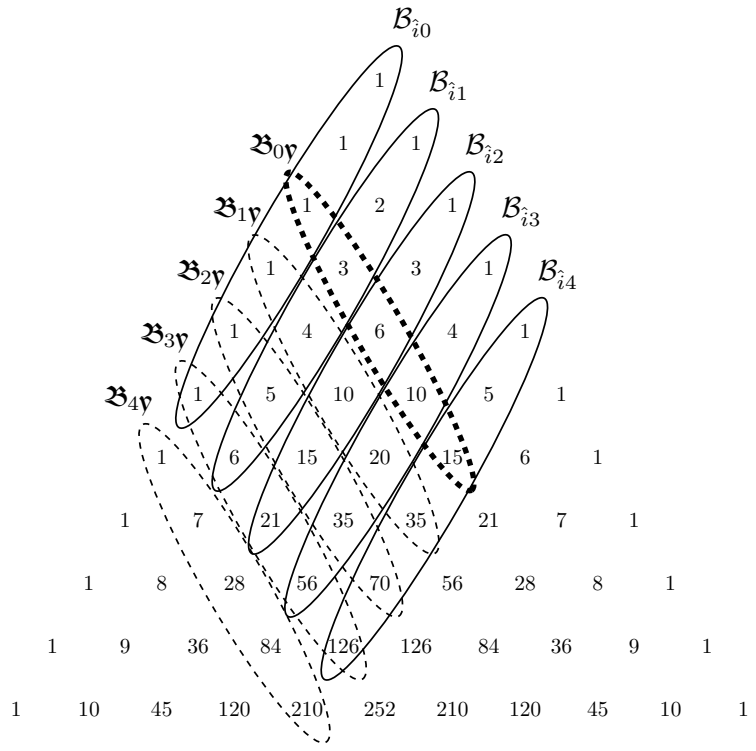

Fig. 6.46: Pascal's triangle; *solid*: $\mathcal{B}_{\hat{i}\hat{j}}$ as factors for $\breve{\mathcal{B}}_{ij\mathfrak{y}\mathfrak{z}}$ with $\hat{i} \in \{\mathfrak{y}+1-\mathfrak{z}, \mathfrak{z}\}$, *dashed*: $\mathfrak{B}_{(i+j)\mathfrak{y}}$, *thick dashed*: $\mathcal{B}_{(i+j)} = \mathfrak{B}_{0(i+j)}$

$$
\begin{array}{ccccccccccc}
\binom{0}{0} \\
\binom{1}{0} & & \binom{1}{1} \\
\binom{2}{0} & & \binom{2}{1} & & \binom{2}{2} \\
\binom{3}{0} & & \binom{3}{1} & & \binom{3}{2} & & \binom{3}{3} \\
\binom{4}{0} & & \binom{4}{1} & & \binom{4}{2} & & \binom{4}{3} & & \binom{4}{4} \\
\binom{5}{0} & & \binom{5}{1} & & \binom{5}{2} & & \binom{5}{3} & & \binom{5}{4} & & \binom{5}{5} \\
\binom{6}{0} & & \binom{6}{1} & & \binom{6}{2} & & \binom{6}{3} & & \binom{6}{4} & & \binom{6}{5} & & \binom{6}{6} \\
\binom{7}{0} & & \binom{7}{1} & & \binom{7}{2} & & \binom{7}{3} & & \binom{7}{4} & & \binom{7}{5} & & \binom{7}{6} & & \binom{7}{7} \\
\binom{8}{0} & & \binom{8}{1} & & \binom{8}{2} & & \binom{8}{3} & & \binom{8}{4} & & \binom{8}{5} & & \binom{8}{6} & & \binom{8}{7} & & \binom{8}{8} \\
\binom{9}{0} & & \binom{9}{1} & & \binom{9}{2} & & \binom{9}{3} & & \binom{9}{4} & & \binom{9}{5} & & \binom{9}{6} & & \binom{9}{7} & & \binom{9}{8} & & \binom{9}{9} \\
\binom{10}{0} & & \binom{10}{1} & & \binom{10}{2} & & \binom{10}{3} & & \binom{10}{4} & & \binom{10}{5} & & \binom{10}{6} & & \binom{10}{7} & & \binom{10}{8} & & \binom{10}{9} & & \binom{10}{10}
\end{array}
\tag{6.264}
$$

After reorganization for efficient computation, the resulting integral approximation to (6.225) on a Cartesian grid, yielding the momentum update due to surface tension, finally reads

$$\vec{\mathcal{U}} = \Delta t \sum_{\mathfrak{d}=1}^{\mathfrak{d}} \frac{1}{\mathfrak{c}_{\mathfrak{d}} \mathfrak{h}} \sum_{\mathfrak{w}=1}^{2} (-1)^{\mathfrak{w}} \underbrace{\left(\frac{\mathfrak{A}_{\mathfrak{p},\mathfrak{q}}}{2} \sum_{\mathfrak{t}=1}^{\mathcal{N}_{\mathfrak{t}_{\mathfrak{d},\mathfrak{w}}}} \frac{(\mathfrak{n}-\mathfrak{o})}{\Delta t} \sum_{\mathfrak{f}=1}^{\mathcal{N}^{\mathfrak{f}}_{\mathfrak{t}_{\mathfrak{d},\mathfrak{w}}}} \left[\frac{\vec{\mathcal{W}}^{(\mathfrak{d},\mathfrak{w},\mathfrak{t},\mathfrak{f})}_{(2(\mathfrak{p}\mathfrak{q}+1))}}{\Delta A_{\mathfrak{d}}} \right] \right)}_{=: \widetilde{\widetilde{\mathcal{F}}}^{(\sigma)}_{\varepsilon,(\mathfrak{d},\mathfrak{w})}} \tag{6.265}$$

with $\frac{(\mathfrak{n}-\mathfrak{o})}{\Delta t}$ as non-dimensional relative time slice size and $\vec{\mathcal{W}}^{\,(\mathfrak{d},\mathfrak{w},\mathfrak{t},\mathfrak{f})}$ as specified in (6.259), considering (6.260) to (6.263c). Coordinates of space-time sub-section corners $\mathfrak{o}$, $\mathfrak{n}$, $\mathfrak{l}$ and $\mathfrak{u}$ are determined in section 6.6.1.6.

6.6.1.4 Coefficients

With definition

$$Z_{\mathfrak{p},\mathfrak{q}} := 2\,(\mathfrak{p}\mathfrak{q}+1)+1 \tag{6.266}$$

the most simple choice

$$\mathfrak{p} = \mathfrak{q} = 1 \tag{6.267}$$

simultaneously is the most efficient one due to a rising number of $(Z_{\mathfrak{p},\mathfrak{q}})^2$ coefficients $\vec{\mathfrak{q}}^{\,(\mathfrak{t},\mathfrak{f})}_{(i+j)\mathfrak{y}}$ in (6.260) at rising $\mathfrak{p}$ and $\mathfrak{q}$. Due to the choice (6.267) equation (6.231) yields the interface normal linear hat function

$$\mathfrak{B}(\eta) = 1 - |\eta| = 1 - \operatorname{sgn}(\eta)\eta \tag{6.268}$$

for approximation of the Dirac distribution as proposed in [48] and sketched in ***Fig. 6.47***, with

$$\mathfrak{A}_{1,1} = 1 \tag{6.269}$$

from equation (6.242). In general the coefficients $\vec{\mathfrak{q}}^{\,(\mathfrak{t},\mathfrak{f})}_{(i+j)\mathfrak{y}}$ in equation (6.265) read

$$\vec{\mathfrak{q}}^{\,(\mathfrak{t},\mathfrak{f})}_{(i+j)\mathfrak{y}} = \sum_{\widetilde{a}=0}^{1} \sum_{\widetilde{b}=0}^{1} \left(\vec{k}^{\vec{f}}_{\widetilde{a}\widetilde{b}}\, \mathbf{Q}_{\left(\operatorname{mod}_{Z_{\mathfrak{p},\mathfrak{q}}}(Z_{\mathfrak{p},\mathfrak{q}}+i-\widetilde{a})\right)\left(\operatorname{mod}_{Z_{\mathfrak{p},\mathfrak{q}}}(Z_{\mathfrak{p},\mathfrak{q}}+j-\widetilde{b})\right)} \right) \tag{6.270}$$

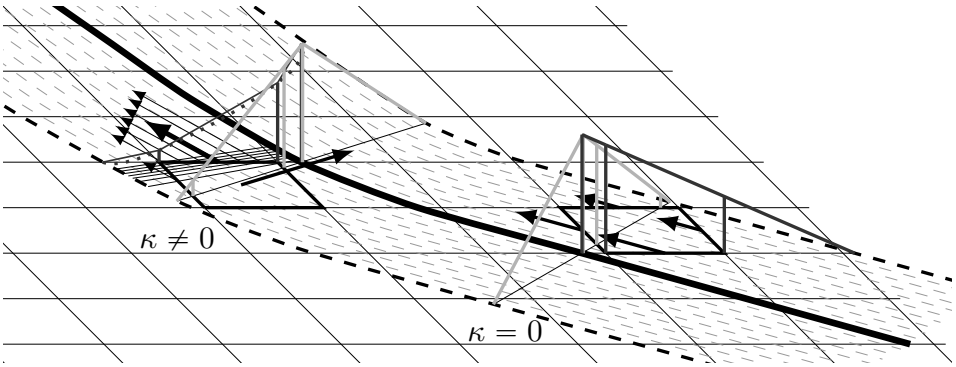

Fig. 6.47: Interface normal linear hat function within the transition region $\mathfrak{B}$ (black lines), interface tangential contributions at grid cell faces (thin arrows) with average at grid cell faces and resulting interface normal effect per grid cell as result of the balance over the grid cell boundary

with

$$0 \leqslant i < Z_{\mathfrak{p},\mathfrak{q}} \tag{6.271a}$$

$$0 \leqslant j < Z_{\mathfrak{p},\mathfrak{q}} \tag{6.271b}$$

and modulo operation $\mathrm{mod}_{Z_{\mathfrak{p},\mathfrak{q}}}$ with respect to division by $Z_{\mathfrak{p},\mathfrak{q}}$. For the choice (6.267), resulting in $Z_{1,1} = 5$, a $Z_{1,1} \times Z_{1,1}$ matrix

$$\mathbf{Q} = \begin{pmatrix} \mathfrak{r}_{0000} & \mathfrak{p}^{0100}_{0001} & \mathfrak{p}^{0101}_{0002} & \mathfrak{r}_{0102} & 0 \\ \mathfrak{p}^{1000}_{0010} & \left(\mathfrak{p}^{0110}_{0011} + \mathfrak{p}^{1100}_{1001}\right) & \left(\mathfrak{p}^{0111}_{0012} + \mathfrak{p}^{1101}_{1002}\right) & \mathfrak{p}^{1102}_{0112} & 0 \\ \mathfrak{p}^{1010}_{0020} & \left(\mathfrak{p}^{0120}_{0021} + \mathfrak{p}^{1110}_{1011}\right) & \left(\mathfrak{p}^{0121}_{0022} + \mathfrak{p}^{1111}_{1012}\right) & \mathfrak{p}^{1112}_{0122} & 0 \\ \mathfrak{r}_{1020} & \mathfrak{p}^{1120}_{1021} & \mathfrak{p}^{1121}_{1022} & \mathfrak{r}_{1122} & 0 \\ 0 & 0 & 0 & 0 & 0 \end{pmatrix} \tag{6.272}$$

is obtained, in which

$$\mathfrak{p}^{\mathfrak{p}\mathfrak{q}\mathfrak{r}\mathfrak{l}}_{\mathfrak{a}\mathfrak{b}\mathfrak{m}\mathfrak{n}} := \mathfrak{r}_{\mathfrak{a}\mathfrak{b}\mathfrak{m}\mathfrak{n}} + \mathfrak{r}_{\mathfrak{p}\mathfrak{q}\mathfrak{r}\mathfrak{l}} \tag{6.273a}$$

$$\mathfrak{r}_{\mathfrak{u}\mathfrak{v}\mathfrak{w}\mathfrak{x}} := \mathcal{K}^{B}_{\mathfrak{u}\mathfrak{v}} \mathfrak{S}^{(\mathfrak{t},\mathfrak{f})}_{\mathfrak{w}\mathfrak{x}} \tag{6.273b}$$

and

$$\mathfrak{S}^{(\mathfrak{t},\mathfrak{f})}_{\mathfrak{w}\mathfrak{x}} = \delta_{(\mathfrak{w}+\mathfrak{x}),0} - \mathrm{sgn}_{\mathfrak{t},\mathfrak{f}}\left(G(\vec{x},t)\right) \mathfrak{Z}_{\mathfrak{w}\mathfrak{x}} \tag{6.274}$$

with δ as the Kronecker delta (5.58) as well as

$$\mathfrak{Z}_{(\mathfrak{a}+\mathfrak{m})(\mathfrak{b}+\mathfrak{n})} = \frac{1}{4}\begin{pmatrix} 2 \\ \mathfrak{a}+\mathfrak{m} \end{pmatrix}\begin{pmatrix} 2 \\ \mathfrak{b}+\mathfrak{n} \end{pmatrix}\left(\mathcal{K}^B_{\mathfrak{a}\mathfrak{b}}\mathcal{K}^G_{\mathfrak{m}\mathfrak{n}} + \mathcal{K}^B_{\mathfrak{m}\mathfrak{n}}\mathcal{K}^G_{\mathfrak{a}\mathfrak{b}} + \mathcal{K}^B_{\mathfrak{a}\mathfrak{n}}\mathcal{K}^G_{\mathfrak{m}\mathfrak{b}} + \mathcal{K}^B_{\mathfrak{m}\mathfrak{b}}\mathcal{K}^G_{\mathfrak{a}\mathfrak{n}}\right) \tag{6.275}$$

subject to

$$0 \leqslant \mathfrak{a} \leqslant 1 \tag{6.276a}$$
$$0 \leqslant \mathfrak{b} \leqslant 1 \tag{6.276b}$$
$$\mathfrak{a} \leqslant \mathfrak{m} \leqslant 1 \tag{6.276c}$$
$$\mathfrak{b} \leqslant \mathfrak{n} \leqslant 1 \tag{6.276d}$$

due to $0 \leqslant (\mathfrak{a}+\mathfrak{m}) \leqslant 2$ and $0 \leqslant (\mathfrak{b}+\mathfrak{n}) \leqslant 2$.

6.6.1.5 Evaluation Simplification

On the one hand, with choice $\widetilde{\mathfrak{m}}_{glob} \geqslant \frac{\mathfrak{D}}{\widetilde{\mathfrak{m}}_{loc}}$ and

$$\mathfrak{D} := \sqrt{\sum_{\mathfrak{d}=1}^{\mathfrak{d}} \mathfrak{c}_{\mathfrak{d}}^2} \tag{6.277}$$

as relative length of the grid cell diagonal with respect to $\mathfrak{h}^{\mathfrak{d}}$, definition (6.235) guarantees, that on each side of the interface at least one grid cell is entirely within the transition region $\mathfrak{B}$, in which the smoothed Dirac is non-zero, independent of the angle between interface and Cartesian grid coordinate system. On the other hand, the choice

$$\widetilde{\mathfrak{m}}_{loc} := \frac{1}{|\nabla G|} \tag{6.278}$$

leads to constant ϵ and B as specified in equation (6.234), which simplifies the presented approach significantly, since in that case

$$\mathcal{K}^B_{00} = B \tag{6.279a}$$
$$\mathcal{K}^B_{01} = \mathcal{K}^B_{10} = \mathcal{K}^B_{11} = 0 \tag{6.279b}$$

and the integrand (6.253) reduces to

$$
\begin{aligned}
(\boldsymbol{F}_S \cdot \vec{\mathfrak{e}}_d)^{(1,1)}_{(\mathfrak{t},\mathfrak{f})} &= \mathfrak{A}_{1,1}\mathcal{K}^B_{00}\left(\sum_{i=0}^{1}\sum_{j=0}^{1}\hat{\mathfrak{S}}^{(\mathfrak{t},\mathfrak{f})}_{ij}\,t^i y^j\right)\left(\sum_{i=0}^{1}\sum_{j=0}^{1}\vec{k}^{\vec{f}}_{ij}\,t^i y^j\right) \\
&= \mathfrak{A}_{1,1}\mathcal{K}^B_{00}\sum_{i=0}^{2}\sum_{j=0}^{2}\hat{\vec{\mathfrak{q}}}^{(\mathfrak{t},\mathfrak{f})}_{ij}\,t^i y^j
\end{aligned}
\tag{6.280}
$$

with

$$
\hat{\mathfrak{S}}^{(\mathfrak{t},\mathfrak{f})}_{\mathfrak{w}\mathfrak{x}} = \delta_{(\mathfrak{w}+\mathfrak{x}),0} - \mathrm{sgn}_{\mathfrak{t},\mathfrak{f}}\left(G(\vec{x},t)\right)\,\mathcal{K}^B_{00}\,\mathcal{K}^G_{\mathfrak{w}\mathfrak{x}} \tag{6.281}
$$

and Kronecker delta δ from (5.58), resulting in less but much easier to handle vector coefficients

$$
\hat{\vec{\mathfrak{q}}}^{(\mathfrak{t},\mathfrak{f})}_{(\mathfrak{a}+\mathfrak{m})(\mathfrak{b}+\mathfrak{n})} = \frac{1}{4}\binom{2}{\mathfrak{a}+\mathfrak{m}}\binom{2}{\mathfrak{b}+\mathfrak{n}}\left(\hat{\mathfrak{S}}^{(\mathfrak{t},\mathfrak{f})}_{\mathfrak{a}\mathfrak{b}}\,\vec{k}^{\vec{f}}_{\mathfrak{m}\mathfrak{m}} + \hat{\mathfrak{S}}^{(\mathfrak{t},\mathfrak{f})}_{\mathfrak{m}\mathfrak{m}}\,\vec{k}^{\vec{f}}_{\mathfrak{a}\mathfrak{b}} + \hat{\mathfrak{S}}^{(\mathfrak{t},\mathfrak{f})}_{\mathfrak{a}\mathfrak{m}}\,\vec{k}^{\vec{f}}_{\mathfrak{m}\mathfrak{b}} + \hat{\mathfrak{S}}^{(\mathfrak{t},\mathfrak{f})}_{\mathfrak{m}\mathfrak{b}}\,\vec{k}^{\vec{f}}_{\mathfrak{a}\mathfrak{n}}\right) \tag{6.282}
$$

with

$$0 \leqslant \mathfrak{a} \leqslant 1 \tag{6.283a}$$

$$0 \leqslant \mathfrak{b} \leqslant 1 \tag{6.283b}$$

$$\mathfrak{a} \leqslant \mathfrak{m} \leqslant 1 \tag{6.283c}$$

$$\mathfrak{b} \leqslant \mathfrak{n} \leqslant 1 \tag{6.283d}$$

due to $0 \leqslant (\mathfrak{a}+\mathfrak{m}) \leqslant 2$ and $0 \leqslant (\mathfrak{b}+\mathfrak{n}) \leqslant 2$. As a result of analytical space-time integration of the integrand (6.280), considering (6.256) and (6.257),

$$
\vec{\mathcal{J}}^{[2]}_{\mathfrak{d},\mathfrak{w},\mathfrak{t},\mathfrak{f}} = (\mathfrak{n}-\mathfrak{o})\frac{\mathfrak{A}_{1,1}}{2}\sum_{i=0}^{2}\sum_{j=0}^{2-i}\left(\hat{\vec{\mathfrak{W}}}^{(\mathfrak{t},\mathfrak{f})}_{ij}\,\mathfrak{n}^i\,\mathfrak{o}^j\right) = (\mathfrak{n}-\mathfrak{o})\,\frac{\mathfrak{A}_{1,1}}{2}\,\vec{\mathcal{W}}_2{}^{(\mathfrak{d},\mathfrak{w},\mathfrak{t},\mathfrak{f})} \tag{6.284}
$$

remains, with $\vec{\mathcal{W}}_2{}^{(\mathfrak{d},\mathfrak{w},\mathfrak{t},\mathfrak{f})}$ as given by equation (6.259) and

$$
\hat{\vec{\mathfrak{W}}}^{(\mathfrak{t},\mathfrak{f})}_{ij} = \frac{1}{\mathcal{B}_{(i+j)}}\sum_{\mathfrak{y}=0}^{2}\left(\hat{\vec{\mathfrak{q}}}^{(\mathfrak{t},\mathfrak{f})}_{(i+j)\mathfrak{y}}\,\mathfrak{w}^{(\mathfrak{t},\mathfrak{f})}_{ij\mathfrak{y}}\right) \tag{6.285}
$$

with $\mathfrak{w}^{(\mathfrak{t},\mathfrak{f})}_{ij\mathfrak{y}}$ according to equation (6.261) as well as $\mathcal{B}$, $\mathfrak{B}$ and $\mathcal{B}$ as given in (6.263a) to (6.263c) and sketched in ***Fig. 6.48***. Determination of the missing geometry based information for computation of $\hat{\vec{\mathfrak{q}}}^{(\mathfrak{t},\mathfrak{f})}_{(i+j)\mathfrak{y}}$ and $\mathfrak{w}^{(\mathfrak{t},\mathfrak{f})}_{ij\mathfrak{y}}$ is given in the next section 6.6.1.6.

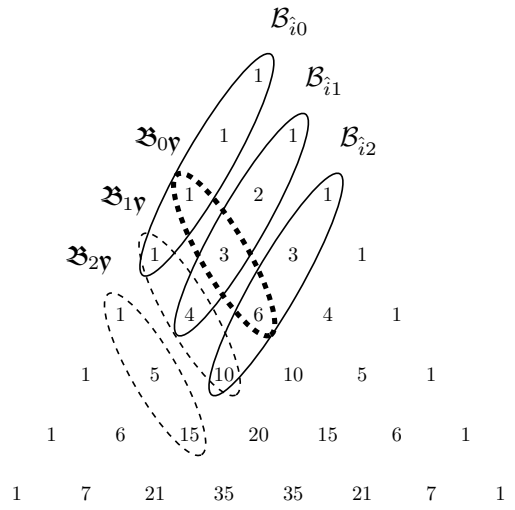

Fig. 6.48: Pascal's triangle; selection of coefficients for simplified evaluation: *solid*: $\mathcal{B}_{\hat{i}\hat{j}}$ as factors for $\breve{\mathcal{B}}_{ij\mathfrak{y}\mathfrak{z}}$ with $\hat{i} \in \{\mathfrak{y}+1-\mathfrak{z}, \mathfrak{z}\}$, *dashed*: $\mathfrak{B}_{(i+j)\mathfrak{y}}$, *thick dashed*: $\mathcal{B}_{(i+j)} = \mathfrak{B}_{0(i+j)}$; see Figure 6.46 and Pascal's triangle in (6.264) for comparison in case of general B

6.6.1.6 Scenarios

For computation of the integrals $\vec{\mathcal{J}}^{[2]}_{\mathfrak{d},\mathfrak{w},\mathfrak{t},\mathfrak{f}}$ over the different space-time sub-sections of each grid cell face according to (6.284) via the vector $\vec{\mathcal{W}}_2^{(\mathfrak{d},\mathfrak{w},\mathfrak{t},\mathfrak{f})}$ – the latter consisting of the different $\hat{\vec{\mathfrak{W}}}^{(\mathfrak{t},\mathfrak{f})}$ according to (6.285) as result of the various $\hat{\vec{\mathfrak{q}}}^{(\mathfrak{t},\mathfrak{f})}$ from (6.282), geometry based weights $\mathfrak{w}^{(\mathfrak{t},\mathfrak{f})}$ from (6.261) and coefficients from Pascal's triangle according to (6.263a) to (6.263c) – the approximated spatio-temporal scenario on each cut grid cell face has to be known as a result of the interface movement. While for determination of the coefficients $\hat{\vec{\mathfrak{q}}}^{(\mathfrak{t},\mathfrak{f})}$ only the sign $\mathrm{sgn}_{\mathfrak{t},\mathfrak{f}}\left(G(\vec{x},t)\right)$ of the level-set function G in each space-time sub-section has to be available in order to determine the coefficients $\hat{\mathfrak{S}}^{(\mathfrak{t},\mathfrak{f})}$ from (6.281), for computation of the geometry based weights $\mathfrak{w}^{(\mathfrak{t},\mathfrak{f})}$ determination of the corner coordinates $\mathfrak{l}(\mathfrak{o})$, $\mathfrak{u}(\mathfrak{o})$, $\mathfrak{l}(\mathfrak{n})$ and $\mathfrak{u}(\mathfrak{n})$ of each space-time sub-section with time slice boundaries $\mathfrak{o}$ and $\mathfrak{n}$ – to be determined as well – is required in order to evaluate equation (6.262). ***Fig. 6.49*** shows the general scenario for general space-time-dependent B. This scenario is the most complex one that can arise within the present surrounding numerical method: A cell face is intersected by an interface (thick solid line) at the beginning of the time step (O), then after a certain period within this time step (horizontal axis) the interface is leaving the grid cell face (top middle downward pointing arrow labeled 2) and the cell face remains un-cut for a certain period in the following, before the interface re-enters the grid cell face (bottom middle upward pointing arrow 2). The latter can happen due to the

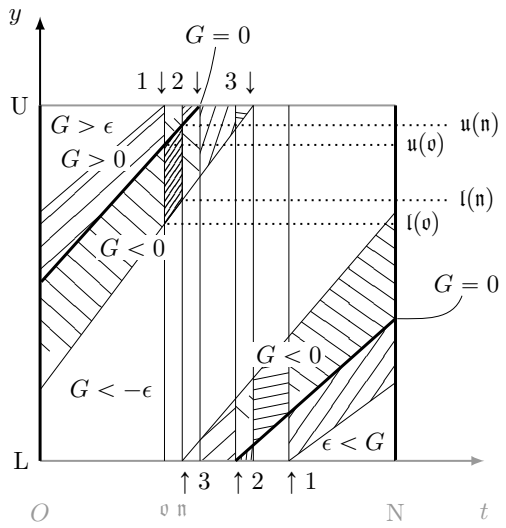

Fig. 6.49: General space-time cell $\widetilde{\partial\Omega}_{\mathfrak{d},\mathfrak{W}}$ with linear time-dependent bounds (interface, band boundary) and temporal sub-slices; the sub-cell limits $\mathfrak{o}$, $\mathfrak{n}$, $\mathfrak{l}(\mathfrak{o})$, $\mathfrak{l}(\mathfrak{n})$, $\mathfrak{u}(\mathfrak{o})$ and $\mathfrak{u}(\mathfrak{n})$ refer to the thick dashed sub-section of the space-time cell; time slices are separated by vertical lines and in general the y-boundaries can change their slopes at the time-slice boundary (resulting in the different dashed sub-sections)

chosen numerical restriction of only up to one intersection per grid cell face at any time. The cell remains cut for the rest of the time step until its end (N). Due to the restriction to maximum one interfacial intersection per grid cell face at the same time, the interface can not re-enter the cell face before a present interface has left the grid cell face. However, the regions around the interface in which the Dirac delta distribution is smoothed and, thus, non-zero, can overlap, both in time only, if the interface leaves and enters the grid cell face within the time step, and - in contrary to the illustration in ***Fig. 6.49*** - in space-time, depending on the chosen band thickness, if more than one intersection is present in the space-time cell.

Fig. 6.50 shows a sub-division of ***Fig. 6.49*** into three different settings (which add up to the one shown in ***Fig. 6.49*** in terms of time slices), referring to three different zero-levels of

$$0 = \mathfrak{S}_i := \begin{cases} G(\vec{x},t) - \epsilon(\vec{x},t) & i = 1 \\ G(\vec{x},t) & i = 2 \\ G(\vec{x},t) - (-\epsilon(\vec{x},t)) & i = 3 \end{cases} \tag{6.286}$$

in order to determine the temporal positions of the time slice boundaries between O and N with both $G(\vec{x},t)$ and, in general, $B(\vec{x},t) = \frac{1}{\epsilon(\vec{x},t)}$ bi-linearly in space-time.

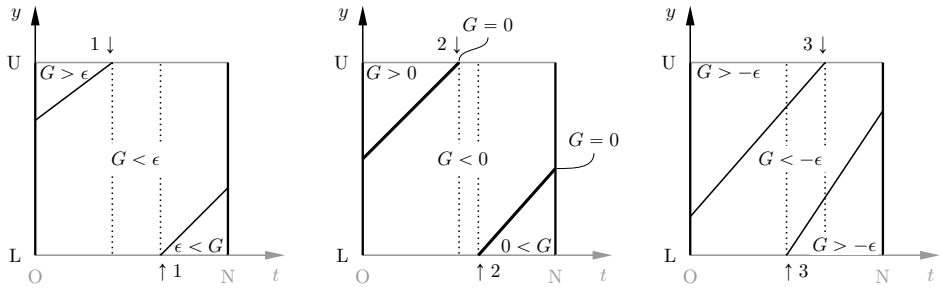

Fig. 6.50: Sub-division of ***Fig. 6.49*** into settings for $\widetilde{\partial\Omega}_{\mathfrak{b},\mathfrak{w}}$ with different zero-levels for: *left:* $G(\vec{x},t) - \epsilon(\vec{x},t)$, *center:* $G(\vec{x},t) - 0$, *right:* $G(\vec{x},t) - (-\epsilon(\vec{x},t))$

For constant B, the lines labeled 1, 2, 3 (downward pointing arrow) in the upper left corner of ***Fig. 6.49*** and ***Fig. 6.50*** are parallel and the lines labeled 1, 2, 3 (upward pointing arrow) in the lower right corner of ***Fig. 6.49*** and ***Fig. 6.50*** are parallel as well.

A new time slice starts, whenever any of the lines in ***Fig. 6.49*** within $\widetilde{\partial\Omega}_{\mathfrak{b},\mathfrak{w}}$ hit the lower or upper spatial bound L or U, which corresponds to the interface or the transition region bounds to leave or enter the grid cell face.

Once all time slice boundaries between O and N are obtained and ordered by magnitude – keeping the label (1, 2 or 3), which identifies the $\mathfrak{S}_i$ that is responsible for the respective time slice boundary, associated with each time slice boundary as shown in ***Tab. 6.2*** for the scenario in ***Fig. 6.49*** – the spatial bounds $\mathfrak{l}$ and $\mathfrak{u}$ of the space-time sub-section at the time slice boundaries $\mathfrak{o}$ and $\mathfrak{n}$ can be determined.

Tab. 6.2: Resulting bounds $\mathfrak{o}$ and $\mathfrak{n}$ of each of the 7 time slices in ***Fig. 6.49*** and corresponding labels of pairs of bounding lines $y(t)$, of which the intersection with the spatial grid cell face bounds L and U border the respective time slice

bounds	$(O \equiv \mathfrak{o}_1)$	$\mathfrak{n}_1$	$\mathfrak{o}_3$	$\mathfrak{n}_3$	$\mathfrak{o}_5$	$\mathfrak{n}_5$	$\mathfrak{o}_7$	$(\mathfrak{n}_7 \equiv N)$
		$\mathfrak{o}_2$	$\mathfrak{n}_2$	$\mathfrak{o}_4$	$\mathfrak{n}_4$	$\mathfrak{o}_6$	$\mathfrak{n}_6$	
labels	-	$1\downarrow$	$3\uparrow$	$2\downarrow$	$2\uparrow$	$3\downarrow$	$1\uparrow$	-
		$1\downarrow$	$3\uparrow$	$2\downarrow$	$2\uparrow$	$3\downarrow$	$1\uparrow$	

This is done by solving equation (6.286) at $\hat{t} \in \{\mathfrak{o}, \mathfrak{n}\}$ per time slice. Considering equation (6.246b) and suitable pairs of time dependent sub-section boundaries $y(t)$ as lower and upper spatial bounds $\mathfrak{l}(t)$ and $\mathfrak{u}(t)$ for each space-time sub-section as well as taking into account that both each grid cell face local time slice is spatially

bounded by L and U in y and that B is constant yields

$$L \leqslant \hat{y}_{(2)} = -\frac{\left(\mathcal{K}_{00}^{G} + \mathcal{K}_{10}^{G}\,\hat{t}\right)}{\left(\mathcal{K}_{01}^{G} + \mathcal{K}_{11}^{G}\,\hat{t}\right)} \leqslant U \tag{6.287a}$$

$$L \leqslant \hat{y}_{(2\mp1)} = -\frac{\left(\tilde{\mathcal{K}}_{00}^{G\pm\epsilon} + \tilde{\mathcal{K}}_{10}^{G\pm\epsilon}\,\hat{t}\right)}{\left(\tilde{\mathcal{K}}_{01}^{G\pm\epsilon} + \tilde{\mathcal{K}}_{11}^{G\pm\epsilon}\,\hat{t}\right)} \leqslant U \tag{6.287b}$$

with $\tilde{\mathcal{K}}^{G\pm\epsilon}$ as bi-linear ansatz coefficients for $G \pm \epsilon$ according to (6.249).

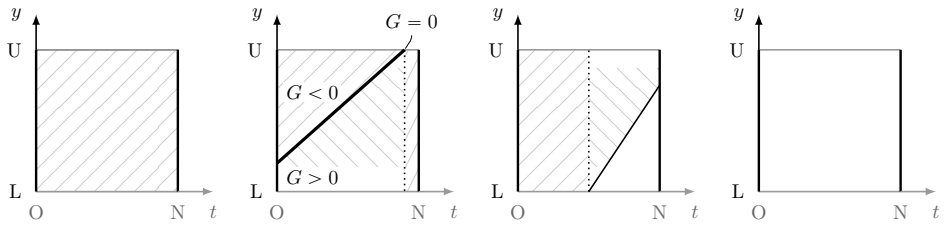

Fig. 6.51: *Left*: entire space-time cell within band of smoothed Dirac around interface, *center left*: space-time cell cut by the interface, *center right*: space-time cell intersected by the boundary of the band of the smoothed Dirac, *right*: entire space-time cell outside the band of smoothed Dirac around interface

Fig. 6.51 finally shows the most simple scenarios, which will arise in most of the cases for $\mathfrak{m}|\nabla G| \geqslant \mathfrak{D}$ on grid cell faces, on which a re-entry of the interface (***Fig. 6.50***, *center*) does not occur. For $1 \leqslant \mathfrak{m}|\nabla G| < \mathfrak{D}$ also the setting shown in ***Fig. 6.44*** on page 254 can arise, while the most general setting from ***Fig. 6.49*** will occur for $\mathfrak{m}|\nabla G| < 1$ only.

6.6.1.7 Dirac Representation along Non-Interface-Normal Paths

In this section the relation between the interface Dirac representation via interface normal linear hat functions due to (6.231) with $\mathfrak{p} = \mathfrak{q} = 1$ and the resulting interface Dirac representation along (straight) paths, which are not perpendicular to the interface in general (as, for example, a Cartesian grid cell face), are given for $\mathfrak{d} = 2$:

A point $\vec{x}$ within $\mathfrak{B}$ can be represented by

$$\vec{x} \;=\; \vec{x}_\Gamma(\tau(\vec{x})) + d(\vec{x})\,\vec{n}_\Gamma(\tau(\vec{x})) \;=\; \vec{x}_\Gamma(\tau_0) + y\,\vec{\mathfrak{e}}_y \;=\; \vec{x}(y) \tag{6.288}$$

with $\vec{n}_\Gamma \cdot \vec{t}_\Gamma = 0$ and, in general, $\vec{\mathfrak{e}}_y \cdot \vec{n}_\Gamma \neq 0$ and $\vec{\mathfrak{e}}_y \cdot \vec{t}_\Gamma \neq 0$, where $\vec{t}_\Gamma$ is the interface tangential vector and $\vec{\mathfrak{e}}_y$ an arbitrary unit vector as sketched in ***Fig. 6.52***. The derivative of the interface normal linear hat function

$$\delta_\Gamma^{(1)} = \frac{\mathfrak{A}}{\varepsilon}\left(1 - \operatorname{sgn}(d(\vec{x}))\frac{d(\vec{x})}{\varepsilon}\right) \tag{6.289}$$

with respect to the coordinate y – with $\frac{\mathrm{d}\operatorname{sgn}(d(\vec{x}))}{\mathrm{d}y} = 0$ assuming the path considered to be located entirely on one side of the interface – reads

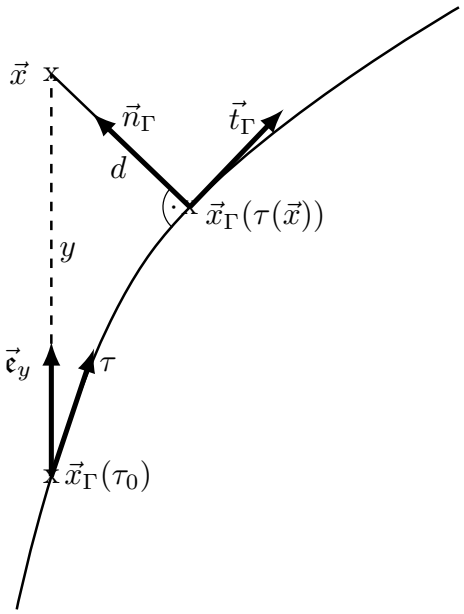

Fig. 6.52: Two different representations of an arbitrary point $\vec{x}$

$$\begin{aligned}
\frac{\mathrm{d}\delta_\Gamma^{(1)}}{\mathrm{d}y} \;&=\; -\frac{\mathfrak{A}}{\varepsilon^2}\operatorname{sgn}(d(\vec{x}))\frac{\mathrm{d}d(\vec{x})}{\mathrm{d}y} \\
&=\; -\frac{\mathfrak{A}}{\varepsilon^2}\operatorname{sgn}(d(\vec{x}))\left(\vec{n}_\Gamma(\tau(\vec{x}))\cdot\left(\frac{\mathrm{d}\vec{x}}{\mathrm{d}y} - \left(\frac{\mathrm{d}\vec{x}_\Gamma(\tau(\vec{x}))}{\mathrm{d}\tau}\circ\nabla\tau(\vec{x})\right)\cdot\frac{\mathrm{d}\vec{x}}{\mathrm{d}y}\right)\right. \\
&\qquad\left. + d(\vec{x})\,\vec{n}_\Gamma(\tau(\vec{x}))\cdot\left[\left(\frac{\mathrm{d}\vec{n}_\Gamma(\tau(\vec{x}))}{\mathrm{d}\tau}\circ\nabla\tau(\vec{x})\right)\cdot\frac{\mathrm{d}\vec{x}}{\mathrm{d}y}\right]\right) \\
&=\; -\frac{\mathfrak{A}}{\varepsilon^2}\operatorname{sgn}(d(\vec{x}))\left(\vec{n}_\Gamma(\tau(\vec{x}))\cdot\vec{\mathfrak{e}}_y - \left(\vec{n}_\Gamma(\tau(\vec{x}))\cdot\frac{\mathrm{d}\vec{x}_\Gamma(\tau(\vec{x}))}{\mathrm{d}\tau}\right)(\nabla\tau(\vec{x})\cdot\vec{\mathfrak{e}}_y)\right. \\
&\qquad\left. + d(\vec{x})\left(\vec{n}_\Gamma(\tau(\vec{x}))\cdot\vec{t}_\Gamma(\tau(\vec{x}))\right)\kappa\Big(\nabla\tau(\vec{x})\cdot\vec{\mathfrak{e}}_y\Big)\right)
\end{aligned} \tag{6.290}$$

after application of both chain and product rule, in which the identities

$$d(\vec{x}) = \vec{n}_\Gamma(\tau(\vec{x}))\cdot(\vec{x} - \vec{x}_\Gamma(\tau(\vec{x}))) \tag{6.291a}$$

$$\vec{x} - \vec{x}_\Gamma(\tau(\vec{x})) = d(\vec{x})\,\vec{n}_\Gamma(\tau(\vec{x})) \tag{6.291b}$$

$$\frac{\mathrm{d}\vec{x}}{\mathrm{d}y} = \vec{\mathfrak{e}}_y \tag{6.291c}$$

from (6.288) are accounted for. Since $\frac{\mathrm{d}\,\vec{x}_\Gamma(\tau(\vec{x}))}{\mathrm{d}\tau}$ is an interface tangential vector and both $\left(\vec{n}_\Gamma(\tau(\vec{x})) \cdot \frac{\mathrm{d}\vec{x}_\Gamma(\tau(\vec{x}))}{\mathrm{d}\tau}\right) = 0$ and $\left(\vec{n}_\Gamma(\tau(\vec{x})) \cdot \vec{t}_\Gamma(\tau(\vec{x}))\right) = 0$,

$$\frac{\mathrm{d}\delta_\Gamma^{(1)}}{\mathrm{d}y} = -\frac{\mathfrak{A}}{\varepsilon^2}\,\mathrm{sgn}(d(\vec{x}(y)))\left(\vec{n}_\Gamma(\tau(\vec{x}(y))) \cdot \vec{\mathfrak{e}}_y\right) \tag{6.292}$$

remains, which is not independent of y and, thus, $\frac{\mathrm{d}\delta_\Gamma^{(1)}}{\mathrm{d}y}$ not constant in general. Therefore the Dirac representation obtained from assuming interface normal linear hat functions is non-linear in non-interface-normal directions and bi-linear approximations in space-time as sketch in ***Fig. 6.45*** in black only approximate the Dirac representation, resulting from interface normal linear hat functions, along $\vec{\mathfrak{e}}_y$, as long as $\vec{\mathfrak{e}}_y \cdot \vec{n}_\Gamma \neq 1$ or $\vec{\mathfrak{e}}_y \cdot \vec{n}_\Gamma \neq 0$ (the latter corresponding to $\kappa \neq 0$). For each of the following special cases the bi-linear approximation matches the chosen Dirac representation exactly (which, in turn, remains an approximation to the true Dirac distribution):

- $\vec{\mathfrak{e}}_y \cdot \vec{n}_\Gamma = 1$ on the entire path along $\vec{\mathfrak{e}}_y$ ($\vec{\mathfrak{e}}_y$ points in interface normal direction)
- $\vec{\mathfrak{e}}_y \cdot \vec{n}_\Gamma = 0$ on the entire path along $\vec{\mathfrak{e}}_y$ ($\vec{\mathfrak{e}}_y$ points in interface tangential direction: $\kappa = 0$)

The second case results from the fact, that the interface normal vector $\vec{n}_\Gamma$ becomes independent of τ for vanishing curvature ($\kappa = 0$).

6.6.1.8 Algorithm

The algorithm for evaluation of (6.225) for constant B as described is as follows, while steps which need to be different for general B are indicated in **bold**:

1. generate and store the required parts of Pascal's triangle according to (6.264) and (6.243) **as shown in *Fig. 6.48***
2. pre-compute and store coefficients $\mathcal{B}$, $\mathfrak{B}$ and $\mathcal{B}$ based on information from Pascal's triangle according to (6.263a) to (6.263c)
3. for each grid cell face $\partial\Omega_{\mathfrak{d},\mathfrak{w}}$ within the narrow band $\mathfrak{N}$ around the interface Γ, which is sufficiently far away from the narrow band boundary, such that all required information can be found within $\mathfrak{N}$, compute ...

(a) ... level-set values G in nodes of space-time cell $\widetilde{\partial\Omega}$ (grid cell face $\partial\Omega_{\mathfrak{d},\mathfrak{w}}$ over time t) according to (6.20) based on surrounding cell data at the corresponding time levels

(b) ... level-set gradient ∇G in nodes of space-time cell $\widetilde{\partial\Omega}$ using cell data

(c) ... **bandwidth** $\epsilon = \varepsilon|\nabla G| = \widetilde{\mathfrak{m}}_{glob}\,\mathfrak{h}$ **according to** (6.234) **in nodes of** $\widetilde{\partial\Omega}$ **considering** (6.278)

(d) ... the product $X := (G + \epsilon)\,(G - \epsilon)$

4. for each face for which $X < 0$ (which means that the respective grid cell face is at least partially within the transition region around the interface during the time step considered) ...

(a) ... set a marker in the grid cells sharing the respective grid cell face

(b) ... pre-compute space-time cell global information such as ...

i. ... bounds of space-time cell $\tilde{\Omega}$ according to (6.252) with $t^n := 0$ and $y_0 := 0$.

ii. ... grid cell face area $\Delta A_{\mathfrak{d}} = \frac{\Delta V}{\mathfrak{c}_{\mathfrak{d}}\,\mathfrak{h}} = \frac{\mathfrak{h}^{\mathfrak{d}}\Pi_{\tilde{\mathfrak{d}}}^{\mathfrak{d}}\mathfrak{c}_{\tilde{\mathfrak{d}}}}{\mathfrak{c}_{\mathfrak{d}}\,\mathfrak{h}} = \mathfrak{h}^{\mathfrak{d}-1}\frac{\Pi_{\tilde{\mathfrak{d}}}^{\mathfrak{d}}\mathfrak{c}_{\tilde{\mathfrak{d}}}}{\mathfrak{c}_{\mathfrak{d}}}$

iii. ... space-time cell size $|\widetilde{\partial\Omega}| = \Delta A_{\mathfrak{d}}\,\Delta t$

iv. ... absolute value $|\nabla G|$ of level-set gradient in space-time cell nodes

v. ... interface normal vector $\vec{n}_\Gamma = \frac{\nabla G}{|\nabla G|}$ in space-time cell nodes based on the level-set gradient ∇G and its magnitude $|\nabla G|$

vi. ... B as the inverse of ϵ (see 3c) in space-time cell nodes

vii. ... **product of surface force** $\vec{f}(\nabla G)$ **and inverse bandwidth** B **(see** (6.244)**) in space-time cell nodes in order to avoid further scaling in the following, reducing the overall number of multiplications**

viii. ... **product of** B **and level-set** G **in space-time cell nodes**

ix. ... **bi-linear ansatz coefficients** $\left(B\,\vec{k}_{ij}^{\vec{f}}\right)$ **and** $\left(B\,\mathcal{K}_{ij}^{G}\right)$**, each according to** (6.249a) **-** (6.249d)**, for the sets determined in 4(b)vii and 4(b)viii**

x. ... number of time slices and time slice boundaries as shown in ***Fig. 6.50***

xi. ... space-time topology (as shown in ***Fig. 6.49*** to ***Fig. 6.51***) regarding lines separating the space-time cell into different sub-sections

(c) for each time slice ...

i. ... determine time slice local boundaries $\mathfrak{v}$ and $\mathfrak{n}$ (see (6.229))

ii. ... extract pairs of lines bounding relevant space-time sub-sections (see ***Tab. 6.2*** for the general example given in ***Fig. 6.49***)

iii. ... for each sub-section in the current time slice ...

A. ... get spatial sub-section node coordinates $\mathfrak{l}(\mathfrak{v})$, $\mathfrak{u}(\mathfrak{v})$, $\mathfrak{l}(\mathfrak{n})$ and $\mathfrak{u}(\mathfrak{n})$ at time slice boundaries $\mathfrak{v}$ and $\mathfrak{n}$ (see (6.229))

B. ... for each sub-section with non-zero space-time volume ...

- ... determine level-set sign $\mathrm{sgn}_{\mathfrak{tf}}\left(G(\vec{x},t)\right)$
- ... compute coefficients $\mathfrak{S}$ **according to** (6.281)
- ... compute coefficients $\vec{\mathfrak{q}}_{ij}$ **according to** (6.282)
- ... compute **weight vector** $\vec{\mathcal{W}}_2$ **(**$z = 2$**) according to** (6.259) by ....
  - ... computing all required scalar base weights $\mathfrak{w}$ according to (6.261),
  - ... computing all required weight vectors $\vec{\mathfrak{W}}_{ij}^{(\mathfrak{t},\mathfrak{f})}$ according to (6.285),
  - ... computing all required products $\mathfrak{n}^i\,\mathfrak{v}^j$,

  and evaluate the respective sum(s) in (6.284) or (6.259)

iv. ... evaluate sum over sub-sections ($\mathfrak{f}$) in time slice $\mathfrak{t}$ in (6.265)

v. ... scale sum with time slice local relative time step size $\frac{\mathfrak{n}-\mathfrak{v}}{\Delta t}$

(d) ... evaluate sum over time slices ($\mathfrak{t}$) in (6.265)

(e) ... scale result with $\frac{\mathfrak{A}_{1,1}}{2} = \frac{1}{2}$ in order to obtain the final space-time average surface force density on the grid cell face.

6.6.2 Present Approach within the Projection Method

As the dynamic pressure $p^{'}$ is treated as time-independent source in the predictor step as shown in section 5.1.4.1 and updated in the second corrector step, the contribution due to surface tension needs to be treated in the same way as discussed at the beginning of this section 6.6. Thus, in the predictor step the space-time integral update (6.265) from t^{n-1} to t^n – stored from the previous time step – is used as momentum source in equation (3.128c) during time integration from t^n to t^{n+1} according to section 6.3. The space-time integral contribution of surface tension during the present time step from t^n to t^{n+1}, computed through surface tension based flux averages

$\overset{\sim}{\overline{\mathcal{F}}}{}^{(\sigma)}_{\varepsilon}$ in (6.265) as described in the previous section 6.6.1, is included in the second corrector step according to

$$\int_{\partial\ddot{\Omega}} (\Delta t\, \theta^{**})\, \nabla\partial\pi' \cdot \vec{n}\mathrm{d}A = \int_{\ddot{\Omega}} \nabla \cdot \mathcal{P}\vec{v}^{**}\mathrm{d}V + \int_{\ddot{\Omega}} \nabla \cdot \theta^{**}\delta\vec{\mathfrak{f}}_{\Gamma}\, \mathrm{d}V \tag{6.293a}$$

$$= \int_{\ddot{\Omega}} \nabla \cdot \theta^{**} \left(\rho\vec{v}^{**} + \delta\vec{\mathfrak{f}}_{\Gamma}\right) \mathrm{d}V \tag{6.293b}$$

$$= \int_{\partial\ddot{\Omega}} \mathcal{P}\vec{v}^{**} \cdot \vec{n}\, \mathrm{d}A + \int_{\partial\ddot{\Omega}} (\Delta t\, \theta^{**})\, \overset{\sim}{\overline{\mathcal{F}}}{}^{(\sigma)}_{\varepsilon}\, \mathrm{d}A \tag{6.293c}$$

where

$$\delta\vec{\mathfrak{f}}_{\Gamma} := \vec{\mathcal{U}}^{(n+1)}_{(n)} - \vec{\mathcal{U}}^{(n)}_{(n-1)} \tag{6.294}$$

represents the difference of surface tension based momentum updates $\vec{\mathcal{U}}$ on primal cells[28] according to (6.225), with discretization (6.265) from the present ($n \rightarrow n+1$) and the previous ($n-1 \rightarrow n$) time step. With exception of the surface tension coefficient (if not constant), $\overset{\sim}{\overline{\mathcal{F}}}{}^{(\sigma)}_{\varepsilon}$ only depends on level-set field data (G, ∇G) at both time levels $O = t^n$ and $N = t^{n+1}$, which can be seen from (6.244) as both $\vec{n}_{\Gamma}$ and B (if not constant) are also functions of G and ∇G only. In the second corrector step both the level-set at the old time level and the final corrected level-set at the new time level are given, such that the space-time integrals (6.265) capture the entire spatio-temporal effect of surface tension.

6.6.2.1 Time Step Restriction

Due to the explicit treatment of the contribution due to surface tension to the momentum equation the allowable time step for the explicit predictor step has to satisfy

$$\Delta t^{\{2\}}_{\max} := \min\left(\Delta t^{\{2\}\#}_{\max},\ \Delta t_{\sigma}\right) \tag{6.295}$$

[28] Discrete evaluation of the right hand side integral of equation (6.293a) is done by first evaluating cell center values according to version (6.293b), to which the discrete integral divergence operator is applied by computation of fluxes across dual grid cell sub-faces – as sketched in the upper right corner of ***Fig. 5.8*** – based on primal cell center values to obtain (6.293c). Another alternative – instead of re-interpolating the flux averages $\overset{\sim}{\overline{\mathcal{F}}}{}^{(\sigma)}_{\varepsilon}$ via primal cell center updates as described – is to compute surface tension based flux averages $\overset{\sim}{\overline{\mathcal{F}}}{}^{(\sigma)}_{\varepsilon}$ across dual grid cell sub-faces according to section 6.6.1.8 directly and add the contributions to that primal grid nodes, which are the centers of the dual grid cells, the flux average across the dual sub-face contributes to. This, however, requires two evaluations of the space-time average surface tension based fluxes: on primal cell boundaries in the predictor (where in the current approach the stored value from the previous time step is used), and on dual cell boundaries in the corrector.

with $\Delta t_{\max}^{\{2\}\#}$ as given in section 6.3.2.1 based on the definition of $\Delta t_{\max}^{\{1\}}$ in equation (5.14) and ***Tab. 5.3***, as well as

$$\Delta t_\sigma := \frac{1}{\sqrt{(2\pi)^{\mathfrak{d}}}} \min_{\Omega} \left(\sqrt{\left(\frac{\rho^{(+)} + \rho^{(-)}}{2} \right) \frac{\mathfrak{h}^3}{\sigma}} \right) \mathfrak{h}^{\frac{3}{2}} \tag{6.296}$$

according to [166].

6.6.2.2 Extension to the Algorithm of the Second Corrector Step

The extensions for including surface tension into the second corrector step on the dual grid are[29]:

1. mark all grid cells which have fractions of at least one grid cell face within the transition region around the interface throughout the time interval considered
2. store the space-time integral flux averages $\overline{\widetilde{\mathcal{F}}}_{\varepsilon}^{(\sigma)}$ due to surface tension, computed in the second corrector step of the previous time step from t^{n-1} to t^n, for later use
3. compute space-time integral flux averages $\overline{\widetilde{\mathcal{F}}}_{\varepsilon}^{(\sigma)}$ due to surface tension in (6.265) on grid cell faces, which have fractions within the transition region around the interface throughout the time interval from t^n to t^{n+1}, according to algorithm 6.6.1.8
4. compute new space-time average update in each marked grid cell from t^n to t^{n+1} according to (6.265) via flux divergence based on the flux averages computed in 3.
5. add the difference of new and old space-time integral based updates (the latter stored in 2.) to the momentum
6. proceed as in section 5.2.2

[29] Note that the algorithm yet only allows for density ratios $\frac{\rho^{(+)}}{\rho^{(-)}} = 1$ and otherwise requires further extension in order to scale effects of the smoothed surface force with the density of the respective fluid phase conservatively, preventing spurious currents in the light fluid phase from scaling with $\frac{\rho^{\text{heavy}}}{\rho^{\text{light}}}$. A possible approach, which is subject of future work, might be based on [129], where the second corrector step is asymptotically split into two sub-problems for sharp interfaces – a first one solved in the heavy fluid only, with zero leading order solution in the light one, and a second corrective problem, which can be solved continuously in the entire domain –, adapted to the present smoothed setting.

6.6.3 Pros and Cons and Open Issues

The advantages and disadvantages of the present discretization of the surface tension tensor in the momentum equation are given in the following, finalized by a list of open issues:

- **Advantages**:
  - conservative both on the continuous level with arbitrary space-time dependent surface tension coefficient σ (naturally including the case of constant surface tension coefficient) and on the discrete level due to flux representation of the space-time average surface force
  - no need for explicit evaluation of interface tangential information
  - no need for interface curvature evaluation
  - no conceptual difference in three space dimensions
  - flux representation offers the possibility of balancing pressure and surface tension force in physically stable situations on the flux level on each grid cell face separately (pressure has to adopt the continuous force profile)
  - analytic integration over a transition region of width $2\,\varepsilon$ offers the possibility of shrinking the transition region size to arbitrarily small values (sub-grid size down to machine accuracy), provided the pressure profile is able to follow this narrow transition region profile
  - required coefficients can be partly determined independent of local information (e.g. Pascal's triangle and products of the coefficients therein), which only needs to be done once per time step or during initialization
- **Disadvantages**:
  - computation of various coefficients, already in two space dimensions
  - computation of numerous coefficients in three space dimensions (since spatial integration needs to be done over two spatial directions per grid cell face instead of one as in two space dimensions)
  - although the concept extends straightforward to three space dimensions, evaluation of the spatio-temporal geometric scenarios on grid cell faces for $\mathfrak{d} = 3$ is quite elaborate
  - more complex implementation as shown in section 6.6.1.8, compared to, for example, a continuous surface force model

- **Open Issues**:
  - inclusion of the present continuous force discretization approach into a sharp interface two-phase flow solver for density ratios $\frac{\rho^{(+)}}{\rho^{(-)}} \neq 1$, avoiding spurious velocities of different orders of magnitude in the different fluid phases
  - limit of vanishing transition region thickness $\varepsilon \to 0$ not yet feasible due to the lack of suitable elliptic solvers that are able to handle the resulting profile in the transition zone with respect to the unknown of the elliptic problem
  - fixes to the issues discussed in the following section 6.6.4

6.6.4 Tests and Results

Before results and findings of numerical computations – focussing on the flux-based surface stress discretization described in sections 6.6.1 and 6.6.2 – are given in section 6.6.4.2 through preliminary studies and in section 6.6.4.3 analyzing oscillating soap bubbles, analytical signed distance functions are given in section 6.6.4.1, which are used as initial conditions for the level-set function in the different examples in sections 6.6.4.2 and 6.6.4.3. The interface representation via the level-set function is the crucial basis of the smoothed surface stress representation.

6.6.4.1 Initial Signed Distance Functions

The initial interfaces in sections 6.6.4.2 and 6.6.4.3 in two spatial dimensions are represented by approximations to the zero levels of the analytically determined signed distance functions given in the following and shown as iso-level plots within the narrow band $\mathfrak{N}$ around the interface in ***Fig. 6.53***. All of these signed distance functions are specified in a structure-local coordinate system. The coordinates of any point $\vec{x}$ can be transformed into this structure-local coordinates system via the coordinate transformation

$$\widetilde{\mathbf{X}} = \boldsymbol{M} \cdot \mathbf{X} \tag{6.297}$$

with

$$\mathbf{X} := \begin{pmatrix} \vec{x} \\ 1 \end{pmatrix} \qquad \widetilde{\mathbf{X}} := \begin{pmatrix} \widetilde{\vec{x}} \\ 1 \end{pmatrix} \tag{6.298}$$

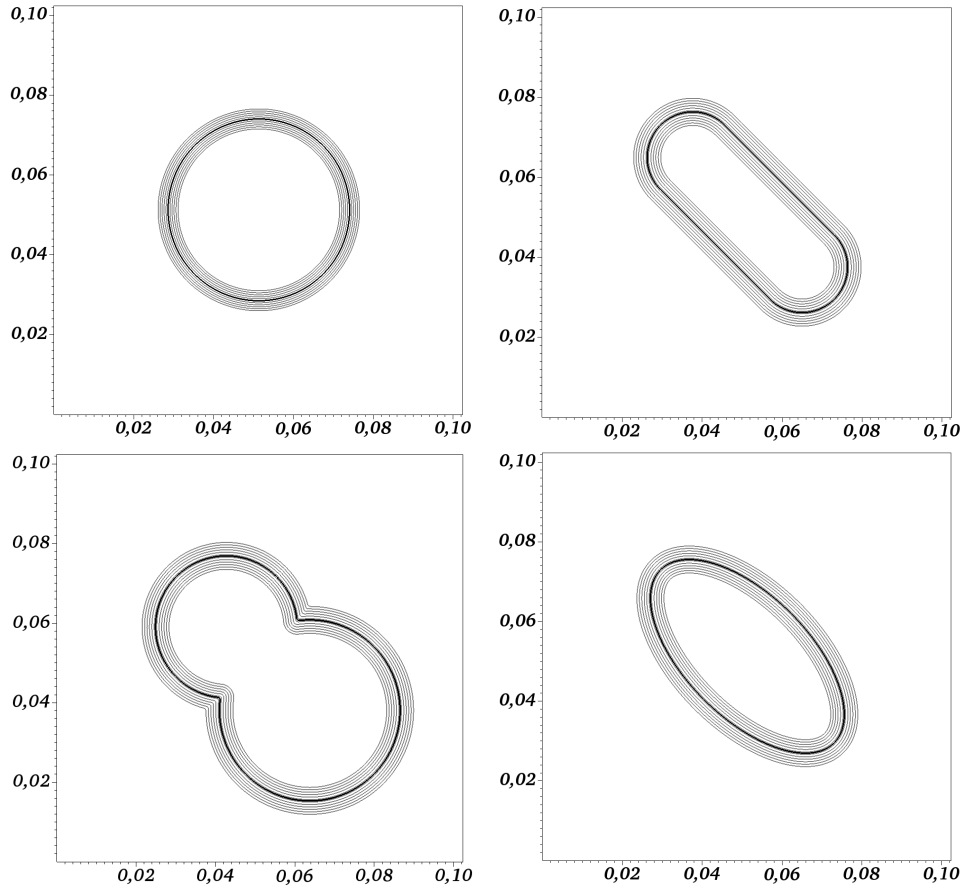

Fig. 6.53: Iso-contours of the level-set functions as determined analytically in sub-sections of section 6.6.4.1 within the narrow band $\mathfrak{N}$ around the interface Γ, each illustrated on the same domain at an angle of 45° between the structure-local coordinate systems and the coordinate system of the underlying Cartesian grid, represented by the domain boundaries

and structure-local coordinates $\vec{\tilde{x}}$, if both the angle ϑ between global and structure-local coordinates system and the offset $\vec{x}^{\,0}$ of the origins of both coordinate systems are known. The transformation matrix

$$\begin{aligned} \boldsymbol{M} = \boldsymbol{R} \cdot \boldsymbol{T} &= \begin{pmatrix} \cos(\vartheta) & -\sin(\vartheta) & 0 \\ \sin(\vartheta) & \cos(\vartheta) & 0 \\ 0 & 0 & 1 \end{pmatrix} \cdot \begin{pmatrix} 1 & 0 & x_1^0 \\ 0 & 1 & x_2^0 \\ 0 & 0 & 1 \end{pmatrix} \\ &= \begin{pmatrix} \cos(\vartheta) & -\sin(\vartheta) & \left(x_1^0 \cos(\vartheta) - x_2^0 \sin(\vartheta)\right) \\ \sin(\vartheta) & \cos(\vartheta) & \left(x_1^0 \sin(\vartheta) + x_2^0 \cos(\vartheta)\right) \\ 0 & 0 & 1 \end{pmatrix} \end{aligned} \tag{6.299}$$

for two-dimensional problems in (6.297) results from the matrix product of rotation matrix

$$\boldsymbol{R} = \begin{pmatrix} \cos(\vartheta) & -\sin(\vartheta) & 0 \\ \sin(\vartheta) & \cos(\vartheta) & 0 \\ 0 & 0 & 1 \end{pmatrix} \tag{6.300}$$

and translation matrix

$$\boldsymbol{T} = \begin{pmatrix} 1 & 0 & x_1^0 \\ 0 & 1 & x_2^0 \\ 0 & 0 & 1 \end{pmatrix} \tag{6.301}$$

in $\mathbb{R}^{(\mathfrak{d}+1)\times(\mathfrak{d}+1)}$. The following signed distance functions are formulated such that no or only minor modifications are required to obtain the corresponding representations in three space dimensions. The two-dimensional transformation given above has to be extended by one dimension and a suitable rotation angle accordingly.

6.6.4.1 - 1 Circle

The signed distance function in point $\vec{x}$ with respect to a circle of radius r with center in point $\vec{x}_0$ is given as

$$d(\vec{x}) = \breve{d}\,(\vec{x}, \vec{x}_0, r) \tag{6.302}$$

with

$$\breve{d}\left(\breve{\vec{x}}, \breve{\breve{\vec{x}}}, r\right) := \operatorname{sgn}\Big(\mathfrak{f}(\breve{\vec{x}}, \breve{\breve{\vec{x}}}, r)\Big)\sqrt{\left|\mathfrak{f}(\breve{\vec{x}}, \breve{\breve{\vec{x}}}, r))\right|} \tag{6.303a}$$

$$\mathfrak{f}(\breve{\vec{x}}, \breve{\breve{\vec{x}}}, r) := \left(\vec{x} - \breve{\vec{x}}\right) \cdot \left(\vec{x} - \breve{\breve{\vec{x}}}\right) - r^2 \tag{6.303b}$$

and sgn as the sign function. The circle is invariant with respect to the above rotation while translation is already accounted for by taking absolute coordinates for the circle center $\vec{x}_0$. The above representation directly applies to a sphere in three space dimensions as well.

6.6.4.1 - 2 Cigar-Shape

This structure consists of two half circles for $\mathfrak{d} = 2$ and two half spheres for $\mathfrak{d} = 3$, both of radius r, connected by a rectangular ($\mathfrak{d} = 2$) / cylindric ($\mathfrak{d} = 3$) segment of

length l. In its local coordinate system the signed distance function reads

$$d(\vec{x}) = \begin{cases} \breve{d}\left(\vec{\widetilde{x}}, \vec{\widetilde{x}}^{+}, r\right) & \forall \quad \widetilde{x}_1 \geqslant \widetilde{x}_1^{+} \\ \breve{d}\left(\vec{\widetilde{x}}, \vec{\widetilde{x}}^{-}, r\right) & \forall \quad \widetilde{x}_1 \leqslant \widetilde{x}_1^{-} \\ \left|\breve{d}\left(\vec{\widetilde{x}}, \breve{\vec{\widetilde{x}}}, 0\right)\right| - r & \forall \quad \widetilde{x}_1^{-} < \widetilde{x}_1 < \widetilde{x}_1^{+} \end{cases} \tag{6.304}$$

with $\breve{d}$ given by equation (6.303a), both $\widetilde{x}_1^{\pm} = \pm\frac{l}{2}$ and $\widetilde{x}_{i\neq 1}^{\pm} = 0$ as center coordinates of the end caps and both $\breve{\widetilde{x}}_1 = \widetilde{x}_1$ and $\breve{\widetilde{x}}_{i\neq 1} = 0$.

6.6.4.1 - 3 *Overlapping Circles*

The signed distance function to the enclosing contour of two overlapping circles with radii r_1 and r_2 as sketched in ***Fig. 6.54*** for two space dimensions is given by

$$d(\vec{\widetilde{x}}) = \left\{ \begin{array}{ll} \breve{d}\left(\breve{d}\left(\vec{\widetilde{x}}, \vec{\widetilde{x}}^{(1)}, r_1\right), \breve{d}\left(\vec{\widetilde{x}}, \vec{\widetilde{x}}^{(2)}, r_2\right)\right) & \text{if } (\mathfrak{C}_1) \\ \left\{ \begin{array}{ll} \breve{d}\left(\breve{d}\left(\vec{\widetilde{x}}, \vec{\widetilde{x}}_{\circ}^{+}, 0\right), \breve{d}\left(\vec{\widetilde{x}}, \vec{\widetilde{x}}_{\circ}^{-}, 0\right)\right) & \text{if } (\mathfrak{C}_2) \\ \left\{ \begin{array}{ll} \breve{d}\left(\vec{\widetilde{x}}, \vec{\widetilde{x}}^{(1)}, r_1\right) & \text{if } (\mathfrak{C}_3) \\ \breve{d}\left(\vec{\widetilde{x}}, \vec{\widetilde{x}}^{(2)}, r_2\right) & \text{otherwise} \end{array} \right. & \text{otherwise} \end{array} \right. & \text{otherwise} \end{array} \right. \tag{6.305}$$

with arguments $\breve{d}$ as specified in (6.303), conditions

$$(\mathfrak{C}_1): \quad \breve{d}\left(\breve{d}\left(\vec{\widetilde{x}}, \vec{\widetilde{x}}^{(1)}, r_1\right), \breve{d}\left(\vec{\widetilde{x}}, \vec{\widetilde{x}}^{(2)}, r_2\right)\right) \;>\; 0 \tag{6.306a}$$

$$(\mathfrak{C}_2): \quad (\mathfrak{C}_{2a}) \vee (\mathfrak{C}_{2b}) \tag{6.306b}$$

$$(\mathfrak{C}_{2a}): \quad (-a_1 < \widetilde{x}_1 \leqslant 0\ ) \;\wedge\; \left(\left|\breve{d}\left(\vec{\widetilde{x}}, \breve{\vec{\widetilde{x}}}, 0\right)\right| \leqslant \left(1 + \frac{\widetilde{x}_1}{a_1}\right) H\right) \tag{6.306c}$$

$$(\mathfrak{C}_{2b}): \quad (\quad 0 < \widetilde{x}_1 < a_2) \;\wedge\; \left(\left|\breve{d}\left(\vec{\widetilde{x}}, \breve{\vec{\widetilde{x}}}, 0\right)\right| \leqslant \left(1 - \frac{\widetilde{x}_1}{a_2}\right) H\right) \tag{6.306d}$$

$$(\mathfrak{C}_3): \quad \widetilde{x}_1 \;\leqslant\; 0 \tag{6.306e}$$

with $\breve{\widetilde{x}}_1 = \widetilde{x}_1$ and $\breve{\widetilde{x}}_{i\neq 1} = 0$ as well as

$$\breve{d}(\breve{d}_1, \breve{d}_2) := \begin{cases} \operatorname{sgn}(\breve{d}_1)\ \grave{d}(\breve{d}_1, \breve{d}_2) & \text{if} \quad \left(\grave{d}(\breve{d}_1, \breve{d}_2) - \left|\breve{d}_1\right|\right) = 0 \\ \operatorname{sgn}(\breve{d}_2)\ \grave{d}(\breve{d}_1, \breve{d}_2) & \text{if} \quad \left(\grave{d}(\breve{d}_1, \breve{d}_2) - \left|\breve{d}_2\right|\right) = 0 \end{cases} \tag{6.307a}$$

$$\grave{d}(\breve{d}_1, \breve{d}_2) := \min\left(\left|\breve{d}_1\right|, \left|\breve{d}_2\right|\right) \tag{6.307b}$$

with

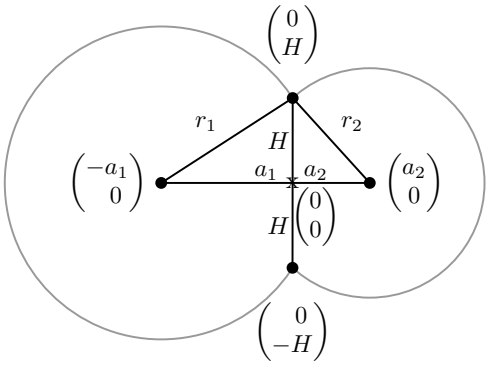

Fig. 6.54: Overlapping circles with radii r_1 and r_2 in structure-local coordinate system with origin labeled X; determination of problem dependent parameters according to ***Tab. 6.5*** on page 300

$$\breve{d}_1 := \breve{d}\left(\vec{\widetilde{x}}, \vec{\widetilde{x}}^{(1)}, r_1\right) \tag{6.307c}$$

$$\breve{d}_2 := \breve{d}\left(\vec{\widetilde{x}}, \vec{\widetilde{x}}^{(2)}, r_2\right) \tag{6.307d}$$

$$\vec{\widetilde{x}}_\circ^{\,\pm} := \begin{pmatrix}0\\ \pm H\end{pmatrix} \tag{6.307e}$$

$$\vec{\widetilde{x}}^{(1)} := \begin{pmatrix}-a_1\\0\end{pmatrix} \tag{6.307f}$$

$$\vec{\widetilde{x}}^{(2)} := \begin{pmatrix}a_2\\0\end{pmatrix} \tag{6.307g}$$

$$H = \sqrt{r_1^2 - a_1^2} \tag{6.307h}$$

$$a_2 = \sqrt{a_1^2 - \left(r_1^2 - r_2^2\right)}. \tag{6.307i}$$

6.6.4.1 - 4 Ellipse

A signed distance function $d(\vec{\widetilde{x}})$ with elliptic zero level Γ can be determined analytically in two space dimensions in an ellipse-local coordinate system with coordinates $\vec{\widetilde{x}} := (\widetilde{x}_1, \widetilde{x}_2)$, such that the intersection of minor and major axes of the ellipse is located at $(0, 0)$ as done in the following.

Note that besides the signed distance function $d(\vec{\widetilde{x}})$, the spatial coordinates $\vec{\widetilde{x}}$ and the interface normal vector $\vec{\widetilde{n}}_\Gamma$ (both in structure local coordinates), all variables in this section have section-local meaning only as defined below and do not refer to any other variable of same name within this work beyond this section 6.6.4.1 - 4. The algorithm for evaluation of the following description is given starting on page 289. Parts of the applied solution procedure are also required in section 6.6.4.3 for determination of the properties of the oscillating pair of soap bubbles based on the given data.

With major and minor axes of length $2\,a$ and $2\,b$ as shown in ***Fig. 6.55***, the elliptic contour (6.308) is represented by

$$\left(\frac{\widetilde{x}_1}{a}\right)^2 + \left(\frac{\widetilde{x}_2}{b}\right)^2 = 1 \tag{6.308}$$

in its ellipse-local coordinate system. The (outward pointing) unit normal vector $\vec{\widetilde{n}}_\Gamma$

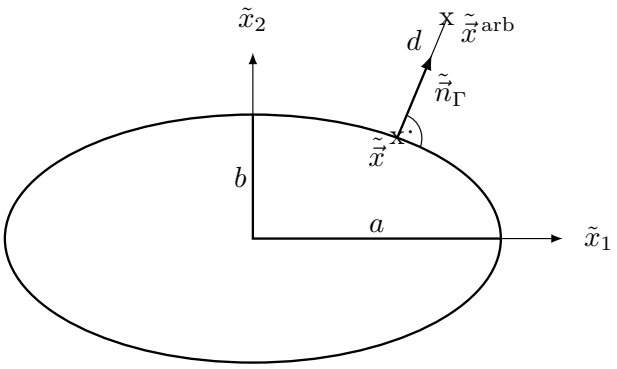

Fig. 6.55: Distance of an arbitrary point $\tilde{x}^{\text{arb}}$ to an ellipse

to the ellipse (6.308) reads

$$\tilde{\vec{n}}_\Gamma := \frac{1}{\sqrt{\left(\frac{\tilde{x}_1}{a^2}\right)^2 + \left(\frac{\tilde{x}_2}{b^2}\right)^2}} \begin{pmatrix} \frac{\tilde{x}_1}{a^2} \\ \frac{\tilde{x}_2}{b^2} \end{pmatrix} = \frac{1}{\sqrt{k^2 x_1^2 + x_2^2}} \begin{pmatrix} k x_1 \\ x_2 \end{pmatrix} \tag{6.309}$$

with relative local quantities

$$0 < k := \frac{b}{a} < 1, \qquad -1 < x_1 := \frac{\tilde{x}_1}{a} < 1, \qquad -1 < x_2 := \frac{\tilde{x}_2}{b} < 1 \tag{6.310}$$

in the ellipse local coordinate system and $(\tilde{x}_1, \tilde{x}_2)$ as arbitrary point on Γ. The relative distance

$$d := \frac{\tilde{d}}{a} \tag{6.311}$$

between Γ and an arbitrary point $\tilde{\vec{x}}^{arb} := \left(\tilde{x}_1^{\text{arb}}, \tilde{x}_2^{\text{arb}}\right)$ can be determined via a straight line

$$\begin{pmatrix} \tilde{x}_1 \\ \tilde{x}_2 \end{pmatrix} + \tilde{d}\, \tilde{\vec{n}}_\Gamma = \begin{pmatrix} \tilde{x}_1^{\text{arb}} \\ \tilde{x}_2^{\text{arb}} \end{pmatrix} \tag{6.312}$$

normal to Γ in the unknown point $(\tilde{x}_1, \tilde{x}_2)$ on Γ through the arbitrary point $\left(\tilde{x}_1^{\text{arb}}, \tilde{x}_2^{\text{arb}}\right)$ as sketched in ***Fig. 6.55*** after transformation to relative coordinates: With

$$m := \frac{\tilde{x}_1^{\text{arb}}}{a} \qquad n := \frac{\tilde{x}_2^{\text{arb}}}{b} \tag{6.313}$$

as well as

$$\mathcal{D} := \frac{d}{\sqrt{k^2 x_1^2 + x_2^2}} \tag{6.314}$$

equation (6.312) transforms to

$$\begin{pmatrix} x_1 \\ x_2 \end{pmatrix} + \mathcal{D} \begin{pmatrix} k x_1 \\ \frac{1}{k} x_2 \end{pmatrix} = \begin{pmatrix} m \\ n \end{pmatrix} \tag{6.315}$$

and solving the upper line for $\mathcal{D}$ yields

$$\mathcal{D} = \frac{m - x_1}{k\, x_1} \tag{6.316}$$

with the restriction $x_1 \neq 0$. **The case $x_1 = 0$ has to be considered separately below**. Further, the resulting relation

$$x_2 = \frac{k^2\, n\, x_1}{m - x_1\,(1 - k^2)} = \frac{N\, x_1}{M - x_1} \tag{6.317}$$

with

$$M := \frac{m}{1 - k^2} \qquad \text{and} \qquad N := \frac{k^2 n}{1 - k^2} \tag{6.318}$$

from the lower line of equation (6.315) is valid, as long as $M - x_1 \neq 0$. **The case $(M - x_1) = 0$ has to be considered separately as well**. Substitution of (6.317) into the relative representation

$$x_1^2 + x_2^2 = 1 \tag{6.319}$$

of equation (6.308) yields the polynomial

$$x_1^4 - M\left(x_1^2 - 1\right)(2\, x_1 - M) - (1 - N^2)\, x_1^2 \;=\; 0 \tag{6.320}$$

in x_1 of degree 4. Analytical solutions of the latter can be obtained via the approach of Ferrari for solving quartic equations by substitution

$$y := x_1 - \frac{M}{2} \tag{6.321}$$

yielding the reduced equation

$$y^4 + P y^2 + Q y + R = 0 \tag{6.322}$$

with

$$P := N^2 - \frac{M^2}{2} - 1, \qquad Q := M\,(1 + N^2), \qquad R := \frac{M^2}{4}\left(\frac{M^2}{4} + N^2 - 1\right) \tag{6.323}$$

of degree 4 as before, however, without the cubic contribution. For $Q \neq 0$ – **the case**

$Q = 0$ **is a third one to be treated separately** – equation (6.322) can be rewritten as

$$\left(y^2 + P\right)^2 = P(y^2 + P) - Qy - R \tag{6.324}$$

after adding $P(y^2+P)$ on both sides of the equation. Extra addition of the expression $z\left(z + 2\left(P + y^2\right)\right)$ with unknown z on both sides of equation (6.324) finally yields

$$\left(y^2 + (P + z)\right)^2 = (P + 2z)\, y^2 - Qy + \left(P^2 - R + z\,(z + 2P)\right) \tag{6.325}$$

in which the right hand side turns to a perfect square if its discriminant with respect to y vanishes:

$$(-Q)^2 - 4\,(P + 2z)\left(P^2 - R + z\,(z + 2P)\right) = 0 \tag{6.326}$$

This is achieved by solving the cubic equation

$$z^3 + \mathfrak{a}z^2 + \mathfrak{b}z + \mathfrak{c} = 0 \tag{6.327}$$

with

$$\mathfrak{a} := \frac{5}{2}P, \qquad \mathfrak{b} := 2P^2 - R, \qquad \mathfrak{c} := \frac{1}{2}\left(P\left(P^2 - R\right) - \left(\frac{Q}{2}\right)^2\right) \tag{6.328}$$

which results from (6.326) after collecting powers of z. After substituting

$$Z := z + \frac{\mathfrak{a}}{3} \tag{6.329}$$

solutions for (6.327) can be obtained according to the approach of Cardano for solving cubic equations via real-valued solutions of the reduced cubic equation

$$Z^3 + pZ + q = 0 \tag{6.330}$$

without quadratic contribution and with

$$p := \mathfrak{b} - \frac{\mathfrak{a}^2}{3} \qquad\qquad q := \mathfrak{c} - \frac{\mathfrak{a}\mathfrak{b}}{3} + \frac{2\mathfrak{a}^3}{27} \tag{6.331}$$

as parameters. These real-valued solutions depend on the discriminant

$$\Delta := \left(\frac{q}{2}\right)^2 + \left(\frac{p}{3}\right)^3 \tag{6.332}$$

as given in ***Tab. 6.3*** with

$$u := \left(-\frac{q}{2} + \sqrt{\Delta}\right)^{\frac{1}{3}} \qquad v := \left(-\frac{q}{2} - \sqrt{\Delta}\right)^{\frac{1}{3}} \tag{6.333}$$

and

$$w := \frac{3q}{p} \qquad r := \sqrt{-\frac{4}{3}p} \qquad \xi := \frac{1}{3}\cos^{-1}\left(-\frac{q}{2}\sqrt{-\left(\frac{3}{p}\right)^3}\right) \tag{6.334}$$

as auxilliary quantities.

Tab. 6.3: Real-valued solutions of the reduced cubic equation (6.330) depending on Δ

	$\Delta > 0$	$\Delta = 0$		$\Delta < 0$
		$p = q = 0$	$p \neq 0$ or $q \neq 0$	
Z_1	$u + v$	0	w	$r\cos(\xi)$
Z_2	-	0	$-\frac{w}{2}$	$-r\cos\left(\xi + \frac{\pi}{3}\right)$
Z_3	-	0	$-\frac{w}{2}$	$-r\cos\left(\xi - \frac{\pi}{3}\right)$

The solutions z_i of (6.327) with $i \in \{1, 2, 3\}$ can then be obtained by re-substitution according to relation (6.329). For each of the corresponding resulting real-valued z_i, equation (6.325) turns into

$$\left(y^2 + (P + z)\right)^2 = (P + 2z)\left(y - \frac{Q}{2\sqrt{(P + 2z)}}\right)^2 \tag{6.335}$$

due to a vanishing discriminant (6.326) of the right hand side of equation (6.325) with respect to y. Thus, a solution to

$$(P + 2z)\, y^2 - Qy + \left(P^2 - R + z\,(z + 2P)\right) = 0 \tag{6.336}$$

is given by $y = \frac{Q}{2\sqrt{(P+2z)}}$. Then $(P + 2z) > 0$ follows from equation (6.335). With that, the root of equation (6.335) yields

$$y^2 + (P + z) = s_1\sqrt{(P + 2z)}\left(y - \frac{Q}{2\sqrt{(P + 2z)}}\right) \tag{6.337}$$

with

$$s_1 \in \{-1, 1\} \tag{6.338}$$

which leads to solving the 6 quadratic equations

$$y^2 - s_{1j}\, U_i\, y + (W_i + s_{1j}\, V_i) = 0, \qquad i \in \{1, 2, 3\}, \quad j \in \{1, 2\} \tag{6.339}$$

with

$$U_i := \sqrt{(P + 2z_i)}, \qquad V_i := \frac{Q}{2U_i}, \qquad W_i := P + z_i \tag{6.340}$$

yielding 12 solutions

$$y_{(4(i-1)+2(j-1)+(h-1)+1)} = \frac{1}{2}\left(s_{1j} U_i + s_{2h}\sqrt{D_i}\right) \tag{6.341}$$

with

$$D_i := U_i^2 - 4\,(W_i + s_{1j}\, V_i) \tag{6.342}$$

and

$$s_2 \in \{-1, 1\} \tag{6.343}$$

as well as $i \in \{1, 2, 3\}$, $j \in \{1, 2\}$ and $h \in \{1, 2\}$. Valid solutions for y are the ones with non-negative discriminant D_i. Of these valid solutions, solutions x_1 are finally obtained after re-substitution via (6.321). The valid ones - indexed l - have to be within the interval $-1 \leqslant x_{1l} \leqslant 1$ and x_{2l} values corresponding to these valid x_1 values can be determined via relation (6.317). The x_{2l} have to be within the interval $-1 \leqslant x_{2l} \leqslant 1$ as well and for valid coordinates (x_{1l}, x_{2l}) the corresponding relative distances d_l can be computed according to

$$d_l = \frac{m - x_{1l}}{k\, x_{1l}} \sqrt{k^2 x_{1l}^2 + x_{2l}^2} \tag{6.344}$$

resulting from (6.314) with (6.316). The absolute value $|d_{l*}|$ for that index l^*, for which $|d_{l*}| = \min_l (|d_l|)$ holds, is the absolute value of the wanted signed distance function. The sign of the signed distance function can then be determined by substituting $(x_{1l*}, x_{2l*}) = (m, n)$ into

$$E := 1 - x_{1l*}^2 - x_{2l*}^2 \tag{6.345}$$

since (m, n) is within the ellipse if $0 < E < 1$, on the elliptic contour if $E = 0$ and outside if $E < 0$.

Special Cases

This section deals with the cases excluded above:

1. $\underline{x_1 = 0}$: This case describes intersections of elliptic contour and minor axis and, thus,
$$|d| = 0 \tag{6.346}$$

2. $\underline{(M - x_1) = 0 \text{ with } x_1 \neq 0}$: In this case $x_1 = M$ and after substitution into equation (6.319)
$$x_1^2 = 1 - M^2 \tag{6.347}$$
with solutions
$$x_1 = \pm\sqrt{1 - M^2} \tag{6.348}$$
and valid real-valued solutions for $M^2 \leqslant 1$. For $M^2 > 1$ (which would lead to non-real-valued solutions) either $M > 1$ or $M < -1$ has to hold, which means that $x_1 > 1$ or $x_1 < -1$. This, however, is beyond the valid range of x_1 and, thus, for $-1 \leqslant x_1 \leqslant 1$ always real-valued solutions are obtained. Finally,
$$|d| = k\sqrt{1 - M^2(1 - k^2)} \tag{6.349}$$
with k as given in (6.310) and M according to (6.318).

3. $\underline{Q = 0 \text{ with } x_1 \neq 0}$: In this case $M = m = 0$ and, thus, the current point is on the minor axis of the ellipse beyond the elliptic contour. Equation (6.320) reduces to
$$x_1^2 - (1 - N^2) = 0 \tag{6.350}$$
with solutions
$$x_1 = \pm\sqrt{1 - N^2} \tag{6.351}$$
which are real-valued for $N^2 \leqslant 1$. This means that $|N| \leqslant 1$ has to hold. Due to $N = \frac{k^2 n}{1-k^2} = \frac{n}{\frac{1}{k^2}-1}$ with $k < 1$ and $k^2 < 1$ and, thus, $\frac{1}{k^2} - 1 > 0$, the relation $|n| \leqslant \frac{1}{k^2} - 1$ is obtained. It follows, that
$$x_2 = \pm N \tag{6.352}$$
and
$$|d| = \sqrt{1 + N^2\left(\frac{1}{k^2} - 1\right)} \tag{6.353}$$

with k as given in (6.310) and N according to (6.318).

Algorithm

For each point in which the signed distance function to the ellipse has to be determined

- perform transformation into ellipse local coordinate system according to (6.297)
- compute k according to (6.310)
- compute m and n according to (6.313)
- if $m = 0$, the current point is on the minor axis of the ellipse and $|d| = 1 - |n|$
- if $m \neq 0$
  - compute M and N according to (6.318)
  - if $n = 0$, the current point $\vec{\tilde{x}}^{arb}$ is on the major axis of the ellipse and valid relative coordinates $\vec{x}$ on the ellipse to compute the distance to are $(1, 0)$, $(-1, 0)$ and $(M, \sqrt{1 - M^2})$; the minimum distance from these points to $(m, 0)$ is the wanted distance for $m \neq 0$ and $n = 0$
  - if $n \neq 0$
    - compute P, Q and R according to (6.323)
    - for $Q = 0$, get the distance from (6.353)
    - for $Q \neq 0$
      - compute $\mathfrak{a}$, $\mathfrak{b}$ and $\mathfrak{c}$ according to (6.328)
      - compute p and q according to (6.331)
      - compute discriminant Δ according to (6.332)
      - compute solutions Z of the reduced third order equation (6.330) based on Δ, Table 6.3 and relations (6.333) and (6.334)
      - re-substitute via (6.329) in order to obtain solutions z to (6.327)
      - for each solution z determine U, V and W according to (6.340) and check for $D_i \geqslant 0$ with D_i according to (6.342) to exclude solutions z which provide a $D_i < 0$ and, thus, not a real-valued solution y according to (6.341)
      - for the remaining real-valued solutions z compute y according to (6.341) considering (6.340), (6.342), (6.338) and (6.343)

  - compute a first ellipse coordinate component x_1 via re-substitution based on (6.321) from each remaining y
  - exclude all x_1 which are beyond $-1 \leqslant x_1 \leqslant 1$
  - for $-1 \leqslant x_1 \leqslant 1$ compute corresponding x_2 values via (6.317)
  - exclude all points (x_1, x_2) for which x_2 is beyond $-1 \leqslant x_2 \leqslant 1$, if necessary
  - for the remaining points (x_1, x_2), compute the distance to point (m, n) according to (6.344)
  - take the distance d with the smallest absolute value $|d|$ as the absolute value of the wanted signed distance function in (m, n)

- scale the obtained relative distance $|d|$ with a in order to get the absolute distance

- determine, if (m, n) is within or outside (or on) the ellipse by evaluating $1 - m^2 - n^2$: if the result is positive, (m, n) is within the ellipse, if it is zero, (m, n) is on the ellipse and if it is negative it is outside the ellipse. Choose the sign for the signed distance function accordingly

Other approaches

Other approaches, like, for example,

- intersecting the ellipse (6.308) with a circle of unknown radius d and center in (m, n) under the constraint that at least two of the up to 4 intersection points have to collapse to one point on the interface

- finding a point on both the ellipse (6.308) and a circle of unknown radius d with center in (m, n) such that both the coordinates of these points and the tangential vectors of ellipse and circle in these points are identical

also lead to polynomial equations of degree 4. The present approach could also be formulated such that a polynomial equation of degree 4 in the unknown distance is obtained directly. However, in that case excluding (ghost) solutions of the respective equations, which are beyond valid ranges for coordinates on the ellipse, is not as straight forward as presented above.

Note that in the following all variables again have their document-global meaning.

6.6.4.2 Preliminary Studies

In this section the discretization described in section 6.6.1 and section 6.6.2 is applied to three different initial settings for preliminary studies at density ratio $\frac{\rho^{(+)}}{\rho^{(-)}} = 1$ and $\widetilde{\mathfrak{m}}_{glob} = 2$ as shown in ***Fig. 6.56***, with analytic signed distance functions for the initial level-set as given in section 6.6.4.1.

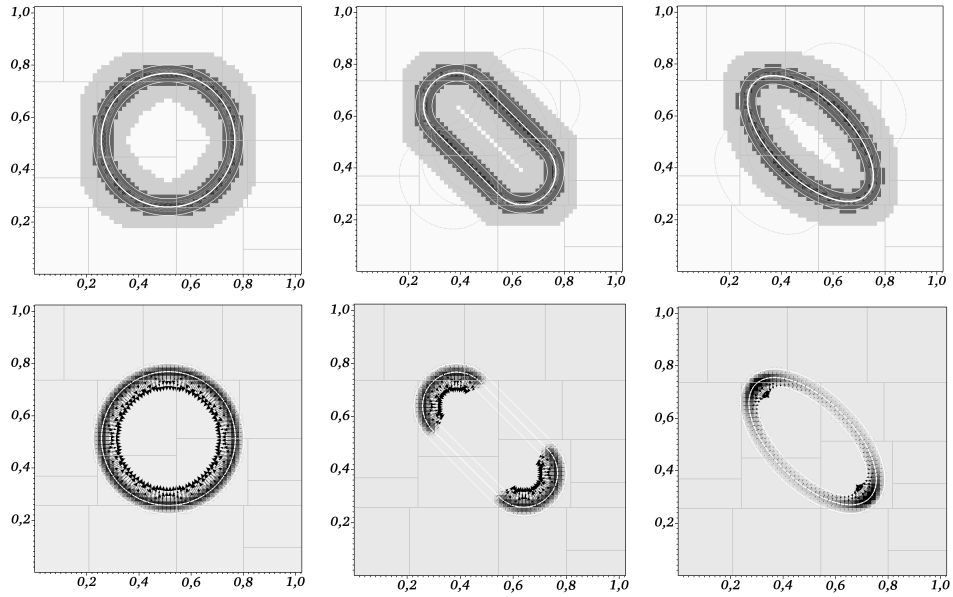

Fig. 6.56: Three different two-dimensional initial settings on various patches for parallel computation on a grid of 64×64 grid cells on a 1.024×1.024 domain each: *left:* circular bubble, *center:* cigar-shaped bubble, *right:* elliptic bubble; *top:* narrow band $\mathfrak{N}$ (medium grey area) with transition region $\mathfrak{B}$ (dark grey area) as a sub-set of $\mathfrak{N}$ and cut cells $\mathfrak{L}$ (black area); *bottom:* resulting surface force per grid cell in $\mathfrak{B}$ (black arrows) and its magnitude (greyscale) within $\mathfrak{B}$; interface Γ (thick white line in center of $\mathfrak{B}$) and transition region bounds (thin white lines) at $\mathfrak{m} = 2$

The initial conditions for flux-based contributions of the surface stress tensor are computed as space-time averages as described in section 6.6.1 by using the identical initial level-set configuration for both time levels involved in the contained space-time evaluation to enforce a stationary case. Thus, all temporal ansatz coefficients are equal to zero initially. Examination of these initial conditions already reveals some valuable information on the present approach for surface tension discretization:

- non-zero forces only arise in grid cells, which are located at least partially within the transition region $\mathfrak{B}$ as expected and shown in ***Fig. 6.56***, ***Fig. 6.57***, ***Fig. 6.58*** and ***Fig. 6.60***.

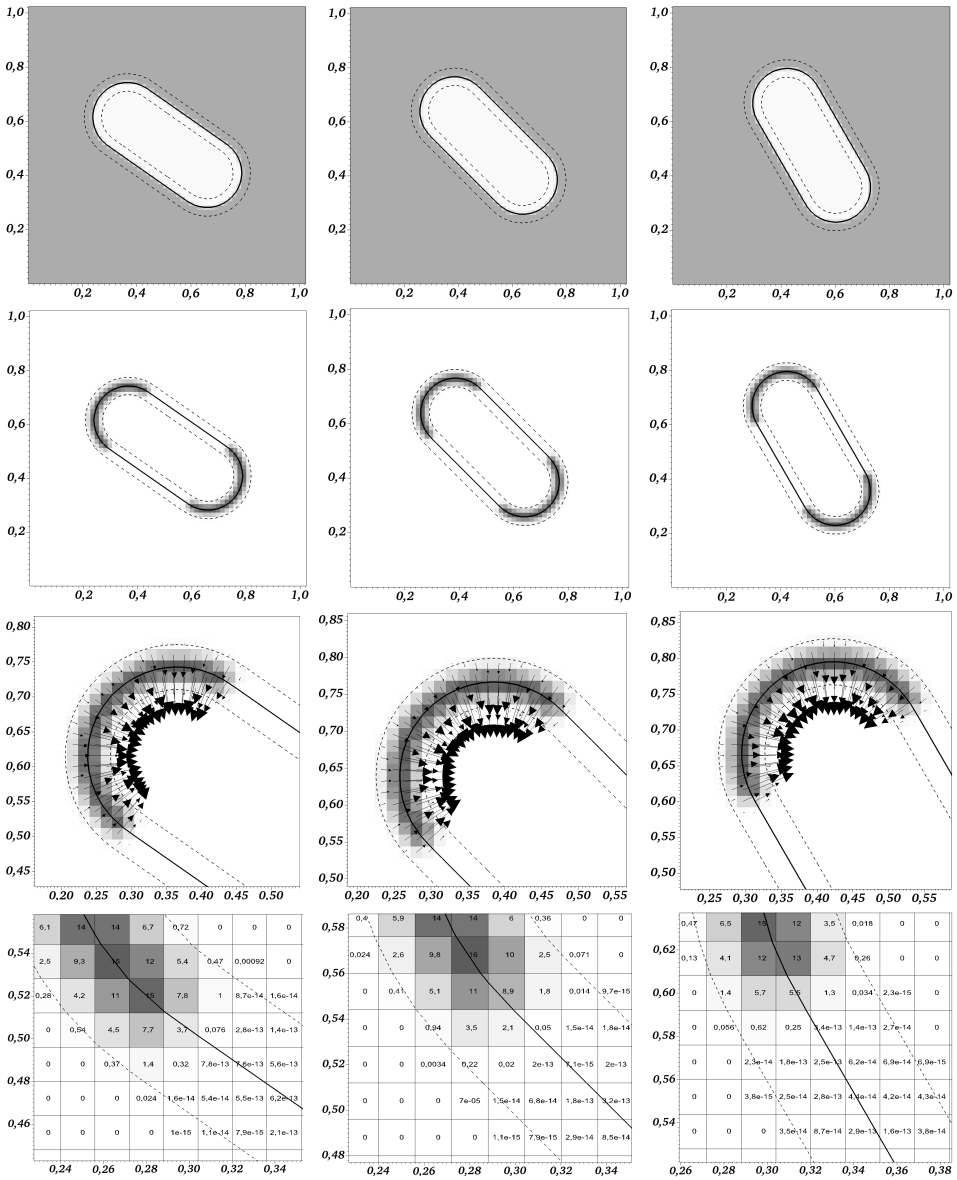

Fig. 6.57: Cigar-shaped bubble at different angles with respect to the coordinate system of the underlying computational Cartesian grid of 64×64 cells on a 1.024×1.024 domain from left to right; *first row*: mass / species mass / phase indicator with intermediate integral averages in cut grid cells only; *second row*: absolute value of resulting force per grid cell after integration of discretized surface stresses over the grid cell boundary; *third row*: detailed view on the resulting interface normal force vectors per grid cell in the transition region $\mathfrak{B}$; *fourth row*: detailed view on the resulting absolute values of interface normal force vectors per grid cell in the lower part of the illustrations in the third row; the resulting forcing vanishes up to machine accuracy where the interface curvature vanishes and is non-zero only within $\mathfrak{B}$; *thick solid line*: interface Γ, *dashed lines*: transition region boundaries; *arrows*: volume force vectors; darker grid cells represent higher absolute values

- the strength of the resulting forces decays towards the boundary of the transition region $\mathfrak{B}$ according to the Dirac approximation as shown in ***Fig. 6.56***, ***Fig. 6.57***, ***Fig. 6.58*** and ***Fig. 6.60*** as well.

- the strength of the resulting forces changes smoothly, if curvature changes smoothly, and scales with the magnitude of curvature (although curvature is not computed explicitly) as shown in the lower part of ***Fig. 6.56***: In the circular case with constant curvature the amplitude of the forcing is constant along the interface. In case of the cigar-shape the amplitude of the forcing is constant along the circular parts with constant curvature and vanishes in areas, where curvature vanishes. The elliptic case shows, that the strength of the forcing scales with the magnitude of the local curvature.

- the forces in each grid cell point in direction of the level-set gradient, corresponding to the interface normal direction, as shown in the third line of ***Fig. 6.57*** and in more detail for the elliptic example in ***Fig. 6.58***, where also the level-set gradient vectors are plotted for comparison. The volume forces are not evaluated as point values in grid cell centers based on the local curvature – as, for example, done in the continuous surface force (CSF) method – but result from the curvature-free balancing of $\mathcal{O}(1)$ vector contributions due to surface stresses at the grid cell faces after integration over those parts of the grid cell boundaries, which are located within transition region $\mathfrak{B}$ around the interface Γ, as described in section 6.6.1 and sketched in ***Fig. 6.59***. As indicated there, the individual vector contributions to these integrals over (segments of) grid cell faces are tangential to the local level-set iso-contours.

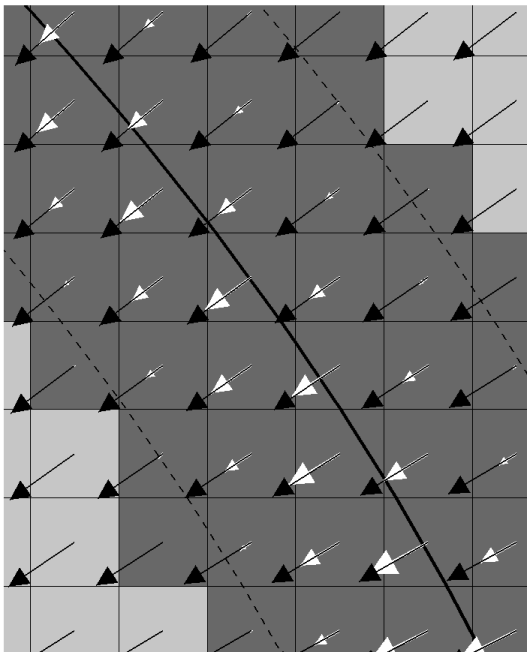

Fig. 6.58: Resulting volume forces (white arrows) in cells within transition region $\mathfrak{B}$ (dark grey areas) around the interface Γ (thick black line) in comparison with vectors pointing in the direction of the local level-set gradient (black arrows)

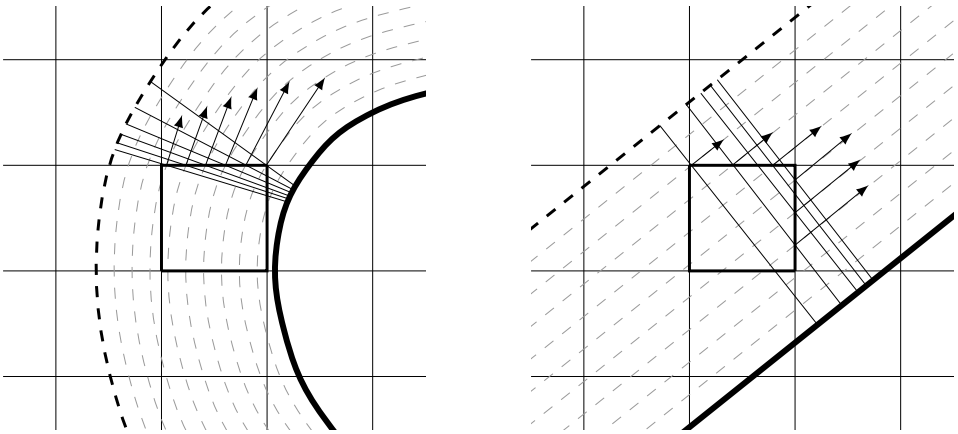

Fig. 6.59: Local (smoothed) surface force contributions $\boldsymbol{F}_S \cdot \vec{\mathfrak{e}}_d$ (arrows) along the Cartesian grid cell boundary (black box) within the transition region $\mathfrak{B}$, tangential to iso-contours (grey dashed lines) of the underlying level-set function representing the interface Γ via its zero level (thick black line)

- although curvature is not computed explicitly and the interface normal volume forces result from balancing of interface tangential $\mathcal{O}(1)$ vector contributions as integrals over grid cell faces, the resulting interface normal forces vanish up to machine accuracy at arbitrary angle of the interface with respect to the Cartesian grid cells in areas, where the curvature vanishes as shown in the fourth line of ***Fig. 6.57***. This is possible, since in regions of zero curvature

  - the interface normal vector $\vec{n}_\Gamma$ becomes independent of the relative coordinate y along the integration path as sketched in ***Fig. 6.59***, and – as a result – all contributions to the integral balance (6.265) are exactly interface tangential on each of the grid cell faces

  - the smoothed Dirac representation along the integration path – resulting from the approximation of the interface Dirac δ_Γ via interface normal linear hat functions within $\mathfrak{B}$ according to equation (6.230) with (6.231) and $\mathfrak{p} = \mathfrak{q} = 1$ according to (6.267) as sketched in ***Fig. 6.47*** – becomes linear as well as shown in section 6.6.1.7. Thus, the piecewise linear approximation of the level-set function G along the integration path – the spatial coordinate y of the space-time cell face – leads to an exact representation of this linear Dirac approximation along the integration path. In general, for non-zero curvatures, the Dirac representation along the integration path is non-linear as given in section 6.6.1.7 as well, and the piecewise

linear level-set approximation along the integration path only provides an approximation to the chosen Dirac representation after application to (6.230) via (6.231) considering (6.232). In grid cells, which are located entirely within the transition zone $\mathfrak{B}$, these approximation errors, however, cancel (largely) pair by pair during balancing over opposing grid cell faces, leading to a higher order error there.

- in grid cells with faces, which are located only partially within the transition region $\mathfrak{B}$, the direction of the resulting volume forces (slightly) deviate from the interface normal direction as can be seen in the lower part of ***Fig. 6.60***. These directional deviations increase with increasing asymmetry of the part of the grid cell, that is within the transition region with respect to the interface normal direction as shown in detail in ***Fig. 6.61***. The most probable but not yet approved source of this behavior is the reduced cancelation property due to the lack of symmetry during the balancing over contributing sections of the grid cell boundary for grid cells which are only partially within the transition region $\mathfrak{B}$ as sketched in ***Fig. 6.62***. The contributions pointing off the interface normal direction, however, are the ones with the smallest magnitudes due to the largest allowable distances from the interface for non-zero values. The described behavior, however, is one of the reasons that yet prevent the thickness of the transition zone $\mathfrak{B}$ from being smaller than the grid resolution, since with smaller transition region width the amplitudes of forces pointing off the interface normal direction increase, and needs to be fixed in future work.

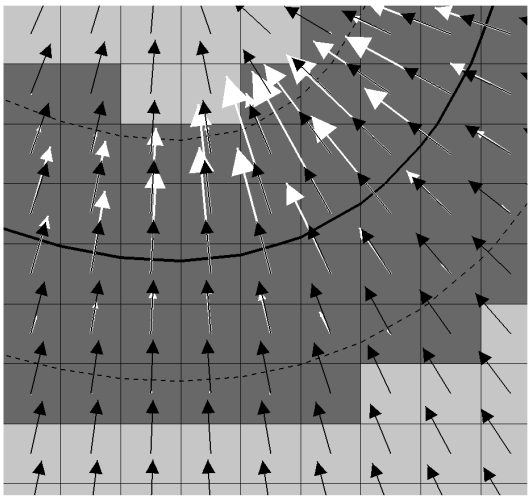

Fig. 6.60: Resulting volume forces (white arrows) in cells within transition region $\mathfrak{B}$ (dark grey areas), bounded by the dashed lines around the interface Γ (thick black line), in comparison with vectors pointing in the direction of the local level-set gradient (black arrows)

- the (smoothed) pressure jump as a measure of curvature approximation at constant surface tension coefficient is reproduced correctly, although curva-

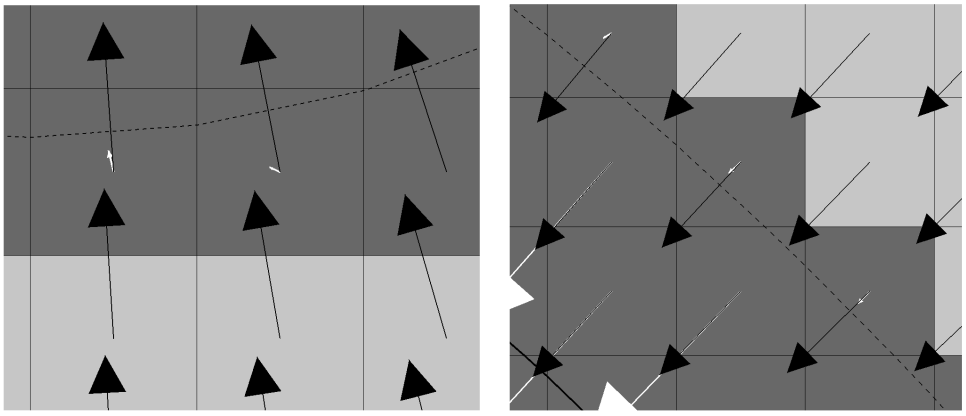

Fig. 6.61: Resulting volume forces (white arrows) in cells at the boundary (dashed line) of the transition region $\mathfrak{B}$ (dark grey areas) around the interface Γ (thick black line), in comparison with vectors pointing in the direction of the local level-set gradient (black arrows)

ture is not computed explicitly, as shown for the circular bubble of radius $r := 0.256\,\mathrm{m}$ from ***Fig. 6.56*** at[30] $\sigma := 5.12 \cdot 10^{-2}\,\frac{\mathrm{kg}}{\mathrm{s}^2}$, centered in a two-dimensional $1.024\,\mathrm{m} \times 1.024\,\mathrm{m}$ domain, with

$$\left[\!\left[p' \right]\!\right] = \sigma\kappa = \sigma\frac{1}{r} = 5.12 \cdot 10^{-2}\frac{\mathrm{kg}}{\mathrm{s}^2}\frac{1}{0.256\,\mathrm{m}} = 0.2\,\frac{\mathrm{kg}}{\mathrm{s}^2\mathrm{m}} \tag{6.354}$$

as theoretical exact value.

However, as shown in ***Tab. 6.4*** for different grid resolutions and different constant relative transition region widths with respect to the grid spacing $\mathfrak{h}$, the maximum pressure amplitude does not improve significantly with grid resolution. The reason for that is on the one hand, that increasing grid resolution implies thinner transition regions, as their width scales with $\mathfrak{h}$, which does not lead to an increasing number of contributing grid cells in interface normal direction. The same computations applying the standard continuous surface force (CSF) method[31] as applied in [164], shown in the right column of ***Tab. 6.4***, in principle show corresponding behavior.

[30] The surface tension coefficient of an air bubble in water, for example, is around $\sigma := 7 \cdot 10^{-2}\,\frac{\mathrm{kg}}{\mathrm{s}^2}$, depending on temperature; the value of $5.12 \cdot 10^{-2}\,\frac{\mathrm{kg}}{\mathrm{s}^2}$ is chosen here to fit into the scheme of numbers as powers of 2 due to $512 = 2^9$, $256 = 2^8$ and $1024 = 2^{10}$ in order to obtain simple results in the physically reasonable order of magnitude.

[31] While the present approach is discretely conservative, independent of grid resolution, the CSF method is only discretely conservative for vanishing transition region width.

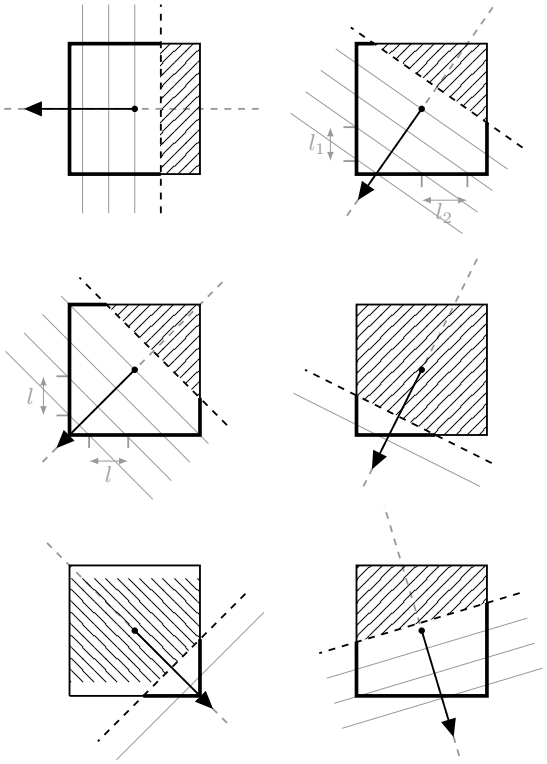

Fig. 6.62: Grid cells only partially within the transition region $\mathfrak{B}$; *left*: symmetric cases, *right*: non-symmetric cases

Tab. 6.4: Relative error $\mathcal{E}$ of maximum (smoothed) interfacial jump in dynamic pressure $p^{'}$ (rounded to two decimal digits) and convergence order $\mathfrak{p}$ (rounded to three decimal digits) for a circular bubble of radius 0.256 in a 1.024×1.024 domain at different grid resolutions and constant relative bandwidth with respect to grid spacing $\mathfrak{h}$ in comparison to the continuous surface force (CSF) model as used in [164]. $\mathcal{E}$ and $\mathfrak{p}$ are defined in appendix section C.

		CSS						CSF	
		$\mathfrak{m}=1$		$\mathfrak{m}=2$		$\mathfrak{m}=4$		$\mathfrak{m}=2$	
cells	$\frac{\mathfrak{h}}{10^{-2}}$	$\frac{\mathcal{E}}{10^{-2}}$	$\mathfrak{p}$	$\frac{\mathcal{E}}{10^{-2}}$	$\mathfrak{p}$	$\frac{\mathcal{E}}{10^{-2}}$	$\mathfrak{p}$	$\frac{\mathcal{E}}{10^{-2}}$	$\mathfrak{p}$
32^2	3.2	2.68	-	1.82	-	5.29	-	2.43	-
64^2	1.6	2.12	0.339	0.97	0.910	1.54	1.779	0.91	1.413
128^2	0.8	2.36	-0.152	0.76	0.361	0.70	1.146	0.48	1.016
256^2	0.4	2.27	0.055	0.73	0.039	0.50	0.489	0.42	0.478
512^2	0.2	2.35	-0.051	0.75	-0.031	0.46	0.135	0.37	0.205
1024^2	0.1	2.47	0.073	0.76	-0.012	0.46	0.000	0.37	0.005

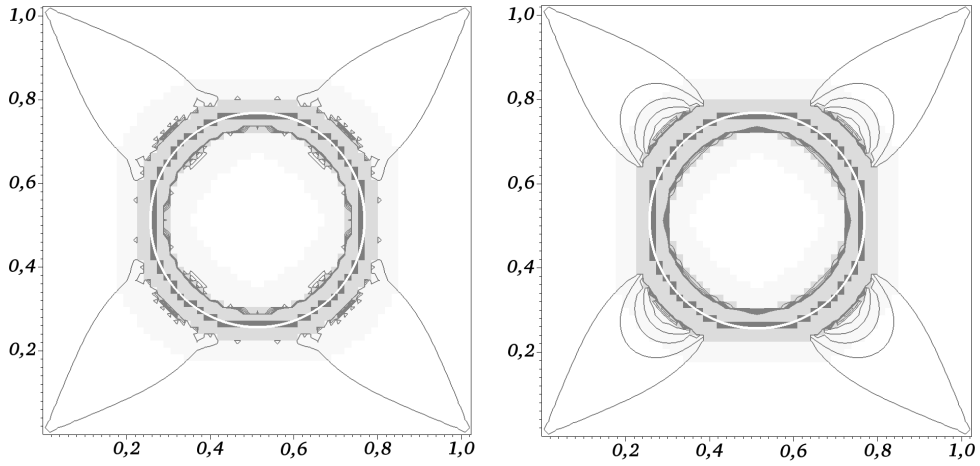

Fig. 6.63: Pressure error at the transition region boundary on a two-dimensional grid of 64×64 cells; *left*: present method, *right*: continuous surface force method as used in [164]; *dark grey lines*: iso-contours of pressure $p^{'}$ beyond values of $(0, 0.2)\frac{\text{kg}}{\text{ms}^2}$, *thick white line*: interface Γ, *dark grey area*: cut grid cells $\mathfrak{C}$, *medium grey area*: transition region $\mathfrak{B}\backslash\mathfrak{C}$ beyond cut cells, *light grey area*: narrow band $\mathfrak{R}\backslash\mathfrak{B}$ beyond transition region, *white area*: computational domain $\Omega^{\square}\backslash\mathfrak{R}$ beyond narrow band

On the other hand, yet an error occurs at the transition region boundary of the present approach as shown in ***Fig. 6.63***. This error causes the results in ***Tab. 6.4*** to be worse than the ones using the CSF method and has two different sources, whose fix is subject of future work: On the one hand, the discretizations of pressure along the entire grid cell face and surface stress contributions only on fractions within the transition region do not necessarily match yet as sketched in ***Fig. 6.64***. On the other hand, the grid cells on the transition region boundary, which only partially contribute to the transition region, lack an implicit symmetry based leading order cancelation property the grid cells which are totally within the transition region benefit from as sketched in ***Fig. 6.62*** and already mentioned above.

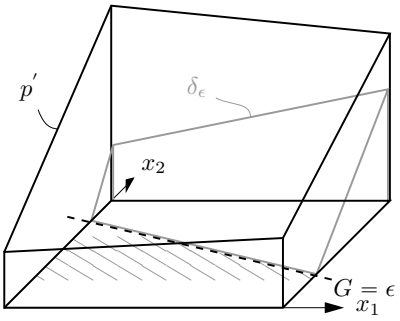

Fig. 6.64: Pressure and surface force profiles in grid cells at the transition region boundary

Fig. 6.63 further shows, that for both methods the largest errors occur on the domain diagonals, where the largest angle ϑ between interface normal and one of the coordinate directions is present. This corresponds to the results from [48], in which a variable bandwidth, depending on ϑ, and usage of a

multi-dimensional Dirac approximation instead of a one-dimensional in interface normal direction are proposed in order to avoid this diagonally dominating errors.

6.6.4.3 Oscillating Pair of Soap Bubbles

In the following two different settings of oscillating soap bubbles according to [97] are considered as shown in ***Fig. 6.65***, each composed of two separate bubbles that have just merged. In ***Tab. 6.5*** the parameters for each setting according to the sketch

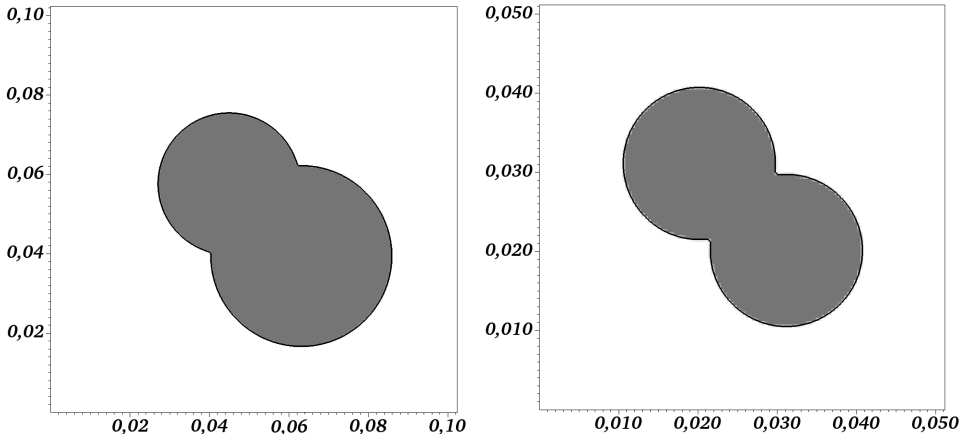

Fig. 6.65: Initial conditions of merged soap bubbles; *left*: initial bubbles of different size (case D) on a $1.024 \cdot 10^{-1}\,\mathrm{m} \times 1.024 \cdot 10^{-1}\,\mathrm{m}$ domain, *right*: initial bubbles of equal size (case E) on a $5.12 \cdot 10^{-2}\,\mathrm{m} \times 5.12 \cdot 10^{-2}\,\mathrm{m}$ domain; settings as specified in ***Tab. 6.5*** and ***Fig. 6.54***

in ***Fig. 6.54*** on page 282 are given, with

- density $\rho^{(+)} = 1.2 \frac{\mathrm{kg}}{\mathrm{m}^3}$ and $\frac{\rho^{(-)}}{\rho^{(+)}} = 1$
- dynamic viscosity $\mu^{(+)} = 1.71 \cdot 10^{-5} \frac{\mathrm{kg}}{\mathrm{m\,s}}$ and $\frac{\mu^{(-)}}{\mu^{(+)}} = 1$
- constant surface tension coefficient $\sigma = 0.034 \frac{\mathrm{kg}}{\mathrm{s}^2}$

according to [97] in both cases. The initial ratio $\frac{a_1}{r_1}$ in ***Tab. 6.5*** is obtained assuming volume conservation by equating the equilibrium volume of the resulting sphere with radius r_{eq} with the sum of the volumes of the initial single bubbles, diminished by the volume of the spherical segments of each initial bubble, that have vanished due to bubble merging.

Tab. 6.5: Settings for oscillating pair of merged bubbles; the quantities in the lower section can be derived from the ones in the upper section, index eq indicates the equilibrium state when the resulting bubble has become a sphere (or circle for $\mathfrak{d} = 2$); $\mathfrak{U}$ is the perimeter of the great circle which is determined in two-dimensional computations

	equal bubbles (case E)	different bubbles (case D)
S_1	$0.00116\,\mathrm{m}^2$	$0.0065\,\mathrm{m}^2$
S_2	S_1	$0.0040\,\mathrm{m}^2$
r_{eq}	$0.012\,\mathrm{m}$	$0.0252\,\mathrm{m}$
r_1	$\sqrt{\frac{S_1}{4\pi}}$	
$\frac{r_2}{r_1}$	1.0	$\sqrt{\frac{S_2}{S_1}}$
$\frac{a_1}{r_1}$	0.80824515133385	0.735263897
$\frac{a_2}{a_1}$	1.0	$\sqrt{1-\left(1-\left(\frac{r_2}{r_1}\right)^2\right)\left(\frac{r_1}{a_1}\right)^2}$
S_{eq}	$4\pi\, r_{\mathrm{eq}}^2$	
$\mathfrak{U}_{\mathrm{eq}}$	$2\pi\, r_{\mathrm{eq}}$	

This results in

$$\left(1-\frac{a_1}{r_1}\right)^2\left(2+\frac{a_1}{r_1}\right)+\left(\frac{r_2}{r_1}-\left(\frac{a_2}{a_1}\right)\frac{a_1}{r_1}\right)^2\left(2\frac{r_2}{r_1}+\left(\frac{a_2}{a_1}\right)\frac{a_1}{r_1}\right) = 4\left(\left(\frac{r_2}{r_1}\right)^3-\mathfrak{R}\right) \tag{6.355}$$

with

$$\mathfrak{R} := \left(\frac{r_{\mathrm{eq}}}{r_1}\right)^3 - 1 \tag{6.356}$$

to solve for $\frac{a_1}{r_1}$, taking into account that in general $\frac{a_2}{a_1}$ is also a function of $\frac{a_1}{r_1}$ as given in ***Tab. 6.5***. In case of equally sized bubbles equation (6.355) reduces to solving

$$\frac{a_1}{r_1}\left(3-\left(\frac{a_1}{r_1}\right)^2\right) = 2\mathfrak{R} \tag{6.357}$$

for $\frac{a_1}{r_1}$. While (6.355) has to be solved numerically, the reduced cubic equation (6.357) without quadratic contribution can be solved analytically as done for equation (6.330) in section 6.6.4.1 - 4, with resulting values as given in ***Tab. 6.6***.

Tab. 6.6: Results during the analytical solution process of the reduced cubic equation (6.357) for $\frac{a_1}{r_1}$ in case E according to solving (6.330) in section 6.6.4.1 - 4. The variable specification in the left column refers to the variables as used in section 6.6.4.1 - 4. The condition $0 < \frac{a_1}{r_1} < 1$ needs to be satisfied for the two bubbles to overlap as shown in ***Fig. 6.54***. Thus, Z_2 is the valid solution for $\frac{a_1}{r_1}$.

quantity from section 6.6.4.1 - 4 as used for solving equation (6.330)	source	representation due to equation (6.357)	value for case E
	Tab. 6.5	$\frac{r_{\text{eq}}}{r_1}$	1.24898488731242
	(6.356)	$\mathfrak{R}$	0.94837052243257
p	(6.330)	-3	-3
q	(6.330)	$2\mathfrak{R}$	1.89674104486514
$\left(\frac{p}{3}\right)^3$	(6.332)	-1	-1
$\left(\frac{q}{2}\right)^2$	(6.332)	$\mathfrak{R}^2$	0.89940664781903
Δ	(6.332)	$\mathfrak{R}^2 - 1$	$\underline{-0.10059335218097}$
ξ	(6.334)	$\frac{1}{3}\cos^{-1}(-\mathfrak{R})$	0.93961815959145
r	(6.334)	2	2
Z_1	***Tab. 6.3***	$r\cos(\xi)$	1.1801926806849
Z_2	***Tab. 6.3***	$-r\cos(\xi + \frac{\pi}{3})$	**0.80824515133385**
Z_3	***Tab. 6.3***	$-r\cos(\xi - \frac{\pi}{3})$	-1.98843783201870

While the case of equally sized bubbles (case E) is solved on a $5.12 \cdot 10^{-2}\,\mathrm{m} \times 5.12 \cdot 10^{-2}\,\mathrm{m}$ domain, the case of different bubbles (case D) is solved on a $1.024 \cdot 10^{-1}\,\mathrm{m} \times 1.024 \cdot 10^{-1}\,\mathrm{m}$ domain, as the bubble radii are about twice in size in the latter case.

The signed distance function for the initial setting as sketched in ***Fig. 6.54*** is given in section 6.6.4.1 - 3. For the present computations an angle of 45° with respect to the Cartesian grid is chosen as illustrated in ***Fig. 6.65***. All domain boundaries are assumed to be periodic and the CFL number is chosen to be $\mathcal{C}_{\mathcal{A}} = 0.48$.

The upper parts of ***Fig. 6.66*** and ***Fig. 6.67*** show the time series of the bubble perimeter, resulting from a two-dimensional computation on a Cartesian grid of 256×256 grid cells for case D with settings according to ***Tab. 6.5*** and on a Cartesian grid of 128×128 grid cells for case E, both computed for the initial period of $0.35\,\mathrm{s}$ at $\widetilde{\mathfrak{m}}_{glob} = 2$. The lower parts show the frequency spectra, resulting from a Fast Fourier Transformation (FFT) of the perimeter time series, performed using MATLAB in a

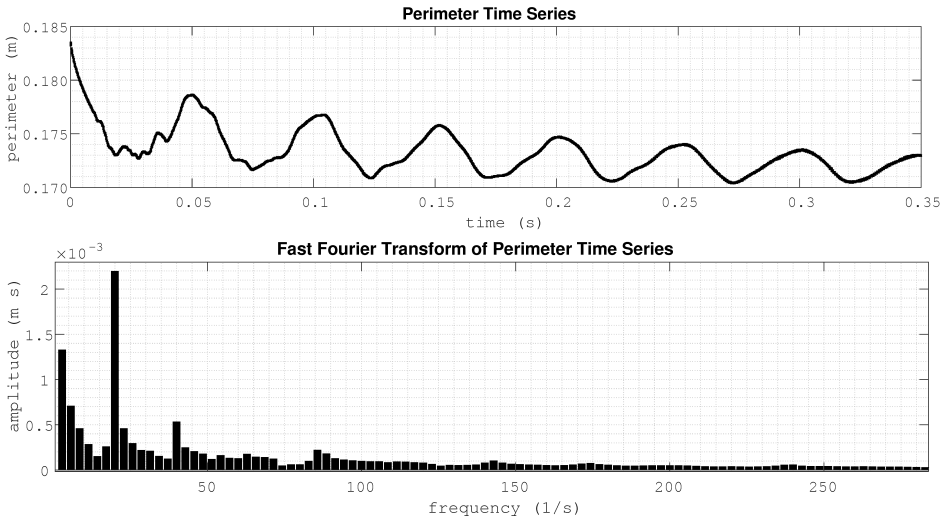

Fig. 6.66: Case D; *top:* Time series of perimeter of pair of bubbles with different radii according to ***Tab. 6.5*** on a two-dimensional grid of 192×192 cells in a $0.1024\,m \times 0.1024\,m$ domain, *bottom*: excerpt of the Fourier transformation result of the top row perimeter time series

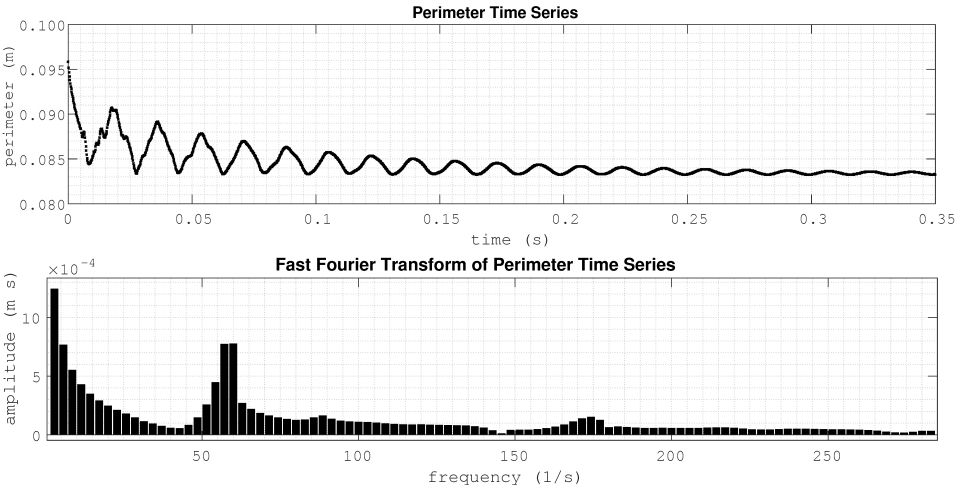

Fig. 6.67: Case E; *top:* Time series of perimeter of pair of bubbles with equal radii according to ***Tab. 6.5*** on a two-dimensional grid of 128×128 cells in a $\overline{0.0512\,\mathrm{m} \times 0.0512\,\mathrm{m}}$ domain, *bottom*: excerpt of the Fourier transformation result of the top row perimeter time series

post-processing step[32]. The corresponding values for the first oscillation modes are given in ***Tab. 6.7*** and ***Tab. 6.8***, corresponding to the frequencies of the coefficients assuming the (local) interface (displacement) to be represented by a linear combination

[32] Simulations are done with the C++ implementation ***STAFSEA***^{2} of the present numerical method: `http://www.mi.fu-berlin.de/w/AgKlein/WelcomeSTAFSEAsquared`.

of different Laplace's spherical harmonics as done in [97].

Tab. 6.7: Frequencies (and corresponding amplitudes) of the first modes resulting from Fourier transformation of the perimeter time series of the oscillating pair of bubbles with different radii (corresponding to surface areas of the individual spherical bubbles of $0.004\,\mathrm{m}^2$ and $0.0065\,\mathrm{m}^2$ in three-dimensional space); comparison of two-dimensional numerical results on a $0.1024\,\mathrm{m} \times 0.1024\,\mathrm{m}$ domain at different grid resolutions, two-dimensional experimental determination from images of three-dimensional flow data (exp.) according to [97] and theoretical computation (theo.) according to [103]

Case D	numerical results				exp.	theo.
	STAFSEA^2				[97]	[103]
mode	$\frac{1}{\mathrm{s}}$ $(10^{-3}\mathrm{ms})$				$\frac{1}{\mathrm{s}}$	$\frac{1}{\mathrm{s}}$
	96^2	128^2	192^2	512^2		
2	19.996 (2.283)	19.998 (2.242)	19.999 (2.197)	19.999 (2.141)	19	20.75
3	39.992 (0.460)	39.996 (0.511)	39.978 (0.531)	39.998 (0.527)	35	39.21
4	59.988 (0.183)	59.994 (0.154)	62.853 (0.174)	62.854 (0.178)	57	59.90
5	82.841 (0.225)	85.706 (0.263)	85.709 (0.219)	88.566 (0.228)	72	82.76

It can be seen, that comparing with

- experimental determination based on two-dimensional images of three dimensional flow data as given in [97] and
- theoretical data in three space dimensions as given in [103]

the frequencies of interfacial oscillation due to the given initial conditions are captured well by the present numerical method although only performed in two spatial dimensions. In contrast to the theoretical and experimental results, for case E also the odd modes are excited due to remaining spurious currents arising from the remaining force-pressure mismatch at the transition region boundary, however, at small amplitudes as shown in ***Fig. 6.67***.

Tab. 6.8: Frequencies (and corresponding amplitudes) of the first modes resulting from Fourier transformation of the perimeter time series of the oscillating pair of bubbles with identical radii (corresponding to surface areas of the individual spherical bubbles of $0.00116\,\mathrm{m}^2$ in three-dimensional space); comparison of two-dimensional numerical results on a $0.0512\,\mathrm{m} \times 0.0512\,\mathrm{m}$ domain at different grid resolutions, two-dimensional experimental determination from three-dimensional flow images (exp.) according to [97] and theoretical computation (theo.) according to [103]

Case E	numerical results					exp.	theo.
	STAFSEA^2					[97]	[103]
mode	$\frac{1}{\mathrm{s}}$ (10^{-3}ms)					$\frac{1}{\mathrm{s}}$	$\frac{1}{\mathrm{s}}$
	48^2	64^2	96^2	128^2	256^2		
2	57.099 (1.111)	57.137 (1.000)	57.140 (0.845)	59.997 (0.776)	59.999 (0.855)	70	63.14
3	82.792 (0.168)	85.706 (0.166)	88.566 (0.160)	88.567 (0.162)	88.571 (0.151)	-	-
4	162.733 (0.162)	168.554 (0.160)	171.419 (0.158)	174.277 (0.151)	177.141 (0.141)	202	182.28
5	196.992 (0.068)	205.693 (0.066)	211.416 (0.064)	217.131 (0.062)	219.998 (0.057)	-	-

In ***Tab. 6.9*** and ***Tab. 6.10*** the ratios between the frequencies of the different modes are given as done in [97].

Tab. 6.9: Ratios of different oscillation modes in comparison with the ones given in [97] for the present case of different initial bubble radii

Case D	numerical results				exp. [97]	theo. [103]
	96^2	128^2	192^2	512^2		
$\frac{mode\ 3}{mode\ 2}$	2.000	2.000	1.999	2.000	1.83	1.89
$\frac{mode\ 4}{mode\ 2}$	3.000	3.000	3.143	3.143	2.96	2.89
$\frac{mode\ 5}{mode\ 2}$	4.143	4.286	4.286	4.429	3.79	3.99
$\frac{mode\ 4}{mode\ 3}$	1.500	1.500	1.572	1.566	1.62	1.53
$\frac{mode\ 5}{mode\ 3}$	2.071	2.143	2.144	2.214	2.07	2.11
$\frac{mode\ 5}{mode\ 4}$	1.381	1.429	1.364	1.409	1.28	1.38

Tab. 6.10: Ratios of different oscillation modes in comparison with the ones given in [97] for the present case of equal initial bubble radii

Case E	numerical results					exp. [97]	theo. [103]
	48^2	64^2	96^2	128^2	256^2		
$\frac{mode\ 3}{mode\ 2}$	1.450	1.500	1.550	1.476	1.476	-	-
$\frac{mode\ 4}{mode\ 2}$	2.850	2.950	3.000	2.905	2.952	2.82	2.89
$\frac{mode\ 5}{mode\ 2}$	3.450	3.600	3.700	3.619	3.667	-	-
$\frac{mode\ 4}{mode\ 3}$	1.966	1.967	1.935	1.968	2.000	-	-
$\frac{mode\ 5}{mode\ 3}$	2.379	2.400	2.387	2.452	2.484	-	-
$\frac{mode\ 5}{mode\ 4}$	1.210	1.220	1.233	1.246	1.242	-	-

In ***Fig. 6.68*** the spatio-temporal surface force averages and the resulting velocity field of the initial phase of case D are shown, where the waves, traveling along the interface, can be seen in regions of maximum forcing at alternating orientation, depending on the local (not explicitly evaluated) curvature.

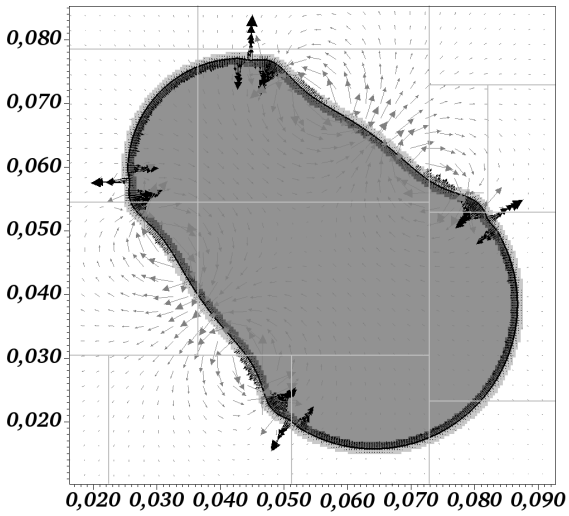

Fig. 6.68: Space-time average surface force (black arrows) within the transition zone $\mathfrak{B}$ around the interface Γ (thick black line) and resulting velocity field (grey arrow) in a periodic $0.1024\,\mathrm{m} \times 0.1024\,\mathrm{m}$ domain of 256×256 grid cells, decomposed into sub-sections (light grey bounded boxes) for parallel computation: Locations of maximum forcing at alternating orientation indicate waves traveling along the interface

Some snapshots of a tracer species, enclosed within the soap bubble and passively advected with the resulting flow, are presented in ***Fig. 6.69*** and ***Fig. 6.70*** during the early phase of the oscillatory process due to the given initial conditions for both case E and case D. On the one hand, it can be seen, that initial symmetry (in the present cases with respect to the domain diagonal) is maintained over a large number of computational time steps, if the initial setting is located symmetrically with respect to the underlying Cartesian grid.

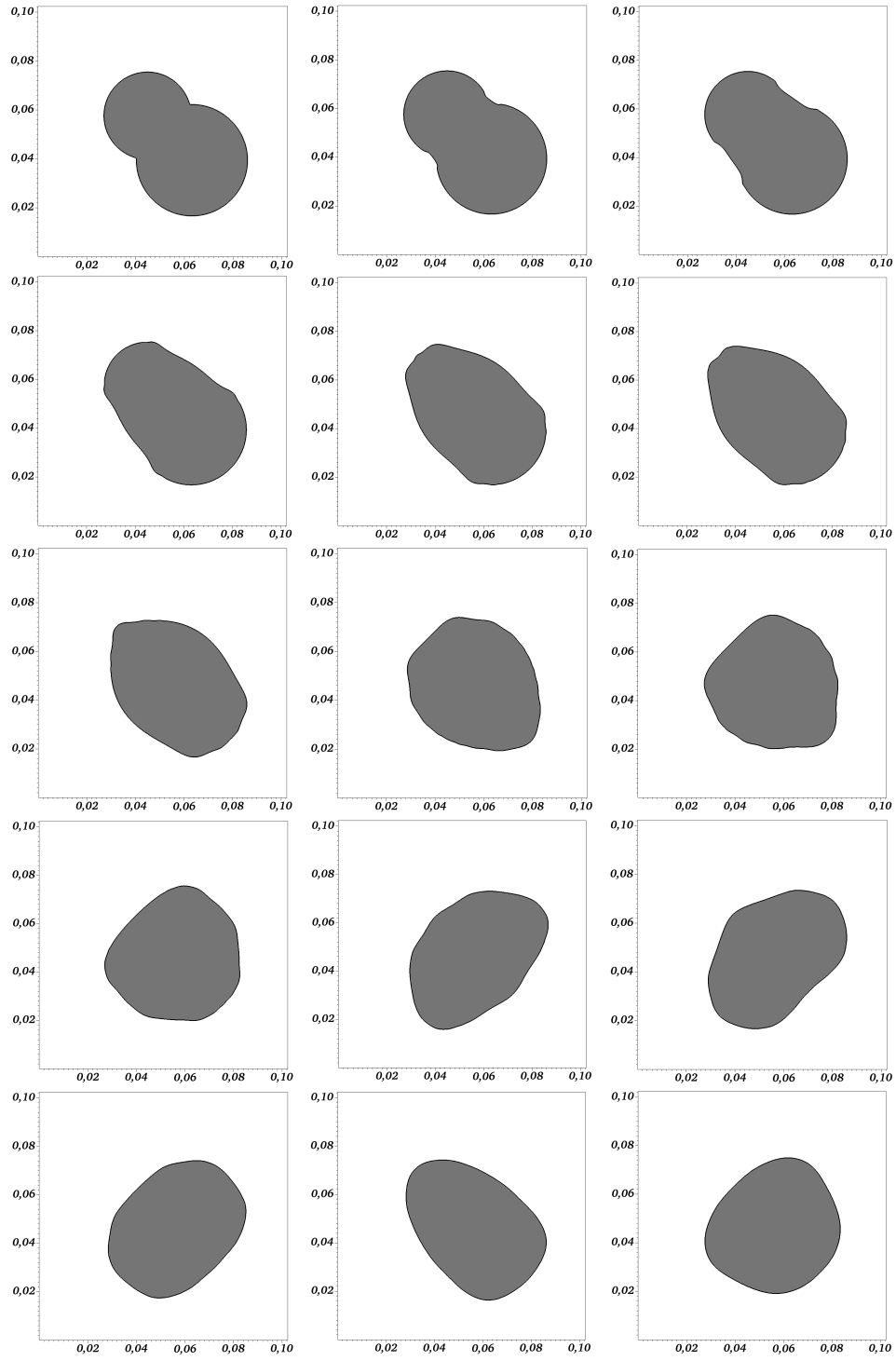

Fig. 6.69: Oscillation snapshots of the pair of merged bubbles of different size (case D) after ((0, 100, 275), (575, 925, 1050), (1350, 2125, 2600), (3050, 5000, 6300), (7100, 11275, 14325)) time steps of size $\Delta t = 9.10107 \cdot 10^{-6}\,\mathrm{s}$ on a two-dimensional Cartesian grid of 256×256 cells on a periodic $0.1024\,\mathrm{m} \times 0.1024\,\mathrm{m}$ domain; computation is done fully explicit at CFL number $\mathcal{C}_{\mathcal{A}} = 0.48$

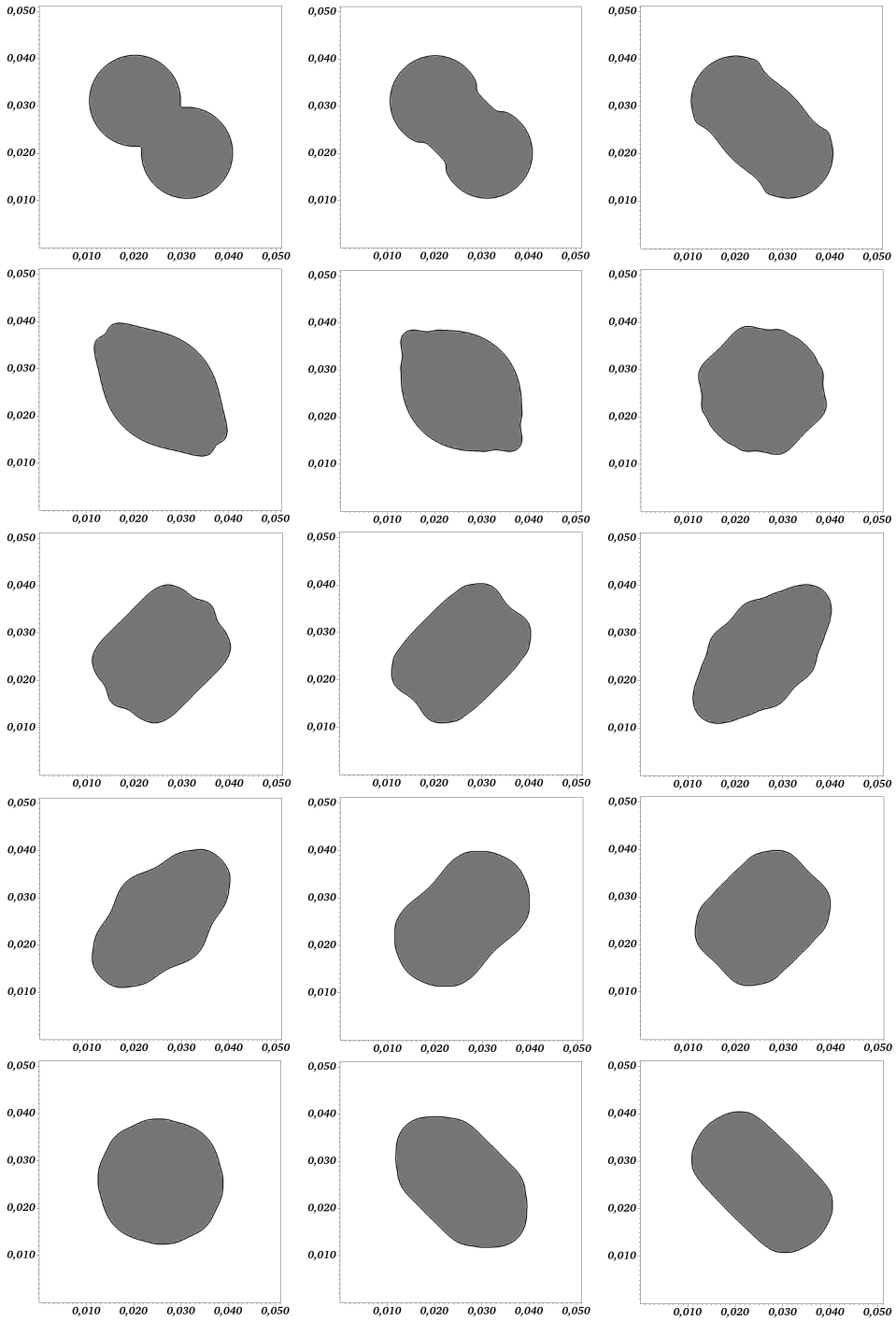

Fig. 6.70: Oscillation snapshots of the pair of merged bubbles of equal size (case E) after ((0, 100, 275), (575, 725, 1000), (1250, 1400, 1925), (2175, 2500, 2800), (3050, 3625, 4050)) time steps of size $\Delta t = 9.10107 \cdot 10^{-6}\,\mathrm{s}$ on a two-dimensional Cartesian grid of 128×128 cells on a periodic $0.0512\,\mathrm{m} \times 0.0512\,\mathrm{m}$ domain; computation is done fully explicit at CFL number $\mathcal{C}_{\mathcal{A}} = 0.48$

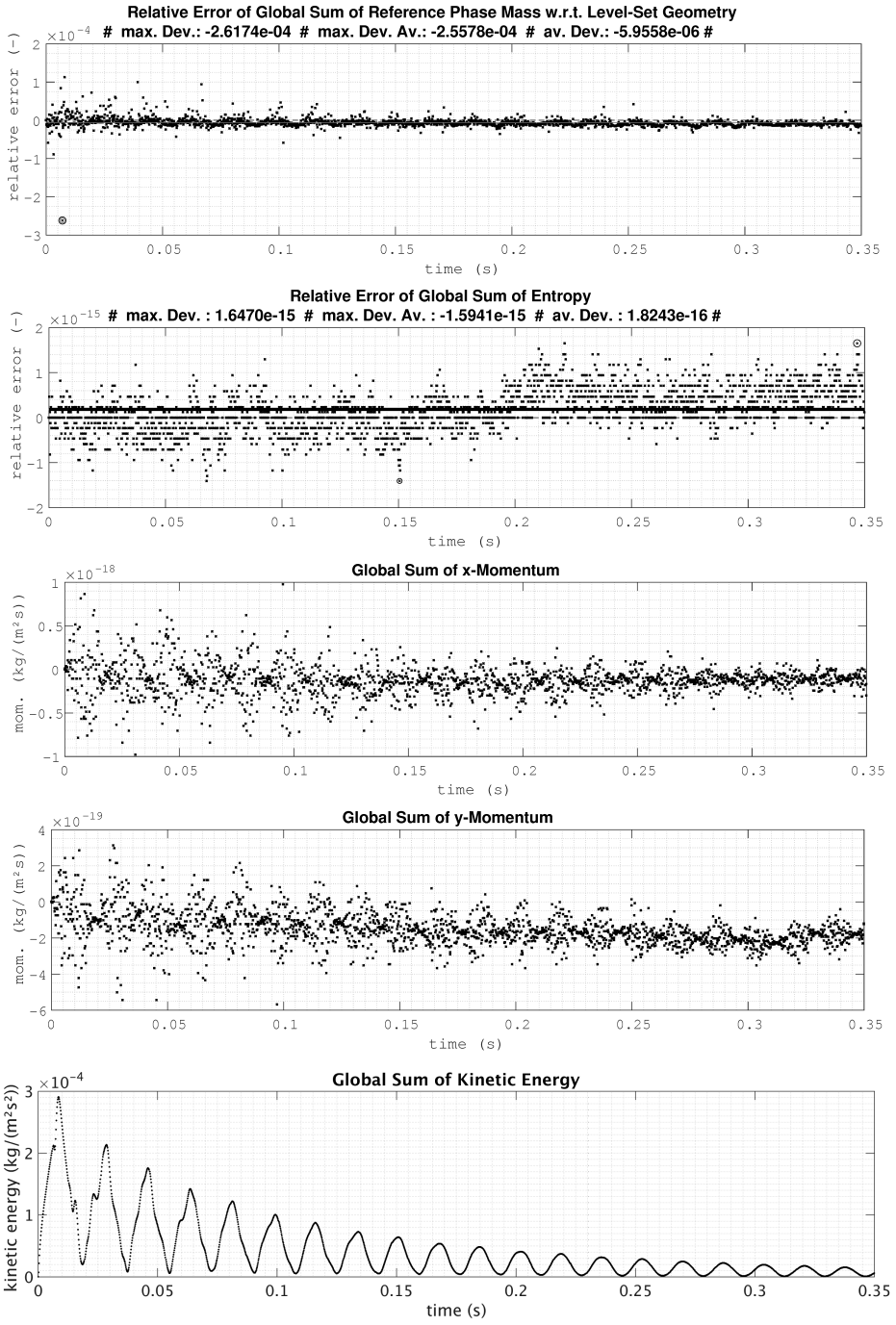

Fig. 6.71: Selected time series of global data for the merged oscillating soap bubbles with identical initial radii, computed on a two-dimensional grid of 128×128 grid cells: *top to bottom*: relative error of level-set based reference phase mass (interface-flow coupling) and entropy measure, followed by absolute values of x_1-momentum component (x), x_2-momentum component (y) and kinetic energy

On the other hand, the tracer species strictly remains within the bubble and intermediate values only occur in cut grid cells as average of portions in each fluid phase within the respective cell.

Finally, ***Fig. 6.71*** shows selected time series of global data. The top graph illustrates the relative error of the interface-flow coupling according to section 6.5.6 based on the strategy described in section 6.5, represented by the relativ error of the mass of the reference fluid within the soap bubble with respect to its initial value and the interface representation based on the level-set. The second plot shows the relative error of the entropy related quantity $\mathcal{P}$ with respect to its initial global sum. The size of the relative deviations over time are in the order of magnitude of machine accuracy, indicating global conservation. The next two plots show the global sums of the momentum components in each coordinate direction, which permanently vanish, despite of the non-trivial arising flow field. The bottom graph shows global kinetic energy as counterpart to the potential energy of the surface due to surface tension, represended by the bubble perimeter in ***Fig. 6.67***.

7. DISCUSSION

This chapter gives an overview of benefits, drawbacks and limitations as well as open issues for a second order accurate numerical method for two-phase flow with sharp interface to work properly, starting with the benefits in section 7.1, followed by the limitations and open issues, discussed in some more detail in section 7.2.

7.1 Benefits

A numerical method for two-phase flow following the concepts presented in this work has the following benefits:

- conservation laws are approximated
- conservative discretizations are used, guaranteeing discrete conservation independent of grid resolution
- consistent and accurate correction of predicted divergence errors without need of evaluation of the discrete divergence (first projection step)
- extendable conceptually straightforward to non-zero divergence constraints
- extendable to weakly compressible and compressible flows
- explicit stability limit is due to the flow speed instead of speed of sound since sound waves are suppressed, allowing for much larger time step sizes during time integration in the predictor step of the projection scheme, compared to solving hyperbolic systems in compressible flow simulations
- no large matrices, since only linear systems for individual scalars need to be solved due to the fractional step projection approach
- no iterative schemes

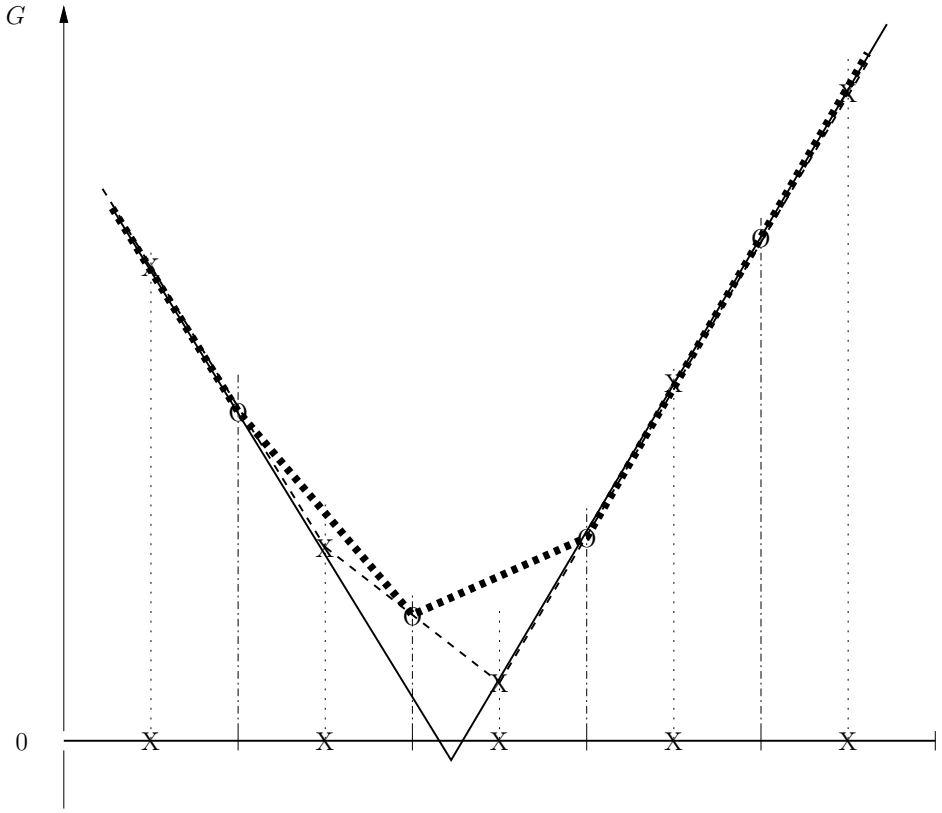

Fig. 7.1: Exact level-set (*thin solid line*) with advected cell center values (X), interpolated level-set node values (O) and piecewise linearly approximated level-set (*thick dotted line*) on a grid in a one-dimensional domain: While the exact level-set has two sign changes within one grid cell, the piecewise linear approximation does not recognize any sign change since the level-set values in both contributing nodes have the same sign. In two space dimensions this one-dimensional plot corresponds to neighboring grid cell faces with parallel normal vectors

7.2 Drawbacks, Limitations and Open Issues

The present method yet suffers from the following drawbacks:

- double (or multiple) intersections per grid cell face (either due to an under-resolved interface or due to interface break-up or merging) can not be detected due to the locally piecewise (bi-)linear approximation of the level-set function as sketched in ***Fig. 6.3*** on page 155 and for a one-dimensional domain in ***Fig. 7.1***. Thus, cell faces, that have been cut at the beginning of the time step, can end up as un-cut grid cell faces although the transport of the exact interface would suggest a double cut on the respective grid cell face. This can occur, if a second cut from a neighboring grid cell face (which is visible as long as it stays

on a different grid cell face) enters the current grid cell face before the already present intersection leaves the same grid cell face. Also, vice versa, grid cell faces can be treated as un-cut at the beginning of the time step by the numerical method until one of the intersections leaves the respective grid cell face, although the grid cell face would be cut twice in the exact case. An example of this behavior is sketched in ***Fig. 7.2***: A fluidic structure with large curvature with respect to the grid resolution is transported parallel to the respective grid cell faces. While in the exact case two intersections are present at the grid cell face at the new time level $n + 1$, the face changes its state from cut to non-cut as soon as the second intersection enters the grid cell face and the entire grid cell (with center labeled X) changes from cut to regular if no other face of that grid cell is intersected. While the mass conservation algorithm from section 6.5 is able to deal with this behavior on the cost of slight shape oscillations over time due to redistribution of mass according to the resulting state as grid cells and faces oscillate between cut and regular in transport direction, space-time integration on such grid cell faces can yield a completely different result from the exact one as sketched in ***Fig. 7.3***, leading to local zero order errors. This problem can be bypassed to some extend by grid refinement around the interface, depending on the magitude of the largest interface (mean) curvature with respect to the grid resolution (see also ***Fig. 7.4*** and the related explanation below). However, depending on the physical phenomena (e.g. thin filaments), it might not be possible to prevent this completely at finite grid resolution.

- multiple intersections of spatio-temporal domains as sketched on the left hand side in ***Fig. 7.3*** only approximate the expected behavior well, as long as there is only one intersection present at any point in time and if both the temporal and the spatial axes are only intersected once per time interval due to the use of only one bi-/tri-linear ansatz function for approximation of quantities on the respective spatio-temoral domain. If two intersections are present at the same time as shown on the left hand side of ***Fig. 7.3***, a single bi-/tri-linear ansatz is not able to represent the true scenario anymore. If ansatz functions are available for each of the spatio-temporal domain fractions, temporal overlaps of intersections can be allowed for as well. However, the use of multiple ansatz functions requires determination of multiple sets of ansatz coefficients involving both spatial and temporal ghost fluid extrapolation for determination of required data for computation of the ansatz coefficients.

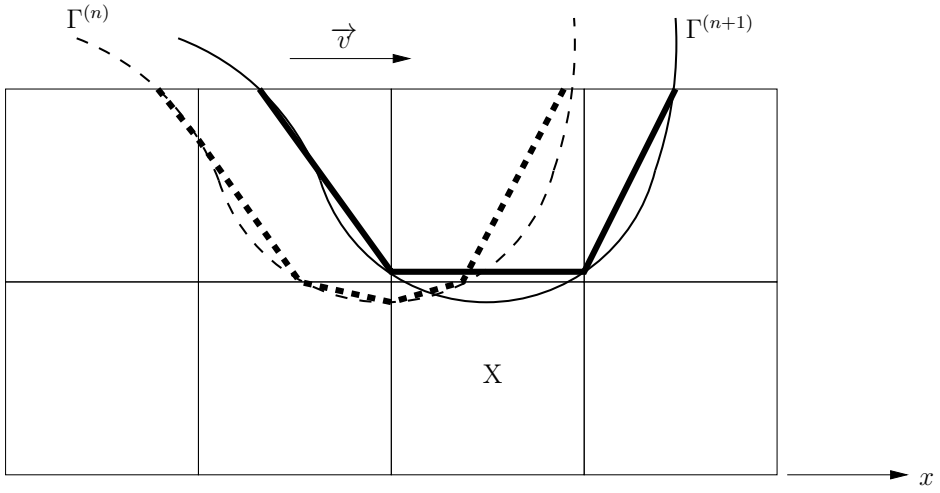

Fig. 7.2: Exact level-set zero level G_0 at old (*thin dashed line*) and new (*thin solid line*) time level and piecewise linear approximation at old (*thick dashed line*) and new (*thick solid line*) time level on a two-dimensional Cartesian grid: While the level-set zero level in the shown configuration is transported along the x-axis, double intersections can be shadowed by the piecewise linear approximation appearing as no intersection. As a consequence the state of grid cells and grid cell faces can oscillate between cut and non-cut

- in case of high interface curvature with respect to the grid spacing, scenarios as sketched in ***Fig. 7.4*** can occur, depending on the magnitude and sign of the cell center level-set values in the surrounding: If the sum of the absolute values of $G_{i+\frac{1}{2},j-\frac{1}{2}}$ and $G_{i+\frac{1}{2},j-\frac{1}{2}}$ (with both negative sign as indicated by $(-)$) is larger than the sum of absolute values of $G_{i-\frac{1}{2},j-\frac{1}{2}}$ and $G_{i+\frac{1}{2},j+\frac{1}{2}}$ (both with positive sign as indicated by $(+)$), which depends on the distance of the respective grid cell centers (X) from the interface, then the interpolation $\frac{1}{2}\left(\frac{G_{i-\frac{1}{2},j-\frac{1}{2}}+G_{i-\frac{1}{2},j+\frac{1}{2}}}{2}+\frac{G_{i+\frac{1}{2},j-\frac{1}{2}}+G_{i+\frac{1}{2},j+\frac{1}{2}}}{2}\right)$ can yield a nodal level-set value $G_{i,j}$ with negative sign in O although it is in the fluid phase where the level-set has positiv sign. In this case all nodal values of the upper right grid cell in ***Fig. 7.4*** are negative, although the cell center value $G_{i+\frac{1}{2},j+\frac{1}{2}}$ is positive, corresponding to numerical separation of a fluidic structure of sub-grid size. Depending on the sign of $G_{i,j}$, the dashed or the dotted approximation applies, however always with $G_{i+\frac{1}{2},j+\frac{1}{2}} > 0$ although beyond the approximated interface.

  This can be prevented by either local grid refinement, depending on the magnitude of the interface curvature with respect to the grid spacing, or by "global" interface refinement in the vicinity of the interface, based on the maximum

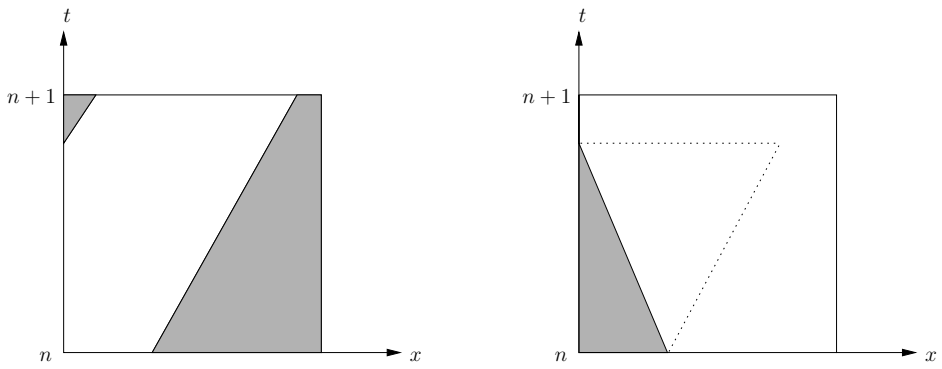

Fig. 7.3: Space-time scenario of the grid cell face that ends up cut twice by the exact level-set zero level G_0 in ***Fig. 7.2*** at the new time level $n+1$: *left:* Exact space-time scenario at constant speed $\vec{v}$, *right:* Resulting approximation of the space-time scenario: The dotted line represents the path of the intersection until the second intersection enters the grid cell face; as a result, the intersection which has been present at time level n seems to move against the flow direction and leave the cell face in upwind direction, resulting in the intersection path approximation represented by the solid line, leading to the shaded/unshaded distribution of space-time fractions

occurring interface curvature. While the first approach, which is the more efficient one, leads to different grid resolutions along the interface, which brings along numerical difficulties in terms of accuracy as velocity data needs to be resolved as fine as the interface representing level-set function, the second approach leads to increased computational cost as the entire vicinity of the interface is resolved depending on local interface properties (largest occuring curvature).

A possible condition for grid refinement is, for example, the relation

$$\mathfrak{h} \min_{\mathfrak{d}} \mathfrak{e}_{\mathfrak{d}} \geqslant \frac{c}{\max_{\mathfrak{i} \in \mathfrak{C}} \kappa_{\mathfrak{i}}} \tag{7.1}$$

in which the left hand side represents the (minimal) grid spacing, the denominator on the right hand side is the largest occuring curvature and $c \geqslant 1$ has to hold in order to prevent poorly resolved structures as sketched in ***Fig. 7.4*** in the top right grid cell.

- although stand-alone level-set and volume-of-fluid methods can handle coalescence and separation of fluidic structures,

  1. the current hybrid approach for mass conservation of each fluid phase as described in section 6.5
  2. the elliptic solvers as presented in [128], [130] and [129]

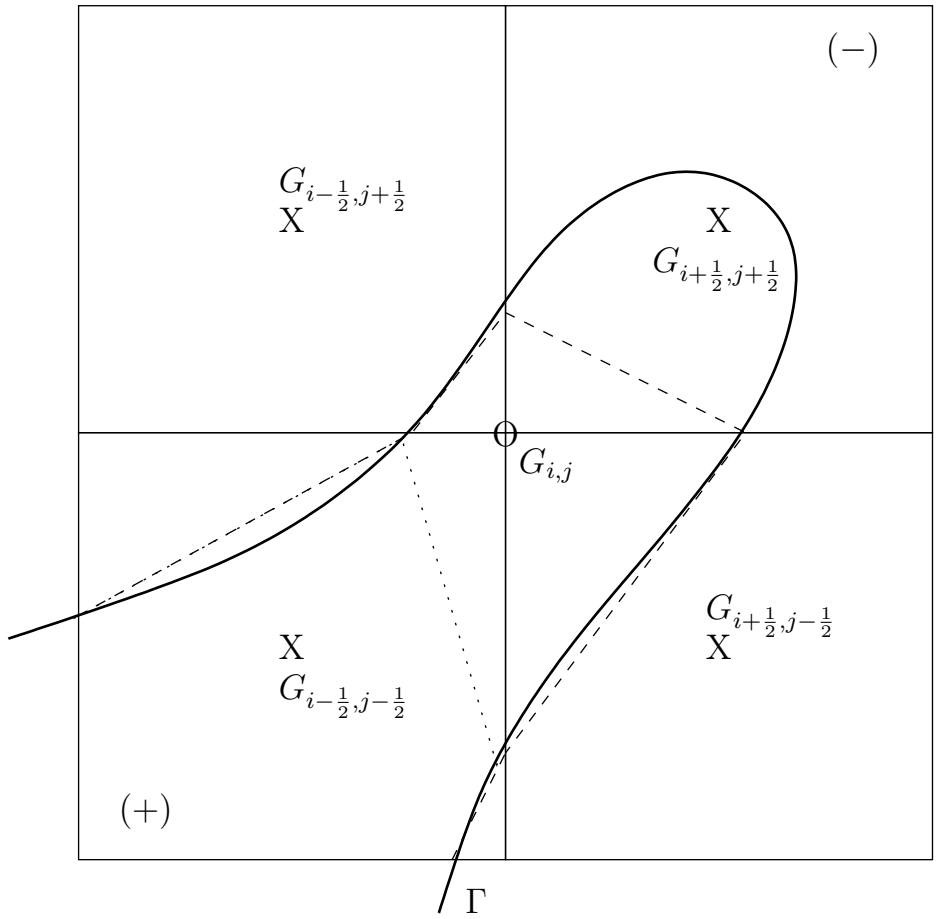

Fig. 7.4: Exact level-set zero level (solid line) representing the interface Γ and approximations, depending on the sign of $G_{i,j}$ in O resulting from the surrounding cell center level-set values in X: *dashed line:* $G_{i,j} > 0$, *dotted line:* $G_{i,j} \leqslant 0$. In both cases, however, $G_{i+\frac{1}{2},j+\frac{1}{2}} > 0$, although – with respect to the approximated interface (dashed or dotted) – the cell center $i + \frac{1}{2}, j + \frac{1}{2}$ is located in the phase in which $G < 0$

3. the limitation to a single cut per grid cell face at the same time as described above

hamper break-up and merging by default without special treatment, which is subject of future research. Concerning 1., the mass stabilization algorithm needs to be extended by both an option for target value determination in cut grid cells with more than two different fluid portions per cut cell and the level-set correction algorithm needs to be able to handle different correction velocities in a single cut cell. The elliptic solvers regarding 2. need to be able to handle more than two fluid portions per cut primal and dual grid cell as well, which,

among others, means that a cut cell has to be able to carry more than two bi-/tri-linear ansatz functions and that suitable inter- and extrapolation algorithms for each fluid portion including ghost fluid data generation need to be provided in order to determine the necessary right hand side values in the arising linear systems for computation of the ansatz coefficients. With respect to 3., sub-grid-models need to be developed, covering the case of two fronts being close enough to each other within one cut cell, such that a grid cell face can be intersected more than once at the same time, guaranteeing that these cases and the involved double (multiple) sub-grid sign change(s) of the level-set function on a single grid cell face can be detected robustly.

- the scaling of the penalizing level-set re-initialization has to be optimized and potentially not yet considered influences have to be discovered and taken into account: while the chosen set of scaling factors yield a reduction of the deviation of the magnitude of the level-set gradient from unity in all presented examples as desired, for each example individual factors can be found, that yield smaller deviations than the common factors and, thus, better results.

- sharp treatment of viscous and diffusive fluxes, in combination with space-time integral sharp interface elliptic solvers with time dependent coefficients, is not yet coupled to the present building blocks and is subject of current research

- test cases with variable density per fluid phase and non-zero divergence constraint, which arise in many typical applications for non-isothermal flow beyond the incompressible assumption, have to be analyzed after extending the method accordingly

- for simulation of practical problems using a Cartesian grid method, a solid wall cut cell method, such as proposed in [22], [21], [112] or [94], needs to be incorporated at the domain boundary allowing for arbitrary domain shapes

- discretization of a transport equation for surface surfactants needs to be added to the system in order to make physical processes available, that change the local surface tension coefficient

- chemical reactions – and with that spatio-temporal dependency of the various coefficients, such as dynamic viscosity and species diffusivity, and non-zero species sources – need to be considered, as, for example, done in [150]. Preliminary work with respect to the implementation into the present method has been done in [61]

Particular issues to be covered for a locally second order accurate two-phase flow method are

- determintion of 4-dimensional space-time weights for source terms in cut grid cells in case of $\mathfrak{d} = 3$
- application of the 3-dimensional space-time weights to the source terms in cut grid cells in case of $\mathfrak{d} = 2$
- second order accurate phase state reconstruction in space-time centroids of cut cell fractions or substitute in cell center incorporating the local gradients
- second order accurate recovery of phase states in centroids of cell face fractions for flux computation or substitute in cell face center
- evaluation of values at space-time centroids in cut cell fractions and on cut face fractions, if more than one spatio-temporal cut is present
- development of a second order accurate time integration strategy for unsplit methods in cut grid cells, e.g. via grid cell face local weights within the Runge-Kutta time integration scheme. Preliminary studies, however, suggest, that consideration of data from a third time level might be required for obtaining second order accuracy in cut grid cells in time locally. However, next to increase of computer storage consumption, this brings along a list of other not yet covered issues.
- suitable strategies for both Poisson solution based pressure update for viscous flow according to [30] and the pressure boundary condition similar to [102] need to be developed for accurate pressure solutions at variable density flows

8. SOFTWARE

The following open source software was used for the given purpose in order to produce the results in the present thesis:

- *GCC*: C++ complier[1]
- *MPICH*: implementation of the message passing interface (MPI) for parallelization[2]
- *SILO*: data storage[3]
- *HDF5*: data storage[4]
- *HYPRE*: solution to linear systems[5]
- *SAMRAI*: parallelization, adaptive mesh refinement, data management, grid generation and extended C++ commands[6]
- *STAFSEA*[2]: the ***ST****ructured* ***A****daptive* ***F****low* ***S****olver for* ***E****ngineering and* ***A****tmospheric* ***A****pplications* that implements the present numerical method in C++[7]
- *VisIt*: visualization of field data[8]
- *Git*: version control[9]

[1] `https://gcc.gnu.org/`, [last visited on July 19th, 2016]
[2] `https://www.mpich.org/`, [last visited on July 19th, 2016]
[3] `https://wci.llnl.gov/simulation/computer-codes/silo`, [last visited on July 19th, 2016]
[4] `https://www.hdfgroup.org/HDF5/`, [last visited on July 19th, 2016]
[5] `https://computation.llnl.gov/project/linear_solvers/software.php`, [last visited on July 19th, 2016]
[6] `https://computation.llnl.gov/project/SAMRAI/`, [last visited on July 19th, 2016]
[7] `http://www.mi.fu-berlin.de/w/AgKlein/WelcomeSTAFSEAsquared`, [last visited on July 19th, 2016]
[8] `https://wci.llnl.gov/simulation/computer-codes/visit/`, [last visited on July 19th, 2016]
[9] `https://git-scm.com/`, [last visited on July 19th, 2016]

- *doxygen*: documentation generation[10]
- *TeX Live*: LaTeX document typesetting[11]
- *TeXShop*: LaTeX editor[12]
- *TikZ*: generation of vector graphics[13]
- *Xfig*: generation of vector graphics[14]
- *Gimp*: transformation of pixel graphics from VisIt into .pdf and .eps graphics (VisIt only provides pixel graphics)
- *fig2pdf*: transforming Xfig figures into pdf files[15]
- *pdfcrop*: truncation of pdf graphics[16]
- *JabRef*: bibliography management[17]
- *Eclipse*: C++ editor[18]
- *Linux* (Debian 8 Jessie): computer operating system

In addition, the following commercial software was used for the given purpose:

- *XCode*: C++ editor and LaTeX editor[19]
- *MATLAB*: visualization of time series data[20]
- *Maple*: computer algebra system (CAS)[21]
- *Mac OSX* (10.6.8, 10.8.5 and 10.10.5): operating systems for Apple computers

[10] `http://www.stack.nl/~dimitri/doxygen/`, [last visited on July 19th, 2016]
[11] `https://www.latex-project.org/`, [last visited on July 19th, 2016]
[12] `http://pages.uoregon.edu/koch/texshop/`, [last visited on July 19th, 2016]
[13] `http://www.texample.net/tikz/`, [last visited on July 19th, 2016]
[14] `http://epb.lbl.gov/xfig/`, [last visited on July 19th, 2016]
[15] `http://fig2ps.sourceforge.net/fig2ps.1.html`, [last visited on Aug. 17th, 2016]
[16] `http://pdfcrop.sourceforge.net/`, [last visited on July 19th, 2016]
[17] `http://jabref.sourceforge.net/`, [last visited on July 19th, 2016]
[18] `http://www.eclipse.org/downloads/packages/eclipse-ide-cc-developers/mars1`, [last visited on July 19th, 2016]
[19] `https://developer.apple.com/xcode/`, [last visited on July 19th, 2016]
[20] `http://www.mathworks.com/products/matlab/`, [last visited on July 19th, 2016]
[21] `http://www.maplesoft.com/products/Maple/`, [last visited on July 19th, 2016]

Part IV

CONCLUSION

9. SUMMARY AND OUTLOOK

The present work serves as starting point for a numerical method for simulation of immiscible chemically reacting zero Mach number variable density two-phase flow with sharp interfaces and its implementation into a newly set up software framework. It combines numerical concepts from [150] – dedicated to combustion – and [92] – addressing meteorological applications and the derivation of a numerical concept for covering different flow regimes – as well as related literature each.

The basic single-phase solver follows one of the variants of the projection method presented in [150], generalized by concepts presented in [92] and, for example, [5] and [6], in order to solve the governing set of Navier-Stokes equations for immiscible chemically reacting two-phase flow at arbitrary equation of state with variable density in the zero Mach number limit (yet without specification of particular reaction kinetics): A predictor step solves the hyperbolic-parabolic part of the equations at time-independent pressure using a second order accurate two-stage Runge-Kutta time integration scheme, applied to an integral Finite Volume flux balance for each grid cell of the underlying fixed Cartesian grid. Applying the generalized concept from [92] allows for a first cell centered correction step to ensure that the advective fluxes on grid cell faces satisfy the divergence constraint arising in the zero Mach number limit without evaluation of the discrete divergence, since divergence errors can be derived from predictor information directly. A second node centered projection step corrects the updated cell centered velocity field to satisfy the divergence constraint as well and determines an update for the node centered pressure field, which has been assumed fix in time during the predictor step, corresponding to an incremental pressure-correction projection method according to [15] on a staggered grid as classified, for example, in [30] and [65].

The single-phase scheme is extended in order to account for suitable overall flux balances in the vicinity of the fluidic interface following concepts from [156] in order to avoid issues due to arbitrarily small grid cell fractions at the fluid interface. The latter is represented by a combination of level-set and volume-of-fluid discretiza-

tions. Both well-established methods suffer from insufficiencies with respect to a discretely conservative numerical method for simulation of fluid flow with different fluid phases, separated by a sharp interface. The concept from [150] and [152] for overcomming these issues, based on work from [28], is modified and adapted to the generalized setup of the present numerical scheme as already briefly sketched in [182]. Different variants of keeping the discretizations of both fluidic interface and fluid flow coupled are analyzed, and in contrast to [150] more weight is put on the level-set function for guiding the resulting correction scheme due to its spatially higher order accurate discretization, while maintaining the mass conservation property provided by volume-of-fluid information. Retention of sharp fluid phase separation without smearing around the interface and stable mass conservation of each fluid phase up to machine accuracy is shown for incompressible flow, while the fluidic interface in terms of the level-set function is coupled second order accurate to the fluid flow, represented by the conserved quantities, serving as basis for split flux computation in the vicinity of the interface in each respective subsequent time step. In addition, a local non-iterative penalization method borrowing from [72] and [42] is proposed, which keeps deviations of the level-set function from a signed distance function bounded. While yet there is space for optimization, the combined approach stabilizes the method by preventing resulting gradients of the discretely transported level-set function from vanishing or heavy steepening.

Further, a discretization technique for approximation of the singular surface stress tensor is proposed. The present yet smoothed approach offers an interesting alternative to a "real" sharp interface approach for treating surface tension, once the remaining open issues are resolved, since it discretizes the influence due to surface tension conservatively. In addition, due to the analytical spatio-temporal integration of ansatz functions, which depend on continuously available data around the interface, small sub-cell transition region widths, approximating the sharp interface case, can be chosen for approximation of the involved smoothed delta Dirac distribution. In this case, the approximation, which depends on the gradient of the level-set function, gets independent of the presented level-set penalization around the interface, since only grid cells with immediate contact to the interface, in which the level-set gradient is restored without penalization according to [72], remain involved in the approximation of the surface stress tensor. However, for making these narrow transition region widths possible, three remaining open issues need to be overcome in future work: On the one hand – in contrast to a "real" sharp interface approach, in which the ansatz functions for pressure determination need to allow for jumps in the

interface normal pressure profile in grid cells cut by the interface – in the present case the ansatz functions for pressure determination need to allow for kinks in grid cells, which are intersected by the transition region boundary for making the ansatzes for both the surface stress tensor and the pressure match. On the other hand, observed deviations of the effective forces due to surface tension from the interface normal direction in grid cells at the transition region boundary need to be corrected due to the lack of an implicit symmetry property in full transition region cells, since with smaller transition region widths the influence of grid cells at the transition region boundary rises both due to the rising relative number of such contributing grid cells and the shorter distance of the latter to the interface, which is equivalent to increased amplitudes of the contributing forces. Additionally, a conservative consistent way of how to include a basically smoothed approach into a sharp interface momentum balance while both keeping arising spurious velocities in both fluid phases in the same order of magnitude and the chosen strategy consistent with the governing equations remains to be found. Therefore the presented examples of merged pairs of oscillating soap bubbles, whose results are in good agreement with both experimental and theoretical investigations from [97] and [103], are restricted to the case of density ratios of one, guaranteeing spurious velocities of the same order of magnitude in both fluid phases.

For a detailed discussion on further open issues the reader is referred to section 7.2, containing a (not necessarily complete) list of necessary future work. The next major step is the coupling of the present building blocks with recent not yet published work on sharp interface elliptic solvers for moving interfaces for the corrector step of the projection method based on developments for stationary interfaces from [128], [130] and [129] in order to yield an applicable method with fully conservative sharp interface discretizations only. The involved techniques are expected to be applicable to discretization of the implicitly treated contributions of friction to the momentum equation and diffusion to the species balances as well. The missing core features in this context are sharp treatment of the Poisson coefficients due to the interfacial movement in time, the respective flux balances while solving the integral elliptic problems, treatment of pressure nodes that change fluid phase during the time step considered and distribution of contributions due to the pressure in the momentum equation to the predictor and the corrector steps. Concluding, fully conservative locally second order accurate discretization of zero Mach number variable density flow with strictly sharp moving interfaces in all the numerical building blocks remains a challenging task, to which this work contributes to, requiring some amout of future work.

APPENDIX

A. CALCULUS

A.1 Matrix and Vector Operations

In this section identities of some matrix and vector operations, used throughout the present work and based on the product rule and the chain rule, are given. Therefore, within this section $s, t \in \mathbb{R}$ are assumed to be arbitrary scalar quantities with $(\blacksquare)_t$ as the partial derivative of $\blacksquare$ with respect to t, $(\vec{n}, \vec{v}, \vec{w}) \in \mathbb{R}^3$ are arbitrary vectors and $\boldsymbol{M} \in \mathbb{R}^{3\times3}$ is an arbitrary matrix. Further, $\boldsymbol{I} \in \mathbb{R}^{3\times3}$ is the identity matrix and $(\nabla \cdot \vec{v}) \in \mathbb{R}$, $(\nabla \cdot \boldsymbol{M}) \in \mathbb{R}^3$, and $(\nabla\vec{v}) \in \mathbb{R}^{3\times3}$ as well as $(\nabla s) \in \mathbb{R}^3$ holds. With that and the identity

$$\vec{v}\vec{w} \equiv \vec{v} \circ \vec{w} \tag{A.1}$$

the following relations are obtained:

$$(\vec{v}\vec{w}) \cdot \vec{n} \;= \vec{v}\,(\vec{w} \cdot \vec{n}) \tag{A.2}$$

$$\nabla \cdot (\,\boldsymbol{M} \cdot \vec{v}\,) \;= (\nabla \cdot \boldsymbol{M}) \cdot \vec{v} + \boldsymbol{M} : \nabla\vec{v} \tag{A.3}$$

$$\nabla \cdot (\,s\vec{v}\,) \;= s\,(\nabla \cdot \vec{v}) + \vec{v} \cdot \nabla s \tag{A.4}$$

$$s\boldsymbol{I} : \nabla\vec{v} \;= s\,(\nabla \cdot \vec{v}) \tag{A.5}$$

$$(\,s\vec{v}\,)_t \cdot \vec{v} \;= \left(\frac{1}{2}s\,(\vec{v} \cdot \vec{v})\right)_t + \frac{1}{2}\,(\,s\,)_t\,(\vec{v} \cdot \vec{v}) \tag{A.6}$$

$$\frac{1}{2}\vec{v} \cdot \nabla\,(\vec{v} \cdot \vec{v}) \;= (\vec{v} \circ \vec{v}) : \nabla\vec{v} \tag{A.7}$$

$$\nabla\left(\frac{1}{s}\right) \;= -\frac{1}{s^2}\nabla s \tag{A.8}$$

Note that both left and right hand sides of (A.3), (A.4), (A.5), (A.6), (A.7) are in $\mathbb{R}$, the ones from (A.2), (A.8) are in $\mathbb{R}^3$ and the ones from (A.1) in $\mathbb{R}^{3\times 3}$. Relation (A.6) results from applying the product rule to $\left(\frac{1}{2}s\left(\vec{v}\cdot\vec{v}\right)\right)_t$, yielding

$$\begin{aligned}\left(\frac{1}{2}s\left(\vec{v}\cdot\vec{v}\right)\right)_t &= \left(\frac{1}{2}\left(s\vec{v}\right)\cdot\vec{v}\right)_t = \frac{1}{2}\left(s\vec{v}\right)_t\cdot\vec{v}+\frac{1}{2}s\vec{v}\cdot\left(\vec{v}\right)_t\\ &= \left(s\vec{v}\right)_t\cdot\vec{v}-\frac{1}{2}\left(s\vec{v}\right)_t\cdot\vec{v}+\frac{1}{2}s\left(\vec{v}\cdot\left(\vec{v}\right)_t\right)\\ &= \left(s\vec{v}\right)_t\cdot\vec{v}-\frac{1}{2}\left(s\right)_t\left(\vec{v}\cdot\vec{v}\right)-\frac{1}{2}s\left(\left(\vec{v}\right)_t\cdot\vec{v}\right)+\frac{1}{2}s\left(\vec{v}\cdot\left(\vec{v}\right)_t\right)\\ &= \left(s\vec{v}\right)_t\cdot\vec{v}-\frac{1}{2}\left(s\right)_t\left(\vec{v}\cdot\vec{v}\right)\end{aligned} \tag{A.9}$$

B. BASIC DERIVATIONS

B.1 Discontinuity of Mass Fractions

Using

- Henry's law
$$C_{\mathfrak{s}}^{(-)} = \frac{1}{\mathcal{H}_{\mathfrak{s}}} C_{\mathfrak{s}}^{(+)} \tag{B.1}$$
with concentration $C_{\mathfrak{s}}$ and non-dimensional Henry's law constant $\mathcal{H}_{\mathfrak{s}}$,
- the definition of the mass concentration (or partial density)
$$\rho_{\mathfrak{s}} := \rho Y_{\mathfrak{s}} = C_{\mathfrak{s}} M_{\mathfrak{s}} \tag{B.2}$$
with
$$\rho = \sum_{\mathfrak{s}} \rho_{\mathfrak{s}} = \sum_{\mathfrak{s}} \rho Y_{\mathfrak{s}} = \rho \underbrace{\sum_{\mathfrak{s}} Y_{\mathfrak{s}}}_{\equiv 1} \tag{B.3}$$
and molar mass $M_{\mathfrak{s}}$ of species $\mathfrak{s}$, and
- the fact that molar mass
$$M_{\mathfrak{s}} = M_{\mathfrak{s}}^{(+)} = M_{\mathfrak{s}}^{(-)} \tag{B.4}$$
of a species $\mathfrak{s}$ is the same in both fluid phases,

the discontinuity of mass concentration can be represented by

$$\begin{aligned}
[\![\, \rho Y_\mathfrak{s} \,]\!] = \rho^{(+)} Y_\mathfrak{s}^{(+)} - \rho^{(-)} Y_\mathfrak{s}^{(-)} &\overset{(B.2)}{=} C_\mathfrak{s}^{(+)} M_\mathfrak{s}^{(+)} - C_\mathfrak{s}^{(-)} M_\mathfrak{s}^{(-)} \\
&\overset{(B.4)}{=} \left(C_\mathfrak{s}^{(+)} - C_\mathfrak{s}^{(-)} \right) M_\mathfrak{s} \\
&= \quad C_\mathfrak{s}^{(+)} M_\mathfrak{s} \left(1 - \frac{C_\mathfrak{s}^{(-)}}{C_\mathfrak{s}^{(+)}} \right) \\
&\overset{(B.2)}{=} \rho^{(+)} Y_\mathfrak{s}^{(+)} \left(1 - \frac{C_\mathfrak{s}^{(-)}}{C_\mathfrak{s}^{(+)}} \right) \\
&\overset{(B.1)}{=} \rho^{(+)} Y_\mathfrak{s}^{(+)} \left(1 - \frac{1}{\mathcal{H}_\mathfrak{s}} \right)
\end{aligned} \tag{B.5}$$

based on one-sided data. The left hand side of the latter equation can be split according to

$$[\![\, \rho Y_\mathfrak{s} \,]\!] = Y_\mathfrak{s}^{(-)} [\![\, \rho \,]\!] + \rho^{(+)} [\![\, Y_\mathfrak{s} \,]\!] \tag{B.6}$$

and solution for $[\![\, Y_\mathfrak{s} \,]\!]$ yields the intermediate result

$$[\![\, Y_\mathfrak{s} \,]\!] = Y_\mathfrak{s}^{(+)} \left(1 - \frac{1}{\mathcal{H}_\mathfrak{s}} \right) - Y_\mathfrak{s}^{(-)} \frac{[\![\, \rho \,]\!]}{\rho^{(+)}} \tag{B.7}$$

for the discontinuity of mass fractions. The density jump can be expressed as sum of equation (B.5) over all species to yield

$$\begin{aligned}
[\![\, \rho \,]\!] = \rho^{(+)} - \rho^{(-)} &= \sum_\mathfrak{s} \rho^{(+)} Y_\mathfrak{s}^{(+)} - \sum_\mathfrak{s} \rho^{(-)} Y_\mathfrak{s}^{(-)} = \sum_\mathfrak{s} [\![\, \rho Y_\mathfrak{s} \,]\!] \\
&= \rho^{(+)} \sum_\mathfrak{s} \left[Y_\mathfrak{s}^{(+)} \left(1 - \frac{1}{\mathcal{H}_\mathfrak{s}} \right) \right] \\
&= \rho^{(+)} \left(1 - \sum_\mathfrak{s} \left(\frac{Y_\mathfrak{s}^{(+)}}{\mathcal{H}_\mathfrak{s}} \right) \right)
\end{aligned} \tag{B.8}$$

resulting in equation (B.7) to read

$$[\![\, Y_\mathfrak{s} \,]\!] = Y_\mathfrak{s}^{(+)} \left(1 - \frac{1}{\mathcal{H}_\mathfrak{s}} \right) - Y_\mathfrak{s}^{(-)} \sum_{\tilde{\mathfrak{s}}} \left[Y_{\tilde{\mathfrak{s}}}^{(+)} \left(1 - \frac{1}{\mathcal{H}_{\tilde{\mathfrak{s}}}} \right) \right] \tag{B.9}$$

which requires consideration of

$$[\![\, Y_\mathfrak{s} \,]\!] := Y_\mathfrak{s}^{(+)} - Y_\mathfrak{s}^{(-)} \tag{B.10}$$

for obtaining the final expression for $[\![\, Y_{\mathfrak{s}} \,]\!]$. The latter reads

$$[\![\, Y_{\mathfrak{s}} \,]\!] := Y_{\mathfrak{s}}^{(+)} \left(1 - \frac{1}{\mathcal{H}_{\mathfrak{s}} \sum_{\tilde{\mathfrak{s}}} \left(\frac{Y_{\tilde{\mathfrak{s}}}^{(+)}}{\mathcal{H}_{\tilde{\mathfrak{s}}}} \right)} \right) \tag{B.11}$$

after replacement of $Y_{\mathfrak{s}}^{(-)}$ in equation (B.9) by $Y_{\mathfrak{s}}^{(+)} - [\![\, Y_{\mathfrak{s}} \,]\!]$ due to equation (B.10) and solving for $[\![\, Y_{\mathfrak{s}} \,]\!]$, taking into account that $\sum_{\mathfrak{s}} Y_{\mathfrak{s}}^{(+)} \equiv 1$.

B.2 Energy Balances

In this section the energy balances for kinetic and potential energy are derived and the pressure formulation of the total energy balance is given.

B.2.1 Kinetic Energy Balance

The kinetic energy balance results from scalar multiplication of the momentum balance (3.43c) with the fluid velocity $\vec{v}$:

$$\vec{v} \cdot \Big[(\, \rho \vec{v} \,)_t + \nabla \cdot (\rho \vec{v} \circ \vec{v}) - \nabla \cdot \boldsymbol{S} - \Big(\rho \vec{g} + \vec{\mathfrak{f}}_\sigma \delta_\Gamma \Big) \Big] = 0 \tag{B.12}$$

Application of the relations (A.3) and (A.6) from appendix section A.1 to the resulting expressions A, B and C in

$$\underbrace{(\, \rho \vec{v} \,)_t \cdot \vec{v}}_{A} + \underbrace{(\nabla \cdot (\, \rho \vec{v} \circ \vec{v} \,)) \cdot \vec{v}}_{B} - \underbrace{(\nabla \cdot \boldsymbol{S}) \cdot \vec{v}}_{C} - \Big(\rho \vec{g} + \vec{\mathfrak{f}}_\sigma \delta_\Gamma \Big) \cdot \vec{v} \;\; = \;\; 0 \tag{B.13}$$

yields

$$\begin{aligned} \overbrace{\Big(\frac{1}{2} \rho \, (\vec{v} \cdot \vec{v}) \Big)_t}^{A} + \underbrace{\frac{1}{2} (\vec{v} \cdot \vec{v}) \, (\, \rho \,)_t}_{D} \;\; + \;\; \overbrace{\underbrace{\nabla \cdot (\, \rho \vec{v} \circ \vec{v} \cdot \vec{v} \,)}_{E} - \rho \vec{v} \circ \vec{v} : \nabla \vec{v}}^{B} \\ + \underbrace{\boldsymbol{S} : \nabla \vec{v} - \nabla \cdot (\boldsymbol{S} \cdot \vec{v})}_{-C} - \Big(\rho \vec{g} + \vec{\mathfrak{f}}_\sigma \delta_\Gamma \Big) \cdot \vec{v} \;\; = \;\; 0 \end{aligned} \tag{B.14}$$

which transforms to

$$\left(\frac{1}{2}\rho\left(\vec{v}\cdot\vec{v}\right)\right)_t + \nabla\cdot\left(\frac{1}{2}\left(\vec{v}\cdot\vec{v}\right)\rho\vec{v}\right) - \nabla\cdot\left(\boldsymbol{S}\cdot\vec{v}\right) + \boldsymbol{S}:\nabla\vec{v} - \left(\rho\vec{g}+\vec{\mathfrak{f}}_\sigma\delta_\Gamma\right)\cdot\vec{v} + \underbrace{\frac{1}{2}\rho\vec{v}\cdot\nabla\left(\vec{v}\cdot\vec{v}\right) - \rho\vec{v}\circ\vec{v}:\nabla\vec{v}}_{F} = 0 \tag{B.15}$$

after applying the mass balance (3.43a) with (3.60a) and relation (A.4) to expression D, relation (A.2) to expression E and simplification. Expression F vanishes due to relation (A.7) and the balance

$$\rho\frac{\mathrm{D}}{\mathrm{D}\,t}\left(\frac{1}{2}\left(\vec{v}\cdot\vec{v}\right)\right) = \nabla\cdot\left(\boldsymbol{S}\cdot\vec{v}\right) - \boldsymbol{S}:\nabla\vec{v} + \left(\rho\vec{g}+\vec{\mathfrak{f}}_\sigma\delta_\Gamma\right)\cdot\vec{v} \tag{B.16}$$

for the kinetic energy remains after subtracting the mass balance (3.43a) with (3.60a).

B.2.2 Potential Energy Balance

As only the vertical component of the vector of gravitational acceleration $\vec{g}$ has a non-zero component $-g$, $\vec{g}$ is irrotational and can be expressed by the gradient $\nabla\mathcal{U}$ of the potential $\mathcal{U}$ which, in addition, is independent of time t due to time independence of $\vec{g}$:

$$\vec{g} = -\nabla\mathcal{U} \tag{B.17}$$

$$\left(\mathcal{U}\right)_t = 0 \tag{B.18}$$

Multiplication of the mass balance (3.43a) considering (3.60a) with the potential $\mathcal{U}$ and application of the product rule results in

$$\left(\rho\mathcal{U}\right)_t - \underbrace{\rho\left(\mathcal{U}\right)_t}_{=0} + \nabla\cdot\left(\rho\mathcal{U}\vec{v}\right) - \rho\vec{v}\cdot\nabla\mathcal{U} = 0 \tag{B.19}$$

which finally yields the balance

$$\rho\frac{\mathrm{D}}{\mathrm{D}\,t}\left(\rho\mathcal{U}\right) = -\rho\left(\vec{g}\cdot\vec{v}\right) \tag{B.20}$$

for potential energy after subtraction of the mass balance (3.43a) considering (3.60a).

B.2.3 Pressure Formulation of Internal Energy Balance

Subtracting the kinetic energy balance (B.16) from the total energy balance (3.43d) yields

$$\begin{aligned}\rho\frac{\mathrm{D}}{\mathrm{D}\,t}\left(e-\frac{1}{2}\,(\vec{v}\cdot\vec{v})\right) &= \rho\frac{\mathrm{D}}{\mathrm{D}\,t}\,(u+\mathcal{U}\,)\\ &= \boldsymbol{S}:\nabla\vec{v}-\rho\vec{g}\cdot\vec{v}-\nabla\cdot(\vec{j}_q+\vec{j}_{\mathrm{e}})+\dot{q}_q-\dot{q}_{\varrho}\end{aligned}\tag{B.21}$$

due to definition (3.6) and after subtraction of the potential energy balance (B.20) from the above result

$$\rho\frac{\mathrm{D}}{\mathrm{D}\,t}\,(u\,)=\boldsymbol{S}:\nabla\vec{v}-\nabla\cdot(\vec{j}_q+\vec{j}_{\mathrm{e}})+\dot{q}_q-\dot{q}_{\varrho}\tag{B.22}$$

remains. This balance of internal energy can be written as

$$\rho\frac{\mathrm{D}}{\mathrm{D}\,t}\,(h\,)=\frac{\mathrm{D}}{\mathrm{D}\,t}\,(p\,)+p\,(\nabla\cdot\vec{v})+\boldsymbol{S}:\nabla\vec{v}-\nabla\cdot(\vec{j}_q+\vec{j}_{\mathrm{e}})+\dot{q}_q-\dot{q}_{\varrho}\tag{B.23}$$

using the definition of enthalpy

$$h:=u+\frac{p}{\rho}\tag{B.24}$$

and the mass balance (3.43a) with (3.60a). Since internal energy u and enthalpy h are functions of the pressure p in general, pressure related expressions have to be extracted from enthalpy. With

$$h=h\,(\rho,p,Y_{\mathfrak{s}})\tag{B.25}$$

and the corresponding total derivative

$$\mathrm{d}h=\left(\frac{\partial h}{\partial\rho}\right)_{p,Y_{\mathfrak{s}}}\mathrm{d}\rho\;+\left(\frac{\partial h}{\partial p}\right)_{\rho,Y_{\mathfrak{s}}}\mathrm{d}p\;+\sum_{\mathfrak{s}=1}^{\mathcal{N}_{\mathfrak{s}}}\left[\left(\frac{\partial h}{\partial Y_{\mathfrak{s}}}\right)_{p,\rho}\mathrm{d}Y_{\mathfrak{s}}\right]\tag{B.26}$$

the material derivative of the enthalpy in equation (B.23) can be replaced by

$$\begin{aligned}\frac{\mathrm{D}}{\mathrm{D}\,t}\,(h\,)=&\left(\frac{\partial h}{\partial\rho}\right)_{p,Y_{\mathfrak{s}}}\left[\,(\,\rho\,)_t+\vec{v}\cdot\nabla\rho\,\right]+\left(\frac{\partial h}{\partial p}\right)_{\rho,Y_{\mathfrak{s}}}\left[\,(\,p\,)_t+\vec{v}\cdot\nabla p\,\right]\\&+\sum_{\mathfrak{s}=1}^{\mathcal{N}_{\mathfrak{s}}}\left[\left(\frac{\partial h}{\partial Y_{\mathfrak{s}}}\right)_{p,\rho}\left[\,(\,Y_{\mathfrak{s}}\,)_t+\vec{v}\cdot\nabla Y_{\mathfrak{s}}\,\right]\right]\end{aligned}\tag{B.27}$$

which finally yields

$$\frac{\mathrm{D}}{\mathrm{D}\,t}\left(\,h\,\right) = \left(\frac{\partial h}{\partial p}\right)_{\rho,Y_{\mathfrak{s}}}\left[\,\left(\,p\,\right)_t + \vec{v}\cdot\nabla p\,\right] - \left(\frac{\partial h}{\partial \rho}\right)_{p,Y_{\mathfrak{s}}}\left[\rho\left(\nabla\cdot\vec{v}\right)\right] + \sum_{\mathfrak{s}=1}^{\mathcal{N}_{\mathfrak{s}}}\left[\left(\frac{\partial h}{\partial Y_{\mathfrak{s}}}\right)_{p,\rho}\left[\varrho_{\mathfrak{s}} - \frac{1}{\rho}\left(\nabla\cdot\vec{j}_{\mathfrak{s}}\right)\right]\right] \tag{B.28}$$

after considering again the mass balance (3.43a) with (3.60a) and the balances of species masses (3.43b). With that and relation (3.30), equation (B.23) reads

$$\begin{aligned}\left(1-\rho\left(\frac{\partial h}{\partial p}\right)_{\rho,Y_{\mathfrak{s}}}\right)\frac{\mathrm{D}}{\mathrm{D}\,t}\left(\,p\,\right) + \overbrace{p\left(\nabla\cdot\vec{v}\right) - p\boldsymbol{I}:\nabla\vec{v}}^{=0} \\ = -\rho\left(\frac{\partial h}{\partial \rho}\right)_{p,Y_{\mathfrak{s}}}\rho\left(\nabla\cdot\vec{v}\right) - \boldsymbol{\mathcal{T}}:\nabla\vec{v} + \nabla\cdot\vec{j}_q - \dot{q}_q \\ + \sum_{\mathfrak{s}=1}^{\mathcal{N}_{\mathfrak{s}}}\left[\left(\frac{\partial h}{\partial Y_{\mathfrak{s}}}\right)_{p,\rho}\left[\rho\varrho_{\mathfrak{s}} - \left(\nabla\cdot\vec{j}_{\mathfrak{s}}\right)\right] + \nabla\cdot h_{\mathfrak{s}}\,\vec{j}_{\mathfrak{s}} + \rho\varrho_{\mathfrak{s}}\left(\Delta h^0\right)_{\mathfrak{s}}\right]\end{aligned} \tag{B.29}$$

considering definitions (3.39) and (3.37). Further, due to relation (A.5) in appendix section A.1, yielding $p\left(\nabla\cdot\vec{v}\right) - p\boldsymbol{I}:\nabla\vec{v} = 0$, and

$$\left(\frac{\partial h}{\partial Y_{\mathfrak{s}}}\right)_{p,\rho} = h_{\mathfrak{s}} \tag{B.30}$$

due to

$$h = \sum_{\mathfrak{s}=1}^{\mathcal{N}_{\mathfrak{s}}}\left(h_{\mathfrak{s}}Y_{\mathfrak{s}}\right) \tag{B.31}$$

the relation

$$\begin{aligned}\frac{\mathrm{D}}{\mathrm{D}\,t}\left(\,p\,\right) + \rho c^2\left(\nabla\cdot\vec{v}\right) = \Xi^{-1}\Bigg[- \boldsymbol{\mathcal{T}}:\nabla\vec{v} + \nabla\cdot\vec{j}_q - \dot{q}_q \\ + \sum_{\mathfrak{s}=1}^{\mathcal{N}_{\mathfrak{s}}}\left(\vec{j}_{\mathfrak{s}}\cdot\nabla h_{\mathfrak{s}} + \rho\varrho_{\mathfrak{s}}\left[h_{\mathfrak{s}} + \left(\Delta h^0\right)_{\mathfrak{s}}\right]\right)\Bigg]\end{aligned} \tag{B.32}$$

results as pressure formulation of the internal energy equation with Ξ as defined in (3.90) and frozen speed of sound c as given in (3.91).

B.3 Integral Average in Cut Grid Cells

The integral average $\overline{\Phi}$ of an arbitrary quantity Φ can be transformed according to

$$\overline{\Phi} := \frac{1}{|\Omega|} \int_{\Omega} \Phi \, \mathrm{d}V = \frac{1}{|\Omega|} \sum_{\varphi} \int_{\Omega^{\varphi}} \Phi^{\varphi} \, \mathrm{d}V \tag{B.33}$$

if sub-sets Ω^{φ} of the domain Ω are occupied by different fluid phases φ with different properties. With definition of the volume fraction

$$\alpha^{\varphi} := \frac{\int_{\Omega^{\varphi}} \mathrm{d}V}{\int_{\Omega} \mathrm{d}V} \equiv \frac{|\Omega^{\varphi}|}{|\Omega|} \tag{B.34}$$

and the integral average

$$\overline{\Phi}^{\varphi} := \frac{\int_{\Omega^{\varphi}} \Phi^{\varphi} \, \mathrm{d}V}{\int_{\Omega^{\varphi}} \mathrm{d}V} \equiv \frac{1}{|\Omega^{\varphi}|} \int_{\Omega^{\varphi}} \Phi^{\varphi} \, \mathrm{d}V \tag{B.35}$$

of fluid phase φ, equation (B.33) transforms to

$$\overline{\Phi} = \sum_{\varphi} \left(\alpha^{\varphi} \, \overline{\Phi}^{\varphi} \right) \tag{B.36}$$

which reads

$$\overline{\Phi} \;=\; \alpha^{(+)} \, \overline{\Phi}^{(+)} + \alpha^{(-)} \, \overline{\Phi}^{(-)} \;=\; \alpha \, \overline{\Phi}^{(+)} + (1 - \alpha) \, \overline{\Phi}^{(-)} \tag{B.37}$$

for two-phase flow with $\alpha := \alpha^{(+)}$ and $\varphi \in \{(+), (-)\}$.

C. ACCURACY

This section is denoted to the accuracy of a numerical method and its order of convergence. Both is discussed in the following sections.

C.1 Integral Average and Centroid Value

Taylor expansion of the scalar quantity Φ in space in the definition

$$\overline{\Phi} = \frac{\int_\Omega \Phi \, dV}{\int_\Omega \, dV} \tag{C.1}$$

of the integral – possibly time-dependent – average $\overline{\Phi}$ over an arbitrary control volume Ω around a reference location $\vec{x}_0$ reads

$$\Phi = \Phi_0 + (\vec{x} - \vec{x}_0) \cdot \left. \frac{\partial \Phi}{\partial \vec{x}} \right|_0 + \frac{1}{2} \sum_{d=1}^{\mathfrak{d}} \sum_{e=1}^{\mathfrak{d}} (x - x_0)_d \, (x - x_0)_e \left. \frac{\partial^2 \Phi}{\partial x_d \partial x_e} \right|_0 + ... \tag{C.2}$$

and the integral average yields

$$\begin{aligned} \overline{\Phi} = \Phi_0 &+ \left(\frac{\int_\Omega \vec{x} \, dV}{\int_\Omega \, dV} - \vec{x}_0 \right) \cdot \left. \frac{\partial \Phi}{\partial \vec{x}} \right|_0 \\ &+ \frac{\sum_{d=1}^{\mathfrak{d}} \sum_{e=1}^{\mathfrak{d}} \left(\left. \frac{\partial^2 \Phi}{\partial x_d \partial x_e} \right|_0 \int_\Omega (x - x_0)_d \, (x - x_0)_e \, dV \right)}{2 \int_\Omega \, dV} + ... \end{aligned} \tag{C.3}$$

since the reference quantities – indexed 0 – are fixed values at the fixed location $\vec{x}_0$ and, thus, do not affect the spatial integration. This further simplifies to

$$\begin{aligned} \overline{\Phi} = \Phi_0 &+ (\vec{x}_c - \vec{x}_0) \cdot \left. \frac{\partial \Phi}{\partial \vec{x}} \right|_0 \\ &+ \frac{\sum_{d=1}^{\mathfrak{d}} \sum_{e=1}^{\mathfrak{d}} \left(\left. \frac{\partial^2 \Phi}{\partial x_d \partial x_e} \right|_0 \int_\Omega (x - x_0)_d \, (x - x_0)_e \, dV \right)}{2 \int_\Omega \, dV} + ... \end{aligned} \tag{C.4}$$

using the common definition of the centroid

$$\vec{x}_c = \frac{\int_\Omega \vec{x}\, dV}{\int_\Omega dV} \tag{C.5}$$

of a region Ω. If now the reference location is chosen to be the centroid of the region Ω, $\vec{x}_0 := \vec{x}_c$, the first order term cancels and

$$\overline{\Phi} = \Phi_c + \Phi^{'} \tag{C.6}$$

with

$$\Phi^{'} := \frac{\sum_{d=1}^{\mathfrak{d}} \sum_{e=1}^{\mathfrak{d}} \left(\frac{\partial^2 \Phi}{\partial x_d \partial x_e}\Big|_c \int_\Omega (x - x_c)_d \, (x - x_c)_e \, dV \right)}{2 \int_\Omega dV} + ... \tag{C.7}$$

remains. If the state Φ is distributed linearly across the control volume Ω and, thus, in the entire control volume $\frac{\partial^2 \Phi}{\partial x_d \partial x_e} = 0$ for any combination of d and e (which also holds for higher derivatives in this case), the integral average over the control volume is represented exactly by the value of Φ in the centroid of the control volume $\vec{x}_c$. For non-linear state distributions and, thus, in general $\frac{\partial^2 \Phi}{\partial x_d \partial x_e} \neq 0$ in the entire control volume, the integral average $\overline{\Phi}$ can be approximated with a spatial second order error by the value Φ_c in the centroid of a control volume as seen from equation (C.6).

C.2 Order of Accuracy

First, the time step local temporal accuracy is examined before discussing the global order of accuracy and the order of accuracy of the approximation of the resulting terms. This is done based on the propagation of a smooth quantity Φ in time by a numerical scheme from $\Phi^{(n)}$ to $\Phi^{(n+1)}$ according to the transport equation

$$\frac{\partial \Phi}{\partial t} + \nabla \cdot \vec{f_\Phi} = \mathfrak{q}, \tag{C.8}$$

where $\vec{f_\Phi}$ represents the flux of Φ. The following issues are also discussed, for example, in Chapter 8 of [106] and in Chapter 2.2 of [120].

C.2.1 Time Step Local Order of Accuracy

Taylor expansion of $\Phi^{(n+1)}$ around the old time level value at level n yields

$$\Phi^{(n+1)} = \Phi^{(n)} + \Delta t \left(\frac{\partial \Phi}{\partial t}\Big|_n + \frac{\Delta t}{2} \frac{\partial^2 \Phi}{\partial t^2}\Big|_n + \frac{\Delta t^2}{6} \frac{\partial^3 \Phi}{\partial t^3}\Big|_n + \mathcal{O}(\Delta t^3) \right) \tag{C.9}$$

leading to

$$\frac{\partial \Phi}{\partial t}\Big|_n = \frac{\Phi^{(n+1)} - \Phi^{(n)}}{\Delta t} - \frac{\Delta t}{2} \frac{\partial^2 \Phi}{\partial t^2}\Big|_n - \frac{\Delta t^2}{6} \frac{\partial^3 \Phi}{\partial t^3}\Big|_n - .... \tag{C.10}$$

and, thus, to an approximation of the time derivative of Φ with a first order error due to

$$\frac{\partial \Phi}{\partial t}\Big|_n = \frac{\Phi^{(n+1)} - \Phi^{(n)}}{\Delta t} + \mathcal{O}(\Delta t) \tag{C.11}$$

In comparison, Taylor expansion around the intermediate time level $n + \frac{1}{2}$ results in

$$\Phi^{(n+1)} = \Phi^{(n+\frac{1}{2})} + \frac{\Delta t}{2} \frac{\partial \Phi}{\partial t}\Big|_{n+\frac{1}{2}} + \frac{\Delta t^2}{8} \frac{\partial^2 \Phi}{\partial t^2}\Big|_{n+\frac{1}{2}} + \frac{\Delta t^3}{48} \frac{\partial^3 \Phi}{\partial t^3}\Big|_{n+\frac{1}{2}} + \frac{\Delta t^4}{384} \frac{\partial^4 \Phi}{\partial t^4}\Big|_{n+\frac{1}{2}} + \mathcal{O}(\Delta t^5) \tag{C.12}$$

for the value at time level $n + 1$ and

$$\Phi^{(n)} = \Phi^{(n+\frac{1}{2})} - \frac{\Delta t}{2} \frac{\partial \Phi}{\partial t}\Big|_{n+\frac{1}{2}} + \frac{\Delta t^2}{8} \frac{\partial^2 \Phi}{\partial t^2}\Big|_{n+\frac{1}{2}} - \frac{\Delta t^3}{48} \frac{\partial^3 \Phi}{\partial t^3}\Big|_{n+\frac{1}{2}} + \frac{\Delta t^4}{384} \frac{\partial^4 \Phi}{\partial t^4}\Big|_{n+\frac{1}{2}} + \mathcal{O}(\Delta t^5) \tag{C.13}$$

for the value at time level n. The difference

$$\Phi^{(n+1)} - \Phi^{(n)} = \Delta t \left(\frac{\partial \Phi}{\partial t}\Big|_{n+\frac{1}{2}} + \frac{\Delta t^2}{24} \frac{\partial^3 \Phi}{\partial t^3}\Big|_{n+\frac{1}{2}} + \mathcal{O}(\Delta t^4) \right) \tag{C.14}$$

can be transformed to

$$\frac{\partial \Phi}{\partial t}\Big|_{n+\frac{1}{2}} = \frac{\Phi^{(n+1)} - \Phi^{(n)}}{\Delta t} - \frac{\Delta t^2}{24} \frac{\partial^3 \Phi}{\partial t^3}\Big|_{n+\frac{1}{2}} + ... \tag{C.15}$$

and, thus, to an approximation of the time derivative

$$\frac{\partial \Phi}{\partial t}\Big|_{n+\frac{1}{2}} = \frac{\Phi^{(n+1)} - \Phi^{(n)}}{\Delta t} + \mathcal{O}(\Delta t^2) \tag{C.16}$$

of Φ with a second order error. This can be written as

$$\Phi^{(n+1)} = \Phi^{(n)} + \Delta t \frac{\partial \Phi}{\partial t}\Big|_{n+\frac{1}{2}} + \mathcal{O}(\Delta t^3) \tag{C.17}$$

or, using the initial transport equation to substitute the time derivative,

$$\Phi^{(n+1)} = \Phi^{(n)} - \Delta t \left(\nabla \cdot \vec{f}_\Phi - \mathfrak{q} \right)^{(n+\frac{1}{2})} + \mathcal{O}(\Delta t^3) \tag{C.18}$$

and after integration over a fix control volume Ω one ends up with the Finite Volume equation

$$\overline{\Phi}^{(n+1)} - \overline{\Phi}^{(n)} = \Delta t \underbrace{\left[\frac{1}{\Delta V} \left(\int_\Omega \mathfrak{q} \, dV - \int_{\partial\Omega} \left(\vec{f}_\Phi \cdot \vec{n} \right) \, dA \right) \right]^{(n+\frac{1}{2})}}_{(\diamondsuit)} + \mathcal{O}(\Delta t^3) \tag{C.19}$$

for determination of the integral average value $\overline{\Phi}^{(n+1)}$ based on the known value $\overline{\Phi}^{(n)}$. The expression $(\diamondsuit)$ needs to be evaluated or approximated at the half time level $n + \frac{1}{2}$ with a truncation error of magnitude $\mathcal{O}(\Delta t^p)$ with $p \geqslant 2$ for keeping the order of accuracy of the approximation of $\overline{\Phi}^{(n+1)}$ at the same accuracy level.

For a predictor-corrector method this means, that if the predictor is a second order accurate method, the predicted value is already second order accurate with a third order local truncation error after a single time step and corrections are only third or higher order terms.

C.2.2 Global Order of Accuracy

As seen, for a second order accurate Finite Volume method, the local truncation error, which is the error made within one single time step of size Δt, is $\mathcal{O}(\Delta t^3)$, while the global truncation error, which is the error accumulated over all performed time steps, is $\mathcal{O}(\Delta t^2)$. The latter can be seen if the difference with respect to the initial value is

considered. While the 'time step local' difference has a truncation error

$$\overline{\Phi}^{(n+1)} - \overline{\Phi}^{(n)} = ... + \mathcal{O}(\Delta t^3) \tag{C.20}$$

the global accumulated error up to time level n is

$$\overline{\Phi}^{(n)} - \overline{\Phi}^{(0)} = ... + n\ \mathcal{O}(\Delta t^3) \tag{C.21}$$

where n is the number of time steps. Since the time passed between time level n and the initial time level equals the number of time steps times the (average) local time step size Δt

$$t^{(n)} - t^{(0)} = n\ \Delta t \tag{C.22}$$

finally the relation

$$\overline{\Phi}^{(n)} - \overline{\Phi}^{(0)} = ... + \left(t^{(n)} - t^{(0)}\right) \mathcal{O}(\Delta t^2) \tag{C.23}$$

is obtained. This holds if n is independent of Δt.

C.3 Order of Convergence

If $\Phi_{\mathfrak{h}}$ is the numerical approximation to the exact solution Φ of a problem, the approximation error

$$E := \Phi_{\mathfrak{h}} - \Phi \tag{C.24}$$

can be defined. The order of convergence $\mathfrak{p}$ represents the global order of accuracy of a numerical method and is defined as

$$\| E \|_{\mathfrak{p}} \leqslant \mathcal{C}\ \mathfrak{h}^{\mathfrak{p}} \tag{C.25}$$

with constant $\mathcal{C}$ independent of $\mathfrak{h}$. If the numerical method has the convergence order $\mathfrak{p}$, the ratio between some norm $\mathfrak{p}$ of the error E and the $\mathfrak{p}^{th}$ power of the step size $\mathfrak{h}$ of interest (e.g. the time step Δt) is smaller than an arbitrary finite constant $\mathcal{C}$, which means, the larger $\mathfrak{p}$ and the smaller the error constant $\mathcal{C}$ is, the better is the numerical

approximation. Typically, the expression

$$\| E \|_{\mathfrak{p}} := \left(\frac{1}{\mathcal{N}} \sum_{\mathfrak{i}=1}^{\mathcal{N}} |E_{\mathfrak{i}}|^{\mathfrak{p}} \right)^{\frac{1}{\mathfrak{p}}} \tag{C.26}$$

with one of the choices

- $\mathfrak{p} = 1$: arithmetic mean of $|E_{\mathfrak{i}}|$
- $\mathfrak{p} = 2$: quadratic mean of $|E_{\mathfrak{i}}|$
- $\mathfrak{p} \to \infty$: maximum of $|E_{\mathfrak{i}}|$

and N as the number of available sample points on the coarser grid is used as finite approximation of the discrete $\mathfrak{p}$-norms (generalized mean), where $\mathfrak{p} \to \infty$ is the most restrictive choice and therefore the most interesting one, since in this case the largest local error needs to satisfy equation (C.25).

The order of convergence can be determined by computing the numerical solutions on two different grids, $\Phi_{\mathfrak{h}_1}$ and $\Phi_{\mathfrak{h}_2}$. The ratio

$$\mathcal{E}_{\mathfrak{p}} := \frac{\| E \|_{\mathfrak{p}}^{(\mathfrak{h}_1)}}{\| E \|_{\mathfrak{p}}^{(\mathfrak{h}_2)}} \tag{C.27}$$

between the resulting error norms is then used to eliminate the unknown resolution independent error constant $\mathcal{C}$ to obtain

$$\mathcal{E}_{\mathfrak{p}} = \mathfrak{r}^{\mathfrak{p}} \tag{C.28}$$

with

$$\mathfrak{r} := \frac{\mathfrak{h}_1}{\mathfrak{h}_2} \tag{C.29}$$

and, thus,

$$\mathfrak{p} = \frac{\ln \mathcal{E}_{\mathfrak{p}}}{\ln \mathfrak{r}} = \log_{\mathfrak{r}} \mathcal{E}_{\mathfrak{p}} \tag{C.30}$$

for a given $\mathfrak{p}$.

C.3.1 Self-Convergence

If no exact solution Φ is available to compare the numerical solution with, there are two other possibilities[1].:

- either an exact solution can be simulated by using a third numerical solution $\Phi_{\mathfrak{h}_3}$ on a much finer grid than the ones to examine, with $\mathfrak{h}_1 = \mathcal{C}_1\,\mathfrak{h}_3$ and $\mathfrak{h}_2 = \mathcal{C}_2\,\mathfrak{h}_3$ as well as $\mathcal{C}_1, \mathcal{C}_2 \in \mathbb{N}, \mathcal{C}_1 \gg 1, \mathcal{C}_2 \gg 1$ (in this case the exact solution Φ in equation (C.24) is replaced by the additional numerical approximation),

- or, since the determination of the numerical solution on a very fine grid can be expensive and time consuming, a third solution $\Phi_{\mathfrak{h}_3}$ is determined with $\mathcal{C}_1 > \mathcal{C}_2 > 1$ and $\frac{\mathcal{C}_1}{\mathcal{C}_2} \in \mathbb{N}$ to define the errors

$$E^{(1,2)} := \Phi_{\mathfrak{h}_1} - \Phi_{\mathfrak{h}_2} \tag{C.31}$$

$$E^{(2,3)} := \Phi_{\mathfrak{h}_2} - \Phi_{\mathfrak{h}_3} \tag{C.32}$$

  with corresponding norms as before. To be able to compute these errors, the values from the finer grid need to be interpolated to the coarser grid by an interpolation method which is of higher order of accuracy than the numerical method which is examined. Again, to eliminate the unknown resolution independent error constant $\mathcal{C}$, the ratio of the error norms is computed using the definitions

$$\mathcal{E}_{\mathfrak{p}} := \frac{\| E^{(1,2)} \|_{\mathfrak{p}}}{\| E^{(2,3)} \|_{\mathfrak{p}}} \tag{C.33}$$

$$\mathfrak{r} := \frac{\mathcal{C}_1}{\mathcal{C}_2} \tag{C.34}$$

  for application to (C.30).

[1] A third possibility is the method of manufactured sulutions as used in [117].

D. POISSON BOUNDARY CONDITION

In this chapter the derivation of a pressure boundary condition for the projection steps of the present numerical method is presented, which incorporates boundary tangential information into the boundary normal Neumann boundary condition. While derived for a simplified setting with constant density in [102] including proof of well-posedness, below the corresponding strategy is followed for more general settings, yet, however, without proof of well-posedness and numerical experiments.

Note that in this chapter a local notation with local meaning of the quantities $\vec{Q}$, $\vec{R}$, $\vec{b}$, β, C, D, K, N, T, ξ, τ, $\mathcal{B}$, $\mathcal{V}$, $\mathcal{S}$, $\mathcal{T}$ **is used**.

With definition of the vector

$$\vec{Q} := \frac{1}{\rho^{(n+1,**)}} \nabla \partial\pi^{(n+\frac{1}{2})} \tag{D.1}$$

which is unknown at the boundary due to unknown $\partial\pi$, the integral Poisson equation

$$\begin{aligned} \int_{\partial\Omega_i \setminus \partial\Omega^{\square}} \left(\beta^{(n+1,**)} \nabla \partial\pi^{(n+\frac{1}{2})} \right) \cdot \vec{n} \, \mathrm{d}A \; &= \int_{\Omega_i} \nabla \cdot \vec{\mathcal{R}}^{\,(n+1,**)} \mathrm{d}V \\ &\quad - \int_{\Omega_i} D^{(n+1,**)} \mathrm{d}V \\ &\quad - \int_{\partial\Omega^{\square}} \left(\beta^{(n+1,**)} \nabla \partial\pi^{(n+\frac{1}{2})} \right) \cdot \vec{n} \, \mathrm{d}A \end{aligned} \tag{D.2}$$

as occurring in (5.104) with

$$\beta^{(n+1,**)} := \frac{\Delta t}{2} \left(\frac{\mathcal{P}}{\rho} \right)^{(n+1,**)} \tag{D.3}$$

$$\vec{\mathcal{R}}^{\,(n+1,**)} := (\mathcal{P}\vec{v})^{(n+1,**)} \tag{D.4}$$

$$D^{\,(n+1,**)} := (\mathcal{P}\mathcal{D})^{\,(n+1,**)} \tag{D.5}$$

transforms to

$$\begin{aligned}\int_{\partial\Omega_i\setminus\partial\Omega^{\square}} \left(\beta^{(n+1,**)}\nabla\partial\pi^{(n+\frac{1}{2})}\right)\cdot\vec{n}\,\mathrm{d}A \;&=\int_{\Omega_i}\nabla\cdot\vec{\mathfrak{R}}^{\,(n+1,**)}\mathrm{d}V\\ &\quad-\int_{\Omega_i}D^{(n+1,**)}\mathrm{d}V\\ &\quad-\int_{\partial\Omega^{\square}}(\rho\beta)^{(n+1,**)}\left(\vec{Q}\cdot\vec{n}\right)\,\mathrm{d}A \qquad \text{(D.6)}\end{aligned}$$

Considering the conservation law

$$(\rho\vec{v})_t+\nabla\cdot(\rho\vec{v}\circ\vec{v})+\nabla p-\left[\nabla\cdot\left(\mu\left(\nabla\vec{v}+[\nabla\vec{v}]^T\right)\right)+\nabla\lambda\nabla\cdot\vec{v}\right]=\rho\vec{g} \qquad \text{(D.7)}$$

of momentum for determination of $\vec{Q}$ at the boundary,

$$(\rho\vec{v})_t+\nabla\cdot(\rho\vec{v}\circ\vec{v})+\nabla p-\mu\left[\nabla\cdot\left(\nabla\vec{v}+[\nabla\vec{v}]^T\right)\right]-\nabla\lambda\,(\nabla\cdot\vec{v})=\rho\vec{g} \qquad \text{(D.8)}$$

is obtained **assuming** $\mu=$ **const.**. Several of the occurring expressions can be rewritten:

- The time derivative can be split applying the product rule:

$$(\rho\vec{v})_t=\rho\vec{v}_t+\rho_t\vec{v} \qquad \text{(D.9)}$$

  Considering the mass balance

$$\rho_t+\nabla\cdot(\rho\vec{v})=0 \qquad \text{(D.10)}$$

  in addition this transforms to

$$(\rho\vec{v})_t=\rho\vec{v}_t-\vec{v}\,\nabla\cdot(\rho\vec{v}) \qquad \text{(D.11)}$$

  and after again applying the product rule

$$(\rho\vec{v})_t=\rho\vec{v}_t-\rho\vec{v}\,(\nabla\cdot\vec{v})-\vec{v}\,(\vec{v}\cdot\nabla\rho) \qquad \text{(D.12)}$$

  is obtained.

- The non-linear advective term can be spit according to

$$\begin{aligned}\nabla \cdot (\rho\vec{v} \circ \vec{v}) &= \rho\vec{v}\,(\nabla \cdot \vec{v}) + \vec{v} \cdot \nabla\,(\rho\vec{v}) \\ &= \rho\vec{v}\,(\nabla \cdot \vec{v}) + \rho\vec{v} \cdot \nabla\vec{v} + \vec{v} \cdot ((\nabla\rho)\vec{v}) \\ &= \rho\vec{v}\,(\nabla \cdot \vec{v}) + \rho\vec{v} \cdot \nabla\vec{v} + (\vec{v} \cdot \nabla\rho)\,\vec{v} \end{aligned} \tag{D.13}$$

- The viscous term transforms to

$$\begin{aligned}&\mu\left[\nabla \cdot \left(\nabla\vec{v} + [\nabla\vec{v}]^T\right)\right] + \nabla\lambda\,(\nabla \cdot \vec{v}) \\ &\quad = \mu\Big(\nabla\,(\nabla \cdot \vec{v}) + \nabla \cdot \nabla\vec{v}\Big) + \nabla\lambda\,(\nabla \cdot \vec{v})\end{aligned} \tag{D.14}$$

  considering $\mu = \text{const.}$

Applied to the momentum equation (D.8), the expression

$$\nabla\partial\pi = \rho\vec{g} - \rho\vec{v}_t - \rho\vec{v} \cdot \nabla\vec{v} - \nabla q + \mu\Big(\nabla\,(\nabla \cdot \vec{v}) + \nabla \cdot \nabla\vec{v}\Big) + \nabla\lambda\,(\nabla \cdot \vec{v}) \tag{D.15}$$

remains, considering $p = q + \partial\pi$. Focusing on the normal component

$$\begin{aligned}\nabla\partial\pi \cdot \vec{n} = \rho\vec{g} \cdot \vec{n} - \rho\vec{v}_t \cdot \vec{n} - \ &(\rho\vec{v} \cdot \nabla\vec{v}) \cdot \vec{n} - \nabla q \cdot \vec{n} \\ &+ \mu\Big(\nabla(\nabla \cdot \vec{v})\Big) \cdot \vec{n} + \mu\Big(\nabla \cdot (\nabla\vec{v})\Big) \cdot \vec{n} + (\nabla\lambda(\nabla \cdot \vec{v})) \cdot \vec{n}\end{aligned} \tag{D.16}$$

of the momentum equation according to (D.15) and replacing the velocity divergence $\nabla \cdot \vec{v}$ at the boundary due to the divergence constraint by

$$\nabla \cdot (\mathcal{P}\vec{v}) = \mathcal{P}\,(\nabla \cdot \vec{v}) + \vec{v} \cdot \nabla\,(\mathcal{P}) \qquad \rightarrow \qquad \nabla \cdot \vec{v} = \frac{1}{\mathcal{P}}\Big(\mathcal{D} - \vec{v} \cdot \nabla\,(\mathcal{P})\Big) \tag{D.17}$$

– yet assuming $\mathcal{P}$ to be a general (conserved) scalar quantity – one obtains

$$\begin{aligned}\nabla\partial\pi \cdot \vec{n} = \rho\vec{g} \cdot \vec{n} - \rho\vec{v}_t \cdot \vec{n} - \ &(\rho\vec{v} \cdot \nabla\vec{v}) \cdot \vec{n} - \nabla q \cdot \vec{n} \\ &+ \ (\mu + \lambda)\left(\nabla\mathcal{D} \cdot \vec{n}\right) - (\mu + \lambda)\left(\nabla\left(\vec{v} \cdot \frac{1}{\mathcal{P}}\nabla\,(\mathcal{P})\right) \cdot \vec{n}\right) \\ &+ \mu\Big(\nabla \cdot (\nabla\vec{v})\Big) \cdot \vec{n} + \mathcal{D}\Big(\nabla\lambda \cdot \vec{n}\Big) - \left(\vec{v} \cdot \frac{1}{\mathcal{P}}\nabla\,(\mathcal{P})\right)\Big(\nabla\lambda \cdot \vec{n}\Big)\end{aligned} \tag{D.18}$$

Considering

$$\blacksquare^{(n+\frac{1}{2})} = \frac{\blacksquare^{(n+1)} + \blacksquare^{(n)}}{2} + \mathcal{O}(\Delta t^2) \tag{D.19}$$

for all quantities $\blacksquare$ and especially for scalars

$$\blacksquare^{(n+\frac{1}{2})} = \frac{\blacksquare^{(n+1)} + \blacksquare^{(n)}}{2} + \mathcal{O}(\Delta t^2) = \frac{\blacksquare^{(n+1,**)} + \blacksquare^{(n)}}{2} + \mathcal{O}(\Delta t^2) = \blacksquare^{(n+\frac{1}{2},**)} \tag{D.20}$$

the velocity $\vec{v}$ at the boundary can be replaced by the known boundary velocity $\vec{b}$ and with

$$\vec{\mathcal{R}} := \frac{1}{(\mathcal{P})^{((n+\frac{1}{2}),**)}} \nabla \left(\mathcal{P}\right)^{((n+\frac{1}{2}),**)} \tag{D.21}$$

and

$$K \ := \mu + \lambda^{((n+\frac{1}{2}),**)} \tag{D.22}$$

equation (D.18) results in

$$\begin{aligned}
\nabla \partial\pi^{(n+\frac{1}{2})} \cdot \vec{n} = {} & \rho^{((n+\frac{1}{2}),**)} \vec{g} \cdot \vec{n} - \rho^{((n+\frac{1}{2}),**)} \vec{b}_t^{(n+\frac{1}{2})} \cdot \vec{n} - \nabla q \cdot \vec{n} \\
& - \left(\rho^{((n+\frac{1}{2}),**)} \vec{b}^{(n+\frac{1}{2})} \cdot \nabla \vec{v}^{(n+\frac{1}{2})} \right) \cdot \vec{n} + \mu \Big(\nabla \cdot \nabla \left(\vec{v}^{(n+\frac{1}{2})} \right) \Big) \cdot \vec{n} \\
& + K \left(\nabla \mathcal{D}^{((n+\frac{1}{2}),**)} \cdot \vec{n} \right) - K \left(\nabla \left(\vec{v}^{(n+\frac{1}{2})} \cdot \vec{\mathcal{R}} \right) \cdot \vec{n} \right) \\
& - \left(\vec{b}^{(n+\frac{1}{2})} \cdot \vec{\mathcal{R}} - \mathcal{D}^{((n+\frac{1}{2}),**)} \right) \left(\nabla \lambda^{((n+\frac{1}{2}),**)} \cdot \vec{n} \right)
\end{aligned} \tag{D.23}$$

with expressions containing $\vec{v}^{(n+\frac{1}{2})}$ remaining to be determined. Assuming the boundary normal vector to be constant in both space and time, restricting to piecewise planar boundary segments with

$$(\nabla \vec{a}) \cdot \vec{n} = \nabla \left(\vec{a} \cdot \vec{n} \right) \tag{D.24}$$

for any vector $\vec{a}$, the expression

$$\begin{aligned}\nabla\partial\pi^{(n+1)}\cdot\vec{n} = {} & \rho^{(n+1,**)}\vec{g}\cdot\vec{n} - \rho^{(n+1,**)}\vec{b}_t^{(n+1)}\cdot\vec{n} - \nabla q\cdot\vec{n} \\ & - \rho^{(n+1,**)}\vec{b}^{(n+1)}\cdot\nabla\left(\vec{v}^{(n+1)}\cdot\vec{n}\right) + \mu\Big(\nabla\cdot\nabla\left(\vec{v}^{(n+1)}\cdot\vec{n}\right)\Big) \\ & + K\left(\nabla\mathcal{D}^{(n+1,**)}\cdot\vec{n}\right) - K\left(\nabla\left(\vec{v}^{(n+1)}\cdot\vec{\mathcal{R}}\right)\cdot\vec{n}\right) \\ & - \left(\vec{b}^{(n+1)}\cdot\vec{\mathcal{R}} - \mathcal{D}^{(n+1,**)}\right)\left(\nabla\lambda^{(n+1,**)}\cdot\vec{n}\right)\end{aligned} \tag{D.25}$$

is obtained due to $(\nabla\vec{n})\cdot\vec{a} = \vec{0}$. This equation has to be considered for all types of boundaries separately and is analyzed in the following for solid no-slip boundaries while slip wall, inflow and outflow boundaries remain to be treated in a similar way.

D.1 Solid No-Slip Boundaries

For solid no-slip boundaries $\vec{b} = \vec{0}$ holds and

$$\begin{aligned}\nabla\partial\pi^{(n+1)}\cdot\vec{n} = {} & \rho^{(n+1,**)}\vec{g}\cdot\vec{n} - \nabla q\cdot\vec{n} \\ & - K\left(\nabla\left(\vec{v}^{(n+1)}\cdot\vec{\mathcal{R}}\right)\cdot\vec{n}\right) + \mu\Big(\nabla\cdot\nabla\left(\vec{v}^{(n+1)}\cdot\vec{n}\right)\Big) \\ & + K\left(\nabla\mathcal{D}^{(n+1,**)}\cdot\vec{n}\right) + \mathcal{D}^{(n+1,**)}\Big(\nabla\lambda^{(n+1,**)}\cdot\vec{n}\Big)\end{aligned} \tag{D.26}$$

remains. Using the boundary normal derivative ($\frac{\partial}{\partial N}$) and the k boundary tangential derivatives ($\frac{\partial}{\partial T_k}$)

$$\mu\Big(\nabla\cdot\nabla\left(\vec{v}^{(n+1)}\cdot\vec{n}\right)\Big) \equiv \mu\frac{\partial}{\partial N}\frac{\partial}{\partial N}\left(\vec{v}^{(n+1)}\cdot\vec{n}\right) + \mu\sum_k\frac{\partial}{\partial T_k}\frac{\partial}{\partial T_k}\left(\vec{v}^{(n+1)}\cdot\vec{n}\right) \tag{D.27}$$

holds with separated boundary normal and boundary tangential derivatives. For solid no-slip boundaries further

$$\mu\sum_k\frac{\partial}{\partial T_k}\frac{\partial}{\partial T_k}\left(\vec{v}^{(n+1)}\cdot\vec{n}\right) = 0 \tag{D.28}$$

applies, since all velocity components vanish at the solid no-slip boundary. Therefore also the change of the normal velocity component in boundary tangential direction

vanishes and the wall tangential change of the latter vanishes as well. Thus,

$$\mu\Big(\nabla\cdot\nabla\left(\vec{v}^{(n+1)}\cdot\vec{n}\right)\Big)=\mu\frac{\partial}{\partial N}\left(\frac{\partial}{\partial N}\left(\vec{v}^{(n+1)}\cdot\vec{n}\right)\right) \tag{D.29}$$

remains. Splitting the velocity divergence constraint at time level $(n+1)$ into boundary normal and boundary tangential components as well, the expression

$$\frac{\partial}{\partial N}\left(\vec{v}^{(n+1)}\cdot\vec{n}\right)=\left(\mathcal{D}^{(n+1,**)}-\vec{v}^{(n+1)}\cdot\vec{\mathcal{R}}\right)-\sum_k\frac{\partial}{\partial T_k}\left(\vec{v}^{(n+1)}\cdot\vec{t}_k\right) \tag{D.30}$$

is obtained considering

$$\nabla\cdot\vec{v}^{(n+1)}=\frac{\partial}{\partial N}\left(\vec{v}^{(n+1)}\cdot\vec{n}\right)+\sum_k\frac{\partial}{\partial T_k}\left(\vec{v}^{(n+1)}\cdot\vec{t}_k\right) \tag{D.31}$$

and finally

$$\begin{aligned}&\mu\Big(\nabla\cdot\nabla\left(\vec{v}^{(n+1)}\cdot\vec{n}\right)\Big)\\&=\mu\frac{\partial}{\partial N}\left[\mathcal{D}^{(n+1,**)}-\vec{v}^{(n+1)}\cdot\vec{\mathcal{R}}-\sum_k\frac{\partial}{\partial T_k}\left(\vec{v}^{(n+1)}\cdot\vec{t}_k\right)\right]\end{aligned} \tag{D.32}$$

remains. Replacing the unknown velocity $\vec{v}^{(n+1)}$ with the projection equation

$$\vec{v}^{(n+1)}=\vec{v}^{(n+1,**)}-\tau^{(n+1,**)}\vec{Q} \tag{D.33}$$

divided by $\mathcal{P}^{(n+1,**)}$ with

$$\tau:=\frac{\rho\beta}{\mathcal{P}}=\frac{\Delta t}{2} \tag{D.34}$$

the expression

$$\begin{aligned}\mu\Big(\nabla\cdot\nabla\left(\vec{v}^{(n+1)}\cdot\vec{n}\right)\Big)=C\frac{\partial}{\partial N}\left[\vec{Q}\cdot\vec{\mathcal{R}}\right]+C\frac{\partial}{\partial N}\left[\sum_k\frac{\partial}{\partial T_k}\left(\vec{Q}\cdot\vec{t}_k\right)\right]\\+\mu\frac{\partial}{\partial N}\Bigg[\mathcal{D}^{(n+1,**)}-\vec{v}^{(n+1,**)}\cdot\vec{\mathcal{R}}\\-\sum_k\frac{\partial}{\partial T_k}\left(\vec{v}^{(n+1,**)}\cdot\vec{t}_k\right)\Bigg]\end{aligned} \tag{D.35}$$

with

$$C := \tau\mu \tag{D.36}$$

is obtained. Further, using definition

$$K_1 := \tau K \tag{D.37}$$

the expression

$$K\left(\nabla\left(\vec{v}^{(n+1)}\cdot\vec{\mathcal{R}}\right)\cdot\vec{n}\right) = K\left(\nabla\left(\vec{v}^{(n+1,**)}\cdot\vec{\mathcal{R}}\right)\cdot\vec{n}\right) - K_1\left(\nabla\left(\vec{Q}\cdot\vec{\mathcal{R}}\right)\cdot\vec{n}\right) \tag{D.38}$$

is obtained. With that and assuming Cartesian grids with

$$\nabla\blacksquare\cdot\vec{n} = \pm\frac{\partial}{\partial N}\blacksquare \tag{D.39}$$

for scalars $\blacksquare$ with positive sign for all boundaries with outward pointing normal vector in positive coordinate direction and negative sign for all boundaries with outward pointing normal vector in negative coordinate direction finally

$$C\frac{\partial}{\partial N}\left[\sum_k \frac{\partial}{\partial T_k}\left(\vec{Q}\cdot\vec{t}_k\right)\right] + (C\pm K_1)\frac{\partial}{\partial N}\left[\vec{Q}\cdot\vec{\mathcal{R}}\right] - \rho^{(n+1,**)}\vec{Q}\cdot\vec{n} \;=\; \mathcal{RHS} \tag{D.40}$$

is obtained, in which

$$\mathcal{RHS} := \mathcal{B} + \mathcal{V} + \mathcal{S} \tag{D.41}$$

with

$$\mathcal{B} := \pm\frac{\partial}{\partial N}q + \rho^{(n+1,**)}g\left(\vec{k}\cdot\vec{n}\right) \tag{D.42a}$$

$$\mathcal{V} := (\mu\pm K)\frac{\partial}{\partial N}\left[\vec{v}^{(n+1,**)}\cdot\vec{\mathcal{R}}\right] + \mu\frac{\partial}{\partial N}\left[\sum_k \frac{\partial}{\partial T_k}\left(\vec{v}^{(n+1,**)}\cdot\vec{t}_k\right)\right] \tag{D.42b}$$

$$\mathcal{S} := \;-\; (\mu\pm K)\frac{\partial}{\partial N}\mathcal{D}^{(n+1,**)} \mp \mathcal{D}^{(n+1,**)}\frac{\partial}{\partial N}\lambda^{(n+1,**)} \tag{D.42c}$$

represents the right hand side. Replacing vector $\vec{Q}$ by its definition (D.1), the left hand side reads

$$C\frac{\partial}{\partial N}\left[\sum_k \frac{\partial}{\partial T_k}\left(\frac{1}{\rho^{(n+1,**)}}\left(\nabla\partial\pi\cdot\vec{t}_k\right)\right)\right] + (C\pm K_1)\,\frac{\partial}{\partial N}\left[\left(\frac{1}{\rho^{(n+1,**)}}\left(\nabla\partial\pi\cdot\vec{\mathcal{R}}\right)\right)\right] - \nabla\partial\pi\cdot\vec{n} \tag{D.43}$$

or

$$C\frac{\partial}{\partial N}\left[\sum_k \frac{\partial}{\partial T_k}\left(\frac{1}{\rho^{(n+1,**)}}\frac{\partial}{\partial T_k}\partial\pi\right)\right] + (C\pm K_1)\,\frac{\partial}{\partial N}\left[\frac{1}{\rho^{(n+1,**)}}\left(\nabla\partial\pi\cdot\vec{\mathcal{R}}\right)\right] \mp \frac{\partial}{\partial N}\partial\pi \tag{D.44}$$

respectively, with tangential vectors $\vec{t}_k$ pointing in positive coordinate direction. The first expression reads

$$C\frac{\partial}{\partial N}\left[\sum_k \frac{\partial}{\partial T_k}\left(\frac{1}{\rho^{(n+1,**)}}\frac{\partial}{\partial T_k}\partial\pi\right)\right] = C\left[\sum_k \frac{\partial}{\partial T_k}\left(\frac{1}{\rho^{(n+1,**)}}\frac{\partial}{\partial T_k}\left(\frac{\partial}{\partial N}\partial\pi\right)\right)\right] + C\left[\sum_k \frac{\partial}{\partial T_k}\left(\left[\frac{\partial}{\partial N}\frac{1}{\rho^{(n+1,**)}}\right]\frac{\partial}{\partial T_k}\partial\pi\right)\right] \tag{D.45}$$

each, with

$$\frac{\partial}{\partial N}\frac{1}{\rho^{(n+1,**)}} = 0 \tag{D.46}$$

after multiple applications of the product rule and considering the symmetry of second derivatives. At the no-slip boundary

$$C\frac{\partial}{\partial N}\left[\sum_k \frac{\partial}{\partial T_k}\left(\frac{1}{\rho^{(n+1,**)}}\frac{\partial}{\partial T_k}\partial\pi\right)\right] = \sum_k \frac{\partial}{\partial T_k}\left(\frac{C}{\rho^{(n+1,**)}}\frac{\partial}{\partial T_k}\left(\frac{\partial}{\partial N}\partial\pi\right)\right) \tag{D.47}$$

remains. The second expression on the left hand side of (D.44) can be split as well according to

$$\begin{aligned}\frac{\partial}{\partial N}\left[\frac{1}{\rho^{(n+1,**)}}\left(\nabla\partial\pi\cdot\vec{\mathcal{R}}\right)\right] &= \frac{1}{\rho^{(n+1,**)}}\frac{\partial}{\partial N}\left[\nabla\partial\pi\cdot\vec{\mathcal{R}}\right] \\ &\quad+\left[\nabla\partial\pi\cdot\vec{\mathcal{R}}\right]\frac{\partial}{\partial N}\frac{1}{\rho^{(n+1,**)}} \\ &= \frac{1}{\rho^{(n+1,**)}}\frac{\partial}{\partial N}\left[\nabla\partial\pi\cdot\vec{\mathcal{R}}\right] \end{aligned} \tag{D.48}$$

and with that the resulting equation reads

$$\begin{aligned}&\sum_k \frac{\partial}{\partial T_k}\left(\frac{C}{\rho^{(n+1,**)}}\frac{\partial}{\partial T_k}\left(\frac{\partial}{\partial N}\partial\pi\right)\right)+\frac{(C\pm K_1)}{\rho^{(n+1,**)}}\frac{\partial}{\partial N}\left[\nabla\partial\pi\cdot\vec{\mathcal{R}}\right]\mp\frac{\partial}{\partial N}\partial\pi \\ &= \mathcal{RHS}\end{aligned} \tag{D.49}$$

subject to be solved for $\frac{\partial}{\partial N}\partial\pi$ which then serves as boundary condition for the Poisson equation

$$\begin{aligned}\int_{\partial\Omega_i\setminus\partial\Omega^{\square}}\left(\beta^{(n+1,**)}\nabla\partial\pi^{(n+1)}\right)\cdot\vec{n}\,dS = &\int_{\Omega_i}\nabla\cdot\vec{\mathcal{R}}^{\,(n+1,**)}\mathrm{d}V \\ &-\int_{\Omega_i}D^{(n+1,**)}\mathrm{d}V \\ &\mp\int_{\Omega^{\square}}\beta^{(n+1,**)}\left(\frac{\partial}{\partial N}\partial\pi\right)dS\end{aligned} \tag{D.50}$$

from (D.2). For **small scale problems** with

$$\nabla(\mathcal{P})=\vec{0} \tag{D.51}$$

as considered in the present work, $\vec{\mathcal{R}}=\vec{0}$ holds and therefore the expression

$$\sum_k \frac{\partial}{\partial T_k}\left(\frac{C}{\rho^{(n+1,**)}}\frac{\partial}{\partial T_k}\left(\frac{\partial}{\partial N}\partial\pi\right)\right)\mp\left(\frac{\partial}{\partial N}\partial\pi\right)=\mathcal{RHS} \tag{D.52}$$

with

$$\mathcal{RHS}:=\mathcal{B}+\mathcal{V}+\mathcal{S} \tag{D.53}$$

and

$$\mathcal{B} := \pm\frac{\partial}{\partial N} q + \rho^{(n+1,**)} g \left(\vec{k}\cdot\vec{n}\right) \tag{D.54a}$$

$$\mathcal{V} := \mu\frac{\partial}{\partial N}\left[\sum_k \frac{\partial}{\partial T_k}\left(\vec{v}^{(n+1,**)}\cdot\vec{t}_k\right)\right] \tag{D.54b}$$

$$\mathcal{S} := -\left(\mu \pm K\right)\frac{\partial}{\partial N}\mathcal{D}^{(n+1,**)} \mp \mathcal{D}^{(n+1,**)}\frac{\partial}{\partial N}\lambda^{(n+1,**)} \tag{D.54c}$$

is obtained.

Where signs have to be chosen, to upper one holds for boundary segments with outward-pointng normal vector in positive coordinate direction, the lower one for boundary segments with outward-pointng normal vector in negative coordinate direction. Further simplifications apply, if the right hand side of the divergence constraint vanishes ($D = 0$), yielding $\mathcal{S} = 0$. In combination with $\nabla(\mathcal{P}) = 0$ the resulting divergence constraint $\nabla\cdot\vec{v} = 0$ arises.

The boundary condition for the equation (D.52) for $\left(\frac{\partial}{\partial N}\partial\pi\right)$, solved on the boundary segment, depends on the neighboring boundary segments. In case of **two spatial dimensions** the sums over the tangential contributions vanish and the Helmholtz equation

$$\frac{\partial}{\partial T}\left(\frac{C}{\rho^{(n+1,**)}}\frac{\partial}{\partial T}\left(\frac{\partial}{\partial N}\partial\pi\right)\right) \mp \left(\frac{\partial}{\partial N}\partial\pi\right) = \mathcal{B}+\mathcal{V}+\mathcal{S} \tag{D.55}$$

on the domain boundary with

$$\mathcal{B} := \pm\frac{\partial}{\partial N} q + \rho^{(n+1,**)} g \left(\vec{k}\cdot\vec{n}\right) \tag{D.56a}$$

$$\mathcal{V} := \mu\frac{\partial}{\partial N}\left[\frac{\partial}{\partial T}\left(\vec{v}^{(n+1,**)}\cdot\vec{t}\right)\right] \tag{D.56b}$$

$$\mathcal{S} := -\left(\mu \pm K\right)\frac{\partial}{\partial N}\mathcal{D}^{(n+1,**)} \mp \mathcal{D}^{(n+1,**)}\frac{\partial}{\partial N}\lambda^{(n+1,**)} \tag{D.56c}$$

remains. The spatial discretization in node (r) with

$$\xi := \frac{\tau}{\Delta x_T^2}\frac{\mu}{\rho} \tag{D.57}$$

reads

$$\begin{aligned}\Bigg[\xi_{(r+\frac{1}{2})}^{(n+1,**)}\left(\frac{\partial}{\partial N}\partial\pi\right)_{(r+1)} + \xi_{(r-\frac{1}{2})}^{(n+1,**)}\left(\frac{\partial}{\partial N}\partial\pi\right)_{(r-1)} \\ - \left[\xi_{(r+\frac{1}{2})}^{(n+1,**)} + \xi_{(r-\frac{1}{2})}^{(n+1,**)} \pm 1\right]\left(\frac{\partial}{\partial N}\partial\pi\right)_{(r)}\Bigg] = \widetilde{\mathcal{RHS}}\end{aligned} \tag{D.58}$$

in which $\widetilde{\mathcal{RHS}}$ is the discretely evaluated right hand side $(\mathcal{B}+\mathcal{V}+\mathcal{S})$.

A boundary condition is required for the boundary node of the boundary segment, which depends on the type of the neighboring boundary segment. If, for example, the nodal velocity values are known in the corners of a two-dimensional domain or along the edges of a three-dimensional domain, the boundary value is obtained according to

$$\begin{aligned}\vec{v}^{(n+1)}\cdot\vec{n} &= \left(\vec{v}^{(n+1,**)} - \tau\vec{Q}\right)\cdot\vec{n} \\ &= \vec{v}^{(n+1,**)}\cdot\vec{n} - \frac{\tau}{\rho^{(n+1,**)}}\nabla\partial\pi\cdot\vec{n} \\ &= \vec{v}^{(n+1,**)}\cdot\vec{n} \mp \frac{\tau}{\rho^{(n+1,**)}}\left(\frac{\partial}{\partial N}\partial\pi\right) \\ &= \vec{v}^{(n+1,**)}\cdot\vec{n} \mp \frac{\tau}{\rho^{(n+1,**)}}\left(\frac{\partial}{\partial N}\partial\pi\right)\end{aligned} \tag{D.59}$$

and with that

$$\left(\frac{\partial}{\partial N}\partial\pi\right)_{(r)^{\square}} = \pm\frac{2}{\Delta t}\left[\rho^{(n+1,**)}\left(\vec{v}^{(n+1,**)} - \vec{v}^{(n+1)}\right)\cdot\vec{n}\right]_{(r)^{\square}} \tag{D.60}$$

holds. Here $\vec{v}^{(n+1)}$ is the target velocity and $\vec{v}^{(n+1,**)}$ the known predicted velocity in the common node of two perpendicular piecewise planar boundary segments. The positive sign again holds for outward pointing normal vectors in positive coordinate direction while the negative sign holds for outward-pointing normals in negative coordinate direction. If $\vec{v}^{(n+1,**)} \equiv \vec{v}^{(n+1)}$ then in the boundary node

$$\left(\frac{\partial}{\partial N}\partial\pi\right)_{(r)^{\square}} = 0 \tag{D.61}$$

holds. Typically this is assumed to be the boundary condition for the entire boundary segment instead of the one for the boundary node.

Summarizing, for piecewise planar boundary segments in small scale problems assuming the dynamic viscosity to be homogeneous in the present more general setting

(with e.g. variable density) a Helmholtz-type equation as (D.55) for two space dimensions is obtained on the domain boundary for determination of the boundary condition of (D.2) as analyzed in [102]. The cases of inhomogeneous dynamic viscosity and/or general locally varying boundary normal vector are not covered yet.

E. ZUSAMMENFASSUNG

Zweiphasenströmungen treten in einer Vielzahl technischer Anwendungen und natürlicher Phänomene auf, weshalb ein großes Interesse an der numerischen Simulation solcher Vorgänge zu Vorhersage- und Analysezwecken besteht. Ein großer Teil dieser Prozesse lässt sich als inkompressibel und somit als Spezialfall einer Klasse von Strömungen mit kleiner Mach-Zahl modellieren. Während es viele verschiedene numerische Methoden zur Berechnung inkompressibler Zweiphasenströmungen bei konstanter Dichte gibt, sind nur wenige Methoden zu finden, die eine variable Dichte zulassen und die entsprechenden Gleichungen in Erhaltungsform lösen und kaum welche, die dabei konsequent diskret konservative Approximationen verwenden und zudem innerhalb des Gesamtkonzepts der numerischen Methode auf andere Regime, wie z.B. schwach kompressible oder kompressible Strömungen, erweiterbar sind. Die vorliegende Arbeit soll den Ausgangspunkt für ein Finite-Volumen-Verfahren bilden, das diese Kriterien erfüllt und zudem auf beliebige Zustandsgleichungen jenseits der Annahme eines idealen Gases als Medium erweiterbar ist. Dabei wird innerhalb dieses verallgemeinerten Rahmens hauptsächlich auf zwei Schlüsselelemente eines numerischen Verfahrens zur Berechnung von Zweiphasenströmung eingegangen und somit zum einen eine Vorgehensweise erläutert, um die numerischen Darstellungen der Trennfläche zwischen den verschiedenen Fluid-Phasen und der Erhaltungsgrößen des Strömungsfeldes gekoppelt und somit das Verfahren stabil zu halten und die Masse jeder Fluid-Phase diskret zu erhalten, zum anderen wird eine Approximation der an der Trennfläche durch die Oberflächenspannung verursachten singulär auftretenden Kraft vorgeschlagen, die es erlaubt, auch diese Einflüsse diskret konservativ zu behandeln. Als zugrundeliegendes numerisches Verfahren zur Lösung des Systems partieller Differentialgleichungen mit elliptischen Einflüssen kommt ein verallgemeinertes Projektionsverfahren zum Einsatz, welches einer hyperbolisch-parabolischen Prädiktorlösung in jedem Zeitschritt nachträglich die elliptischen Eigenschaften aufprägt. Da solche Verfahren (mit Ausnahme der Lösung von linearen Systemen für einzelne Skalare) ohne Iterationen auskommen, sind die einzelnen Bestandteile des numerischen Verfahrens ebenfalls iterationsfrei gehalten.

BIBLIOGRAPHY

[1] ABADIE, T. ; AUBIN, J. ; LEGENDRE, D. : On the combined effects of surface tension force calculation and interface advection on spurious currents within Volume of Fluid and Level Set frameworks. Journal of Computational Physics, Vol. 297, pp. 611–636, 2015. (*on page 252*).

[2] ALAND, S. ; LOWENGRUB, J. ; VOIGT, A. : Two-phase flow in complex geometries: A diffuse domain approach. Computer Modeling in Engineering & Sciences, Vol. 57, No. 1, pp. 77–106, 2010. (*on page 4*).

[3] ALAZARD, T. : A minicourse on the low Mach number limit. Discrete and Continuous Dynamical Systems Series, Vol. 1, No. 3, pp. 365–404, 2008. (*on page 53*).

[4] ALMGREN, A. S. ; BELL, J. B. ; COLELLA, P. ; HOWELL, ; L., M.: WELCOME: A conservative adaptive projection method for the variable density incompressible Navier-Stokes equations. Journal of Computational Physics, Vol. 142, pp. 1–46, 1998. (*on pages 6, 56, and 104*).

[5] ALMGREN, A. S. ; BELL, J. B. ; RENDLEMAN, C. A. ; ZINGALE, M. : Low Mach Number Modeling of Type Ia Supernovae. I. Hydrodynamics. The Astrophysical Journal, Vol. 637, pp. 922–936, 2006. (*on pages 10, 45, 56, 101, 104, and 323*).

[6] ALMGREN, A. S. ; BELL, J. B. ; RENDLEMAN, C. A. ; ZINGALE, M. : Low Mach Number Modeling of Type Ia Supernovae. II. Energy Evolution. The Astrophysical Journal, Vol. 649, pp. 927–938, 2006. (*on pages 10, 45, 56, 101, and 323*).

[7] ALMGREN, A. S. ; BELL, J. B. ; RENDLEMAN, C. A. ; ZINGALE, M. : Low Mach Number Modeling of Type Ia Supernovae. III. Reactions. The Astrophysical Journal, Vol. 684, pp. 449–470, 2008. (*on pages 45, 101, and 144*).

[8] ALMGREN, A. S. ; BELL, J. B. ; SZYMCZAK, W. G. : A Numerical Method for the Incompressible Navier-Stokes Equation Based on an Approximate Projection. SIAM Journal of Scientific Computing, Vol. 17, No. 2, pp. 358–369, 1996. (*on page 56*).

[9] ANDERSON, J. D. JR. : Hypersonic and High-Temperature Gas Dynamics. AIAA Education, Second Edition, 2006. (*on page 31*).

[10] ANISZEWSKIA, W. ; MŃENARDA, T. ; MAREK, M. : Volume of Fluid (VOF) type advection methods in two-phase flow: A comparative study. Computers & Fluids, Vol. 97, pp. 52–73, 2014. (*on page 5*).

[11] ANJOSA, G. ; MANGIAVACCHIBN, N. ; BORHANIA, N. ; THOMEA, J. R. : 3D ALE Finite-Element Method for Two-Phase Flows With Phase Change. Heat Transfer Engineering, Vol. 35, No. 5, pp. 537–547, 2014. (*on pages 4 and 5*).

[12] ARMFIELD, S. ; STREET, R. : The Fractional-Step Method for the Navier-Stokes Equations on Staggered Grids: The Accuracy of Three Variations. Journal of Computational Physics, Vol. 153, pp. 600–665, 1999. (*on page 65*).

[13] ASHBY, S. F. ; FALGOUT, R. D. : A Parallel Multigrid Ppreconditioned Conjugate Gradient Algorithm For Groundwater Flow Simulations. Nuclear Science and Engineering, Vol. 124, pp. 145–159, 1996. (*on page 113*).

[14] BASTIAN, P. : A fully-coupled discontinuous Galerkin method for two-phase flow in porous media with discontinuous capillary pressure. Computers & Geoscience, Vol. 18, pp. 779–796, 2014. (*on page 4*).

[15] BELL, J. B. ; COLELLA, P. ; GLAZ, H. M. : A second-order projection method for the Navier-Stokes equations. Journal of Computational Physics, Vol. 85, pp. 257–283, 1989. (*on pages 6, 56, 65, 101, 112, and 323*).

[16] BELL, J. B. ; DAY, M. S. ; RENDLEMAN, C. A. ; WOOSLEY, S. E. ; ZINGALE, M. : Adaptive low Mach number simulations of nuclear flame microphysics. Journal of Computational Physics, Vol. 195, No. 2, pp. 677–694, 2004. (*on page 10*).

[17] BELL, J. B. ; MARCUS, D. L. : A Second-Order Projection Method for Variable Density Flows. Journal of Computational Physics, Vol. 101, pp. 334–348, 1992. (*on pages 6, 56, and 99*).

[18] BENACCHIO, T. : A Blended Semi-Implicit Numerical Model for Weakly Compressible Atmospheric Dynamics. PhD thesis, Freie Universität Berlin, 2014. (*on pages 10 and 145*).

[19] BENACCHIO, T. ; O'NEILL, W. P. ; KLEIN, R. : A Blended Soundproof-to-Compressible Numerical Model for Small- to Mesoscale Atmospheric Dynamics. Monthly Weather Review, Vol. 142, pp. 4416–4438, 2014. (*on pages 7, 10, 32, 43, 47, and 145*).

[20] BERGER, M. ; AFTOSMIS, M. J. : Progress towards a Cartesian Cut-Cell Method for Viscous Compressible Flow. 50th AIAA Aerospace Sciences Meeting Including the New Horizons Forum and Aerospace Exposition, 2012. (*on page 86*).

[21] BERGER, M. ; HELZEL, S. : A Simplified h-box Method for Embedded Boundary Grids. SIAM Journal of Scientific Computing, Vol. 34, No. 2, pp. A861–A888, 2012. (*on page 317*).

[22] BERGER, M. J. ; HELZEL, C. ; LEVEQUE, R. J. : h-box methods for the approximation of hyperbolic conservation laws on irregular grids. SIAM Journal on Numerical Analysis, Vol. 41, No. 3, pp. 893–918, 2003. (*on page 317*).

[23] BERGER, S. A. : CRC Handbook of Thermal Engineering, CRC Press, 1999. (*on page 15*).

[24] BIRD, R. B. ; STEWART, W. E. ; LIGHTFOOT, E. N. : Transport Phenomena. Wiley, 1960. (*on pages 21 and 23*).

[25] BOGER, M. : Numerical Modeling of Compressible Two-Phase Flows with a Pressure-Based Method. PhD thesis, Universität Stuttgart, 2014. (*on pages 7 and 10*).

[26] BOTHE, D. ; KOEBE, M. ; WIELAGE, K. ; PRÜSS, J. ; WARNECKE, H. J. : Bubbly Flows, Springer, 2003. (*on page 4*).

[27] BÖTTCHER, K. : Numerical solution of a multi-component species transport problem combining diffusion and fluid flow as engineering benchmark. Inter-

national Journal of Heat and Mass Transfer, Vol. 53, pp. 231–240, 2010. (*on page 22*).

[28] BOURLIOUX, A. : A Coupled Level-Set Volume-of-Fluid Algorithm for Tracking Material Interfaces. In: 3rd Annual Conference of the CFD Society in Cananda, 1995. (*on pages 9, 148, 153, 181, and 324*).

[29] BRACKBILL, J. U. ; KOTHE, D.B. ; ZEMACH, C. : A Continuum Method for Modelling Surface Tension. Journal of Computational Physics, Vol. 100, pp. 335–354, 1992. (*on pages 5 and 252*).

[30] BROWN, D. L. ; CORTEZ, R. ; MINION, M. L. : Accurate Projection Methods for the Incompressible Navier-Stokes Equations. Journal of Computational Physics, Vol. 168, pp. 464–499, 2001. (*on pages 54, 55, 65, 101, 112, 113, 318, and 323*).

[31] CASTOR, J. I. : Radiation Hydrodynamics. Cambridge University Press, 2004. (*on page 69*).

[32] CHOPP, D. L. : Some Improvements of the Fast Marching Method. SIAM Journal of Scientific Computing, Vol. 23, No. 1, pp. 230–244, 2001. (*on page 151*).

[33] CHORIN, A. J. : A Numerical Method for Solving Incompressible Viscous Flow Problems. Journal of Computational Physics, Vol. 2, pp. 12–26, 1967. (*on pages 53, 54, and 56*).

[34] CHORIN, A. J. : Numerical Solution of the Navier-Stokes Equations. Mathematics of Computation, Vol. 22, pp. 745–762, 1968. (*on pages 54 and 98*).

[35] CHOW, E. ; CLEARY, A. J. ; FALGOUT, R. D. : Design of the hypre Preconditioner Library. In: SIAM Workshop on Object Oriented Methods for Inter-operable Scientific and Engineering Computing, 1998. (*on page 113*).

[36] CLANET, C. ; HÉRAUD, P. ; SEARBY, G. : On the Motion of Bubbles in Vertical Tubes of Arbitrary Cross-Sections: Some Complements to the Dumitrescu-Taylor Problem. Journal of Fluid Mechanics, Vol. 519, pp. 359–376, 2004. (*on page 41*).

[37] COURANT, R. ; FRIEDRICHS, K. ; LEWY, H. : On the Partial Difference Equations of Mathematical Physics. IBM Journal of Research and Develop-

ment, Vol. 11, No. 2, pp. 215–234, 1967. [originally published in 1928 in German]. (*on pages 71, 156, and 196*).

[38] CRANK, J. ; NICOLSON, P. : A practical method for numerical evaluation of solutions of partial differential equations of the heat conduction type. Mathematical Proceedings of the Cambridge Philosophical Society, Vol. 43, No. 1, pp. 50–67, 1947. (*on page 74*).

[39] CROCE, R. ; M., GRIEBEL ; SCHWEITZER, M. A. : Numerical Simulation of bubble and droplet deformation by a level set approach with surface tension in three dimensions. International Journal for Numerical Methods in Fluids, 2009. (*on page 5*).

[40] CUTNELL, J. D. ; JOHNSON, K. W. : Physics. Wiley, 1997. (*on page 41*).

[41] DELHAYE, J. M. : Jump conditions and entropy source in two-phase systems. Local instant formulation. International Journal of Multipphase Flow, Vol. 1, pp. 395–409, 1974. (*on page 17*).

[42] DESJARDINS, O. ; MOUREAU, V. ; PITCH, H. : An accurate conservative level set/ghost fluid method for simulating turbulent atomization. Journal of Computational Physics, Vol. 227, pp. 8395–8416, 2008. (*on pages 4, 147, 209, and 324*).

[43] DESJARDINS, O. ; PITCH, H. : A Spectrally Refined Interface Approach for Simulating Multiphase Flows. Journal of Computational Physics, Vol. 228, pp. 1658–1677, 2009. (*on page 147*).

[44] DING, Y. ; YANG, L. ; YUAN, L. : A finite difference real ghost fluid method on moving meshes with corner-transport upwind interpolation. Computers & Fluids, Vol. 49, No. 1, pp. 247–257, 2011. (*on page 4*).

[45] DREW, D. A. ; PASSMANN, S. L. : Theory of Multicomponent Fluids. Springer, 1999. (*on pages 18 and 19*).

[46] DURRAN, D. R. : Improving the anelastic approximation. Journal of the Atmopheric Sciences, Vol. 46, pp. 1453–1461, 1989. (*on pages 38, 43, and 144*).

[47] ENGBERG, R. F. ; KENIG, E. Y. : Numerical simulation of rising droplets in liquid-liquid systems: A comparison of continuous and sharp interfacial force models. International Journal of Heat and Fluid Flow, Vol. 50, pp. 16–26, 2014. (*on page 252*).

[48] ENGQUIST, B. ; TORNBERG, A.-K. ; TSAI, R. : Discretization of Dirac Delta Functions in Level Set Methods. Journal of Computational Physics, Vol. 207, No. 1, pp. 28–51, 2005. (*on pages 252, 255, 263, and 298*).

[49] ENRIGHT, D. ; FEDKIW, R. ; FERZIGER, J. ; MITCHELL, I. : A Hybrid Particle Level Set Method for Improved Interface Capturing. Journal of Computational Physics, Vol. 183, pp. 83–116, 2002. (*on page 147*).

[50] FAINERMAN, V. B. ; MÖBIUS, D. ; MILLER, R. , eds.: Surfactants - Chemistry, Interfacial Properties and Application. Elsevier, 2001. (*on page 34*).

[51] FALGOUT, R. D. : An Introduction to Algebraic Multigrid. Computing in Science and Engineering, Vol. 8, pp. 24–33, 2006. (*on page 113*).

[52] FALGOUT, R. D. ; YANG, U. M. : hypre: a Library of High Performance Preconditioners. In: Computational Science - ICCS 2002 Part III, Sloot, P. M. A. ; Tan, C. J. K. ; Dongarra, J. J. ; Hoekstra, A. G. , eds., Vol. 2331, Springer, 2002, pp. 632–641. (*on page 113*).

[53] FATTORI, M. : A Level Set and Sharp Interface Approach for Simulating Incompressible Two-Phase Flow. Master's thesis, University of Waterloo, 2014. (*on page 6*).

[54] FECHTER, S. ; MUNZ, C.-D. : A discontinuous Galerkin-based sharp-interface method to simulate three-dimensional compressible two-phase flow. International Journal for Numerical Methods in Fluids, Vol. 78, No. 7, pp. 413–435, 2015. (*on page 6*).

[55] FRANCOIS, M. M. ; CUMMINS, S. J. ; DENY, E. D. ; KOTHE, D. B. ; SICILIAN, J. M. ; WILLIAMS, M. W. : A balanced-force algorithm for continuous and sharp interfacial surface tension models with a volume tracking framework. Journal of Computational Physics, Vol. 213, pp. 141–173, 2006. (*on page 251*).

[56] FRUCHTMANN LAI, M. : A Projection Method for Reacting Flow in the Zero Macu Number Limit. PhD thesis, University of California, Berkley, 1994. (*on page 53*).

[57] GERLACH, D. ; TOMAR, G. ; BISWAS, G. ; F., DURST : Comparison of volume-of-fluid methods for surface tension-dominant two-phase flows. Inter-

national Journal of Heat and Mass Transfer, Vol. 49, pp. 740–754, 2006. (*on page 5*).

[58] GHIDERSA, B. E. : Finite Volume-based Volume-of-Fluid Method for the Simulation of Two-Phase Flows in Small Rectangular Channels. PhD thesis, Forschungszentrum Karlsruhe in der Helmholtz-Gemeinschaft, 2004. (*on pages 4 and 17*).

[59] GIRALDO, F. X. ; RESTELLI, M. : A study of spectral element and discontinuous Galerkin methods for the Navier-Stokes equations in nonhydrostatic mesoscale atmospheric modeling: Equation sets and test cases. Journal of Computational Physics, Vol. 27, pp. 3849–3877, 2008. (*on pages 138, 139, and 140*).

[60] GODA, K. : A multistep technique with implicit difference schemes for calculating two- or three-dimensional cavity flows. Journal of Computational Physics, Vol. 30, pp. 76–95, 1979. (*on page 55*).

[61] GOETZE, U. : Numerische Analyse des Strang-Splitting-Fehlers bei einem Diffusions-Reaktionsmodell. Master's thesis, Freie Universität Berlin, 2016. [in German]. (*on pages 70 and 317*).

[62] GOTTLIEB, S. ; SHU, C.-W. ; TADMOR, E. : Strong Stability-Preserving High-Order Time Discretization Methods. SIAM Review, Vol. 43, No. 1, pp. 89–112, 2001. (*on pages 72 and 73*).

[63] GRESHO, P. M. ; CHAN, S. T. : On The Theory Of Semi-Implicit Projection Methodes For Viscous Incompressible Flow And Its Implementation Via A Finite Element Method That Also Introduces A Nearly Consistent Mass Matrix. Part 2: Implementation. Journal for Numerical Methods in Fluids, Vol. 11, pp. 621–659, 1990. (*on page 114*).

[64] GROSS, S. ; REUSKEN, A. : Numerical Methods for Two-phase Incompressible Flows. Vol. 40 of Springer Series in Computational Mathematics, Springer, 2011. (*on page 4*).

[65] GUERMOND, J. L. ; MINEV, P. ; SHEN, J. : An overview of projection methods for incompressible flows. Computer Methods in Applied Mechanics and Engineering, Vol. 195, pp. 6011–6045, 2006. (*on pages 7, 53, 55, 65, 112, 113, and 323*).

[66] GUERMOND, J. L. ; SHEN, J. : On the Error Estimates for the Rotational Pressure-Correction Projection Methods. Mathematics of Computation, Vol. 73, No. 248, pp. 1719–1737, 2003. (*on page 101*).

[67] GUEYFFIER, D. ; LI, J. ; NADIM, A. ; SCARDOVELLI, R. ; ZALESKI, S. : Volume-of-Fluid Interface Tracking with Smoothed Surface Stress Methods for Three Dimensional Flows. Journal of Computational Physics, Vol. 152, pp. 423–456, 1999. (*on page 5*).

[68] GUO, Z. ; LIN, P. : A thermodynamically consistent phase-field model for two-phase flows with thermocapillary effects. Journal of Fluid Mechanics, Vol. 766, pp. 226–271, 2015. (*on page 5*).

[69] HARLOW, F. H. ; AMSDEN, A. A. : A simplified MAC technique for incompressible fluid calculations. Journal of Computational Physics, Vol. 6, pp. 322–325, 1970. (*on page 5*).

[70] HARLOW, F. H. ; WELCH, J. E. : Numerical Calculation of Time-Dependent Viscous Incompressible Flow of Fluid with Free Surface. Physics of Fluids, Vol. 8, No. 12, pp. 2182–2189, 1965. (*on pages 5, 19, and 91*).

[71] HARTMANN, D. : A Level-Set Based Method for Premixed Combustion in Compressible Flow. PhD thesis, Fakultät für Machinenwesen, Rheinisch-Westfälische Technische Hochschule Aachen, Germany, 2010. (*on page 149*).

[72] HARTMANN, D. ; MEINKE, M. ; SCHRÖDER, W. : Differential equation based constrained reinitialization for level set methods. Journal of Computational Physics, Vol. 227, pp. 6821–6845, 2008. (*on pages 149, 212, 214, and 324*).

[73] HAYES, W. D. ; PROBSTEIN, R. F. : Hypersonic Inviscid Flow. Dover Publications, 2004. (*on page 31*).

[74] HENSON, V. E. ; YANG, U. M. : BoomerAMG: A parallel algebraic multigrid solver and preconditioner. Applied Numerical Mathematics, Vol. 41, No. 1, pp. 155–177, 2002. (*on page 113*).

[75] HIRSCH, C. : Numerical Computation of Internal and External Flow: The Fundamentals of Computational Fluid Dynamics. Butterworth-Heinemann (Elsevier), 2. edition, 2007. (*on page 71*).

[76] HIRT, C. W. ; NICHOLS, B. D. : Volume of fluid (VOF) method for the dynamics of free boundaries. Journal of Computational Physics, Vol. 39, No. 1, pp. 201–225, 1981. (*on pages 5 and 151*).

[77] HOSSEINI, S. M. ; FENG, J. J. : Pressure boundary conditions for computing incompressible flows with SPH. Journal of Computational Physics, Vol. 230, pp. 7473–7487, 2011. (*on page 113*).

[78] HOU, T. Y. ; LOWENGRUB, J. S. ; SHELLEY, M. J. : Boundary Integral Methods for Multicomponent Fluids and Multiphase Materials. Journal of Computational Physics, Vol. 169, pp. 302–362, 2001. (*on page 4*).

[79] HUTTER, C. ET AL. : Continuum Mechanics in Environmental Sciences and Geophysics. Springer, 1993. (*on page 15*).

[80] INAMURO, T. ; OGATA, T. ; TAJIMA, S. ; KONISHI, N. : A lattice Boltzmann method for incompressible two-phase flows with large density differences. Journal of Computational Physics, Vol. 198, No. 2, pp. 628–644, 2004. (*on page 4*).

[81] ISHII, M. ; HIBIKI, T. : Thermo-fluid dynamic theory of two-phase flow. Springer, 1975. (*on page 17*).

[82] JACQMIN, D. : An Energy Approach to the Continuum Surface Method. In: AIAA 96-0858, presented at the 34th Aerospace Sciences Meeting, Reno, NV, 1996. (*on pages 28 and 252*).

[83] JAKOBSEN, H. A. : Chemical Reactor Modeling: Multiphase Reactive Flows. Springer, 2008. (*on page 15*).

[84] JEMISON, M. ; LOCH, E. ; SUSSMAN, M. ; SHASHKOV, M. ; ARIENTI, M. ; OHTA, M. ; WANG, Y. : A Coupled Level Set-Moment of Fluid Method for Incompressible Two-Phase Flows. Journal of Scientific Computing, Vol. 54, No. 2, pp. 454–491, 2013. (*on page 148*).

[85] JOSEPH, D. D. ; RENARDY, Y. Y. : Fundamentals of Two-Fluid Dynamics, Part 1: Mathematical Theory and Applications. Vol. 3 of Interdisciplinary Applied Mathematics, Springer, 1993. (*on pages 19 and 26*).

[86] KARDIOGLU, S. Y. ; KLEIN, R. ; MINION, M. L. : A fourth-order auxiliary variable projection method for zero-Mach number gas dynamics. Journal of

Computational Physics, Vol. 227, No. 3, pp. 2012–2043, 2008. (*on pages 9, 114, 116, 128, 130, and 132*).

[87] KATAOKA, I. : Local Instant Formulation of Two-Phase Flow. Institute of Atomic Energy, Kyoto University, Vol. 23, pp. 1–33, 1985. (*on pages 18, 19, and 24*).

[88] KLEIN, B. : A high-order Discontinuous Galerkin solver for incompressible and low-Mach number flows. PhD thesis, Technischen Universität Darmstadt, 2015. (*on page 7*).

[89] KLEIN, R. : Semi-Implicit extension of a Godunov-type scheme based on low Mach number asymptotics I: One-dimensional Flow. Journal of Computational Physics, Vol. 121, pp. 213–237, 1995. (*on pages 38 and 41*).

[90] KLEIN, R. : Numerics in Combustion. In: Introduction to Turbulent Combustion, Vervisch, L. ; Veynante, D. ; Olivari, D. , eds., 99-04, The von Karman Institute for Fluid Dynamics, Rhode-Saint-Genèse, Belgium, 1999. (*on pages 10, 38, 40, 108, and 172*).

[91] KLEIN, R. : Asymptotic Analyses for Atmospheric Flows and the Construction of Asymptotically Adaptive Numerical Methods. ZAMM - Journal of Applied Mathematics and Mechanics, Vol. 80, No. 11-12, pp. 765–777, 2000. (*on page 38*).

[92] KLEIN, R. : Asymptotics, structure, and integration of sound-proof atmospheric flow equations. Theoretical and Computational Fluid Dynamics, Vol. 23, No. 3, pp. 161–195, 2009. (*on pages 6, 7, 9, 10, 32, 38, 43, 47, 56, 65, 72, 83, 90, 91, 96, 99, 144, and 323*).

[93] KLEIN, R. ; ACHATZ, U. ; BRESCH, D. ; KNIO, O. ; SMOLARKIEWICZ, P. K. : Regime of Validity of Soundproof Atmospheric Flow Models. Journal of the Atmospheric Sciences, Vol. 67, pp. 3226–3237, 2010. (*on page 144*).

[94] KLEIN, R. ; BATES, K. ; NIKIFORAKIS, N. : Well Balanced Compressible Cut-Cell Simulation of Atmospheric Flow. Philosophical Transaction of the Royal Society, Vol. 367, No. 1907, pp. 4559–4575, 2009. (*on page 317*).

[95] KLEIN, R. ; BOTTA, N. ; SCHNEIDER, T. ; MUNZ, C. D. ; ROLLER, S. ; MEISTER, A. ; HOFFMANN, L. ; SONAR, T. : Asymptotic adaptive methods

for multi-scale problems in fluid mechanics. Journal of Engineering Mathematics, Vol. 39, pp. 261–343, 2001. (*on pages 27, 32, 35, 38, 40, 41, and 99*).

[96] KLEIN, R. ; PAULUIS, O. : Thermodynamic Consitstency of a Pseudo-Incompressible Approximation for General Equations of State. Journal of the Atmospheric Sciences, Vol. 69, No. 3, pp. 961–968, 2012. (*on page 144*).

[97] KORNEK, U. ; MÜLLER, F. ; HARTH, K. ; HAHN, A. ; GANESAN, S. ; TOBISKA, L. ; STANNARIUS, R. : Oscillations of soap bubbles. New Journal of Physics, Vol. 12, 2010. (*on pages 299, 303, 304, 305, and 325*).

[98] KRAMER, W. ; CLERCX, H. J. H. ; VAN HEIJST, G. J. F. : Vorticity dynamics of a dipole colliding with a no-slip wall. Physics of Fluids, Vol. 19, 2007. (*on pages 132 and 133*).

[99] KRYLOV, A. N. : On the numerical solution of the equation by which in technical questions frequencies of small oscillations of material systems are determined. News of Academy of Sciences of the USSR, Vol. 7, No. 4, pp. 491–539, 1931. [in Russian]. (*on page 113*).

[100] LAFAURIE, B. ; NARDONE, C. ; SCARDOVELLI, R. ; ZALESKI, S. ; ZANETTI, G. : Modelling Merging and Fragmentation in Multiphase Flows with SURFER. Journal of Computational Physics, Vol. 113, No. 1, 1994. (*on pages 28 and 252*).

[101] LAKEHAL, D. ; MEIER, M. ; FULGOSI, M. : Interface Tracking Towards the Direct Simulation of Heat and Mass Transfer in Multiphase Flows. International Journal of Heat and Fluid Flow, Vol. 23, pp. 242–257, 2002. (*on page 19*).

[102] LAKIN, S. : Eine implizite Druckrandbedingung für die nichtstationäre Stokes-Gleichung. Master's thesis, Freie Universität Berlin, 2012. [in German]. (*on pages 10, 55, 113, 318, 347, and 358*).

[103] LAMB, H. : Hydrodynamics. Cambridge University Press, 1932. (*on pages 303, 304, 305, and 325*).

[104] LE CHENADEC, V. ; PITSCH, H. : A 3D Unsplit Forward/Backward Volume-of-Fluid Approach and Coupling to the Level Set Method. Journal of Computational Physics, Vol. 233, pp. 10–33, 2013. (*on pages 5, 148, and 149*).

[105] LE CHENADEC, V. ; PITSCH, H. : A monotonicity preserving conservative sharp interface flow solver for high density ratio two-phase flows. Journal of Computational Physics, Vol. 249, pp. 185–203, 2013. (*on page 6*).

[106] LEVEQUE, R. J. : Finite Volume Methods for Hyperbolic Problems. Cambridge Texts in Applied Mathematics, Cambridge University Press, 2002. (*on pages 72 and 340*).

[107] LI, C. ; XU, C. ; GUI, C. ; FOX, M. D. : Level set evolution without re-initialization: a new variational formulation. In: IEEE Computer Vision and Pattern Recognition, 2005. (*on pages 209 and 240*).

[108] LI, Z. ; M.-C., LAI : The immersed interface method for the Navier-Stokes equations with singular forces. Journal of Computational Physics, Vol. 171, pp. 822–842, 2001. (*on page 4*).

[109] LIU, J.-G. ; LIU, J. ; PEGO, R. : Stability and convergence of efficient Navier-Stokes solver via a commutator estimate. Communications on Pure and Applied Mathematics, Vol. 60, pp. 1443–1487, 2007. (*on page 113*).

[110] LIU, X. ; GUO, L. ; MORITA, K. ; ZHANG, S. : Development of a hybrid particle-mesh method for two-phase flow simulations. International Journal for Numerical Methods in Fluids, 2016. (*on page 5*).

[111] MAJDA, A. ; SETHIAN, J. : The Derivation and Numerical Solution of the Equations for Zero Mach Number Combustion. Combustion Science and Technology, Vol. 42, pp. 185–205, 1985. (*on page 38*).

[112] MAY, S. ; BERGER, M. : A mixed explicit implicit time stepping scheme for Cartesian embedded boundary meshes. In: Finite Volumes for Complex Applications VII - Methods and Theoretical Aspects, Fuhrmann, J. ; Ohlberger, M. ; Rohde, C. , eds., Vol. 77 of Springer Proceedings in Mathematics & Statistics, Springer, 2014, pp. 393–400. (*on page 317*).

[113] MAZUMDER, S. : Critical assessment of the stability and convergence of the equations of multi-component diffusion. Journal of Computational Physics, Vol. 212, pp. 383–392, 2006. (*on page 22*).

[114] MCCASLIN, J. O. ; DESJARDINS, O. : A local re-initialization equation for the conservative level set method. Journal of Compuational Physics, Vol. 262, pp. 408–426, 2014. (*on pages 211, 212, and 250*).

[115] MENARD, T. ; TANGUY, S. ; BERLEMONT, A. : Coupling level set/VOF/ghost fluid methods: Validation and application to 3D simulation of the primary break-up of a liquid jet. International Journal of Multiphase Flow, Vol. 33, pp. 510–524, 2007. (*on page 4*).

[116] MITTAL, J. ; IACCARINO, G. : Immersed Boundary Methods. Annual Review of Fluid Mechanics, Vol. 37, pp. 239–261, 2005. (*on page 6*).

[117] MÜLLER, A. : Untersuchungen zur Genauigkeit adaptiver unstetiger Galerkin Simulationen mit Hilfe von Luftblasen-Testfällen. PhD thesis, Johannes Gutenberg-Universität Mainz, 2012. [in German]. (*on pages 139, 140, and 345*).

[118] MUNZ, C.-D. ; DUMBSER, M. ; ROLLER, S. : Linearized acoustic perturbation equations for low Mach number flow with variable density and temperature. Journal of Computational Physics, Vol. 224, pp. 352–364, 2007. (*on page 7*).

[119] MUNZ, C. D. ; ROLLER, S. ; KLEIN, R. ; GERATZ, K. J. : The extension of incompressible flow solvers to the weakly compressible regime. Computers & Fluids, Vol. 23, pp. 173–196, 2003. (*on page 7*).

[120] MUNZ, C.-D. ; WESTERMANN, T. : Numerische Behandlung gewöhnlicher und partieller Differentialgleichungen. Springer, 2006. [in German]. (*on page 340*).

[121] MURADOGLU, M. ; TRYGGVASON, G. : A front-tracking method for computation of interfacial flows with soluble surfactants. Journal of Computational Physics, Vol. 227, pp. 2238–2262, 2008. (*on page 34*).

[122] NGUYEN, V.-T. ; PERAIRE, J. ; CHEONG, K. B. ; P.-O., PERSSON : A Discontinuous Galerkin Front Tracking Method for Two-Phase Flows with Surface Tension. Computers & Fluids, Vol. 39, No. 1, pp. 1–14, 2010. (*on page 4*).

[123] NGUYEN VAN YEN, R. ; FARGE, M. ; SCHNEIDER, K. : Energy Dissipating Structures Produced by Walls in Two-Dimensional Flows at Vanishing Viscosity. Physical Review Letters, Vol. 106, No. 184502, pp. 1–4, 2011. (*on page 132*).

[124] NGUYEN VAN YEN, R. ; KLEIN, R. ; WAIDMANN, M. : Non-stationary boundary layers and energy dissipation in incompressible flows. Talk given at Universidade Federal do Rio de Janeiro, 2012. (*on page 132*).

[125] NGUYEN VAN YEN, R. ; WAIDMANN, M. ; FARGE, M. ; SCHNEIDER, K. ; KLEIN, R. : Production of dissipative vortices by solid bodies in incompressible fluid flows: comparison between Prandtl, Navier-Stokes and Euler solutions. In: International Congress of Mathematicians, Seoul (Korea), 2013. (*on page 132*).

[126] NGUYEN VAN YEN, R. ; WAIDMANN, M. ; KLEIN, R. ; FARGE, M. ; SCHNEIDER, K. : Energy dissipation caused by boundary layer instability at vanishing viscosity. [to be published]. (*on pages 10 and 132*).

[127] NI, M.-J. : Consistent projection methods for variable density incompressible Navier-Stokes equations with continuous surface forces on a rectangular collocated mesh. Journal of Computational Physics, Vol. 228, pp. 6938–6956, 2009. (*on page 251*).

[128] OEVERMANN, M. ; KLEIN, R. : A Cartesian grid finite volume method for the solution of the Poisson equation with variable coefficients and embedded interfaces. Journal of Computational Physics, Vol. 219, No. 2, pp. 749–769, 2006. (*on pages 99, 100, 180, 315, and 325*).

[129] OEVERMANN, M. ; KLEIN, R. : An asymptotic solution approach for elliptic equations with discontinuous coefficients. Journal of Computational Physics, Vol. 261, pp. 230–243, 2014. (*on pages 43, 180, 276, 315, and 325*).

[130] OEVERMANN, M. ; SCHARFENBERG, C. ; KLEIN, R. : A sharp interface finite volume method for elliptic equations on Cartesian grids. Journal of Computational Physics, Vol. 228, No. 14, pp. 5184–5206, 2009. (*on pages 99, 100, 180, 315, and 325*).

[131] OLSSON, E. ; KREISS, G. : A conservative level set method for two phase flow. Journal of Computational Physics, Vol. 210, No. 1, pp. 225–246, 2005. (*on pages 5 and 148*).

[132] ONEA, A. ; WÖRNER, M. ; CACUCI, D. G. : A qualitative computational study of mass transfer in upward bubble train flow through square and rectangular mini-channels. Chemical Engineering Science, Vol. 64, pp. 1416–1435, 2009. (*on page 4*).

[133] O'NEILL, W. P. : A thermodynamically consistent formulation of the pseudo-incompressible equations for atmospheric modelling with an extension to moist processes. PhD thesis, Freie Universität Berlin, 2015. (*on pages 10, 40, 47, and 144*).

[134] O'NEILL, W. P. ; KLEIN, R. : A Moist Pseudo-Incompressible Model. Atmospheric Research, Vol. 142, pp. 133–141, 2014. (*on pages xiii, 10, 46, 47, 48, and 144*).

[135] OSHER, S. ; SETHIAN, J. A. : Fronts propagating with curvature-dependent speed: Algorithms based on Hamilton-Jacobi formulations. Journal of Computational Physics, Vol. 79, pp. 12–49, 1988. (*on page 148*).

[136] OWKES, M. ; DESJARDINS, O. : A discontinuous Galerkin conservative level set scheme for interface capturing in multiphase flows. Journal of Computational Physics, Vol. 249, pp. 275–302, 2013. (*on page 149*).

[137] PANDOLFI, M. ; MARSILIO, R. : Frozen and Equilibrium Speeds of Sound in Non-equilibrium Flows. In: Advances in Kinetic Theory and Continuum Mechanics, Springer Berlin Heidelberg, 1991, pp. 185–194. (*on page 31*).

[138] PARK, Y.-C. ; KAJISHIMA, T. : Application of CIP Method to Two-Phase Flow in Gas-Lift Pumping System to Reduce Numerical Dissipation. Geosystem Engineering, Vol. 13, No. 4, pp. 127–132, 2010. (*on page 5*).

[139] PATANKAR, S. V. : Numerical Heat Transfer and Fluid Flow. Series in computational methods in mechnaics and thermal science, Hemisphere Publishing Corporation, 1980. (*on page 53*).

[140] PERSSON, P.-O. : High-Order LES Simulations using Implicit-Explicit Runge-Kutta Schemes. 49th AIAA Aerospace Sciences Meeting including the New Horizons Forum and Aerospace Exposition, 2011. (*on page 73*).

[141] PETERS, N. : Fifteen Lectures on Laminar and Turbulent Combustion. Aachen, Germany, 1992. (*on pages 22, 27, and 30*).

[142] PIELKE, R. A. : Mesoscale Meteorological Modeling. Academic Press, 1. edition, 1984. (*on page 144*).

[143] PROSPERETTI, A. ; TRYGGVASON, G. : Computational Methods for Multiphase Flow. Cambridge University Press, 2007. (*on pages 4 and 19*).

[144] PUCKET, E. G. ; ALMGREN, A. S. ; BELL, J. B. ; MARCUS, D. L. ; RIDER, W. J. : A High-Order Projection Method for Tracking Fluid Interfaces in Variable Density Incompressible Flows. Journal of Computational Physics, Vol. 130, No. 2, pp. 269–282, 1997. (*on page 5*).

[145] REN, H. ; ZHANG, G. ; GUAN, H. : Three-dimensional numerical simulation of a vortex ring impinging on a circular cylinder. Fluid Dynamics Research, Vol. 47, 2015. (*on page 133*).

[146] RIDER, W. J. ; KOTHE, D. : Reconstructing volume tracking. Journal of Computational Physics, Vol. 141, pp. 112–152, 1998. (*on pages 5, 241, 245, and 248*).

[147] RUSSO, AND SMEREKA P. G.: A remark on computing distance functions. Journal of Computational Physics, Vol. 163, pp. 51–67, 2000. (*on page 212*).

[148] SARMIN, E. N. ; CHUDOV, L. A. : On the stability of the numerical integration of systems of ordinary differential equations arising in the use of the straight line method. USSR Computational Mathematics and Mathematical Physics, Vol. 3, No. 6, pp. 1537–1543, 1963. (*on page 72*).

[149] SATO, Y. ; NICENO, B. : A conservative local interface sharpening scheme for the constrained interpolation profile method. International Journal for Numerical Methods in Fluids, Vol. 70, No. 4, pp. 441–467, 2012. (*on page 5*).

[150] SCHNEIDER, T. : Verfolgung von Flammenfronten und Phasengrenzen in schwachkompressiblen Strömungen. PhD thesis, Fakultät für Machinenwesen, Rheinisch-Westfälische Technische Hochschule Aachen, Germany, 2000. [in German]. (*on pages 6, 7, 9, 10, 38, 56, 71, 72, 74, 125, 148, 153, 179, 181, 183, 188, 199, 220, 252, 317, 323, and 324*).

[151] SCHNEIDER, T. ; BOTTA, N. ; GERATZ, K. J. ; KLEIN, R. : Extension of Finite Volume Compressible Flow Solvers to Multi-dimensional, Variable Density Zero Mach Number Flows. Journal of Computational Physics, Vol. 155, No. 2, pp. 248–286, 1999. (*on pages 6, 10, 38, 72, 90, and 99*).

[152] SCHNEIDER, T. ; KLEIN, R. : Overcoming Mass Losses in Level-Set-Based Interface Tracking Schemes. In: 2nd International Conference on Finite Volume for Complex Application, Editions Hermes, 1999. (*on pages 5, 153, 181, 199, 228, 230, and 324*).

[153] SCHOCHET, S. : The Mathematical Theory of Low Mach Number Flows. ESAIM: Mathematical Modelling and Numerical Analysis, Vol. 39, No. 3, pp. 441–458, 2005. (*on page 38*).

[154] SESTERHENN, J. ; MÜLLER, B. ; THOMANN, H. : Computation of compressible low Mach number flow. Computational Fluid Dynamics, Vol. 2, pp. 829–883, 1992. (*on page 38*).

[155] SETHIAN, J. A. : Level Set Methods and Fast Marching Methods: Evolving Interfaces in Computational Geometry, Fluid Mechanics, Computer Vision, and Materials Science. Cambridge University Press, 1999. (*on pages 151 and 183*).

[156] SMILJANOVSKI, V. ; MOSER, V. ; KLEIN, R. : A Capturing-Tracking Hybrid Scheme for Deflagration Discontinuities. Combustion Theory and Modelling, Vol. 1, No. 2, pp. 183–215, 1997. (*on pages 5, 156, 179, 181, and 323*).

[157] SPELT, P. D. M. ; DING, H. ; SHAW, S. J. : Computational Methods for Two-Phase Flows. Vol. 1 of Advances in Computational Fluid Dynamics, World Scientific Publishing Company, 2017. [to be published]. (*on page 6*).

[158] STEWART, P. A. ; LAY, N. ; SUSSMAN, M. ; OHTA, M. : An Improved Sharp Interface Method for Viscoelastic and Viscous Two-Phase Flows. Journal of Scientific Computing, Vol. 35, No. 1, pp. 43–61, 2008. (*on page 6*).

[159] STRANG, G. : On the construction and comparison of difference schemes. SIAM Journal on Numerical Analysis, Vol. 5, pp. 506–517, 1968. (*on page 68*).

[160] SÜLI, E. ; MAYERS, D. : An Introduction to Numerical Analysis. Cambridge University Press, 2003. (*on page 73*).

[161] SUN, D. L. ; TAO, W. Q. : A coupled volume-of-fluid and level set (VOSET) method for computing incompressible two-phase flows. International Journal of Heat and Mass Transfer, Vol. 53, pp. 645–655, 2010. (*on page 148*).

[162] SUSSMAN, M. : A second order level set and volume-of-fluids method for computing growth and collapse of vapour bubbles. Journal of Computational Physics, Vol. 187, pp. 110–136, 2003. (*on page 5*).

[163] SUSSMAN, M. : A parallelized, adaptive algorithm for multiphase flows in general geometries. Computers & Structures, Vol. 83, pp. 435–444, 2005. (*on page 148*).

[164] SUSSMAN, M. ; ALMGREN, A. S. ; BELL, J. B. ; COLELLA, P. ; HOWELL, L. H. ; L., WELCOME M. : An Adaptive Level Set Approach for Incompressible Two-Phase Flow. Journal of Computational Physics, Vol. 148, pp. 81–124, 1999. (*on pages 5, 252, 296, 297, and 298*).

[165] SUSSMAN, M. ; HUSSAINI, M. Y. ; SMITH, K. ; WEI, R.-Z. : A second order adaptive sharp interface method for incompressible multiphase flow. In: Proceedings of the Third International Conference on Computational Fluid Dynamics, 2004. (*on page 148*).

[166] SUSSMAN, M. ; OHTA, M. : A Stable and Efficient Method for Treating Surface Tension in Incompressible Two-Phase Flow. SIAM Journal on Scientific Computing, Vol. 31, No. 4, pp. 2447–2471, 2009. (*on page 276*).

[167] SUSSMAN, M. ; P., SMEREKA ; S., OSHER : A Level Set Approach for Computing Solutions to Incompressible Two-Phase Flow. Journal of Computational Physics, Vol. 114, pp. 146–159, 1994. (*on pages 4, 5, 71, and 252*).

[168] SUSSMAN, M. ; PUCKETT, E. G. : A Coupled Level Set and Volume-of-Fluid Method for Computing 3D and Axisymmetric Incompressible Two-Phase Flows. Journal of Computational Physics, Vol. 162, pp. 301–337, 2000. (*on page 147*).

[169] SUSSMAN, M. ; SMITH, K. M. ; HUSSAINI, M. Y. ; OHTA, M. ; ZHI-WEI, R. : A sharp interface method for incompressible two-phase flow. Journal of Computational Physics, Vol. 221, pp. 469–505, 2007. (*on pages 5 and 6*).

[170] TANGUY, S. ; MENARD, T. ; BERLEMONT, A. : A level set method for vaporizing two-phase flows. Journal of Computational Physics, 2006. (*on page 5*).

[171] TEIGEN, K. E. ; SONG, P. ; LOWENGRUB, J. ; VOIGT, A. : A diffuse-interface method for two-phase flows with soluble surfactants. Journal of Computational Physics, Vol. 230, No. 2, pp. 375–393, 2011. (*on page 6*).

[172] TEMAM, R. : Sur l'approximation de la solution des équations de Navier-Stokes par la méhode des pas fractionnaires II. Archive for Rational

Mechanics and Analysis, Vol. 3, pp. 377–385, 1969. [in French]. (*on page 98*).

[173] TRYGGVASON, G. ; BUNNER, B. ; EBRAT, O. ; W., TAUBER : Computation of Multiphase Flows by a Finite Difference/Front Tracking Method. I. Multi-Fluid Flows. In: 29th Computational Fluid Dynamics Lecture Series, von Karman Institute for Fluid Dynamics, 1998. (*on pages 18 and 19*).

[174] TRYGGVASON, G. ; BUNNER, B. ; ESMAEELI, A. ; JURIC, D. ; AL-RAWAHI, N. ; TAUBER, W. ; HAN, J. ; NAS, S. ; JAN, Y.-J. : A Front Tracking Method for the Computations of Multiphase Flow. Journal of Computational Physics, Vol. 169, No. 2, pp. 708–759, 2001. (*on page 5*).

[175] TRYGGVASON, G. ; JURIC, D. ; CHE, J. ; H., NOBARI M. R. ; NAS, S. : Computation of Multiphase Flows by a Finite Difference/Front Tracking Method III. Variable Surface Tension and Phase Change. In: 29th Computational Fluid Dynamics Lecture Series, von Karman Institute for Fluid Dynamics, 1998. (*on page 34*).

[176] TRYGGVASON, G. ; SCARDOVELLI, R. ; ZALESKI, S. : Direct Numerical Simulations of Gas-Liquid Multiphase Flows. Cambridge University Press, 2011. (*on pages 4, 6, 17, 18, 19, 20, 28, 29, 147, 149, and 252*).

[177] VAN DER PIJL, S. : Computation of Bubbly Flows with a Mass-Conserving Level-Set Method. PhD thesis, Delft Universtity of Technology, 2005. (*on page 148*).

[178] VAN DER VORST, H. A. : Bi-CGSTAB: A Fast and Smoothly Converging Variant of Bi-CG for the Solution of Nonsymmetric Linear Systems. SIAM Journal on Scientific and Statistical Computation, Vol. 13, No. 2, pp. 631–644, 1992. (*on page 113*).

[179] VAN LEER, B. : Towards the ultimate conservative difference scheme II. Monotonicity and conservation combined in a second order scheme. Journal of Computational Physics, Vol. 14, No. 4, pp. 361–370, 1974. (*on page 83*).

[180] VATER, S. ; KLEIN, R. : Stability of a Cartesian grid projection method for zero Froude number shallow water flows. Numerische Mathematik, Vol. 113, pp. 123–161, 2009. (*on pages 6, 56, 65, 90, 91, and 99*).

[181] VOLPE, G. : On the use and accuracy of compressible flow codes at low mach numbers. AIAA Paper 91-1662, 1991. (*on page 38*).

[182] WAIDMANN, M. ; GERBER, S. ; OEVERMANN, M. ; KLEIN, R. : A Conservative Coupling of Level-Set, Volume-of-Fluid and Other Conserved Quantities. In: Finite Volumes for Complex Applications VII - Methods and Theoretical Aspects, Fuhrmann, J. ; Ohlberger, M. ; Rohde, C. , eds., Vol. 77 of Springer Proceedings in Mathematics & Statistics, Springer, 2014, pp. 457–465. (*on pages 9, 148, 182, 194, 205, 233, 234, 252, and 324*).

[183] XU, S. ; WANG, Z. J. : An immersed interface method for simulating the interaction of a fluid with moving boundaries. Journal of Computational Physics, Vol. 216, pp. 454–493, 2006. (*on page 4*).

[184] YANENKO, N. N. : The Method of Fractional Steps. The Solution of Problems of Mathematical Physics in Several Variables, Springer, 1971. (*on page 53*).

[185] YANG, J. ; STERN, F. : A Sharp Interface Method for Two-Phase Flows Interacting with Moving Bodies. 18th AIAA Computational Fluid Dynamics Conference, AIAA 2007-4578, 2007. (*on page 6*).

[186] YANG, X. ; JAMES, A. J. ; LOWENGRUB, J. ; ZHENG, X. ; CRISTINI, V. : An adaptive coupled level-set/volume-of-fluid interface capturing method for unstructured triangular grids. Journal of Computational Physics, Vol. 217, pp. 364–394, 2006. (*on page 148*).

[187] YEOH, G. H. ; TU, J. : Computational Techniques for Multiphase Flows. Butterworth-Heinemann (Elsevier), 2010. (*on pages 28 and 252*).

[188] YOUNGS, D. L. : Time-dependent multi-material flow with large fluid distortion, Numerical Methods for Fluid Dynamics, Academic Press, 1982. (*on page 152*).

[189] ZHENG, X. ; BABAEE, H. ; DONG, S. ; CHRYSSOSTOMIDIS, C. ; KARNIADAKIS, G. E. : A phase-field method for 3D simulation of two-phase heat transfer. International Journal of Heat and Mass Transfer, Vol. 82, pp. 282–298, 2015. (*on page 5*).

[190] ZIENKIEWICZ, O. C. ; TAYLOR, R. L. ; NITHIARASU, P. : The Finite Element Method for Fluid Dynamics. Butterworth-Heinemann (Elsevier), 7. edition, 2014. [first published in 1967]. (*on page 71*).